JAEA-Review
2009-041

JAEA-Review

JAEA Takasaki Annual Report 2008

(Ed.) Shigeru TANAKA

Takasaki Advanced Radiation Research Institute

December 2009

Japan Atomic Energy Agency

日本原子力研究開発機構

本レポートは独立行政法人日本原子力研究開発機構が不定期に発行する成果報告書です。
本レポートの入手並びに著作権利用に関するお問い合わせは、下記あてにお問い合わせ下さい。
なお、本レポートの全文は日本原子力研究開発機構ホームページ（http://www.jaea.go.jp）
より発信されています。

独立行政法人日本原子力研究開発機構　研究技術情報部　研究技術情報課
〒319-1195　茨城県那珂郡東海村白方白根 2 番地 4
電話 029-282-6387, Fax 029-282-5920, E-mail:ird-support@jaea.go.jp

This report is issued irregularly by Japan Atomic Energy Agency
Inquiries about availability and/or copyright of this report should be addressed to
Intellectual Resources Section, Intellectual Resources Department,
Japan Atomic Energy Agency
2-4 Shirakata Shirane, Tokai-mura, Naka-gun, Ibaraki-ken 319-1195 Japan
Tel +81-29-282-6387, Fax +81-29-282-5920, E-mail:ird-support@jaea.go.jp

JAEA-Review 2009-041

JAEA Takasaki Annual Report 2008

(Ed.) Shigeru TANAKA

Takasaki Advanced Radiation Research Institute

Japan Atomic Energy Agency

Watanuki-machi, Takasaki-shi, Gunma-ken

(Received October 26, 2009)

JAEA Takasaki annual report 2008 describes research and development activities performed from April 1, 2008 to March 31, 2009 with Takasaki Ion Accelerators for Advanced Radiation Application (TIARA, four ion accelerators), and electron/gamma-ray irradiation facilities (an electron accelerator and three ^{60}Co gamma-ray irradiation facilities) at Takasaki Advanced Radiation Research Institute, Japan Atomic Energy Agency (JAEA Takasaki). These activities are classified into four research fields: 1) space, nuclear and energy engineering, 2) environmental conservation and resource security, 3) biotechnology and medical application, and 4) advanced materials, analysis and novel technology. This annual report contains 161 reports consisting of 153 research papers and 8 status reports on operation/maintenance of the irradiation facilities described above, and a list of publications, related press-releases, TV programs, patents, and the type of research collaborations as Appendices.

Keywords: TIARA, Ion Accelerators, Electron Accelerator, Gamma-ray Facilities, Nuclear and Energy Engineering, Environmental Conservation, Resource Security, Biotechnology, Medical Application, Advanced Materials, Analysis, Novel Technology, Materials for Space, Semiconductors, Inorganic Materials, Organic Materials, Functional Materials, Radiation Chemistry, Radiation Biology, Radioisotope Production, Nuclear Chemistry, Material Analyses, Solid State Physics, Microbeam Technology, Accelerator Technology, Accelerator Operation, Safety Control

高崎量子応用研究所研究年報 2008

日本原子力研究開発機構 高崎量子応用研究所
（編） 田中 茂

（２００９年１０月２６日受理）

高崎量子応用研究所研究年報 2008 は、同研究所にある TIARA 施設（イオン加速器 4 基）及び電子･ガンマ線照射施設（電子加速器 1 基、^{60}Co ガンマ線照射施設 3 棟）を利用して 2008 年 4 月 1 日から 2009 年 3 月 31 日までの間に行われた研究・技術開発成果をまとめたものである。この研究年報には、１）宇宙・原子力・エネルギー、２）環境・資源、３）バイオ技術・医学応用、４）先端材料・計測・基盤技術の 4 分野に分類した 153 編の論文及び 8 編の施設の運転･管理状況報告からなる合計 161 編を収録する。また、論文リスト、新聞発表、テレビ放映、出願特許、及び研究実施形態・利用施設の一覧表を付録として含む。

高崎量子応用研究所：〒370-1292 群馬県高崎市綿貫町 1233
編集委員：（著者代表）田中 茂、田中 淳、玉田 正男、小嶋 拓治、
鳴海 一雅、松橋 信平、水橋 清、福田 豊、中村 義輝

PREFACE

This report covers research and development activities in Takasaki Advanced Radiation Research Institute, JAEA, during the period from April 2008 to March 2009 conducted with TIARA (Takasaki Ion Accelerators for Advanced Radiation Application), electron beam and Co-60 γ-ray irradiation facilities.

This annual report contains 161 papers in the fields of

1) Space, Nuclear and Energy Engineering,
2) Environmental Conservation and Resource Security,
3) Biotechnology and Medical Application,
4) Advanced Materials, Analysis and Novel Technology,
5) Status of Irradiation Facilities.

In the field of Space, Nuclear and Energy Engineering, radiation induced degradation of solar cells and malfunction of semiconductor devices have been examined by using high energy electrons, protons and heavy ions to develop the next generation electronic systems for artificial satellites. Single event transient currents induced in semiconductor devices by energetic ions have been investigated experimentally and theoretically for completing prediction models of device malfunction caused by cosmic-rays. Radiation resistant devices have also been developed based on wide bandgap semiconductors like SiC. Radiation degradation of organic materials has been tested for the purpose of practical use in nuclear energy systems, e.g., chemicals, rubbers and cables for nuclear fuel treatment and fabrication systems as well as the components of the ITER remote maintenance system. Radiation effects on metallic materials, inter alia, structural and cladding materials for LWR, and blanket materials for fusion reactor have been intensively studied using TIARA for securing reactor safety. Development of high-performance polymer electrolyte membranes for hydrogen fuel cells has been conducted by track etching pores, radiation grafting and cross-linking technique using ion beams, electron beams and gamma-rays, fabricated with different base polymers such as poly (vinylidene fluoride), poly (ethylene-co-tetrafluoroethylene), poly (ether ether ketone) and their modified polymer membranes.

In the field of Environmental Conservation and Resource Security, radiation cross-linking technique has been adopted to improve the heat stability of biodegradable poly(L-lactic acid) in order to use the dummy lens of eyeglasses. Hydro-gels produced from carboxymethyl cellulose have also been investigated on the use of an additive to prevent the shrinking of traditional Japanese paper. Fibrous catalyst for trans-esterification has been developed with radiation grafting technique and applied to biodiesel production. R&Ds of the decomposition and removal of trace amount of pollutants such as persistent pharmaceuticals in waste water using gamma-rays have been performed to develop new process technologies

for environmental conservation.

In the field of Biotechnology and Medical Application, analyses of DNA damage and subsequently induced mutation by heavy ions were progressed. The ion beam breeding has been continuously applied for many kinds of higher-plants and microorganisms such as crops, flowers, fruits, *Aspergillus oryzae* and yeasts to obtain new varieties that show phenotypic or genotypic alteration. Single cell-targeting irradiation experiments using heavy-ion microbeams revealed that the radiation-induced bystander response played an important role in the process of the induction of radioadaptive responses, and that nitric oxide was actually an initiator or mediator of the radioadaptive response. A series of new results highlighted that high-LET heavy ions might be a promising modality for radio- and chemo-resistant Bcl-2 over-expressing tumors. The positron imaging method has been applied to various practical topics in agriculture; non-uniform translocation of photoassimilates into an eggplant fruit was observed with a result suggesting a hint to control the shape of the products. Radiolabeled-antibody ^{177}Lu-DOTA-NUB2 was developed as a medicine both applicable for the therapy and the diagnosis of cancer; the treatment with the ^{177}Lu-DOTA-NUB2 showed remarkable decrease of tumor with less adverse reactions. The in-air micro-PIXE system has been utilized mainly to investigate behavior of intracellular trace elements in bio-medical samples. This technique has been also applied to analyze both the contents and the distribution of asbestos in few-mg lung-tissues for the diagnosis of “asbestos lung”. A new technique to analyze 3D distribution of trace elements in a minute sample has also been developed on this system.

In the field of Advanced Materials, Analysis and Novel Technology, irradiation effects were applied to materials science to modify the material properties; superconductivity of B-doped diamond thin films and YBCO thin films, hydrogen absorption of La-Ni based alloys, gasochromism of WO_3 films, hardness of FeCu alloys, photoluminescence of SiC nanotubes, and hydrogen selectivity of SiC membranes, and the fabrication of various nanostructures. Technique of synthesis of nano-wires/fibers has been developed based on the cross-linking reactions of the polymers in a single-ion track induced by a high-energy heavy ion. Si nanocrystals in fused-silica substrates and Au/Pt nanoclusters on graphite substrates were fabricated. Ion-implantation-induced nitriding process of Ti thin films on NaCl substrates was observed in-situ with the transmission electron microscope combined with the ion implanter. Interaction between positrons and radiation-induced He bubbles in Si and sputtering-related phenomena were investigated. Surface-plasmon excitation was also studied with reflection high-energy positron diffraction. Studies on the radiolysis of aqueous solutions were carried out with the development of radiolysis techniques. The Proton-Beam-Writing technique was also applied to fabricate an electric micro filter. The studies using single carbon-cluster-ions with the energy of MeV/atom, e.g. C_2-C_{10} and

$C_{60,}$ were performed with the measurement of secondary ions/electrons or luminescence emitted from target materials. Different kinds of beam detectors, fluence monitors, and dosimeters were developed for the measurement of single-pulse ion-beam, high-energy neutrons, and electrons. Developments of fast single-ion hit, uniform wide-beam formation, and micro-beam production technologies were in progress for the cyclotron and the electrostatic accelerators at TIARA on the basis of various techniques for magnetic field control, beam-detection, beam attenuation, and beam position control.

About the Status of Irradiation Facilities, all the accelerators in TIARA; namely the AVF cyclotron, the 3-MV tandem accelerator, the 3-MV single-ended accelerator and the 400-kV ion implanter, have been operated steadily and safely as well as an electron accelerator and irradiation systems in Co-60 gamma-ray irradiation facilities. A uniform beam of 10-MeV H^+ was successfully formed within an area of 6 cm × 6 cm with the uniformity of 6%, using the multi-pole magnet system installed last year at the downstream of the AVF cyclotron beam line. Total operation times of the tandem accelerator, the single-ended accelerator, and the ion implanter were 30,322, 34,448, and 26,857 hours, respectively, since the beginning of their operation. The total number of experiments made by various users using the AVF cyclotron was 7,492 from the first beam extraction in 1991 to March 2008, as a result of continuous efforts such as regular maintenance and trouble-shooting.

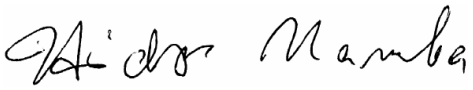

Hideki Namba,
Director General
Takasaki Advanced Radiation Research Institute
Japan Atomic Energy Agency

This is a blank page.

Contents

1. Space, Nuclear and Energy Engineering

This is a blank page.

1-01 Evaluation of Radiation Hardened Logic Circuits by Using 90 nm CMOS Technology

H. Shindou [a)], A. Maru [a)], Y. Satoh [a)], S. Kuboyama [a)], T. Hirao [b)] and T. Ohshima [b)]

[a)] Aerospace Research and Development Directorate, Japan Aerospace Exploration Agency (JAXA),
[b)] Environment and Industrial Materials Research Division, QuBS, JAEA

In recent years, there is increasing demand to improve the performance of integrated circuits for space application. Radiation-Hardness-by-design (RHBD) methodology utilizing a deep sub-micron process for semiconductor devices has been extensively investigated as a possible candidate methodology[1,2]. In our previous study, we successfully demonstrate the effectiveness of RHBD methodology for 0.15 μm CMOS/SOI process[3]. However, these techniques lead some penalties on the size of circuit, operation speed and power consumption. In addition, the deep sub-micron technologies are generally believed to be more sensitive to Single-Event Effect (SEE) than the older technology.

In this study, we evaluated basic SEE sensitivities of 90 nm CMOS commercial technologies with RHBD methodology. We designed test chip which include the standard latch circuit (i.e. non-RHBD circuit) and Dual Interlocked Storage Cell (DICE) latch circuit[4]. DICE is one of the well known RHBD approarch. Figure 1 illustrates the block diagram of DICE latch. It has a unique structure in which stored information is retained in two separate nodes. Corrupted information at one node cannot propagate to another node and is recovered automatically by the correct node.

In order to evaluate the effectiveness of RHBD applorach for 90nm CMOS processes, we performed the heavy ion irradiation for the test chip by using AVF cyclotron at JAEA. The SEU cross-section was simply calculated by dividing a number of error bits by the total fluence after the irradiation. Cocktail ion beam (M/Q=5) was used for our evaluation.

Figure 2 shows SEU cross-sections as a function of linear energy transfer (LET) for each test circuits. The cross-section was simply calculated by dividing a number of error bits by the total fluence. It is clearly said from the result that SEU tolerance is greatly improved by using RHBD methodology for 90 nm CMOS process. However, in our experiment case, some SEUs were observed in DICE latch though the cross-section is very small. These errors may be attributable to the multiple transistors upset by a single incident ion. It is thought that the actual distance of the two adjacent transistors in the off state to hold the logic state is one of the critical parameters to prevent SEUs observed in DICE latch circuit. Optimizations of the actual layout of the circuit are needed in order to achieve SEU immunity up to 64 MeV/(mg/cm^2) of LET for future work. We also plan to evaluate other types of RHBD circuit for space application.

References

1) Joseph M. Benedetto, IEEE NSREC Data Workshop Record, (2005) 58.
2) R. C. Lacoe, et al., IEEE Trans. Nucl. Sci., Vol. 47 (2000) 2334.
3) A. Makihara et al., IEEE Trans. Nucl. Sci., Vol. 52 (2005) 2524.
4) T. Calin et al., IEEE Trans. Nucl. Sci., Vol. 43 (1996) 2874.

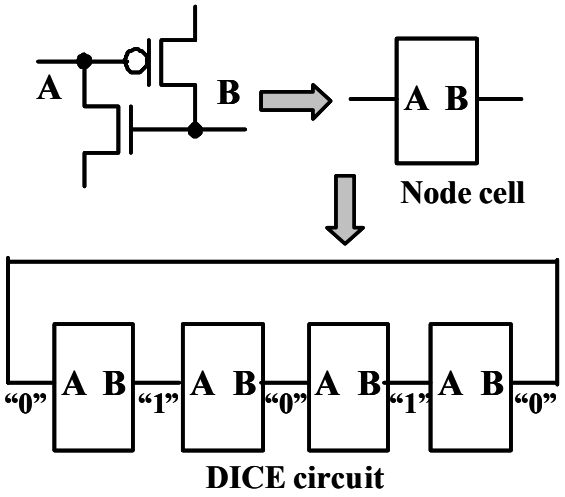

Fig. 1 Block diagram of Dual Interlocked Storage Cell (DICE) latch circuit.

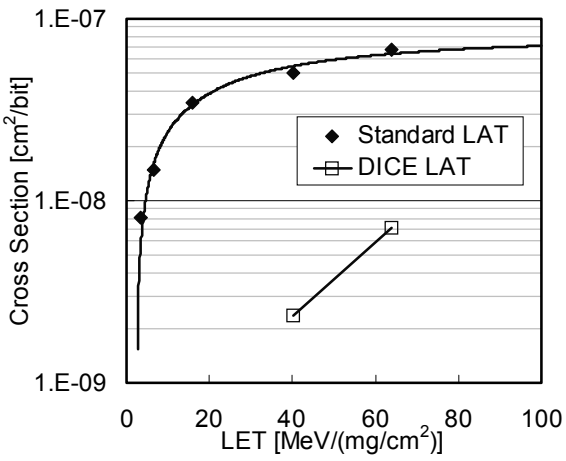

Fig. 2 SEU cross-sections as a function of Linear energy transfer for Standard and DICE latch circuits.

1-02 Development of Transient Ion Beam Induced Current System with High-energy Focused Microbeams

T. Hirao [a], T. Makino [b], D. Kobayashi [b], K. Hirose [b], S. Onoda [a] and T. Ohshima [a]

[a] Environment and Industrial Materials Research Division, QuBS, JAEA,
[b] Institute of Space and Astronautical Science, Japan Aerospace Exploration Agency (ISAS/JAXA)

1. Introduction

Transient errors in logic LSI systems mounted on satellites are caused by high energy cosmic rays. These transient errors are called soft errors. A single event transient (SET) has emerged as a new factor that causes soft errors. SET is momentary voltage noise due to a direct ion hit in the logic cell that configures logic LSI systems. The noise pulse (SET pulse) causes a soft error when they reach a flip-flop or other memory element. SET could dominate the soft error response of logic LSIs operating in space at clock frequencies of 100 MHz or higher. No effective hardening designs are available to prevent this SET from occurring because few data have been obtained on time duration of digital SET pulse (SET pulse-width) for hardening designs. Therefore, we used test circuits to gather knowledge on the SET pulse-width.

2. Experimental

a) Test Condition

We measured SET pulses originating in inverter (INV) cells fabricated by fully-depleted (FD) silicon-on-insulator (SOI) technology [1] to reveal the LET dependence of SET pulse-widths. Heavy ion irradiation tests were performed using the AVF cyclotron. Heavy ions were irradiated in a vacuum chamber with broad beams of Kr (322 MeV) or Xe (454 MeV) at 0 and 45 degrees. We also used a Kr beam at 49 degrees. Kr provides effective LETs, LET_{effs}, of 40, 56, and 62 MeV•cm^2/mg at 0, 45, and 49 degrees, respectively. Xe provides LET_{effs} of 68 and 92 MeV•cm^2/mg at 0 and 45 degrees, respectively. Effective LETs were defined as 1/cosine of incident angles of heavy ions. We calculated the LET value by using SRIM code.

b) Experimental Results

Figure 1 shows measured SET pulse width distribution originated in INV cells. Pulse-width originating in the inverter cell was distributed in a range of 0.1 to 1.0 ns with a peak near the center of the distribution. We replotted peak values of the distributions as a function of LETs to reveal the LET dependence of SET pulse-width.

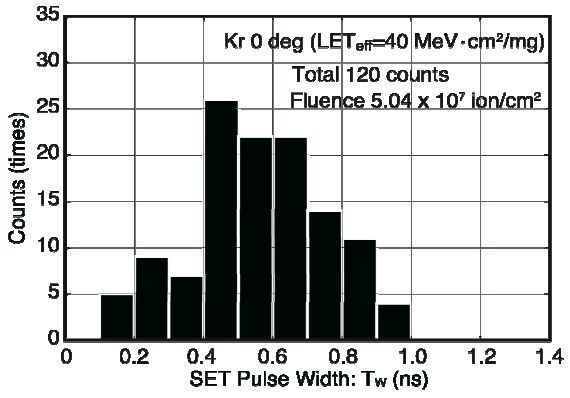

Fig. 1 SET pulse widths plotted as a function of measured SET pulse-width Tw.

3. Summary

Figure 2 shows LET dependence of SETs in an FD-SOI CMOS inverter. The resultant relationship exhibits that the pulse-widths became saturate as LET increases. Also, pulse-widths in the range of LET_{eff} from 40–92 MeV•cm^2/mg were shorter than 1.0 ns. These results imply that most of the pulses generated in the space environment would be shorter than 1.0 ns because few heavy ions have LET_{effs} over 100 MeV•cm^2/mg. The SET pulse-width exists in a range up to 1.0 ns with a peak near the center of the distribution for all cases [2].

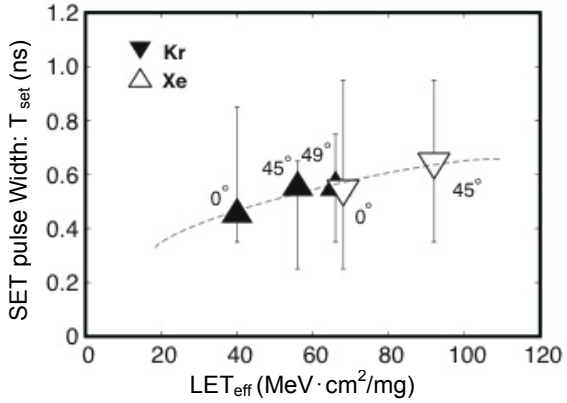

Fig. 2 SET pulse widths plotted as a function of effective LET. Symbols represent peak values, pulse widths observed most frequently, and vertical bars full-width half maximum for each distributions.

In this collaboration study, we also experimentally validated a scan technology for measuring error rates of logic circuits [3] and a technique for estimating error probabilities in circuits from SET pulse width measurements [4].

References

1) T. Makino et al., Trans. Nucl. Sci. 56 (2009) 202-207.
2) Y. Yanagawa et al., Trans. Nucl. Sci. 53 (2006) 3575-3578.
3) Y. Yanagawa et al., Trans. Nucl. Sci. 56 (2009) to be published.
4) T. Makino et al., Ext. Abs. 66th JSAP Spring Meeting Mar. 2009, 30p-V-16.

1-03 Dependence on Irradiation Energy of Soft Error Rates in Bulk and SOI SRAMs

S. Abo [a)], S. Onoda [b)], T. Hirao [b)], T. Ohshima [b)], T. Iwamatsu [c)] and M. Takai [a)]

[a)] Center for Quantum Science and Technology under Extreme Conditions, Osaka University,
[b)] Environment and Industrial Materials Research Division, QuBS, JAEA,
[c)] Advanced Device Development Department, Renesas Technology Corporation

A single event upset (SEU) due to excess carriers generated by high energy particles, which are originated from cosmic rays, becomes more serious problem in advanced semiconductor devices. In a conventional (bulk) device, the whole excess carriers generated along the particle track are accumulated to a drain electrode, resulting in SEU. On the contrary, a silicon-on-insulator (SOI) device has an advantage over the conventional (bulk) device for SEU [1, 2], in which a channel region is insulated from the Si substrate by a buried oxide layer. Thus, the excess carriers in the Si substrate are not accumulated to the drain electrode. However, the excess carriers generated in a SOI layer are kept in the SOI layer or accumulated to the drain and source electrodes. In particular, the generated holes increase the SOI body potential, which results in the abnormal drain current (i.e., floating body effect) and SEU [1].

In this study, the difference of soft error rates (SERs) in bulk and SOI static random access memories (SRAMs) with a technology node of 90 nm was investigated by helium ion probes with energies ranging from 0.8 to 6.0 MeV. The SOI SRAM has a body-tie structure for suppressing the floating body effect. The top over-layers were 4 Cu metal and polyimide passivation layers. A memory cell included 4 n-channel metal oxide semiconductor field effect transistors (MOSFETs) and 2 p-channel MOSFETs. A size of the memory cell, a critical charge and a capacity of the SRAM chip were 1.25 μm^2, 1.8 fC and 8 Mbits, respectively. The amount of the soft error was monitored after the helium probe irradiation. The SRAM chips were put into a vacuum and were shielded with a package resin of SRAM for uniform probe irradiations and other large peripheral circuits and connecting cables were in the air. The irradiation time was 60 s with a beam current of 20 pA, corresponding to 1.25 particles/μm^2 s.

Figure 1 shows the SERs as a function of helium ion probe energy on bulk and SOI SRAMs. No soft error occurred in both bulk and SOI SRAMs with helium ion probe energies of less than 1.8 MeV. This indicates that the helium ion probes with energies of less than 1.8 MeV were shielded by the over-layers of MOSFET. The value of SER for bulk SRAM was saturated with helium ion probe energies more than 2.5 MeV. On the contrary, the value of SER for SOI SRAM becomes the highest at 2.5 MeV and decreases with increasing the helium ion probe energy at and above 2.5 MeV. This indicates that the advantage of SOI SRAM for the soft error. Figure 2 shows the lost energy in the SOI layer after over-layers transmission for SOI SRAM as a function of helium ion probe energy simulated by SRIM code [3]. The amount of the generated charge in the SOI layer was much less than the critical charge (1.8 fC). The amount of the generated charge in SOI SRAM became the highest at about 2.5−3.0 MeV. The measured SER (Fig. 1) also indicates the highest at the same helium ion probe energy. These results indicate that SER in SOI SRAM depends on the amount of the generated charge by helium ion irradiation in the SOI layer.

References

1) J.-P. Colinge, Silicon-on-insulator Technology: Materials to VLSI, Kluwer Academic Publishers, Boston/Dordrecht/London, (1997).
2) F. Assaderaghi, G. Shahidi, Electrochem. Soc. Ser. 99.
3) J. Ziegler, http://www.srim.org.

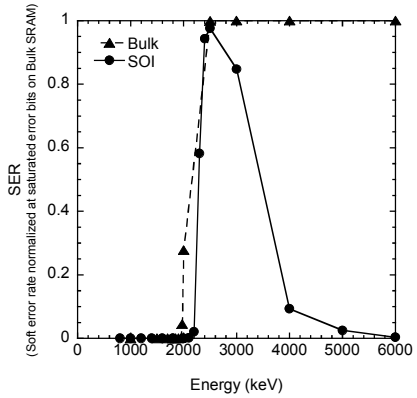

Fig. 1 SER (Soft error rate normalized at saturated error bits on Bulk SRAM) as a function of helium ion probe energy on bulk and SOI SRAMs.

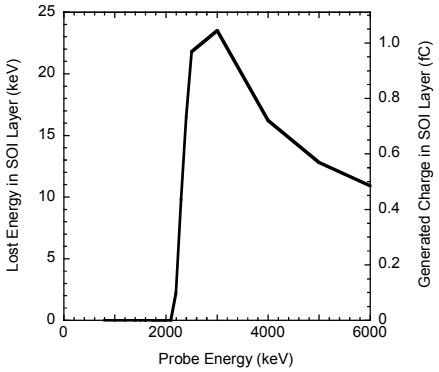

Fig. 2 Lost energy and generated charge in the SOI layer after over-layers (passivation and wiring layers) transmission as a function of helium ion probe energy.

1-04 Heavy-ion Induced Gate Current in SOI Devices

Y. Takahashi [a)], R. Imagawa [a)], A. Ohwaki [a)] ,H. Takeyasu [a)],
T. Hirao [b)], S. Onoda [b)] and T. Ohshima [b)]

[a)] Nihon University, [b)] Environment and Industrial Materials Research Division, QuBS, JAEA

One of the most detrimental effects on semiconductor devices in radiation environments is the single-event effect (SEE). Recently, silicon-on-insulator (SOI) technology has been developed to reduce SEE in devices, because it was believed that the charge collection is suppressed by the existence of a buried oxide (BOX) layer [1)]. However, anomalous charge collection through the BOX layer was also reported [2)]. So it is important to clarify the charge collection mechanism through the oxide layer. In the present work, we have investigated the heavy-ion induced transient gate currents in MOS structures, and we concluded that the transient current through a gate oxide layer is dominated by a displacement current[3)]. In this study, the heavy-ion induced transient current in SOI pn junction diode was investigated, in order to discuss the features of transient current in SOI devices.

The Al gate p^+n junction diodes with the junction area of 100 μm in diameter were fabricated on n-type bulk Si or SOI substrate. In SOI substrate, the thicknesses of top silicon layer and BOX layer are 1.5 μm and 0.3 μm, respectively. The transient currents in diodes induced by 15 MeV Oxygen ions were measured. The LETs and project range of the ions are 6.5 MeV/(mg/cm^2) and 12.3 μm, respectively. Heavy-ion irradiation tests were carried out using the Single Ion hit (SIH) system in JAEA and the transient current caused by the single ion was measured by Transient Ion Beam Induced Current (TIBIC) measurement system. DC bias voltage is applied through a bias tee, and the transient current induced by heavy-ion irradiation is measured with a high speed oscilloscope with a bandwidth of 3 GHz.

Figure 1 shows the transient current and the total collected charge, the integration value along a time after irradiation, in a bulk p^+n diode, in which the reverse bias of 20 V is applied during irradiation test. The peak height of the current signal is 620 μA, and the current approached the noise level about 10 ns after irradiation. The total collected charge is 550 fC that corresponds to the charges generated along the ion track up to 8.2 μm due to irradiation.

Figure 2 shows the transient current and the total collected charge in a SOI p^+n diode, in which the reverse bias of 20 V is applied during irradiation. The peak height of the current signal is 28 μA, corresponds to 1/20 of the data of bulk sample. The duration of the signal is longer than the bulk data, because the serial resistance in SOI device is higher than the bulk device. The maximum collected charge is 170 fC, that is less than 1/3 of the bulk data. These results indicate that the SEE effects can be reduced using the SOI devices. However, the charge generated in top silicon due to irradiation is 100 fC, and the measured charge is 1.7 times as much as the generated charge. In Fig. 2, it is also found that the measured current becomes negative at 20 ns after irradiation, and collected charge is reduced. We considered that the negative current is induced by the displacement current through the BOX layer. In order to clarify the charge collection mechanism in SOI device, further experimental and more detail investigations are necessary.

References

1) O. Musseau, IEEE Trans. Nucl. Sci., NS-43, 2 (1996) 603-613.
2) T. Hirao et al., Nucl. Instrum. Meth. Phys. Res., B-206 (2003) 457-461.
3) Y. Takahashi et al., Nucl. Instrum. Meth. Phys. Res., B-260 (2007) 309-313.

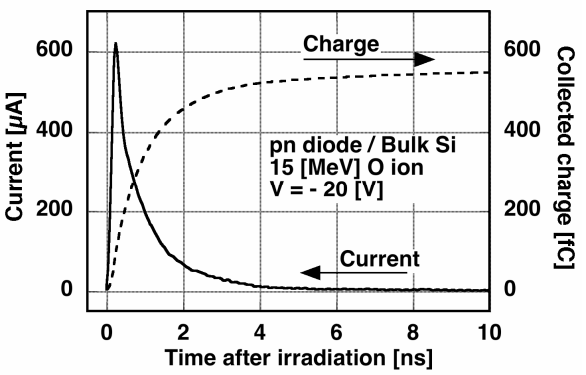

Fig. 1 Transient current and total collected charge in a bulk p^+n diode.

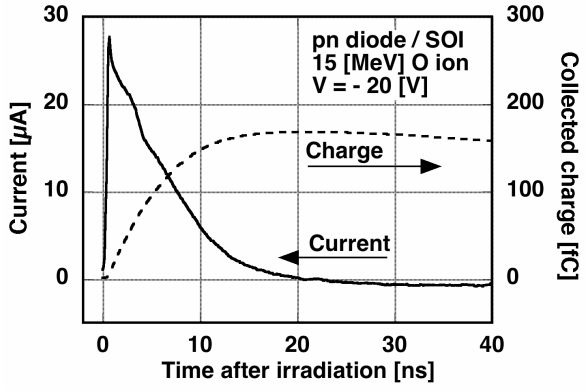

Fig. 2 Transient current and total collected charge in a SOI p^+n diode.

1-05 Development of Transient Ion Beam Induced Current System with High-energy Focused Microbeams

S. Onoda, T. Hirao and T. Ohshima

Environment and Industrial Materials Research Division, QuBS, JAEA

Single Event Effects (SEEs) are well known as a malfunction of microelectronics devices caused by the impact of the Galactic Cosmic Ray (GCR) such as high energy heavy ions. Generally, SEEs are triggered by unexpected transient currents induced by an ion incidence. The focused ion microbeam has a key advantage in evaluating the transient currents at specific region of a device with a high resolution. However the available energy range of microbeams connected to 3MV Tandem Accelerator is much lower than that of the GCR. In order to realize test conditions closer to the real radiation environment, the high energy microbeam has been recently developed at AVF Cyclotron[1]. To measure the transient current at specific region of device by using high energy microbeam, we develop new measurement system. In this paper the peak current mapping on diodes is demonstrated.

Figure 1(a) shows the schematic diagram of the Transient Ion Beam Induced Current (TIBIC) system developed at TIARA facility. The TIBIC system contains following; (1) a chopper, (2) a beam focusing system including a beam shifter, micro slits, divergence defining slits, an XY scanner, and quadruplet quadrupole magnets, (3) a chamber, and (4) an electronics for TIBIC measurements including a bias-t, an amplifier (amp.), a power supply, and 3 GHz Digital Storage Oscilloscope (DSO). In this system, the beam chopping system is also used for controlling the beam current. In addition, the beam current can be reduced by the beam attenuators located next to the chopper although not shown here. The beams accelerated by the AVF Cyclotron are optimized by the focusing system. The details of how to focus the high energy heavy ion beam is described elsewhere[1]. The focused microbeam is transported into the irradiation chamber. The scintillator film (ZnS) and the #1000 Copper (Cu) mesh lie in the same plane of the DUT in the irradiation chamber. These are used for detecting the microbeam position and for evaluating the Full Width at Half Maximum (FWHM) of the microbeam spot size, respectively.

Software control sequence for TIBIC imaging proceeds as follows. First a constant reverse bias is applied to the Device Under Test (DUT). During this period the beam is removed using a chopping system controlled by a Transistor-Transistor Logic (TTL) signal provided by a Device Acquisition (DAQ) board. Next the microbeam is electro-statically scanned by the raster method with a speed of about 330 sec/frame. The beam flux is controlled to be several tens ions per second. When a transient current is generated by an ion strike, the DSO is triggered and the beam is again stopped by the TTL signal from DSO. DAQ board also receives the TTL signal from DSO and simultaneously records the x-y positions. After the transient current and positions are stored in Personal Computer (PC), the process is repeated over the complete scan area. Finally, we perform the Pulse Shape Analysis (PSA) on each transient current and generate images based on extracted PSA parameters, such as the charge, the peak current, the fall time, and the rise time. After each scan, the current-voltage and the capacitance- voltage curves can be measured to assess the level of displacement damage introduced by the beam. Figure 1(b) shows the TIBIC peak mapping on diodes. This image illustrates that the diode region covered with the circular electrode is SEE sensitive.

Reference

1) M. Oikawa *et al.*, Nucl. Instrum. Meth. B260 (2007) 85.

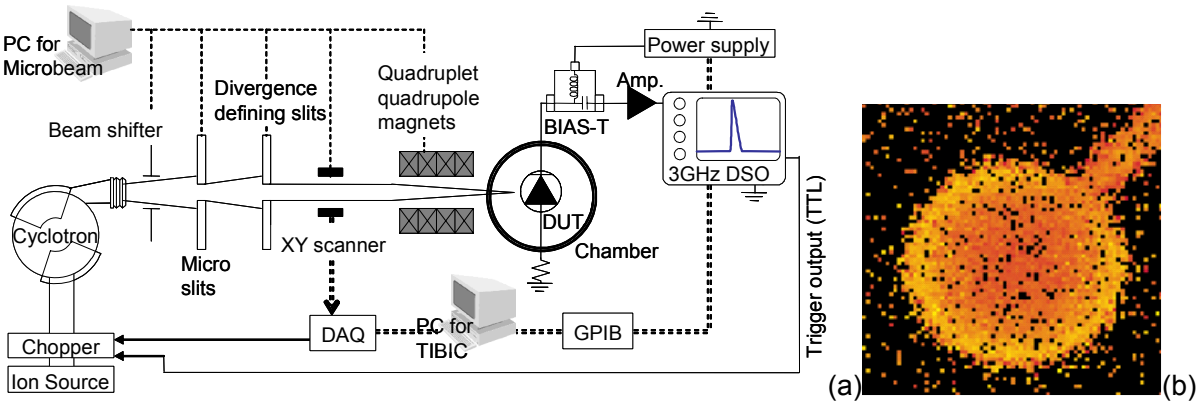

Fig. 1 Schematic diagram of the TIBIC system connected with high-energy heavy ion microbeam system and the AVF Cyclotron (a). TIBIC peak images measured by using the focusing microbeam (b).

1-06 Simulated Space Degradation of Transparent Film for Thin-film Space Solar Cells

K. Shimazaki [a)], Y. Kobayashi [a)], M. Takahashi [a)], M. Imaizumi [a)], T. Ohshima [b)], S. Sato [b)] and K. Kibe [a)]

[a)] Aerospace Research and Development Directorate, JAXA,
[b)] Environment and Industrial Materials Research Division, QuBS, JAEA

Paper-like III-V multi-junction solar cells are the most promising materials for the next generation of space solar cells because of its high efficiency[1]. A coverglass (100 μm thickness) is typically attached on the space solar cells using high transparent silicone adhesive. However, covering thin film solar cells with the conventional coverglass counteracts the advantages of the flexibility and light weight of the cells. Flexible and high transparent films are therefore needed for surface protection of the solar cells. Optical degradation of the films caused by space radiation must be evaluated since it decreases the amount of transmitted sunlight falling on solar cells and degrades the cell output power.

Space radiations are omnidirectional charged particles and have energies that range from near-zero up to several hundred million electron volts. However, the present ground tests are different from the actual space radiation environment. Ground tests usually utilize the mono-energetic and normal incident charged particles. For simulating the same level of degradation as the actual space radiation environment, we calculated the energies deposited in the films using PHITS [2,3] (Particle and Heavy Ion Transport code System). The space radiation environments were calculated using NASA-developed AP8 (for trapped proton) [4], AE8 (for trapped electron) models [5], and JPL-91 (for solar proton) model [6]. The selected example was for a low earth orbit for the mission duration of 5 years. The interest sample was transparent film with 75 μm thickness. Figure 1 illustrates the calculated depth profiles of the deposited energy by space radiations and ground-based monoenergetic radiations. Table 1 tabulates the calculated particle energies and fluences for simulating the space degradation. Calculation results show that the space radiations deposit the more energy in the vicinity of the surface (less than 5 μm) than within the materials. According to the calculation results, we performed irradiation tests for the transparent films. For the comparison, we selected two experiments. One is only 1 MeV-electron irradiation and the other was three energies of proton irradiations followed by 1 MeV-electron irradiation. Figure 2 depicts the changes of the spectral transmittance of the films. No significant difference was found in optical degradation between two experiments although their transmittances slightly degraded around 400 nm. This result demonstrates that the interest transparent film has a high radiation tolerance on the optical properties for the low earth orbit for the 5-year-mission.

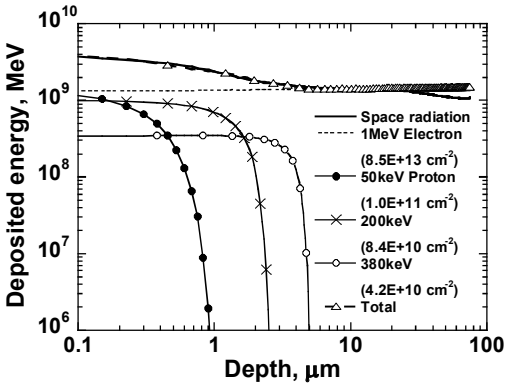

Fig. 1 Calculated depth profile of deposited energies in transparent film.

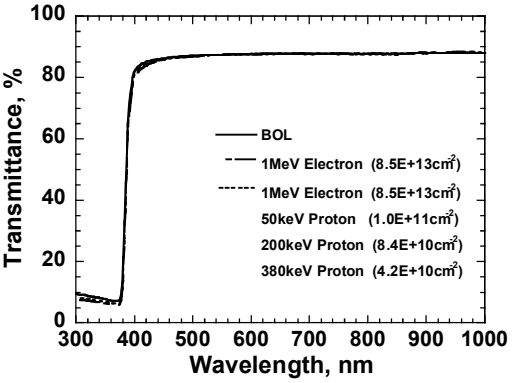

Fig. 2 Changes in transmittance of transparent film.

Table 1 Particle energies and fluences for simulating the space degradation under low earth orbit conditions (5 years).

	Electron	Proton		
Energy	1 MeV	50 keV	200 keV	380 keV
Fluence, cm^{-2}	8.5×10^{13}	1.0×10^{11}	8.4×10^{10}	4.2×10^{10}

References

1) T. Kodama et al., Tech. Digest Int. PVSEC-17, 6O-B11-03 (2007).
2) H. Iwase et al., J. Nucl. Sci. Technol. **39** (2002) 1142.
3) K. Niita et al., Radiat. Meas. **41** (2006) 1080.
4) D. M. Sawyer and J. I. Vette, NASA Publication NSSCE 76-06 (1976).
5) J. I. Vette, NASA Publication NSSDC 91-24 (1991).
6) J. Feynman et al., J. Geophys. Res. 98 No. A8 (1993) 13281-13294.

1-07 Hydrogen Observation of Ion-Irradiated a-Si:H Thin Films by Using *In-Situ* ERD System

S. Sato [a)], T. Ohshima [a)], and M. Imaizumi [b)]

[a)] Environment and Industrial Materials Research Division, QuBS, JAEA,
[b)] Aerospace R&D Directorate, JAXA

I. Introduction

Hydrogenated amorphous silicon (a-Si:H), which is used as thin film transistor or thin film solar cell, has high radiation tolerance[1)]. Since a-Si:H thin film solar cell also has advantages from the point of view of resource saving, high output per weight, low cost, and so on, it is expected as solar cell for space applications. The conversion efficiency of single-junction a-Si:H solar cell is nowadays about 10%[2)]. Furthermore, multi-junction solar cell, of which the efficiency is expected to be higher than that of single-junction solar cells, becomes a mainstream in present day. For instance, the target value of the efficiency of a-Si:H/a-SiGe:H/μc-Si:H triple-junction solar cell is 15%[3)].

Extensive studies of light-induced degradation for a-Si:H materials, i.e., Staebler-Wronski (SW) effect[4)], have been performed since three decades ago. In contrast to this, radiation effects on a-Si:H materials have not been well investigated. However, it is necessary to elucidate the radiation effects in order to utilize a-Si:H devices in radiation environments. One of the most important points is the knowledge about hydrogen diffusion in a-Si:H induced by charged particles, since the hydrogen atoms saturate dangling-bonds and enable conductivity control.

The purpose of this study is to develop ERD measurement system at variable temperature condition and to observe hydrogen behavior in ion-irradiated a-Si:H thin film with rising a sample temperature. So far, we have developed the low temperature ERD system in the dual beam irradiation chamber (MD2). As the chamber connected to both the 400 kV Ion Implanter and from the 3MV Single-Ended Accelerator, ERD measurement using beams from the former one can be performed for a sample just after the ion irradiation (implantation) from the latter one.

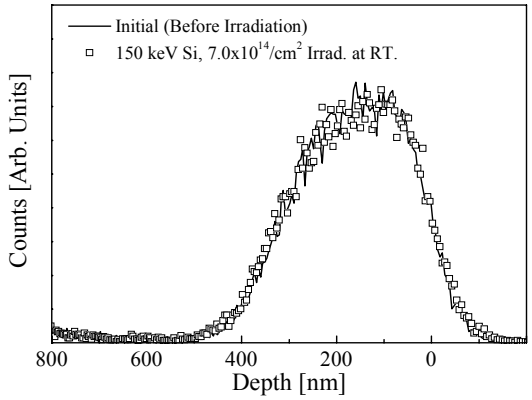

Fig. 1 ERD spectrum of an a-Si:H thin film before and after 150 keV Si^+ irradiation at 7.0×10^{14} /cm^2.

II. Experimental

The samples used in this study were a-Si:H thin films fabricated on Fz-Si substrates by Plasma Enhanced Chemical Vapor Deposition (PECVD) at National Institute of Advanced Industrial Science and Technology (AIST). The thickness of the a-Si:H thin film was estimated to be 300 nm.

Figure 1 shows the results of the ERD measurements before and after 150 keV Si^+ at the fluence of 7.0×10^{14} /cm^2. The ERD measurements were carried out at room temperature after the irradiation. No specific change of the hydrogen distribution was observed between before and after the irradiation. One hundred fifty keV Si ions was implanted into the a-Si:H thin film and the average projected range was 220 nm according to the calculation results of SRIM. Atomic concentration of the implanted Si even in the peak region was 4.2×10^{19} /cm^3, which value was merely below 0.1% of Si concentration in the a-Si:H thin film. This indicates that Si implantation in the amorphous network doesn't induce hydrogen diffusion in the case that the implantation dose is low so that the atomic composition doesn't change.

For the next step, we will perform low temperature *in-situ* ERD measurement to the samples irradiated with Si or H ions. Additionally, we also plan to improve the sample holder and install a heater to the sample holder for temperature control.

Finally, we would like to thank H. Sai of AIST for fabricating the a-Si:H samples.

References

1) N. Wyrsch et al., J. Non-Cryst. Solids **352** (2006) 1797-1800.
2) The 3rd working paper of the Research Center for Photovoltaics, Adv. Ind. Sci. and Technol (2007).
3) X. Xu et al., *Proceedings of the 33rd IEEE PVSC*, San-Diego US, May, (2008) 246.
4) D.L. Staebler and C.R. Wronski, Appl. Phys. Lett. **31** (1977) 292.

1-08 Gate Controllable Light Emitting FET Based-on Rare-Earth Ion Doped AlGaN/GaN HEMT

A. Wakahara [a)], H. Okada [a)], K. Takemoto [a)], T. Shimojyo [a)], T. Hata [a)], T. Ohshima [b)] and S. Sato [b)]

[a)] Department of Electrical and Electronic Engineering, Toyohashi University of Technology,
[b)] Environment and Industrial Materials Research Division, QuBS, JAEA

Gate controllable light emitting FET devices were fabricated and investigated in this study. Fabricated devices showed excellent *I-V* characteristics as FET. A reddish luminescence was found at the Eu implanted region when applying drain bias of 20 V. This luminescence was caused by the impact excitation of rare-earth ions (REIs) associated with two-dimensional electron gas (2DEG) acceleration.

我々は、イオン注入法により窒化物半導体に添加した希土類元素の発光特性について、フォトルミネセンス(PL)やカソードルミネセンス(CL)による評価を行ってきた[1), 2)]。希土類元素の内殻遷移に基づく発光は、単色性に優れ、温度消光が少ないといった特徴を有していることから、発光素子や光通信素子への応用に魅力的である。電流注入により直接的に希土類元素を励起することができれば、発光素子とドライバ・トランジスタを一体化した三端子型の発光デバイスが期待できる。本研究では、新しい窒化物半導体三端子型発光デバイスを開発し、その特性を評価した。

Figure 1にデバイスの断面構造を示す。AlGaN/GaNの高電子移動度トランジスタ(HEMT)構造を基本とし、希土類元素であるユーロピウム(Eu)のイオン注入領域を設けている。2次元電子ガス(2DEG)層中の電子はドレイン電界によって加速された後、ドレイン電極端に選択的にイオン注入した希土類元素を衝突励起し、希土類元素の発光が得られると期待している[3)]。

デバイス作製では、まず、AlGaN/GaNのHEMT構造に、イオン注入のマスクとしてSiO_2層を堆積し、フォトリソグラフィにより注入領域の窓開けを行った後、Euのイオン注入を100 keVで行った。TRIM2008によるシミュレーションから、EuはAlGaN/GaNの界面の2DEG層にピークを持つ注入分布になるものと予想された。Euの注入濃度は、PLおよびCL評価で強い発光強度が得られた5×10^{14} cm^{-2}とした[2)]。イオン注入後に注入損傷の回復のためにNH_3とN_2混合ガス雰囲気中で1100 °C、2分間のアニールを行った。ソース・ドレイン電極にはTi/Al/Ti/Auを、ゲート電極にはAuを用い、それぞれリフトオフ法により形成した。

このようにして作製したデバイスは、室温でゲートバイアスによるドレイン電流制御など、良好な電界効果トランジスタ(FET)の動作を示した(Fig. 2)。Fig. 3に、ドレイン－ソース間電圧V_{DS} = 20 V、ゲート－ソース間電圧V_{GS}=0 V印加時のデバイス上面の写真を示す。ドレイン電極端で赤色の発光が観測された。V_{GS}=-1 Vの印加によりドレイン電流が減少するとともに発光強度も減少した。V_{GS}=-5 Vでは、ドレイン電流はゼロになり、発光しなくなった。これらの結果から、発光は衝突励起により得られたものと考えられ、本研究で提案したデバイスが、新しい三端子型発光デバイスに有望であることを示すことができた。また、従来の発光デバイスは、キャリア再結合に基づく発光機構を利用しており、放射線照射によって形成される少数キャリアトラップの影響を強くうけるが、本デバイスは多数キャリアによる希土類元素励起を利用しており、宇宙用発光素子としても期待できる。

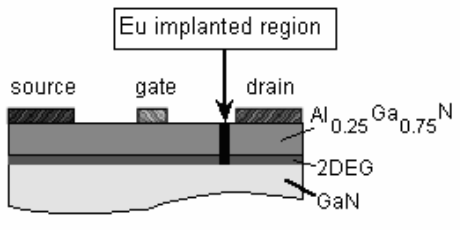

Fig. 1 A Cross-section of light emitting FETs.

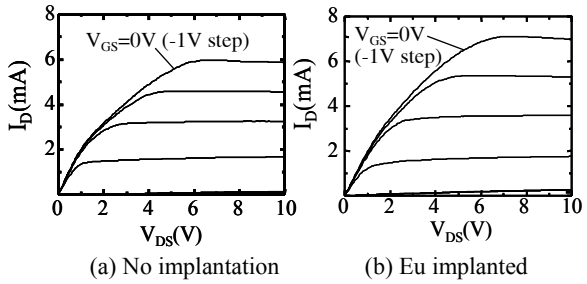

(a) No implantation (b) Eu implanted

Fig. 2 I_D-V_{DS} characteristics of the devices.

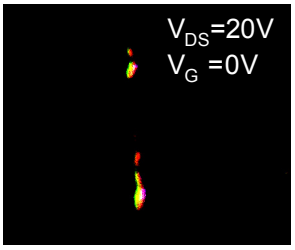

Fig. 3 A luminescence of the light emitting FET.

References

1) Y. Nakanishi et al., Nucl. Instrum. Meth. Phys. Res. B 206 (2003) 1033.
2) Y. Nakanishi et al., Phys. Stat. Sol. (c) 0 (2003) 2623.
3) T. Nakazato et al., Jpn. J. Appl. Phys. 41 (2002) 1990.

1-09 Damage Factors of Charge Collection Efficiency in SiC for Gamma-rays, Electrons and Protons

S. Onoda [a)], N. Iwamoto [a, b)], K. Kojima [c)], K. Kawano [b)] and T. Ohshima [b)]

[a)] Environment and Industrial Materials Research Division, QuBS, JAEA,
[b)] The University of Electro-Communications,
[c)] National Institute of Advanced Industrial Science and Technology

The particle detectors operating in severe radiation environments such as Japan Proton Accelerator Research Complex (J-PARC), super Large Hadron Collider (super-LHC), and outer space must have radiation hardness. Presently, in these environments, Si based semiconductor devices are applied to a particle detector. However, it is considered that Si detectors do not have enough radiation tolerance. Therefore, developing particle detectors with superior radiation tolerance is required. Since Silicon Carbide (SiC) is regarded as one of the candidate materials for electronic devices with high radiation hardness, we study the radiation hardness of the SiC detectors from the viewpoint of Charge Collection Efficiency (CCE).

Six cyclic hexagonal-type SiC (6H-SiC) n^+p diodes were fabricated on a p-type 50 μm thick epitaxial layer grown on a p-type substrate (CREE, 3.5° off Si-face). The epitaxial layer was grown by a hot-wall chemical vapor deposition system at the National Institute of Advanced Industrial Science and Technology (AIST). The n^+ region was formed by three fold P ion implantations of 60, 90, and 140 keV at 800 °C and subsequent annealing at 1650 °C for 3 min in Ar ambient. During the annealing, samples were covered with carbon coating in order to suppress the degradation of the surface morphology. The diameter of n^+ region and its average P concentration were 250 μm and 5×10^{19} cm^{-3}, respectively. For the surface termination, field oxide of 100 nm thick was formed by pyrogenic oxidation at 1,100 °C for 90 min. To form electrodes on the backside, deposition of Al followed by sintering at 850 °C for 5 min in Ar ambient, and re-deposition of Al to100 nm thickness were carried out. On the front side, contacts on the n^+ region and bonding pads were formed by Al deposition.

We performed the irradiations to samples by using Co-60 gamma-rays, 1 MeV electrons, and 65 MeV protons. After irradiations the CCE decreased with the increase in the irradiation fluence. It is known that the decrease in CCE is expressed by the following classical damage model; $Q_\Phi / Q_0 = 1/(1+K\Phi)$, where K is the damage factor of CCE, Φ is the fluence, and Q_0 and Q_Φ are the total collected charge before and after irradiation, respectively. By fitting this equation to the data, the damage factors of CCE were estimated to be 1.16×10^{-18}, 5.65×10^{-18}, and 4.56×10^{-15} cm^{-2} for Co-60 gamma-rays, 1 MeV electrons, and 65 MeV protons, respectively. The decrease in CCE by 1MeV neutrons has been reported [1,2]. According to the reported data, the damage factors for 1 MeV neutrons were estimated to be in the range from 1.38×10^{-15} to 2.58×10^{-16} cm^{-2}.

It is well known that the observed damage factors are independent of the radiation source and energy according to Non-Ionizing Energy Loss (NIEL). To date however, NIEL analysis has mostly been applied to solar cell parameters, and little attention has been given to CCE. Here we discussed whether NIEL analysis could be applicable to the damage factors of CCE in SiC. The damage factors of CCE as a function of NIEL are shown in Fig. 1. For purposes of comparison, the damage factors in Si for 15 MeV Oxygen, 15 MeV Carbon, 15 MeV Iron, and 10 MeV Gold ions were represented[3]. Note that the damage factors in SiC were slightly higher than those in Si. The possible reason for this difference is that the number of defects causing degradation of CCE differs from the number of primary knock-on atoms (PKAs), which is directly related to NIEL. Another reason for this difference is the error associated with the sample fabrication process and test conditions, etc. As shown in Fig. 1, it was suggested that the damage factors of CCE in SiC also were linearly proportional to NIEL.

References

1) F. Nava *et al.*, IEEE Trans. Nucl. Sci. **53** (2006) 2977.
2) F. Moscatelli *et al.*, IEEE Trans. Nucl. Sci. **53** (2006) 1557.
3) S. Onoda *et al.*, AIP Journal **1099** (2009) 1010.

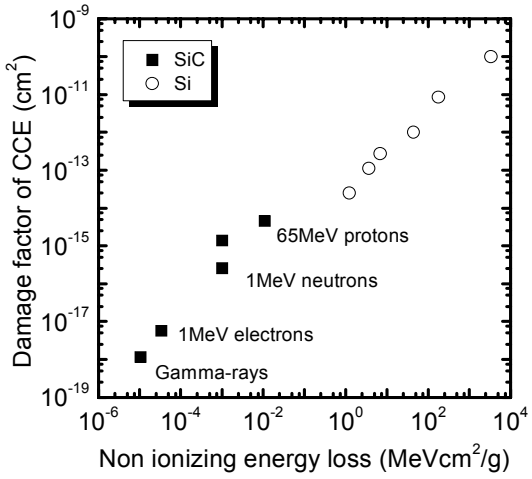

Fig. 1 Damage factors of CCE as a function of NIEL. The closed squares and open circles indicated the damage factors of CCE in SiC and Si.

1-10 Mechanisms of Reduction in Hole Concentration in Al-doped 4H-SiC by 200 keV Electron Irradiation

H. Matsuura [a], N. Minohara [a] and T. Ohshima [b]

[a] Dept. of Electronic Engineering and Computer Science, Osaka Electro-Communication University,
[b] Environment and Industrial Materials Research Division, QuBS, JAEA

By comparing the radiation damage in 4H-SiC with that in Si[1,2], it was found that the reduction in hole concentration, p(T), in Al-doped p-type 4H-SiC by electron irradiation was much larger than that in p-type Si. Since the large reduction in p(T) in Al-doped 4H-SiC by electron irradiation was an unexpected result, the decrease in p(T) by irradiation with different electron energies was investigated[2]. Since 200 keV electrons can displace only substitutional C atoms in SiC, we have investigated the reduction in p(T) in Al-doped p-type 4H-SiC by the irradiation of 200 keV electrons at several fluences.

A 10-μm-thick Al-doped p-type 4H-SiC epilayer on n-type 4H-SiC was cut to a size of 1×1 cm^2. The value of p(T) was obtained by Hall-effect measurements, in the van der Pauw configuration, within the temperature range of 120-650 K in a 1.4 T magnetic field. p(T) for the samples irradiated with total fluences (Φ) of 0, 1, 3, 5, 7, and 9×10^{16} cm^{-2} were measured, which are shown in Fig. 1.

The densities and energy levels of acceptors were determined by free carrier concentration spectroscopy (FCCS)[1,2] using the experimental p(T) shown in Fig. 1. Here, FCCS is a graphical peak analysis method that can determine the densities and energy levels of acceptors and hole traps from the experimental p(T) without any assumptions regarding acceptor species and hole traps.

Figure 2 shows the fluence dependence of the density (N_{Al}) of shallow acceptors at E_V+0.2 eV or the density (N_{DA}) of deep acceptors at E_V+0.37 eV, denoted by open circles or solid squares. The shallow acceptors are assigned to Al acceptors, whereas the origin of the deep acceptors is unknown up to now.

The value of N_{Al} is decreased by the displacement of C atoms neighboring to Al atoms because only the Al atom bonding to four C atoms works as an Al acceptor. Therefore, the following differential equation describing the fluence dependence of N_{Al} is obtained:

$$\frac{dN_{Al}}{d\Phi} = -\kappa_{Al} N_{Al} \quad , \tag{1}$$

where κ_{Al} is the removal coefficient of Al acceptors and Φ is the fluence of 200 keV electrons. In the case that the 200 keV electron irradiation creates the deep acceptors from Al acceptors and extinguishes the deep acceptors, the fluence dependence of N_{DA} is obtained:

$$\frac{dN_{DA}}{d\Phi} = -\frac{dN_{Al}}{d\Phi} - \kappa_{DA} N_{DA} \quad , \tag{2}$$

where κ_{DA} is the removal coefficient of the deep acceptors.

The N_{Al} and N_{DA} simulated from eqs. (1) and (2) are qualitatively in agreement with the experimental data in Fig. 2, respectively[3].

References

1) H. Matsuura et al., Jpn. J. Appl. Phys. 45 (2006) 2648.
2) H. Matsuura et al., Physica B 376-377 (2006) 34.
3) H. Matsuura et al., J. Appl. Phys. 104 (2008) 043702.

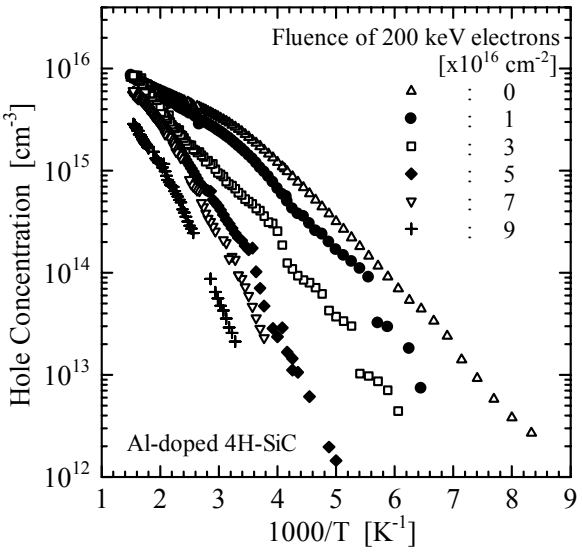

Fig. 1 Temperature dependence of hole concentration for Al-doped 4H-SiC unirradiated or irradiated by 200 keV electrons.

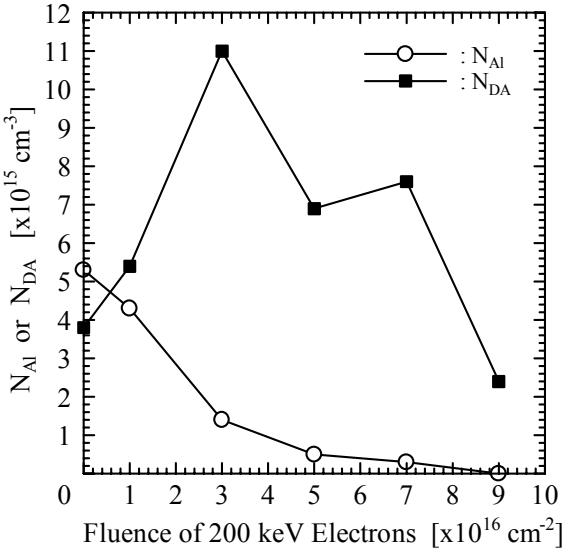

Fig. 2 Fluence dependence of shallow or deep acceptor density.

1-11 EPR Identification of Dicarbon Antisite Defect in Electron-irradiated *n*-Type 4*H*-SiC

T. Umeda [a)], N. Mizuochi [a)], J. Isoya [a)], N. Morishita [b)], S. Onoda [b)] and T. Ohshima [b)]

[a)] Graduate School of Library, Information and Media Studies, University of Tsukuba,
[b)] Environment and Industrial Materials Research Division, QuBS, JAEA

Silicon carbide (SiC) potentially has applications in power electronic devices of high performances. Moreover, the high radiation-hardness is especially suited to the semiconductor devices used in space. A problem is that SiC device fabrication technology has not progressed in controlling defects far enough to attain the electrical-characteristics close to those expected for this material. In recent years, through a combination of electron paramagnetic resonance (EPR) measurements and *first-principles* calculations, we identified vacancy-related defects in 4*H*-SiC, monovacancies, V_{Si}^- ($V_{Si}^-$and T_{V2a}), EI5:$V_C^+(k)$, EI6:$V_C^+(h)$, and HEI1:$V_C^-(h)$, divacancies, P6/P7:$[V_{Si}V_C]^0$, (S=1), antisite-vacancy pairs, HEI9/HEI10:$[C_{Si}V_C]^+$ and SI5: $[C_{Si}V_C]^-$.[1)] Several forms of thermally-stable interstitial-related defects have been predicted by theoretical studies. The carbon interstitial C_i can be stabilized by a dumbbell or dicarbon (C_2) structure at either the carbon or silicon site. At higher temperatures, aggregation of C_i proceeds to various forms such as $[(C_2)_C]_2$, $[(C_2)_{Si}]_2$, $(C_3)_{Si}$, and $[(C_2)_C$-$(C_2)_{Si}]$. It has been pointed out that the defects stable even after thermal annealing above 1500 °C, which were observed by deep-level transient spectroscopy (DLTS) and photoluminescence (PL) spectroscopy, are likely to be aggregated forms of carbon interstitials.

We have identified the negatively charged dicarbon antisite defect $(C_2)_{Si}$, in which two carbon atoms share a silicon site, in electron-irradiated *n*-type 4*H*-SiC by means of combined EPR measurements and *first-principles* calculations[2)]. The samples used were single-crystals of 4*H*-SiC (nitrogen-doped, room-temperature carrier concentration 1×10^{17} cm^{-3}). The samples were irradiated by 2 MeV electrons at different temperatures (60 °C, 400 °C and 800 °C) and to various doses ($2\times10^{17}\sim4\times10^{18}$ e/cm^2).

The HEI5 and HEI6 EPR centers (S=1/2, C_{1h} symmetry) are associated with dicarbon antisite defects $(C_2)_{Si}$ at Si(k) and Si(h) site, respectively. This assignment is based on a comparison of the measured and calculated hyperfine tensors of ^{13}C and ^{29}Si atoms as far as the second neighborhood around the dicarbon (C_1-C_2) at silicon site. Each of C_1 and C_2 atoms is strongly bonded to three carbon atoms with sp^2 hybrid orbital. The unpaired electron is localized (54% and 53% for HEI5 and HEI6, respectively) on 2p (π) orbital of the C_1 atom. The 2p (π) orbital of the C_2 atom is doubly occupied. The calculated (0/-) and (-/2-) levels of $(C_2)_{Si}$ are E_C–1.4 eV and E_C–0.4 eV, respectively. Thus, dicarbon antisites are stable in a single negative charge state under a wide range of *n*-type samples. We found that the defects can be created under a wide range of irradiation conditions. Observation of the immediate formation of HEI5/6 centers at the minimum dose of 2×10^{17} e/cm^2 suggests the existence of carbon antisite defects C_{Si} in the *as-grown* samples. Annealing studies revealed several atomic processes such as recombination of carbon interstitials with carbon vacancies and formation of carbon aggregates. Those processes were activated at about 1000 °C, which is consistent with the temperature range for forming PL centers likely to be related to carbon aggregates. As theoretically predicted, the dicarbon antisite $(C_2)_{Si}$ is much more stable than the dicarbon interstitial defect (or carbon split interstitial) $(C_2)_C$, in which two carbon atoms share a carbon site.

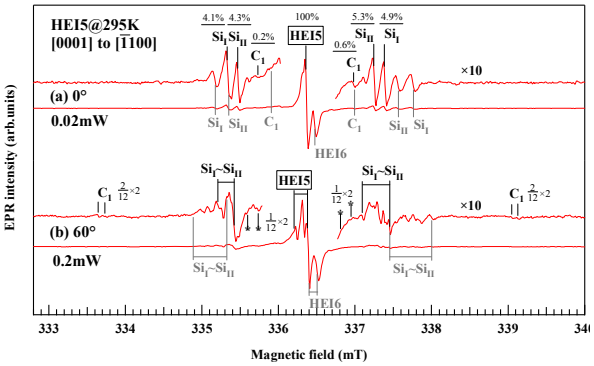

Fig. 1 Hyperfine structure of HEI5 center in 4*H*-SiC.

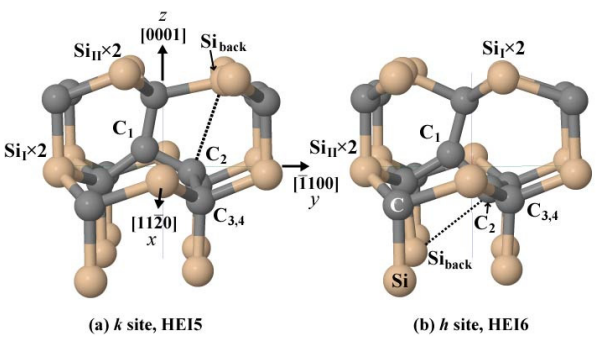

Fig. 2 Atomic structure of dicarbon antisite defects (HEI5/6 centers) in 4*H*-SiC calculated by *first-principles* calculation.

References

1) J. Isoya *et al.*, Phys. Status Solidi B 245 (2008) 1298.
2) T. Umeda *et al.*, Phys. Rev. B 79 (2009).

1-12 Development and Test of Internal Charge Measurement System for Satellite

H. Miyake, S. Numata, Y. Tanaka and T. Takada

Tokyo City University

The charge accumulation in dielectric materials irradiated by high energy particles in space environment causes the discharge accident. Therefore, we need to measure the charge distribution in the bulk of dielectric materials. We have had many experiences to measure the charge distribution in dielectric materials under electron-beam irradiation. However, the charge accumulation measurement in dielectrics irradiated by proton-beam was not carried out by any researchers. We have carried out the measurement of space charge distribution in PI films which are used for MLI during proton-beam irradiation. From the results, we could obtain charge accumulation behaviour in the bulks.

放射線帯の捕捉荷電粒子による人工衛星の帯・放電を起因とした運用異常が近年多数報告されている[1)]。そこで、本研究では人工衛星の表面材料に使用されているポリイミド(PI)試料に放射線帯の荷電粒子であるプロトンを照射し、PI材料内の帯電挙動について計測、検証を行った。

宇宙機の表面材料に用いられるPIフィルム125 μmを試料に用いた。プロトン照射には日本原子力研究開発機構、高崎量子応用研究所所有の3MVタンデム加速器を用いた。プロトン照射は真空下で加速電圧2.5 MV、電流30 nA/cm^2、照射時間20分である。照射前、照射中・後にかけて連続的にPEA法により空間電荷分布測定を行った。また、照射5日後に、表面帯電を模擬し直流高電圧を試料に60分間印加し空間電荷分布の測定を行った。印加電圧は印加電界が100 kV/mmになるように12.5 kVとし、プロトン照射面側から印加した。内部帯電の計測はパルス静電応力法(PEA法)を用いて行った[2)]。

Fig. 1にプロトン照射PI試料内の空間電荷分布と電界分布を示す。a)はプロトン照射開始1分後の最大電荷蓄積時の空間電荷分布結果を、b)には照射5日後に直流高電圧を印加した際の材料内の空間電荷分布の経時変化の測定結果を、c)には同b)での印加直後、印加終了直前、直後の電界分布をそれぞれ示している。a)より、照射側電極より90 μmの位置に11.5 C/m^3 の正電荷の蓄積が観察された。同実験条件によるPI試料内のプロトン飛程を算出すると84 μmとなる。試料内正電荷ピークと比較し7%程度の誤差であり、正電荷信号は照射されたプロトンに起因するものであると考えられる。照射を行った試料に直流高電圧を印加すると、b)より、材料内に多量の正負のヘテロ電荷の蓄積が観察される。ヘテロ電荷の蓄積量は電圧印加時間の経過と共に増加している。ヘテロ電荷の形成位置は計算飛程と一致する。c)より高電圧印加終了直後の電界分布は終了直前の電界分布とヘテロ電荷形成前の電界分布との差分に一致することも確認でき、プロトン照射時の正電荷蓄積位置近傍を境に電界が反転している。更に、試料内の未照射の試料では同様の高電圧印加を行っても試料内に電荷蓄積は確認できないことから、材料内のヘテロ電荷はプロトンによって材料の分子構造が切断されたことに起因する空間電荷分極によって形成されているものと考えられる。今後は照射線量や印加電界等の条件を変更し、プロトン照射材料の電荷挙動の解析を行っていく予定である。

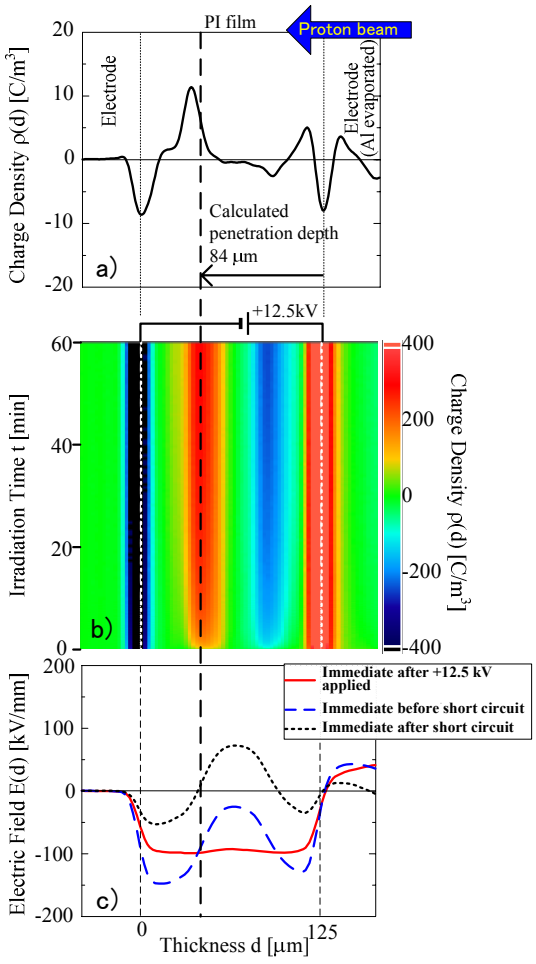

Fig. 1 Charge density and electric field distribution in PI film irradiated by protons. a) Charge density distribution (Maximum accumulation), b) Charge accumulation behavior under +12.5 kV with time progress, c) Electric filed distribution.

References

1) H. C. Koons et al., Proc. of the 6th Spacecraft Charging Technology Conference, Air Force Research Laboratory, (1998) 7-11.
2) T. Takada et al., IEEE Trans. Plasma Sci., Vol. 34, No. 5, (2006) 2176-2184.

1-13 Gamma-Ray and Electron Irradiation Tests of Quartz Optical Fiber Transmission Line for Commercially Available Multi-kW High Power Yb-doped Fiber Lasers

E. Minehara [a)], T. Kitagaki [b)] and T. Washiya [b)]

[a)] Laser Science and Technology Promotion Office at Turuga, KPSI, JAEA / Research and Development Department, The Wakasa Wan Energy Research Center,
[b)] Advanced Reprocessing Unit, ANSRD, JAEA

In order to cut and to disassemble pressure vessels and many kinds of structural components in nuclear reactor plants using a commercially available multi-kW high power Yb-doped fiber laser, we need a quartz optical fiber transmission lines to feed the powerful fiber laser light from the fiber laser to the old nuclear power plants components and other material around and inside radio-isotope activated and contaminated devices and components of the nuclear power plants. The figure 1 shows a typical industrial laser example of fiber laser device. The laser oscillator amplifiers, laser diodes and other vital components are installed in the one box far away from radio-activated area of the nuclear power plant shown in Fig. 1, but the optical fiber must be used and hanged very close to the most-activated area in the plant. Therefore, we have to use the radiation-resistant optical fibers in the nuclear power plant disassembling programs.

A few years ago, we tested to irradiate the optical fibers for 1,000 hours or longer using Takasaki Co60 gamma-ray irradiation facility, while we had intermittently and regularly injected to transmit the multi-kW fiber laser light through the transmission line optical fiber once an hour or so. We resultantly found all of the IPG GmbH packaged optical fibers were damaged and burned out after the hundreds of kGy exposure. On the other hands, the irradiation-resistant optical fiber made by one Japanese company showed very long life-time or no deteriorated performance over thousands of hours under 10 kGy/h or higher exposure rate with no transmission of the high power laser light. Here, we plan to reproduce the gamma-ray damages and fiber-laser burning accidents for the radiation-resistant optical fibers using the 54 domestic quartz optical fibers, Takasaki Co60 irradiation facility and the fiber laser at Yokohama factory of LX Co. Ltd.

In the experiments shown in Figs. 1, 2, and 3, we decided to make 2 steps to irradiate the fibers with the gamma-rays and to inject the high power laser light into the irradiated fibers. We irradiated 7 times the 54 our gamma-ray exposure fibers by the gamma rays for about 10 kGy, 100 kGy, 1 MGy, 1 MGy, 2 MGy, 2 MGy and 10 MGy exposures. Whenever the gamma-ray exposure was finished, we used to send them to the LX Yokohama factory, and we tried to inject and to transmit the high power laser light through the 54 fibers under the clean filtered air. The first accident happened to damage thin two stainless-steel pipes of the No.3 fiber-receptacle socket around the inlet fiber edge after the 100 kGy exposure. And resultantly the third of the four 0.8 mm diameter core fibers was damaged seriously and its outer Nylon film burned out and the third did not become usable again. The second accident also eventually happened to damage quartz optical fiber edge surface and to burn two other fibers around the damaged one because tiny dusts remained after our repeated wet and dry compressed and flammable DME gas cleaning. Up to now and up to 20 MGy, we could conclude we could not find any fiber line broken accident like the IPG GmbH fibers except for the edge damage accident and receptacle damage one. These accidents are thought to be no intrinsic deterioration of the fiber. Electron irradiation was not performed here because of some difficulties in interpolating both irradiations data.

Fig. 1 IPG-made Fiber laser, 3-dimensional work bench, fibers, monitor-microscope and power meter.

Fig. 2 Home-made fiber edge receptacles in the breadboard.

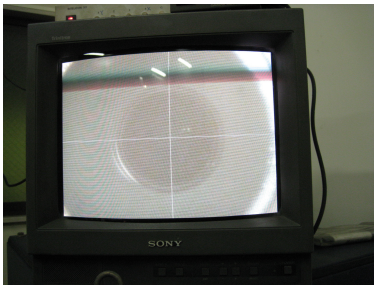

Fig. 3 A video image of the fiber edge surface and a dust.

1-14 Radiation Resistance of Optical Fibers for Laser Transmission

T. Kitagaki [a)], E. Minehara [b)], T. Kobayashi [a)], T. Washiya [a)] and M. Myochin [a)]

[a)] Advanced Reprocessing Unit, ANSRD, JAEA [b)] Quantum Beam Science Directorate, QuBS, JAEA

ANSRD is developing advanced laser cutting technology with the optical fiber transmission for the future reprocessing plant. In this study, radiation resistance of optical fibers was estimated by gamma-ray irradiation test.

Irradiation test was executed to evaluate the influence on the laser characteristics and the difference of dose rate, so the dose rate and the exposure time under gamma-ray irradiation condition were parameterized. The specifications of the optical fibers are shown as follows. Supplier is Mitsubishi Cable, core material is pure silica, length is 40 m and core diameter is φ0.2 mm and φ1.0 mm.

The irradiation test is carried out at the Co-60 gamma ray irradiation facility in JAEA Takasaki. The dose rates were 0.2 kGy/h, 1.0 kGy/h, 10 kGy/h and the exposure time was adjusted as a total dose was 200 kGy respectively. The transmittance was measured by near-infrared spectroscope at outside of the irradiation cell and halogen lamp was used as the light source. Moreover, transmittance at the longer irradiation time with high dose rate and recovery effect of transmittance by laser transmission called photo-breaching effect were evaluated in this test. The average output power is 160 W of pulse YAG laser used as the laser transmission and the laser beam transmission was executed two minutes at every one hour interval. The output power transmitted from the optical fiber is measured by a power meter.

Figure 1 shows the test result as the dose rate is parameter. The transmittance at a wavelength of 1070 nm that is the wavelength area of fiber laser and YAG laser was evaluated. When the dose rate is 1.0 kGy/h and 10 kGy/h, the transmittances of the core diameter φ1.0 mm is slightly lower compared with φ0.2 mm, but differences between two kinds of core diameter are little. When the dose rate is 10 kGy/h, transmittances decreases to about 70%, although other conditions at the same dose decreases to about 80%. Therefore, it found out that the effect of core diameter is a little, but high dose rate more than 1.0 kGy/h accelerate defect. Decrease of transmittance occurred by inside defects in silica corresponding to several wavelengths. In the low dose rate, the defect is thought to be affected by NBOHC [2)], one of the inside defect. In the high dose rate, it seems that different inside defect occurred.

Figure 2 shows the test result when the irradiation time was long and the YAG laser was transmitted. When the total dose was 10 MGy, transmittance of the core diameter φ0.2 mm was about 60%. When the total dose was 2 MGy, transmittance of the YAG laser was about 95%. Although the core diameter of the fiber transmitted YAG laser was different from the others, the difference of the core diameter hardly affects transmittance as previously indicated. So, it was found that the recovery rate of transmittance by the photo breaching effect is about 15% at 2 MGy.

The energy of the laser beam equivalent for the decrease of transmittance is absorbed to the optical fiber and exchanged into heat, therefore the heat influence on the clad layer is concerned. However, it is little problem because the radiation deterioration was enough little when the YAG laser was transmitted. In the future, the photo breaching effect should be evaluated when the laser power is different from the YAG laser used in this test.

In conclusion, the influence on the diameter of the optical fibers and the differences of dose rate were evaluated. The deterioration mechanism that is caused when a dose rate is higher than 1 kGy/h will be clarified in the future.

References

1) Y. Tooya et al., Proc. GLOBAL2005.
2) K. Toh et al., Meas. Sci. Technol. 17 (2006) 955-959.

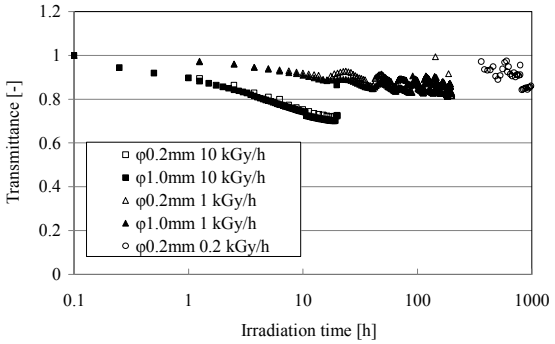

Fig. 1 Transmittance change when dose rate and core diameter of optical fibers is parameter, and total dose is 200 kGy.

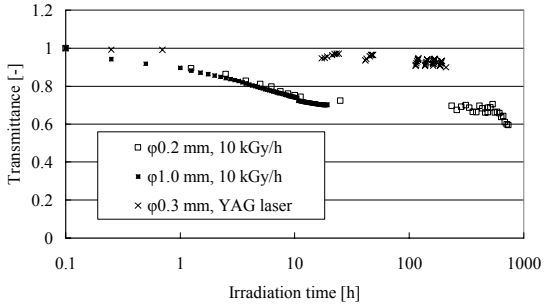

Fig. 2 Transmittance change as the irradiation term is long and the YAG laser is transmitted.

1-15 Performance Test of AC Servo Motor for ITER Blanket Remote Robot under High Gamma Ray Radiation

S. Kakudate [a)], N. Takeda [a)], K. Taguchi [a)], Y. Matsumoto [a)], A. Idesaki [b)], N. Morishita [b)], K. Shibanuma [c)] and K. Koizumi [a)]

[a)] Division of ITER Project, FRDD, JAEA,
[b)] Environment and Industrial Materials Research Division, QuBS, JAEA,
[c)] Division of Advanced Plasma Research, FRDD, JAEA

The inner lining (termed a "blanket") of the vacuum vessel (VV) of the International Thermonuclear Experimental Reactor (ITER) will be activated by 14 MeV neutrons generated by fusion reactions. Maintenance of the blanket in the VV must be carried out under high gamma ray radiation conditions (~0.5 kGy/h) and in the presence of contaminated dust such as beryllium, carbon and steel. All interventions inside the VV therefore must be performed remotely. The blanket is composed of about 400 modules, designed for remote individual replacement[1)].

Figure 1 shows the robot for maintenance of the blanket module. The robot has 18 degrees of freedom and is driven by an electrical AC servo motor[2)] with sensor for position measurement. Irradiation tests for AC servo motor were carried out from 1995 to 2001 with the cooperation of JAEA QuBS to develop the electrical insulator and the mechanical lubricant under high gamma ray irradiation[3)]. However, the AC servo motor that was developed is too expensive. It is necessary to reduce the manufacturing cost of this developed AC servo motor in order to satisfy ITER requirements. To reduce costs, a commercially available AC servo motor used in viewing/inspection robots that are designed for fission reactor was selected. The Objective of this irradiation test is to clarify the performance limits of a commercially available AC servo motor under gamma ray irradiation. Table 1 shows the materials for AC servo motor used in these irradiation tests.

We have carried out this irradiation test of six AC servo motors under gamma rays from the beginning of Nov. 2007. As a result, one of six motors stopped due to radiation damage of electric insulator under total dose of 3.47 Gy. The remained five motors continued to work after having been irradiated with a total dose of about 8 MGy as shown in Fig. 2. We will confirm the criteria for estimating the life time of AC servo motor through this irradiation test.

References

1) ITER Technical Basis, ITER EDA Documentation Series No. 24, IAEA, Vienna (2002).
2) H. Sugimoto et al., Sougou-denshi-shuppan, (2005) (in Japanese).
3) K. Obara et al., JAERI-Tech 99-003(1999).

Fig. 1 Robot for remote maintenance for ITER blanket.

Table 1 Materials AC servo motor.

Parts for AC servo motor	Materials
- Insulator of winding for motor stator	Varnish (Polyester)
- Grease for lubricant	Rad-hard grease(GK-1)
-Cable for power and sensor	Insulator: Ethylene Tetra Fluoro
	Outer cover: Chlorosulfonated polyethylene
- Connection for lead line	Sensor: polylefin
	Motor: Ethylene Tetra Fluoro

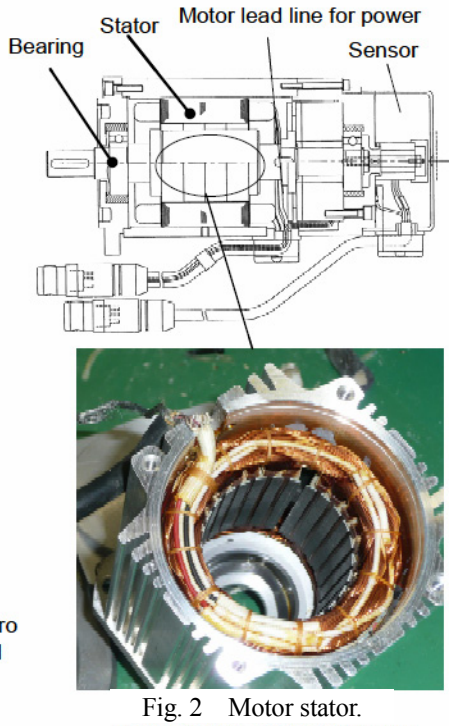

Fig. 2 Motor stator.
(total dose : around 8 MGy)

1-16 Gamma-Ray Irradiation Test to Investigate Acceptable Total Dose of Amplifier Circuit for Strain Gauge Using Rad-Hard Operational Amplifier for Remote Maintenance System of ITER

N. Takeda [a)], K. Taguchi [a)], S. Kakudate [a)], Y. Matsumoto [a)], H. Kozaka [a)], A. Idesaki [b)], M. Gokan [b)], N. Morishita [b)], S. Baba [c)], H. Okamoto [c)] and T. Hirose [c)]

[a)] Division of ITER Project, FRDD, JAEA, [b)] Environment and Industrial Materials Research Division, QuBS, JAEA, [c)]Ryoei Technica Corp.

The ITER, an international fusion experimental reactor, requires remote maintenance for its components because of the hostile environment in the reactor, especially gamma-rays. The radiation environment during the maintenance operation is about 0.5 kGy/h and therefore, the total dose is 1 MGy if the maintenance operation takes three months.

The irradiation test has been performed for components of the ITER remote maintenance system [1,2]. Regarding instrumentation and operational amplifiers for strain gauges, an irradiation test was performed in order to examine which amplifier on the market can be used from the viewpoint of radiation-hardness and a rad-hard operational amplifier, HS1-5104ARH-Q, functioned without deviation of characteristics from specification until the guaranteed value, 1 kGy, and had continued to function from 2 kGy till 471 kGy with some of characteristics deviating from specification [3,4]. The present study aimed at continuation of the irradiation test to investigate the behavior of the actual circuit for the strain gauge using the tested amplifier, HS1-5104ARH-Q.

The dose rate in the irradiation test was almost the same value as that in the real environment of the ITER maintenance operation, 0.5 kGy/h. Figure 1 shows the tested amplifier circuit. Three samples (No. 5542, 5543, 5545) of the operational amplifier HS1-5104ARH-Q were used for the irradiation test with one reference sample (No. 5536). The circuit was irradiated continuously for 1,653 hours and 6 minutes with the average dose rate of 0.45 Gy/hr and the total does was therefore 744 Gy. Several in-situ measurements were performed and one of the items was to measure the output voltage of the amplifier circuit with certain value of AC/DC bridge input voltage. Before and after the irradiation, their electrical characteristics were also measured such as input bias current, offset voltage, open-loop gain and so on.

Regarding the electrical characteristics, the open-loop gains Avol+ of the samples had drastically reduced: it was 286.1 kV/V before the irradiation and was 1.8 kV/V after the irradiation for the sample No. 5542, as an example. However, the effect of irradiation was not clearly found on the characteristics of the amplifier circuit. Figure 2 shows trend of the output voltage of the amplifier circuit for the bridge input voltage of DC -5 V. The output voltages indicates almost the same value as the initially estimated value (-1.05 V) and no effect can be found in the graph during the irradiation. The same tendency can be seen for the AC bridge input voltage. Therefore, there is a possibility that the amplifier circuit can be used continuously during the irradiation, even after the operation amplifier is severely damaged. The further investigation is needed to identify the effect of the irradiation on the amplifier circuit.

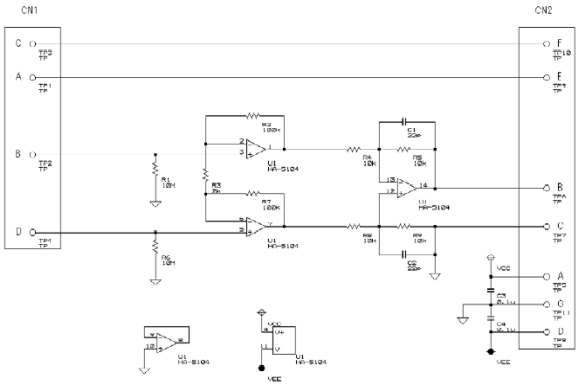

Fig. 1 Amplifier circuit for irradiation test.

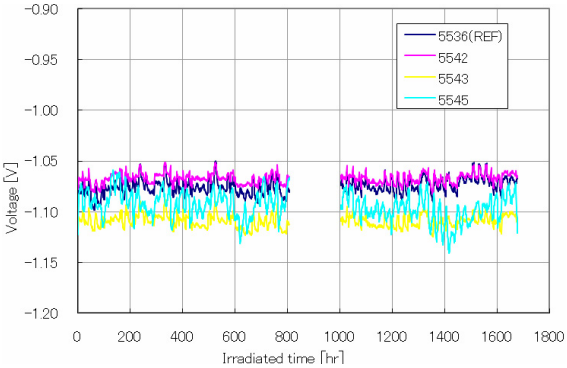

Fig. 2 Trend of output voltage for bridge input voltage of DC -5 V.

References

1) K. Obara et al., JAERI-Tech 99-003 (1999).
2) K. Obara et al., J. Robot. Mechatron. Vol. 10, No. 2 (1998) 121-132.
3) N. Takeda et al., JAEA Takasaki Ann. Rep. 2006 (2008) 18.
4) N. Takeda et al., JAEA Takasaki Ann. Rep. 2007 (2008) 17.

1-17 Gamma-Ray Irradiation Test of Centrifugal Contactor with Magnetic Bearing System

K. Kosugi, K. Fujizaku, N. Okamura, H. Ogino and Y. Nakajima

Nuclear Cycle Engineering Department, NFCEL, JAEA

In Japan Atomic Energy Agency (JAEA), an innovative centrifugal contactor system has been developed for the advanced aqueous reprocessing of FBR fuel. In this study, we carried out gamma-ray irradiation test of centrifugal contactor with magnetic bearing system to estimate the radiation resistance. The equipments stopped several times under irradiation, and were not finally reactivated of two different factors, one was abrasion of the touchdown bearing and adhesion to main shaft, the other was a trouble of the IC. Accumulated dose of the equipments was 3.7-4.7×10^8 R.

JAEAでは、次世代の使用済み核燃料の再処理用の抽出装置として小型で高性能を有する遠心抽出器の開発を進めている。転がり軸受型遠心抽出器の装置寿命は駆動部に依存し、その構成部品である転がり軸受の機械的劣化、あるいはグリース劣化が主要な寿命因子である。とくに、グリース劣化は荷重や発熱、磨耗粉やミストの混入、放射線等が複合的に影響を及ぼすため、潤滑寿命を定量的に推定することが難しい。現行機では、グリースの耐放射線性を考慮すると、1～1.5万時間程度が装置寿命となるものと考えられる。プラント機器としては、プラント稼働率、保守コスト、廃棄物発生量等の観点から、装置寿命は長いほど有効であることは明白である。そこで、装置寿命の飛躍的向上を図るため、寿命推定の不確定要素が多いグリースを使わず、回転軸を浮上させ非接触でロータを回転できる磁気軸受に着目し、これを駆動部に適用した磁気軸受型遠心抽出器を開発している[1)]。

これまでの開発の中で、磁気軸受型遠心抽出器に対し10^8 R程度のγ線照射を実施し、その結果、モータの巻線等に耐放射線性を有する材料を使用する必要があることが明らかとなった[2)]。これに伴い、モータの配置を内蔵型からマグネットカップリングを介し軸受部・ロータ部と接続する外置型へ設計変更し製作した。

この耐放射線性磁気軸受型遠心抽出器2台を用い、耐放射線性能の確認及び設計変更した箇所の運転時の安定性等の評価を目的とし、高崎量子応用研究所ガンマ線照射施設にて照射線量10^9 Rを目途とした照射試験を実施した。

本試験では、遠心抽出器はその中心が線源カバー表面から約90 cmとなる位置に設置し（Fig. 1参照）、3500 rpmの定常運転状態で照射を行った。平均線量率は1.5 × 10^5 R/hであった。照射量の増加に伴い頻繁に制御不良による停止が発生するようになり、最終的に、1号機は累積照射線量4.7×10^8 R、2号機は3.7×10^8 Rの照射で再起動が不可能となった。1号機の再起動不能となった制御不良の原因は、アミド樹脂製の下部タッチダウンベアリングの摩耗により発生した摩耗粉が主軸に固着したことで浮上制御ができなくなったためであった。Fig. 2に1号機の主軸及びその付着物の状況並びに摩耗した下部タッチダウンベアリングを示す。2号機の制御不良の原因は、照射室内に配置した中継ボックス内の方形波発生ICの不具合により位置センサ搬送波が出力されなくなったためであった。

実施設における抽出器の年間照射線量の評価値は約1.0×10^8 R/年であり、今回の結果は3-5年の運転に相当する。今後は、下部タッチダウンベアリングの照射線量と摩耗状況及び他の材料の適用等について検討を進め、遠心抽出器の性能向上を図る。

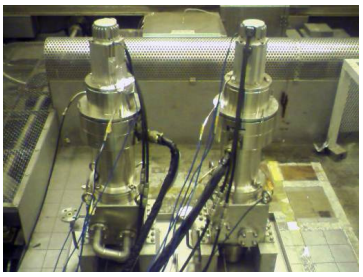

Fig. 1 Irradiated centrifugal contactors with magnetic bearing system.

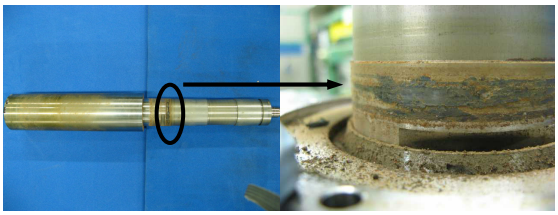

Main shaft and adhesion material

Lower touchdown bearing

Fig. 2 Main shaft and lower touchdown bearing of No.1 equipment.

References

1) N. Okamura et al., Proc. Global 2007, Boise, Idaho.
2) Y. Arai et al., Proc. Fall Meeting of AESJ, Sapporo, Japan (2006).

1-18 Gamma-Ray Irradiation on Electric Cables Used in Nuclear Fuel Fabrication Plants

A. Sasahara [a)], H. Narita [b)], S. Yamakawa [b)], K. Shirai [b)] and H. Abe [c)]

[a)] Nuclear Technology Research Laboratory, Central Research Institute of Electric Power Industry,
[b)] Civil Engineering Research Laboratory, Central Research Institute of Electric Power Industry,
[c)] Nuclear Facility Safety Research Unit, NSRC, JAEA

In nuclear grade electric cables used under gamma-ray field such as nuclear fuel fabrication area, the properties of organic polymers as electric cable insulation and covered materials may be affected by gamma-ray exposure [1)] and consequently, the burning behavior of the electric cables under fire events may be changed [2)]. In this study, gamma-ray exposed electric cable samples are prepared for use in the flame test to investigate the burning behaviors.

The nuclear grade electric cables used in this study are no-halogen flame retardant cables. They are mainly composed to copper wire and polyethylene sheath. Two types of cables, electric power transmission and control signal cables, are exposed in this study. Table 1 shows the size and number of cables.

The gamma-ray exposure to the electric cables was carried out at the cell No.6 of the Takasaki Advanced Radiation Research Institute of Japan Atomic Energy Agency (JAEA). The plate geometry ^{60}Co (45 cm (height) × 160 cm (length)) was used as gamma-ray source whose intensity was about 7.4 PBq in Dec. 2008. Target dose was determined around 10^5 Gy in which the degradation in the mechanical properties of organic polymers will appear. Thus, sixteen hours exposure was continuously carried out at JAEA. The irradiated positions of cable samples from the front of plate gamma-ray source, where can archive target dose, were estimated on the basis of measured dose rate for the cell No.6, JAEA and they were from 18 to 28 cm, depending on the horizontal axial length positions along the plate source.

The eighteen cable samples were fastened up narrow area (18 cm × 100 cm) on the wire netting and their center was adjusted to that of the plate gamma-ray source to achieve uniform exposure. The size of wire netting is 25 cm in width and 100 cm in length and its both ends were held by two poles keeping parallel to the plate gamma-ray source. The wire netting was put at around 30 cm distance from the plate source as shown in Fig. 1 and the samples were continuously exposed for 16 hours from on 15th to on 16th December 2008.

Dose for cable samples slightly depends on fastened position on the wire netting and its range was estimated from 0.8×10^5 to 0.95×10^5 Gy. This range met target one.

References

1) A. Charlesby, *Atomic Radiation and Polymers*, Pergmon Press LTD, (1960).
2) A. Nakayama *et al.*, Hitatch Densen 26 (2007) 67-70.

Table 1 Size and number of cable samples.

Type of cable	Size and length	Number
Electric power transmission	ϕ10 × 400 mm	3
	ϕ10 × 700 mm	3
	ϕ10 × 1500 mm	3
Control Signal	ϕ10.5 × 400 mm	3
	ϕ10.5 × 700 mm	3
	ϕ10.5 × 1500 mm	3

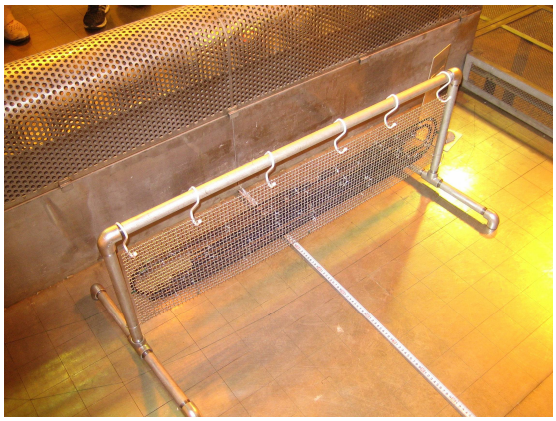

Fig. 1 Exposure geometry of cable samples.

1-19 Gamma-ray Irradiation Durability of Silica Based TRPEN Adsorbents for the Extraction Chromatography

Y. Koma, K. Matsumura, Y. Sano and S. Watanabe

Advanced Reprocessing Unit, ANSRD, JAEA

In the framework of the Fast Reactor Cycle Technology Development Project (FaCT Project), the extraction chromatography technology is under development for Am and Cm (actinides(III)) recovery process as a part of spent fuel reprocessing[1]. The technology uses the porous SiO_2 support coated with styrene-divinylbenzene polymer (SiO_2-P) and an extractant on its surface. Some extractants including TODGA (N,N,N,N-tetra(n-octyl)diglycolamide) and R-BTP (2,6-bis(5,6-dialkyl-1,2,4-triazine-3-yl)-pyridine) were examined on their property of degradation due to gamma-ray irradiation[2]. In succession, extractant TRPEN (N,N,N',N'- tetrakis((5-alkoxypyridin-2-yl)meth-yl)ethylenediamine) for actinides(III)/lanthanides(III) separation was investigated in order to compare candidate extractants.

The TRPEN/SiO_2-P adsorbents of R=octyl (namely TOPEN) were immersed in HNO_3 solution, and they were irradiated at room temperature with Co-60 gamma-rays at a dose rate of 3 kGy/h. The maximum accumulated dose was 4 MGy. The adsorbents separated from the acid solution were provided for the batch adsorption/elution experiments, and the concentrations of the TOC in the residual acidic solution were evaluated to estimate the amount of the eluted organic compounds. Colors of the adsorbents and solutions turned to yellow or brown by irradiation. The resulted adsorbent was provided for TG/DTA analysis.

Figure 1 shows the distribution coefficients of Cd as a stand-in of Am/Cm onto the TRPEN/SiO_2-P adsorbent irradiated with the gamma-ray. The distribution coefficient for unirradiated adsorbent was 6.4 cm^3/cm^3, whereas that was somewhat decreased with absorbed dose up to 4 MGy, although the values were rather scattered. Concentration of the HNO_3 influenced to lower the distribution coefficient. Decrease of adsorption capability is less than other extractants tested[2].

Figure 2 shows leakage of TRPEN into the nitric acid solution during irradiation. For the 0.1 M HNO_3 solution, the leakage was almost constant at 4-5% for dose of 1 MGy or higher. On the other hand, the leakage was proportional to the dose for 1 M $NaNO_3$ solution, and reached at 17% for 4 MGy irradiation. This must be explained in consideration of protonation reaction at high acidity. The behavior of the distribution ratio and the leakage for TRPEN adsorbent was inconsistent. This result and the GC-MS analysis of solution suggest that octyl group of TRPEN is cleaved to dissolve in aqueous solution, and the resulting extractant of counterpart holds extractability as a hypothesis.

The unirradiated adsorbent contacted with nitric acid decomposes at 270 °C or higher and shows exothermic peaks at 270, 350 and 500 °C in air. Due to irradiation, the peaks disappeared and the weight of adsorbent starts to decrease at 140 °C. The adsorbent seems stable up to 140 °C even when irradiated.

Acknowledgements

We would like to thank Mr. R. Yamagata at Irradiation Service Section in TARRI for his assistance on the experiment. Present study is the result of "Development of Extraction Chromatography for Am and Cm Recovery" entrusted to JAEA by the Ministry of Education, Culture, Sports, Science and Technology of Japan (MEXT).

References

1) H. Funasaka and M. Itoh, Global 2007, Boise, USA (2007) 259-267.
2) Y. Koma, Y. Sano, S. Watanabe, et al., JAEA Takasaki Ann. Rep. 2007 (2008) 21.

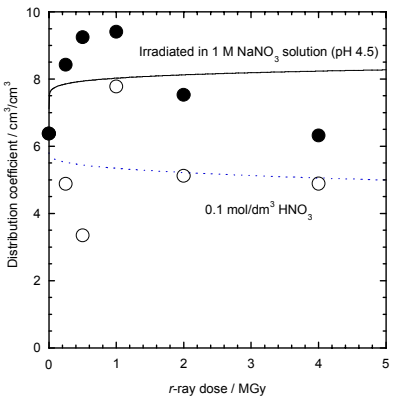

Fig. 1 Distribution coefficient of Cd onto the irradiated TRPEN adsorbents from 0.025 M Cd solution.

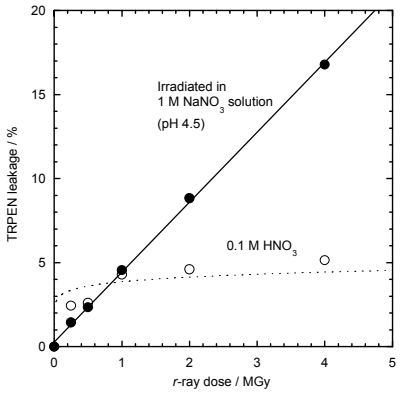

Fig. 2 Leakage of TRPEN into the solution during irradiation.

1-20 Study on Stability of Cs·Sr Solvent Impregnated Resin against Gamma Irradiation

H. Hoshi [a)], T. Kikuchi [a)], Y. Morita [a)] and T. Kimura [b)]

[a)] Division of Fuels and Materials Engineering, NSED, JAEA,
[b)] Division of Environment and Radiation Sciences, NSED, JAEA

Minimization of radioactive waste from reprocessing process of spent nuclear fuel is strongly desired. We develop an advanced technology for separation of heat generating elements (Cs and Sr) from high level waste to optimize radioactive waste by its characteristics. Recently, some analogues of calix-crown or crown ether extractant were reported on specific selectivity for Sr or Cs, respectively[1,2]. In our previous study, some novel solvent impregnated resins (SIRs) were prepared and these SIRs indicated promising ability to separate Cs and Sr from other typical fission products dissolved in nitric acid solution.

An extractant and a modifier were impregnated into porous silica, which is embedded styrene divinyl benzene polymer on the surface. These adsorbents contacting with nitric acid solution were exposed to gamma ray in a vial. After the gamma irradiation, adsorbents were filtrated through a membrane filter. The adsorption capacity was examined by using irradiated adsorbents after drying.

Cs SIR has a significant selectivity for Cs by size exclusion. As shown in Fig. 1, the capacity of Cs decreased with concentration of nitric acid solution (> 4 mol/dm^3). In dilute nitiric acid solution (< 4 mol/dm^3), the difference of capacity between irradiated resin and non-irradiated one was neglibibly small. Thus, dissolution of extractant into aqueous phase is more significant than the decomposition by irradiation in dilute nitric acid solution. As the irradiated resin was analyzed by TG, peak area ratio indicated that alcohol modifier was decomposed more than extractant and it was presumed that decrease of capacity was due to the degradation of alcohol used as a modifier of adsorbent.

The capacity of Sr from 2 mod/dm^3 nitric acid solution onto irradiated Sr SIR at 25 ºC was shown in Fig. 2. As described above, similar tendency, the capacity of Sr decreased with concentration of nitric acid solution (> 4 mol/dm^3), was observed. However, Sr SIR showed remarkable stability against acidity and irradiation in dilute nitric acid solution (< 4 mol/dm^3) and capacity of Sr after irradiation was almost as same as fresh one. The irradiated Sr SIR was also analyzed by TG and some thermal peaks from degradation products were observed.

It is concluded that both Cs SIR and Sr SIR maintained their high selectivity for Cs and Sr, respectively, after irradiation. Decreasing ratio of adsorption capacity by irradiation can be estimated from these results. It contributes significantly for conceptual design of separation plant.

Present study is the result of "Development of separation technology of transuranium elements and fission products by using new extractants and adsorbents" entrusted to JAEA by the Ministry of Education, Culture, Sports, Science and Technology of Japan (MEXT). We are very grateful to Mr. Yamagata for his valuable cooperation in this study.

References

1) P. V. Bonnesen et al., Solve. Extr. Ion Exch., 18 (2000) 1079.
2) J. F. Dozol et al., EUR 19605EN, 2000.

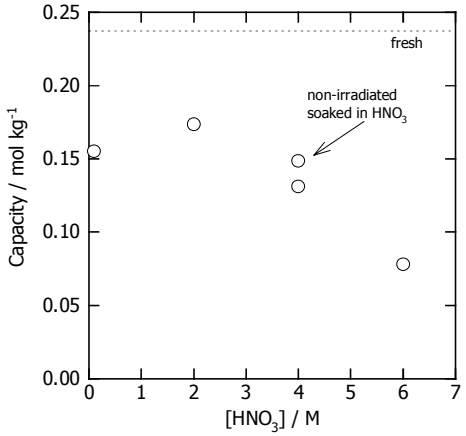

Fig. 1 Capacity of Cs onto Cs SIR from 4 mol/dm^3 nitric acid solution. SIR was irradiated by contacting with nitric acid solution. Capacity of Cs was obtained at 25 ºC. Dose: 267 kGy, rate: 2.3 kGy/h, time: 116 h.

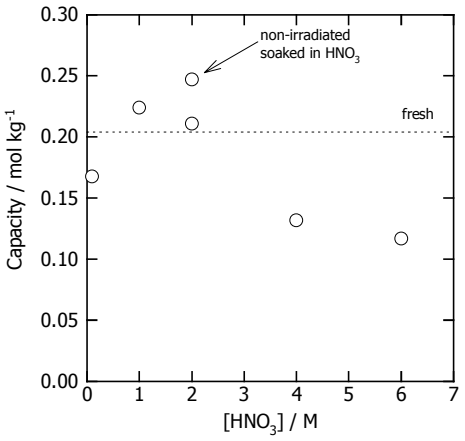

Fig. 2 Capacity of Sr onto Sr SIR from 2 mol/dm^3 nitric acid solution. SIR was irradiated by contacting with nitric acid solution. Capacity of Sr was obtained at 25 ºC. Dose: 267 kGy, rate: 2.3 kGy/h, time: 116 h.

1-21 Study on Degradation Properties of NBP Precipitant by γ-Ray Irradiation

M. Nogami [a)], Y. Sugiyama [a)], T. Kawasaki [a)], M. Harada [a)], Y. Kawata [b)], Y. Morita [b)], T. Kikuchi [c)] and Y. Ikeda [a)]

[a)] Research Laboratory for Nuclear Reactors, Tokyo Institute of Technology,
[b)] Division of Fuels and Materials Engineering, NSED, JAEA, [c)] Mitsubishi Materials Corporation

We have been developing a novel reprocessing system for spent FBR fuels based on two precipitation processes[1,2]. In this system, only U(VI) species firstly precipitate in nitric acid solutions dissolving spent fuels by using a pyrrolidone derivative (NRP) with low hydrophobicity and donicity which bring lower precipitation ability. Secondly the residual U(VI) and Pu(IV, VI) precipitate simultaneously using another NRP with higher precipitation ability. For developing the system, it is necessary to evaluate the stability of the precipitants under γ-ray irradiation. In our previous studies on the stability for several NRPs, their applicability was confirmed by the examination of the precipitation abilities of the samples irradiated in 3 mol·dm^{-3} (= M) HNO_3 solutions for U(VI)[3]. In this study, influence of concentrations of HNO_3 on the stability by irradiation was examined for *N*-*n*-butyl-2-pyrrolidone (NBP) which is one of the NRPs for lower precipitation ability, and the degradation mechanism was investigated.

A HNO_3 solution up to 6 M containing 2 M NBP was put into a Pyrex glass tube. Gamma-ray irradiation by the ^{60}Co source was performed at 12.2 or 13.0 kGy/h up to 1 MGy at room temperature under ambient atmosphere. One MGy is equivalent to the dose for some dozen cycles of use. The irradiated sample solutions were analyzed by a liquid chromatograph to determine the residual ratio of NBP.

For the appearances of the sample solutions of NBP after the irradiation, oil drops were observed in the samples irradiated in 6 M HNO_3 for 0.48 MGy and more. The drops disappeared afterward. Also, a gas continues to generate from all the samples of 6 M HNO_3 after irradiation. Almost no changes were observed for the other samples except coloration in the samples of lower concentrations of HNO_3. The changes in the residual ratio of NBP versus dose are shown in Fig. 1. The residual ratios of the samples for HNO_3 solutions up to 3 M are found to be decreased identically and linearly. Circa 20 % of NBP is degraded after the irradiation of 1 MGy. On the other hand, as expected from the appearances, it is found that the degradation of the samples of 6 M HNO_3 is more distinguished. The concentration of HNO_3 in the first precipitation step in our system is supposed to be 2 M, which has been found appropriate from the viewpoint of the degradation of NBP.

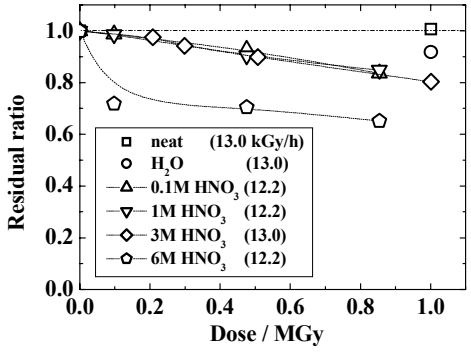

Fig. 1 Changes in residual ratio of NBP by γ-ray irradiation.

Oxalic acid (OX) was identified as one of the anionic degraded species as the result of the analysis of the irradiated samples in 3 M HNO_3 by ion chromatography. The concentration of OX was found to be increased with an increasing dose and OX was expected to be the major final degraded product. It was evaluated that ca. one third of the degraded NBP turned into OX, meaning that the rest is other degraded products. Although some other new peaks were observed in the chromatograms, they have not been identified. It was also found in the chromatograms that the concentration of HNO_3 was decreased with an increasing dose. In addition, the MS analysis revealed that almost all of the peak intervals of m/z in the irradiated sample were the multiples of 16.

It was proposed from the above results that the degradation of NBP starts from the cleavage of the pyrrolidone ring by the addition of oxygen atom originating from HNO_3, followed by the formation of chain monoamides and C4 compounds by the continuous addition of oxygen, leading to the generation of OX.

Acknowledgment

Present study is the result of "Development of Advanced Reprocessing System Using High Selective and Controllable Precipitants" entrusted to Tokyo Institute of Technology by the Ministry of Education, Culture, Sports, Science and Technology of Japan (MEXT). The authors also greatly thank Dr. R. Yamagata, Department of Advanced Radiation Technology, TARRI, JAEA, for his help at the irradiation facility.

References

1) Y. Ikeda et al., Proc. Intl. Conf. on Adv. Nucl. Fuel Cycles and Systems (GLOBAL2007), (2007) 1503.
2) Y. Morita et al., Proc. Intl. Conf. on Adv. Nucl. Fuel Cycles and Systems (GLOBAL2007), (2007) 1508.
3) M. Nogami et al., JAEA Takasaki Ann. Rep. 2007 (2008) 23.

1-22 Alpha-radiolysis of Organic Extractants for Separation of Actinides

Y. Sugo [a], M. Taguchi [b], R. Nagaishi [c], Y. Sasaki [a], K. Hirota [b] and Y. Morita [a]

[a] Division of Fuels and Material Engineering, NSED, JAEA, [b] Environment and Industrial Materials Research Division, QuBS, JAEA, [c] Division of Environment and Radiation Sciences, NSED, JAEA

1. Introduction

The radiolytic stabilities of the organic extractants for the separation of actinides have been commonly evaluated by the irradiation with gamma-rays as the most convenient method. However in the actual partitioning process of high-level radioactive waste from nuclear fuel reprocessing, the extractants will be exposed to alpha-rays emitted from actinides, as well as beta- and gamma-rays from various fission products. In this study, alpha-radiolysis of *N,N,N′,N′*-tetraoctyldiglycolamide (TODGA) in *n*-dodecane was investigated by the irradiation with helium ion beam accelerated by a tandem accelerator using the TC1 irradiation apparatus in the TIARA facility. The sample was also irradiated with ^{60}Co gamma-rays for comparison of the radiation chemical yields between alpha- and gamma-rays.

2. Experimental

The incident energy and the penetration ranges of helium ions were calculated by the IRACM code system [1]. The calculated incident energies of helium ions on the surface of the sample are plotted against a distance from the beam window to the sample in Fig. 1. The distance was adjusted to 35 mm so as to that the incident energy would be 5.0 MeV corresponding to the typical energies of the alpha-rays emitted from actinides. The penetration range of 5.0 MeV helium ions in the sample was evaluated to be 42 μm. Fluence F [ions nA^{-1} cm^{-2}] normalized by ion beam current per pass through the beam by moving up or down of the sample holder was determined to be 5×10^7 by a solid state track detector CR-39.

Since the thickness of the sample (500 μm) was sufficiently larger than the penetration range of the ions, absorbed dose was estimated on the assumption that whole the incident energy was given to the sample, and the sample solution was homogeneous. Dose D [Gy] per pass was calculated as follows.

$$D = 1.602 \times 10^{-10} F E_0 I \sigma w^{-1}, \quad (1)$$

where E_0 is the incident energy of the ions [MeV], I is the beam current [nA] monitored by Faraday cup, σ is the area of the sample [cm^2], and w is the sample weight [g]. Dose was controlled by changing the number of moving up and down of the sample holder.

The concentration of TODGA before and after irradiation was determined using a capillary gas chromatograph.

3. Results and Discussion

The concentration of TODGA in *n*-dodecane is plotted against dose in Fig. 2, in comparison between alpha- and gamma-radiolyses. This figure indicates the yield for the degradation of TODGA by alpha-rays is not more than that by gamma-rays. Radiation chemical yield G [μmol J^{-1}] was calculated using the following equation.

$$G = 10^3 C_0 k' \rho^{-1}, \quad (2)$$

where C_0 is the initial concentration of TODGA before irradiation [mol L^{-1}], and ρ is density of the solution [kg L^{-1}]. The coefficient k' [kGy^{-1}] obtained by fitting to the exponential curve. G-values for the degradation of TODGA by irradiation with alpha- and gamma-rays are 0.022 ± 0.001 and 0.080 ± 0.003 μmol J^{-1}, respectively. This result indicates that the radiolytic degradation of TODGA has been hitherto overestimated only by the irradiation with gamma-rays as the conventional means.

Acknowledgments

The authors are grateful to Dr. T. Kimura for his useful discussion. They are much indebted to Dr. K. Akamatsu and Dr. Y. Hase for their help with the irradiation.

Reference

1) S. Tanaka et al., JAERI-Data/Code 97-019 (1997).

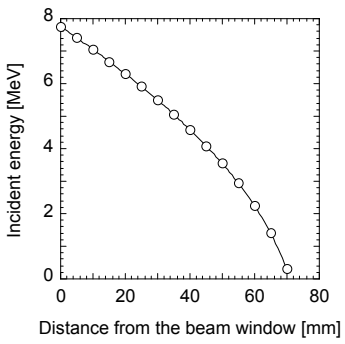

Fig. 1 Incident energy of helium ions on the surface of the sample.

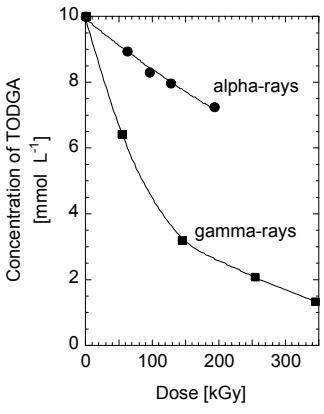

Fig. 2 Degradation of TODGA in *n*-dodecane by irradiation with alpha- and gamma-rays.

1-23 Effect of Electron Beam and Gamma-ray Irradiation to Anion Exchange Membrane on Efficiency of its Nitrate Ion Permeation

Y. Meguro, Y. Watanabe, A. Kato and K. Takahashi

Nuclear Cycle Backend Technology Development Unit, NCBD, JAEA

Radioactive liquid wastes including high concentrated nitrate salt have been generated from nuclear fuel facilities. It is necessary to remove nitrate ion from the waste prior to solidification of the waste, from perspectives of safety assessment and environmental impact of the waste disposal. The authors have been developed a method to remove sodium nitrate from the liquid wastes by electrodialysis separation with ion-exchange membranes. We already fundamentally demonstrated that this method had promise as a denitration method. In order to clarify feasibility of the method, we need to know radiation resistance of the ion-exchange membrane. In this study, electron beam and gamma-ray were irradiated to an anion exchange membrane and then permeation efficiency of nitrate ion through the membrane was determined.

NEOSEPTA ACS membrane (ASTOM Co., Ltd.) was employed as an anion exchange membrane. The membrane was irradiated by electron beam at 10, 50, or 250 kGy in the electron beam irradiation facility or gamma-ray at 4, 20, or 100 kGy in the second Co-60 irradiation facility. Membrane was also irradiated by electron beam at 50 kGy and gamma-ray at 20 kGy. The irradiated membrane was placed in an electrodialyzer, which constructed of two cells, an anode, a cathode, liquid control pumps and a commutator. Sodium nitrate solutions were employed as electrolyte solutions, 5 mol/dm^3 for catholyte and 0.2 mol/dm^3 for anolyte. Nitrate ion was permeated from the catholyte to the anolyte through the membrane by turning of electricity at 0.75 A for 6 hours, and then the amount of permeated nitrate ion was determined. The permeation efficiency (PE) of nitrate was calculated by

$$PE = (C_{t,a} - C_{0,a}) * F/I/t,$$

where $C_{t,a}$ and $C_{o,a}$ are the amount of nitrate ion in the anolyte at time = t and 0 (mol), respectively, and F, I, and t are Faraday constant (C/mol), current (A), and time (s), respectively.

The membranes were examined visually after the irradiation. The color of the membrane was thickened up with high dose irradiation; those were 250 kGy of electron beam and 100 kGy of gamma-ray.

The permeation efficiency of nitrate ion was determined using a non-irradiated membrane or the irradiated membranes. The results are summarized in Table 1. The permeation efficiencies of nitrate ion were high enough for the non-irradiated membrane and all of the irradiated membranes except the irradiated one at higher dose. The efficiency decreased about 10% with 250 kGy of electron beam and 100 kGy of gamma-ray. However this membrane separation method targets low radioactive liquid wastes generated from operation of reprocessing facilities and exposure dose of the membrane from the wastes by electron beam and gamma-ray is estimated to be less than 10 kGy/year. Therefore the present results suggest that this anion membrane has sufficiently-high radiation resistance in practical.

In this study we investigated the irradiation effect on permeation efficiency. This membrane can selectively transfer monovalent anions. The irradiation effect on this property has to be investigated as well as that on physical durability of the membrane in future.

Acknowledgement

Present study is the result of "METI commissioned R&D project on geological disposal in FY2008: TRU waste disposal technology - Combined development of nitrate salt removal technology and an assessment system for the impact of nitrate on the co-locational disposal of TRU waste and HLW."

Table 1 Permeation efficiency of nitrate ion through anion exchange membrane at 0.75 A for 6 hours.

Irradiation		The amount of permeation of NO_3^- / mol	Permeation efficiency
Electron beam / kGy	Gamma-ray / kGy		
-	-	0.176 ± 0.001 (n=3)	1.05 ± 0.01 (n=3)
10	-	0.171	1.02
50	-	0.183	1.09
250	-	0.156± 0.001 (n=3)	0.931± 0.006 (n=3)
-	4	0.186	1.11
-	20	0.165	0.984
-	100	0.151	0.897
50	20	0.168	0.999

1-24 Alpha-Ray Irradiation Damage on CSM Rubber Applied for Glove Box for Plutonium Powder Treatment

K. Saito, Y. Nogami and H. Endo

Plutonium Fuel Development Center, NFCEL, JAEA

Facilities as a MOX plant which handles much plutonium consume a lot of expensive rubber gloves applied for glove boxes. Currently, for economical reasons, newly improved long-lasting glove is desired and under development at Plutonium Fuel Development Center, Tokai, JAEA. For the purpose of the development of the new glove, the deteriorative factors (oxygen, ozone, ionizing radiation etc.) and the mechanism of damage to raw material are needed to be well-known. However, in spite of strong α rays from plutonium, the present status of experimental data of direct and indirect α-ray effects on glove is very poor. Therefore, in order to evaluate the α-ray effects, helium ion irradiation experiments have been conducted. The experiment was done at vacuum environment at first in the previous year[1]. Then, as a next step almost the same experiment was performed atmospherically. Comparison between the results of these two experiments would give us some knowledge of the effect of air at α-particle irradiation.

Sample material is chlorosulfonated polyethylene (CSM) glove which SANKO CHEMICAL INDUSTORY CO. Ltd. manufactures and Plutonium Fuel Development Center mainly employs. JIS K 6251-7 dumbbell-shaped pieces cut from a CSM glove were irradiated in the air with He^{2+} ion beams from AVF cyclotron in TIARA. The kinetic energy of the accelerated ion was 20 MeV initially and was degraded to 5 MeV close to the average energy of α rays emitted from plutonium isotopes during passing through titanium foil at the beam duct end, 40 μm-thick nickel foil set close to the titanium foil, helium and air. Ion flux and duration were 1.25×10^{9} p/cm^2/s and 1~122 min, respectively, and the corresponding absorbed dose was 0.012~1.4 MGy. Since the deterioration-promoting effect under stress by γ-ray irradiation is known[2], 100%-elongation stress parameter was set additionally. Four samples were simultaneously irradiated under the same condition: fluence and stress. The irradiated samples are sent to visual inspection and two tensile tests: tensile strength and elongation at break. Experiments were divided into two parts and they were done at September and November. Since temperature may impact the result of tensile tests, zero-fluence samples were tested in each experiment.

In the present experiment up to the fluence of 9.1×10^{12} cm^{-2}, α-ray effects were not observed at all for surface appearance. However, in the previous experiment in vacuum environment, faint discoloration was observed for the same fluence level mentioned above. There are two main differences of the experimental conditions. One is environment in the air or a vacuum. The other is ion flux intensity. The flux for the previous experiment were $7.5\sim15\times10^{10}$ p/cm^2/s, which is 60~120 times higher than that of the present one. This is because 3MV tandem was adopted for the previous experiment. Therefore, temperature increase caused by the ion flux was so small that no effect might be observed at the present experiment.

Figure 1 shows the results of tensile tests. Any systematic variation with fluence was not observed, either. In the previous experiment, the elongated samples exhibit a clearly faster decrease than the without-stress samples in tensile strength in the region of more than 9.2×10^{12} cm^{-2}. In the present experiment, although the maximum fluence for the elongated samples reached the half of without-stress samples, no indication of decrease is observed yet. In the previous report [1], the result of the weakening of tensile strength according to fluence at first glance was supposed to be attributed to temperature increase for one thing. Also the present result stemmed from little heat load on the samples as well as the result of surface state.

Unfortunately, any knowledge of the effect of air existence expected in this experiment was not drawn.

References

1) K. Saito et al., JAEA Takasaki Ann. Rep. 2007 (2008) 20.
2) T. Seguchi et al., private communication.

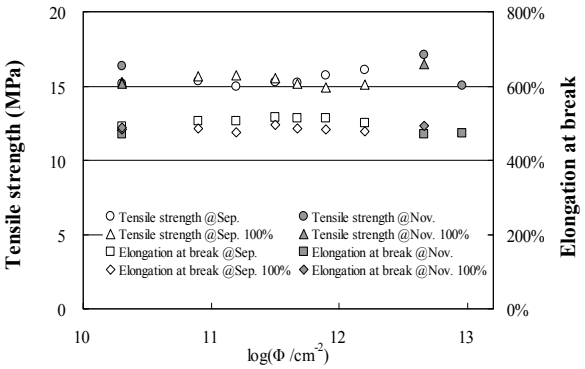

Fig. 1 Tensile strength and elongation at break according to ion fluence. Values are the medians of four samples for one irradiation condition. Data for non-irradiation are set at 2×10^{10} cm^{-2} of log-scale of abscissa. Tensile tests were performed at the temperatures of 24 ~ 25 °C (open symbols) and 18 ~ 21 °C (gray symbols). "100%" indicates elongated samples.

1-25 Research on Radiation Resistant of Heat-resistant Rubber Materials

F. Masukawa [a)], S. Nakatsukasa [b)], K. Asakura [b)] and T. Tabasaki [b)]

[a)] Safety Division, J-PARC, JAEA, [b)] Hayakawa Rubber Co. Ltd.

Higher radiation resistance is required for the rubber materials installed on the accelerator and fluoro rubber (FKM) that has the highest heat resistant ability, is generally used. Conventional rubbers, which use the materials like FKM do not have sufficient resistance against radiation for long term use. In this work, rubber materials with heat-resistant ability are examined by comparing to FKM. The samples were irradiated with γ rays at the Cobalt-60 irradiation facility in Takasaki Advanced Radiation Research Institute, JAEA. The irradiations were made up to 2 MGy at room temperature in air environment. For the irradiated rubber's functions such as hardness deteriorated, it was confirmed that the examined rubber sample showed better elasticity than FKM.

１．はじめに

放射線環境下の汎用器材に使用されるゴムの選定は、耐放射線性に限らず対象流体、温度条件などの要因も重要視されて利用されている。ここでは、従来よりゴム製Oリングに使用されている耐熱性に優れたフッ素ゴムと開発中のゴムにγ線照射を行い、機械特性の調査を行なった。

２．照射ゴムの選定

γ線照射に使用したゴムの種類をTable 1 に示す。耐放射線特性が高いと考えられる合成ゴムから2種類、フッ素ゴムから2種類を選んだ。ここで評価したEPDMは、大強度陽子加速器(J-PARC)のエキスパンションジョイントに使用した耐放射線性が高い止水材[1)]と異なり、耐熱性向上のための配合処方としている。

Table 1 Types of materials.

Test No.	Characteristics
EPDM (No.362)	Ethylene Propylene Diene Terpolymers. Heat-Resistant
FKM (No.1021) (No.1041)	Fluororubber General grade Chemical-Resistant grade
Synthetic rubber (No981)	Oil proof grade

３．試験方法

試料への照射はJAEA高崎研究所のCo60γ線照射施設にて室温空気中で行なった。各種の機械特性試験はJIS規格に準じて硬度試験(JIS-K6251)、強度・伸び試験(JIS-K6251)、圧縮永久ひずみ(JIS-K6262)を0, 0.5, 1, 2 MGyの各照射線量の試料で測定した。

４．結果および考察

Figure 1に伸び率の結果を示す。フッ素ゴムの試料は照射による表面軟化劣化のため一部データを取ることができない状況となった。開発中の材料でも特にEPDMは2 MGyまでの吸収線量においても弾性を保持しており、他の特性評価についても類似した傾向を確認した。

Figure 2に25%圧縮永久歪みの結果を示す。フッ素ゴムは内部硬化劣化も同時に進行したために試料破損も発生したのに対して、開発品のNo362とNo981は弾性を残していた。

今後は真空シールとして使用可能かどうかを評価していく予定である。

Reference

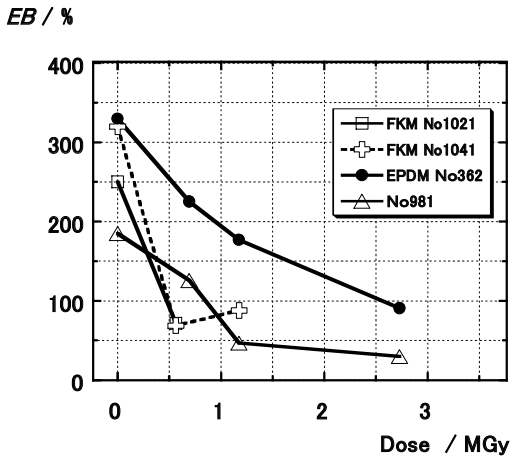

Fig. 1 JIS-K6251; Elongation measurement results. No.1021 and No.1041 are FKM, and at 0.5 or higher than 1 MGy, taking samples became extremely difficult.

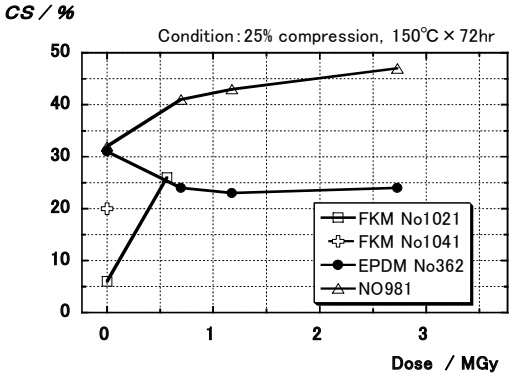

Fig. 2 JIS-K6251; Showing results on compression set. FKM samples destroyed after irradiation or with more than 1 MGy irradiation.

1) 中務定義 他、日本ゴム協会誌、**79**（2006）429.

1-26 Studies on Microstructure and Elemental Distributions of Barrier Materials for Geological Disposal of Radioactive Waste

T. Kozaki [a], R. Koike [a], N. Miyasaka [a], K. Yoshi [a], S. Sato [a], N. Kozai [b] and T. Satoh [c]

[a] Graduate School of Engineering, Hokkaido University, [b] Advanced Science Research Center, JAEA, [c] Department of Advanced Radiation Technology, TARRI, JAEA

Introduction

Compacted bentonite is a candidate buffer material for geological disposal of radioactive waste. The major clay mineral of bentonite is montmorillonite. When compacted and saturated with water, bentonite has significant advantageous features such as low hydraulic conductivity, high ability of sorption and low diffusivities of radionuclides, resulting in high performance as a barrier to retard the migration of radionuclides from waste to the biosphere as well as another potential barrier of host rock. In a disposal system using steel waste container (i.e. overpack for high-level radioactive waste), the bentonite is expected to alter due to the interactions between iron and bentonite. One of the most probable alterations is the formation of Fe(II)-bentonite, i.e. ion exchange of Na- montmorillonite with Fe(II) ions which could be released from the corrosion of carbon steel. Therefore, for safety assessment of the geological disposal of radioactive waste, the properties of the altered bentonite materials and the impacts of the Fe(II)-bentonite formation on the performance of the barrier should be clarified through basic studies.

In this study, two types of Fe-bentonite samples, Fe(II)- and Fe(III)-bentonites, were prepared, and characterized by several analytical methods. Micro-PIXE analyses were performed for Fe(III)-bentonite sample to evaluate re-distribution of Fe in the sample during the sample preparation.

Experimental

Fe(III)-bentonite samples were prepared through the ion exchange reaction of Na-bentonite (Kunipia F, Kunimine Industries Co. Ltd., Japan) with Fe(III) in $FeCl_3$ solution. Twenty grams of Na-bentonite were suspended in 800 cm^3 of 0.2 M $FeCl_3$ solution for 16 h. After the suspension was allowed to settle overnight, the supernatant was removed by decantation. The four-hour-ion-exchange treatment was repeated twice. Excess salt was removed by rinsing with dilute HCl solution prior to the rinse with deionized water. The rinse was repeated until no Cl^- ions in the supernatant were detected using $AgNO_3$ solution. After the Fe(III)-bentonite was vacuum-dried at 298 K, the Fe(III)-bentonite was crushed and sieved to obtain samples with grain sizes of 75-150 μm.

Fe(II)-bentonite samples were prepared through the ion exchange reaction using Fe(II)-nitrilotriacetate complex (Fe(II)-NTA solution) instead of $FeCl_3$ solution. The ion-exchange treatment was made under Ar gas bubbling. Detail procedure of the preparation of Fe(II)-bentonite using Fe(II)-NTA solution was described elsewhere [1].

Both Fe(II)- and Fe(III)-bentonite samples were characterized by XRD and chemical analyses. Distribution of elements in the Fe(III)-bentonite sample was determined by Micro-PIXE method. The samples for micro-PIXE analyses were prepared by drying Fe(III)-bentonite suspension which had been dropped on a carbon plate.

Results and Discussion

Fe(III)-bentonite prepared through ion exchange treatment using $FeCl_3$ solution has Fe content of 126 mmol/100 g-clay, which is slightly higher than that of the cation exchange capacity of the bentonite (110 meq/ 100 g-clay). Figure 1 shows two-dimensional elemental mappings of Si, Al and Fe for Fe(III)-bentonite sample. The region where both Si and Al are observed has high Fe content, indicating the presence of Fe-bearing silicates, i.e. Fe(III)-bentonite. However, the region where only Fe was observed can be seen in Fig. 1, suggesting that Fe(III) oxides (or hydroxides) is present in the sample. This could be attributed to the precipitation of Fe(III) ions during the process of excess salt removal with deionized water. Careful pH conditionings seem to be essential for the preparation of pure Fe(III)-bentonite.

Fe(II)-bentonite sample prepared by the method using Fe(II)-NTA solution contains Fe of 55 mmol/100 g-clay. The result of chemical analysis by the o-phenanthroline method indicates that 98% of Fe in the sample was divalent. Therefore, the Fe content of the sample is in good agreement with the cation exchange capacity of the bentonite, suggesting complete ion exchange of bentonite sample. Micro-PIXE analyses are planned to be made for Fe(II)-bentonite next financial year so as to confirm the absence of Fe(II) precipitations.

Reference

1) J. Manjanna, et al., J. Nucl. Sci. Technol. 44 (2007) 929.

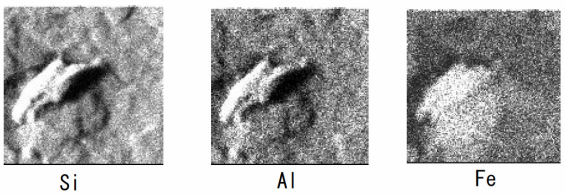

Fig. 1 Two-dimensional elemental mappings of Si, Al and Fe for Fe(III)-bentonite sample.

1-27 Interaction between *Paramecium bursaria* and Heavy Elements

N. Kozai [a], T. Ohnuki [a] and T. Satoh [b]

[a] Advanced Science Research Center, JAEA,
[b] Department of Advanced Radiation Technology, TARRI, JAEA

It is known that activity of microorganisms such as bacteria, algae, and yeasts has a great impact on the geological migration of the radionuclides leached from the radioactive waste forms buried underground. Retardation of the radionuclides migration by adsorption on the cells is the most desirable function of those microorganisms. It is also known that protozoa, who prey those microorganisms, are found not only in surface water and soil but also in deep ground water. Protozoa are defined as one-celled (unicellular) organisms and control the number of those bait-microorganisms. However, no knowledge on the role of protozoa on the radionuclide migration is available. The chemical forms of the radionuclides sorbed on or taken up by those bait-microorganisms may change during the process of digestion and absorption by protozoa. Protozoa may take up radionuclides directly from water. The objective of this study is therefore to elucidate the role of protozoa in the migration of radionuclides. In the present report, uptake or sorption of metals in aqueous solutions by paramecia was investigated. Paramecia are the most common species of protozoa in fresh waters and most extensively used in research. Depending on the species, paramecia are 70-350 μm length and several tens of μm wide. This size is suitable for micro-PIXE analysis considering the special resolution, less than 1 μm, of the micro-PIXE analyzing system in the TIARA facility.

This study used *Paramecium bursaria* as a paramecium species. *P. bursaria* is 80–150 μm length and has a mutualistic symbiotic relationship with green alga, Zoochlorella. Because of the alga inside the *Paramecium* cells, *P. bursaria* looks green. This study investigated the behavior of *P. bursaria* in solutions containing Eu(III), Pb(II), and Sr(II). An inorganic medium containing 200 mg/L $Ca(NO_3)_2 \cdot 4H_2O$, 20 mg/L $MgSO_4 \cdot 7H_2O$, 0.8 mg/L $Fe_2(SO_4)_3 \cdot nH_2O$, and 590 mg/L NaCl was prepared by dissolving these salts in purified water. The metal solutions were prepared by dissolving one of the following metal salts, $Eu(OCOCH_3)_3 \cdot nH_2O$, $Pb(OCOCH_3)_2 \cdot 3H_2O$, or $Sr(NO_3)_2$, in the inorganic medium to have one of the metal at 0.05 mM. The pH of the metal solutions was adjusted to 7.0 with a dilute NaOH solution. The cells of *P. bursaria* were precultured with yeast cells. After the preculture, the cells were roughly separated from the yeast cells and the other excretion precipitates of the Paramecium by collecting the *P. bursaria* cells gathered using their positive phototaxis on the surface of the culture medium. To further clean the collected *P. bursaria* cells, the cells were passed through a net filter with a mesh opening of 180 μm pore size, collected on a net filter with a mesh opening of 10 μm, washed on the filter four times with an inorganic medium at pH 7.0, and finally transferred in a beaker with the same medium. All of the *P. bursaria* cells in the suspended medium thus prepared were alive. A portion (1 mL) of the cell suspension was introduced to 9 mL of the metal solutions in glass beakers. The beakers were sealed and kept at 25 ^{o}C. After 24 h, the cells were collected on a membrane filter and washed with purified water three times. The cells moving around were sampled, put on carbon plates, and dried in air at room temperature. In control experiments, the *P. bursaria* cells precultured and cleaned were put on carbon plates, dried in air, and covered with the metal solutions. After 24 h, the metal solutions were removed and the cells on the carbon plates were washed with purified water three times and dried in air at room temperature. The cells of *P. bursaria* on carbon plates can be easily detected by mapping of phosphate (Fig. 1).

When the cells alive were contacted with the Sr solutions, all of the cells were still alive and moving around after 24 h. In the Eu and Pb solutions, most of the cells lost their original form and died. For the surviving cells, micro-PIXE analysis hardly detected Eu and Sr on/in the cells (Fig. 1) but many dots of Pb were detected on the cells. In the control experiments using the pre-dried *P. bursaria* cells, Eu and Sr were also hardly detected after the cell-metal contact. A few dots of Eu were detected on the cells, however, we could not tell whether those Eu dots were the Eu sorbed on and taken up by the cells or the Eu with the other origin. The Eu dots might be sorbed on the excretion precipitates unremoved from the *P. bursaria* cell suspension. On the other hand, Pb was clearly detected on the whole part of the cells (figure not shown). These results suggest that *P. bursaria* cells have different sorption/uptake behaviors depending on the elements.

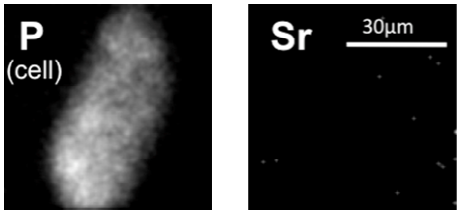

Fig. 1 Distribution of P and Sr in a *P. bursaria* cell.

Further study on the sorption or uptake of metals by *P. bursaria* cells during the culture of *P. bursaria* cells with bait-microorganisms on which metals were sorbed beforehand is currently underway.

1-28 Effect of Groundwater Radiolysis on the Disposal System of High-Level Radioactive Waste

M. Yamaguchi [a] and M. Taguchi [b]

[a] Geological Isolation Research Unit, GIRDD, JAEA,
[b] Environment and Industrial Materials Research Division, QuBS, JAEA

High-level radioactive waste (HLW) is planned to be disposed of in a deep underground repository. In the current Japanese design concept of the HLW disposal system, a canister of HLW is encapsulated in a carbon steel overpack. This waste package is emplaced in the repository and surrounded by buffer materials (bentonite). The radiation effect from HLW on the disposal system may occur in two different phases: the period of overpack physical containment and that after its breaching. Alpha and beta radiation can be shielded completely by the overpack in the former phase, while gamma-radiation from HLW will penetrate through the overpack and into the buffer material, where radiolysis of the porewater of bentonite might affect the chemical conditions of the buffer and corrosion behavior of the overpack materials. It is found so far that oxidative corrosion of carbon steel is accelerated by gamma-radiation in the aqueous phase system, while its behavior seems to become non-reactive under the system of compacted bentonite. If this process of buffering effect can be well-understood quantitatively, it would be greatly helpful to provide feedback to the design of overpack, which could eventually contribute to optimize the construction and operational costs of the repository.

In the later phase, i.e. after the overpack finally loses its integrity and the porewater water comes into contact with the HLW (it is typically assumed 10^3 years in performance assessment for the disposal system in Japan), radiolysis resulting from alpha-radiation has to be taken into account as dose rates of beta and gamma-radiation becomes negligible small at this stage. It is anticipated that radiolytic oxidizing species such as H_2O_2 and O_2 may accelerate release of radionuclides from HLW matrix and make the retardation (barrier) funtion weaker due to higher oxidizing condition. Actually the processes seem more complicated as solutes in porewater would affect the radiolytic process. High concentration of dissolved H_2 may be generated by anoxic corrosion of overpack. However, effects of these species on radiolysis of water have not yet been systematically understood.

Thus we have studied following two issues in accordance with two different phases mentioned above:

1. Role of compacted bentonite for gamma-radiolysis: This is aiming to understand the experimental observations of carbon steel corrosion under gamma-radiation. Apart from the corrosion, the effect of clay materials for radiolysis of porewater is poorly understood. We are currently trying to design experimental setups and have obtained preliminary results: Montmorillonite, a kind of smectite clay mineral which is the main component of bentonite and act as a barrier for radionuclides migration due to its extensive swelling property, was added to 0.5 M NaCl aqueous solutions. Hydrogen concentration in gas and liquid phases were analyzed by gas-chromatograph and gas-selective electrode, respectively, after gamma-irradiation at 10 kGy/h. By increasing added amount of Montmorillinote to the same volume of NaCl solution, the H_2 concentration in the gas phase decreased significantly, while dissolved H_2 concentration increased. Latter values were higher than estimated from the volume of liquid phase by model calculation with homogeneous reaction in liquid phase and gas/liquid mass transfer. This may be due to dispersed clay particles which might have induced H_2 formation. More detailed studies including both on experiment and modeling are necessary to elucidate the effect of clay particles on gamma-radiolysis of water.

2. Effect of solutes on helium ion beam radiolysis of water: Helium ion beam radiolysis of aqueous solutions have been employed to study the effects of solutes on alpha-radiolysis of groundwater. Irradiation was performed with the AVF cyclotron in TIARA. We have studied the effect of bicarbonate[1] and chloride ions on radiolysis of water which are commonly found in groundwater. Aerated water and NaCl solutions were irradiated with $^4He^{2+}$ at 20 MeV for 10 minutes. Concentrations of H_2O_2 increased almost linearly with accumulated dose, but H_2O_2 accumulation rate in 0.5 M NaCl was about half of that in pure water. G-values of 0.5 M NaCl were derived by simulating H_2O_2 concentration. The effect of dissolved H_2 was also studied by using H_2O_2 aqueous solution. While dissolved H_2 can reduce H_2O_2 concentration effectively in the case of gamma-radiolysis, it was not effective at high-LET radiation such as proton or helium ions, although model calculation predicted almost complete decomposition of H_2O_2.[2] In our preliminary experiments H_2O_2 was decomposed almost completely in aqueous solutions saturated with H_2 after $^4He^{2+}$ beam radiolysis. Further study is necessary to clarify the effect of dissolved H_2 on high-LET radiolysis of water by controlling dissolved oxygen concentration which seems to be crucial in this case.

This study is a part of the Project for assessment methodology development of chemical effects on geological disposal system funded by the Ministry of Economy, Trade and Industry, Japan.

References

1) M. Yamaguchi et al., 2nd APSRC, 1P-25 (2008).
2) B. Pastina et al., J. Phys. Chem. A105 (2001) 9316.

1-29 Damage Level Dependence of Irradiation Hardening of α-Fe Alloys and a Reduced Activation Steel F82H

S. Jitsukawa [a)], M. Ando [b)], N. Okubo [a)], T. Onitsuka [a,c)], Y. Abe [a)], K. Shiba [a)] and T. Sawai [a)]

[a)] Division of Fuels and Materials Engineering, NSED, [b)] Division of Fusion Reactor Engineering, FRDD, [c)] Division of Applied Heat Technology, NSED, JAEA

Mechanical properties of the reactor core component materials exhibit large changes by the irradiation damage of high-energy neutrons. Changes depend on the damage levels and irradiation temperature. At relatively low temperatures, irradiation mainly causes hardening and toughness degradation. Materials even for fast reactors and fusion machines often exhibit irradiation hardening.

For the modeling of irradiation hardening, bcc Fe alloys and high chromium martensitic steels have been irradiated. Some of the alloys were modified by addition of Ni and Cu atoms. Ni and Cu atoms often cause hardening by producing fine precipitations during irradiation [1)].

Model Fe alloys doped with 0.3%Cu and 1%Ni were used, as well as pure iron, a reduced activation martensitic steel F82H and F82H+1%Ni; F82H contains Fe 8Cr 2W 0.2V 0.04Ta 0.1C tempered at 1023 K for 1 h after normalizing at 1313 K. Plates of the alloys were cut into 3 mm × 6 mm × 0.8 mm in size, and rectangular surfaces with 6 mm × 0.8 mm of the specimen were irradiated at about 573 K with 10.5 MeV Fe^{3+} ions and He and H ions. Average damage rate was 1.0×10E-3 dpa/s at a depth of 1 micro-meter.

After the irradiation, ultra-microhardness tests have been performed. Direction of indentation was chosen to be parallel to the ion beam axis. Hardness tests were performed with a penetration depth of about 400 nm to avoid the effect of depth dependence of the ultra-microhardness. Indentation load ranging from 10 to 16 mN was used.

Figure 1 shows damage level dependence of hardening by ion-irradiation at 553-573 K. Hardness increased with damage levels in the damage range above 0.5-1 dpa. The hardening is thought to be the result of the increase in dislocation density: growth of irradiation induced interstitial type of dislocation loops. Fe specimens doped with Cu and Ni exhibited higher hardness after irradiation (scatters are rather large), as well as that of F82H doped with 1% Ni. These larger hardness might be caused by the fine precipitation formed during irradiation. The damage level dependence of the yield stress levels of pure-Fe and A533B and 9Cr-1Mo steels obtained at ORNL are re-plotted in Fig. 2. The irradiation was conducted at temperatures below 373 K [2)]. Yield stress increased with damage level with an exponent of 0.1-0.2, as those seen in Fig. 1. Similar exponent values suggest that the hardening was dominated by the same mechanism of the increase as that in dislocation density. Onitsuka et al. had also reported that Fe-0.3%Cu alloy hardened to a considerable degree after exposure to electrons to 1 mdpa, comparing with pure Fe [3)]. These suggest that the damage level dependences of the alloys could be schematically shown by Fig. 3. At relatively low damage levels, alloys doped with Cu exhibited hardening caused by fine precipitations. This was followed by the hardening by the increase of dislocation density.

References

1) T. Taguchi et al., J. Nucl. Mater. 335 (2004) 457.
2) T. Byun and K. Farrel, Acta Mater. 52 (2004) 1597.
3) T. Onitsuka, JAEA Takasaki Ann. Rep. 2007 (2008) 27.

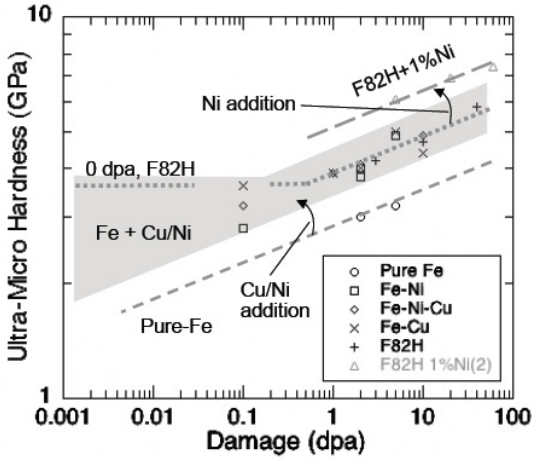

Fig. 1 Damage level dependence of hardness after ion-irradiation at about 573 K.

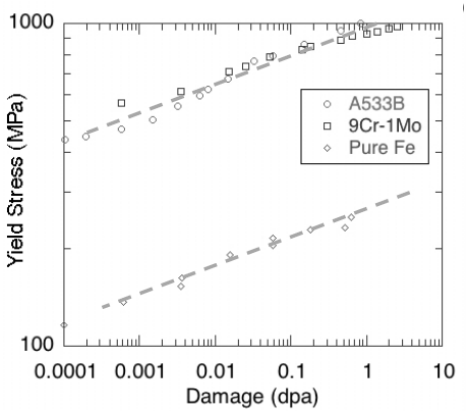

Fig. 2 Damage level dependence of yield stress after neutron irradiation below 373 K.

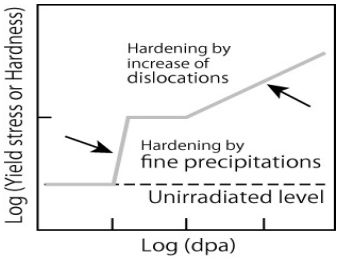

Fig. 3 A schematic damage level dependence of irradiation hardening.

1-30 Effects of Microstructual Evolution in low-alloy Steels for Radiation Hardening under Electron Irradiation

T. Onitsuka [a)], Y. Abe [b)], N. Okubo [b)], M. Ando [b)], T. Sawai [b)] and S Jitsukawa [b)]

[a)] Division of Applied Heat Technology, NSED, JAEA,
[b)] Division of Fuels and Materials Engineering, NSED, JAEA

Understanding the mechanisms at the origin of radiation hardening and associated embrittlement is of great interest for predicting the evolution of reactor pressure vessel steel during nuclear power plant running. In the present study, to examine the behavior of different solutes under irradiation, radiation hardening behavior in 3 model alloys (Fe-2%Ni, Fe-2%Ni-0.5Cr, and Fe-0.6%Cu) and pure Fe under electron irradiation was investigated.

The alloy ingots of Fe-2%Ni, Fe-2%Ni-0.5%Cr, and Fe-0.6%Cu (in weight percent) were made by means of vacuum induction melting method in order to reduce impurities to very low level. Highly purified (99.99%) iron sheet supplied by Nilaco Co. Ltd., was used as pure Fe. After cold-rolling to sheets of about 5mm thickness, Fe-2%Ni and Fe-2%Ni-0.5%Cr were water-quenched after annealing at 950 °C for 1 hour and tempered at 750 °C for 1 hour, and Fe-0.6%Cu was water-quenched after solution treatment at 825 °C for 4 hours to keep the copper in supersaturated solution. Pure Fe was annealed at 800 °C for 4 hours and air cooled. After heat treatment, specimens with 15 mm × 15 mm × 0.5 mm in dimension were made from inner part of each sheet and irradiated with 2.0 MeV electrons using a Dynamitron accelerator at JAEA-Takasaki to doses of 3.5×10^{23} e^-/m^2, corresponding to calculated atomic displacement doses of 1.2×10^{-3} dpa. The irradiation temperature was kept at 200 °C or less and the dpa rate was 3.0×10^{-9} dpa/s. The indentation hardness test and the positron annihilation lifetime (PAL) measurement were performed before and after irradiation.

Figure 1 shows the dpa dependence of the increases in indentation hardness of the irradiated materials. The change in hardness in Fe-0.6%Cu alloy showed remarkable increase and tends to be saturated at the high dose. This result has good agreement with the previous work[1)]. The difference between the result of Fe-2%Ni and Fe-2%Ni-0.5%Cr alloy indicates that the addition of Cr enhanced the radiation hardening in Fe-2%Ni alloy. Figure 2 shows the result of positron lifetime parameters in irradiated specimens to doses of 3.5×10^{23} e^-/m^2. In conclusion, the results indicate the formation of precipitates that suppress the increase in positron lifetime component in Fe-2%Ni as well as Fe-0.6%Cu, which shows good agreement with the result of irradiation hardening data shown in Fig. 1. Further experiments and investigations by using small angle x-ray scattering (SAXS) measurements and TEM observations will be made in the future.

Reference

1) T. Tobita et al, J. Nucl. Mater. 299 (2001) 267.

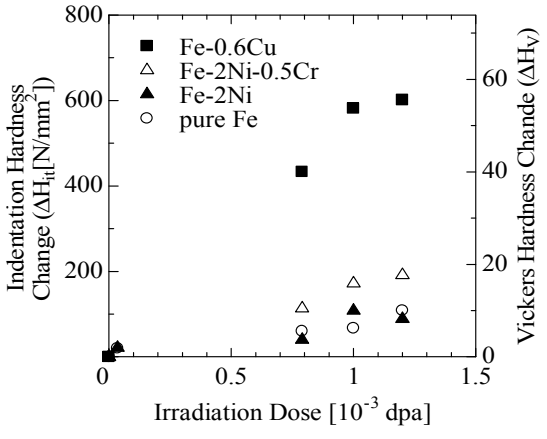

Fig. 1 Increases in indentation hardness as a function of irradiation dose for pure Fe, Fe-2Ni, Fe-2Ni-0.5Cr, and Fe-0.6Cu alloy. Here, calculated Vickers hardness change is indicated at the right side of the vertical axis for the convenience.

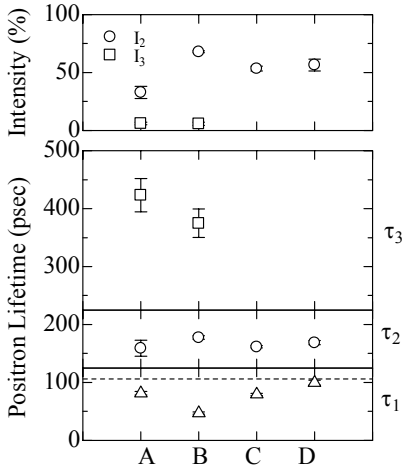

Fig. 2 Result of PAL parameters obtained from irradiated specimens doses to 3.5×10^{23} e^-/m^2. A-D correspond to pure Fe, Fe-2Ni, Fe-2Ni-0.5Cr and Fe-0.6Cu alloy, respectively. Usually τ_1, τ_2 and τ_3 associated with positron lifetime components for bulk, monovacancy and nanovoids. I_2 and I_3 are the fractional intensities of τ_2 and τ_3. The dashed line presents τ_1 obtained from non-irradiated bulk Fe (106 psec) for reference.

1-31 Irradiation Simulation of Neutron Damage Microstructure in Extra High Purity Fe-25Cr-35Ni Austenitic Stainless Steels

I. Ioka [a)], Y. Ishijima [b)], H. Ogawa [b)] and Y. Nakahara [b)]

[a)] Nuclear Engineering Research Collaboration Center, JAEA,
[b)] Division of Fuels and Materials Engineering, NSED, JAEA

1. Introduction

The ultra high burn-up of LWR is considered to be an important technology for establishing nuclear power plants as one of the most promising future energy systems from a view-point of reducing radioactive waste and greenhouse gas. Cladding materials with the long excellent performance under heavy irradiation are required to these developments. The high chromium and high nickel austenitic stainless steel (Extra high purity (EHP) alloy, Fe-25Cr-35Ni) [1,2] was selected as one of candidates that are possible to be made by the new engineering technology.

Microstructural evolution induced by irradiation is believed to be the key variables responsible for degradation of materials in LWR. Months to years of irradiation time are required to obtain a change in microstructure of materials at dozens of dpa. Charged particle simulation with accelerated damage rate is often used in such situations as to forecast the behavior of neutron-irradiated materials. By establishing the correlation between charged particle- and neutron- irradiated microstructures of EHP alloy, the results from charged particle-irradiation can be used to provide valuable information on microstructure evolution in EHP alloy in LWR cores.

This work is focused on investigating the microstructure of EHP alloy irradiated by neutron. The dislocation loop density and size, the void density and size are determined, and are compared to those for charged particle-irradiations of EHP alloy.

2. Experimental Procedures

The materials were Fe-25Cr-35Ni and Fe-25Cr-20Ni EHP alloys. The chemical compositions are shown in Table 1. The configuration of specimen is 3 mm in diameter and 0.2 mm in thickness. The surface of specimen was polished with #2400 emery paper and 0.1 μm diamond paste before neutron-irradiation.

Table 1 Chemical compositions of EHP alloys.

Materials	Fe	Cr	Ni	Ti	C	O
Fe-25Cr-35Ni	bal.	24.85	35.05	0.17	0.0018	0.0009
Fe-25Cr-20Ni	bal.	24.23	21.61	0.21	0.0006	0.0005
	N	Si	Mn	P	S	B
Fe-25Cr-35Ni	0.0020	<0.005	0.001	0.001	0.0010	−
Fe-25Cr-20Ni	0.0010	<0.01	<0.01	0.001	0.002	<0.0005

The specimens were irradiated at 553 ± 20 K in a helium and nitrogen mixture gas atmosphere for 25,000 h using the Japan Research Reactor No.3. The fast neutron fluence was estimated to be 1.5×10^{25} n/m^2 corresponded to a damage level of 1.8 dpa.

3. Results

Figure 1 shows the bright field image of neutron-irradiated Fe-25Cr-35Ni and Fe-25Cr-20Ni. The images show that irradiation defects such as dislocation loops are induced by neutron-irradiation. Voids were not observed in both specimens. Figure 2 shows the number density and the average diameter of dislocation loops of irradiated Fe-25Cr-35Ni and Fe-25Cr-20Ni. The number density and the average diameter of dislocation loops of Fe-25Cr-35Ni were less than those of Fe-25Cr-20Ni. It is considered that Ni is effective to suppress the initiation and growth of irradiation defects. In future, microstructural evolution of charged particle-irradiated specimens will be analyzed.

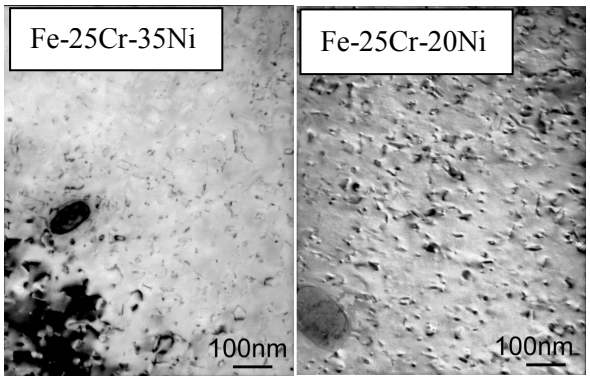

Fig. 1 Bright field image of both irradiated specimens.

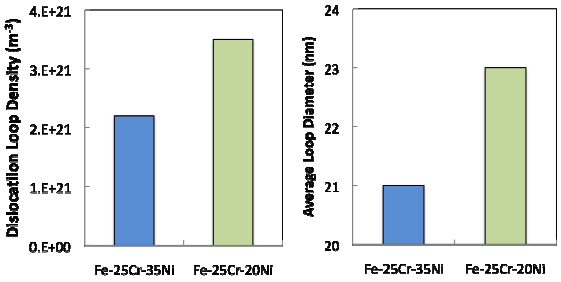

Fig. 2 Density and size of dislocation loops of specimens.

References

1) K. Kiuchi et al., IAEA TCM, Argentina, Nov. 15-19, (1999).
2) K. Kiuchi et al., ICAPP, June 9-13, Florida (2002).

1-32 Evaluation of Microstructure Change in Extra High Purity Austenitic Stainless Steel under BWR Condition Simulated by Triple Ion Irradiation

Y. Ishijima, I. Ioka and M. Yamamoto

Division of Fuels and Material Engineering, NSED, JAEA

1. Introduction

The ultra high burn-up of LWR is considered to be an important technology for establishing nuclear power plants as one of the most promising future energy systems from a view point of reducing radioactive waste and greenhouse gas. Cladding materials with the long excellent performance under heavy irradiation are required to these developments. The extra high purity (EHP) grade (C + N + O + Si + Mn + P + S + B< 100 wppm) and high Cr and Ni (> 20 wt%) austenitic stainless steel was selected as one of candidates that are possible to be made by the present engineering technologies. However, it is not clear what the best chemical composition of EHP grade austenite stainless steel for claddings. The purpose of this study is to evaluate Ni concentration effect on irradiation behavior for EHP grade stainless steel.

In this paper, triple ion irradiation that simulates BWR condition was carried out for the EHP grade Fe-25Cr-35Ni and Fe-25Cr-20Ni (SUS310) alloys. After irradiation, TEM observations are carried out, and then evaluation of swellings, and measurements of number density and diameter of dislocation loops are made.

2. Experimental Procedures

The chemical compositions are shown in Table 1. The specimens were cut to a size of $\phi 3 \times 0.2$ mm. The area to be irradiated was then mechanically and electro-chemically polished to a specular finish.

Table 1 Chemical compositions of EHP alloys.

Materials	Fe	Cr	Ni	Ti	C	O
Fe-25Cr-35Ni	bal.	24.85	35.05	0.17	0.0018	0.0009
Fe-25Cr-20Ni	bal.	24.23	21.61	0.21	0.0006	0.0005
	N	Si	Mn	P	S	B
Fe-25Cr-35Ni	0.0020	<0.005	0.001	0.001	0.0010	–
Fe-25Cr-20Ni	0.0010	<0.01	<0.01	0.001	0.002	<0.0005

Triple ion irradiation simulating BWR neutron irradiation condition was performed using Ni^{3+} (12 MeV), He^{+} (1.1 MeV) and H^{+} (0.38 MeV) ion beams. Aluminum film degraders were used to spread He^{+} and H^{+} irradiated area. Irradiation temperatures were 573, 673, and 773 K. Irradiation damage and ion-implantation depth were calculated using TRIM code. The TEM observation was carried out to evaluate dislocation loops and swellings.

3. Results

Figure 1 shows the bright field image of Fe-25Cr-35Ni at each irradiation temperature. The images show that irradiation defects such as dislocation loops and voids are induced by charged particle-irradiation. Voids were observed in Fe-25Cr-35Ni at irradiation temperature of 773 K. In Fe-25Cr-20Ni, voids were also observed at 773 K.

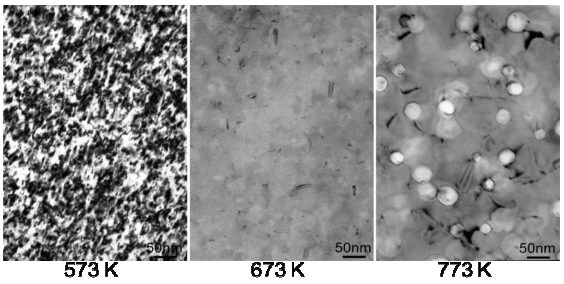

Fig. 1 Bright field image at each irradiation temperature.

Figure 2 shows the number density of dislocation loops and swelling as functions of irradiation temperature. The swelling was calculated from void volume. The number density of dislocation loops decreased with increasing irradiation temperature. The density for Fe-25Cr-35Ni was lower than that for Fe-25Cr-20Ni. In feature, microstructural evolution of neutron irradiated specimens would be analyzed.

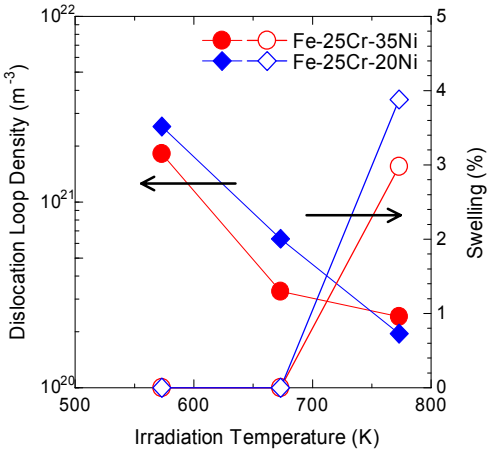

Fig. 2 Dislocation loop density and swelling of EHP alloys.

1-33 Damage Process in Hafnium Irradiated with Energetic Electrons

Y. Chimi, J. Ogiyanagi and S. Hanawa

LWR Long-term Reliability Research Unit, NSRC, JAEA

In the commercial light water reactors, pure hafnium metal is used as one of the neutron absorbers for control rods due to long nuclear lifetime and good corrosion resistance. In recent years, many cracks on the control rods using hafnium plates have been found in Japanese boiling water reactors. The cause of the crack is strongly concerned with the irradiation growth of hafnium. However, the irradiation behavior of hafnium has been hardly reported in literature so far. In the present work, in order to study the fundamental damage process in hafnium, defect production and recovery behaviors of hafnium irradiated with energetic electrons have been investigated.

The specimen was a polycrystalline pure hafnium foil with ~25 μm in thickness. Electron irradiation in the energy range of 1.0-2.5 MeV was performed at temperatures below 20 K using a 3-MV single-ended accelerator in TIARA, JAEA-Takasaki. The change in electrical resistivity of the specimen, $\Delta\rho$, was measured *in situ* at ~8 K during irradiation as a function of electron fluence, Φ. After irradiation, the thermal recovery of $\Delta\rho$ was observed by means of isochronal annealing. For comparison, a polycrystalline pure zirconium foil with ~25 μm in thickness was also adjacent to the hafnium foil, and those foils were irradiated and measured simultaneously.

Figure 1 shows the electron energy dependence of electrical resistivity change rate, $d(\Delta\rho)/d\Phi$, for hafnium and zirconium. For each electron energy, $d(\Delta\rho)/d\Phi$ is simply proportional to the defect production cross-section, because $\Delta\rho$ increases linearly with Φ. The calculated displacement cross-sections for the relativistic electrons[1] are also shown in the figure after normalization to $d(\Delta\rho)/d\Phi$ at 2.5 MeV. Assuming that the values of displacement threshold energy, E_d, are 28 eV and 35 eV for hafnium and zirconium, respectively, the trends of calculated cross-sections generally agree with $d(\Delta\rho)/d\Phi$. For zirconium, the value of 35 eV corresponds to the literature data[2], but it is noted that E_d is dependent on the crystal orientation, especially for anisotropic materials such as zirconium and hafnium. The thermal recovery behavior of $\Delta\rho$ is shown in Fig. 2. While for zirconium, there is a large peak of the recovery at ~100 K, which indicates the migration of irradiation-produced single interstitial atoms[2], a large peak at different temperature is found for hafnium. It implies that the migration energy of single interstitial atoms for hafnium is different from that for zirconium.

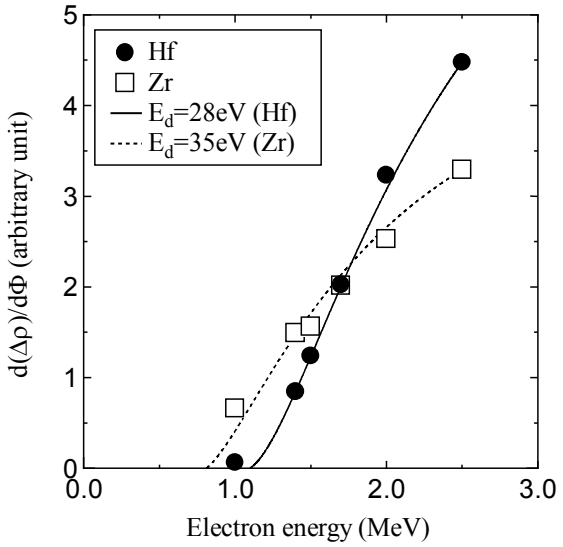

Fig. 1 Electron energy dependence of electrical resistivity change rate, $d(\Delta\rho)/d\Phi$, for hafnium (Hf) and zirconium (Zr). Calculated displacement cross-sections are also shown by solid and dotted lines.

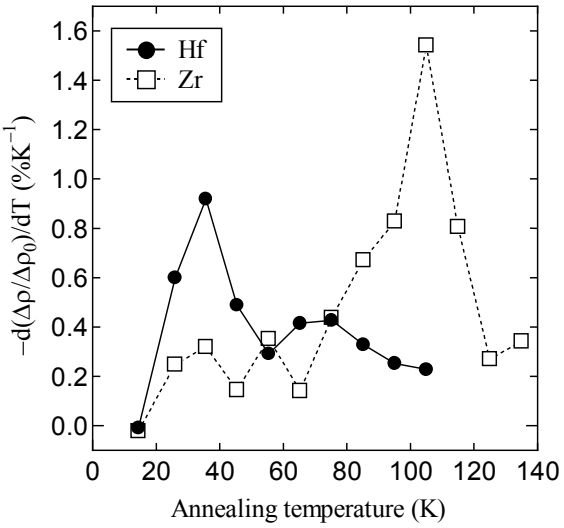

Fig. 2 Thermal recovery behavior of irradiation-induced electrical resistivity change, $-d(\Delta\rho/\Delta\rho_0)/dT$, for hafnium (Hf) and zirconium (Zr), where $\Delta\rho_0$ denotes initial value of $\Delta\rho$ before annealing.

References

1) F. Seitz and J.S. Koehler, in: F. Seitz, D. Turnbull (Eds.), Solid State Physics, vol.2, Academic Press, New York, (1956) 305.
2) P. Ehrhart et al., in: H. Ullmaier (Ed.), Atomic Defects in Metals, Landolt-Börnstein, Numerical Data and Functional Relationships in Science and Technology, Springer, Berlin, (1991), Group III, vol. 25.

1-34 High-sensitivity Chemical Etching for Preparation of Nano-sized Poly(vinylidene fluoride) Ion-track Membranes

T. Yamaki, H. Koshikawa, S. Sawada, S. Hasegawa, M. Asano and Y. Maekawa

Environment and Industrial Materials Research Division, QuBS, JAEA

Quite recently, ion-track membranes of poly(vinylidene fluoride) (PVDF) have attracted a renewed interest for their applications to next-generation electrochemical devices such as fuel cells[1,2]. In order to produce track-etched pores in PVDF films, several kinds of etching solutions were previously employed. In most cases[3], a highly concentrated aqueous KOH solution with a $KMnO_4$ additive was kept at a high temperature (85 °C). These severe etching conditions provided irreversible chemical damage all over the film including the non-irradiated part, thereby destroying some distinctive properties of PVDF. Therefore, in this study, we attempted to prepare PVDF ion-track membranes of up to a few hundred nm pore diameter without any oxidant additives in the alkaline etching solution. Instead of the oxidant agent-induced activation, the effect of the pretreatment was considered to enhance the efficiency of chemical etching even under milder conditions[4,5]. The pretreatment involves heating at a high temperature (but far below the melting temperature of PVDF, about 180 °C) in air after the irradiation, with the expectation of a sufficient oxidation of the chemical species within the latent tracks, which accelerates the chemical dissolution.

A 25-μm thick PVDF film was irradiated at room temperature with ^{129}Xe at an energy of 3.5 MeV/n from the TIARA cyclotron. The fluence ranged from 3×10^6 to 3×10^{11} ions/cm^2. As a pretreatment, the irradiated films were heated in air at 120 °C for 30 days prior to etching. The film storage at 25 °C (room temperature) was also done for comparison. Track etching was then performed in a 9 M KOH aqueous solution at 80 °C. After depositing a gold coating, the surface of the 24-hour etched membranes was imaged by scanning electron microscopy (SEM). In order to measure the track etch rate, V_T, the etching was performed in an electrolytic conductivity cell. A bulk etch rate, V_B, was estimated by taking the decrease in film thickness during one-month etching. Using the ratio V_T/V_B, we obtained the track etching sensitivity, Q, according to

$$Q = (V_T/V_B) - 1. \quad (1)$$

Figure 1 shows SEM images of the surface of the PVDF ion-track membranes obtained by the chemical etching after storage at 120 and 25 °C. The surface pore diameter was around 180 nm for the track-etched membranes prepared through pretreatment at 120 °C, while the storage at 25 °C produced smaller pores of approximately 120 nm. This clearly confirms that the thermal pretreatment accelerated the pore growth in the range of hundreds of nanometers.

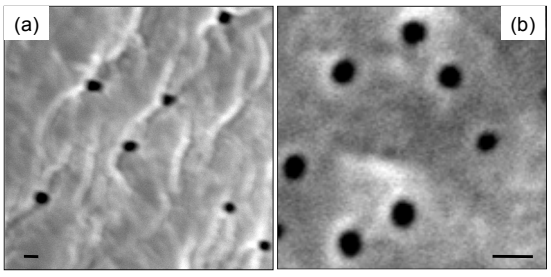

Fig. 1 SEM images of the PVDF track-etched membranes obtained with the pretreatment at (a) 120 and (b) 25 °C. A bar on each image means a length scale of 250 nm.

Table 1 summarizes the results of the etching of ^{129}Xe-irradiated PVDF films after their storage in air at different temperatures. As seen in the table, a V_T value at 120 °C was estimated to be 6.6 μm/h, which was four times higher than that at 25 °C. Among a very limited number of previous conductometry-based studies on PVDF ion-track membranes, Daubresse et al.[3] reported an extremely high V_T reaching nearly 50 μm/h for the chemical etching in KOH-$KMnO_4$ mixed solutions. In our case, there should be an important conclusion: like the $KMnO_4$ addition, heating in high-temperature air also worked as a pretreatment for accelerating the track etching.

As another aspect to be considered for clarifying the advantage of the no-oxidant alkaline etching, it must be noted that V_B was extremely small at both the temperatures, suggesting very mild etching conditions for PVDF, in marked contrast to a few hundreds nm/h for etching in the $KMnO_4$ containing solution[3]. In a strong alkaline medium at high temperatures, virgin PVDF undergoes deprotonization and the consecutive elimination of fluorine to afford –CH=CF- or –CH=CF$_2$. In the absence of the additives, however, these modifications should be restricted to the outermost film layer because there is basically no wetting at the polymer/solution interface.

Consequently, the combined SEM and conductometric analyses revealed that our pretreatment, simply heating in air, was quite effective for facilitating the etching of the latent tracks, while it was insensitive to the irradiation-damage-free polymer outside the track. These results enabled us to obtain very high etching sensitivity for the preparation of cylindrical through-pores in PVDF.

References

1) T. Yamaki et al., E*CS Transactions* 3 (2006) 103.
2) T. Yamaki et al., *Electrochemistry* 75 (2007) 175.
3) C. Daubresse et al., *Nucl. Instrum. Meth. B* 105 (1995) 126.
4) T. Yamaki et al., *Kobunshi Ronbunshu*, 65 (2008) 273.
5) R. Rohani et al., *Nucl. Instrum. Meth. B* 267 (2009) 554.

Table 1 Results of the etching of irradiated PVDF films after their storage in air at two different temperatures.

Temperature (ºC)	V_T (μm/h)	V_B (nm/h)	Q	Pore diameter (nm)
120	6.6	0.31	21000	182±26
25	1.6	0.46	3500	118±11

1-35 Improvement of Chemical Stability of Grafted Electrolyte Membranes by Ion-Beam-Induced Crosslinking: Comparison with γ-ray Irradiation

H. Koshikawa, T. Yamaki, M. Asano, M. Yoshida and Y. Maekawa

Environment and Industrial Materials Research Division, QuBS, JAEA

Chemical stability of radiation-grafted electrolyte membranes has been one of the most important issues in our extensive research of fuel-cell materials. We previously have prepared new poly(ethylene-co-tetrafluoroethylene) (ETFE)-based membranes by ^{60}Co γ-ray irradiation in an oxygen-free atmosphere after the radiation grafting of styrene-derivatives[1]. These membranes possessed multiply-crosslinked structures between the base membranes and grafted polymers, which improved their chemical stability. On the other hand, the present study concerns the use of ion beams as a crosslinking tool instead of γ-rays. This is actually motivated by the fact that the crosslinking yield of polystyrene (PSt) increased with the high LET of radiation[2].

The membranes were prepared by the following procedures. (i) pre-γ-irradiation dose of 15 kGy on ETFE membranes under argon gas at room temperature, and grafting of styrene (St) into ETFE membranes with St /toluene 25 /75 vol% solution under argon gas at 60 ºC for 24 h, (ii) post-crosslinking of ETFE-g-PSt by γ-irradiation of 1,000 kGy or ^{16}O ions irradiation of 6.3 MeV/n (26 kGy as an absorbed dose), and (iii) sulfonation of the post-crosslinked ETFE-g-PSt in a 0.2 mol/L chlorosulfonic acid solution of 1,2-dichloroethane at 50 ºC for 6 h, hydrolyzed in distilled water at 50 ºC for 6 h.

For the estimation of the crosslinking of the post-irradiation, the ETFE base material and the ETFE-g-PSt membrane were evaluated by a tensile test. Figure 1 shows the result of the stress and strain at break of the ETFE base material and the ETFE-g-PSt membranes.

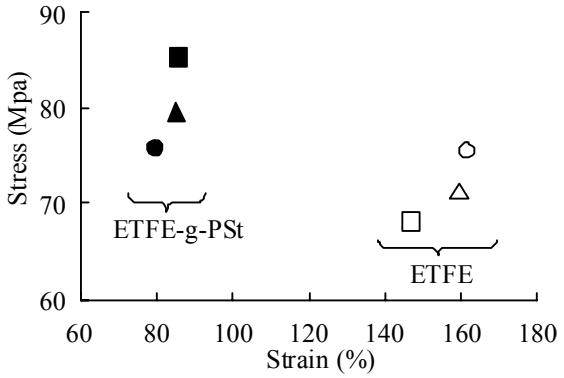

Fig. 1 Stress and strain at break of the ETFE base material and the ETFE-g-PSt membranes which were non-crosslinked (circle) and post-crosslinked with (b) γ-rays (triangle) and (c) ^{16}O ions (square).

It has been clear that the strain of the ETFE base material decreases greatly by the graft of St. Furthermore, the ^{16}O irradiation is 1.9 times more effective to increase the stress of the membranes than γ-rays irradiation. These results indicated that crosslinking of the grafted St chain was effectively introduced by ^{16}O ion beams irradiation than the γ-ray irradiation.

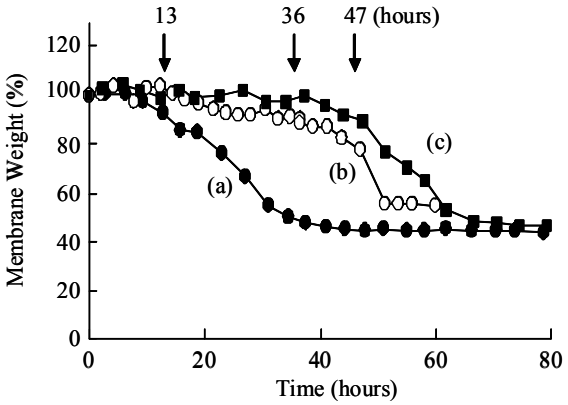

Fig. 2 The change in the membrane weight in 3% H_2O_2 aqueous solution at 60 ºC. (a) non-crosslinked and post-crosslinked with (b) γ-rays and (c) ^{16}O ions.

Figure 2 shows representative results of the accelerated chemical stability test, in which the change in membrane weight was measured during the course of oxidative degradation in a 3% H_2O_2 aqueous solution at 60 ºC. The time when the severe weight loss started, i.e., the degradation onset time (indicated by arrows in the figure), was longer for the post-crosslinked membranes than the non-crosslinked one. Very interestingly in the accelerated chemical stability test, the irradiation with ^{16}O ions gave high stability than the γ-irradiated membrane though the dose of γ-irradiation was quite more than that of ^{16}O ions. This means the LET effect on the crosslinking, that is, bombardment of each ion should form multiply crosslinked networks along its latent track, thereby improving the chemical stability of the membranes noticeably. High density in-track crosslinking (probably due to an LET effect) will be useful as a method for membrane modification.

References

1) J. Chen et al., Mater. J. Power Sources 158 (2006) 69.
2) S.Bouffard et al., Nucl. Instrum. Meth. Phys. Res. B 131 (1997) 79.

1-36 Preparation of Poly(ether ether ketone)-based Polymer Electrolytes for Fuel Cell Membranes Using Grafting Technique

S. Hasegawa, Y. Suzuki and Y. Maekawa

Environment and Industrial Materials Research Division, QuBS, JAEA

A radiation grafting technique is one of the most promising tools for preparing a high performance polymer electrolyte membrane (PEM) in fuel cell developments. Sulfonated aromatic polymer membranes formed the basis of super engineering plastics have been attractive owing to their high thermal stability as well as excellent barrier properties against fuels (methanol, H_2) and oxygen. However, super engineering plastic films such as poly(ether ether ketone) (PEEK) have high chemical resistance, and thus it is difficult to introduce grafting monomers into the films except for a few reports [1,2]. In this work, we successfully prepared PEEK-based PEMs by radiation grafting of a styrene monomer into PEEK films and the consequent selective sulfonation of the grafting chains in the film state. Using milder sulfonation, the sulfonation reactions proceeded at the grafted chains in preference to the phenylene rings of PEEK main chains (Fig. 1).

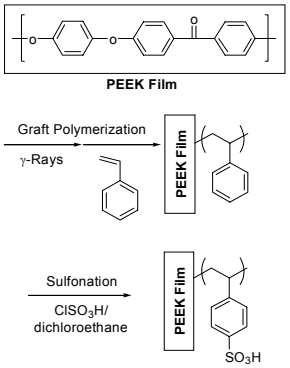

Fig. 1 Radiation grafting of styrene onto a PEEK film and subsequent sulfonation of grafting chain.

High crystalline PEEK films, 25 μm in thickness, were irradiated with doses ranging at 30 kGy (dose rate: 10 kGy/h) using γ-rays from a ^{60}Co source under an argon atmosphere at room temperature. The preirradiated films were immersed in bulk styrene or the solutions of styrene in organic solvents (1/1 v/v) at 80 °C under an argon atmosphere. The grafting degree (*GD*) was calculated from the following equation, $100=(W_g \times W_0)/W_0$, where W_0 and W_g are the film weights before and after the grafting, respectively. The *GD*s gradually increased and leveled off at *GD*s of about 20% and 70% after 48 h (Table 1).

Table 1 Conditions of radiation grafting of styrene onto PEEK with resulting grafting degrees.

Dose (kGy)	Solvent [a)]	Temp. (°C)	GD (%) [b)]
30	-	80	1.4
30	1-PrOH	80	65
30	1-PrOH	90	83

a) Monomer concentration: 50 vol%., b) Reaction time: 48h.

All the sulfonation reactions of the grafted PEEK films with various *GD*s were conducted in the above 0.05 M $ClSO_3H$ solution at 0 °C for 8 h. Ion exchange capacity (IEC) was determined by acid–base titration. Proton conductivity was obtained by impedance spectroscopy measurement at room temperature using a Solartron 1269 analyzer.

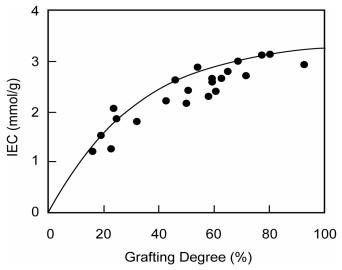

Fig. 2 Radiation grafting of styrene onto a PEEK film and subsequent sulfonation of grafting chain.

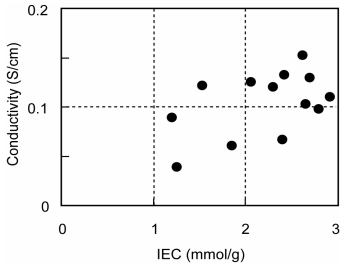

Fig. 3 Relation between the conductivity (S/cm) and IEC (mmol/g) of the grafted PEEK electrolyte membranes.

The sulfonation reactions of the grafted PEEK films were conducted under milder conditions of 0.05 M $ClSO_3H$ in dichloroethane at 0 °C compared with conventional sulfonation condition (0.2 M at 60 °C). Figure 2, most of the membranes exhibited sulfonation degrees near 100%, calculated on the basis of number of polystyrene grafting units. These results strongly suggest that the sulfonation reaction mainly occurs on the styrene units in the graft chains in preference to the phenylene rings of PEEK backbone. The conductivities of the grafted PEEK electrolyte membranes are plotted against the IEC (mmol/g) in Fig. 3. Most of the grafted PEEK electrolyte membranes have higher conductivity (0.09 S/cm) than that of Nafion®(0.07 S/cm). By controlling *GD*s, the IEC and conductivity of the membranes can be controlled in the range of 1.2–2.9 mmol/g and 0.03–0.18 S/cm, respectively.

References

1) H. Ghassemi et al., Polymer 45 (2004) 5855.
2) S. Zhong et al., J. Power Sources 162 (2007) 51.

1-37 A Breakthrough in Development of High-temperature Polymer Electrolyte Membrane Fuel Cells

J. Chen, M. Asano and Y. Maekawa

Environment and Industrial Materials Research Division, QuBS, JAEA

Polymer electrolyte membrane fuel cells (PEMFCs) are very promising as power sources for automotive applications. However, the currently used Nafion® is too expensive. For this reason, inexpensive membranes with high performance have been extensively studied[1-8]. In this study, ethyl styrenesulfonate (ETSS) was grafted onto a divinylbenzene-treated poly(ether ether ketone) (PEEK) films, followed by hydrolysis of the ETSS graft chains, so that a new electrolyte membrane (ssPEEK) was obtained.

The prepared ssPEEK membrane is a highly branched material, containing poly(styrenesulfonic acid) side chains and the PEEK backbones. The PEEK backbones maintain the excellent properties while the grafted side chains give the high proton conductivity.

The ssPEEK membrane-based cell was operated at 95 °C and 80 RH-% to test its long-term membrane durability, as shown in Fig. 1. It was interesting that the ssPEEK membrane-based cell could be stably run for more than 1,025 h at the high temperature of 95 °C. The open circuit voltage (OCV) degradation rate was about 29 μV/h, and the voltage degradation with current density at 0.3 Acm^{-2} was about 18 μV/h. Such a slow degradation rate is believed to satisfy the requirement of automotive fuel cells. Drastic degradation of the OCV and the cell voltage at 0.3 Acm^{-2} was observed after 980 h and 1,025 h, respectively.

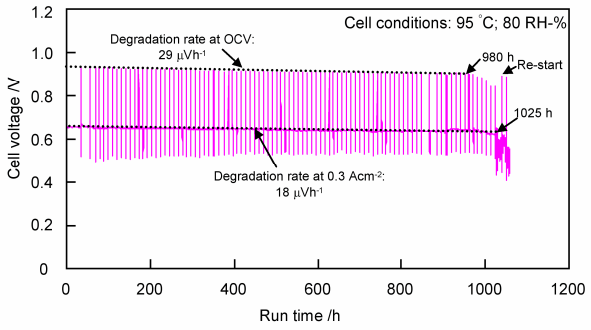

Fig. 1 Durability of the polymer electrolyte membrane fuel cell using the ssPEEK membrane.

However, with a re-start of the fuel cell after 5 min drying treatment, the OCV almost returned to its the initial value, indicating that the gas crossover through the membrane had not yet significantly increased; the drastic decrease in OCV as well as in the cell voltage at 0.3 Acm^{-2} was mainly due to the degradation which occurred in the catalyst layer.

After the durability test, the anode and cathode catalyst together with the catalyst before use were investigated by XRD and TEM. Through the XRD measurement and calculation by the Scherrer equation[9], we found that the size of the Pt particles in the anode and cathode was 4.9 and 6.5 nm, respectively, while in a new membrane electrode assembly (MEA) before any test, it was 2.6 nm. Therefore, the Pt particles aggregated significantly and were sintered during the cell durability test; this degradation was more severe on the cathode side. Similar Pt aggregation and sintering were also observed in the TEM images.

The ssPEEK membrane after the durability test was also analyzed. The thickness of the active area of the membrane, especially near the cathode inlet, was somewhat decreased. On the other hand, the proton conductivity at the active area decreased to about one third of the initial value. From the FT-IR/ATR analysis, it can be found that both the active surface of the anode and the cathode lost about 20% of their sulfonic acid groups. The deterioration on the cathode side of the membrane was more severe than that on the anode side.

In conclusion, an ssPEEK membrane was developed and a fuel cell using this membrane was successfully run at 95 °C for more than 1,000 h. Development of such a high performance polymer electrolyte membrane will bring a big breakthrough for the practical application of fuel cell using the hydrogen as the fuel.

References

1) J. Chen et al., J. Membr. Sci., 256(2005) 38; 277 (2006) 249; 269 (2006) 194; 283 (2006) 373; 296 (2007) 77; 319 (2008) 1-4.
2) J. Chen et al., J. Appl. Polym. Sci., 100 (2006) 4565; 101 (2006) 2661; 103 (2007) 1966.
3) J. Chen et al., J. Mater. Sci., 41 (2006) 1289; 42 (2007) 1330.
4) J. Chen et al., J. Power Sources, 158 (2006) 69.
5) J. Chen et al., Electrochem. Solid-State Lett., 9 (2006) G184; 9 (2006), G326.
6) J. Chen et al., J. Polym. Sci. A, Polym. Chem., 45 (2007), 2624; 46 (2008) 5559-5567.
7) J. Chen et al., Polymer, 48 (2007), 6002.
8) D. Li et al., NIMB 267 (1) (2009) 103-107.
9) H.P. Klug and L.E. Alexander, in "X-ray Diffraction Procedures for Polycrystalline and Amorphous Materials", Wiley, New York (1973).

1-38 Water Transport Properties of Crosslinked-PTFE Based Electrolyte Membranes

S. Sawada [a,b], T. Yamaki [a], H. Nishimura [b], M. Asano [a], A. Suzuki [b], T. Terai [b] and Y. Maekawa [a]

[a] Environment and Industrial Materials Research Division, QuBS, JAEA,
[b] Department of Nuclear Engineering and Management, Graduate School of Engineering, The University of Tokyo

During the operation of a proton-exchange-membrane (PEM) fuel cell, water in a hydrated membrane is transported by an electro-osmotic drag and concentration gradient-driven back diffusion [1]. These phenomena would determine water distribution across a PEM. The structure of the hydrophilic region, where water and sulfonic acid (SO_3H) groups aggregate, must be considered for the better understanding of the water transport properties. For example, the hydrated Nafion® membrane is believed to possess the spherical hydrophilic clusters with a diameter of 3-5 nm.

We recently developed crosslinked-poly(tetrafluoroethylene) (PTFE) based PEMs by a radiation-induced grafting method [2], which exhibited restricted water swelling due to their crosslinking structures [3]. Here, the water transport properties of these novel PEMs at such low water content were clarified in relation to their microscopic structure.

The PEM synthesis was carried out as already reported [2]. We used, as a base material, a 42 μm thick film of PTFE crosslinked with electron beam at total doses of 100 and 400 kGy. Here, because the irradiation dose is known to determine the density of crosslinks, the 400 kGy irradiated-PTFE film would be more highly crosslinked than the 100 kGy-irradiated one. The film was pre-irradiated with 15 kGy γ-rays in an Ar atmosphere at room temperature, and then immersed in a styrene monomer at 60 °C for 4-8 hours. For sulfonation, the grafted film was immersed in a 0.2 M chlorosulfonic acid/1,2-dichloroethane mixture at 50 °C for 6 hours. Finally, the resulting PEM was rinsed with pure water and then dried in a vacuum oven. The ion exchange capacity (IEC) of the PEM was evaluated by back titration with a standardized 0.1 M NaOH solution.

We investigated the water transport properties by a tritium-labeled-water (HTO) permeation method using a two-compartment cell. Each of the compartments separated by a PEM was filled with pure or HTO-containing water. The HTO concentration in the receiving compartment, C, was measured by a scintillation counting technique. The water permeability, P, was estimated from the slope of the C vs. time line based on the Fick's diffusion theory.

P is expressed as the product of the water volume fraction, ϕ, and water diffusion coefficient, D. In order to have a deeper insight into the behavior of the individual water molecules, D was calculated by the following equation:

$$D = P/\phi . \quad (1)$$

Table 1 shows the D values of the PEMs based on the crosslinked and non-crosslinked (i.e., the crosslinking dose of 0 kGy) PTFE at similar IECs of 1.6-1.7 meq/g. As the crosslinking dose increased up to 400 kGy, D reached a minimum of 2.1×10^{-10} m^2/s, which was 55% and 43% of those in non-crosslinked PEM (3.8×10^{-10} m^2/s) and in Nafion® (4.9×10^{-10} m^2/s), respectively. As mentioned in the introduction, ϕ was also reduced with an increase of the crosslink density. Accordingly, the crosslinked structure of PTFE main chains suppressed the expansion of hydrophilic regions, thereby decreasing the values of D.

Then, we consider water uptake, represented by the number of water molecules per SO_3H group, λ, to account for the above results. According to the previous report [4], five water molecules were required for complete formation of the first hydration shell around a SO_3H group. The crosslinked PEM synthesized by 400 kGy irradiation showed the λ of 8.1 (see Table 1), and therefore, more than half of water molecules in the PEM could be bound to the SO_3H groups, which is likely the main reason for low water mobility. This implies that the water transport pathway has condensed SO_3H groups even in the hydrated state because the PTFE crosslinks would make the membrane water poor.

References

1) G. Xie et al., J. Electrochem. Soc. 142 (1995) 3057-3062.
2) T. Yamaki et al., Polymer 45 (2004) 6569-6573.
3) S. Sawada et al., Trans. Mater. Res. Soc. Jpn. 30 (2006) 943-946.
4) S. J. Paddison, J. New Mater. Electrochem. Syst. 4 (2001) 197-207.

Table 1 D and λ of the non-crosslinked and crosslinked PTFE based PEMs with similar IECs of 1.6-1.7 meq/g. This table also shows the results for Nafion®.

Base film	Crosslinking dose (kGy)	D ($\times 10^{-10}$ m^2/s)	λ
PTFE	0	3.8	23
	100	2.9	13
	400	2.1	8.1
Nafion®	–	4.9	22

2. Environmental Conservation and Resource Security

This is a blank page.

2-01 Improvement of Heat Stability of Poly(L-lactic acid) by Radiation-induced Crosslinking and Post-processing

N. Nagasawa, N. Kasai and M. Tamada

Environment and Industrial Materials Research Division, QuBS, JAEA

Poly(L-lactic acid) (PLLA) is a transparent and hard plastic and is produced by either polymerization of L-lactic acid obtained by a fermentation method or ring-opening polymerization of L-lactide (cyclic dimmer) in the presence of catalyst. The raw materials are renewable resources such as sugar or corn starch. Therefore, PLLA is one of the most attractive materials because of the most promising candidates as a replacement of petrochemical products. It is expected that the PLLA can be applied to dummy lens of eyeglasses as a replacement of one made from poly (methyl methacrylate) (PMMA). However, PLLA briefly deformed at temperature higher than its glass transition temperature (*Tg*) of approximately 55 ºC, because of the bulk in cargo ship heated up to 70 ºC when eyeglasses products sent overseas.

Radiation-induced crosslinking is an effective tool for improvement of heat stability of polymer materials. Therefore, this technique was applied to produce PLLA requiring high thermal stability. We found that triallyl isocyanurate (TAIC) has been proved as an effective crosslinker for PLLA to improve the above-mentioned property[1, 2]. However, in this application to optical lens, it is not enough to improve the thermal deformation of PLLA under stressing at 70 ºC. Composition with inorganic compounds and crystallization by heat-processing are used to improve the heat stability of thermoplastics. In this study, the radiation-induced crosslinking of PLLA / silicon dioxide (SiO_2) composite with TAIC and the post processing of crosslinked PLLA composite by heating were further investigated on the viewpoint of thermal deformation.

PLLA (trade name: LACEA® H100), TAIC and SiO_2 powder (trade name: NS-P) used in this study were kindly contributed from Mitsui Chemicals, Inc., Shin Nakamura Chemicals, Co., Ltd, and Tosoh Silica Co., Japan, respectively. PLLA and the additive were mixed in a laboplastomill at mixing speed of 20 rpm at 180 °C for 10 min. The PLLA / SiO_2 composite films, 1 mm thick, were prepared by hot-pressing at 180 ºC for 5 min and then irradiated by EB accelerator with dose ranges from 10 kGy to 100 kGy. The gel content was estimated by weighing insoluble part of the crosslinked PLLA composite film after immersion in chloroform for 48 h at room temperature. The thermal property and dynamic rheology of crosslinked PLLA composite films were measured by differential scanning calorimeter (DSC) and ARES-RFS III rheometer.

The crosslinking structures are formed in irradiated PLLA /SiO_2 composite films with TAIC. Gel fraction of the composite films represented to the crosslinking density increased with TAIC content and radiation dose. Gel fraction seems to saturate at doses higher than 50 kGy.

DSC measurements of crosslinked samples irradiated at 50 kGy show typical crosslinking in PLLA / 10 % SiO_2 composite mixed with more than 5 % TAIC. Neither crystallization peak nor melting peak of PLLA crystals can be observed in DSC of PLLA / SiO_2 / TAIC composite irradiated at doses higher than 50 kGy like non-irradiated one.

Figure 1 shows the temperature dependence of share storage modulus (*G'*) analyzed in the crosslinked PLLA / SiO_2 composite films. Non-crosslinked PLLA (a) becomes soft from about 55 °C, which is *Tg,* and then its *G'* rapidly decreases until 70 °C. Even if it is crosslinked, it exhibits almost the same action. However, after composition with SiO_2 and heating, its decrease level became less with SiO_2 added, although it slowly turned soft at about 55 °C. After it was crosslinked, PLLA / SiO_2 composite heat-treated at 100 °C for half an hour exhibited the least change of *G'*. From the above results, it was found that thermal deformation could be controlled by adding inorganic substances and applying heat treatment.

The post-heated crosslinked PLLA composite became more stable at higher temperature of 70 ºC than *Tg*. The combination of composition with SiO_2, radiation crosslinking and crystallization by post-heating caused significant improvement of heat stability of PLLA material.

References

1) H. Mitomo et al., *Polymer*, **46**(3) (2005) 4695.
2) N. Nagasawa et al., *Nucl. Instrum. Meth. Phys. Res., Sect. B,* **236**(1-4) (2005) 611.

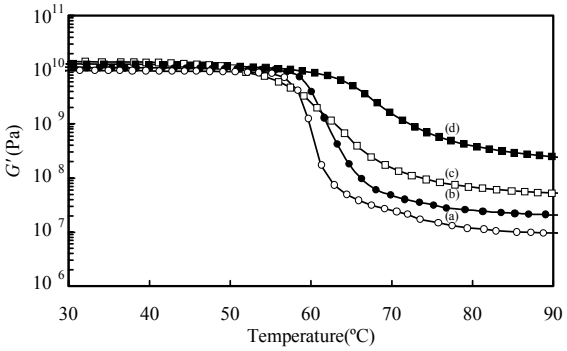

Fig. 1 Temperature dependence of share storage modulus (*G'*) of crosslinked PLLA films with 5 % TAIC by EB-irradiation at 50 kGy and post processed sample. (a) Unirradiated PLLA, (b) Crosslinked PLLA, (c) Crosslinked PLLA / 10 % SiO_2, d) Crosslinked PLLA / 10 % SiO_2 post-heated at 100 ºC for 0.5 h.

2-02 Effects of Molar Mass of CMC on Mechanical Properties of CMC-Acid Gel

M. Takigami [a)], A. Hiroki [b)], N. Nagasawa [b)], T. Kasahara [c)], S. Takigami [c)], Y. Maehara [d)] and M. Tamada [b)]

[a)] Gunma Industry Support Organization, [b)] Environment and Industrial Materials Research Division, QuBS, JAEA, [c)] Gunma University, [d)] Tomioka General Hospital

Carboxymethyl cellulose (CMC) is a widely used water-soluble polymer derived from wood pulp. Because of its safe and environmentally friendly properties, its use extended after gelation by multivalent metal ions, crosslinking agents and radiation crosslinking [1-3]. We found that sodium salt of CMC formed a gel (CMC-acid gel) by mixing CMC with acid [4,5]. The mechanism of gel formation was elucidated as a replacement of sodium with hydrogen in carboxymethyl group existing as a counter ion. Commercial CMC is generally in the form of sodium salt owing to the production process. CMC in the form of sodium salt is easily soluble in water, however, it is not soluble in water once it is replaced with hydrogen. As the result, CMC molecules became close enough to form hydrogen bonds between the molecules and gel was formed in this way. The resultant gel is elastic, adherent and strong. Those characters were very specific as for polysaccharide gels.

CMC-acid gel can be prepared also under the coexistence of other carbohydrates. CMC-Konjac glucomannan (KM) acid system was examined [6]. Molar mass of KM had a big influence on mechanical properties of the gel. However, we have not examined the effects of molar mass of CMC on mechanical properties of the CMC-acid gel.

We reported a method to decrease molar mass of polysaccharides using acid hydrolysis at elevated temperature and pressure [7]. By the method, KM with varieties of molar masses was prepared without chemical structural changes. Applying the method, CMC was hydrolyzed with citric acid to prepare CMC with various molar masses.

CMC 1380 having a degree of substitution of 1.36 and viscosity of 1820 mPa·s (1 % solution, 25 °C), produced by Daicel Chemical Industries, Ltd., Japan, was used throughout the experiment. CMC was mixed with a 0.5 M citric acid solution at the concentration of 10 %. For mixing, a hybrid defoaming mixer (AR-250, Thinky Cooperation, Japan) was used. The mixture was molded into a cylinder with a thickness of 10 mm and a diameter of 20 mm and mechanical properties of the gels were measured using a Table-Top Universal Tester (EZ-Test, Shimadzu Co.). The CMC-acid gel cylinders were pressed at 2 mm/min.

Gels made of CMC with less molar mass became stronger after long time storage, while those made of higher molar mass CMC became slightly brittle after storage. The phenomena were elucidated by number of hydrogen bonds in gel. Too many hydrogen bonds made the gels fragile. Controlling the number of hydrogen bonds in gel, some of the CMC-acid gels recovered the initial thickness after compression to 80 % thickness of the gel. Elastic and strong gels were formed. Such gels are under investigation to look for applications.

As an example of application of CMC-acid gel, a gel was under investigation to provide clear magnetic resonance imaging (MRI) as shown in Fig. 1. The left imaging was measured without using CMC-acid gel and showed artifact (white part in a circle), which did not exist actually. Most of the artifact disappeared in the right imaging measured putting CMC-acid gel on shoulders. The CMC-acid gel was effective to provide clear MRI without showing its own strong signal.

Acknowledgement

The authors are grateful for the sponsorship of Japan Science and Technology Agency to achieve Gunma Prefecture Collaboration of Regional Entities for the Advancement of Technological Excellence.

References

1) B. Fei et al., J. Appl. Polym. Sci. 78 (2000) 278.
2) R. A. Wach et al., J. Appl. Polym. Sci. 81 (2001) 3030.
3) R. A. Wach et al., Rad. Phys. Chem. 68 (2003) 771.
4) M. Takigami et al., Fiber Preprints, Japan, Vol. 61, No. 3 (autumn Meeting, 2006) 158, The Society of Fiber Science and Technology, Japan.
5) M. Takigami et al., Trans. Mater. Res. Soc. Jpn. 32 (2007) 713.
6) T. Kasahara et al., Trans. Mater. Res. Soc. Jpn. 33 (2008) 927.
7) M. Takigami et al., Trans. Mater. Res. Soc. Jpn. 31 (2006) 723.

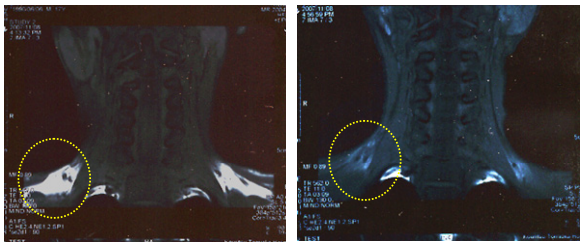

Fig. 1 Magnetic resonance imaging of human shoulder.
Left: Measured without CMC-acid gel,
Right: Measured using CMC-acid gel.

2-03 Development of Low Shrinking Echizen Japanese Paper with CMC Gel

N. Kasai [a)], F. Yoshii [a)], M. Tamada [a)], H. Ishikawa [b)] and K. Iwai [c)]

[a)] Environment and Industrial Materials Research Division, QuBS, JAEA,
[b)] Ishikawa paper mills, LTD, [c)] The Wakasa Wan Energy Research Center

Polysaccharides such as cellulose and starch are renewable materials, but those materials are typical degradation polymer under ionizing radiation. Thus it is difficult to lead crosslinked structure in polysaccharide molecules as a solid state. Polysaccharides derivatives such as carboxymetnylcellulose (CMC) and carboxy-mechylstarch (CMS) and carboxymethylchitosan (CM-chitosan) dissoluble in water were irradiated at a high concentration (paste-like condition) to lead crosslinking structure in polysaccharides. It was found that this condition is effective to induce crosslinking for polysaccharide derivatives and form hyrdogel. CMC to induce crosslinking was homogeneously kneaded with water at high concentration. Hydrogels are achieved at the concentration over 10%, after exposing those solution to ionizing irradiation. The crosslinking of CMC was affected by factors such as concentration, molecular weight and degree of substitution (DS). As shown in Fig. 1, the gel generated with a low dose by large DS, and the gel fraction was obtained by 1～2% with 2 kGy, the gel of more than 40% with 5 kGy.

In the application, the CMC gel was impregnated in the Echizen Japanese paper (Washi) to retard shrinkage by moist change of climate. The gel was made from the solution at the low concentration, 1% and the gel was impregnated in an Echizen Washi sheet during processing as illustrated in Fig. 2. On the other hand, CMC with the high gel fraction is not dispersed easily to water. Hence, 2 and 5 kGy irradiated CMC hydrogel was used for modification of Echizen Washi. CMC gel was observed to homogeneous disperse in the Echizen Washi fibrous by using electron microscopy. Shrinkage of Echizen Washi could be reduced to 0.8% from 1.3% by impregnating of CMC gel. The Echizen washi is used for gold-leafed folding screen and crack is often induced for gold foil on Echizen Washi by shrinkage. It is expected that lower shrinking Echizen Washi is effective for prevention crack of gold foil adhered on the Washi by lowering of shrinking (Fig. 3). It was found that Echizen Washi impregnated gel are effective for improvement of other physical properties except for reduction of shrinkage. Tensile strength, surface strength and elongation at break were 1.5, 2.0 and 1.4 times higher compared with those of the control, respectively. And it was found further advantage that, penetration of water for Echizen Washi impregnated gel was retarded.

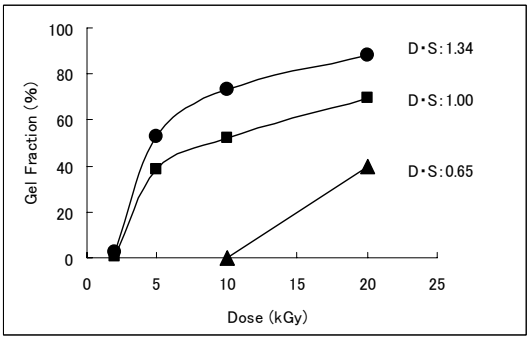

Fig. 1 Effect of DS on gel fraction of CMC.

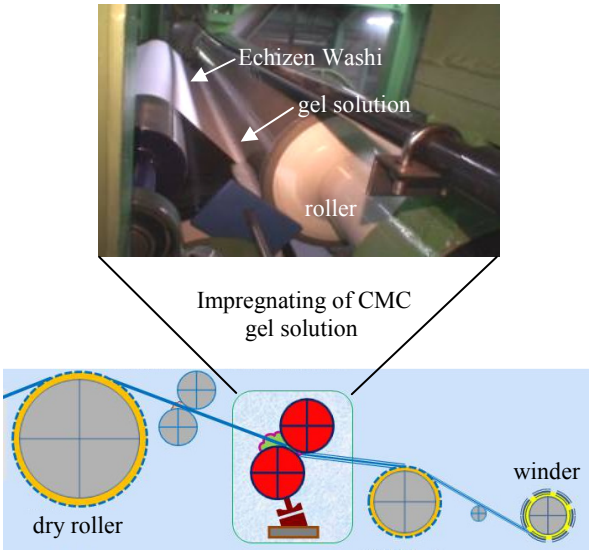

Fig. 2 Impregnating of CMC gel solution for Echizen Washi.

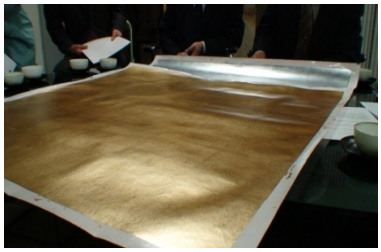

Fig. 3 Wallpaper pasted gold foil.

This study was supported by a grant for "The development of the Low Shrinking Echizen Japanese Paper which used the CMC gel" from METI-KANSAI.

2-04 Preparation and Characterization of DNA-BSA Hybrid Hydrogels Using γ-ray Irradiation

H. Saito [a)], K. Furusawa [a)], T. Dobashi [a)], N. Nagasawa [b)] and M. Tamada [b)]

[a)] Department of Chemistry and Chemical Biology, Graduate School of Engineering, Gunma University, [b)] Environment and Industrial Materials Research Division, QuBS, JAEA

We have prepared DNA-BSA (bovine serum albumin) hybrid hydrogels using γ-ray irradiation of concentrated solutions of DNA and BSA. The gel fraction and acridin orange adsorption measurements suggest that the hydrogel prepared by the present method is a candidate of materials for carcinogen adsorption.

1. はじめに

工場排水や産業廃棄物等には微量であるが発ガン性を有する有害物質が含まれ、人体への影響や環境汚染が問題視されている。DNA は、発ガン性有害物質を吸着することから、DNA を固定化した吸着材の研究開発が行われている。最近、我々は、化学薬品を使用せずに橋かけできる放射線橋かけ技術を応用し、カルボキシメチルセルロースなどの多糖類誘導体との濃厚混合水溶液にγ線を照射することにより、DNA を固定化したゲルを合成できることを見いだした [1)]。本研究では、多糖類誘導体よりも DNA との親和性が高いタンパク質である牛血清アルブミン(BSA)を用いて DNA 含有ゲルをγ線照射により合成し、得られたゲルのゲル分率、膨潤度ならびに発ガン性モデル物質であるアクリジンオレンジの吸着性について調べた。

2. 実験方法

試料は ICN Biomedicals 製 BSA（66 kDa）と、日本化学飼料より提供された鮭白子由来 DNA（平均塩基対数 10 kbp、約 200 kDa）を用いた。BSA 水溶液を各濃度（5~40 wt%）に調製し、1.0 wt%の DNA 水溶液に各濃度（10~40 wt%）の BSA 水溶液と等容混合し、BSA-DNA ブレンド水溶液を調製した。各溶液をマイクロチューブに 1 mL 入れ、遠心分離器（回転数 10,000 rpm、15 分間）で脱泡後、室温で所定線量（10~160 kGy、線量率 10 kGy/h）γ線を照射した。照射サンプルを水洗浄し凍結乾燥後、ゲル分率及び膨潤度を算出した。乾燥ゲル 0.01 g に対して 15 μg/mL のアクリジンオレンジ溶液 5 mL の割合で、2 日間室温にて浸漬し、その上澄み溶液の 495 nm における吸光度から吸着特性を評価した。

3. 結果と考察

Fig. 1 に 10 wt% BSA＋0.5 wt% DNA 溶液から合成した BSA-DNA ゲル（または溶液）のゲル分率の線量依存性について示す。ゲル化開始点は BSA 単独の水溶液では 90 kGy、BSA-DNA ブレンド水溶液では 60 kGy であった。また、線量の増加に伴い、ゲル分率が増加する傾向が見られ、120 kGy 以上では、70~80%前後のゲル分率となった。また、得られたブレンドゲルの膨潤度について、BSA 単独では 90 kGy で約 600、BSA-DNA では 60 kGy で約 150 であったが、100 kGy 以上では DNA の有無に関わらず同程度の約 100 であった。BSA 濃度の影響を検討するため、100 kGy 照射で作製した BSA-DNA ブレンドゲルの BSA 初期濃度とゲル分率との関係について調べた。BSA 濃度が増加するにつれ、ゲル分率も増加した。5 wt%では 48%になるが、10 wt%では 65%になり、それ以上の高濃度では 65%であった。また、BSA 濃度が増加すると、膨潤度が減少した。DNA は BSA と親和性が高く複合体を形成することから、複合体形成による分子鎖の運動性制御によってゲル化が促進したものと考えられる。100 kGy 照射によって合成し、ほぼ同等の膨潤度（約 150）を有する BSA ゲル、BSA-DNA ゲルのアクリジンオレンジ吸着特性を評価した。BSA-DNA ゲルが 0.015 μg 吸着し、BSA ゲルよりも 15 倍吸着した事が分かった。以上より、BSA-DNA ゲルは濃度と線量によってゲル分率や膨潤率の制御でき、アクリジンオレンジを吸着することから、γ線照射により合成した BSA-DNA ゲルは発ガン性物質浄化材としての応用が期待される。

Reference

1) K. Furusawa et al., *J. Biomater. Sci. Polymer Edn,* 19 (2008) 1159-1170.

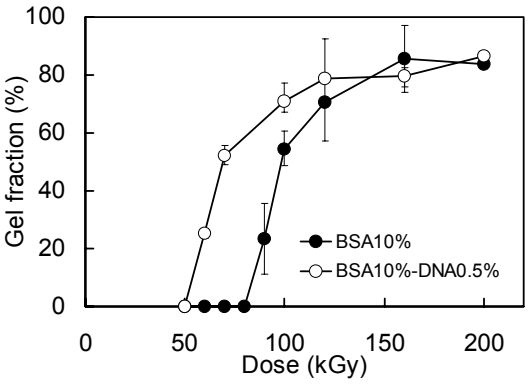

Fig. 1 Dose dependence of Gel fraction.

2-05 Preparation of Hydrogels for a Simple Identification of Fe (II) Content

R. Shirotani [a], A. Hiroki [b], M. Tamada [b] and Y. Jigata [a]

[a] Saitama Industrial Technology Center,
[b] Environmental and Industrial Materials Research Division, QuBS, JAEA

A simple metallic identification method based on hydrogels was investigated. Poly(vinyl alcohol) gel membranes synthesized by electron beam irradiation were immersed into an acidic aqueous solution containing 1, 10-phenanthroline (phen) as a colorimetric reagent and an ascorbic acid as a reducing agent to prepare chromogenic gel membranes. As the obtained gel membranes were pasted onto the copper alloy with Fe content, it was found that the transparent hydrogel turned red gradually. The absorbance of the colored hydrogels at 510 nm increased with increasing Fe content in the copper alloy, resulting in the formation of the Fe (II)-phen complex. Fe (II) content in the alloy could be quantified simply by changing in a color of the gel membranes.

金属資源の価格高騰に伴い、金属廃材の再利用が注目されている。金属廃材を再利用し、目的組成の材料を製造するためには、溶融段階での組成調整が不可欠である。金属廃材の材種（組成）をオンサイトで判定できれば、リサイクル率及び製品の品質向上に繋がる。そこで、本研究では、高価な機器を必要とせず、簡便に金属成分を定量できる分析法の開発に取り組み、銅合金中の鉄分簡易判定用ゲルを作製したので報告する。

ポリビニルアルコール(PVA) の 20 wt%水溶液を調製し、冷却プレスにより厚さ 1 mm の薄膜を作製した。この薄膜に所定線量の電子線を照射し、橋かけ反応により PVA ゲルシートを作製した。作製したゲルシートを発色試薬（1,10-フェナントロリン, phen)、還元剤（アスコルビン酸）を含む酸水溶液に 24 時間浸漬し、溶液から取り出した後、表面の余分な溶液を拭き取り発色ゲルシートとした（Fig. 1)。発色ゲルシートを鉄含有量が異なる 6 種類の銅合金にそれぞれ 10 分間貼り付け、発色度合いを目視観察するとともに、発色したゲルの吸光度を測定した。

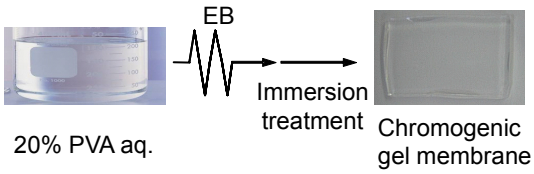

Fig. 1 Preparation of hydrogels for metal identification.

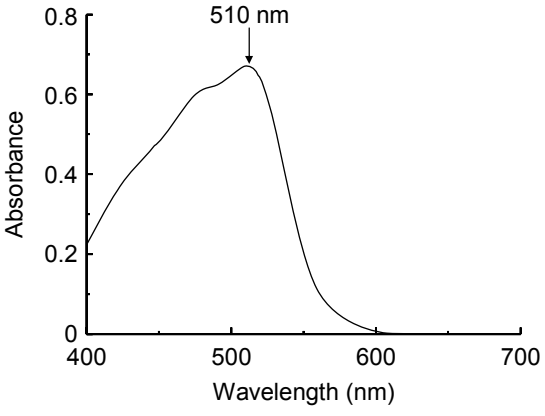

Fig.2 Absorption spectra of the PVA gel membrane containing Fe(II)-phen complex.

5 g/L の phen、0.1 g/L のアスコルビン酸を含む酸水溶液(pH＝2)への浸漬により作製した透明な発色シートを、鉄含有量 4 wt.%の銅合金に 10 分間貼り付けた結果、ゲルシートは、赤く発色することが分かった。発色したシートの吸収スペクトルを Fig. 2 に示す。発色したゲルは、510 nm にピークを示した。Fe(II) と phen は、pH 2～9 の水溶液中で安定な錯体 $[Fe(phen)_3^{2+}]$ を形成し、波長 510 nm に吸収極大を示すことが知られている [1]。従って、PVA ゲル内においても安定な Fe(II) - phen 錯体を形成できることが明らかとなった。更に、溶液中の発色試薬及び還元剤の濃度の影響について調べた結果、それぞれを 10 g/L, 1 g/L まで増加しても 510 nm の吸光度はほぼ同じであることが分かった。

鉄含有量が 0, 1, 2, 3, 3.5, 4 wt.%の銅合金に 10 分間貼り付けた後の発色ゲル（5 g/L の phen、1 g/L のアスコルビン酸を含む酸水溶液(pH＝2)に 24 時間浸漬により作製）の写真を Fig. 3 に示す。鉄含有量の増加に伴い発色の度合いが強くなることが分かった。波長 510 nm の吸光度測定の結果、吸光度は鉄含有量増加に伴い緩やかに増加していることが明らかとなった。しかし、鉄含有量 1%以下の銅合金では発色を確認できなかった。そこで、貼付時間を長くした結果、吸光度は貼付時間の増加に伴い直線的に増加し、20 分でおよそ 2 倍にまで達することが分かった。従って、鉄含有量 1%以下の目視での発色確認が困難な銅合金（0.26 wt.%）に対しては、貼付時間を長くすることで材種判定できることが分かった。

以上のように、発色の度合いから銅合金中の鉄含有量を簡易定量できるゲルシートを作製できた。

Reference

1) 大西寛、束原巌、吸光光度法－無機編、共立出版、(1983) 101.

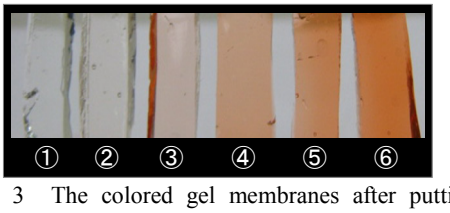

Fig. 3 The colored gel membranes after putting onto the copper alloys. Fe content in the alloy; ①0%, ② 1%, ③ 2%, ④ 3%, ⑤ 3.5%, ⑥ 4%.

2-06 Identification of Carboxymethyl Cellulose Radicals by ESR Method

S. Saiki [a,b], N. Nagasawa [a], A. Hiroki [a], N. Morishita [a], M. Tamada [a], H. Kudo [b] and Y. Katsumura [b,c]

[a] Environment and Industrial Materials Research Division, QuBS, JAEA,
[b] Graduate School of Engineering, The University of Tokyo,
[c] Advanced Science Research Center, JAEA

Cellulose and their derivatives are well known as radiation-degradation polymer. However, it was found that some kinds of water-soluble cellulose derivatives at highly concentrated aqueous solution undergo crosslinking reactions by ionizing irradiation [1-3]. Carboxymethyl cellulose (CMC), having a structure as shown in Fig. 1, is one of water-soluble cellulose derivatives. Radiation -induced crosslinking and degradation of polymer in aqueous solution are generally caused by water radiolysis, especially OH radical. OH radical is easy to abstract hydrogen atom from carbon atom of polymer chains, and then polymer radicals are produced. The polymer radicals are contributed to crosslinking and degradation. In this work, to identify CMC-radical produced by reaction with OH radical in an aqueous solution, CMC radical produced using UV photolysis of hydrogen peroxide (H_2O_2), were observed by electron spin resonance (ESR) method.

In this ESR measurement, UV photolysis and flow system were adopted as shown in Fig. 2. The sample solution contained CMC (degree of substitution 2.34) and H_2O_2 was continuously bubbled with N_2 gas to remove oxygen. As sample solution flows, ESR spectra are measured.

As a result of adjusting many parameters, we succeed in detecting ESR spectrum of CMC radical produced by reaction with OH radical (Fig. 3). As it can be seen, there are large and small splits. Because the left-and-right spectra are not same shape, it is assumed that a number of radicals are overlapped in this spectrum.

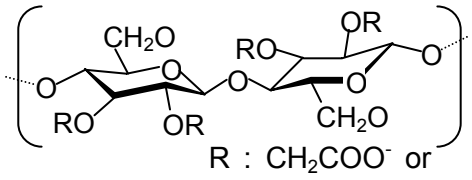

Fig. 1 Carboxymethyl cellulose.

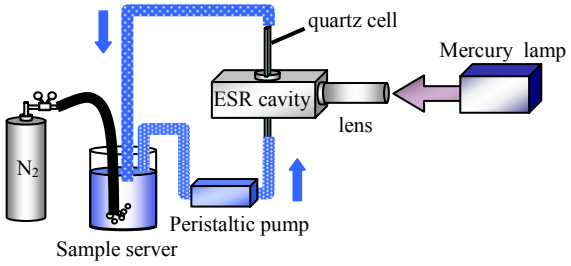

Fig. 2 ESR measurement system.

Here, candidates of radical sites were considered from a point of view of chemical structure. Considering that OH radical is easy to abstract hydrogen atom from carbon atom, it is assumed that radicals are located on carbon atom of glucopyranose ring or of carboxymethyl group. To identify radical sites, radicals, which have similar chemical structure around radicals with these candidates, should be compared with experimental ESR spectra from a point of view of split pattern and width, which reflect on chemical structure information about hydrogen atom position around the radical. As for radical on glucopyranose ring, compared with glucose radical [4], split pattern and width are very different from experimental results, therefore it is speculated that radicals on glucopyranose ring are not included in experimental results. Next, as for radicals on carboxymethyl groups, compared with benzyl ethyl ether radical [5], split pattern and width are almost coincident with experimental results.

In conclusion, experimental ESR spectrum was identified as radicals on carboxymethyl groups.

References

1) B. Fei et al., J. Appl. Polym.Sci., 78 (2000) 278-283.
2) R. A. Wach et al., J. Appl. Polym. Sci., 81 (2001) 3030-3037.
3) F. Yoshii et al., Nucl. Instrum. Meth. Phys. Res. B, 208 (2003) 320-324.
4) B. C. Gilbert et al., J. Chem. Soc. Perkin II, 8 (1981) 1186-1189.
5) S. Steenken et al., J. Phys. Chem., 79 (1975) 763-764.

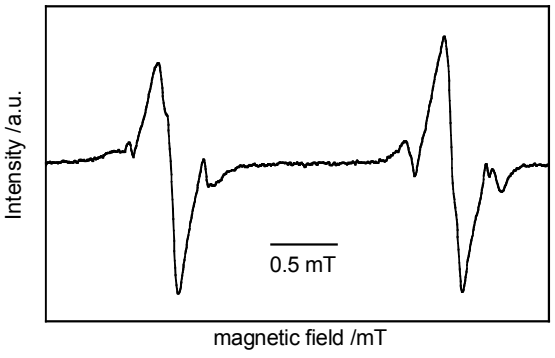

Fig. 3 ESR spectra of CMC radical produced by OH radical.

2-07 Synthesis of Fibrous Catalyst for Biodiesel Production

Y. Ueki [a], N. H. Mohamed [b] and M. Tamada [a]

[a] Environment and Industrial Materials Research Division, QuBS, JAEA,
[b] Radiation Processing Technology Division, Malaysian Nuclear Agency

1. Introduction

Fossil fuel resources are decreasing daily. Biodiesel, which is produced from vegetable oils and animal fats, has been attracting attention as an alternative to petroleum diesel fuel, since it is a non-toxic, biodegradable, renewable and carbon-neutral fuel. At present, the homogenous alkali-catalyzed method using NaOH or KOH as a catalyst is the mainstream for the industrial production of biodiesel. Recently, novel synthesis techniques, such as acid-, ion-exchange resin-[1], lipase-, and metal oxide-catalyzed method and non-catalytic supercritical methanol method[2], have been investigated and developed by numerous researchers. The objectives of this study are to synthesize a sophisticated fibrous catalyst for biodiesel production through the radiation-induced graft polymerization and to evaluate its catalytic performance through the transesterification of triglyceride and alcohol.

2. Expermental

Nonwoven polyethylene (NWPE) fabric (fiber diameter: 13 μm) was irradiated with an electron beam up to 100 kGy in nitrogen atmosphere at dry ice temperature. The irradiated NWPE fabric was reacted with an aqueous emulsion solution, which was composed of 4-chloromethylstyrene (CMS), polysorbate 20 (Tween 20) and deionized water, in a deaerated glass ampoule for 4 h at 40 ºC. After grafting, the CMS-grafted NWPE fabric was further treated with 0.25 M trimethylamine (TMA) aqueous solution at 50 ºC to introduce a quaternary ammonium group. The fibrous catalyst was pretreated with 1 M NaOH, before using for transesterification of triglyceride and alcohol. The degree of grafting (Dg) was evaluated by the increased weight after grafting, and the TMA group density was estimated by the nitrogen content of fibrous catalyst. The concentrations of triglyceride and biodiesel were measured by using high performance liquid chromatography (HPLC) system, in a similar manner to the method described M. Holčapek et al[3].

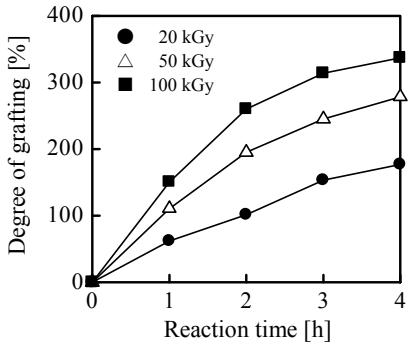

Fig. 1 Effect of irradiation dose on Dg.

3. Results and Discussion

As shown in Fig. 1, the Dg of NWPE fabric could be controlled in the range of up to 340% (5.1 mmol-CMS/g-catalyst) by optimizing the grafting conditions (irradiation dose: 100 kGy, CMS concentration: 3 wt%, Tween 20 concentration: 0.3 wt%, reaction temperature: 40 °C, reaction time: 4 h). The amination of the CMS-grafted NWPE fabric was finished within 30 min, regardless of the Dg. The degree of amination reached over 85%, and the TMA group densities were 2.7, 3.3, and 3.6 mmol- TMA/g-catalyst for the Dg of 100%, 200%, and 300%, respectively. This TMA group density is comparable to that of commercially available particulate resin (DIAION PA306S: 3.4 mmol-TMA/g-resin).

The performance of the fibrous catalyst was evaluated by the transesterification of triolein (purity: 60%) and ethanol. The transesterification was done by adding fibrous catalyst (0.5 g, 3.5 mmol-TMA/g-catalyst) in reaction solution (triolein: 2.8 g, ethanol: 7.2 g, decane: 10 g) at 50 ºC for 4 h. The molar ratio of triolein to ethanol was fixed at 1:50. As seen in Fig. 2, before transesterification, only triglyceride peaks were observed in the retention time range of 21–24 min. As the transesterification continued, the triglyceride peaks were reduced and, in contrast, biodiesel peaks were gradually appeared in the retention time range of 11–14 min. The conversion ratio of triglyceride reached 23%, 48%, 70%, 82%, and 95% at 10 min, 30 min, 1 h, 2 h, and 4 h, respectively.

References

1) N. S. Kitakawa et al., *Bioresour. Technol.* **98** (2007) 416.
2) D. Kusdiana et al., *J. Chem. Eng. Jpn.*, **34** (2001) 383.
3) M. Holčapek et al., *J. Chromatogr. A*, **858** (1999) 13.

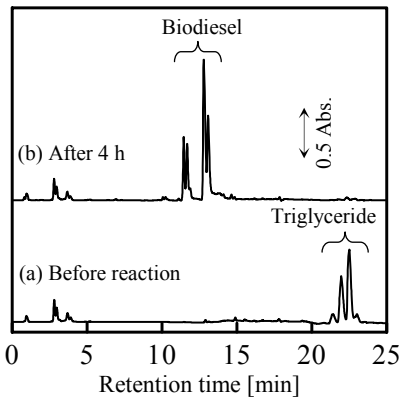

Fig. 2 Production of biodiesel from triglyceride.

2-08 Effect of Irradiation on Chitin Fiber

H. Tamura [a)], Y. Maeda [a)], T. Furuike [a)], S. Tokura [a)], N. Nagasawa [b)] and M. Tamada [b)]

[a)] Kansai University, [b)] Environment and Industrial Materials Research Division, QuBS, JAEA

Chitin is known to be biodegradable polymer in nature and in the animal body[1-3], and to be low toxicity when administrated into animal body. However, chitin is insoluble in general solvents due to its high crystallinity, which is based on the hydrogen bond through the acetamide group and hydrogen bonds[4-6]. Although several research works have been reported to dissolve chitin, the solvents caused to decrease the molecular weight of chitin during the dissolution procedure. In recent years, calcium chloride dihydrate saturated methanol was found to be the mild solvent for chitin [7-8]. Solubility of deacetylated chitin depended on the degree of deacetylation and also molecular weight. The limitation of solubility by the chitin of higher molecular weight seems to be such a high viscosity in spite of fast dissolution of N-acetylated chitosan. Chitosan with high degree of deacetylation was insoluble in calcium chloride saturated methanol, thus fiber spinning using the solvent was successful in a milder condition.

Since α-chitin solution in calcium chloride dihydrate-saturated methanol is stable for a long period at room temperature, the solution was used as dope solution for chitin fiber spinning. The coagulation was done using acetone/methanol mixed solvent system. The surface of the α-chitin fiber was smooth and relatively high tensile strength. However, the knot strength which is important for practical property for fiber, was very poor. Therefore, gelatin was added some extent in the chitin dope solution to improve the knot character of the chitin fiber. As a result, such properties of obtained chitin/gelatin composite fiber were improved with the increase of the added gelatin.

In this study, gamma-ray irradiation was performed to the chitin/gelatin composite fiber. The irradiation to the composite fiber will improve the fiber properties as well as sterilization.

The composite fiber with the gelatin composition of 20% against chitin content was used. The gamma-ray irradiation was performed at 0, 10, 30 and 50 kGy. The result of the tensile test of the fiber is shown in Fig. 1. The tensile strength of the composite fiber increased drastically with the increase of the irradiation dose. About 2 times improvement was observed irradiating 50 kGy. In contrast, the elongation decreased with the increase of the irradiation dose. Therefore, Young's modulus of the composite fiber increased with the increase of the irradiation dose. Irradiated composite fibers were subject to the swelling experiment in water. The result is shown in Fig. 2. All the composite fibers reached a maximum swelling within 1 hour. The maximum swelling decreased with the increase of the irradiation dose. In addition, lysozyme hydrolysis experiment was performed. The lysozyme is an enzyme which favor chitin as substrate. Although, the degradation percentage of chitin alone fiber was 30% after 1 month, that of irradiated fiber decreased (10 kGy: 16%, 50 kGy: 8%). These results suggest that the irradiation to the composite fiber prompts the cross linking in chitin and gelatin.

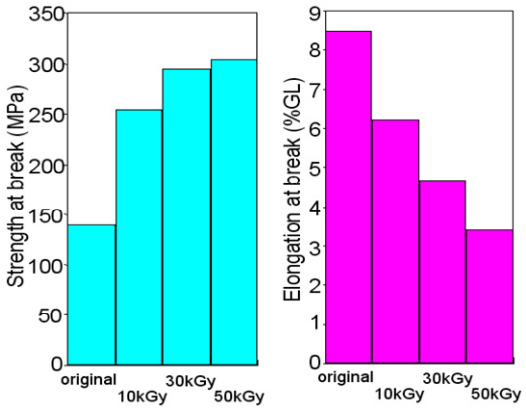

Fig. 1 Tensile test of irradaiated chitin composite fibers.

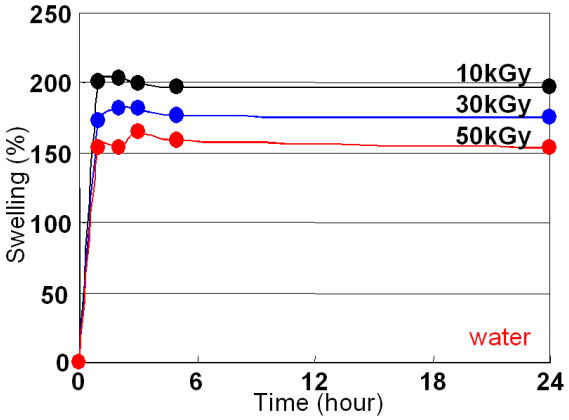

Fig. 2 Effect of irradiation on swelling behavior of chitin composite fibers.

References

1) S. Hirano et al., *J. Agric. Food Chem*., 38 (1990) 1214.
2) H. Sashiwa et al., *Int. J. Biol. Macromol*., 12 (1990) 295.
3) H. Sashiwa et al., *in chitin Enzymology, R. A. A. Muzzarelli, Ed., Ancona*, (1993) 177.
4) R. Minki, J. Blackwell, *J. Mol Biol*., 120 (1978) 167.
5) P. R. Austin, Purification of chitin. U.S.Patent, 3, 879 (1975) 377.
6) K. Kaifu et al., *Polym. J*., 13 (1981) 241.
7) A. Shirai et al., *Chitin and Chitosan. Eds*. Zakaria, B.B., Muda, W.M.W., Abdullah, M.P. Bangi, Penerbit Universiti, Kebangsaan Malaysia. (1995) 53-60.
8) S. Tokura et al., *Macromol.Symp*., 101 (1996) 389.

2-09 Characterization of γ-Irradiated Konjac Glucomannan by Light Scattering Probe Microscope

T. Makabe [a)], S. Komiya [a)], P. Prawitwong [a)], R. Takahashi [a)]. M. Takigami [b)], N. Nagasawa [c)], M. Tamada [c)] and S. Takigami [a)]

[a)] Gunma University, [b)] Gunma Industry Support Organization,
[c)] Environment and Industrial Materials Research Division, QuBS, JAEA

Konjac glucomannan (KM) is a water-soluble glucomannan with high molar mass. KM aqueous solution shows extremely high viscosity. KM can be depolymerized by γ-rays irradiation [1,2]. Molar mass of irradiated KM decreased with increase of absorbed dose. The chemical structure of KM scarcely changed by γ-irradiation. The viscosity of γ-irradiated KM aqueous solutions decreased with decrease of molar mass. High molar mass KM solution showed pseudo-plastic fluids behavior of non-Newtonian fluid at semi-dilute solution region and changed to Newtonian fluid with decrease of molar mass. Low molar mass KM solution showed behavior of Newtonian fluid behavior at semi-dilute region[3].

In this study, characteristic features of γ-irradiated KM were investigated using a size exclusion chromatograph equipped with a multiangle static light-scattering (SEC-MALS) and a scanning probe microscopy (SPM).

Commercial konjac flour (Akagi Ohodama species) was supplied by Ogino Shoten Co. Ltd. The flour was purified by washing with aqueous ethanol solution several times before use.

The purified KM was irradiated with ^{60}Co γ-rays under reduced pressure (below 10^{-3} Torr) at room temperature. The dose rate was in the range of 0.5 to 3.33 kGy/h and the absorbed dose was varied from 1 to 10 kGy.

Molar mass of KM samples was determined by SEC MALS equipped with a MALS detector from DAWN DSP (Wyatt Technology) with a vertically polarized He-Ne laser operated at wavelength of 632.8 nm. The photometer, which was calibrated using pure toluene, was connected to a SEC column of $GMPW_{XL}$ (Tosoh) and a differential refractive index detector RI-71S (Shodex), which was used to determine KM concentration at each position of elution peak. The temperatures of the MALS flow cell and the column were controlled at 40 °C.

The KM sample solution was filtered through a 0.45 μm cellulose acetate membrane filter (Sartorius). Scattered light intensities at scattering angles between 14.4° and 163° were measured. Fifty mM $NaNO_3$ solution was used as both solvent and eluent at 1 mL/min.

The irradiated KM was dissolved in Barnstead water and filtered through a 0.45 μm cellulose acetate membrane filter (Sartorius). KM solution (5×10^{-3} mg/mL) was deposited on freshly cleaved mica and was dried under nitrogen gas stream for 3 h. KM molecular chains were observed by alternating current (AC) mode using a JSPM-5200 scanning probe microscope (JEOL) equipped with a silicon cantilever (NSC35/ALBS, μ-masch).

Figure 1 shows effect of absorbed dose on molar mass and weight average radius of gyration (R_G) of γ-irradiated KM. The molar mass of original KM was 1020 kDa. The molar mass decreased significantly with increase of absorbed dose up to 2 kGy and then decreased gradually. The molar mass of 10 kGy irradiated KM was 236 kDa. The R_G of original KM was 98 nm. The R_G value decreased significantly with increase of dose up to 2 kGy and then decreased to 46.4 nm at 10 kGy of absorbed dose. KM molecules were solvated in the form of random coils in water. The flexibility of molecular chain increased with raising temperature.

SPM image of KM molecular chain showed rod-like pattern and the chain thickness was ca. 1.6 nm. The chain length decreased significantly with decrease of molar mass. However, the chain height scarcely changed regardless of molar mass. The chain lengths of low molar mass KM with 507 kDa and 236 kDa were 440 nm and 250 nm, respectively.

References

1) P. Prawitwong et al., Food Hydrocol. 21 (2007) 1362.
2) P. Prawitwong et al., Trans. Mat. Res. Soc. Jpn. 31 (2006) 727.
3) T. Makabe et al., Trans. Mat. Res. Soc. Jpn. 33 (2008) 471.

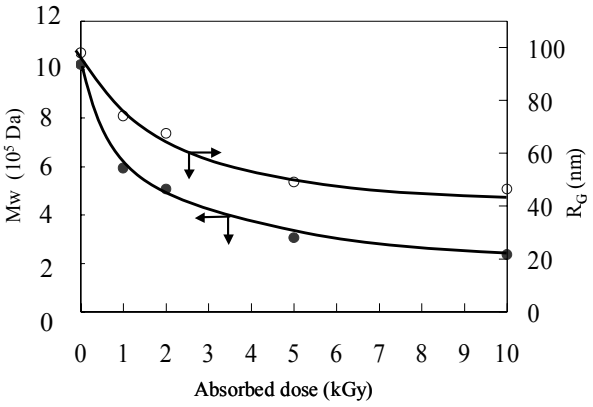

Fig. 1 Effect of absorbed dose on Mw and R_G for irradiated KM.

2-10 Determination of the Concentration of OH Radicals in EB-irradiated Humid Gases Using Oxidation of CO

T. Hakoda [a)], A. Shimada [a)], K. Matsumoto [b)] and K. Hirota [a)]

[a)] Environment and Industrial Materials Research Division, QuBS, JAEA, [b)] Iwasaki Electric Co., Ltd.

Electron beam (EB) technology has an advantage for treating dilute environmental pollutants in gases due to high-concentration of active oxidizing species. In general, OH radicals play an important role of initiating the decomposition and removal of such pollutants. Accordingly, the determination of OH-radical concentration is quite important for developing efficient decomposition/removal processes of pollutants. The formation of OH radicals in humid gases has been examined by chemical modeling simulation based on a number of kinetic data [1)]. According to this simulation, the OH radicals are mainly produced from the reaction of radiation-induced N_2^+ and O_2^+ with water vapor. However, the attempt on the practical measurement of OH-radical concentration has not been performed for EB-irradiated gases. On the other hand, quantitative analysis of OH radicals using the oxidation of CO into CO_2 has been used in atmospheric chemistry [2)]. This method is based on the higher reaction rate constants of OH radicals against CO compared with other oxidizing species. This method has been applied to the measurement of the concentration of OH radicals produced by pulsed discharge plasmas in CO/humid Ar [3)]. In the present study, the number of OH radicals, produced in humid N_2 under 1-MeV EB irradiation, was indirectly determined using an index of oxidation of CO to CO_2.

The 1st accelerator at JAEA Takasaki was used for the irradiation of a sample gas. An average dose of a sample gas was evaluated from the concentration of N_2 produced from the irradiation of pure N_2O gas at the same flow rate of a sample gas. The concentration of CO in an irradiated sample gas was measured using a gas chromatograph equipped with a methanizer and flame ionizing detector. The concentration of CO_2 was measured using a total organic carbon analyzer and the gas chromatograph.

Under insufficient CO concentration, OH radicals disappear through its bimolecular reaction before reacting with CO. Under insufficient water vapor condition, N_2^+ disappears through neutralization with secondary electrons and negative ions before reacting with water vapor. Prior to application of the CO oxidation method to the determination of the OH-radical concentration, the concentration of CO to scavenge OH radicals and that of water vapor to fully react with N_2^+/excited species were examined from the concentration of CO_2 produced under different concentrations of CO and water vapor. As shown in Fig. 1, such concentrations of CO and water vapor were 2,000 and 8,000 ppmv, respectively, under irradiation at doses of 2.0–10.0 kGy with dose rates of 0.17–2.55 kGy/s.

The experiment using such concentrations of CO and water vapor demonstrated that the concentration of CO_2, produced from the reaction of CO with OH radicals, lineally increased with doses of 0–10 kGy (Fig. 2). The G(OH) was estimated as 4.90 from its slope. This G(OH) was 1.5 times larger than the value expected from the interaction of N_2^+ with water vapor. The OH radicals would be also produced from the reaction of water vapor with the excited species of N_2 besides N_2^+.

References

1) H. Mätzing, Adv. Chem. Phys. 80 (1991) 315.
2) M.J. Campbell et al., J. Atmos. Chem. 4 (1986) 413.
3) Z.-Z. Su et al., J. Phys. D: Appl. Phys. 35 (2002) 3192.

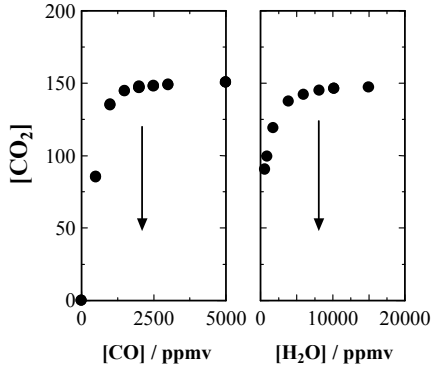

Fig. 1 (A) The concentration of CO_2 produced in an irradiated 10,000-ppmv H_2O/N_2 gas at 10 kGy as a function of the initial concentration of CO and (B) That in an irradiated 2,000-ppmv CO/N_2 gas at 10 kGy as a function of water vapor concentration.

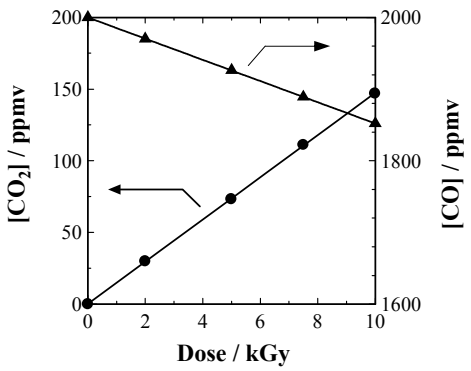

Fig. 2 The concentration of CO_2 and CO in 2,000-ppmv CO/10,000-ppmv water vapor/N_2 gas as a function of dose at dose rates of 0.17–2.55 kGy/s; ●: CO_2, and ▲: CO.

2-11 Decomposition of Persistent Pharmaceuticals by Ionizing Radiation

A. Kimura, M. Taguchi and K. Hirota

Environment and Industrial Materials Research Division, QuBS, JAEA

Introduction

The concentrations of pharmaceuticals in the water environment have increased because of population growth and the advanced medical diversification. Pharmaceuticals appear physiological activity and cure diseases. They, however, are doubtful to have chronic and reproduction toxicities, and may give ill effect to animals. There is a growing tendency to establish a guideline of their treatments in Japan, whereas it is difficult to carry out the risk management of pharmaceuticals having great benefits for human life. The direct methods such as activated sludge system and advanced oxidation technologies are considered to be suitable for the treatment of pharmaceuticals in wastewater. A report for the monitoring test of pharmaceuticals in wastewater indicated that some pharmaceuticals were not decomposed by activated sludge system[1]. Therefore, the development of a new treatment method is required to minimize their risk. Persistent chemicals in wastewater are effectively decomposed by ionizing radiation method, which produces hydroxyl radicals homogeneously[2]. The purpose of this work is to treat pharmaceuticals by an ionizing radiation in combination with activated sludge.

Experimental

Ibuprofen, 17β-estradiol, carbamazepine, mefenamic acid, naproxen, and ketoprofen were selected as samples because of a high consumption in the world and a high persistency[1]. A real wastewater of pH value at 7.45 and the amount of TOC at 2.5 to 5 g/L was collected at an effluent of a water treatment facility. Each pharmaceutical was dissolved in the wastewater at 3.5 to 5 μmol/L.

The γ-ray irradiation of each pharmaceutical solution was carried out at 298 K using ^{60}Co γ-ray sources at JAEA, Takasaki, to the doses in the range of 50 to 20,000 Gy (Gy = J kg^{-1}) at dose rates ranging from 100 to 10,000 Gy h^{-1}. Activated sludge was supplied by a treatment plant using activated sludge system and used for the experiment of biodegradation. The sludge was acclimated by adding 1 g/L glucose and levulose of 300 mL/day. The acclimated sludge solution of 50 mL was mixed with equal amount of the pharmaceuticals solution, and the mixed solution were stirred at 100 rpm and aerated at 100 mL/min for 24 hours. Each pharmaceutical solution was analyzed by HPLC, ion chromatography, and LC-MS. Estrogen activity of 17β-estradiol aqueous solution was evaluated by the ELISA.

Result and Discussion

Decomposition of pharmaceuticals in the wastewater was carried out by γ-ray irradiation. Concentration of the pharmaceuticals in the wastewater decreased exponentially with increase of dose. Mefenamic acid, ketoprofen, and 17 β-estradiol were eliminated at 2.0 kGy, and carbamazepine, naproxen, and ibuprofen were decomposed at 1.0 kGy. The wastewater mixed equal amount of 6 pharmaceuticals at 5 μmol/L was irradiated with γ-ray as shown in Fig. 1. The required doses for the elimination of mixed pharmaceuticals solution were almost the same with that of each pharmaceutical solution. The decomposition efficiency of pharmaceuticals in the mixed solution would not be reduced by the competition reaction of pharmaceuticals with hydroxyl radicals because the pharmaceuticals coexisted a large amount of impurities in the wastewater. Ionizing radiation method was suitable for the treatment of pharmaceutical in the wastewater, but some irradiation products having physiological activity may remain in the treated wastewater. When pharmaceuticals in wastewater are treated by the combination method of the ionizing radiation and the activated sludge system, the irradiation products having physiological activity would be decomposed by activated sludge.

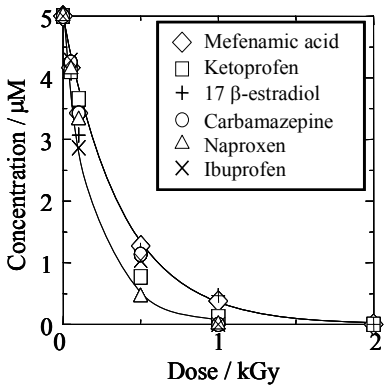

Fig. 1 Decomposition of real wastewater mixed equal amount of 6 pharmaceuticals by γ-ray irradiation.

Treatment of pharmaceuticals in wastewater was carried out by the combination method of ionizing radiation and activated sludge. 17 β-Estradiol in the wastewater at 3.5 μmol/L was decomposed at 500 Gy of γ-ray irradiation, but the wastewater after the irradiation also had estrogen activity. The estrogen activity of the wastewater was eliminated by the activated sludge for 15 h. Combination method of the ionizing radiation and the activated sludge was available for the treatment of pharmaceuticals in wastewater.

References

1) K. Fent et al., *Aquatic Toxicology*, 76 (2006) 122-159.
2) A. Kimura et al., *Radiat. Phys. Chem.*, 76 (2007) 699-706.

2-12 Chemical and Biological Assays of γ-ray Irradiated Aqueous Chlorophenol Solutions

M. Taguchi [a], A. Kimura [a], F. Shiraishi [b] and K. Hirota [a]

[a] Environment and Industrial Materials Research Division, QuBS, JAEA,
[b] Environmental Quality Measurement Section, Research Center for Environmental Risk, National Institute for Environmental Studies

Introduction

The organic pollutants, which induce biological effects even at a very low concentration in a river or lake water, are reported very much. We investigated a radiation processing for the treatment of wastewater containing endocrine disrupting chemicals[1-3]. On the other hand, the chlorinated organic compounds, which have the acute toxicity like dioxin and PCB, also exists in real wastewater. Generally, chlorinated organic compounds are persistent in nature, and have the property to accumulate in the living body. Ionizing radiation is a good tool to generate homogeneously and quantitatively reactive species, for example, hydroxyl (OH) radical and hydrated electron, in water. The chlorinated organic pollutants in wastewater will be decomposed by taking advantage of radiation induced oxidation by the OH radicals and reduction by the hydrated electron. The decompositions of chlorophenol, which have a basic molecular structure of chlorinated organic pollutants, were investigated by chemical analyses using a chromatography and biological assays using a luminescence bacteria.

Experimental

2- and 4-Chlorophenols were dissolved in pure water to prepare samples at the concentration of 1 mmol L^{-1}. The aqueous chlorophenol solutions were poured in glass vials and bubbled with oxygen or nitrogen during irradiation. The γ-ray irradiations were carried out at 298 K using ^{60}Co sources in JAEA/Takasaki. A HPLC (Agilent, 1100 series) with a reverse phase column (Shodex, RS pak DE-613) was used for the qualitative and quantitative analyses. Toxic intensity of the sample solutions were evaluated from the amount of a reduction of luminescence intensity of luminescence bacteria (*photobacterium phosphoreum*).

Results and Discussion

The concentrations of 2-chlorophenol (2CP) and 4-chlorophenol (4CP) decreased exponentially with dose. Chlorophenols were decomposed by the addition of the OH radicals on benzene ring and reduction with the hydrated electron to release chlorine. As a result, in the case of 4CP, chlorocatechol, chlororesorcinol and phenol were produced as primary products as shown in Scheme 1. These primary products were decomposed by a further irradiation.

Toxicity changes of the aqueous chlorophenol solutions before and after γ-ray irradiation are shown in Fig. 1. The aqueous 2CP solution had a weak acute toxicity before irradiation, and the toxicity increased monotonously with dose irrespective of the existence of the dissolved oxygen.

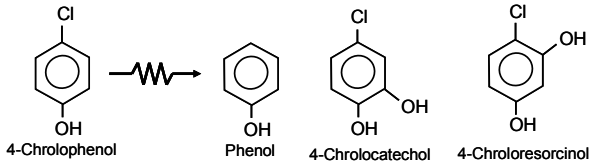

Scheme 1 Decomposition mechanism of 4-chlorophenol in water under oxygen saturated condition by γ-ray irradiation.

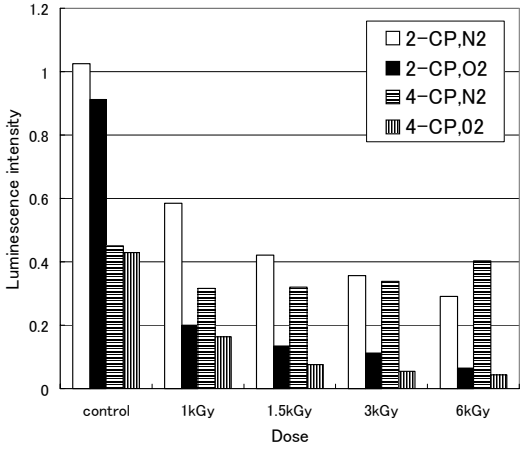

Fig. 1 Toxicity of aqueous chlorophenol solutions under oxygen or nitrogen saturated condition after γ-ray irradiation.

On the other hand, the aqueous 4CP solution had a strong toxicity before irradiation. The toxicity reinforced with the increase in dose under the oxygen saturated condition. The toxicity, however, increased and then decreased with dose under the nitrogen saturated condition.

Most of 2CP and 4CP, and their primary products were decomposed by the higher dose irradiation. That is, the toxicities after γ -ray irradiation are considered to be based on a components of not only chlorophenols and primary products but also secondary products such as organic acid and aldehyde.

References

1) A. Kimura et al., *Radiat. Phys. Chem.*, 69 (2004) 295-301.
2) A. Kimura et al., *Radiat. Phys. Chem.*, 75 (2006) 61-69.
3) A. Kimura et al., *Radiat. Phys. Chem.*, 76 (2007) 699-706.

3. Biotechnology and Medical Application

This is a blank page.

3-01 Quantitative Analyses of DNA Damage Induced by $^{12}C^{5+}$ and $^{4}He^{2+}$ Ion Beams Using a Renewal Dosimetry System at TC1 Port

K. Akamatsu

Division of Environment and Radiation Sciences, NSED, JAEA

1. Introduction

Chemical structures of DNA lesions and their distribution are quite important to clarify following biological repair procedures. In case of ionizing radiations, especially, it is expected that three-dimensional distribution of DNA damages is diversified as well as their chemical structures, and the diversity makes investigations of physicochemical processes in radiation effects difficult. In fact, double-strand breaks produced by high linear energy transfer (LET) alpha particles are more difficult to rejoin in living cells than those produced by low LET ^{137}Cs γ-rays [1]. So far, we have investigated difference of DNA damage spectrum between radiations using an analytical method [2], however, the accuracy in ion beam dosimetry have been not sophisticated because of instability of He ion source itself and limitation of picoammeter used. In this report, we reveal a newly-constructed dosimetry system and the results of unaltered nucleobase release from DNA induced by ion beams ($^{4}He^{2+}$, $^{12}C^{5+}$) in comparison with that of ^{60}Co γ-rays (7cell, Takasaki). The ion beams used were obtained from TC1 port in TIARA.

2. Construction of millisecond pulse beam for actual fluence measurement at an experimental beam current

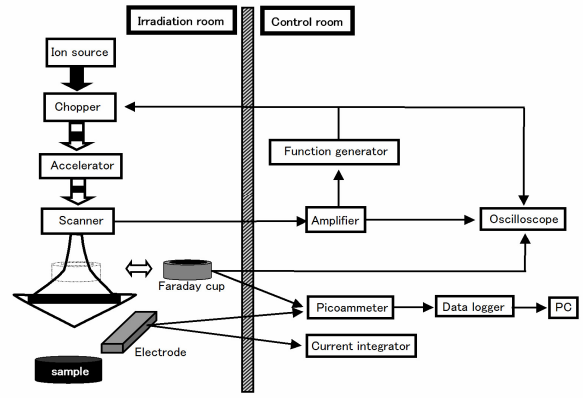

Fig. 1 Pulse beam generation system.

We have obtained fluence values at nA-order beam current by extrapolation of pit density at 10 ± 3 pA using CR-39® dosimeter. This means that the extrapolated fluence contains inevitable error (± 30 %). Then, we constructed millisecond pulse beam generation system to measure actual fluence at an experimental beam current (~10 nA) as shown in Fig. 1. The obtained fluence rate using the pulse beam is $9.1 \pm 0.06 \times 10^5$ particles/nA/cm^2/ms, which is almost the same as theoretical value (9.2×10^5 particles/nA/cm^2/ms). Then, we can trustingly use the value in calculation of radiation chemical yields with accuracy.

In addition, beam current monitoring system (Fig. 1) was also constructed. A part of the beam during an irradiation experiment was picked up to monitor fluctuation of the current (Fig. 1). This system enables us to obtain accurate total particle or coulomb number on a sample.

3. Experiments

Linear formed pUC19 plasmid DNA digested by Sma I (pUC19/Sma I) was used. pUC19/Sma I aqueous solution was mounted on a glass plate and dried thoroughly in vacuum at 4 °C for a few days. Each sample was irradiated with $^{4}He^{2+}$ beam with LET of ~ 85 keV/μm or $^{12}C^{5+}$ with ~ 700 keV/μm (around the Bragg peak) at given doses at r.t. The doses were determined based on the theoretical fluence rate (9.2×10^5 particles/nA/cm^2/ms) which is also authorized by actual fluence measured by the pulse system. The irradiated DNA samples were recovered by water at 0 °C. The aqueous solutions of irradiated DNA were ultrafiltrated (< Mw 5,000 cut-off) to obtain bases released. Each of the filtrated solutions was analyzed by HPLC.

4. Results and Discussion

Figure 2 shows dose-response relationships of unaltered nucleobase generation by the ion beam irradiation. At a glance, the slopes for both ions are three times larger than that for the γ-rays. Similar tendency was reported using $^{16}O^{7+}$ beam [3]. This result suggests that efficiency of radiation chemical reactions leading to base release for high-LET radiation are higher than that for a low-LET one at least in case of direct radiation effect on DNA.

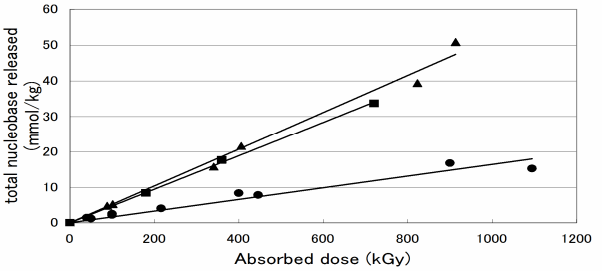

Fig. 2 Base release profiles of ion beam- irradiated pUC19/Sma I compared with that of ^{60}Co γ-rays in the solid state (●: ^{60}Co γ-rays, ▲: $^{4}He^{2+}$, ■: $^{12}C^{5+}$).

5. Acknowledgments

We would like to gratefully thank Drs. M. Taguchi, Y. Saito, Y. Sugo, and Y. Kobayashi for optimizing dosimetry system and maintaining the TC line.

References

1) C. M. deLala et al., Radiat. Res. 144 (1995) 43.
2) K. Akamatsu, Anal. Biochem. 362 (2007) 22.
3) M. Gromova et al., J. Chem. Soc., Parkin Trans. 2 (1998) 1365.

3-02 Lethal and Mutagenic Effects of He Ion Particles in *Escherichia coli*

T. Suzaka [a,b], H. Tauchi [a], N. Shikazono [b], K. Fujii [b] and A. Yokoya [b]

[a] Department of Environmental Sciences, Faculty of Science,
[b] Advanced Science Research Center, JAEA

Non-DSB type of clustered damage is known to be induced by ionizing radiation and is proposed to cause deleterious effects to cells[1]. Their yields and configurations likely depend on the radiation qualities, such as particle energy or ionization density along the particle track characterized by LET (linear energy transfer)[1,2]. To date, various biological consequences of radiation of both low and high LETs have been extensively studied with varieties of organisms, including bacteria, yeasts, higher plants, and mammalian cells. It is, however, still difficult to make clear the LET dependence on both the yield and the extent of repair of non-DSB type of clustered damage *in vivo*, because most of the studies uses only repair-proficient wild type cells. In this project, we fully utilize repair-deficient mutants to find out the features of damage as well as how and to what extent the induced damage is processed. Lethal and mutagenic effects for radiation of different qualities are being investigated. Here, we present the results of wild type *E. coli* cells exposed to soft X-rays and He ion particles with different LETs.

The cells of CC104 (wild type *E. coli*) were incubated in 0.2 % glucose minimal medium at 37 °C unless otherwise stated. Six hundred μL of overnight culture were inoculated in 30 mL of fresh medium and incubated until the OD values at 600 nm reached 0.3. Three mL each of culture was washed with 0.15 M NaCl and cells were resuspended with 30 mL of 0.15 M NaCl. Subsequently, 10 mL of the resuspended solution was filtered through a nitrocellulose membrane of a diameter of 1 cm. To prevent cells from drying, the membrane was placed on a filter paper pre-wetted with 300 μL of 0.15 M NaCl solution with 20 % glycerol. Subsequently, the membrane with the filter paper was placed on 0.15 M NaCl agar in a Petri dish, and then the dish was covered with a polyimide film (Kapton film) of 7.5 μm thickness. Cells on the membrane were irradiated with soft X-rays (tungsten target, tube voltage 150 kV, tube current 6 mA) at a dose rate of 0.47 Gy/sec, and He ion particles at dose rates of 1~4 Gy/sec. LETs of He ions were altered by placing a Ni foil in front of the sample. After irradiation, the membrane was vortexed in 1 mL of 0.15 M NaCl to recover the cells. Recovered cells were incubated overnight and the fraction of survived cells was determined by dividing the number of survived cells by that of unirradiated cells. In this study, the reverse mutation frequency of *lacZ* was measured. G to T transversion in the *lacZ* gene reverts the cells so that they could grow on a medium with lactose as the only carbon source [3]. In determining the mutation frequency, irradiated cells were initially propagated in 0.2% glucose minimal medium at 37 °C for 16 hours to fix mutations. Six hundred μL of the culture were added to 30 mL of fresh medium and further incubated at 37 °C. When the OD at 600 nm reached 0.3, the cells were collected and resuspended with 0.15 M NaCl. Cells were plated on a 0.2 % lactose/glucose minimal medium, and were incubated at 37 °C for 40 hours. The reverse mutation frequency was determined by dividing the number of colonies on the lactose plate by that on the glucose plate.

Lethal and mutagenic effects of radiations with different quality were assessed from dose response curves. Lethal effects of soft X-rays and He ion particles at an LET of 18 keV/μm did not differ significantly, whereas He ion particles at an LET of 89 keV/μm had slightly stronger effect on lethality than the other two types of radiation (data not shown). All types of radiation showed similar dose responses for mutation induction (Fig. 1), demonstrating that the occurrence of transversion does not strongly depend on LET in wild type *E. coli*. Studies with base-excision repair deficient strains are now underway.

References

1) N. Shikazono et al., J. Radiat. Res. 50 (2009) 27.
2) H. Nikjoo et al., Radiat. Res. 156 (2001) 577.
3) C.G. Cupples and J.H. Miller, Proc. Natl. Acad. Sci. USA 86 (1989) 9163.

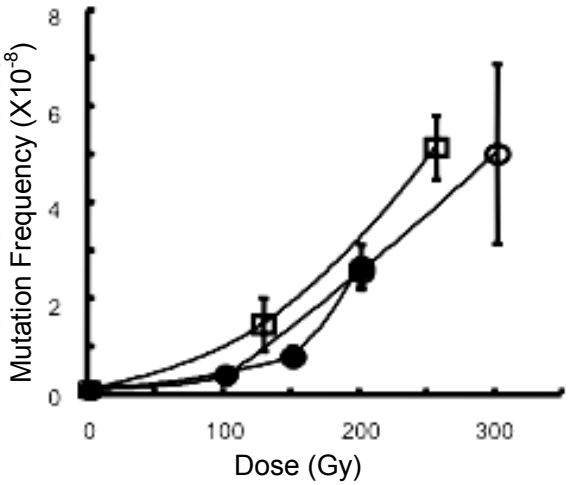

Fig. 1 Reverse mutation frequencies of wild type *E. coli* (CC104) at the *lacZ* gene. Cells were exposed to soft X-rays (□), He ions with an LET of 18 keV/ μm (○), and 89 keV/μm (●).

3-03 SMAP2 Protein Potentially Mediates the Response to Synthetic Auxin, 2,4-D, in *Arabidopsis thaliana*

A. Nakasone [a,b], M. Kawai-Yamada [b,c,d], T. Kiyosue [e], I. Narumi [a], H. Uchimiya [b,f] and Y. Oono [a]

[a] Radiation-Applied Biology Division, QuBS, JAEA, [b] University of Tokyo, [c] Saitama University, [d] JSTA, Core Research for Environmental Science and Technology, [e] Kagawa University, [f] Iwate Biotechnology Research Center

The phytohormone auxin has roles in controlling various mechanisms in growth, proliferation, and differentiation of plants throughout the life stages[1, 2]. Elucidating the signal transduction mechanism of auxin is one of the core goals of the plant scientific field. As a research initiative, the analysis of novel mutants created by ion-beam mutagenesis is an effective method[3].

By using ion beam, we previously isolated a novel auxin-related mutant, *aar1*, which shows a reduced response to the putative anti-auxin, *p*-chlorophenoxyisobutyric acid (PCIB)[3,4]. The mutant *aar1* is a unique auxin-signaling mutant that exhibits 2,4-dichlorophenoxyacetic acid (2,4-D)-specific resistance without any changes in 2,4-D transport or metabolism[4]. The *SMAP1* gene, which is one of the missing genes in the 44-kbp DNA region that is possibly deleted by ion beams in the *aar1-1* genome, is responsible for the 2,4-D / PCIB-resistant phenotype of *aar1*[4]. SMAP1 is a small acidic protein of unknown function with a conserved phenylalanine / aspartic acid-rich domain in its C-terminal region. Similar genes are present in the genomes of a wide variety of plants and animals, implying that the *SMAP* genes are evolutionally indispensable for living organisms. The *Arabidopsis* genome has another copy of the *SMAP* gene, *SMAP2*. In this study, to better understand the biological function of the *SMAP2* gene and its relationship to the mode of action of 2,4-D, we investigated the expression pattern of the *SMAP2* gene and the phenotypic complementation of *SMAP2* in the *aar1* mutant.

RNA hybridization revealed that *SMAP2* transcripts were observed only in siliques while *SMAP1* transcripts were observed in most *Arabidopsis* tissues. RNA was also extracted from whole flowers, petals, pistils, anthers and green siliques, and examined by semi-quantitative RT-PCR. *SMAP2* was strongly expressed in anthers and moderately in green siliques.

The fact that *SMAP2* is expressed only in limited tissues prompted us to examine the effect of overexpression of the *SMAP2* gene in transgenic plants. We also wanted to determine whether *SMAP2* has the same function as *SMAP1*. To address these questions, the *SMAP2* and *SMAP1* coding regions were cloned under the cauliflower mosaic virus *35S* promoter and introduced to *aar1-1* plants and the transgenic seeds were plated on 40 nM 2,4-D and 20 μM PCIB, and subsequently the root lengths of those plants were measured at 10 d (Fig. 1). The length of wild-type roots was reduced by both 2,4-D and PCIB, whereas the length of *aar1-1* roots was not much reduced as wild-type, in agreement with previous results[4]. Overexpression of *SMAP1* in an *aar1-1* background (*35S:SMAP1/aar1-1*) restored 2,4-D and PCIB sensitivity, as expected. Furthermore, two independent lines of *35S*:*SMAP2*/*aar1-1* showed reduced root length on 2,4-D and PCIB medium, suggesting that overexpression of *SMAP2* also restored 2,4-D and PCIB sensitivity in *aar1-1* (Fig. 1). These results suggest that the biological activity of SMAP2 is similar to that of SMAP1 and that SMAP2 is able to mediate the 2,4-D / PCIB responses in *Arabidopsis* roots when its expression is enhanced.

References

1) M. J. Bennett et al. Science 273 (1996) 948.
2) P. J. Davies, Plant Hormones, Kluwer Academic Publishers, Dordrecht (1995).
3) Y. Oono et al., Plant Physiol. 133 (2003) 1135.
4) A. Rahman et al., Plant J. 47 (2006) 788.

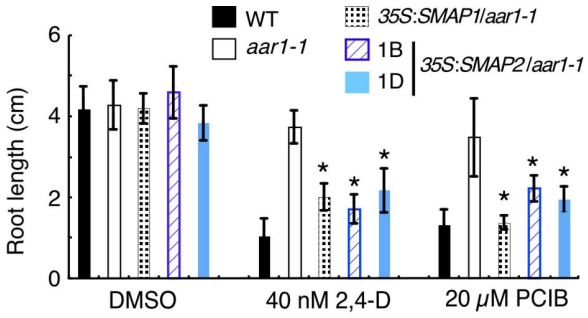

Fig. 1 Root length of 10-d-old wild-type, *aar1-1*, *35S*:*SMAP1*/*aar1-1* and *35S*:*SMAP2*/*aar1-1* plants grown on GM containing DMSO, 40 nM 2,4-D and 20 μM PCIB. Error bars show mean ± SD for at least 13 seedlings.

3-04 Efficient Induction of Flower-Color Mutants by Ion Beam Irradiation in Petunia Seedlings Treated with High Sucrose Concentration

Y. Hase [a)], M. Okamura [b)], D. Takeshita [a)], I. Narumi [a)] and A. Tanaka [a)]

[a)] Radiation-Applied Biology Division, QuBS, JAEA,
[b)] Plant Research Center, Kirin Agribio Company, Limited

Ionizing radiation has been used for several decades to produce new plant varieties. Many attempts have been made to increase the mutation efficiency. If we could control the direction of mutation, it is very useful to increase the mutation efficiency. Nagatomi et al. reported that the flower-color mutants were obtained with higher frequency when the cultured petals were irradiated rather than the cultured leaves [1)]. They hypothesized that the genes involved in flower-color synthesis are easily mutated where these genes are highly expressed. Nagatomi et al. compared the mutagenic effect in petals and leaves with the same irradiation doses. In addition, mutations other than flower color were not examined as an internal standard for general mutation frequency. Therefore, it has not yet been clearly shown if the condition of the cells alters the mutation frequency of particular genes. Expression of genes involved in anthocyanin pigment biosynthesis is known to be activated by stresses, such as high-intensity light, UV light, low temperature and sugar. We hypothesized that if the condition of the cell could alter the mutation frequency of particular genes, the stress treatment increases the frequency of flower-color mutation. In this study, we examined the effect of stress treatments on the frequency of flower-color mutants in petunia.

To find the suitable stress conditions that stimulate pigment biosynthesis, we examined the effects of sucrose, UV light and low-temperature treatment in petunia seedlings. We found that treatment with 3% sucrose effectively stimulated pigment accumulation (Fig. 1). Then, we examined the radiation sensitivity of petunia seedlings to 320-MeV carbon ions. We concluded 8 Gy to be an appropriate dose for mutagenesis in this experiment. It was thought that the sucrose treatment did not affect the mortality of the seedlings.

The petunia seedlings treated with or without sucrose were exposed to the carbon ions, and the M2 seeds were collected from individual M1 plants. In this study, the mutant screening in M2 lines was repeated twice using independent plant materials. In Experiment 1, the frequencies of M2 lines that contained chlorophyll mutants were 0.56% for sucrose-treated group and 0.48% for non-treated group. In Experiment 2, the frequencies were 0.39% for sucrose-treated group and 0.33% for non-treated group. There was no significant difference between the two groups in these two independent experiments. No chlorophyll mutant was obtained in the un-irradiated control group. Flower-color mutants that included magenta, purple and light pink were obtained from the original color of violet (Fig. 2). The frequencies of M2 lines that contained flower-color mutants were 1.52 and 1.20% in the sucrose-treated group and 0.56 and 0.58% in non-treated group. The sucrose treatment resulted in a more than two-fold increase in flower-color mutant frequency in the two independent experiments. These results show that sucrose treatment specifically increases the frequency of flower-color mutation following ion-beam irradiation. Our results show the possibility that the direction of mutation can be controlled to some extent.

A part of this study was supported by a grant for the Research and Development Program for New Bio-industry Initiatives from Bio-oriented Technology Research Advancement Institution.

Reference

1) S. Nagatomi et al., IRB Technical News No.60 (1997).

Fig. 1 Effect of stress treatments on accumulation of pigments in petunia seedlings. (A) 3% sucrose, (B) 15 kJ/m^2 of UV-B, (C) 4 °C for 24 h, (D) control.

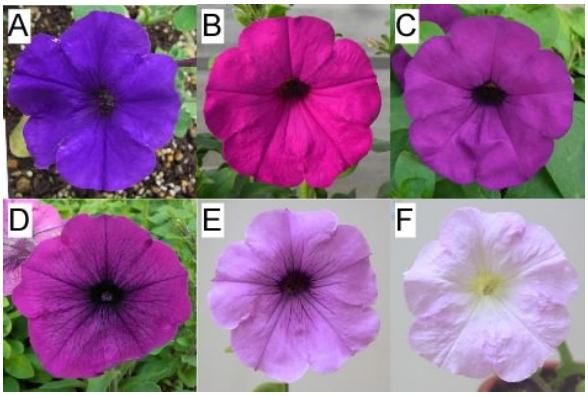

Fig. 2 Flower-color mutants obtained in this study. (A) Parental line, (B) Magenta, (C) Purple, (D) Purple vein, (E) Light purple, (F) Light pink.

3-05 Mutation Spectrum Induced by γ-rays and Carbon Ion Beams in Plant

R. Yoshihara, Y. Hase, S. Nozawa and I. Narumi

Radiation-Applied Biology Division, QuBS, JAEA

Biological effects of γ-rays and ion beams have been extensively studied in animal and bacteria. These studies showed that the lethal effect and the induction of DNA double strand break (DSB) per absorption dose of ion beams were higher than those of γ-rays because ion beams with high linear energy transfer (LET) deposits high-density energy to DNA compared to γ-rays. Moreover LET of ion beams changes along the ion particle path, and almost stopping ion particle has maximum LET (Bragg peak). Gamma-rays and ion beams have been used for mutagenesis in mutation breeding, however, their mutational effects were little known in plant. Mutation breeding is one of the valuable breeding techniques that can produce various new phenotypes. It is necessary to investigate which types of mutation are induced by γ-rays and ion beams for improvement of mutation breeding techniques. In this study, we analyzed mutation spectrum induced by γ-rays, 220 MeV carbon ions (220 MeV C) and carbon ions in high LET region near the Bragg peak (Bragg C) to show the mutational effects of these radiations. We will apply our results to upgrade our mutation breeding methods.

To detect the mutation induced in plant, we used *rpsL* transgenic *Arabidopsis* (Arabidopsis/rpsL) mutation detection system [1]. In this system the plasmid carrying *rpsL* gene is integrated in *Arabidopsis* chromosomal DNA, and the mutations occurred in *rpsL* region are detected via plasmid rescue. By using the system, intragenic mutations can be detected.

We irradiated to Arabidopsis/rpsL dry seed with 740 Gy, 140 Gy and 64 Gy of γ-rays, 220 MeV C and Bragg C, conferring same biological effect on survival, respectively (80% shoulder dose (Dq) of survival curves) (Table 1). Although mutant frequency in γ-rays and 220 MeV C irradiated groups were increased by 2.8 and 2.6 times, respectively, that in Bragg C irradiated group remained background level (MF in Table 1). Lethality of Bragg C was more than 2 and 10 times higher than that of 220 MeV C and γ-rays, respectively (Dq in Table 1). From these observations, it is suggested that intragenic mutation in Bragg C irradiated group was seldom detected because of its high lethal effect. Excessively high LET radiation might be not suitable for mutation breeding.

Mutation spectrum induced by γ-rays and 220 MeV C were analyzed. Both radiation induced higher incidence of G:C to A:T transition and > 2 bp deletions/insertions. The frequency of −2 and −1 frameshifts were higher in γ-rays irradiated group (Fig. 1). These observation suggested that γ-rays and 220 MeV C have different mutational effects each other. It is said that G:C to A:T transition induced by radiation is related to oxidative DNA damage. This damage causes misincorporation of wrong nucleotide during DNA replication, and induces point mutations [2]. Deletions and insertions were caused during repair process of DSB by non-homologous end joining (NHEJ). Although NHEJ can rejoin the broken ends of DSB efficiently, the repair process is error-prone because broken ends are modified during rejoining [3]. We found rejoined site of −2 frameshift in γ-rays irradiated group have similar traits to deletion mutation caused by NHEJ. Recently it is shown that about half of the −1 frameshift induced by γ-rays related to DSB repair by NHEJ [4]. From these viewpoints, we speculated that γ-rays and 220 MeV C induced DSB with structurally different broken ends, causing different types of deletion mutation. From our mutation spectrum analysis, it was shown that γ-rays and carbon ions have different mutational effects. It would be effective for mutation breeding to use both γ-rays and ion beams as the situation demands to induce different types of mutation.

Acknowledgement

We would like to thank Prof. Takimoto, Yamaguchi University, for providing Arabidopsis/rpsL seeds.

References

1) R. Yoshihara et al., J. Radiat. Res. 47 (2006) 223.
2) S. Bjelland & E. Seeberg, Mutat. Res. 531 (2003) 37.
3) J. Y. Bleuyard et al., DNA repair 5 (2006) 1.
4) E. Heidenreich & H. Eisler, Mutat. Res. 556 (2004) 201.

Table 1 Shoulder dose (Dq) and mutant frequency (MF).

	Dq (Gy)	MF
Background	−	3.4×10^{-5}
γ-rays	930	9.8×10^{-5}
220 MeV C	180	9.1×10^{-5}
Bragg C	80	3.1×10^{-5}

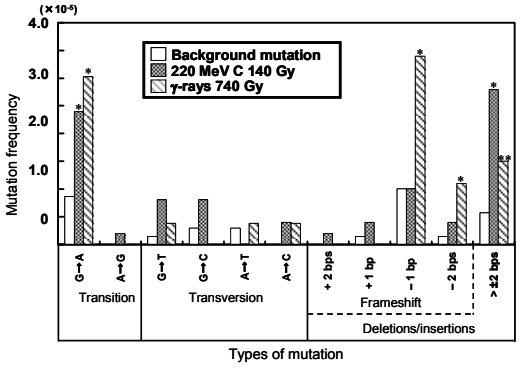

Fig. 1 Frequency of each type of mutation. Mutation frequency is indicated as the ratio of mutants to total rescued clones. Statistical analysis was performed according to Poisson distribution (*: $p<0.01$, **: $p<0.05$).

3-06 Production of Visibly Altered Mutants by Ion Beam Irradiation in Soybean

A. Kanazawa [a)], S. Arase [a)], J. Abe [a)], H. Hase [b)], A. Tanaka [b)] and I. Narumi [b)]

[a)] Research Faculty of Agriculture, Hokkaido University,
[b)] Radiation-Applied Biology Division, QuBS, JAEA

Soybean (*Glycine max*) is an important crop in terms of production of food, oil, and forage. However, existing mutant lines of soybean is very limited, which is a constraint on performing a genetic study and breeding of this plant. Soybean is considered to have derived from ancestral plant(s) that have a tetraploid genome, and as a consequence, more than 90% of nucleotide sequence in the soybean genome is duplicated[1)]. It is conceivable that such a duplicated nature of the genome brought about a low frequency of mutant production by conventional methods for mutagenesis such as γ-ray or X-ray irradiation as well as chemical treatments. In these circumstances, we have started to examine whether ion beam irradiation is effective in producing a mutant in soybean because ion beam irradiation is expected to cause genomic changes that are more drastic than those induced by conventional mutagenesis.

We have previously analyzed the effects of ion beam irradiation on plant growth and morphology in soybean by exposing dried seeds to the 320 MeV carbon ions with the range of 0.2-25 Gy[2)]. The irradiated seeds were sown on soil and plants were grown for three weeks in a greenhouse. We found that irradiation doses higher than approximately 5 Gy affect plant growth rate. In order to establish a plant population that can be available for screening mutants, we further examined the effects of irradiation by growing plants in a field. We found that both plant height and the ratio of the number of plants that survived until seed-setting per the number of seeds sown in the field depended on the doses of irradiation. We tentatively concluded that irradiation doses around 2.5 Gy are suitable for producing mutants[3)].

Based on these results we grew plants from irradiated seeds in a large scale to obtain a population of M2 seeds: 3,200 seeds and 3,320 seeds irradiated at 5 Gy and 2.5 Gy, respectively, were sown in the field and seeds were harvested. The harvested M2 seeds were sown in the field next year and generation of individuals with visibly altered phenotypes was examined.

An observed striking change was unscheduled generation of stem(s) from the node where cotyledons were formed. However, although this phenomenon was detected at a high frequency in the M1 plants, its frequency in the M2 population was as low as non-irradiated plants (Table 1). Accordingly, it is likely that the high frequency of the alteration in the M1 plants may involve physical stress on cells in the growing point of plants and most of observed changes in the M2 generation are not heritable.

The other observed change was yellowish green-colored leaves (Fig. 1). Frequency of this type of change was 0.10% (n = 1911) and 0.19% (n = 1038) for M2 plants irradiated with 2.5 Gy and 5.0 Gy, respectively. We confirmed that this phenotypic change was heritable. In petunia, the frequency of M2 lines that contained chlorophyll mutants was ~0.3-0.5% when irradiated at 80% of a dose equivalent to the shoulder of survival curve (Hase et al., unpublished data). Taken into account the fact that the frequency of the yellowish mutants in soybean includes only the frequency of mutants that survived until trifoliate leaves are produced, these results suggest that irradiation with doses 2.5-5.0 Gy is suitable for producing mutants in soybean and soybean mutants may be obtained at a frequency equivalent to the experiments in petunia. We are currently working on screening more mutants as well as producing more M2 populations.

References

1) R. C. Shoemaker et al., Genetics 144 (1996) 329.
2) A. Kanazawa et al., JAEA Takasaki Ann. Rep. 2006 (2008) 88.
3) A. Kanazawa et al., JAEA Takasaki Ann. Rep. 2007 (2008) 71.

Table 1 Frequency of unscheduled branching.

Plants	Frequency (%)	No. of plants examined
Non-irradiated	4.4	641
M1 (2.5 Gy)	23.1	654
M2 (2.5 Gy)	7.2	710
M2 (5.0 Gy)	5.0	1038

Fig. 1 Mutant soybean plant observed in the M2 population. A representative plant with yellowish-green leaves (left) and a visibly unaltered plant (right) are shown.

3-07 New Type Flower Colored Petunia Obtained by Ion Beam Irradiation at JAEA-TIARA

M. Okamura [a)], D. Takeshita [a)], Y. Hase [b)], I. Narumi [b)] and A. Tanaka [b)]

[a)] Plant Research Center, Kirin Agribio Co., LTD., [b)] Radiation-Applied Biology Division, QuBS, JAEA

1. Introduction

New carnation varieties have been developed by ion beam breeding in the joint R&D between Kirin Agribio Co., LTD. and JAEA. They have been commercialized in Japan and Europe [1)], and their wholesale market has amounted to 550 million yen per year.

We have developed an advanced application system of ion beams in chrysanthemum to improve plants that have acquired useful characteristics such as tolerance to multi-diseases by recombinant DNA techniques[2)].

Cultivars of *Petunia hybrida* (petunias) have been bred since early 1830s and are now available as a popular bedding plants that have enormous market worldwide. This paper reports the production of new type flower color variations in petunia obtained by ion beam irradiation at JAEA-TIARA.

2. Materials and Methods

Very vigorous variety of petunia cv. “Kirin Hana- Saka Rose” that has a bright rose flower was used as a plant material. Buds placed in petri-dishes containing Murashige and Skoog medium were irradiated with 320-MeV carbon ions of 10 Gray generated by an AVF cyclotron at TIARA. Regenerated plants were grown in a green house to examine flower color.

3. Results and Discussions

1) Mutants with new type flower color

In total 1,010 individuals were generated from the irradiation. As a result, the individual of the pink color and the cherry color appeared respectively at the frequency of 1%. In addition, the individual that has minutely striped white (HS-MS) and the individual with the petal of a spotted pattern (HS-SP) appeared.

2) Characteristics of the mutants

Minutely striped white mutant (Fig. 1: HS-MS) has the same basal petal color as the parent. Its growth is a bit slower. The striped type cultivars have been reported in the morning-glory since Edo period. Recently, the cause is analyzed using carnation [3)]. In white part, transposon insertion into the pigment gene causes the inactivation of pigment synthesis. In the colored part the transposon excision induces the recovery of the pigment gene. It seems that "HS-MS" obtained here has the same mechanism of floral phenotype.

Spotted pattern mutant (Fig. 2: HS-SP) has the same basal petal color and growth habit, but the spot pattern is unique. Moreover HS-SP changes its flower color from spotted rose to spotted magenta and finally to spotted purplish blue. This unique characteristic is supposed to come from the change of vacuolar pH due to the mutation of either the genes that adjust pH or the genes that control aging of flowers.

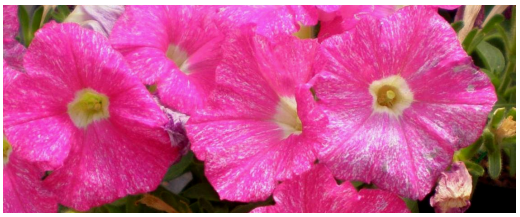

Fig. 1 Flower color mutant with minute white striped type obtained from ion beam breeding of petunia “Hana-Saka Rose”.

Fig. 2 Flower color mutant (right) of newly spotted color with changing color from rose to purplish blue, by ion beam breeding of petunia cv. “Hana-Saka Rose”(left).

In this study, we produced fascinating new mutants generated by ion beams that give us useful gene resources. We demonstrated the great impact of ion beams on the breeding of carnation, chrysanthemum and petunia and on floricultures.

A part of this study was supported by a grant in aid for Research and Development Program for New Bio-industry Initiatives.

References

1) M. Okamura et al., In J. Teixeira da Silva (ed.) Floriculture, Ornamental and Plant Biotechnology Vol. I, Global Science Books (2006) 619.
2) M. Okamura et al., JAEA Takasaki Ann. Rep. 2006 (2008) 82.
3) Y. Ito et al., Plant Cell Physiol. 43 (2002) 578.

3-08 Generating New Ornamental Plant Varieties Using Ion Beams

A. H. Affrida [a)], S. Shakinah [a)], A. Zaiton [a)], R. Yoshihara [b)], I. Narumi [b)], Y. Hase [b)] and Y. Oono [b)]

[a)] Agrotechnology and Biosciences Division, Malaysian Nuclear Agency,
[b)] Radiation-Applied Biology Division, QuBS, JAEA

Chrysanthemum is one of the leading temperate flowers in Malaysia, and contributes 22.62% of the total value of cut flower production (Lim *et al.*, 1998). Most of Malaysia's cut flowers are exported to Japan and the export values are increasing every year. Malaysian growers obtain chrysanthemum planting materials from foreign companies, propagate the plants locally and pay royalty based on the number of stalk sold at auction centers.

Ion beam is proven to be a useful mutagen for obtaining new commercial varieties with various flower colours in a short time, especially in ornamental plants like chrysanthemum, carnation and verbena. The objectives of this research are to develop an effective method for mutation induction of local varieties chrysanthemum using ion beams and to determine the optimum dose for callus formation using petals.

Fig. 1 *Chrysanthemum morifolium* cv Reagan Red (left) and *Chrysanthemum morifolium* cv Lameet (right).

Petals of *Chrysanthemum morifolium* cv Reagan Red and *Chrysanthemum morifolium* cv Lameet [1)] were cultured on 6 cm sterile petri dishes containing MS medium [2)] supplemented with 0.5 mg/L α-naphthalene acetic acid (NAA) and 2.0 mg/L 6-benzylaminopurine (BAP). The samples covered with Kapton films were irradiated with 320 MeV $^{12}C^{6+}$ ion beam at 0, 0.2, 0.5, 1.0, 2.0, 5.0, 8.0, 10, 20, 30 and 40 Gray (Gy) from the TIARA AVF cyclotron (JAEA, Takasaki). The irradiated petals were transferred onto fresh media and incubated at 25±2 °C under 16-hour photoperiod for proliferation. After 4 weeks, the number of survived petal was scored.

Irradiated petals that were able to produce callus and green in colour were considered to have survived the irradiation, whilst those that turned brown were not. No shoot regeneration was observed within four weeks after irradiation and therefore, only the increase in callus size was measured, which indicated that the callus were growing and multiplying.

The dose response curve of *Chrysanthemum morifolium* cv Reagan Red culture is shown in Fig. 2. The percentages of survived culture irradiated at 0-5.0 Gy were less than that of 8.0 Gy. This was because most cultures turned brown after being transferred to fresh media. The percentage of survived petals also decreased drastically at doses above 20 Gy.

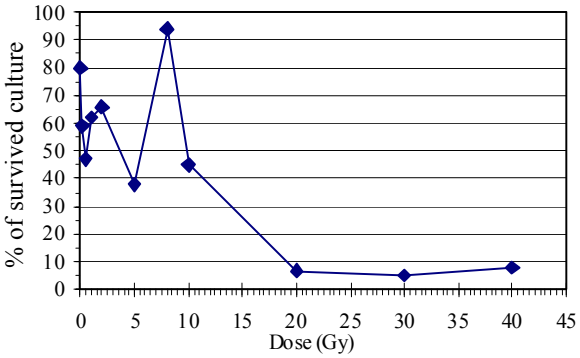

Fig. 2 Percentage of survived petal culture against dose after 4 weeks in *Chrysanthemum morifolium* cv Reagan Red.

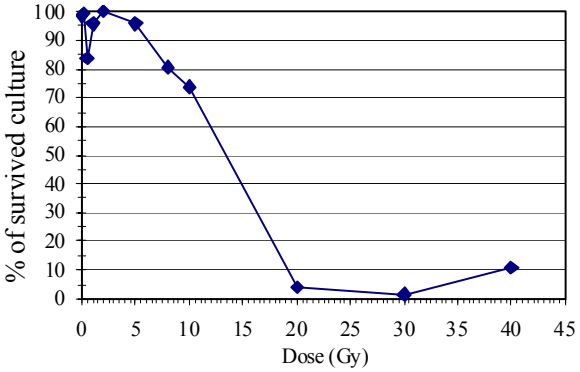

Fig. 3 Percentage of survived petal culture against dose after 4 weeks in *Chrysanthemum morifolium* cv Lameet.

The dose response curve of *Chrysanthemum morifolium* cv Lameet culture is shown in Fig. 3. The percentage of survived cultures was more than 90% at doses below 7.5 Gy. Irradiation at dose 20 Gy and higher were found lethal, as the percentage of survived cultures were less than 10%.

The results reported here were from the first irradiation experiments for both varieties. The experiment will be repeated to obtain more accurate dose response curve. Meanwhile all of the calluses were sub-cultured until they produce shoots.

References

1) H. J. Lim et al., Cut Flower Production in Malaysia. FAO Corporate Document Repository (1998) (http://www.fao.org /docrep/005/ac452e/ac452e06.htm)
2) T. Murasige and F. Skoog, Physiol. Plant, 15 (1962) 473.

3-09 Mutation induction in Lavandin: Plant Regeneration from $^{12}C^{6+}$ Beam Irradiated-lateral Meristems and -isolated Cultured Cells

M. Tsuro [a)], M. Inazawa [a)], S. Nozawa [b)] R. Yoshihara [b)] Y. Hase [b)] and I. Narumi [b)]

[a)] Faculty of Agriculture, Meijo University,
[b)] Radiation-Applied Biology Division, QuBS, JAEA

In order to develop a new lavandin, *Lavandula* × *intermedia* Emeric., plant with different fragrance from original plant, effect of several doses of $^{12}C^{6+}$ beam on shoot formation from lateral meristem was analysed. $^{12}C^{6+}$ beam did not affect shoot formation below 32.0 Gy, while shoot formation rate was decreased with increase of irradiation dose of over 32.0 Gy. In root initiation, any medium with or without IBA and NAA was not stimulated. Furthermore, the trials for root formation and plant regeneration from $^{12}C^{6+}$ beam and gamma ray irradiated-isolated cells derived shoots, as previously reported, were also conducted. In $^{12}C^{6+}$ beam irradiation, few shoots (<10%) formed roots in every medium tested. On the other hand, efficient root formation rates (>80%) were observed in medium with or without IBA, in gamma ray irradiation. These results suggested root formation was significantly affected by the kinds of radiations. Regenerated plants are now grown in the greenhouse for analysis of essential oils.

ラベンダーのエッセンシャルオイルは多くの化合物で構成されており、その成分比の違いにより香調が大きく変化することから新しい香りの創出が期待されている。

これまでに香調が変異したラベンダーの作出を目的として、$^{12}C^{6+}$ビームおよびガンマ線を単離培養細胞に照射し、細胞の増殖およびシュートの形成に及ぼす影響を調査した(Tsuro et al., 2007, 2008)。本研究では、腋芽分裂組織に$^{12}C^{6+}$ビームを照射し、線量がシュート伸長に及ぼす影響を調査するとともに、前述で得られた細胞由来シュートとあわせてシュートからの発根条件を検討して再分化個体の獲得を試みた。

植物材料としてラバンジン（真正ラベンダーとスパイクラベンダーとの雑種）品種'スーパーセビリアンブルー'を用いた。温室で育成した植物体の上位5 cm程度で木質化していない部位を切り取り、常法により滅菌した後、葉をすべて取り除いた茎を節ごとに切断し、1外植片につき1個の腋芽が得られるように節部に対生に着生した腋芽を残して正中面に半分に切り取ったものを腋芽外植片として用いた。0.2 mg/L ベンジルアデニン(BA)を添加した1/2 MS固形培地に腋芽を上に向けて置床し、320 MeV $^{12}C^{6+}$ビームを0, 0.5, 1.0, 2.0, 4.0, 8.0, 16.0, 32.0, 64.0および128.0 Gyの線量で照射した。照射後、25 °C、16時間明条件で培養を行い、シュートの伸長を促した。培養2週間後に腋芽からのシュート形成率を調査した。

腋芽より伸長したシュートおよび既報(Tsuro et al., 2007, 2008)で得られた$^{12}C^{6+}$ビームおよびガンマ線照射細胞由来カルスより形成したシュートが1～2 cmに伸長したとき、シュートを切り取り、0.2 mg/Lのナフタレン酢酸(NAA)またはインドール酪酸(IBA)を添加あるいは無添加の1/4 MS固形培地に移植して、25 °C、16 時間明条件で培養し、発根を誘導した。

$^{12}C^{6+}$ビームを腋芽に照射し、2週間培養したときのシュート形成率をFig. 1に示した。32.0 Gy以下の線量では形成率が高く、照射に対する伸長抑制反応は認められなかった。また、64.0 Gyおよび128.0 Gy区でシュート形成率の低下が認められたが、全個体が枯死するまでに至らなかった。

$^{12}C^{6+}$ビームおよびガンマ線照射細胞由来カルスから形成したシュートおよび上述の$^{12}C^{6+}$ビーム照射腋芽から伸長したシュートを各種発根培地に移植して培養したときの発根率をFig. 2に示した。発根率は概してガンマ線照射区で高く、腋芽由来シュートで低かった。ガンマ線照射区では培地に添加した成長調節物質が発根に大きな影響を与えており、IBA添加区およびフリー区で9割以上のシュートが発根していたのに対し、NAA添加区では37.8%と著しく低下しており、NAAの添加によって発根が抑制されることが示唆された。一方、$^{12}C^{6+}$ビーム照射区では培地による発根率の差異が認められず、総じてガンマ線照射区より発根率が低かった。特に、腋芽由来シュートからはほとんど発根が認められず、再分化個体は8.0 Gyを超える線量区からほとんど得られなかった。

本研究で得られた再分化個体は現在屋外で育成している。今後、植物体の形態調査に加え、生殖成長期に見られる出穂日やエッセンシャルオイル成分の変異等の形質を調査する予定である。

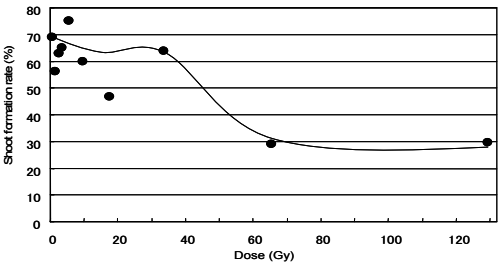

Fig.1 Effect of $^{12}C^{6+}$ beam irradiation on shoot formation from lateral meristem in lavandin.

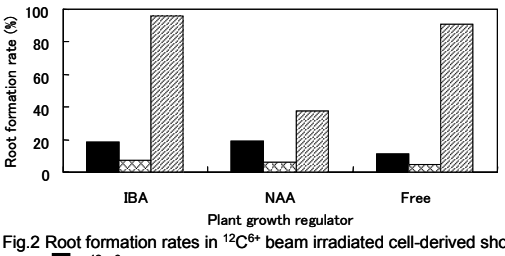

Fig.2 Root formation rates in $^{12}C^{6+}$ beam irradiated cell-derived shoot (■), $^{12}C^{6+}$ beam irradiated lateral meristem-derived shoot (▨) and gamma ray irradiated cell-derived shoot (▨).

3-10 Selection of Salinity Tolerant Lines in Strawberry (*Fragaria* × *ananassa*) Irradiated with Helium Ion Beam

N. Chiba [a)], K. Arakawa [a)], T. Itabashi [a)], S. Nakamura [a)], N. Takahashi [a)], Y. Iwasaki [a)], R. Yoshihara [b)], S. Nozawa [b)], Y. Hase [b)] and I. Narumi [b)]

[a)] Miyagi Prefectural Agriculture and Horticulture Research Center,
[b)] Radiation-Applied Biology Division, QuBS, JAEA

We irradiated helium ion to strawberry (*Fragaria* × *ananassa*) and examined growth of 804 M_1 plants under half concentration of MS solid medium containing 50 mM sodium ion *in vitro*. Thirty six M_1 plants showed salinity tolerance under the tested condition and the rate of selection was 4.5%. Helium ion irradiation seems to be an effective technique to develop salinity tolerant lines in strawberry.

１．はじめに

イチゴ（*Fragaria* × *ananassa*）は耐塩性の低い作物であり、土壌中の過剰な塩類は収量と品質に悪影響を及ぼす。本試験ではイオンビームを利用した変異誘発により、イチゴの耐塩性が改良できるかを試験した。

２．実験方法

材料はイチゴ品種「もういっこ」と「章姫」を用いた。2008年9月4日に無菌培養条件の腋芽を含む切片に対してヘリウムイオン(50 MeV, $^4He^{2+}$)を照射し、その後に6-ベンジルアデニン0.4 μMを含む1/2MS固体培地で切片から再生したイチゴの幼植物体をM_1世代（突然変異第１世代)とした。塩類ストレスにより変異株を選抜するため、塩化ナトリウムの添加によりNa^+濃度を50 μMに調節した1/2MS固体培地を選抜培地として使用した。照射後約130日に腋芽から再生したM_1世代をプラントボックス（7 cm(W)×7 cm(D)×10 cm(H)）内の選抜培地へ移植した。栽植密度はプラントボックス1個当たり4株とした。耐塩性の選抜は、移植後約70日の観察において無照射株との生育比較により行った。

３．結果及び考察

以前に試験[1)]したイオンビームに対する腋芽からの再生の線量反応を参考に、線量4～32 Gyで変異誘発し、選抜培地による塩分ストレス条件下で「もういっこ」M_1世代136株と「章姫」M_1世代668株（合計804株）の生育経過を観察した。無照射株及び耐塩性を獲得していない照射株は、生育抑制と葉枯れが見られた。一方，耐塩性を獲得した変異株は塩化ナトリウム無添加培地で生育した無照射株と同程度に生育し，葉枯れの程度も軽微であった（Fig. 1）。両品種の無照射株間において耐塩性の品種間差違は見られなかった。照射後約200日に選抜した耐塩性変異株は両品種の合計で36株，選抜率は「もういっこ」で5.9%，「章姫」で4.2%，試験全体で4.5%であった（Table 1）。線量と選抜率の関係については明瞭な傾向が無かった。

耐塩性イチゴ変異株の選抜率（4.5%）は，以前にイオンビームにより作出したユリの突然変異株から花器における諸形質の変異率と同程度の値であった[2),3)]。竹久らの報告[4)]ではNa^+濃度50～100 mMの塩害水田において、イオンビームで誘発したイネ耐塩性変異株を選抜している。今回は実験室内で選抜試験を行った結果であり、今後は野外施設においてNa^+濃度100 mM程度の設定でイチゴ変異株系統の高次選抜を行う予定である。

Table 1 Number of tested and selected M_1 plants of strawberry (*Fragaria*×*ananassa*) cultivar ‘Mouikko’ and ‘Akihime’.

Dose	N of tested M_1		N of selected M_1	
(Gy)	Mouikko	Akihime	Mouikko	Akihime
4	16	160	1	7
8	36	172	4	9
16	28	156	3	3
32	56	180	0	9
Total	136	668	8 (5.9 %)	28 (4.2 %)

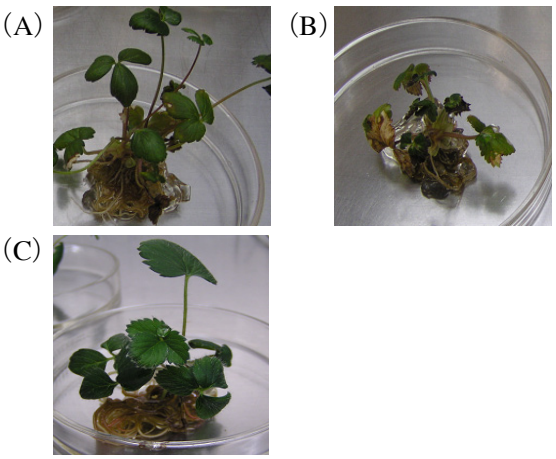

Fig. 1 Selection of salinity tolerance in strawberry (*Frgaria* × *ananassa*) cultivar ‘Mouikko’.
(A): Selected salinity tolerant mutant,
(B): Salinity intolerant plant,
(C): Unirradiated plant in no addition of sodium ion.

References

1) N. Chiba et al., JAEA Takasaki Ann. Rep. 2007 (2008) 78.
2) N. Chiba et al., JAEA Takasaki Ann. Rep. 2005 (2007) 92.
3) N. Chiba et al., JAEA Takasaki Ann. Rep. 2006 (2008) 77.
4) H. Takehisa et al., Radiation & Industries 121 (2009) 22.

3-11 Development of Commercial Variety of Osteospermum by a Stepwise Mutagenesis by Ion Beam Irradiation

T. Okada [a)], M. Iizuka [a)], R. Yoshihara [b)], Y. Hase [b)] and I. Narumi [b)]

[a)] Gunma Agricultural Technology Center, [b)] Radiation-Applied Biology Division, QuBS, JAEA

Introduction

Osteospermum is one of the composite perennials, and characterized by a long flowering period. Recently, the production of Osteospermum has increased as pot plants and bedding materials. Besides the ordinary cross breeding, bud mutation has been used for the breeding of new varieties. However, development of more efficient mutagenesis techniques with an artificial manner is expected at production fields. Previously, we irradiated Osteospermum 'Mother Symphony' with ion beams, and selected the unprecedented pastel color variant, which was applied to the variety registration as 'Vient Flamingo (tentative name)' in March 2007[1)]. Usually, Osteospermum has different colors between the each side of petals. But, we could obtain the orange- and yellow-isochroous variants from irradiated 'Mother Symphony'. However, we could not obtain a white- isochroous variant that has a potentially high market value. Therefore, we irradiated again the white petal variant OM7 of 'Mother Symphony' with ion beams to obtain white-isochroous petals[2)]. As a result of that, the OM706 that has light yellow in the back side of the petal was obtained. This result suggested that Osteospermum mutated in a stepwise manner with ion beams[3)]. Then, in an effort to obtain variants with white- isochroous petals, we irradiated again OM706 with ion beams.

Materials and Methods

(1) *Preparation of re-irradiation material*

Leaf sections (quadrilateral pieces with 0.5 to 1 cm in size) of the 2 times irradiated variant OM706 of Osteospermum 'Mother Symphony' were put on 1/2 MS medium supplemented with 0.1 mg/L NAA and 1.0 mg/L BA. After irradiation and post-cultivation, the re-differentiated individuals were obtained.

(2) *Selection of variants using the optimized dose*

Leaf disc sections were irradiated with carbon ions (220 MeV $^{12}C^{5+}$ and 320 MeV $^{12}C^{6+}$) at a range of 0.5 to 5 Gy. After 24 h, the leaf disc sections were transferred to fresh 1/2 MS medium supplemented with 0.1 mg/L NAA and 1.0 mg/L BA to induce adventitious buds. After about 1 month, grown adventitious buds were transplanted on fresh 1/2 MS medium, and cultivated to obtain plantlets. The resultant plantlets were acclimatized and then grown in a greenhouse to investigate flower color and morphological changes.

Results and Discussion

OM706 that has the white petal in the upper side and the light yellow petal in the back side was derived from re-irradiated the white petal variant OM7. By third irradiation of OM706, we obtained 132 individuals that have variation in petal color, petal shape and plant type from total 1,144 flowering plants which were raised until now this year (Table 1). Third irradiation induced a lot of mutations in petal color or plant type compared to the first and second irradiation. In color variation, yellowish white, whitish light orange, whitish light yellow and pale yellow mutants and lighter yellow in the back side of the petal than OM706 were obtained. So far, many variants show discoloration in the back side of the petal more than OM706, but we could not obtain a perfect white petal variant. However, thousand irradiated individuals before flowering are grown in a greenhouse now. Appearance of perfect white petal individuals is expected among plants flowering from now.

Table 1 Mutants in OM706 by the irradiation of 0.1～5 Gy $^{12}C^{5+}$ and $^{12}C^{6+}$ ion beams.

Radiation	No. of hardening	No. of hardening	
$^{12}C^{5+}$ (220 MeV)	834	color	60 (7.2)[z]
		plant type	26 (3.1)
$^{12}C^{6+}$ (320 MeV)	310	color	27 (8.7)
		plant type	19 (6.1)

[z] The percent is shown in the parenthesis.
Color variation: yellowish white 8, whitish light orange 6, whitish light yellow 9, pale yellow 40, lighter yellow in the back side of the petal than OM706 20, others 4
Plant type variation: type of petal 33, dwarf 9, others 3

References

1) M. Iizuka et al., JAEA Takasaki Ann. Rep. 2005 (2007) 81.
2) M. Iizuka et al., JAEA Takasaki Ann. Rep. 2006 (2008) 71.
3) M. Iizuka et al., JAEA Takasaki Ann. Rep. 2007 (2008) 65.

3-12 Mutants Induced by Ion Beam Irradiation in Delphinium 'Momoka'

S. Chinone [a)], K. Tokuhiro [a)], K. Nakatsubo [a)], Y. Hase [b)] and I. Narumi [b)]

[a)] Kaneko Seeds CO., LTD., [b)] Radiation-Applied Biology Division, QuBS, JAEA

To obtain mutants of Delphinium'Momoka', we irradiated 320 MeV carbon ion beams. Ion beams irradiation induced some mutants of flower colour, spike and plant height. The flower colour changed into light pink, red pink and yellow pink flower from deep pink. We suggested the suitable doses for mutant induction in Delphinium were around 0.5-1.0 Gy.

イオンビーム照射による突然変異は，ガンマ線などの従来の変異原と比較して誘発の効果やs変異スペクトルが大きく，キクやカーネーションでは花色や花形の変化，腋芽数の減少のなどの変異が報告されている[1)]。

カネコ種苗㈱育成のデルフィニウム'ももか'は濃いピンク色の花色を有する品種である。本研究では，淡ピンク色や黄色などの花色変異体の獲得を目的にイオンビーム照射を行った。

無菌的に培養しているデルフィニウム'ももか'の葉身を60 mmシャーレに置床し約1～2週間後にイオンビームの照射を行った．照射は日本原子力研究開発機構イオンビーム照射研究施設（TIARA）のAVFサイクロトロンを用いて，炭素イオン（$^{12}C^{6+}$，320 MeV）を照射した。2008年の照射は前報で適正線量と推測された炭素イオン0.5～1.0 Gyを照射した[2)]。照射後，再分化培地に移植し，7～8ヵ月後にパイプハウスに定植し，開花検定を行った。

2007年に照射した174個体，2008年に照射した188個体の開花検定を行った結果，花色や花型，花穂の形状，草丈の変異が認められた（Table 1）。

炭素イオンの線量が2および4 Gyでは，矮性個体や奇形花などが見られ，有用な変異体は認められなかった。

花色変異は薄いピンク色から黄色がかったピンク色，赤味の強いピンク色などが見られた（Fig. 1）。その他の変異として小花が密に着生する個体や花弁数が増加する個体などが認められた。その中から，花色の変異体を9個体，小花が密に着生する変異体を1個体選び，培養を行った。増殖後，変異の安定性について再度検定を行う予定である。

開花検定の結果，有用な変異の誘発には0.5～1.0 Gyが適正と推察された。

Table 1 The number of mutants induced by carbon ion beam irradiation.

Time	Dose (Gy)	Number of plants	Number of mutants		Mutation Type			
					Flower colour	Malformed flower	Spike	Dwarf
2007	0.5	59	5	(8.5%)	3	1	0	1
	1	43	5	(7.0%)	2	1	1	1
	2	28	4	(7.1%)	0	3	0	1
	4	3	2	(66.7%)	0	0	0	2
2008	0.5	105	8	(7.6%)	3	2	1	2
	1	83	7	(7.2%)	0	2	1	4

Fig. 1 Mutants induced by ion-beam irradiation. Upper: 'Momoka', Bottom left: Flower-color mutant, Bottom right: Mutant with increased number of spikes.

References

1) M. Okamura, et al., TIARA Takasaki Ann. Rep. 2005 (2007) 82.
2) S. Chinone, et al., TIARA Takasaki Ann. Rep. 2007 (2008) 68.

3-13 Molecular Analysis of Carbon Ion Induced Mutations in the Yeast *ogg1* and *msh2* Mutants

Y. Matuo [a)], S. Nishijima [a)], Y. Hase [b)], S. Nozawa [b)], A. Sakamoto [b)], I. Narumi [b)] and K. Shimizu [c)]

[a)] Graduate School of Engineering, Osaka University,
[b)] Radiation-Applied Biology Division, QuBS, JAEA,
[c)] Radioisotope Research Center, Osaka University

Breeding technology using mutations induced by ion beam irradiation has undergone major developments, and has been applied in various fields. To investigate the molecular mechanism of the mutagenesis caused by ion beam irradiation, we used the yeast mutant strains *ogg1* and *msh2*, which are deficient in mismatch repair.

S. cerevisiae strains used in this study are S288C (RAD^+), *ogg1*, *msh2*. OGG1p is a DNA glycosylase / AP lyase that excises guanine lesions such as 8-oxoguanine (8-oxoG). MSH2p is the mismatch repair (MMR) protein that mediates DNA repair through the recognition of 1 and 2-bp mismatches. The yeast strains were irradiated with carbon ions ($^{12}C^{5+}$; 220 MeV) with the dose of 50 to 100 Gy. The LET was 107 keV/μm. Carbon ion beams were generated from AVF cyclotron in JAEA-Takasaki. Selection of *ura3* cells was accomplished by plating the cells on the media containing 5-fluoroorotic acid (5-FOA). The mutation sites of *ura3* mutants were determined by DNA sequencing.

Mutation frequencies are shown in Fig. 1. The mutation frequencies induced by carbon ions in *ogg1* and *msh2* were 1.4- and 1.2- fold higher than that of the wild-type cells at 100 Gy, respectively. These results indicate that *OGG1* and *MSH2* play an important role in reducing the occurrence of mutations caused by ion beam irradiation.

Table 1 shows summaries of the sequence analyses. Our previous results showed that the types of base changes in carbon-ion induced mutants in wild type cells included GC to TA transversions (41%), other types of base substitution (41%) and deletions/insertions (18%). In the case of *ogg1,* GC to TA transversions were largely observed (70%). GC to TA transversions are caused by misincorporation of 8-oxodG into DNA. The high frequency of GC to TA events in *ogg1* and *msh2* strains strongly suggests that 8-oxodG is the predominant mutagenic lesion induced by ion-beam irradiation of yeast. Therefore, this result probably implies that the concentration of 8-oxodG in *ogg1* mutant cells is higher than that in wild type cells, since the 8-oxodG produced by ion-beam irradiation is removed less efficiently in *ogg1* mutant cells than in wild type cells.

In the *msh2* mutant strain, the mutational spectrum exhibited a predominance towards small deletions (- 1 bp deletion mutation), with the mutations unequally distributed over the *URA3* gene region. Moreover, in the *msh2* mutant strain, the largest class of base substitution mutations was GC to TA transversions. These results suggest that the high rates of base substitutions observed in MMR deficient strains are, at least partially, caused by the misincorporation of oxidatively damaged DNA bases such as 8-oxodG. Our results show that that the oxidative stress caused by carbon-ion irradiation induces the formation of 8-oxodG in DNA, which, if not repaired, can be a major cause of genetic instability.

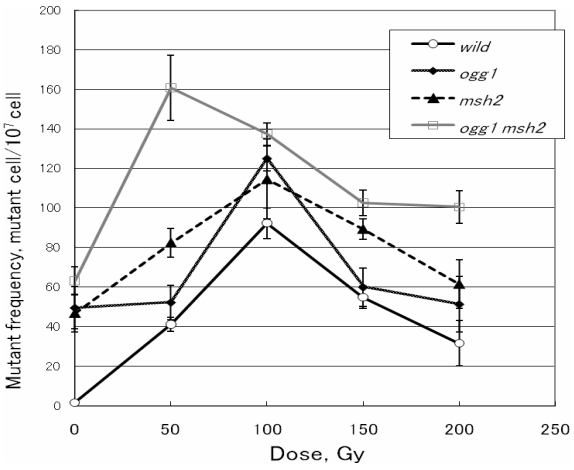

Fig. 1 Frequency of *ura3* mutants after irradiation with a carbon ion beam.

Table 1 Type of mutations induced by carbon-ion irradiation.

Type of mutation	*ogg1* Number	*ogg1* Percentage	*msh2* Number	*msh2* Percentage	*Wild* Number	*Wild* Percentage
Base substitution						
Transversions	47	94.0	16	32.0	35	68.7
G:C to T:A	36	77	13	81	21	63
G:C to C:G	0	0	2	13	12	31
A:T to C:G	7	15	0	0	1	3
A:T to T:A	4	8	1	6	1	3
Transitions	3	6.0	10	20.0	7	13.7
G:C to A:T	3	100	9	90	7	100
A:T to G:C	0	0	1	10	0	0
Deletions	0	0	23	46.0	8	15.7
Insertions	0	0	1	2.1	1	1.9
Total	50	100.0	50	100.0	51	100.0

3-14 Effects of Heavy Ion beam Irradiation in Citrus

Y. Matsuo [a)], Y. Hase [b)], S. Nozawa [b)], R. Yoshihara [b)] and I. Narumi [b)]

[a)] Saga Prefectural Agricultural Fruit Tree Experiment Station,
[b)] Radiation-Applied Biology Division, QuBS, JAEA

Radiation breeding is one of the useful methods to develop new varieties of fruit tree. To apply the carbon-ion beams to citrus breeding, we examined radiation sensitivity of five citrus varieties. In Carrizo citrange, the regeneration rate form the irradiated hypocotyl decreased to 60.0% at 4 Gy and 38.5% at 8 Gy. In Neiha kumquat, the regeneration rate was 79.5% at 8 Gy. In Kawano-natsudaidai, the regeneration rate was more than 90 % up to 8 Gy, and 58.3% at 16 Gy. Our results show that there is a difference in radiation sensitivity between the citrus varieties.

果樹等木本植物の増殖は、栄養繁殖を中心に増殖が行われており、突然変異等を利用して作出された個体は、接木などを利用し増殖することが可能である。放射線を利用し突然変異を効率よく誘発する育種法は、果樹育種において重要な品種改良の一つである。しかし、カンキツにおいては、重イオンビーム等を利用した突然変異誘発事例の報告は少ない。このため、本試験では前報でのユズに重イオンビームを照射した試験結果をもとにカンキツ類に重イオンビームを照射し、放射線感受性の程度を調査した。

供試品種は、キャリゾシトレンジ、ニンポーキンカン、福原オレンジ、川野ナツダイダイ、シークヮーサー用いた。種子を1/2MS培地に播種後、3週間目に胚軸を2 cm程度残し切断した。さらに、1週間後に切断面より発生したカルスに重イオンビームを照射した。照射線種はCイオン（$^{12}C^{6+}$, エネルギー320 MeV）を用い、照射線量は2 Gy、4 Gy、8 Gy、16 Gy、32 Gy、の5線量区とした。照射施設は原子力機構高崎量子応用研究所のAVFサイクロトロンを用いた。照射後、出芽・伸長を開始した個体は、馴化培地へ継代し、更に培土に鉢上げを実施し、ガラス室で育苗した。照射4 Weeks後の再分化率、再分化植物伸長量等の調査を行った。

各品種とも前回のユズへの照射試験を基準に照射を実施した。再分化率は各品種によりバラつきがみられた（Table 1、Fig. 1）。キャリゾシトレンジでは、再生率が2 Gyを超えると60%以下となり、重イオンビームに対する感受性程度が高いと思われた。ニンポーキンカンでは、種子は他の品種に比べ小粒であったが、8 Gyまではほぼ80%程度以上再分化した。しかし、16 Gyを超えると再分化率は24%程度と急速に低下するが、32 Gy以上でも唯一再分化個体が確認できた。福原オレンジでは、ユズとほぼ同様に4 Gyまでは80%以上の再分化率を示した。川野ナツダイダイでは、今回調査した5品種の中で一番重イオンビームに対する感受性が低く、8 Gyまでは、90%以上の個体が再分化した。また、16 Gyでも60%以上の個体に再分化が見られた。また、平均伸長も他の品種より長かった。シークァーサーでは、各線量区とも再分化率が低い結果となった。また、16 Gyでは再生率が5%程度と非常に低い結果となった。これは、前処理条件を他品種同様に行った結果、小粒種子で且つ初期生育が緩慢であったため、照射前までに健全な照射個体に生育できなかったものと思われ、再度条件検討を行う必要があると思われた。

以上の結果を踏まえ、今後は品種ごとに最適線量を決定して、照射試験を実施する。また、明確な再分化曲線が描けなかった品種については、引き続き条件検討を実施する。

References

1) Y. Matsuo et al., Hort. Res. (JAPAN) 6 Suppl.1 (2007) 40.
2) Y. Matsuo et al., JAEA Takasaki Ann. Rep. 2007 (2008) 74.

Table 1 Shoot regeneration rate from hypocotyls and length of shoots of five citrus cultivars irradiated with carbon ions.

Cultivar		Dose (Gy)					
		0	2	4	8	16	32
Carrizo citrange	Regeneration rate (%)	92.3	79.5	60.0	38.5	30.4	0.0
	Shoot length (mm)	9.7	7.8	5.3	6.4	9.7	0.0
Neiha kumquat	Regeneration rate (%)	100.0	96.6	94.4	79.5	24.2	5.0
	Shoot length (mm)	6.5	5.6	5.8	3.9	0.8	1.0
Fukuhara orange	Regeneration rate (%)	90.0	80.0	84.6	38.5	22.2	0.0
	Shoot length (mm)	6.4	5.1	2.1	8.8	4.3	0.0
Kawano natsudaidai	Regeneration rate (%)	91.7	100.0	95.7	96.0	58.3	0.0
	Shoot length (mm)	15.3	16.6	7.8	11.0	2.5	0.0
Shiikuwasha	Regeneration rate (%)	66.7	85.7	82.6	52.0	5.0	0.0
	Shoot length (mm)	2.3	2.7	2.3	1.6	1.2	0.0

3-15 Mutation Induction in *Asclepias* Using Ion Beam Irradiation

N. Kobayashi [a)], S. Kano [a)], S. Sasaki [a)], K. Tasaki [a)], A. Nakatsuka [a)], S. Nozawa [b)], Y. Hase [b)] and I. Narumi [b)]

[a)] Faculty of Life and Environmental Science, Shimane University,
[b)] Radiation-Applied Biology Division, QuBS, JAEA

1. Introduction

Creation of new flower and plant form is expected for mutation breeding especially in ornamental plants [1),2)]. *Asclepias* is one of the perennial ornamentals native to Central America, using for cutting, potting and bed flowers. For the purpose to obtain flower and/or plant form mutation, *Asclepias* seeds were irradiated by ion beams. The seed germination rates, growth and survival rate of seedlings obtained from ion beam irradiated seeds are investigated[3)].

2. Materials and Methods

Open pollinated seeds of *Asclepias curassavica* L. 'Silky gold' and 'Silky red' were irradiated with carbon ion beams (220 MeV $^{12}C^{5+}$) at 0, 25, 50, 100, 150, 200, 250, 300, 400 and 500 Gy. Irradiated seeds were sowed in green house and germinated seedlings were transplanted into pots. After 10 months, these plants were planted in the field and maintained with a conventional cultivation method. The germination and survival rates, morphological variation of leaf and flower, and flowering time were investigated.

3. Results and Discussion

Seed germination rate decreased from 200 Gy irradiation with increasing doses and any seeds could not germinate in 500 Gy. Survival rate of seedlings decreased below 50% in 150 and 200 Gy and all seedlings were molted in 250 Gy and higher doses irradiation (Fig. 1). In 50 Gy and higher doses irradiated seedlings, abnormal morphology of leaves; rounded apical leaf, branched leaf and narrow lanceolated leaf were observed and appearance of abnormal leaf was increased in higher doses irradiation (Fig. 1). Compared with 0 Gy irradiated plants, flowering time in a part of plants irradiated with 25, 50, and 100 Gy was earlier and most of plants irradiated with 150 and 200 Gy flowered later. These results suggested the optimal irradiation doses for *Asclepias* seeds were consider being 50 to 200 Gy. Selection and evaluation of mutant seedlings with new ornamental traits is conducting.

References

1) N. Kobayashi et al. JAEA Takasaki Ann. Rep. 2005 (2007) 96.
2) N. Kobayashi et al. JAEA Takasaki Ann. Rep. 2006 (2008) 87.
3) S. Kano et al. Abst. Chugoku-Shikoku Br., Japan. Soc. Hort. Sci. 46 (2007) 40.

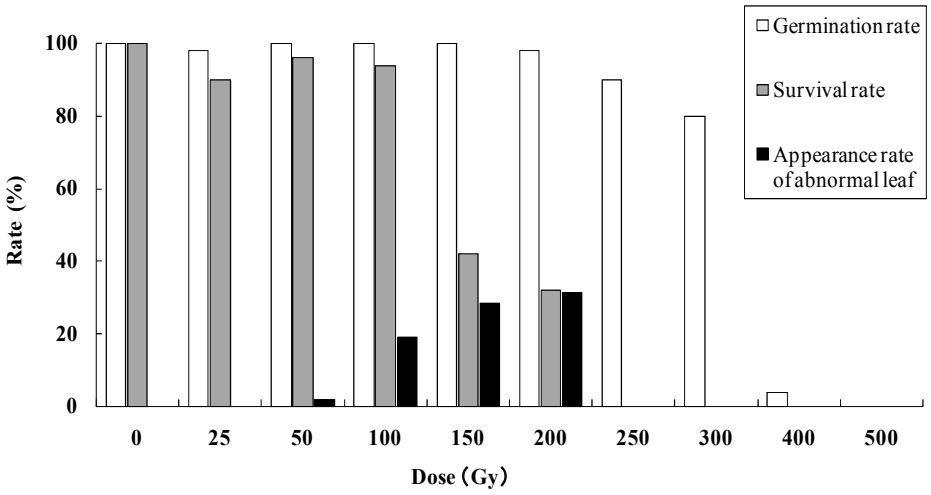

Fig. 1 Effects of ion beam irradiation for seed germination, seedling growth and leaf form in *Asclepias*.

3-16 Producing New Gene Resources in Fig by Using Ion-beam Irradiation

I. Asami [a)], S. Fukuta [a)], S. Kuroyanagi [a)], M. Yamada [a)],
Y. Hase [b)],Y. Yoshihara [b)] and I. Narumi [b)]

[a)] Aichi-ken Agricultural Research Center, [b)] Radiation-Applied Biology Division, QuBS, JAEA

The goles of our study are to produce new gene resources in fig by mutation induction with ion-beam irradiation, because the breading by varietal crossing in fig is very difficult. As the third paper of our study, we report the influences of carbon ion beams irradiation to *in vitro* lateral buds on mutation induction in fig 'Noire de Caromb' and 'White Genoa'. *In vitro* buds were irradiated with carbon ion beams (320 MeV $^{12}C^{6+}$) at TIARA. The efficiency of survival rate of buds, the fresh weight and the length of lateral shoots, and the rate of shoot that grows over 1 cm were observed. The optimum doses for carbon ion beams was 5-6 Gy of 320 MeV $^{12}C^{6+}$. So, we concluded that there was not a difference in radiation sensitivity of latelal buds in 4 varieties including 'Masui- Dauphine' and 'Banane'.

日本のイチジク産地で栽培されている品種は、ほとんどが“桝井ドーフィン”である。また、日本での栽培に適したフィッグ型イチジク品種はほとんど雌花しか着生しない[1)]ことから他品種との交雑育種は困難であり、これまで遺伝子資源の拡大はされてこなかった。そこで本課題では、イオンビームを利用して高品質で特徴ある新品種開発につながる遺伝子資源を創成する。本年度は過去2ヶ年とは異なるイチジク品種の培養苗腋芽に炭素イオンビームを照射し、放射線感受性の品種間差の有無を調査する。

無菌培養したイチジク品種“ヌアードカロン”と“ホワイトゼノア”の葉を切除した茎部を節ごとに切断し、6 cm径シャーレ内にのMS液体培地（ショ糖3%）を含ませた育苗用オアシス®（発砲フェノール樹脂）を入れ、腋芽の向きを上に揃えて挿した。同試料に加速した炭素イオン粒子（320 MeV・$^{12}C^{6+}$、LET：86 keV／μm）を種々の線量で照射した(腋芽30～40節／区)。照射試料は液体培地を含ませたオアシス®に挿し、プラントボックス内で育てた。培養は25 ℃、照明6 μmol/m^2/s^1、16 時間日長で行い、培養60日後の腋芽の生存率、10 mm以上伸長した腋芽の割合、腋芽の茎長及び重量を調査した。

“ヌアードカロン”の腋芽に炭素イオンビームを2.5 Gyから15 Gyまで段階照射したところ、10 Gyを越えると生存率がやや低下した。また、伸長した腋芽の茎長及び重量は5 Gy照射で非照射区（0 Gy）の平均値に対して50%程度にまで低下した（Fig. 1）。“ホワイトゼノア”の腋芽に炭素イオンビームを2.5 Gyから10 Gyまで段階照射したところ、生存率に大きな差はなかった。伸長した腋芽の茎長及び重量は約6 Gy照射で非照射区の平均値に対して50%程度にまで低下した（Fig. 2）。

放射線感受性を、照射した腋芽の生存率ではなく、照射後の腋芽の生育量から判断した場合、前年度までに調査した“桝井ドーフィン”と“バナーネ”で非照射区の平均値に対して生育量が50%に低下する線量は、本年度と同様に、およそ5 Gy～7.5 Gyであった[2),3)]ことから、培養苗腋芽に照射する本方法においては放射線感受性の品種間差はほとんど無いと判断できた。

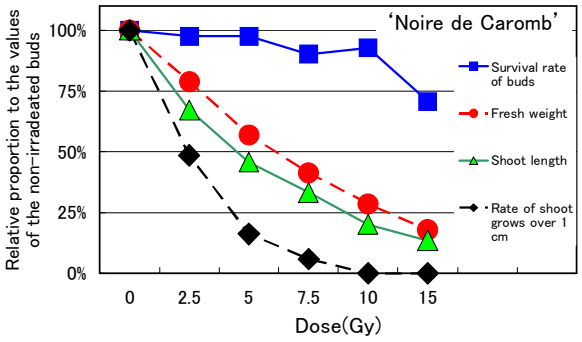

Fig. 1 Influence of 320 MeV carbon ion beam irradiation on growth of *in vitro* lateral buds in fig 'Noire de Caromb'.

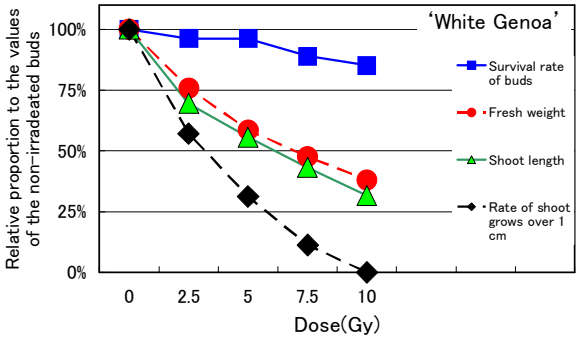

Fig. 2 Influence of 320 MeV carbon ion beam irradiation on growth of *in vitro* lateral buds in fig 'White Genoa'.

References

1) 平田尚美.農業技術体系-果樹編５,東京,農文協.イチジク,基29 (1993).
2) I.Asami, et al., JAEA Takasaki Ann. Rep. 2006 (2008) 80.
3) I.Asami, et al. ,JAEA Takasaki Ann. Rep. 2007 (2008) 76.

3-17 Ion Beam Breeding of Summer-to-Autumn Flowering Chrysanthemum 'Floral-Yuka'

T. Shirao [a)], T. Nagatani [a)], S. Nozawa [b)], Y. Hase [b)], A. Tanaka [b)] and I. Narumi [b)]

[a)] Kagoshima Biotechnology Institute,
[b)] Radiation-Applied Biology Division, QuBS, JAEA

We used ion beam irradiation to improve flower habit and unusual petal flowering in long day of summer-to-autumn flowering Chrysanthemum 'Floral-yuka'. In the individual selection, 20 individuals were selected from 3,858 regenerated from tissue cultured plants, and then various flower shapes and leaf shapes were observed in the mutants. Also the decreases in the amount of DNA and the plant heights of mutants were detected as dose of ion beam irradiation increased. After vegetative propagation of selected individuals, the line selections were performed by flowering in August, and five lines were selected. However, the rest of lines were showed downsizing of flower buds.

夏秋輪ギク「フローラル優香」は、秀品率が高く、鹿児島県内の夏秋輪ギクの主力品種の一つとなっているが、草丈伸長のためのジベレリン処理や長日期には日長操作のためのシェード管理が必要などの改良すべき点がある。我々は、2004年からイオンビーム育種の手法を用いて、長日条件下の無シェード栽培でも舌状花異常が発生せずに開花が正常に行われる優良系統の育成に取り組んできたが、これまでに有望なものは得られていない。そこで、2007年の個体選抜試験及び2008年の系統選抜試験では、簡易シェードで高品質な切り花生産が可能となる優良個体の育成を図ることとし、消灯後の日長管理を95%遮光ネットを用いて13時間日長で選抜を行った。

供試材料には、「フローラル優香」の無菌植物から切り出した葉片（2×4 mm）をMS培地（IAA:5 mg/L、BA：1 mg/L）に置床後、原子力機構高崎研のAVFサイクロトロンにより発生させたイオンビーム（320 MeV・$^{12}C^{6+}$）を1～5 Gy照射し、不定芽経由により得た再生個体を用いた。これらの再生個体は、8月開花の作型の個体選抜試験に供試し、併せて照射線量が生育やDNA量に及ぼす影響等を調査した。さらに、選抜した個体は、翌年、系統選抜試験に供試した。

個体選抜試験には3,858個体を供試し、到花日数がコントロールと同等もしくは短縮しており、花弁の乱れが無く花容が優れる20個体を選抜した。2004～2006年の無シェード条件下で実施した個体選抜試験では、供試個体のほとんどがコントロールよりも到花日数が長くなり、コントロールと同等もしくは短縮した個体の出現率は2%程度であったが、本試験では、到花日数がコントロールと同等もしくは短縮した個体の出現率は、試験区間で異なるものの18.6～36.5%と増加した。しかし、イオンビーム照射線量と到花日数が短縮した個体の出現率には一定の傾向は認められなかった。イオンビーム照射のDNA量に対する影響については、照射線量の増加に伴い、DNA量が減少するとともに試験区内での個体間のバラツキが増大する傾向が認められた。また、開花時の草丈についても、イオンビームを照射した試験区内では個体間のバラツキが大きくなるとともに、照射線量の増加に伴い草丈が低くなった個体が多数観察された。さらに、花容については、花弁数の減少や舌状花の丸弁化、わい化等の変異が、葉形については、わい化や丸葉化、欠刻が深くなる等の変異が観察された。これらの変異は無照射区においてもわずかながら観察されたことから、イオンビーム照射による変異とともに培養変異も影響していると考えられる。

個体選抜試験で選抜した20個体は、翌年の系統選抜試験に供試し、同じく8月開花の作型で選抜特性の保持状況を調査した。到花日数については、FY07-W10、FY07-W20の2系統がコントロールよりも3日程度短縮されており、他系統もコントロールと同程度であった。花容については、花弁の乱れや貫生花の発生は無かったものの、系統によっては、やや扁平花になる傾向が認められた。また、多くの系統で、開花時の花のボリュームが減少しており、切り花品質が低下した。本試験では、開花時の花のボリュームがコントロールと比較して同等以上で、草姿が優れるFY07-W2、FY07-W4、FY07-W9、FY07-W17、FY07-W19の5系統を選抜した（Table 1及びFig. 1）。特にFY07-W19は、花弁数が多いとともに、1枚1枚の舌状花も大きいものとなっていた。これらの選抜系統については、引き続き生育特性の調査を継続する予定である。

以上の結果，イオンビーム育種による「フローラル優香」の特性改良については，長日期の開花習性や異常花の発生といった形質は改良可能であることが示されたものの、切り花のボリューム低下を考慮した選抜が必要であると考えられる。

Table 1 Characteristics of the selected lines in 2008.

Line	Dos (Gy)	ND	Plant height (cm)	Flower diameter (cm)	Flower weight (g)	Number of florets
FY07-W2	1	49	92	12.5	17.2	348
FY07-W4	1	47	85	13.0	18.7	328
FY07-W9	1	47	91	12.5	19.8	353
FY07-W17	3	50	97	12.5	21.0	340
FY07-W19	3	50	91	13.5	24.4	441
Floral-yuka (Control)	-	49	100	11.5	20.1	377

NDF : The number of days to flowering.

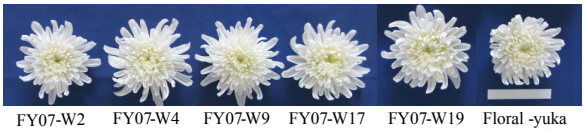

FY07-W2 FY07-W4 FY07-W9 FY07-W17 FY07-W19 Floral -yuka (Control)

Fig. 1 Flower shapes of selected lines. bar:10 cm

3-18 Dose Response of Ion Beam Irradiation in Strawberry (*Fragaria×ananassa*) Leaf Explants

J. Takano [a)], K. Namai [a)], R. Yoshihara [b)] Y. Hase [b)] and I. Narumi [b)]

[a)] Tochigi Prefectural Agricultural Experiment Station,
[b)] Radiation-Applied Biology Division, QuBS, JAEA

In order to obtain Fusarium wilt resistant mutants in strawberry cultivar "Tochiotome" which is most popular in Japan, leaf explants was irradiated with 320-MeV carbon ion beam. Results show that the suitable doses for mutation induction were estimated to be 2.5 Gy or below. Resistance of regenerated plants are being evaluated at the present time.

栃木県が育成したイチゴ品種「とちおとめ」[1)]は、作付面積が全国一であり、優れた果実品質を有するが、最重要病害の萎黄病に罹病性である。そのため、生産者からは、耐病性品種の育成が強く望まれている。イオンビームによる変異誘発は、原品種の特性を維持しつつ、一部の特性を改良するのに適している。そこで本研究では、イオンビームを用いた「とちおとめ」の萎黄病耐病性個体を作出することを目的とした。本年度はイオンビームの最適な照射条件を検討した。イオンビームには日本原子力研究開発機構、イオン照射研究施設（TIARA）のAVFサイクロトロンで加速された炭素イオン（$^{12}C^{6+}$, エネルギー320 MeV）を用いて照射を実施した。

とちおとめ無菌培養苗の葉片を約5 mm角に調製し、TDZ 1.0 mg/L、2,4-D 0.1 mg/Lおよびブドウ糖18 g/Lを添加した1/3MS培地（前培養培地）で1日間液体培養した。その後、前培養培地に0.8%寒天を添加した培地（カルス誘導培地）を10 mL分注した60 mmシャーレに置床し、イオンビーム照射まで4日間培養した。照射後、カルス誘導培地を30 mL分注した90 mmシャーレで1ヶ月間培養し、TDZ 1.0 mg/Lおよびブドウ糖18 g/Lを添加したMS培地（寒天0.8%）に移植して再分化を誘導した。ただし、1/3MS培地はMS培地成分のKNO_3, NH_4NO_3およびKH_2PO_4のみを1/3量に改変した。培養条件は、カルス誘導時の光強度を7 μmol $m^{-2}sec^{-1}$、再分化誘導時には40 μmol $m^{-2}sec^{-1}$とし、14時間日長、25 ℃で管理した。イオンビームは、2.5, 5.0, 7.5, 10.0 Gyの線量で照射した。再分化率は、再分化誘導1ヶ月後に調査した。

再分化率は、2.5 Gy照射区で7.2%、5 Gy照射区で6.1%、7.5 Gy照射区で3.3%、10 Gyで0.7%と照射強度が上昇するにしたがって低下した（Fig. 1）。この結果より、2.5 Gy照射区が再分化に最も影響を与えないと考えられ、それ以下が適正な照射線量と考えられた。今後は、2.5 Gy以下の線量で照射した再分化個体を作出していく予定である。また、再分化したシュートは、発根培養、順化の後、耐病性検定を行う予定である（Fig. 2）。

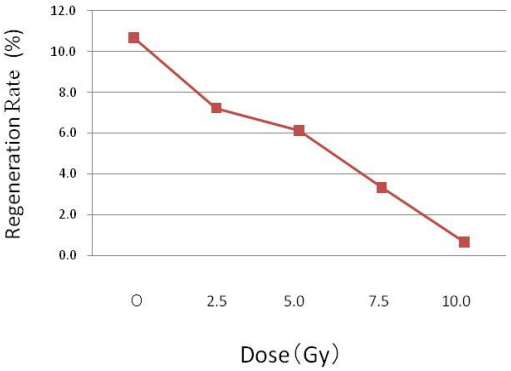

Fig. 1 Effect of ion beam irradiation on regeneration rate in strawberry (cv. Tochiotome).

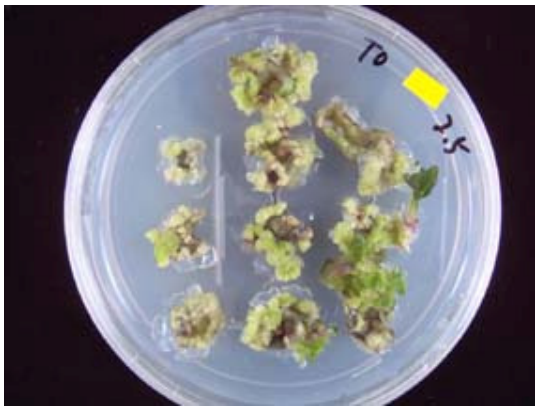

Fig. 2 Regeneration from ion beam irradiated leaf explants.

Reference

1) Y. Ishihara et al., 栃木県農業試験場研究報告44 (1996) 109.

3-19 Development of *Deinococcus grandis*/*Escherichia coli* Shuttle Vector

K. Satoh [a,b], Z. Tu [c], H. Ohba [a,b] and I. Narumi [a,b]

[a] Radiation-Applied Biology Division, QuBS, JAEA, [b] Research Unit for Quantum Beam Life Science Initiative, QuBS, JAEA, [c] College of Animal Sciences, Zhejiang University

Introduction

There is a wide diversity of radioresistance in the domain Bacteria, among which *Deinococcus* is the best known genus [1]. The genus *Deinococcus* comprises more than 30 species that exhibit extraordinary resistance to UV or ionizing radiation in the absence of a differentiated resting stage. Among these, *D. radiodurans* has been intensively studied in an effort to unravel mechanisms pertaining to DNA repair [1]. Despite the variety of *Deinococcus* species presently known, genetic engineering investigations have predominantly been applied to *D. radiodurans* and *D. geothermalis*. The development of new host-vector systems is therefore required to expand applications to a broader variety of *Deinococcus* species. In this study, attention was focused on the small 2.5-kb cryptic plasmid pUE30 from *Deinococcus radiopugnans* [2] towards the development of new shuttle vectors for *Deinococcus* species.

Experimental Procedures

The complete nucleotide sequence of pUE30 was determined with DNA sequence. The hybrid plasmids were constructed by ligating pUE30 to a derivative of pKatCAT, a vector developed for gene disruption studies in *D. radiodurans* [3]. In an effort to determine the region required for autonomous replication of the shuttle vectors in *D. grandis*, several deletion plasmids were constructed (Fig. 1). The expression of functional exogenous gene in *D. grandis* was analyzed by luciferase assay.

Results and Discussion

The nucleotide sequence of the small cryptic plasmid pUE30 from *Deinococcus radiopugnans* was determined. The 2,467-bp plasmid possesses two open reading frames, one encoding 88 amino acid residues (Orf1) and the other encoding 501 amino acid residues (Orf2). The predicted amino acid sequence encoded by Orf1 exhibits homology to a limited region of replication proteins encoded by *repABC*-type plasmids of α-proteobacteria. On the other hand, the predicted amino acid sequence encoded by Orf2 exhibits homology to replication proteins encoded by plasmids of *D. radiodurans* SARK and *Thermus* species.

Hybrid plasmids pZT23 consisting of pUE30 and pKatCAT5, which replicates in *E. coli* with a chloramphenicol resistance determinant, were shown to autonomously replicate in *D. grandis*. Transformation analysis using the deleted shuttle vectors (pZT27~30) revealed that Orf2 was necessary for replication of the plasmids in *D. grandis* (Fig. 1). On the other hand, Orf1 showed deleterious effects on the stability of the plasmids in *D. grandis*.

In an effort to express a functional exogenous gene in *D. grandis*, an expression plasmid (pZT90) that possesses the *D. radiodurans* minimal *groE* promoter was constructed based on the shuttle vector pZT29, and a firefly luciferase gene was successfully and stably expressed in *D. grandis* under non-selective conditions (Fig. 2).

The *D. grandis* host-vector system developed in this study should prove useful in the bioremediation of radioactive waste and for the investigation of DNA repair mechanisms.

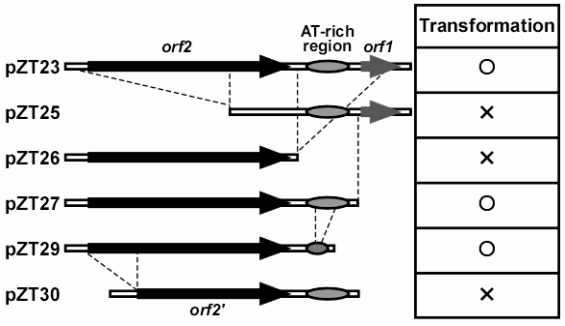

Fig. 1 Construction and transformation of several deletion plasmids.

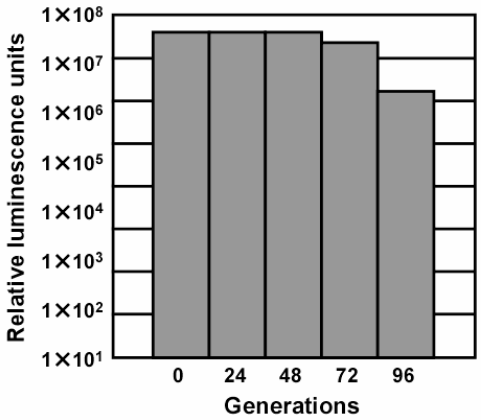

Fig. 2 Luciferase activity of *D. grandis* transformant under non-selective conditions.

References

1) M. M. Cox and J. R. Battista, Nat. Rev. Microbiol. 3 (2005) 882.
2) M. W. Mackay et al., Arch. Microbiol. 141 (1985) 91.
3) T. Funayama et al., Mutat. Res. 435 (1999) 151.

3-20 Analysis of Mutagenic Effect Induced by Ion Beams for Breeding of *Aspergillus oryzae*

Y. Toyoshima [a)], H. Tanaka [a)], J. Watanabe [a)], T. Yamazaki [a)], K. Iwashita [b)], S. Mikami [b)], K. Satoh [c)] and I. Narumi [c)]

[a)] Soy Sauce Laboratory, Manufacturing Division, YAMASA CORPORATION,
[b)] National Research Institute of Brewing, [c)] Radiation-Applied Biology Division, QuBS, JAEA

In this study, we investigated the mutagenic effect induced by ion beams for breeding of *A. oryzae*. To examine the mutation pattern in detail, we selected three *sB* deficient mutants in which large structural alterations in chromosomal DNA pattern were inferred from genomic southern analysis. Genome walking from *sB* break point suggested a possibility of chromosomal recombination, which was verified by pulsed-field gel electrophoresis and Southern analyses. These results suggest that ion beams are usable for acquisition of *A. oryzae* mutants that have large and complex structural genomic alterations.

【緒言】

麹菌（*Aspergillus oryzae*）は醤油、清酒、味噌などの醸造産業において利用される重要な微生物である。そのため、麹菌の育種が精力的に行われてきた。

これまで、イオンビーム照射による麹菌育種を検討した結果、凍結乾燥処理を行った麹菌分生子へのイオンビーム照射では 400 Gy で遺伝子変異が高い割合で生じていることが示唆された[1)]。また、パルスフィールド電気泳動などの結果から、染色体が大規模に欠失した株も見出され、イオンビーム照射により、麹菌ゲノムの大規模な変異を生じさせることを確認している[2)]。

今年度は、ゲノム構造の大きな変化が予想される株について、ゲノムウォーキングを行い、変異点の詳細な解析を行った。

【実験方法】

A. oryzae niaD300 の分生子を凍結乾燥し、照射サンプルとした。TIARAのAVFサイクロトロンを用いて加速した$^{12}C^{5+}$（220 MeV, 107 keV/μm）を照射サンプルに300～500 Gy 照射した。スクリーニング方法、サザン解析、パルスフィールド電気泳動については前報に準じて実施した[1,2)]。

【結果】

sB 遺伝子領域のサザン解析により、大規模な遺伝子構造の変化が予想された 3 株（400-7、400-11、400-15）を用いて、ゲノムウォーキングを行った。その結果、いずれの株についても染色体間組換えを示唆するシークエンスが得られた。

次に、パルスフィールド電気泳動で、染色体の泳動パターンを調べたところ Fig. 1 に示すように、親株に比べてバンドパターンが大きく異なっていた。

そこで、*sB* 遺伝子領域から上流、下流に約 3 kbp 離れた領域にプローブを作成し、このゲルを用いてサザン解析を行った（Fig. 2）。その結果、異なる染色体部位へプローブのハイブリダイゼーションが確認された。このバンドサイズは、ゲノムウォーキングにより推定された染色体組換えのサイズとほぼ一致することから、これら 3 株において、イオンビーム照射による染色体間の組換え誘発が確認された。

以上から、イオンビーム照射は、大規模な遺伝子欠損や染色体間組換えなど、麹菌ゲノム構造のダイナミックな変化を誘発することが明らかとなった。

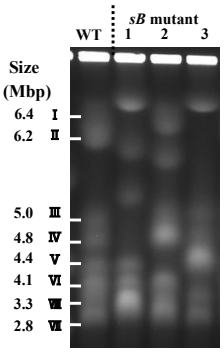

Fig. 1 Separation of *A .oryzae* Chromosomal DNAs; WT, niaD300 as DNA size marker; Lanes 1 to 3, *sB* mutants (1, 400-7; 2, 400-11; 3, 400-15); Ⅰ - Ⅷ, Chromosomal number.

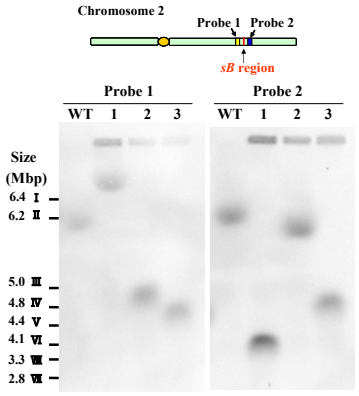

Fig. 2 Genomic Southern analysis of *sB* gene of *A. oryzae*; WT, niaD300; Lanes 1 to 3, *sB* mutants (1, 400-7; 2, 400-11; 3, 400-15); Ⅰ-Ⅷ, Chromosomal number.

References

1) Y. Toyoshima et al., JAEA Takasaki Ann. Rep. 2006 (2008) 97.
2) Y. Toyoshima et al., JAEA Takasaki Ann. Rep. 2007 (2008) 84.

3-21 Mutation Breeding of *Zygosaccharomyces rouxii* Induced by Ion Beams

K. Ito [a)], Y. Hanya [a)], K. Satoh [b)], Y. Hase [b)] and I. Narumi [b)]

[a)] R&D Division, Kikkoman Corp., [b)] Radiation-Applied Biology Division, QuBS, JAEA

Introduction

More than 300 aroma compounds have been confirmed in soy sauce. Many of them are produced during fermentation and the yeasts play an important role for production of them. Some of volatile aroma compounds, for example, HEMF, which is very important as the characteristic aroma component of soy sauce, are produced by the yeasts. Because these compounds have an influence on quality of soy sauce, many soy sauce researchers have tried to breed the yeasts to improve aroma components of soy sauce[1)]. However, it was difficult to breed the yeasts by traditional mutation, because of low mutation frequency. Therefore, we focused on ion beam mutagenesis that had a high mutation frequency and a broad spectrum of mutation in *Aspergillus* species[2)]. In this report, we investigated survival rate and mutation frequency of a salt-resistant soy sauce yeast, *Zygosaccharomyces rouxii* IFO1876 (haploid cell), to determine an optimal irradiation condition for ion beam mutagenesis.

Materials and Methods

(1) Survival rate

The suspension containing 10^2 - 10^7 cells (logarithmic growth phase) were spread on complete medium (YPD) plate. The cells were irradiated with 220 MeV ^{12}C (121.8 keV/μm) ion beams accelerated by AVF cyclotron at JAEA, in a dose range of 50-300 Gy. Irradiated cells were cultured at 30 ˚C for 3 days before the colonies were enumerated.

(2) Mutation frequency

The 10^6 cells were spread on YPD plate and irradiated with ion beams as described above. After cultivation for 6 hours, the irradiated cells were suspended with sterilized water. This cell suspension was spread on minimum medium (MM) plate containing 3.0 mg/mL of 5-fluoroorotate (5FOA). Mutation frequency was measured by counting the number of 5FOA resistant colonies. In order to isolate auxotrophic mutants, the irradiated cell suspension was treated with nystatin[3)] and spread on YPD plate. The colonies grown on YPD plate were replica plated on both MM and YPD plate. The colonies that failed to grow on MM plate were defined as auxotrophic mutants.

Results and Discussion

(1) Survival rate

One way to maximize the characteristics of ion beam mutagenesis is to irradiate an organism in a dry form, by which the generation of hydroxyl radicals resulted from water radiolysis is kept to the minimum. However, *Z. rouxii* IFO1876 was very sensitive to a dry form, the recovery rate after desiccation was below 1.0%. Therefore, *Z. rouxii* IFO1876 was irradiated on YPD plate. Figure 1 shows the survival rate of *Z. rouxii* IFO1876. The survival rate of *Z. rouxii* IFO1876 was similar to that of *Aspergillus* species[2)].

(2) Mutation frequency

We tried to obtain the 5FOA resistant mutants for measurement of mutation frequency, but no mutant was obtained. *Z. rouxii* IFO1876 was resistant to various other drugs. Therefore, we tried to obtain auxotrophic mutants by using a classical replica method. The 4,774 colonies grown on YPD plate after nystatin enrichment were replica plated on MM medium. The 49 auxotrophic mutants were obtained (Table 1). The number of auxotrophic mutants reached a maximum at 150 Gy. The irradiation at 150 Gy might be an optimal condition.

In the 49 mutants, the 47 mutants were adenine auxotrophic mutants, and other two mutants were amino acid auxotrophic mutants. In *Saccharomyces cerevisiae*, adenine auxotrophic mutants that are deficient in *ade1* or *ade2* gene form red-colored colonies. But, all 47 mutants didn't form red-colored colonies. These mutants might have a mutation in genes for adenine synthesis other than *ade1* and *ade2* genes.

References

1) T. Aoki et al., Agric. Biol.Chem. 54 (1990) 273.
2) K. Ito et al., JAEA Takasaki Ann. Rep. 2007 (2008) 94.
3) K. Ouchi et al., Hakokogaku Kaishi 61 (1983) 349.

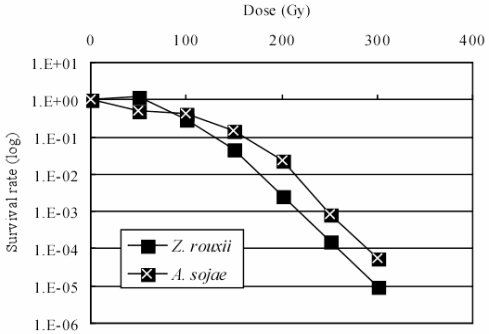

Fig. 1 Survival rate of cells after irradiation with carbon ion beams in *Z. rouxii* IFO1876.

Table 1 The number of auxotrophic mutants.

Dose (Gy)	replicated colonies	auxotrophic mutants[a)]
50	960	0
100	1440	20 (18)
150	1364	27 (27)
200	1010	2 (2)
Total	4474	49 (47)

[a)] The number of adenine auxotrophic mutants indicates in parentheses.

3-22 Ion Beam Breeding of "Sake Yeast"

T. Masubuchi [a)], O. Kamiyama [a)], K. Satoh [b)], Y. Hase [b)] and I. Narumi [b)]

[a)] Gunma Industrial Technology Center, [b)] Radiation-Applied Biology Division, QuBS, JAEA

We are trying to obtain high etyl caproate producing Sake yeast by carbon-ion irradiation. Freeze-dried yeast was irradiated with 220 MeV carbon ions by AVF cyclotron at JAEA at doses of 50-300 Gy. We isolated 774 cerulenin resistant mutants of sake yeast "Kyokai-901". Sake brewed with 3 mutants on 200 g micro-scale fermentation contained 4.4-5.3 ppm etyl caproate, whereas sake brewed with a parent strain contained 1.6 ppm etyl caproate.

清酒の消費は他の飲料との競合により全体では減少傾向が続いているが、吟醸酒や純米酒など、付加価値を有するものについては踏みとどまっており、各酒造蔵はこの分野に生き残りを賭け注力している。群馬県では、県内清酒の高品質化・差別化を意図して平成 3 年度から県独自の清酒酵母育種を開始し、平成 12 年度に「群馬 KAZE 酵母」として実用化した。当該酵母使用の清酒は全国新酒鑑評会等で入賞を重ねる実績をあげている。しかし消費者の嗜好は時代と共に変化していくため、新たなタイプの酵母開発を続け、市場ニーズに適応していくことが必要である。

新たな酵母を得るためには、もろみや自然界からのスクリーニング、既存酵母の変異処理などの手法がある。本研究では、吟醸酒に使用するためにカプロン酸エチルを主とした香気成分高生産株の取得を主目的とするため、発酵力が良好で吟醸酒での使用実績も多いきょうかい 901 号酵母を親株とし、変異処理で更に優良酵母を得ることを試みた。変異処理にはエチルメタンスルフォネート（EMS）を用いることが多いが、今回は炭素イオンビーム照射を行い、薬剤処理とは異なる変異スペクトルの発現を期待した。

イオンビーム照射に供する試料は、酢酸セルロースメンブラン上に塗布し、60 mm 径シャーレ中で凍結乾燥後にカプトン膜で上面を覆った。凍結乾燥の保護材として 10%グリセリン、10%スキムミルク+1%グルタミン酸ナトリウムの両者を検討したが、いずれも効果が認められず、操作性も悪かった。よって保護材を用いず、十分に培養した菌体を 0.9% NaCl で洗菌および再懸濁した後、減圧濾過ユニット（ADVANTEC 社 KP47-S）を用いてメンブラン上に濾別し、凍結乾燥する方法を採った。

照射に関しては、TIARA の AVF サイクロトロンを用いて加速した $^{12}C^{5+}$ (220 MeV)で、50～300 Gy の範囲で実施した。試料は照射後、YPD 培地 5 mL を添加して 30 ℃、2 時間保持し、適宜集菌、希釈して培地に塗布した。

カプロン酸エチル高生成株を取得するための選択培地は、市川ら[1)]の方法に準じセルレニン12.5 μMを含む YPD寒天培地を用いた。これに生育したセルレニン耐性変異株を齋藤ら[2)]の方法を改変した発酵試験に供し、15 ℃ 7日間の培養後に重量減少量（CO_2放出量）を測定し発酵力の目安とした。また、得られた上清をヘッドスペースガスクロマトグラフにより、イソアミルアルコール、酢酸エチル、酢酸イソアミル、カプロン酸エチルの各成分を定量して香気生成能を評価した。

発酵試験は774株について実施し、うち香気生成能が良好な35株について、布宮ら[3)]の変即二段仕込みを改変した方法で小仕込み試験（総米200 g）を行った。最も良好な結果を示した3株の変異株のうち、No.227および231は125 Gy、No.218は150 Gyの照射区分で得られたものである。これらの小仕込み試験について、群馬KAZE酵母（1号および2号）および親株であるきょうかい901酵母と比較した結果を示す(Table 1)。

変異株 No.227 は若干発酵力が弱い傾向があるが、他の２株は親株に劣らない発酵力を有し、カプロン酸エチル生成能も親株に比較して格段に向上している。しかし、現有の KAZE 2 号酵母にはまだ及ばないため、更なる検討を要する。

Table 1 Components contained in sake by micro brewing.

Strain No.	Alcohol content (%)	Sake meter	Acidity (mL)	Amino acidity (mL)	Sake cake ratio(%)
231	18.2	+5.2	2.2	1.9	76.8
227	17.5	-2.2	2.5	2.0	83.0
218	18.2	+5.3	2.3	1.9	79.4
Kyokai-901	18.2	+5.5	2.4	1.7	79.2
KAZE-1	18.1	+3.5	2.2	1.9	78.1
KAZE-2	17.6	+1.0	2.2	2.0	79.3

Strain No.	Isoamyl alcohol (ppm)	Etyl acetate (ppm)	Isoamyl acetate (ppm)	Etyl caproate (ppm)
231	200.6	95.7	7.3	4.4
227	187.9	80.4	5.9	5.3
218	225.5	111.4	11.0	4.7
Kyokai-901	221.3	143.3	12.2	1.6
KAZE-1	195.5	107.6	8.2	4.9
KAZE-2	200.3	85.6	7.5	7.0

References

1) 市川英治 et al., 1988年度日本農芸化学会大会講演要旨集、435.
2) 齋藤久一 et al., 醸協 87(1992) 915.
3) 布宮雅昭 et al., 醸協 90(1995) 217.

3-23 Detection Method for Irradiated Garlic Using ESR

M. Ukai [a)], H. Kameya [a)], H. Nakamura [a)], S. Todoriki [b)], M. Kikuchi [c)], T. Sakashita [c)], T. Funayama [c)] and Y. Kobayashi [c)]

[a)] Hokkaido University of Education, [b)] National Food Research Institute,
[c)] Radiation-Applied Biology Division, QuBS, JAEA

By Electron Spin Resonance (ESR) spectroscopy, we revealed free radicals in irradiated garlic. The representative ESR spectrum of garlic is composed of a singlet at the *g*-value of 2.0. The signal is due to organic free radicals. Upon γ-irradiation, new signals appeared. To analyze the irradiation effects, we proposed an ESR detection method of irradiated garlic.

Introduction

放射線照射は効果的な殺菌法として国際的に認められている[1)]。電子スピン共鳴（ESR）法は、放射線照射食品に関する品質表示の正しさを担保する検知技術に応用されており、EU では公定法として導入し照射の有無の判別を行っている。われわれはすでに照射コショウを用い ESR による検知法を報告[2)-3)]している。本研究では、照射ニンニクに誘導されるラジカルの挙動を ESR により詳細に検討した。

Materials and Methods

試料は中国産の分球ニンニクを用いた。照射には ^{60}Co γ 線を用い、原子力機構高崎量子応用研究所において、50 Gy、5 kGy の各吸収線量で実施した。試料を 300 mg 秤取し、ESR 試料管（99.9%石英ガラス）に封入し、測定サンプルとした。ESR 測定には ESR 分光器（EMX-Plus、Bruker）を用い、マイクロ波の周波数を X バンド（9.3 GHz）、掃引磁場を 0～500 と 345～355 mT とした。

Results and Discussions

Fig. 1 に未照射ニンニクの ESR 信号を示す。本スペクトルは 345～355 mT の外部磁場掃引によって測定された。ニンニクの ESR 信号は g =2.0 における鋭く強い一本線であり、有機フリーラジカル由来の信号と考えられる。芽止め線量に相当する 50 Gy を照射したニンニクの ESR スペクトルは g =2.0 に観測される一本線であり未照射試料のスペクトルと比べ変化はなかった。しかしながら、低磁場側でわずかな分裂が見られた。殺菌線量に相当する 5 kGy を照射したニンニクの ESR 測定を行った結果を Fig. 2 に示した。g =2.0 の信号は 6 本に分裂し、これらの信号の両サイドにも新たな信号を観測した。

ニンニクの ESR 測定では、照射処理により g =2.0 の位置に観測される一本線の分裂が観察され、この分裂現象は照射依存性があった。以上のことから、照射ニンニクに誘導されるラジカルは ESR 信号として計測でき検知法として有用であると考えられた。今後は、ESR 測定の高精度化を行っていくつもりである。

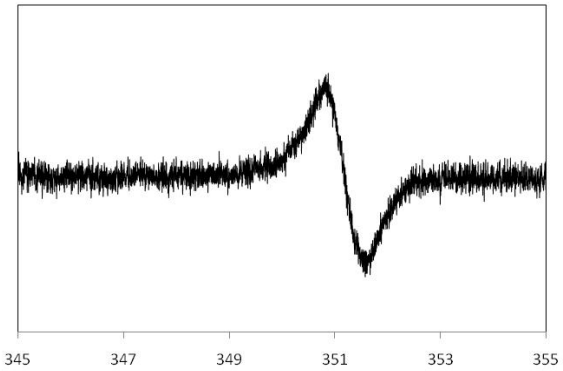

Fig. 1 An ESR spectrum of the garlic.

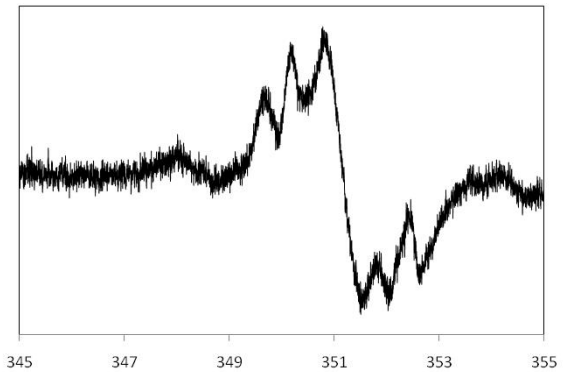

Fig. 2 An ESR spectrum of the irradiated garlic.

References

1) R. A. Molirs, Food Irradiations, John Wiley, (2001) 1.
2) M. Ukai et al., Spectrochim. Acta, **63**(4) (2006) 879.
3) M. Ukai et al., Appl. Magn. Reson., **24** (2003) 1.

3-24 ESR Method for Detecting Irradiated Fresh Mangoes

M. Kikuchi [a)], M. S. Hussain [b)], N. Morishita [a)], T. Sakashita [a)], T. Funayama [a)], M. Ukai [c)], Y. Shimoyama [d)] and Y. Kobayashi [a)]

[a)] Radiation-Applied Biology Division, QuBS, JAEA, [b)] Bangladesh Atomic Energy Commission, [c)] Hokkaido Univ. Education, [d)] Muroran Inst. Tech.

When tropical fruits are imported, quarantine treatments are required for preventing plant pests. The irradiation is a choice of the quarantine treatments for tropical fruits in the world. When the irradiation is utilized as the treatment, detection methods are required to endorse the reliability of labels for consumers. In protocols of CEN, electron spin resonance (ESR) spectroscopy is employed as an analytical tool of irradiation by the radical detection from foods containing bone, cellulose and crystalline sugar. In this paper, we will describe on radical detection from irradiated mangoes.

Mangoes, the product of the Philippines, were purchased in a market, and irradiated with ^{60}Co γ-rays. The mangoes after irradiation were stored at 4 °C for maximum 9 days. Skin and flesh of the mangoes were separated, freeze-dried and powderized. An ESR spectrometer (JEOL RE-3X) was used at 25 °C with sweep ranges of 0 to 500 mT, or 331 to 341 mT.

ESR signals were recorded as the first derivatives of the resonance signal. First, when searching detectable ESR signals in a fresh mango, we could observe that the ESR signals of each sample had a strong main peak at 335.9 mT (g = 2.00), showing the stable radicals remains in mango flesh (Fig. 1). The peak-to-peak height of the main peak was saturated around 3 mW, indicating that the main peak is attributed to organic free radicals of the mango. The ESR signal intensity was examined against absorbed doses (Fig. 2), shown that the main peak in mango flesh was increased gradually with increasing doses till 25 kGy although the signal intensity in skin was not so increased by the irradiation. At lower doses used for practical quarantine treatment (0.4 to 1 kGy), however, the main peak in specimens showed the difference of mango individuality that may be due to ripeness, temperature and period of storage. Therefore, each comparable background mango as reference is required to evaluate mango specimens, indicating that the main peak is not applicable for the detection of irradiated mangoes.

Next, when searching radiation-responsible ESR signals, we found two side peaks at 333.3 mT (g = 2.02) and 339.4 mT (g=1.98) beside the main peak (Fig. 3). The side peaks in 3 kGy-irradiated mango were clearly different from those in non-irradiated specimen. When we employed the side peaks, the peak height had a good dose response at quarantine doses. Therefore, we could distinguish the 0.3 kGy-irradiated mangoes from the reference. The peaks are still detectable a week later of irradiation.

In conclusion, while the ESR main peak is not applicable to the mango detection, the side peaks is an effective indicator to detect fresh mangoes irradiated to dose range of quarantine treatment. Since ESR method is able to measure without complicate preparation, this technique is useful to detect the irradiation treatment against a wide variety of foods.

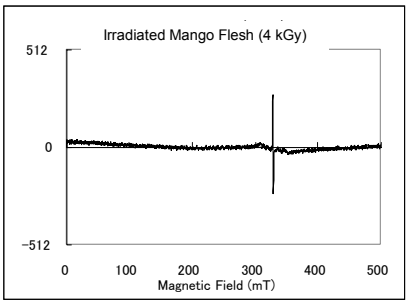

Fig. 1 ESR main peak obtained from irradiated fresh mango.

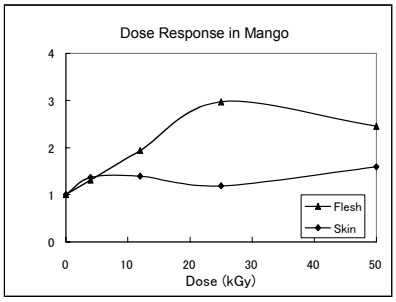

Fig. 2 Dose response of main peak.

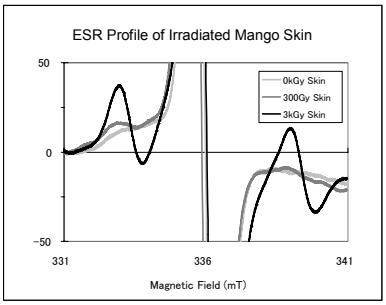

Fig. 3 ESR side peaks responsible to absorbed doses.

3-25 Combined Treatment of Human Tumor Cells with Carbon-ion Irradiation and the Telomerase Inhibitor

Y. Yokota [a)], T. Funayama [a)], N. Hamada [a, b)], T. Sakashita [a)], M. Suzuki [a)] and Y. Kobayashi [a, b)]

[a)] Radiation-Applied Biology Division, QuBS, JAEA,
[b)] Gunma University Graduate School of Medicine

Heavy particle radiotherapy is a useful means to eradicate solid tumors because of its physical, chemical and biological properties. It is, however, needed to accumulate the more evidence for the combined therapy between heavy particles and chemical agents for overcoming intractable tumors. The purpose of our study is to investigate combination effects of heavy-ion irradiation and chemical agents.

Indefinite proliferation of tumor cells is mostly due to expression of telomeric DNA reverse transcriptase (TERT) whose expression is downregulated in normal somatic cells. In this regard, TERT inhibitors have been developed to target tumor cells selectively. Of these, the inhibitor MST-312 is reported to suppress proliferation of leukemia cells and shorten their telomere at 1 μM concentration [1)]. Moreover, it is reported that down-regulation of TERT expression reduced the rejoining efficiency of DNA double-strand breaks [2)]. Based on such evidence, we expect that MST-312 treatment enhances cell-killing effect of heavy-ion irradiation. In this study, we investigate a combination effect of carbon-ion irradiation and MST-312 treatment in tumor cells.

Human cervical cancer HeLa cells and normal diploid fibroblast BJ cells were used here. Firstly, both cells were cultured for 24 h at various concentrations of MST-312 and 10 mM DMSO (solvent of MST-312). After treatment, cells were reseeded in fresh medium without MST-312 and DMSO. Colonies having more than 50 cells were counted at day 14 to determine the survival. The survival of HeLa cells and BJ cells, which were cultured for 24 h in graded concentrations of MST-312, is plotted in Fig. 1. The survival of HeLa cells decreased with increasing MST-312 concentration more dramatically than that of BJ cells. HeLa cells could not form any colonies at 5 μM. From this result, it is expected that there is a concentration of MST-312 for killing tumor cells selectively. At higher concentration, cells were detached from the culture dish and cell debris floated in the medium was observed. Cell-killing effect of MST-312 might be mainly induced through the apoptotic pathway.

Secondly, HeLa cells were cultured for 24 h with or without 1 μM MST-312, and then, irradiated with carbon ions (LET=110 keV/μm) to evaluate the combined effect of carbon-ion irradiation and MST-312 treatment. After irradiation, cells were reseeded in fresh medium without MST-312 and colonies were counted as described above. The survival of HeLa cells, which were cultured with or without 1 μM MST-312 and irradiated with carbon ions, is plotted in Fig. 2. The survival of the irradiated cells additively decreased in combination with MST-312 treatment. Carbon-ion irradiation and MST-312 treatment might inactivate the clonogenic potential of tumor cells through independent mechanisms. The dose of carbon ions that was needed to reduce the survival of irradiated cells to 10% of sham-irradiated cells (D_{10}) was 0.5 Gy and 1.2 Gy in the presence and absence of MST-312, respectively. MST-312 pre-treatment may reduce the dose needed for a curative effect in heavy-particle radiotherapy.

References

1) H. Seimiya et al., Mol. Cancer Ther. 1 (2002) 657.
2) K. Masutomi et al., Proc. Natl. Acad. Sci. U.S.A. 102 (2005) 8222.

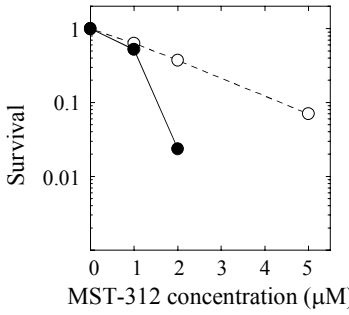

Fig. 1 Cytotoxicity of MST-312. HeLa cells (closed circle) and BJ cells (open circle) were cultured for 24 h at various concentrations of MST-312. The scale is semilogarithmic.

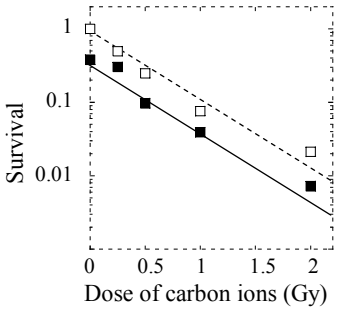

Fig. 2 Combined treatment with carbon-ion irradiation and MST-312. HeLa cells were cultured for 24 h with (closed square) or without (open square) 1 μM MST-312, followed by carbon-ion irradiation. The scale is semilogarithmic.

3-26 Comparative Study of Several Behaviors in *Caenorhabditis elegans* following High-LET Radiation Exposure

T. Sakashita [a)], M. Suzuki [a)], N. Hamada [a,b)], K. Fukamoto [a)], Y. Yokota [a)], S. Sora [a)], T. Kakizaki [c)], S. Wada [c)], T. Funayama [a)] and Y. Kobayashi [a, b)]

[a)] Radiation-Applied Biology Division, QuBS, JAEA, [b)] Department of Quantum Biology, and The 21st Century COE Program, Gunma University Graduate School of Medicine, [c)] Department of Veterinary Medicine, Kitasato University Graduate School of Veterinary Medicine and Animal Sciences.

Exposure to high linear energy transfer (LET) radiation has been reported to affect the function of the nervous system in mammals. However, little is known about that in other species. Therefore, we investigated the effects of high-LET radiation on the several behaviors in the nematode, *Caenorhabditis elegans*, in comparison with those of the low-LET radiation.

Tested behaviors include chemotaxis to NaCl[1)], the locomotory rate as a motor behaviour[2)], and the salt chemotaxis learning as a learning behaviour[1)]. In particular, the effects of ionizing radiation on the salt chemotaxis learning were investigated on both of the ability of the salt chemotaxis learning and the chemotaxis during learning on NaCl and benzaldehyde [1)]. Well-fed adults *C. elegans* incubated at 20 °C for 3 days were used in all experiments. In the previous studies, we reported that low-LET irradiation with 500 Gy did not affect the chemotaxis to NaCl in *C.elegans*[1)]. To compare with the same radiation dose, animals were exposed to accelerated carbon ions (^{12}C, 18.3 MeV/u, LET = 113.3 keV/μm) at the dose of 500 Gy.

Exposure to high-LET radiation did not affect the chemotaxis to NaCl, the locomotory rate, and the ability of the salt chemotaxis learning in *C. elegans* (Table 1). In addition, high-LET irradiation did not induce the decline of the locomotory rate observed in low-LET irradiation[2)]. The cause of no-effect on the locomotory rate is still unknown. We reported that low-LET-radiation-induced reduction of the locomotory rate was masked by the bacterial mechanosensation[3)]. The report suggests that ionizing-radiation-induced reduction of the locomotory rate is caused by signals via a neuronal network. To reveal the difference in the radiation effects between low- and high-LET radiations, the future work will be needed on the mechanism of radiation responses in the neuronal network. On the other hand, chemosensation to NaCl during learning was significantly affected, but not to benzaldehyde (Table 1). The results support those of the previous low-LET irradiation experiments[1)]. Thus, the effect of high-LET radiation on the chemotaxis during learning might be also induced in the same way as low-LET radiation did[1)]. In the next step, we will test the *gpc-1* mutants, which defects in the GPC-1 signal-transduction protein.

The comparison of high-LET with low-LET irradiation in several behaviors of *C. elegans* revealed the differences and common points of radiation effects on the basis of LET. To address these issues, further studies focused on the mechanism of radiation responses in the nervous system will be needed.

References

1) T. Sakashita et al., FASEB J. 22 (2008) 713.
2) T. Sakashita et al., J. Radiat. Res. 49 (2008) 285.
3) M. Suzuki et al., J. Radiat. Res. 50 (2009) 119.

Table 1 Comparison of the effects of high- and low LET radiations on the several behaviors in *C. elegans*. We used the reference dose of 500 Gy. "–" and "+" indicate the non-significant and significant effects, respectively.

Ionizing radiation	Behaviors in *C. elegans*				
	Chemotaxis	Locomotory rate	Ability of the salt chemotaxis learning	Chemotaxis during learning	
				NaCl	Benzaldehyde
High-LET radiation (carbon ions)	–	–	–	+	–
Low-LET radiation (γ-rays)	–[a]	+[b]	–[a]	+[a]	–[a]

[a] The data from Sakashita et al.[1)], [b] The data from Sakashita et al.[2)]

3-27 Development of New Cell Targeting System for Collimating Heavy-ion Microbeam System

T. Funayama, K. Fukamoto, Y. Yokota, M. Suzuki, T. Sakashita and Y. Kobayashi

Radiation-Applied Biology Division, QuBS, JAEA

The collimating heavy-ion microbeam system at JAEA-Takasaki has provided target irradiation of heavy charged particles to biological material at atmospheric pressure [1]. The system generates heavy-ion microbeam of a minimum beam size 5 μm in diameter by collimating beams using a microaperture which is made from tantalum or gold disk (100-500 μm thick) comprising various pinhole sizes.

A variety of biological material has been irradiated using this microbeam system including cultured mammalian and higher plant cells, isolated fibers of mouse skeletal muscle, silkworm (*Bombyx mori*) embryos and larvae, *Arabidopsis thaliana* roots, and the nematode *Caenorhabditis elegans*. For more than 15 years, the system has been applied and contributed to the investigation of mechanisms within biological organisms not only in the context of radiation biology, but also in the fields of general biology such as physiology, developmental biology and neurobiology.

Since more than 15 years has been passed from the beginning of the system operation, the Nikon TMD-300 microscope of existing targeting system became decrepit and the automatic objective revolver became inoperative. However, because of the lacking of maintenance parts, we could not repair the existing microscope. Therefore we updated whole targeting system to newly designed one.

The new system consists of a full automatic inverted microscope (Olympus IX81 model) which can be controlled its function fully from connected PC, and automatic sample stage which has submicron positioning accuracy by close loop control using optical microscale encoder (Fig. 1). According to the change in hardware components of the system, the control software for targeting cells was also redeveloped and replaced (Fig. 2). The software, named "MH System", basically takes over a concept of previous targeting software "Irradiate", but its software source codes were redeveloped without previous code base. The new software becomes capable to control not only microscope and stage, but also high-voltage power supply and counter-time NIM module. The complicated system of controlling remote microscope using network connection from irradiation room was omitted, and replaced to simple hardware solution, which extend the console lines of the control PC placed in irradiation room to the preparation room.

The new software supports not only conventional offline-online targeting method, which has potential targeting errors arisen by offline-online sample transfer, but also enable online-target detection. Thus it is expected that the targeting accuracy of cellular sample will be improved by this system update. Another planned function to be incorporated into the new system is so called "live-targeting function". This function enables real-time tracking and target-irradiation of moving objects such as non-paralyzed nematode. This updated system will allow a novel biological application that utilized high fluence characteristics of collimating heavy-ion microbeam system and contribute to explore the effect of heavy-ion radiation on various biological systems.

Reference

1) T. Funayama et al., J. Radiat. Res. 49 (2008) 71.

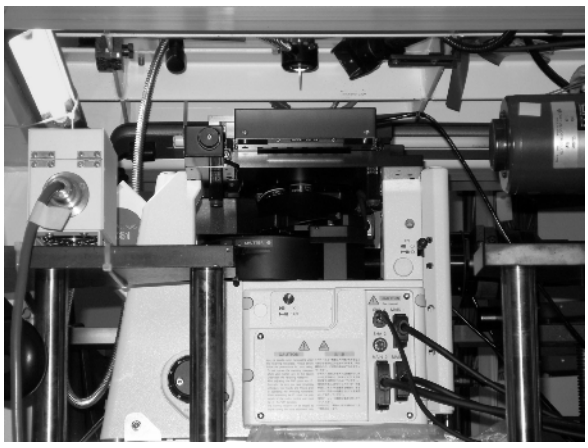

Fig. 1 New cell targeting system of collimating heavy-ion microbeam system.

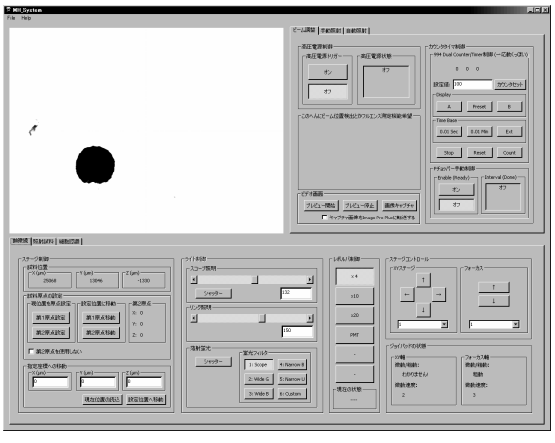

Fig. 2 Newly developed software for new cell targeting system.

3-28 Bcl-2 as a Potential Target for Heavy-ion Therapy

N. Hamada [a,b], T. Hara [a,b], K. Kataoka [a,b], S. Sora [a,b], T. Funayama [b], T. Sakashita [b], Y. Yokota [b], M. Omura-Minamisawa [c] and Y. Kobayashi [a,b]

[a] Department of Quantum Biology, Division of Bioregulatory Medicine, and The 21st Century Center of Excellence (COE) Program for Biomedical Research Using Accelerator Technology, Gunma University Graduate School of Medicine, [b] Radiation-Applied Biology Division, QuBS, JAEA, [c] Department of Radiology, Yokohama City University Graduate School of Medicine

Biological effectiveness differs with the linear energy transfer (LET) of ionizing radiation. In contrast to conventional low-LET photons like X-rays and γ-rays, high-LET heavy ions offer the potential therapeutic advantage of their excellent spatial dose distribution, and higher relative biological effectiveness (RBE) with less cell-cycle and oxygen dependency of radiosensitivity [1-6]. Recent biological studies have illustrated that heavy ions overcome tumor radioresistance due to *p53* mutations and intratumor hypoxia, and possess anti-angiogenic and anti-metastatic potential [1]. So far, heavy-ion therapy has achieved good cancer controllability in short treatment times while sparing critical normal organs.

Bcl-2 is an anti-apoptotic protein that was initially identified as an oncogene in follicular B-cell lymphoma where the t(14;18) chromosomal translocation leads to constitutive upregulation of Bcl-2 expression. The overexpression of Bcl-2 is found in nearly half of human cancers, and has been associated with resistance against conventional photons and chemotherapeutic agents. Restoring susceptibility by nullifying the effects of Bcl-2 has thence emerged as an attractive strategy to improve the efficacy of cancer therapy. A series of studies have addressed tumor sensitization to photons by chemical or antisense-based Bcl-2 inhibitors; however, the potential impact of heavy ions on Bcl-2 overexpressing tumors remains uncharacterized. Here we set out to address whether heavy-ion irradiation alone or its combination with the Bcl-2 inhibitor alters tumor radioresistance caused by Bcl-2 overexpression. Cells used in this study were Bcl-2 cells (human cervical cancer-derived HeLa cells that stably overexpress Bcl-2) and Neo cells (neomycin resistant gene-expressing HeLa cells), where the former express 9-fold higher levels of Bcl-2 than the latter [7].

Firstly, the effect of heavy-ion irradiation alone was examined [8]. The clonogenic survival assay revealed that on one hand, Bcl-2 cells were more resistant to ^{60}Co γ-rays (0.2 keV/μm) and helium ions (16.2 keV/μm) than Neo cells. On the other, heavy ions (76.3-1610 keV/μm) yielded similar survival regardless of Bcl-2 overexpression, among which carbon ions (108 keV/μm) gave the maximum RBE both in Bcl-2 and Neo cells. Next, irradiated cells were assessed for apoptosis and cell cycle distribution, showing that carbon-ion exposure decreased the difference in the apoptotic incidence between Bcl-2 and Neo cells, and prolonged G_2/M arrest that occurred more extensively in Bcl-2 cells than in Neo cells. These findings indicate that high-LET heavy ions overcome tumor radioresistance caused by Bcl-2 overexpression, which may be explained at least in part by the enhanced apoptotic response and prolonged G_2/M arrest. Thus, heavy-ion therapy may be a promising modality for Bcl-2 overexpressing radioresistant tumors.

Second, the combined effects of heavy-ion irradiation and the Bcl-2 inhibitor HA14-1 were analyzed [9]. HA14-1 is a nonpeptidic small-molecule ligand of a Bcl-2 surface pocket, which was recently identified from *in silico* screens [10]. A growing body of evidence has shown that HA14-1 selectively disturbs the interaction between Bcl-2 and Bax [11], and sensitizes tumors to photons [12]. The clonogenic survival assay revealed that pre-irradiation treatment with a noncytotoxic concentration of HA14-1 sensitized human cervical cancer-derived Bcl-2 and Neo cells, but not AG01522 normal human fibroblasts, to carbon ions. This suggests that HA14-1 preferentially potentiates tumor cell killing by heavy ions.

In conclusion, our results highlight that high-LET heavy ions may be a promising modality for radio- and chemoresistant Bcl-2 overexpressing tumors, and that Bcl-2 may be an attractive target to improve the efficacy of heavy-ion therapy. The mediating molecular mechanisms and the *in vivo* validity need to be further examined. There is mounting evidence that some chemicals (e.g., docetaxel), *p53* gene transfer and hyperthermia potentiate heavy ion-induced cell killing [1]. Such combined treatments may enhance the effectiveness of heavy-ion therapy.

References

1) N. Hamada, J. Radiat. Res. 50 (2009) 1.
2) N. Hamada et al., Mutat. Res. 637 (2008) 190.
3) N. Hamada et al., Mutat. Res. 639 (2008) 35.
4) N. Hamada et al., Biol. Sci. Space 22 (2008) 41.
5) N. Hamada et al., Biol. Sci. Space 22 (2008) 46.
6) N. Hamada et al., Radiat. Res. 166 (2006) 24.
7) N. Hamada et al., Cancer Lett. 268 (2008) 76.
8) N. Hamada et al., Radiother. Oncol. 89 (2008) 231.
9) N. Hamada et al., Radiother. Oncol. 89 (2008) 227.
10) J. L. Wang et al., Proc. Natl. Acad. Sci. USA 97 (2000) 7124.
11) F. Manero et al., Cancer Res. 66 (2006) 2757.
12) J. An et al., Oncogene 26 (2007) 652.

3-29 Biological Effect of High Linear Enegy Transfer Charged Particle and X-ray on Human Brain Cancers

S. Ishiuchi [a,b], Y. Yoshida [b,c], K. Tsuzuki [d], M. Hasegawa [b,e], M. Hosaka [f], N. Hamada [b,g,h] T. Funayama [h], S. Wada [b,g,h], Y. Kobayashi [b,g,h],Y. Nakazato [i] and T. Nakano [b,c]

[a] Department of Neurosurgery, Gunma University School of Medicine, [b] 21st Century COE Program, Gunma University Graduate School of Medicine, [c] Department of Radiation Oncology, Gunma University Graduate School of Medicine, [d] Department of Neurophysiology, Gunma University Graduate School of Medicine, [e] Department of Radiation Oncology, Nara Medical School, [f] Department of Molecular Medicine, Institute for Molecular and Cellular Regulation, Gunma University, [g] Department of Quantum Biology, Gunma University Graduate School of Medicine, [h] Radiation-Applied Biology Division, QuBS, JAEA, [i] Department of Human Pathology, Gunma University Graduate School of Medicine

We examined radiobiological effect of high linear energy transfer charged particle (LET) as well as X-rays on brain cancers. Both high LET and X-rays induced senescence-like death as revealed by staining of senescence-associated β-galactosidase (SA-β-Gal) at PH 6. Genechip analysis showed that expression was not significantly changed between cells irradiated by high LET and X-rays.

重イオンマイクロビームを用いた細胞の放射線応答の解析を、主にヒト神経膠芽腫細胞を用いて行った。確立した培養系[1,2]を用いて複数の重粒子線(Ar,Ne,C)の腫瘍細胞に対する移動性、増殖性および細胞死に関してX線と対比して解析した。細胞障害性は物理線量を同じにすると重粒子線のほうが3～4倍強い細胞障害性を認めたが、誘発される細胞死の形式はX線および重粒子線とも差異はなくsenescence-associated β-galactosidase (SA-β-Gal)で陽性に染色され、また自家蛍光を発することから老化様細胞死であった（Fig. 1）。

細胞走行性に関しては、非照射細胞と比較するとX線で2倍、重粒子線(Ar,Ne,C)で3倍の遊走亢進作用が認められた。このX線および重粒子線の細胞走行性の亢進現象に関しては、確立されたモデル動物による評価を行い、培養系で得られた知見を支持する結果となった。すなわち、炭素線を照射した腫瘍細胞はヌードマウス脳移植モデルにおいて著しい浸潤性を示した。脳移植マウスにX線照射しても著しい浸潤能の亢進を認めた。X線、炭素線照射群とも、グルタミン酸受容体拮抗薬併用で治療した群では腫瘍細胞はすべて老化様細胞死に陥った。

X線および重粒子線照射による分子生物学的変化を照射細胞のoligonucleotide arrayを用いて解析し、発現亢進及び低下する遺伝子群を同定した(Affymetrix GeneChip Human Genome U133 Plus 2.0 arrays) 。発現亢進遺伝子数はX線で140個、炭素線で219個、そのうち82個が共通であり、発現低下した遺伝子数はX線で143個、炭素線で220個、そのうち78個が共通であった。両照射群は連動しており、X線で亢進しかつ炭素線で発現低下する遺伝子や、X線で発現低下しかつ炭素線で亢進する遺伝子は１つも認めなかった。X線および重粒子線照射群で照射により活性化するシグナル伝達路も連動する傾向を示した。

以上を総括すると、炭素線はX線に比較して3倍の細胞障害性を示すものの、誘発する細胞死の様式にX線と差異は認めなかった。細胞走行性に関しても、高エネルギー付与である炭素線のほうがさらに高い遊走亢進作用を示した。照射細胞の遺伝子変化、シグナル伝達路の活性化様式にも本質的な差異は認めなかった。臨床応用の観点からは、ヌードマウス脳移植モデルにて遊走阻害剤を併用することで、効果的に細胞死を誘導できることが判明し、炭素線の短所を補いより効果的で有効な治療法の樹立の可能性が示唆された。

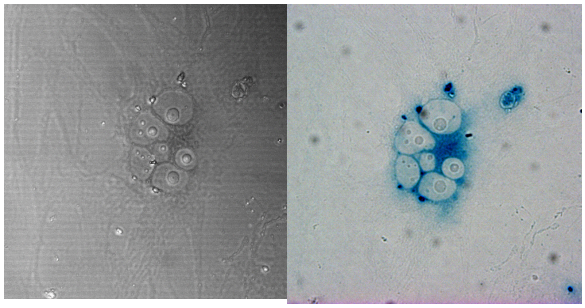

Fig. 1 Image of Multinucleated giant cells, higher magnification(Left). A cell showed senescence –like death as revealed by the positive staining of SA-β-Gal (Right).

References

1) S. Ishiuchi et al., Nat. Med. 8 (2002) 971.
2) S. Ishiuchi et al., J. Neurosci. 27 (2007) 7987.

3-30 Analysis of Molecular Mechanisms for Radiation-Induced Bystander Effects Using Heavy Ion Microbeams

H. Matsumoto [a)], M. Hatashita [a)], M. Tomita [b)], K. Otsuka [b)], T. Funayama [e)], T. Sakashita [e)], N. Hamada [c,d,e)] and Y. Kobayashi [c,d,e)]

[a)] Faculty of Medical Science, University of Fukui, [b)] Central Research Institute of Electric Power Industry, [c)] Gunma University Graduate School of Medicine, [d)] The 21st Century Center of Excellence Program for Biomedical Research Using Accelerator Technology, [e)] Radiation-Applied Biology Division, QuBS, JAEA

The objective of this project is to elucidate molecular mechanisms of the bystander response using heavy ion microbeams in JAEA. We examined how many targeted cells were required to induce the radioadaptive response using argon microbeams for a priming irradiation. We found that when 10 to 50 cells in a population of ten thousand cells were irradiated with argon microbeams as priming dose at 5 particles per cell, followed by the incubation for 4 to 6 h at 37 °C, the radioadaptive response could be induced after challenge irradiation with argon broad beams at 1 to 5 Gy. The induction of radioadaptive response was almost completely suppressed by the addition of carboxy-PTIO to the medium. These findings strongly suggest that the radiation-induced bystander response plays an important role in the process of the induction of radioadaptive response, and that nitric oxide is actually an initiator or mediator of the radioadaptive response.

低線量／低線量率放射線に対して生物が示す特異的な応答様式の一つに放射線誘発バイスタンダー応答がある [1)]。我々は、日本原子力研究開発機構において開発された重イオンマイクロビーム細胞照射システム（細胞局部照射装置）を用いて、この放射線誘発バイスタンダー応答の分子メカニズムを明らかにすることを計画した。

1. 実験方法

(1)細胞：ヒト非小細胞肺がん H1299 細胞に正常型 *p53* を導入した H1299/wt*p53* 細胞を使用した。

(2)培養：35 mm ディッシュの中央 1 か所に 1×10^6 ～ 2×10^7 cells/mL の細胞懸濁液 10 μL をスポットし(1×10^4 ～ 2×10^5 cells/colony)、15~20 時間培養したものを照射実験に供した。

(3)照射：Funayama ら [2)]の方法に従って、コロニーの細胞 1 ～ 50 個に 5 粒子の 460 MeV $^{40}Ar^{13+}$を HZ1 ポートにおいて照射した。その後 4 ～ 6 時間の培養を経て、460 MeV $^{40}Ar^{13+}$を HY1 ポートにおいて 1 ～ 5 Gy 照射した。

(4)HY1 ポートでの照射直後に細胞を回収し、T25 フラスコに一定数の細胞を播種し、コロニー形成を行い、細胞の生存率を測定した。

(5)c-PTIO 処理：HZ1 ポートでの照射 2 時間前に 10 μM の c-PTIO を添加し、コロニー形成完了までその条件を維持した。

2. 結果および考察

(1)予備照射として 2×10^5 個の細胞当たり 1 ～ 50 個の細胞に 5 粒子の 460 MeV $^{40}Ar^{13+}$を照射しても、生存率をエンドポイントとした放射線適応応答の誘導は認められなかった。

(2)予備照射として 1×10^4 個の細胞当たり 1 ～ 5 個の細胞に 5 粒子の 460 MeV $^{40}Ar^{13+}$を照射しても、生存率をエンドポイントとした放射線適応応答の誘導は認められなかった。

(3)予備照射として 1×10^4 個の細胞当たり 10 ～ 50 個の細胞に 5 粒子の 460 MeV $^{40}Ar^{13+}$を照射すると、生存率をエンドポイントとした放射線適応応答の誘導が認められた（Fig. 1）。

(4)予備照射として 1×10^4 個の細胞当たり 10 ～ 50 個の細胞に 5 粒子の 460 MeV $^{40}Ar^{13+}$照射により誘導された生存率をエンドポイントとした放射線適応は 10 μM の c-PTIO の添加によりほぼ完全に抑制された（Fig. 1）。

以上の結果より、放射線適応応答の誘導過程において NO ラジカルを介したバイスタンダー応答が重要な役割を果たしていることが強く示唆された [3,4)]。

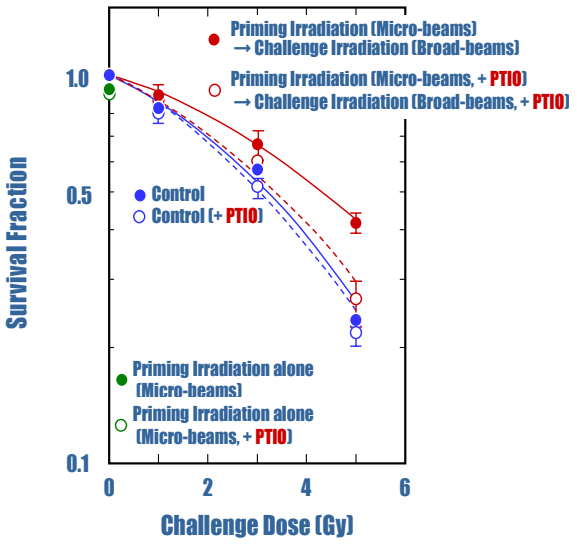

Fig. 1 Induction of radioadaptive response by the priming irradiation with Ar-microbeams.

References

1) H. Matsumoto et al., J. Radiat. Res. 48 (2007) 97.
2) T. Funayama et al., Radiat. Res. 163 (2005) 241.
3) H. Matsumoto et al., Cancer Res. 67 (2007) 8574.
4) H. Matsumoto et al., J. Radiat. Res. 50, Suppl. (2009) A67.

3-31 Irradiated Culture Medium Mediated Bystander Cell-killing Effect Induced by Carbon-ion Microbeams

M. Suzuki [a)], Y. Furusawa [a)], T. Funayama [b)], K. Fukamoto [b)], Y. Yokota [b)], N. Hamada [b,c)], C. Tsuruoka [a)] and Y. Kobayashi [b,c)]

[a)] Research Center for Charged Particle Therapy, NIRS, [b)] Radiation-Applied Biology Division, QuBS, JAEA, [c)] Department of Quantum Biology, Gumma University Graduate School of Medicine

We reported here past two years that bystander cellular effects, such as cell-killing and mutagenic effects, were observed in normal human cells irradiated with carbon-ion microbeams using the 256 (16×16)-cross-stripe irradiation method. Furthermore, we characterized one of the possible mechanism(s) in which gap-junction mediated cell-cell communications played an important role. Previous studies have shown that the culture medium irradiated with ionizing radiations transferred to non-irradiated cultures could induce increased biological effects. Mothersill and Seymour first demonstrated a significant reduction in cloning efficiency in non-irradiated human cells that had received medium from cultures irradiated with ^{60}Co gamma rays[1]. This year we examined the potential contribution of unknown factors secreted from irradiated cell itself into the culture medium to bystander cellular effects.

Carbon-ion microbeams ($^{12}C^{5+}$, 220 MeV) were generated with the HZ1 port. Approximately 6×10^5 exponentially growing normal human skin fibroblasts were inoculated into each of microbeam dish, which was made of acrylic resin ring with 36 mm diameter and attached 7.5 μm-thick polyimide film on the bottom of the ring, 2 days before the microbeam irradiation. In order to block up cell-cell communication, half of the sample dishes were treated with a specific inhibitor of gap-junction mediated cell-cell communication (40 μM of gamma-isomer of hexachloro-cyclohexane) one day before the irradiation. At the irradiation period, cultures were confluent and around 93% of the cells stayed in G_0/G_1 phase (data not shown). Irradiation was carried out using the 256 (16 × 16)-cross-stripe irradiation method described in the previous report. The value of linear energy transfer (LET) was estimated to be 103 keV/μm at the sample position. Microbeams of 20 μm in diameter were irradiated in each point with 8 delivered ions.

Figure 1 showed cell-killing effect, which was detected with a colony-forming assay as a reproductive cell death, in microbeam-irradiated dishes with (L+IR) / without (IR) a specific inhibitor of gap-junction mediated cell-cell communication. The percent cell survival after 3 h irradiation without a specific inhibitor of gap junctions (a) was around 87%, suggesting the bystander cell-killing effect because in our 256 (16×16)-cross-stripe irradiation method the maximum number of the carbon-ion direct hit cells was estimated around 0.2% of all cells in the dish. And the cell survival increased around 100%, when using a specific inhibitor of gap junctions. On the other hand, the percent cell survival after 24 h irradiation (b) was around 100% and no difference was observed between with and without a specific inhibitor of gap junctions. The results suggest two phenomena as follows;

(1) Unknown factor(s) secreted from the C-ion-irradiated cultures did not contribute to induce a cell killing against C-ion-unirradiated bystander cells at least within 24 h of the irradiation.

(2) Bystander cell-killing effect observed in the cell population re-plated after 3 h of the irradiation was completely recovered within 24 h of the irradiation.

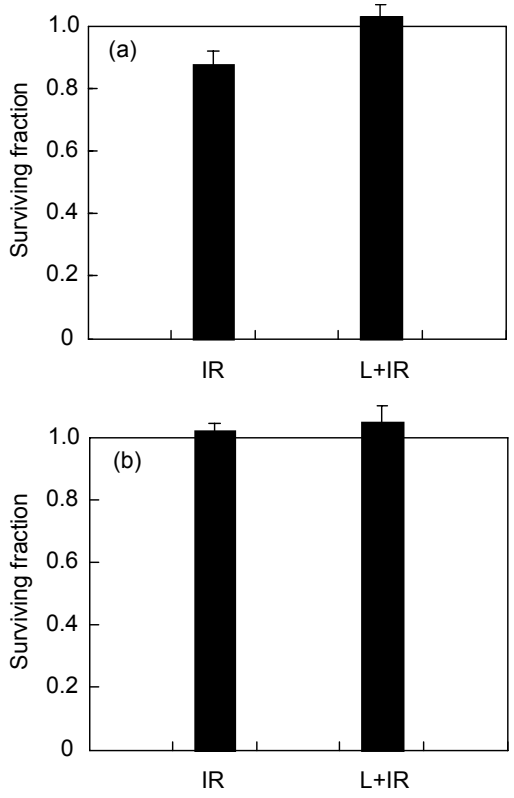

Fig. 1 Cell-killing effect in normal human fibroblasts irradiated with carbon-ion microbeams treated with (L+IR) / without (IR) a specific inhibitor of gap-junction mediated cell-cell communication. The cells were re-plated in dishes after 3 h (a) and 24 h (b) of the irradiation. The data at the 3 h (a) is taken from the report in 2006. The results are the means and standard errors from 3-5 independent beam times.

Reference

1) C. Mothersill and C. B. Seymour, Int. J. Radiat. Biol. 71 (1997) 421.

3-32 Induction of Autophagy in C2C12 Myoblast by Heavy-Ion Beam Irradiation

M. Hino [a)], N. Hamada [b)], Y. Tajika [a)], T. Funayama [c)], Y. Morimura [a)], T. Sakashita [c)], Y. Yokota [c)], K. Fukamoto [c)], Y. Kobayashi [c)] and H. Yorifuji [a)]

[a)] Department of Anatomy, Gunma University Graduate School of Medicine, [b)] Division of Pathophysiology, Institute of Development, Aging and Cancer, Tohoku University, [c)] Radiation-Applied Biology Division, QuBS, JAEA

The induction of autophagy by heavy-ion beam irradiation was analyzed. The C2C12 myoblasts were irradiated with ^{40}Ar (11.2 MeV/u) and ^{20}Ne (12.8 MeV/u) and the induction of autophagy was assayed by electron microscopy, immunofluorescence staining using LC-3 antibody (Fig. 1) and LysoTracker staining. These morphological observations showed that autophagy is induced by the irradiation of heavy-ion beam in C2C12 myoblasts.

我々はこれまでに骨格筋単離筋線維の重粒子線照射による構造変化を電子顕微鏡を用い解析を行ってきた[1,2]。その結果照射領域の細胞膜では不規則な突起と陥凹、基底板の断片化が見られた。また照射領域の細胞質では筋原線維の配向の乱れ、筋小胞体の内腔の拡大が見られた。またオートファジー小体が多数観察された。

オートファジーは真核生物に普遍的な現象で、細胞質の一部を新たに形成された膜系が取り囲み、隔離し分解する機構である。オートファジーの基本的な生理的機能は、栄養飢餓状態で自己の細胞質を分解することでアミノ酸などの栄養素を産生することとされている。一方で一定の領域の細胞質やミトコンドリア等のオルガネラをまとめて分解することができる機構であることから飢餓応答以外にも障害をうけた細胞質領域やオルガネラをバルクに除去することで細胞質のホメオスタシスを維持していると考えられている。

今回我々は、重粒子線照射により誘導されるオートファジーについてマウス由来の骨格筋筋芽細胞C2C12株を用いてより詳細な検討を行った。

(1) C2C12細胞に重粒子線 (^{40}Ar, 11.2 MeV/u ; ^{20}Ne, 12.8 MeV/u)を照射した後30分までの各時点で細胞を固定し透過型電子顕微鏡による観察を行った。その結果照射細胞においてオートファジー小体が観察された。

(2) LC-3はオートファジーの初期に隔離膜が細胞質を隔離する過程に必須の因子である。オートファジーが活性化した細胞ではLC-3の抗体染色像の増強が見られることからオートファジーの初期過程のマーカーとして用いられる。そこでC2C12細胞に重粒子線を照射後30分の時点で固定し、抗LC-3抗体を用いて蛍光抗体染色を行った（Fig. 1）。重粒子線照射により蛍光強度の増強が見られた。

(3) オートファジー小体ではリソソームと融合することで内容物の分解が行われるため、成熟したオートファジー小体の内側は酸性である。C2C12細胞を酸性オルガネラのマーカーであるLysoTracker試薬存在下で培養し、重粒子線を照射後30分の時点で細胞を固定し、オートファジー小体形成を観察した。重粒子線照射によりLysoTracker 染色の蛍光強度の増強が見られた。

以上三点の結果は筋芽細胞C2C12において重粒子線照射がオートファジーを誘導することを示している。

(4)オートファジーに対する阻害剤3-methyladenineの存在下、非存在下でコロニー形成法による生存率を比較したが、有意な差は見られなかった。

近年がんに対する放射線治療においてアポトーシスと並んでオートファジー性細胞死が注目を集めている。重粒子線によるオートファジー誘導の解明は重粒子線治療の効果を高める上でも有意義と考えられる。

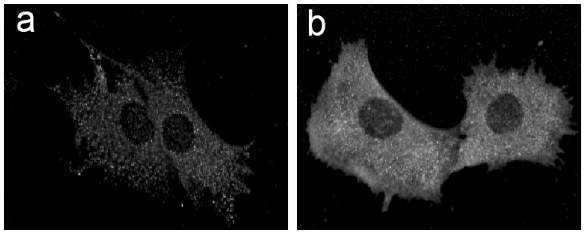

Fig. 1 C2C12 myoblasts 30 min after irradiation (b, ^{20}Ne 260 MeV, 2 Gy) and control (a) were stained with LC-3 antibody.

References

1) M. Hino et al., Cell Struct. Funct. 32 (2007) 51.
2) M. Hino et al., Cell Struct. Funct. 34 (2009) 11.

3-33 Analysis of Enhanced Lethal Effect Induced by Low Dose Ion Beams in Glioma Cells

S. Wada [a)], E. Nakagawa [a)], Y. Hayakawa [a)], T. Kakizaki [a)], T. Funayama [b)], T. Sakashita [b)], Y. Kobayashi [b)] and N. Ito [a)]

[a)] Department of Veterinary Medicine, Kitasato University,
[b)] Radiation-Applied Biology Division, QuBS, JAEA

Recently enhanced lethal effect induced by low dose ion beams was observed. In this study we investigated if the enhanced lethal effect induced by low dose ion beams was relative to sphingomyelinase (SMase), which is membrane traffic molecular. Cell lines used for this experiment were radioresistant glioma cell lines. These cells were irradiated with 220 MeV $^{12}C^{5+}$ ions (108 keV/μm). Enhanced lethal effect of low dose carbon ion irradiation was inhibited by the treatment of sphingomyelinase inhibitor. The production of radicals (OH radical and NO radical) after low dose carbon irradiation was suppressed by the treatment of sphingomyelinase inhibitor. These results suggested that enhanced lethal effect induced by low dose ion beams was led by cellular membrane response.

1. はじめに

これまでに低線量炭素線照射による生存率は、高線量域の生存曲線からの外挿値よりも低い値を示し、低線量炭素線照射でも高い細胞致死効果が得られることを明らかにした。この低線量炭素線照射による細胞致死効果の増強のメカニズムは炭素線による細胞核への影響ではなくて、細胞膜への影響によると考えられたが詳細は明らかにされていない。細胞は放射線によって細胞膜も損傷され、この細胞膜損傷はスフィンゴミエリナーゼによって修復される。さらに、このスフィンゴミエリナーゼによって生成されるセラミドはセカンドメッセンジャーとして細胞内ラジカル産生などのさまざまな生体応答に関与する。そこで、本研究では、低線量炭素線照射による細胞致死効果の増強と細胞膜応答分子であるスフィンゴミエリナーゼの関係を解析した。

2．実験方法

グリオーマ細胞を用い、AVFサイクロトロンによって加速された220 MeV C^{5+}（LET=108 keV/μm）を照射した。細胞致死効果の評価にはcolony formation assayを用いた。照射後に産生されるOHラジカルおよびNOラジカルを測定するため、細胞内Reactive Oxygen Species (ROS) に特異的な蛍光プローブCM-H_2DCF-DAおよび細胞内NOに特異的な蛍光プローブDAF-FM DAを用いて蛍光強度をマイクロプレートリーダで測定した。さらに、炭素線による細胞致死効果の細胞膜応答との関与を検証するため、スフィンゴミエリナーゼ阻害剤による生存率および細胞内ラジカル産生量の算出を行った。

3. 結果および考察

低線量域での炭素線の細胞致死効果の増強のメカニズムとしての細胞膜応答の関与を検討するため、スフィンゴミエリナーゼ阻害剤処置による細胞致死効果を観察した（Fig. 1）。スフィンゴミエリナーゼ阻害剤処置と無処置の生存率を比較したとき、0.1、0.4 Gyにおいてスフィンゴミエリナーゼ阻害による有意な生存率の上昇が認められた。この結果は低線量炭素線照射による細胞致死効果にはスフィンゴミエリナーゼが関与することを示唆している。さらに、低線量放射線照射による細胞致死効果には照射後の細胞内ラジカル産生が関与すると考えられている。そこで、照射後のラジカル産生とスフィンゴミエリナーゼの関係を検討するため、スフィンゴミエリナーゼ阻害剤による細胞内ラジカル産生の変化を観察した（Fig. 2）。炭素線照射後に細胞内のROS量およびNO量が増加することが観察され、特に0.1 Gyにおいて有意な増加が観察された。さらに、スフィンゴミエリナーゼ阻害剤を処置することによって、炭素線照射による細胞内ラジカル産生は認められなかった。この結果は炭素線照射後の細胞内ラジカル産生にはスフィンゴミエリナーゼを介する機構の存在を示唆している。これらのことから、低線量炭素線照射による細胞致死効果には細胞膜や細胞質応答を担うスフィンゴミエリナーゼが関与すると考えられた。

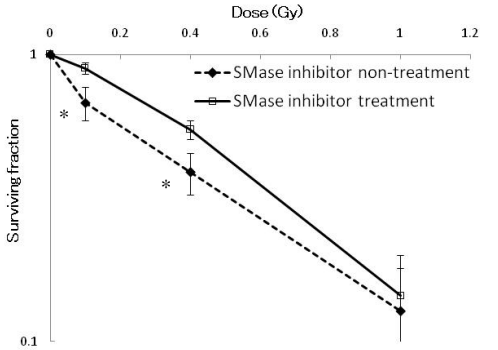

Fig.1 Comparison of lethal effect by SMase inhibitor treatment after low dose carbon ion irradiation.* $p<0.05$

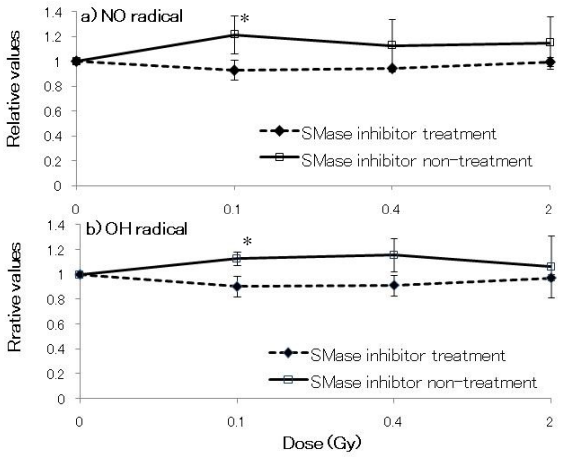

Fig. 2 Comparison of intercellular OH radical levels a) and NO radical levels b) by SMase inhibitor treatment. * $p<0.05$

3-34 The Expression of Glutathione Peroxidase and p53 of Human Retinal Vascular Endothelial Cells Irradiated by Gamma Ray

K. Akeo [a), b)], T. Funayama [c)], Y. Kobayashi [c)] and Y. Akeo [a)]

[a)] Akeo Eye Clinic, [b)] Department of Ophthalmology, Keio University School of Medicine, [c)] Radiation-Applied Biology Division, QuBS, JAEA

It is well-known that the damage of retinal endothelial (RE) cells was one of causes as pathogenesis in senile macular degeneration. The retrospective experience in the treatment of macular degeneration with gamma knife radiosurgery (GKR) was reported that the treatment was delivered in a single shot of 12 Gy, the majority of patients maintained stable visual acuity after treatment, and further studies were needed to better define the role of GKR in the treatment of macular degeneration [1].

The gamma ray (^{60}Co) causes ionization uniformly in the whole irradiated tissue. The gamma irradiation is known to result in a dose-dependent decline in the activities of glutathione peroxidase (GPX) in the skin of mice [2]. We found out that high dose of gamma irradiation prevented programmed cell death regulated by p53 and bcl-2 genes in the ciliary body dissected from living body, and was useful for preservation of organ after culture by the protective influence of inflammatory reaction [3].

GPX, a selenium-dependent and lipid peroxide-scavenging enzyme that effectively reduces lipid peroxides with the concomitant oxidation of glutathione distributed in mitochondria [4]. Faucher et al. measured the expression of two bcl-2 family members, bax and bcl-2, in a human endothelial like cell-line overexpressing the organic hydroperoxide-scavenging enzyme GPX, in the absence of any apoptotic/oxidant stimulus, and showed that overexpressing an antioxidant gene such as GPX in endothelial cells is able to change the basal mRNA and protein bax levels without affecting those of p53 and bcl-2. This phenomenon could be useful to antiatherogenic therapies which use antioxidants with the aim of protecting the vascular wall against oxidative stress injury [5].

We applied the gamma ray as the induction of the oxidative stress that influenced GPX against in the RE cells, and measured the expression GPX with Light Cycler system as a real time- reverse-transcriptase polymerase chain reaction (RT-PCR). We investigated how the gamma ray irradiation influenced GPX that prevented from damage of phospholipid of cell membrane of the RE cells, and how the expression of GPX related to the expression of p53 that regulated the programmed cell death.

Established human RE cells in vitro were exposed to 20 Gy gamma ray radiation (^{60}Co). We obtained the RE cells after 0, 4, 8, 24 h of the irradiation and extracted total cellular RNA and cDNA was synthesized. We used the Primer3 website to design the primers for RT-PCR amplification of the cDNA of GPX, p53, and 18S RNA. The reactions were carried out at the following temperature: 95 ºC, for denaturation; 60 ºC, for annealing; and 72 ºC, for extension for 17–27 cycles. After mixing the cDNA, primer and SYBR green, the expression of 18S RNA, GPX and p53 was measured using the LightCycler system. The technology of this system is extremely innovative and enables rapid and simultaneous evaluation PCR experiments. Fluorometric analysis of the formed PCR products was performed as a real-time measurement either continuously or at specifically defined time points during each PCR cycle.

The expression of GPX and p53 in RE cells increased significantly by the gamma ray irradiation as the result of the LightCycler analysis, the quantitative real-time RT-PCR. The increase of p53 expression was significantly more than that of GPX expression. The gamma ray irradiation induced the programmed cell death by the expression of p53 genes. The increase of GPX indicated the defense mechanism against lipid peroxidation in RE cells by the gamma ray irradiation.

References

1) M.A. Henderson et al., Stereotact Funct. Neurosurg. 85 (2007) 11.
2) J.G. Chandra et al., Clin. Chim. Acta 332 (2003) 111.
3) K. Akeo et al., Exp. Animals. 55 (2006) 375.
4) K. Watanabe, Tran. Soc. Pathology Jpn. 76 (1986) 39.
5) K. Faucher et al., Mol. Cell Biochem. 277 (2005) 81.

3-35 Analyses of Effects of Heavy-ion Beam Irradiation on Cellular and Viral Genes

N. Shimizu [a)], A. Oue [a)], T. Mori [a,b)], T. Ohtsuki [a,b)], I. Salequl [a,b)], S. Wada [b,c)], Y. Kobayashi [b,c)] and H. Hoshino [a,b)]

[a)] Department of Virology and Preventive Medicine,
[b)] 21st Century COE Program, Gunma University Graduate School of Medicine,
[c)] Radiation-Applied Biology Division, QuBS, JAEA

We have found that heavy-ion irradiation up-regulates the susceptibility of human glioblastoma cell line, NP-2/CD4/CCR5, although irradiation with protons and X-rays showed no effects on it. In this study, the encompassing analyses for the mRNA expression levels of NP-2/CD4/CCR5 cells irradiated with heavy ions, protons, or X-rays was done by DNA microarray. We found that many genes whose expression was up- or down-regulated by heavy ion irradiation are different from those affected by proton or X-ray irradiation. Those genes related to heavy-ion irradiation may contain the genes whose expression is involved in the determination of the susceptibility of the cell to HIV-1.

重粒子線は、X 線などの放射線とは異なる生物学的効果をヒト培養細胞株に与える。重粒子線照射によって特定の遺伝子が活性化あるいは不活化される可能性がある。我々は、ヒト免疫不全ウイルス 1 型（HIV-1）に対する感染感受性を指標にして、重粒子線を照射した細胞の性質の変化を解析した。これまでの解析から、比較的低い線量の重粒子線照射によって、細胞の HIV-1 感受性が上昇することを見出した。このような現象は、X 線や陽子線照射では見られなかった。また、重粒子線照射した細胞では、重粒子線照射した細胞では、CD133 や NF-kB の mRNA 発現の増加が見られた。histon deacetylase（HDAC）、Ku-80、poly-ADP ribose polymerase などの発現は低下した。これらの因子の発現の変化と細胞の HIV-1 感受性の変化との関連はまだ明らかでない。特異的阻害剤を用いた解析では、G2/M アレスト、アポトーシス誘導、酸化ストレス、ならびに HDAC や N 型糖鎖合成の阻害は、NP-2/CD4/CCR5/LTR-GFP 細胞の HIV-1 感受性上昇を誘起しなかった。重粒子線照射によっても細胞に生じることが予想されるこれらの現象は、HIV-1 感受性上昇に関与しないことが示唆された。一方、5-azacytidine、neuraminidase、あるいは PI3 キナーゼ阻害剤である Wortmannin 処理によって、細胞の HIV-1 感受性が上昇した。重粒子線照した細胞の HIV-1 の転写の上昇には、細胞の脱メチル化、リン酸化阻害、あるいは細胞膜因子の糖鎖修飾変化などが関与する可能性が示唆された。

本年度は、細胞の遺伝子発現を網羅的に解析することで、重粒子線によって特異的に発現が影響を受ける遺伝子の同定を目的とした。

ヒトグリオーマ由来 NP-2 細胞に CD4 と CCR5 を発現させた NP-2/CD4/CCR5 細胞[1]に、異なる線量の重粒子線（炭素線）（0、1.0、4.0 Gy）、陽子線（0、1.0、4.0 Gy）、あるいは X 線（0、5.0、20 Gy）を照射した。49 時間培養した後、ISOGEN 法（日本ジーン）を用いて細胞の全 RNA を抽出して cDNA を合成し、DNA マイクロアレイ解析を行った（タカラバイオ）。

DNA マイクロアレイ解析の結果では、放射線未照射での値が極端に低いもの（500 以下）については、誤差が大きくなることが予想されたために除外した。また、未照射の値の偏差が大きな遺伝子も除外した。その上で、放射線照射によって、値が 1.5 倍以上増加、あるいは 0.6 倍以下に低下した遺伝子を集計した（Table 1）。

重粒子線照射によって発現が増加あるいは減少した遺伝子は 50 種類以下であった。X 線照射によって発現量が変化した遺伝子数も同程度であった。陽子線照射によって発現量が変化した遺伝子は、重粒子線と X 線と比較して、数倍から 10 倍以上多かった。しかし、照射で発現量が変化する遺伝子は、陽子線と重粒子線の間、あるいは陽子線と X 線の間でほとんど重複はしなかった。

細胞の遺伝子発現への影響は、重粒子線と陽子線では、かなり異なることが明らかになった。今後は、それぞれの線種特異的に発現量が変化する遺伝子を同定し、それらの発現と HIV-1 感受性変化との関係を明らかにしたい。

Table 1 Numbers of gene whose mRNA expression was affected by radiations.

Radiation-dose	Increased	Decreased	Total
C-1	7	20	27
C-4	8	19	27
C-1 or C-4	10	35	45
C-1 and C4	5	4	9
X-5	7	1	8
X-20	24	13	37
X-5 or X-20	29	14	43
X-5 and X-20	2	0	2
P-1	119	165	284
P-4	164	194	358
P-1 or P-4	185	336	521
P-1 and P-4	98	23	121
C and X	6	5	11
C and P	0	0	0
P and X	3	0	3

C, carbon-ions; P, protons; X, X-rays.

Reference

1) Y. Soda et al., Biochem. Biophys. Res. Commun. 258 (1999) 313.

3-36 Effect of Heavy Ion Irradiation on the Lepidopteran Insect Cell Line, Sf9

S. Tsuchiya [a)], K. Fukamoto [a,b)], K. Shirai [a)],T. Funayama [b)] Y. Yokota [b)], T. Sakashita [b)], K. Kobayashi [b)] and K. Kiguchi [a)]

[a)] Division of Applied Biology, Faculty of Textile Science and Technology, Shinshu University,
[b)] Radiation-Applied Biology Division, QuBS, JAEA

Heavy ion beams are an extremely useful tool for radio-microsurgery and for studying cellular differentiation. Heavy ion beams deposit more energy in target tissues, organs or cells than X-rays or gamma rays.

Using the heavy ion beams, we demonstrated that locally-targeted irradiation of heavy ion beams at egg and larval stages of the silkworm, *Bombyx mori*, could disrupt or prevent the development of specific organs or tissues such as legs, wings, eyes and antennae in the resultant larvae or adults[1)]. From results obtained to date, it appears that the insect cells, especially epidermal cells, were relatively resistant to the carbon ions[2)].

Lepidopteran insect cells are generally known to be more resistant to radiation compared with mammalian cells, but the detail mechanisms of this resistance have not been understood. As compared with yeast and bacteria, insects are evolutionarily much closer to mammals, and have the radioresistant systems that are similar to the mammalian systems. So the insect cells can be considered to be as useful models for identifying the mechanisms underlying extreme radioresistance.

To clarify the molecular mechanisms of radioresistance in insect cells to heavy ions, we investigated the effect of carbon ion ($^{12}C^{5+}$) irradiation on insect cells, Sf9.

Cell viability at 96 h after the irradiation was studied using carbon ions. No effects of carbon ion irradiation on the viability of Sf9 cells were observed even at a dose of 400 Gy (Fig. 1).

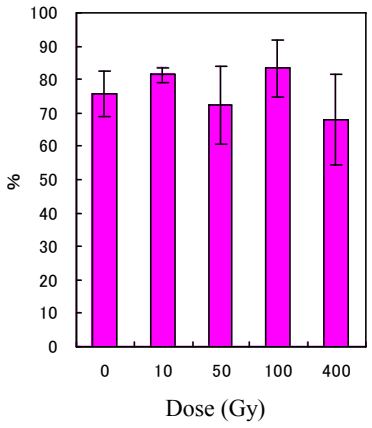

Fig. 1 Viability of Sf9 cells after carbon ion irradiation at an indicated dose. Viability was tested by stainability to trypan blue. Error bars indicate the standard deviation of 5-7 experiments.

The dose-dependent inhibition of cell proliferation was found. No significant effect on cell proliferation was detected at up to 10 Gy. At 50 Gy, cell growth was significantly inhibited, while cells exposed to over 100 Gy showed severe growth inhibition noticed up to 144 h post-irradiation. The D_0 value was about 84 Gy at 144 h after irradiation. This value is quite similar to the value of previous report using gamma-rays (85 Gy)[3)]. However, biphasic survival response curve that found on the gamma ray irradiation experiment[3)] was not obtained in this study.

Radiation-induced cellular hypertrophy was observed in Sf9 cells at a dose of 50 Gy (Fig. 2). The cells also lost adherence, then were flowing in the medium. However, at two weeks post-irradiation, the cells recovered gradually to the normal size and morphology, then cell proliferation restarted.

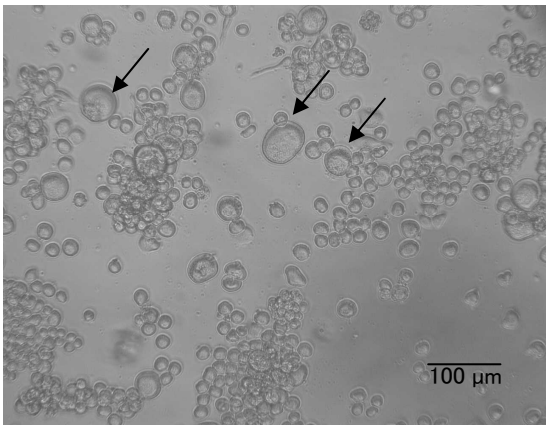

Fig. 2 Radiation-induced cellular hypertrophy in Sf9 cells. Arrows indicate hypertrophic cells.

In this study, the effects of heavy ion irradiation on the insect cells were investigated. As a result, it is clearly shown that Sf9 are highly resistant to the heavy ion irradiation and not detected apoptosis up to 400 Gy, notably. Now, we are going to address the irradiation induced bystander effects on the incest cells using heavy ion beams.

References

1) Z-L. Tu et al., J. Seric. Sci. Jpn 683 (1999) 443.
2) K. Fukamoto et al., J. Insect Biotech. Sericol. 75 (2006) 107.
3) S. Chandna et al., Int. J. Radiat. Biol. 80 (2004) 301.

3-37 Anhydrobiosis-Related Activity of Antioxidants as a Possible Explanation of High Resistance of an African Chironomid to Gamma-Ray Irradiation

O. Gusev [a)], Y. Nakahara [a)], A. Fujita [a)], M. Watanabe [a)], T. Kikawada [a)], T. Okuda [a)], T. Sakashita [b)], T. Funayama [b)], N. Hamada [b,c)] and Y. Kobayashi [b,c)]

[a)] Anhydrobiosis Research Unit, National Institute of Agrobiological Sciences,
[b)] Radiation-Applied Biology Division, QuBS, JAEA,
[c)] Department of Quantum Biology, Gunma University Graduate School of Medicine

DNA is the principal cellular target governing loss of viability after exposure to gamma irradiation. DNA damage occurs predominantly by the indirect action of gamma rays, which interact with other atoms or molecules, particularly water, to produce reactive free radicals. Larvae of anhydrobiotic chironomid *Polypedilum vanderplanki* show high resistance to gamma rays, surviving for 2 days after irradiation with the dose more than 2,000 Gy in active form (wet) and more than 5,000 Gy in anhydrobiotic (dry) form[1)].

Previously we found that a number of stress-responsive RNA and DNA repair enzymes are accumulated during anhydrobiosis in the larvae[2)]. We assumed that this process would be something to do with the resistance to high and low LET irradiation in the larvae[1,3)].

In the present study we have analyzed recovery of DNA in the fat body cells of the larvae after 70 Gy of gamma irradiation. Furthermore, we investigated expression of a gene encoding catalase in the larvae during anhydrobiotic process and after gamma irradiation. Alive larvae were put into a plastic vials with 5 ml of distilled water and irradiated with 70 Gy of gamma-rays from a Cobalt-60 source at 60 Gy/min. Control samples were sham-irradiated and manipulated in parallel with the test samples. DNA breaks and their repair were analyzed with alkaline Comet Assay standard technique using the fat body cells as a model cell type. Total RNA from irradiated larvae and anhydrobiotic larvae was extracted in serial fixation and expression was estimated using qRT-PCR method.

We found that 70 Gy gamma irradiation causes less damage to DNA of the larvae (Fig. 1), compared with the same dose of heavy ions irradiation[2)]. The damaged DNA by gamma rays was recovered within 24 h after irradiation (Fig. 1), while it took more than 48 h for DNA recovery after the same dose of ^{4}He ions[2)]. The possible explanation of faster recovery of the cells after gamma irradiation would be an improved activity of antioxidants in the irradiated larvae. We found that a gene encoding catalase is highly up-regulated in the larvae both during entering anhydrobiosis and exposed to the gamma irradiation (Fig. 2). Our preliminary analysis demonstrated that appearance of reactive oxygen species (ROS) occurring already on the very early stages of dehydration had a negative effect, i.e. DNA breaks and also triggered synthesis of trehalose, LEA proteins, anti-oxidants, DNA repairing enzymes and other molecules essential for the successful anhydrobiosis.

The DNA damage by gamma irradiation is thought to be due to occurrence of ROS. As *P. vanderplanki* larvae experience severe oxidative stress in the course of anhydrobiosis, it is plausible that the activity of ROS-regulating cascades adopted for the drought stress in the larvae could be contributing to the prompt DNA reparation after gamma irradiation stresses.

References

1) M. watanabe et al., Int. J. Radiat. Biol. 82 (2006) 587.
2) O. Gusev et al., JAEA Takasaki Ann. Rep. 2007 (2008) 103.
3) M. Watanabe et al., J. Insect Physiol. 53 (2007) 573.

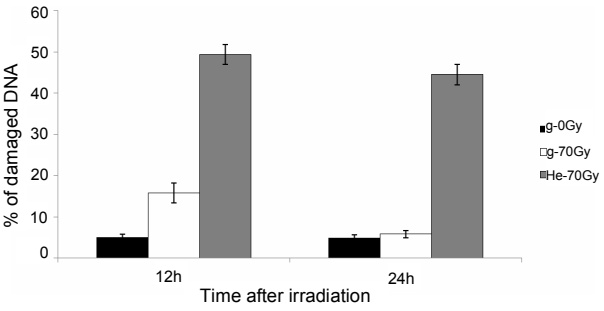

Fig. 1 Dynamic of DNA reparation in the fat body of larvae of *P. vanderplanki* exposed to gamma-rays (70 Gy) and ^{4}He ions (70 Gy). The values are calculated using DNA comets in alkaline buffer.

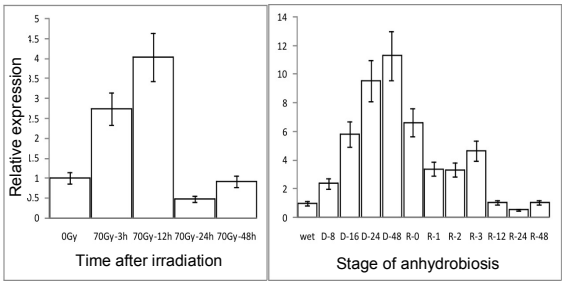

Fig. 2 Relative expression of CAT in the larvae of *P. vanderplanki* after irradiation with 70 Gy of gamma-rays from a Cobalt-60 source (left) and during anhydrobiosis (right). D: hours of dehydration, R: hours of rehydration.

3-38 Crosstalk between Signal Transduction Pathways in Response to Irradiation of Radiation and Innate Immunity of *C. elegans*

T. Kimura [a)], T. Takanami [a)], T. Sakashita [b)], N. Hamada [b, c)], S. Wada [d)], M. Suzuki [b)], Y. Kobayashi [b, c)] and A. Higashitani [a)]

[a)] Graduate School of Life Sciences, Tohoku University,
[b)] Radiation-Applied Biology Division, QuBS, JAEA, [c)] Department of Quantum Biology, and The 21st Century COE Program, Gunma University Graduate School of Medicine,
[d)] Department of Veterinary Radiology and Radiation Biology, Kitasato University

C. elegans microarray analyses including our experiments indicate that several genes in response to irradiation of ionizing radiation (IR) show the alterations similar to those on the infection with *Pseudomonas aeruginosa* [1,2]. It strongly suggests that there is a crosstalk between signal transduction pathways in IR response and innate immune response. In this study, to clarify the signal transduction pathways, we have characterized transcriptional control(s) of a gene *F49F1.6* induced by both IR exposure and *P. aeruginosa* infection. Two to four hours after IR irradiation, the expression levels were drastically increased by more than 20-fold in a dose dependent manner. Its upregulation was transiently, and the expression became steady-state level 24 h after IR irradiation [1]. In addition, at 4 h after irradiation of body-surface at 10 μm depth with 100 Gy of $^{12}C^{5+}$ ions (TIARA 3MV tandem accelerator), the expression level in L1 larvae was increased by 2-fold, but not in the adult hermaphrodites. *F49F1.6* gene product has a signal peptide and Metridin-like ShK toxin domain and shows good similarity to the N-terminal region of mammalian Mucin-2 precursor. These results suggest that *F49F1.6* gene product probably functions in the intestine of body center.

In the transcriptional promoter region of *F49F1.6*, we could find a consensus sequence for GATA-1 transcriptional factor. In the nematode *C. elegans*, *elt-2* encodes a GATA-type transcriptional factor most similar to the vertebrate GATA4-6 transcriptional factors and is required for initiating and maintaining terminal differentiation of the intestine[3]. In addition, ELT-2 is required specifically for infection responses and survival on pathogens *P. aeruginosa* and *Cryptococcus neoformans* [4,5]. We therefore performed RNAi experiment of *elt-2* to elucidate whether IR induction of *F49F1.6* is also dependent on ELT-2 function. The result clearly indicated that the induction was completely repressed in the *elt-2* RNAi animals (Fig. 1).

It has been also reported that upregulation of certain innate immune response genes by infection with *P. aeruginosa* is controlled through a stress activated MAPK (p38: *pmk-1*) signal transduction pathway [2]. To study a crosstalk between IR response and immune response through stress activated MAPK pathway(s), we used some mutants involved in p38 and JNK pathways. The results indicate that the IR induction of *F49F1.6* needed p38 MAPK pathway but not JNK-1 pathway (Fig. 2). Altogether, we succeed in discovery of a novel crosstalk between responses to IR and innate immunity through a GATA transcription factor ELT-2 and p38 signal transduction pathway in *C. elegans*.

References

1) T. Kimura et al., Bioelectromagnetics 29 (2008) 605.
2) E.R. Troemel et al., PLoS Genet. 2 (2006) e183.
3) T. Fukushige et al., Dev. Biol. 198 (1998)286.
4) M. Shapira et al., Porc. Natl. Acad. Sci. USA 103 (2006) 14086.
5) S. Kerry et al., PLoS ONE 1 (2006) e77.

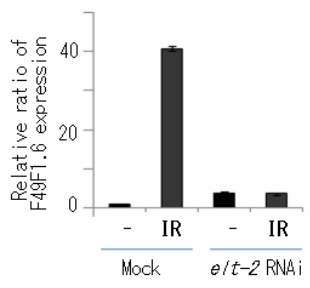

Fig. 1 A GATA factor ELT-2 is required for *F49F1.6* gene expression induced by 100 Gy X-ray irradiation.

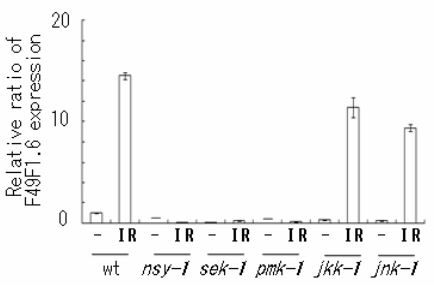

Fig. 2 p38 MAPK (PMK-1) pathway is essential for *F49F1.6* gene expression, but not JNK-1 pathway.

3-39 Imaging for Carbon Translocation to a Fruit with $^{11}CO_2$ and Positron Emission Tomography

N. Kawachi [a], K. Kikuchi [b], H. Watabe [c], N. Suzui [a], S. Ishii [a], N. S. Ishioka [a] and S. Fujimaki [a]

[a] Radiation-Applied Biology Division, QuBS, JAEA, [b] Molecular Genetics and Physiology Research Team, NIVTS, NARO, [c] Department of Investigative Radiology, NCVC

Recently, radionuclide imaging technologies have been providing researchers with exciting opportunities to study biology. In particular, the positron emission tomography (PET) has made great progress and has allowed us to obtain the present images of molecular dynamics for quantitating physiological functions noninvasively in clinical and animal studies. In the field of plant science, most of the radionuclide-based methods for studying plants are invasive and require a statistical process with a large number of test plants. The positron-emitting tracer imaging system (PETIS), is one of the most powerful techniques used for plant researches of the distribution and translocation of water, photoassimilates, mineral nutrients, and environmental pollutants. Most of the higher plants studied in laboratory experiments are thin and small, and hence, two-dimensional planar images are sufficient for studying these plants. However, it is difficult to provide images of photoassimilate translocation and distribution in the fruits of the "s*ink organs*" with planar imaging, because fruits are three-dimensional (3D) living structures; therefore, the PET approach has to be used to study fruits growth and development.

In order to validate the present technique, we performed PET studies on a plant with a fruit, a "sink organ". Tomato (*Lycopersicon esculentum* L. 'Momotarou') seeds were sown in cell plug trays, and after three weeks, several of the seedlings were transplanted into plastic pots (diameter: 13 cm) filled with a standard growing medium. Approximately 6 weeks after pollination, two fruits of a plant were selected and subjected to the PET experiment. The mass of the fruits was 77 g in the maturation period and 0.9 g in the developmental period. A leaf of the plant was installed into the exposure cell in order to produce ^{11}C-labeled photosynthetic compounds. The scanner used was a microPET Focus 120 (Siemens Medical Solutions, Inc.), which has an imaging field of view that is 76 mm in diameter and 67 mm in axial length. The spatial resolution of the scanner is 1.45 mm in full width at half maximum at the center of the field of view. An ordered-subset expectation maximization algorithm with a 3D mode, 2 iterations, and 12 subsets was used for image reconstruction. The positron emitting $^{11}CO_2$ gas radioactive intensity was 100 MBq at the time when PET began acquiring images. Room air containing nonradioactive CO_2 was pumped into the exposure cell. $^{11}CO_2$ gas was supplied through the inlet duct of the cell for approximately 30 s; PET scanning was performed simultaneously in the list mode for 2 h.

Approximately 30 min after PET start, ^{11}C appeared in the area in the field of view where the fruit was placed, and after that, it flowed into the two tomatoes (Fig. 1). This indicated that ^{11}C-labeled photosynthate was synthesized from the assimilated $^{11}CO_2$ in the leaf and transported via phloem, and that it finally reached the fruits. These images depicted the fine structure of the phloem path and the fruit's bioactivity; that is, the developing fruit exhibited more activity than the matured one in the PET images. Further, basic physiological functions were analyzed from the carbon kinetics in the dynamic PET images. In conclusion, we have successfully obtained 3D images of the carbon translocation to a tomato fruit by using PET and $^{11}CO_2$. This experimental method will be useful in not only investigating plant physiology, such as the mechanism of fruit growth under various physiological conditions, but also in improving agricultural techniques, such as the cultivation conditions to gain the best harvest in quality and quantity.

Reference

1) K. Kikuchi et al., J. J. S. Horti. Sci, 77 (2008) 199-205.

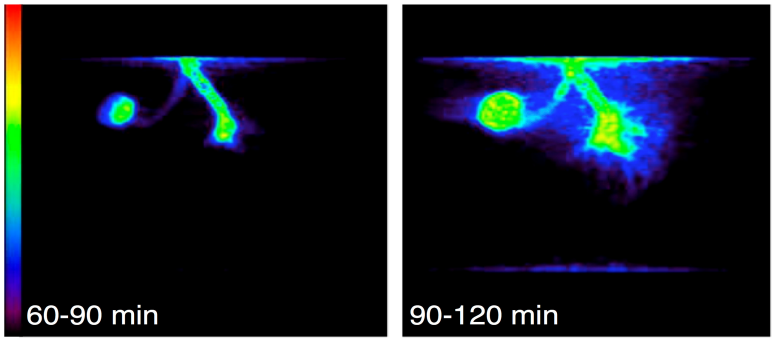

Fig. 1 Volume rendering 3D images (60-90 min, 90-120 min) of [^{11}C]photoassimilate translocation into the tomatoes.

3-40 Kinetic Analysis of Cadmium Uptake in Oilseed Rape Plants Using Positron Multi-Probe System

N. Suzui [a)], S. Nakamura [b)], S. Ito [a)], N. Kawachi [a)], N.S. Ishioka [a)] and S. Fujimaki [a)]

[a)] Radiation-Applied Biology Division, QuBS, JAEA,
[b)] Faculty of Bioresource Sciences, Akita Prefectural University

Cd accumulation in the human body causes serious health problems when Cd is taken via the farm products. In order to decrease Cd accumulation in these products, it is necessary to understand mechanisms of uptake, transport and accumulation of Cd in the plant body. In the last few years, we have tried to elucidate mechanisms of Cd transport and accumulation by visualizing Cd dynamics in the plant body using ^{107}Cd and positron emitting tracer imaging system (PETIS) [1)]. However, uptake process of Cd by plants was not been observed directly using PETIS because ^{107}Cd radioactivity of tracer solution in PETIS experiments was above the level of quantification of the PETIS apparatus. In this study, we have developed a monitoring system of ^{107}Cd radioactivity in tracer solution using Positron Multi-Probe System (PMPS) that enables the noninvasive measurement of the amounts of ^{107}Cd uptake by an intact plant.

Figure 1 shows set-up of this monitoring system. Two-week old oilseed rape plant (*Brassica napus* L.) was placed into a plastic cylindrical container containing 30 mL of 0.5 mM $CaCl_2$ solution with approximately 10 MBq of ^{107}Cd, which was produced by bombarding silver plate with an energetic proton beam delivered from AVF cyclotron at TIARA (Takasaki Ion Accelerators for Advanced Radiation Application) and was purified following previously described method [2)]. The cylindrical container was divided by nylon mesh into two compartments, the root of the plant was immersed in the upper compartment, and a pair of PMPS detectors was placed outside the bottom compartment. The tracer solution was gently stirred by bubbling air in order to prevent a concentration gradient of solvent between the two compartments, and the radioactivity in the solution was measured continuously.

Figure 2 shows the time-course change in ^{107}Cd radioactivity in the tracer solution over 24 hours. The time-course data for ^{107}Cd radioactivity can be fitted to an exponential decreasing curve with a plateau. This indicates that the rate of Cd uptake by the plant was proportional to the Cd remaining in the tracer solution. To date we could simultaneously monitor the uptake amounts in 4 individual oilseed plants by shielding each detector head with lead blocks. The detailed analysis of the kinetics in various experimental conditions would provide valuable information concerning the mechanism of Cd uptake in plant.

References

1) S. Fujimaki et al., JAEA Takasaki Ann. Rep. 2005 (2007) 127.
2) N. S. Ishioka et al., JAEA Takasaki Ann. Rep. 2005 (2007) 162.

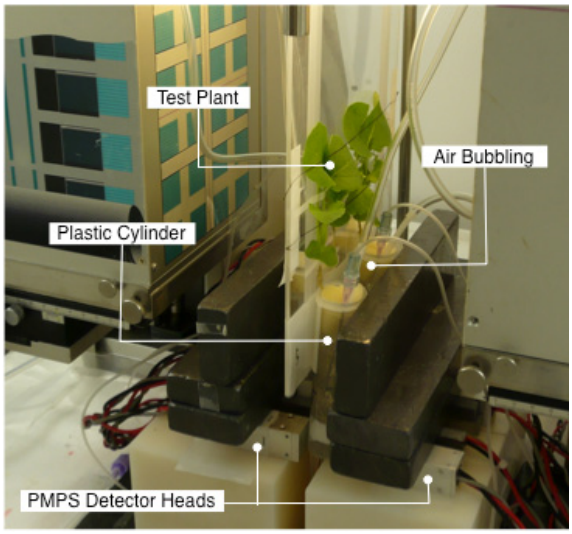

Fig. 1 Set up of the monitoring system of ^{107}Cd radioactivity in tracer solution. A pair of PMPS detector detected an annihilation gamma-ray from ^{107}Cd and the resulting radioactivity was recorded.

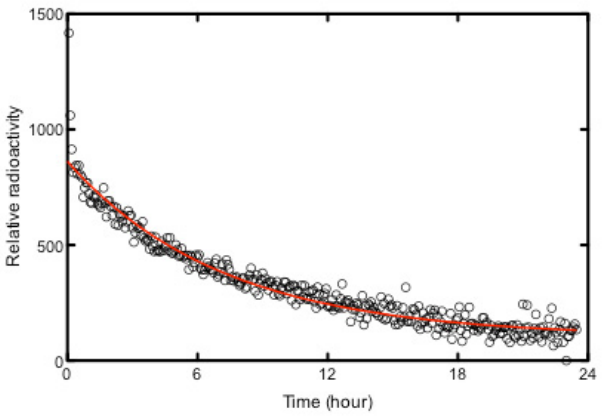

Fig. 2 Time-course change of ^{107}Cd radioactivity in the tracer solution. Data were acquired every 4 minutes and decay correction applied. The red curve indicates least-square fitting of the data to an exponential function.

3-41 Visualization of ^{107}Cd Translocation in Tobacco Plants

S. Nakamura [a)], N. Suzui [b)], N.S. Ishioka [b)], N. Kawachi [b)], S. Ito [b)], H. Hattori [a)], M. Chino [a)] and S. Fujimaki [b)]

[a)] Faculty of Bioresource Sciences, Akita Prefectural University,
[b)] Radiation-Applied Biology Division, QuBS, JAEA

Cadmium (Cd) is regarded as one of the toxic heavy metals. Cd can enter human food chain via farm products easily. Cd accumulation in the human body causes serious health problems. In order to reduce Cd accumulation in farm products, it is necessary to understand the mechanisms of Cd long-distance transport and control them. However, these mechanisms are not fully understood so far. We tried to elucidate mechanisms of Cd long-distance transport by visualizing Cd transport of in the plant body of tobacco plants using positron emitting tracer imaging system (PETIS). PETIS is a planner imaging system. We can obtain serial images of distribution of positron emitting molecules in the plant body non-invasively[1)]. In this research, we used tobacco plants. Because tobacco is one of model plants which enable us to manipulate its gene expression, it is expected to create crop plants with low Cd content in the future.

^{107}Cd (half-life: 6.5 h) was used as a positron-emitting radioactive tracer in our experiment. ^{107}Cd was produced by bombarding silver plate with an energetic proton beam delivered from AVF cyclotron at TIARA (Takasaki Ion Accelerators for Advanced Radiation Application). ^{107}Cd was purified, following the method of Ishioka et al.[2)]. Tobacco plants (*Nicotiana tabacum*) were grown hydroponically in a growth chamber where the growth conditions of plants were controlled completely for two weeks after sowing. PETIS experiments were also performed in the growth chamber under controlled growth conditions. After setting plants in the chamber, PETIS experiments were started by adding purified ^{107}Cd in nutrient solutions. In these experiments 0.1 μM Cd was added as a carrier to hydroponic solutions. This Cd concentration (0.1 μM) is comparable to that in soil solution from non Cd-polluted soils. Time-series images of the ^{107}Cd distribution were obtained with the PETIS apparatus. Each image was obtained every four minute for 36 hours.

We succeeded to obtain fine serial images of Cd transport and accumulation in tobacco plants. Strong ^{107}Cd signals were observed in the roots of tobacco plants. We also could see strong signals of ^{107}Cd in the stems. In leaves, ^{107}Cd signals were distributed thoroughly. The pattern of Cd signal distribution in the tobacco plants was similar to that in oilseed plants[3)]. These results demonstrated that dicotyledonous plants had the similar pattern of Cd distribution when plants were treated at low concentration of Cd.

References

1) S. Fujimaki, ITE *Let.* (2007) 8, C1-C10.
2) N.S. Ishioka et al., JAEA Takasaki Ann. Rep. 2005 (2007) 162.
3) N. Suzui et al., JAEA Takasaki Ann. Rep. 2007 (2008) 112.

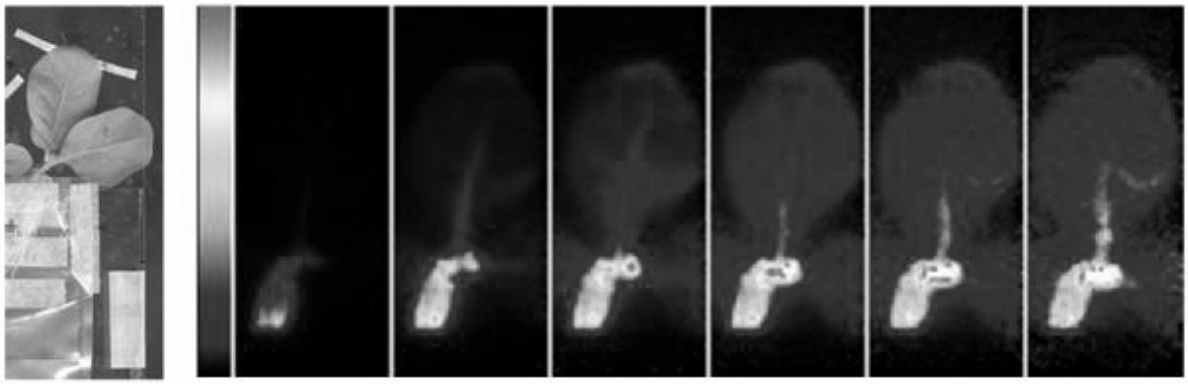

Fig. 1 Accumulation of ^{107}Cd signals in tobacco plants. Each image is integration of 90 original frames, corresponding to six hours.

3-42 Cadmium Transport in Young Soybean Plant Using a Positron-emitting ^{107}Cd

S. Ito, N. Suzui, N. Kawachi, N.S. Ishioka and S. Fujimaki

Radiation-Applied Biology Division, QuBS, JAEA

Cadmium (Cd) is one of the most serious pollutants for foods over the world. Recently, Cd accumulation in soybean seed is considered one of the acute agricultural problems in Japan. However, characteristics of Cd transport and accumulation in soybean plants are unclear so far. In this study, the mechanism of Cd transport in young soybean plants was characterized using tracer of a positron-emitting ^{107}Cd (half-life: 6.5 hours) and the positron-emitting tracer imaging system (PETIS), which presents a movie of changing distribution of a positron-emitting radioactive tracer within an intact test plant. After the PETIS experiment, ^{107}Cd distribution within test plant was obtained with autoradiography by using bio-imaging analyzer system (BAS).

Soybean (*Glycine max* [L.] Merr. cv. Williams) seeds were inoculated with a suspension of *Bradhyrhizobium japonicum* (strain USDA110) and were sown on vermiculite. They were grown in a growth chamber under following conditions: 12 h light at 28 ºC and 12 h dark at 20 ºC. Seven days after sowing, they were transferred to a hydroponic culture excluding Cd. About 3 weeks after sowing, they were transplanted to plastic tubes containing 0.5 mM $CaCl_2$ solution and subjected to the experiments. The test plants were placed between a set of the PETIS detector heads in another growth chamber. ^{107}Cd was produced according to the method established by Ishioka et al.[1] and was added to the $CaCl_2$ solution with 0.1 μM non-radioactive Cd. The imaging with PETIS was performed for 36 hours. After the PETIS experiments, the test plants were sampled. The sampled plants were ironed and pressed. ^{107}Cd distribution in the test plants was analyzed using the BAS.

In the field of view of PETIS, ^{107}Cd was observed very weakly (Fig. 1). Cd appeared in the shoot base at about 10 hours after Cd feeding, which timing was 10 times later compared with the results of rice by Fujimaki et al.[2]. Cd was not reached the leaves within 36 hours, which is different from the results in sorghum and oilseed rape plants [3].

Also with the autoradiography, ^{107}Cd signal was limited in the stem base but not detected in the leaves (Fig. 2). These results may indicate that Cd transport might be particularly slow in soybean plants. Longer-term experiments will be performed in the next study.

References

1) N.S. Ishioka et al., JAEA Takasaki Ann. Rep. 2005 (2007) 162.
2) S. Fujimaki et al., JAEA Takasaki Ann. Rep. 2005 (2007) 127.
3) S. Nakamura et al., JAEA Takasaki Ann. Rep. 2006 (2008) 123.

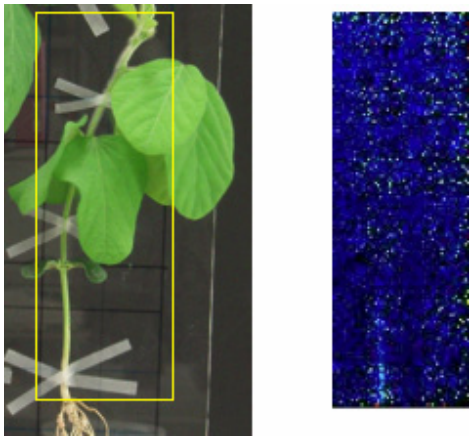

Fig. 1 Photograph (left) and PETIS image (right) in young soybean plant. This image is integration of all original frames, corresponding to 36 hours.

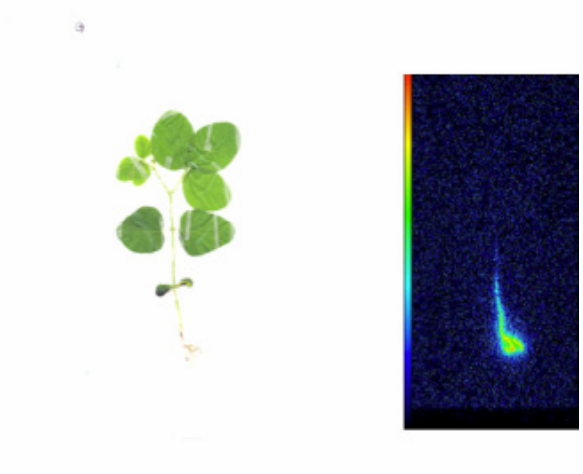

Fig. 2 Optical image (left) and BAS image (right) in young soybean plant.

3-43 Analysis of Translocation and Distribution of Photoassimilates in Eggplant Fruit in Relation to Positions of the Source Leaves Using the Positron-emitting Tracer Imaging System

K. Kikuchi [a)], N. Kawachi [b)], S. Ishii [b)], N. Suzui [b)], S. Ito [b)], N. S. Ishioka [b)], I. Honda [a)] and S. Fujimaki [b)]

[a)] National Institute of Vegetable and Tea Science, National Agriculture and Food Research Organization, [b)] Radiation-Applied Biology Division, QuBS, JAEA

Introduction

In the eggplant cultivation, defoliation is normally used to prevent the disease and insect as well as raise the efficiency of light interception for efficient fruit production. However the general guideline for defoliation is not established yet because fundamental knowledge about effects of defoliation on the nutritional balance in individuals has hardly been obtained. For these reason, it is important to clarify the accumulation mechanism of the photoassimilates which is translocated from each leaf to the fruit in eggplant. Previously, we succeeded to observe translocation of ^{11}C-labeled photoassimilates from a leaf into a fruit and established a method for the quantitative analysis of photoassimilates using the positron-emitting tracer imaging system (PETIS) (2008). PETIS can noninvasively visualize the movement of ^{11}C-labeled photoassimilates in plants and repetitive analyses using one plant are possible due to the short half-life (20 min) of ^{11}C. In this study, we analyzed translocation of photoassimilates from each of major leaves to a fruit, and estimated the contribution of the respective leaves to accumulation of photoassimilates in the fruit using $^{11}CO_2$ and PETIS.

Material and Method

Eggplants (*Solanum melongena* L., line AE-P03) were grown in the growth chamber under a controlled temperature (28/18 °C, day/night) and a 14 h light photoperiod. Their first flowers were hand-pollinated at anthesis. Thirteen days after pollination, the plants whose fruits grow normally were selected and subjected to the PETIS experiment. One leaf from the eighth (immediately above the second fruit), seventh (immediately below the second fruit) and sixth leaf (Fig. 1 (A)) was selected, and $^{11}CO_2$ was fed to this leaf 9 h after the beginning of the light period, and the translocation of ^{11}C into the fruit was measured by PETIS to estimate the photoassimilate translocation. The PETIS images were collected every 10 sec and integrated. The repetitive experiments were conducted in the next days under the same conditions with the same plant, but with different leaves to be fed $^{11}CO_2$.

Result and Discussion

Figure 1 (B), (C) and (D) show serial PETIS images integrated every 60 min after $^{11}CO_2$ feeding. When $^{11}CO_2$ was fed to the sixth leaf, the accumulation of ^{11}C-labeld photoassimilates into one side of the fruit was observed (Fig. 1 (D)). On the other hand, accumulation of them in a central part of fruit was observed when we used the seventh leaf (Fig. 1 (C)). These results indicate that photo-assimilates translocated from the sixth and the seventh leaves accumulated into the different parts in the fruit. When the eighth leaf was fed, the translocation of the ^{11}C-labeled photoassimilates to the fruit was faintly observed (Fig. 1 (B)). Similar pattern was obtained in most of the plants tested. We calculated the amount of the photoassimilates accumulated in the fruit one hour after the first detection of ^{11}C in the fruit. When the seventh leaf was fed, the value was highest and that of sixth leaf was also nearly equal. However, that of eighth leaf was approximate quarter of that from the seventh leaf. These results indicate that the distribution part and the volume of photoassimilate translocation from a leaf to a fruit depend on the leaf position. It is known that the amount of photoassimilates translocated from leaf to fruit greatly influences the growth of fruits. Moreover it is assumed that the uneven distribution of the photosynthesis is involved in the development of curved or malformed fruit. These findings obtained here may contribute to the development of defoliation technique and a method for efficient fruit production in the near future.

Reference

1) Kikuchi et al., J. Japan. Soc. Hort. Sci. 77 (2008) 199-205.

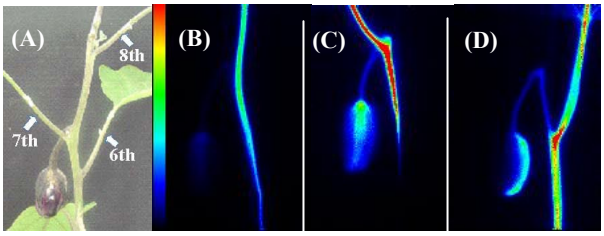

Fig. 1 (A) plant photograph in the experiment. (B), (C), (D) Serial PETIS images when $^{11}CO_2$ was fed to the (B) 6th (C) 7th (D) 8th leaves.

3-44 The Production of ^{13}N-labeled Nitrogen Gas Tracer and the Imaging of Nitrogen Fixation in Soybean Nodules

S. Ishii [a,b], N. Suzui [a], S. Ito [a], N. S. Ishioka [a], N. Kawachi [a], S. Matsuhashi [a], N. Ohtake [b], T.Ohyama [b] and S. Fujimaki [a]

[a] Radiation-Applied Biology Division, QuBS, JAEA,
[b] Graduate School of Science and Technology, Niigata University

The nodule is a symbiotic organ of leguminous plants with rhizobium. Soybean plants utilize nitrogen (N) fixed by nodules from atmospheric N_2. Until now, ^{15}N, a stable isotope, has long been used for studies of N_2 fixation. However, because this method is invasive, it has been difficult to analyze an instant response to environmental (ex. temperature, light) changes.

The purpose of our study is to image the N_2 fixation noninvasively and analyze the kinetics quantitatively and by using nitrogen gas labeled with ^{13}N (half life: 10 min), a positron emitting isotope, and PETIS (positron-emitting tracer imaging system). Previously, we succeeded in producing ^{13}N-labeled nitrogen gas ($[^{13}N]N_2$)[1]. However, it was required to purify the gas because it was likely to contain physiologically active ^{13}N-labeled impurities. In this paper, we report development of a new method of production of pure $[^{13}N]N_2$ and the imaging of nitrogen fixation.

The scheme of the production of $[^{13}N]N_2$ tracer is indicated in Fig. 1. ^{13}N was produced using the ^{16}O (p, α) ^{13}N nuclear reaction. CO_2 was filled in a target chamber and irradiated with proton ions at energy of 18.3 MeV and electric current of 5 μA for 10 min delivered from a cyclotron located at Takasaki Ion Accelerators for Advanced Radiation Application (TIARA). All CO_2 was absorbed and removed from irradiated gas with powdered soda-lime in a syringe, and helium gas was also added to the syringe. The resulting gas was injected into gas chromatography and separated. Thirty five mL of gas including the peak of $[^{13}N]N_2$ was collected. The gas was mixed with 10 mL of O_2 and 5 mL of N_2, and used for the tracer experiment. The production process took only about 15 min after the irradiation. Finally, approximately 10 - 30 MBq of $[^{13}N]N_2$ was produced.

Soybean plants, *Glycine max* [L.] cv. Williams, inoculated with rhizobium (*Bradyrizobium japonicum* strain USDA 110) and hydroponically cultivated with a N-free medium for 25 - 30 days after sowing was used for the PETIS experiments.

The $[^{13}N]N_2$ tracer gas was fed to the underground part of intact nodulated soybean plants for 10 min. Then the tracer gas was flushed out by flowing fresh ambient air. The serial images by PETIS were collected for 1 h (360 frames × 10 second).

Distribution of ^{13}N in the root of the soybean was shown in Fig. 2. Obvious signals of ^{13}N were observed at the positions of clump of nodules (the red circle) and sparse nodules (yellow arrowhead). Similar results were obtained in all the six plants tested.

In conclusion, we succeeded in the real-time imaging of nitrogen fixation in intact soybean plants with nodules using $[^{13}N]N_2$ tracer and PETIS.

Reference

1) S. Ishii et al., JAEA Takasaki Ann. Rep. 2007 (2008) 111.

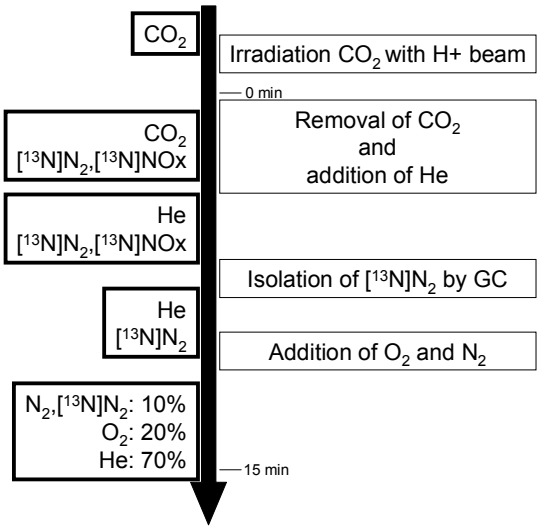

Fig. 1 Scheme of the production of $[^{13}N]N_2$ tracer.

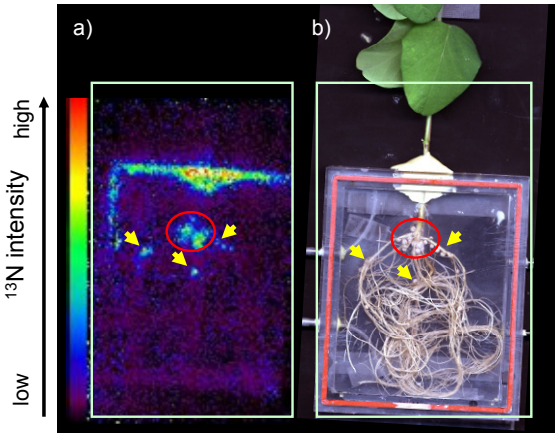

Fig. 2 Distribution of ^{13}N signal in the root of a soybean plant. a) PETIS image. This image was integrated 110 frames after flushing out of the tracer. b) Optical image.

3-45 ^{76}Br-*m*-Bromobenzylguanidine (^{76}Br-MBBG) for in vivo Imaging of Neuroendcrine-tumor with PET

Sh. Watanabe [a)], H. Hanaoka [b)], J. X. Liang [a)], Y. Iida [b)], Sa. Watanabe [a)], K. Endo [b)] and N. S. Ishioka [a)]

[a)] Radiation-Applied Biology Division, QuBS, JAEA,
[b)] Gunma University Graduate School of Medicine

Introduction

^{131}I-*m*-Iodobenzylgunanidine (^{131}I-MIBG), functional analogue of norepinephrine, has been employed for the therapy of neuroendcrine tumors which express norepinephrine transporter (NET). ^{123}I-MIBG scintigraphy has been also used for diagnosis of NET positive tumors such as detecting metastasis, investigating suitability and monitoring response to the treatment with ^{131}I-MIBG. However, ^{123}I-MIBG scintigraphy has been not enough for diagnosis of neuroendcrine tumors due to poor sensitivity and resolution. Positron emission tomography (PET) is superior to spatial resolution and quantitative capability. Positron emitter labeled MIBG has potential to improve diagnostic ability of NET positive neuroendcrine tumors. ^{76}Br ($t_{1/2}$ = 16.1 h, β^+ = 57%) is a positron emitter which has similar chemical properties to iodine. ^{76}Br-labeled *m*-bromobenzylguanidine (^{76}Br-MBBG) can be applied for the diagnosis of NET positive tumor with PET imaging.

In this study, we have synthesized no-carrier-added ^{76}Br labeled ^{76}Br-MBBG, and evaluated in vitro stability. Biodistribution studies performed with neuroendcrine tumor xenografted nude mice in order to assess the possibility of application for the *in vivo* imaging of neuroendcrine tumors with PET.

Materials and Methods

No-carrier-added ^{76}Br was produced using enriched $Cu_2{}^{76}Se$ target (99.7% enrichment, 365 mg) at JAEA-TIARA AVF cyclotron. ^{76}Br was separated from the irradiated Cu_2Se target with the dry distillation method[1)]. ^{76}Br was characterized with HPGe detector connected to Multi Channel Analyzer (Seiko, CE&G). Radioactivity was determined by γ-ray at 520 keV. ^{76}Br-MBBG was synthesized with halogen exchange method in the presence of *in situ* generated Cu^+ catalyst as shown in Fig. 1[2)]. Characterization was carried out with TLC (C-18 reverse phase) and HPLC analysis. (Mobile phase: 15% acetonitrile in 0.01M Na_2HPO_4 solution; Flow rate: 3 mL/min.; Column: μBondapak C-18 300 mm×7.6 mmi.d., Waters).

For in vitro stability, ^{76}Br-MBBG was incubated in saline or serum at 37 °C for 24 hours. The stability was evaluated with the radiochemical purity of ^{76}Br-MBBG calculated from HPLC analysis under abovementioned conditions.

Biodistibution studies were performed in rat pheochromocytoma (PC-12) xenografted nude mice. ^{76}Br-MBBG (37 kBq) and ^{125}I-MIBG (3.7 kBq) was injected in the tail vein. Five of mice were sacrificed at 0.5, 1, 3, and 6 hours postinjection (p.i.). Blood, liver, kidney, adrenal, intestine, stomach, spleen, pancreas, lung, heart, muscle, and tumor were removed and weighed. Radioactivity was measured by well-type γ counter, and tissue concentration was calculated as % dose/g.

Results and Discussions

^{76}Br-MBBG was synthesized with 50% of labeling yield. R_f value in TLC analysis was 0.28 and retention time in HPLC analysis was 27 min, which are identical to non-radioactive MBBG. Radiochemical purity was >97% and no other radiobromine compound was contaminated.

Results of *in vitro* stability showed that the radiochemical purity of ^{76}Br-MBBG after incubation for 24 hours was >97%, and no ^{76}Br-decomposition was detected. Consequently, it revealed that ^{76}Br-MBBG is stable in saline and serum until 24 hours.

In biodistribution studies, ^{76}Br-MBBG was taken up highly in tumor (32 %ID/g at 3 h p.i.) and cleared rapidly from blood (0.8 %ID/g at 1 h p.i.), as shown in Table 1. Tumor to blood ratio was 64.1 at 3 h p.i.. Tumor uptake of ^{76}Br-MBBG was the highest in all organs. Uptake in target organs (adrenal and heart) were also higher than that of non-target one. In comparison to ^{125}I MIBG, uptake of ^{76}Br-MBBG in tumor and target organs are higher than that of ^{125}I-MIBG (25 %ID/g at 3 h p.i.). Whereas, uptake in non-target organs were identical.

These results clearly indicated that ^{76}Br-MBBG was accumulated selectively to tumors and has potential to apply for *in vivo* imaging of NET positive tumors with PET.

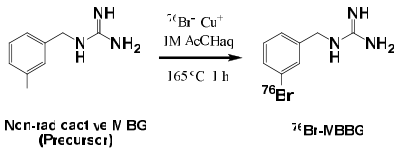

Non-radioactive MIBG (Precursor) ^{76}Br-MBBG

Fig. 1 Labeling scheme and chemical structure of ^{76}Br-MBBG.

Table 1 Biodistribution of ^{76}Br-MBBG and ^{125}I-MIBG in PC-12 xenografted nude mice.

Tissue	Tissue concentration (% dose/g)			
	30 min. p.i.	1 h p.i.	3 h p.i.	6 h p.i.
Tumor	20.3 ± 7.5	22.0 ± 10.3	32.0 ± 19	23.7 ± 5.9
	16.2 ± 6.1	18.1 ± 8.3	25.1 ± 15	19.4 ± 4.9
Blood	0.865 ± 0.11	0.834 ± 0.02	0.587 ± 0.10	0.522 ± 0.03
	0.998 ± 0.14	0.910 ± 0.14	0.545 ± 0.12	0.316 ± 0.04
Adrenal	14.9 ± 3.3	12.9 ± 2.6	16.5 ± 4.2	17.3 ± 4.4
	12.4 ± 1.7	9.92 ± 1.8	12.6 ± 4.1	11.4 ± 3.2
Heart	16.8 ± 1.7	13.2 ± 0.95	14.2 ± 5.3	9.04 ± 0.73
	14.8 ± 1.5	11.4 ± 0.74	12.5 ± 4.7	8.10 ± 0.68
Liver	8.39 ± 0.45	7.62 ± 0.37	3.95 ± 0.38	2.30 ± 0.11
	8.52 ± 0.65	7.78 ± 0.43	4.17 ± 0.42	2.22 ± 0.12
Kidney	2.03 ± 0.28	1.62 ± 0.12	1.36 ± 0.18	1.07 ± 0.17
	2.29 ± 0.33	1.69 ± 0.13	1.37 ± 0.25	0.942 ± 0.19
Intestine	5.45 ± 0.45	4.83 ± 0.16	3.58 ± 0.23	3.58 ± 0.23
	5.36 ± 0.43	4.92 ± 0.27	5.39 ± 0.60	3.79 ± 7.5

Values are presented as mean ± SD. Upper column in every tissue shows results of ^{76}Br-MBBG, and lower column shows those of ^{125}I-MIBG.

References

1) N. S. Ishioka et al., JAEA Takasaki Ann. Rep. 2007 (2008) 113.
2) C. Loc'h et al., Nucl. Med. Biol., **21** (1994) 49-55.

3-46 Production of Radioisotopes for Nuclear Medicine Using Ion-beam Technology and Its Utilization for both Therapeutic and Diagnostic Application in Cancer

Y. Iida [a) b)], H. Hanaoka [a)], Sa. Watanabe [d)], Sh. Watanabe [d)] N. S. Ishioka [d)], H. Yoshioka [c)], S. Yamamoto [c)], P. Paudyal [c)], B. Paudyal [c)], T. Higuchi [c)], N. Oriuchi [c)] and K. Endo [b) c)]

[a)] Department of Bioimaging Information Analysis, [b)] 21st Century COE Program and [c)] Department of Diagnostic Radiology and Nuclear Medicine, Gunma University Graduate School of Medicine, [d)] Radiation-Applied Biology Division, QuBS, JAEA

As antibody binds specifically to corresponding antigens, radiolabeled antibody also binds to cells expressing antigens on surface membranes. Large amounts of antibodies labeled with cytotoxic radionuclides are administered intravenously in cancer patients, after diagnostic imaging using the tracer amount of radiolabeled antibody. In this study, we developed this therapy, called radioimmunotherapy, for effective treatment in cancer patients without damaging normal cells which do not express antigens. We developed ^{177}Lu-DOTA-NuB2 using carrier-free lutetium(Lu)-177, and obtained remarkable results for decreasing tumor. Tumor specific radionuclide therapy using ^{177}Lu is effective therapy with less adverse reactions.

現在、放射性薬剤を体内に投与して治療を行う放射性同位元素内用療法に用いられる放射性核種（RI）は^{131}I、^{90}Y、^{89}Srのみであるが、治療での有効性が期待されるRIは他にも多数存在する[1)]。一方で、内用放射線療法の治療効果は標的となる癌組織の大きさ、性状と放射線のエネルギーとのバランスに左右され、個々の標的に対して最も効率的なエネルギーが存在する可能性が示唆されている[2)]。すなわち、性質の異なる種々のRIを利用することで、個々の病態に適した個別化医療を実現できる可能性がある。さらにこれらのRIを併用することでより高い治療効果が期待できる。そこで新規治療用RIを製造し、癌治療における有効性を調べるとともに、最適な治療を実現するための個別化医療、併用療法の可能性を基礎的に検討した。

新しい治療用核種として^{177}Luの有用性について検討した。^{177}Luは^{90}Y よりも半減期が長く（^{90}Y：半減期64.1 時間、^{177}Lu：6.73 日)、主なβ線のエネルギーは0.176、0.384、0.497 MeVでβ線のほかγ線も放出するため治療と同時に診断も行える利点を有しており、より治療効果の高い放射免疫療法薬剤の開発が期待できる。^{177}Lu は ^{176}Yb(n,γ)^{177}Yb($T_{1/2}$ = 1.91 時間)→^{177}Lu ($T_{1/2}$=6.73日)により製造し、化学分離法の開発により無担体の^{177}Luの分離精製に成功した。そこで悪性リンパ腫の標的となるCD20を抗原とする抗体：NuB2に^{177}Luを結合し(^{177}Lu-DOTA-NuB2)、RPMI1788腫瘍移植マウスに投与して体内動態を調べた結果、^{177}Lu-DOTA-NuB2は高く腫瘍に移行し（投与24時間後で約16.2 %dose/g）、滞留することが分かった（Fig. 1）。これらの結果に基づきRAMOS細胞移植ヌードマウスに^{177}Lu-DOTA-NuB2を投与し、経時的にその抗腫瘍効果を調べたところ、14.8 MBqの投与により腫瘍サイズが縮小することを認めた（Fig. 2）。

癌治療に腫瘍特異的な方法、新規RIを用いることは患者の副作用を軽減し、治療効果の増大とともに患者のQOLの向上に貢献することが期待できる。

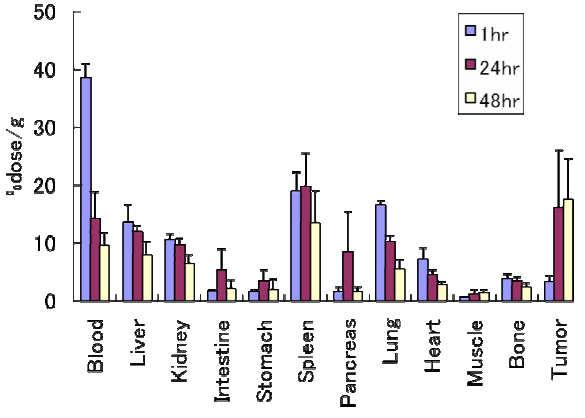

Fig. 1 Biodistribution of ^{177}Lu-DOTA-NuB2 in SCID mice bearing RPMI1788. For each time point, data were acquired from five animals.

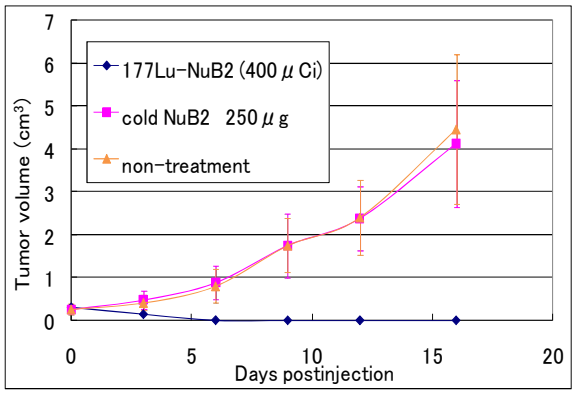

Fig. 2 Therapeutic effect of ^{177}Lu-DOTA-NuB2 in nude mice bearing RAMOS tumor.

References

1) Barbet J et al., Eur. J. Nucl. Med. Mol. Imaging 33 (2006) 627-30.
2) van Dieren EB et al., Int. J. Radiat. Oncol. Biol. Phys. 36 (1996) 197-204.

3-47 Production of Lu-177 Capable of Labeling Antibodies

Sa. Watanabe [a)], K. Hashimoto [a)], Sh. Watanabe [a)], Y. Iida [b)], H. Hanaoka [b)], K. Endo [b)] and N. S. Ishioka [a)]

[a)] Research Unit for Quantum Beam Life Science Initiative, QuBS, JAEA,
[b)] Gunma University Graduate School of Medicine

Lutetium-177 is considered to have potential for application in radionuclide therapy, because it emits β-particles ($E_{\beta,max}$ = 498 keV) suitable to penetrate small tumors and its physical half-life of 6.734 days is long enough for ^{177}Lu-labeled agents to accumulate to tumor sites. In addition, the energy of γ-rays (E_{γ} = 113 keV and 208 keV) emitted from ^{177}Lu is particularly suitable for imaging by single photon emission computed tomography. Lutetium-177 can be usually produced in nuclear reactors with high yield and high specific radioactivity by the ^{176}Lu(n, γ)^{177}Lu reaction with very high cross section of 2090 barns. However ^{177}Lu with higher specific radioactivity are required in the field of radioimmunotherapy using labeled monoclonal antibodies. Thus, an alternative production route, the ^{176}Yb(n, γ)^{177}Yb($T_{1/2}$ = 1.911 h)→ ^{177}Lu process (thermal neutron cross sections σ(^{176}Yb) = 2.85 b) was studied using enriched $^{176}Yb_2O_3$ to produce no-carrier-added (nca) ^{177}Lu in the present work. The important point is purification of ^{177}Lu in the separation of nca ^{177}Lu from macroscopic amounts of the ytterbium target, because of labeling with monoclonal antibodies. Therefore, in the present paper, production of highly-purified nca ^{177}Lu capable of labeling antibodies is developed using reversed-phase ion-pair liquid chromatography with 2-hydroxyisobutyric acid (2-HIBA) and 1-octanesulfonic acid sodium salt as a complexing reagent and an ion-paring agent, respectively.

The experimental nca ^{177}Lu production was carried out by a modified form of the method described in detail before[1]. About 2 mg of enriched $^{176}Yb_2O_3$ target (^{176}Yb: 95.3%-99.7%) in a quartz ampoule was irradiated for 6 hours at JAEA JRR-3 with a thermal neutron flux of 1×10^{14} n·cm^{-2}·s^{-1}. The irradiated $^{176}Yb_2O_3$ was then dissolved in 6 M HCl and 30% H_2O_2 with heating. The solution was evaporated to dryness and the residue was dissolved in 0.01 M HCl. The solution was loaded on a reversed-phase column (connected in series of three Resolve C_{18} Radial-Pak column segments). Elution was done with 0.25 M 2-HIBA/0.1 M 1-OS (pH=2.2-2.4) at a flow rate of 2 mL/min. The pure ^{177}Lu fraction separated from ytterbium was collected and loaded on a cation-exchange column (AG50w-x8, H^+ type), then washed with 300 mL of 0.1 M HCl to eliminate 2-HIBA/1-OS. The pure ^{177}Lu was eluted with 6 M HCl, and evaporated to dryness. Finally the residue was dissolved in acetic acid. For the ^{177}Lu labeling of DOTA (1,4,7,10-tetraazacyclododecan-N,N,N'',N'''-tetraacetic acid) conjugated NuB2 (anti CD20 antibody), acetate buffer (3 M, pH=6.0) was added to the acetic acid solution of ^{177}Lu. After the mixture was allowed to stand for 5 min at room temperature, a solution of DOTA-NuB2 (5 mg·mL^{-1}) was added. After incubating for 1.5 hours at 40 °C, to convert the unreactive ^{177}Lu into ^{177}Lu-EDTA, a solution of 2 mM EDTA was added. After 15 min incubation, the radiochemical yield, which was defined as a percentage of the radioactivity of ^{177}Lu-DOTA-NuB2 to that of ^{177}Lu used for the labeling, was determined with thin layer chromatography on ITLC/SG (Gelman Sciences Inc., USA) using saline solution as a developing solvent. The ^{177}Lu-DOTA-NuB2 remains at the origin point of a silica gel ITLC strip and the ^{177}Lu-EDTA moves to the solvent front.

The radiochemical yield of the ^{177}Lu-DOTA-NuB2 was less than 5%. The low radiochemical yield of the ^{177}Lu-DOTA-NuB2 must be due to the metallic impurity included into the final solution of ^{177}Lu. Therefore, the determination of metallic impurity in the final 6 M HCl solution of ^{177}Lu was carried out by ICP-MS. The concentrations of Ca, Fe and Zn, which can be labeled with DOTA-NuB2 and are major impurities, were 87, 340 and 77 ppb, respectively. With those large amounts of the metallic impurity, the labeling of ^{177}Lu-DOTA-NuB2 is inhibited. Those metallic impurities were found to be responsible for the regents of 2-HIBA and 1-OS. Therefore, to eliminate the metallic impurities, the 2-HIBA solution was purified by a cation exchange column (Bio Rad AG50W-x8), and the 1-OS solution was by a chelating ion exchange column (Bio Rad Chelex 100). The metallic impurities in the final ^{177}Lu solution reduced to 18, 83 and 10 ppb for Ca, Fe and Zn, respectively. The radiochemical yield of the ^{177}Lu-DOTA-NuB2 increased to 35%. To eliminate further metallic impurities, an anion exchange process was added after the cation exchange process. The metallic impurities finally reduced to 13, 18 and 9 ppb for Ca, Fe and Zn, respectively. The radiochemical yield of the ^{177}Lu-DOTA-NuB2 increased more than 80%. Consequently, production of nca ^{177}Lu capable of labeling antibodies was succeeded.

Acknowledgments

A part of this study is the result of "Development of RI-DDS for advanced cancer diagnosis and therapy" carried out under the Strategic Promotion Program for Basic Nuclear Research by the Ministry of Education, Culture, Sports, Science and Technology of Japan.

Reference

1) K. Hashimoto et al., J. Radioanal. Nucl. Chem., 255 (2003) 575.

3-48 Three-Dimensional Measurement of Elemental Distribution in Minute Samples by Combination of In-Air Micro-PIXE and STIM

T. Satoh [a)], A. Yokoyama [a)], T. Ohkubo [a)], Y. Ishii [a)], K. Saito [b)], T. Kamiya [a)], K. Arakawa [a)], S. Matsuyama [c)] and K. Ishii [c)]

[a)] Department of Advanced Radiation Technology, TARRI, JAEA,
[b)] Takasaki University of Health and Welfare, [c)] Tohoku University

1. Introduction

A technique of measuring three-dimensional (3D) distribution of trace elements in a minute sample was developed using the in-air micro-PIXE (Particle Induced X-ray Emission) system[1]. A 3D distribution was acquired by means of reconstructing numbers of projection images of the sample obtained by micro-PIXE analyses from different directions. This is basically the same technique as X-ray CT (Computed Tomography). However, when this technique was applied to the in-air micro-PIXE analysis, the X-ray yields should be corrected in taking account of parameters such as the X-ray production cross section, the X-ray attenuation coefficient, the energy of an incident particle, and the 3D densities of major elements in the analysis sample. In this paper, STIM (Scanning Transmission Ion Microscopy) –CT[2] was used to obtain the 3D density map of the sample.

2. Experiment

In this experiment, 3 MeV proton microbeam was scanned over the target. The target was glued on a metal needle and was rotated by 180 degrees at intervals of 15 degrees. For STIM experiment, the surface barrier detector was placed at just behind the target, while a Faraday cup was placed at the same position in the case of micro-PIXE analysis. The metal adsorbent fiber with radiation-induced graft polymerization containing sulfur and iron developed by Environmental Polymer Group of JAEA[3] was used as a test target. The fiber was useful for confirming accuracy of the 3D analysis, because analysis of the characteristic X-ray of sulfur is influenced significantly by attenuation of the X-rays in the target though the effect is small in the case of iron.

3. Result

The 3D structure of the test target is shown in Fig. 1. It was reconstructed from twelve STIM images using FBP (Filtered Back-Projection) and the Shepp and Logan filter[4]. Figure 2 shows two-dimensional micro-PIXE images of sulfur and iron in the target. The concentration of sulfur at left side of the target seems to be low due to absorption of sulfur K X-rays (2.31 keV), because there was the lithium-drifted silicone detector at right side. Using the 3D STIM data, such detected intensities of the X-rays must be corrected according to linear attenuation coefficients of major elements in the target. Figure 3 shows 3D distributions of sulfur and iron reconstructed using FBP and micro-PIXE. The image indicated with 'A' in Fig. 3 was a reconstructed distribution of sulfur without correction. Sulfur seemed to be uniformly contained in the fiber. However significant artifacts were produced as a result of the image reconstruction without correction. The artifacts in the reconstructed image of sulfur were successfully reduced by the correction as shown in 'B' images in Fig. 3, while iron was really localized in the analysis target as shown in 'C' in Fig. 3. These results indicated that STIM-CT and our correction method were useful for accurate reconstruction of the micro-PIXE images in the case of the elements which have low energy characteristic X-rays.

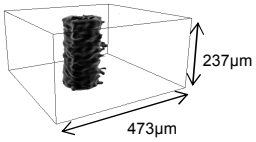

Fig. 1 3D structure of the target. It was reconstructed using FBP and STIM-CT analysis.

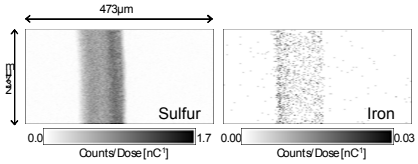

Fig. 2 A two-dimensional micro-PIXE image of sulfur and iron. The gray scale shows the counts of the characteristic X-ray per dose.

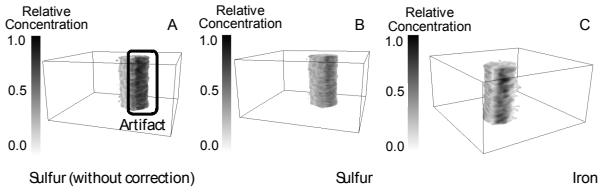

Fig. 3 Reconstructed 3D distributions of sulfur and iron using FBP. The images indicated with 'B' and 'C' were reconstructed distribution of sulfur and iron with correction.

References

1) T. Sakai et al., Int. J. PIXE 10 Nos. 3 & 4 (2000) 91.
2) J. C. Overley et al., Nucl. Instrum. Meth. B 30 (1988) 337.
3) N. Seko et al., Nucl. Technol. 144 (2003) 274.
4) L. A. Shepp et al., IEEE Trans. Nucl. Sci. 21 (1974) 21.

3-49 Measurement of Trace Metal in Methamphetamine Treated Mice Brain Slices by In-Air Micro-PIXE

E. Sakurai [a)], K. Yanai [a)], K. Ishii [a)], K. Yamanaka [a)], S. Okura [a)], H. Yamazaki [a)], S. Matsuyama [a)], N. Okamura [a)], T. Kamiya [b)], T. Satoh [b)] and K. Arakawa [b)]

[a)] Tohoku University, [b)] Department of Advanced Radiation Technology, TARRI, JAEA

Stress might induce cognition decline. Our previous reports have shown that the bromine levels were decreased in mice brain subjected chronic-restraint stress [2)] or social isolation stress [1)] when compared with that of control mice. In this report, we analyzed a distribution change of trace metals in methamphetamine treated mice brain slices. It is well known that repeated administration of methamphetamine (METH) caused abnormal behavior and impaired cognitive function [3)]. Therefore, evil influences of drug abuse become a serious social issue. There is a report [4)] suggested that cognitive impairment may be closely associated with neuroanatomical damage and zinc metabolism in Alzheimer's disease. To examine the change of the distribution on trace metal in a brain slices of treated by abuse drugs might be useful information to establish for a new pharmaco-therapeutics of mental disorders resulting from drug abuse.

PIXE (Particle Induced X-ray Emission) is a powerful method for the analysis of trace elements. In-air micro-PIXE was developed at the Takasaki Ion Accelerators for Advanced Radiation Application (TIARA), JAEA. Micro-PIXE allows analyzing the spatial distribution of the elements quantitatively.

Figure 1 shows the beam irradiation image in region of 90×90 μm^2 in the brain slice of control and METH treated mice, and the image of bromine and calcium in the slices of both mice. Mice were injected i.p. with METH once per day for consecutive seven days. One week and two weeks after, the mice were injected i.p. with METH once again. The control mice were injected saline at the same schedule of METH administration. The mice were given a daily 50 mg/kg of 5-bromo-2'-deoxyuridine (BrdU) injection for five consecutive days before remove the brains.

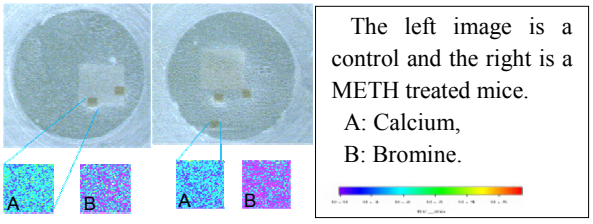

Fig. 1 Beam irradiation, calcium and bromine image (90×90 μm) of brain slices.

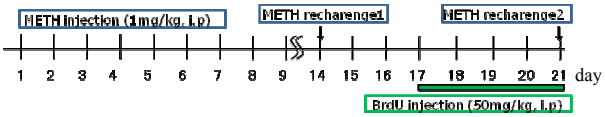

Fig. 2 Drug administration schedule.

After 2-h final BrdU injection, the brain were removed and immediately quick-frozen in dry ice to –40 °C. Each brain was cryosectioned sagittally at 16 μm thickness. The brain slices were mounted on polycarbonate films, which were processed with 5N sulfuric acid. The brain slices were examined with beam currents of almost 120 pA. PIXE data were obtained using incident 3 MeV proton microbeams.

All experiments were performed in accordance with institutional guidelines, and experiments protocols were approved by the Animal Care Committee of Tohoku University.

Figure 2 shows an administration schedule of METH for male C57BL/6 mice. Mice were injected with METH (1 mg/kg, i.p.) once per day for consecutive seven days. In this condition, METH administration mice might be becomes a state of psychotic disease.

The amounts of trace metal in the slices are shown in Fig. 3. The amount of bromine in brain slice of METH administered mice was lower than that of control mice. However, in the case of calcium and zinc, those amounts were little higher than that of control mice.

These results suggested that the neurogenesis of METH clonic administration mice might be lower than that of their Wild type mice. Abuse drugs might cause neurodegenenesis in mice.

References

1) Sakurai E et al., JAEA Takasaki Ann. Rep. 2007 (2008) 122.
2) Sakurai E et al., JAEA Takasaki Ann. Rep. 2006 (2008) 182.
3) Dai H et al., Psychopharmacology 183 (2005) 285-293.
4) Youdim MB., Neurotox Res. 14 (2008) 45-56.

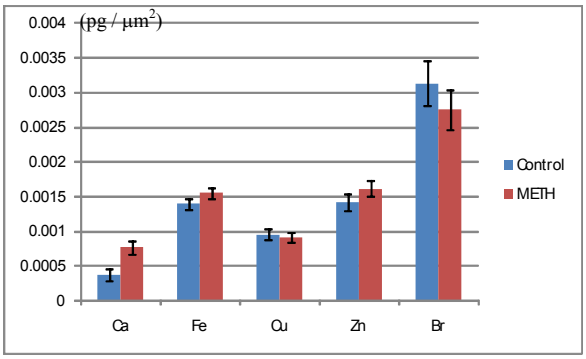

Fig. 3 Amount of trace metals in 1 μm^2 of brain slices.

3-50 Direct Visualization and Quantification of Anticancer Agent cis-diamminedichloro-platinum(II) in Human Lung Cancer Cells Using In-Air Micro-PIXE Analysis

H. Sakurai [a)], M. Okamoto [a)], M. Hasegawa [b)], T. Satoh [c)], M. Oikawa [d)], T. Kamiya [c)], K. Arakawa [c)] and T. Nakano [a)]

[a)] Gunma University Graduate School of Medicine, [b)] Nara Medical University, [c)] Department of Advanced Radiation Technology, TARRI, JAEA, [d)] National Institute of Radiological Sciences

An elemental analysis system using an ion micro-beam combined with a particle-induced X-ray emission (PIXE) method (in-air micro-PIXE system) was used to develop an imaging and quantification method for intracellular cis-diamminedichloro-platinum(II) (CDDP) in a human lung cancer cell line[1]. A human lung adenocarcinoma cell line, A549, was cultured and nuclear labeling was carried out by incubating the cells with BrdU. The cells were then exposed to CDDP at concentrations ranging from 1 μM to 1 mM, for 30 min to 24 h. After drug treatment, samples were washed and frozen with liquid nitrogen, and freeze-dried for 24 h. Standard samples were made using agar containing several concentrations of CDDP. Experiments using standard samples showed a linear correlation between CDDP concentration and platinum signal strength. No clear platinum signal was detected after exposure to CDDP for 24 h at doses between 1 and 100 μM. However, significant Pt signals were observed at 1 mM. In that case, the Pt image of in-air micro-PIXE had enough quality to visualize nucleus and cytoplasm (Fig. 1). The detected signals of CDDP were stronger in the nucleus than in the cytoplasm (Fig. 1). A time-course study showed increased CDDP uptake in cells after longer drug exposure periods (Fig. 2). The use of this system enables the high-resolution visualization of intracellular CDDP distribution and measurement of intracellular CDDP concentrations.

The present results showed that the accumulation of CDDP in human lung cancer cells increased with drug exposure time. Because the concentration of CDDP is very high and most cells lose viability after 24 h exposure to CDDP, the uptake of CDDP in the cells must occur by a passive mechanism under no physiological condition. Further efforts are needed to increase the sensitivity of the authors' system for detecting lesser amounts of platinum in the cells.

In conclusion, the present study demonstrates the application of elemental analysis using in-air micro-PIXE to biomedical samples. The use of this system enabled the high-resolution visualization of intracellular CDDP distribution and measurement of intracellular CDDP concentrations. In the postgenomic era, the use of trace elements through this technique may promote new findings in cancer research.

Reference

1) H. Sakurai et al., Cancer Science 99 (2008) 901-904.

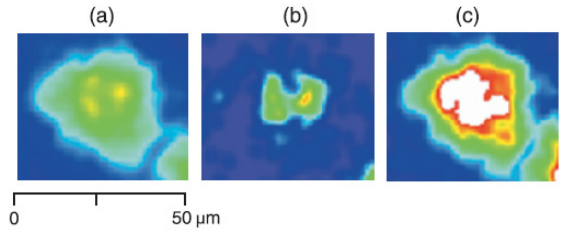

Fig. 1 Elemental maps of (a) phosphorus, (b) bromine and, (c) platinum in a human lung cancer cell line, A549. The cells were periodically treated with 10 μmol bromodeoxyuridine (BrdU) before exposure to 1 mmol *cis*-diamminedichloro-platinum(II) (CDDP) for 24 h. Diffused intracellular phosphorus distribution is observed, and bromine accumulation is apparent in cell nuclei. The platinum signal detected in the intracellular nucleus is stronger than that in the cytoplasm.

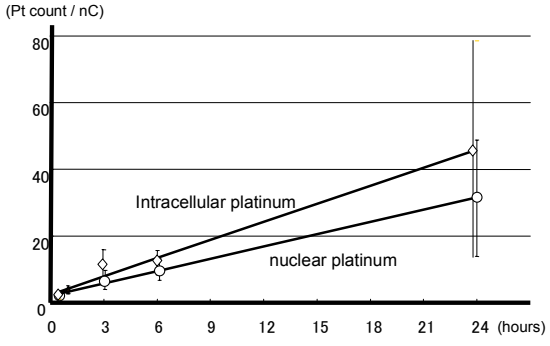

Fig. 2 Intracellular and nuclear platinum count/nC after exposure to 1 mM CDDP. Increased CDDP uptake is observed in cells with linear correlation after longer drug exposure. CDDP uptake is higher in the nucleus than in the cytoplasm.

3-51 Measurement of Fluorine Distribution in Carious Enamel around Fluoride-containing Materials Using PIGE/PIXE System

H. Komatsu [a], Y. Matsuda [a], T. Kijimura [a], K. Okuyama [a], H. Yamamoto [b], Y. Iwami [b], S. Ebisu [b], M. Nomachi [b], K. Yasuda [c], T. Satoh [d] and M. Oikawa [e]

[a] Hokkaido University, [b] Osaka University Graduate School of Dentistry, [c] The Wakasa wan Energy Research Center, [d] Department of Advanced Radiation Technology, TARRI, JAEA, [e] National Institute of Radiological Sciences

Introduction

It is well established that the fluorine is a possible agent for caries prevention. The fluoride that contained some restorative material was also demonstrated as a great benefit for preventing dental caries. The purpose of this study is to measure the fluorine distribution in carious enamel around fluoride-containing materials using an in-air micro-PIGE/PIXE system at TIARA[1].

Material and Methods

Class V cavities in the buccal surfaces of 7 extracted human teeth were drilled and filled with glass ionomer cements (fluoride-containing); Fuji IX FAST (FN), Fuji VII (FS), and RIVA S/C (RV). Two 170 μm longitudinal sections including the filling material were obtained from each tooth. All tooth surfaces, except the outer surface of enamel, were coated with a wax. In order to simulate daily acid attack occurring in the oral cavity, the pH-cycling (pH 7.0-pH 4.5) was carried out for 5 weeks for preparing artificial carious enamel using an automatic pH cycling system[2]. After pH-cycling, F distribution of the outer lesion in each specimen was evaluated using micro-PIGE/PIXE system[1]. The fluorine distribution in carious enamel was analyzed at more than 100 μm separation from the cavity wall. The outermost surface of the carious lesion was at the spot containing 5 % of the calcium concentration in intact enamel. For the comparison of fluorine distribution, the average fluorine concentration in each specimen was calculated at area of about 10 μm from the defined surface. The cumulative amount of F in the outer 150 μm of the lesion was then calculated.

Results

F distribution of the specimens after 5-week pH-cycling clearly showed the F uptake from all fluoride-containing materials into the outer lesion (Fig. 1). For fluoride-containing materials, the amount of F uptake had significantly higher value comparing to those before pH-cycling. There was no significant difference in the F uptake between the materials. When compared with each material, there were wide differences in the cumulative amount of F uptake and/or the depth in highest F concentration among the specimens.

Discussion

In this study, the amount of F uptake from all materials increased after pH cycling. In a previous report[3], we demonstrated that it was possible to reduce dissolution rate in artificial carious enamel adjacent to another glass ionomer cement from materials used in the present study. It was also confirmed in the previous report[3] that the amount of F uptake increased after pH cycling. The amount of F uptake from all materials in present study was similar to that in the previous report. Therefore, this result suggested a possibility for reducing the dissolution rate in tooth enamel adjacent to all materials used in this study.

Regarding the wide differences among the specimens in each material, it could be related to tooth variation and analytical method such as the decision making for the outermost surface of carious lesion. However, it was unclear, so it is necessary to further study for estimating analytical methods such as beam energy and gamma-ray detector.

Conclusion

It was confirmed that the amount of F uptake increased after pH cycling for all fluoride-containing materials used in the current study. Although further research is warranted, it can be speculated that it will reduce dissolution rate in tooth enamel.

References

1) H. Yamamoto et al., Nucl. Instrum. Meth. B **210** (2003) 388.
2) Y. Matsuda et al., Dent. Mater. J. 24 (2006) 280.
3) H. Komatsu et al., Nucl. Instrum. Meth. B 260 (2007) 201.

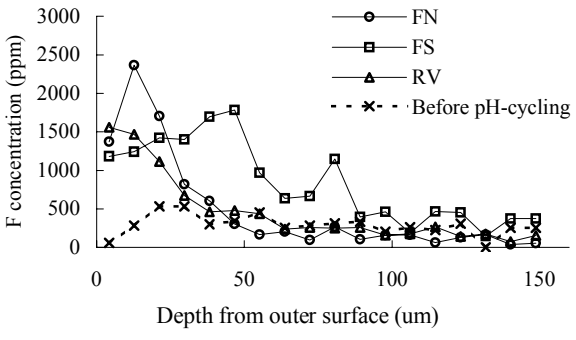

Fig. 1 Mean F distribution of the specimens after 5-week pH-cycling.

3-52 Evaluation of Intracellular Trace Element in Response to Microenvironment in Esophageal Squamous Cell Carcinoma

M. Sakai [a)], E. Yamaki [a)], N. Tanaka [a)], H. Kimura [a)], T. Inose [a)], M. Sohda [a)], M. Nakajima [a)], H. Kato [a)], T. Asao [a)], H. Kuwano [a)], M. Oikawa [b)], T. Satoh [b)] and T. Kamiya [b)]

[a)] Gunma University, Graduate School of Medicine,
[b)] Department of Advanced Radiation Technology, TARRI, JAEA

The interaction between microenvironmental components and tumor cells is bidirectional. Tumor cells and their products are capable of regulating and altering gene expression in nontumor cells residing in or infiltrating into the microenvironment and exert selective pressures on such cells, thereby shaping their phenotype. Conversely, microenvironmental components regulate gene expression in tumor cells thereby directing the tumor into one or several possible molecular evolution pathways, some of which may lead to metastasis [1)]. Thus, investigating the bidirectional interaction can serve to clarify the nature of tumors. Extracellular microenvironment consists of several factors, such as hypoxia, hyposerum, hypoglucose, and hypodensity. Among these factors, tumor hypoxia appears to be strongly associated with tumor propagation, malignant progression, and resistance to therapy and it has thus become a central issue in tumor physiology and cancer treatment. Previous studies suggest that intratumoral oxygen levels may influence a series of biologic parameters that also affect the malignant potential of a neoplasm [2)]. However, the molecular mechanism of these interactions between microenvironmental components and tumor cells at the trace element level has not been fully clarified.

The aim of our study is to evaluate intracellular trace element in response to oxygenation state in a single tumor cell (TE-2: esophageal squamous cell caner (ESCC) cell line) using In- Air Micro- PIXE, the device that enable to visualize trace element distribution in a single cell. For the candidate of microelement to examine in this study, we selected cis-diamminedichloroplatinum (II) (CDDP), which is a key anticancer agent in ESCC.

Cell sample preparation was performed as described previously [3)] but modified as follows. Exponentially growing TE-2 cells were labeled with 100 μL (per 10-cm dish) bromodeoxyuridine (BrdU; BD Biosciences, San Jose, CA, USA) for 24 h. The 4-μm thick Mylar films were stretched between Pyrex glass and Viton rings, followed by immersion in 5 mol sulfuric acid for 2 h and washing with distilled water three times. Twenty-four hours after the BrdU labeling procedure, cells were trypsinized and counted using a hemocytometer, then 1×10^6 cells were seeded on a Mylar film in a culture dish for 24 h under normoxia (O2 : 21%) or hypoxia (O2 : 1%). Before CDDP exposure, CDDP containing medium (0.5-mmol CDDP) was prepaired. The original medium on Mylar film was then replaced with CDDPcontaining medium. After 2 h of drug exposure, this medium was removed and cells were washed five times with a tris-hydroxymethylaminomethane-HNO3 solution (pH 7.4). The cells were then cryofixed by soaking the samples in isopentane at liquid nitrogen temperature. The frozen samples were dried for 24 h in a freeze-drier and kept in a desiccator until PIXE analysis. The In-Air Micro-PIXE analysis was performed as described previously [3)]. We used the calibration curve constructed by Sakurai et al [3)] for the quantitative evaluation of cisplatin.

Figure 1 shows the comparison of intracellular and nuclear CDDP concentration in TE-2 cultured under normoxia and hypoxia. Intracellular CDDP concentration in TE-2 cultured under hypoxia was significantly lower than that of under normoxia. Nuclear CDDP concentration in TE-2 cultured under hypoxia had a tendency to be lower than that of under normoxia. Our results show that tumor hypoxia affect intracellular and nuclear CDDP concentration. The result obtained in this study can be interpreted as indicating the evaluation of intracellular trace element distribution in response to microenvironment.

References

1) IP Witz, Adv. Cancer Res. 100 (2008) 203-229.
2) M. Hockel et al., J. Natl. Cancer Inst. 93 (2001) 266-276.
3) H. Sakurai et al., Science 99 (2008) 901-904.

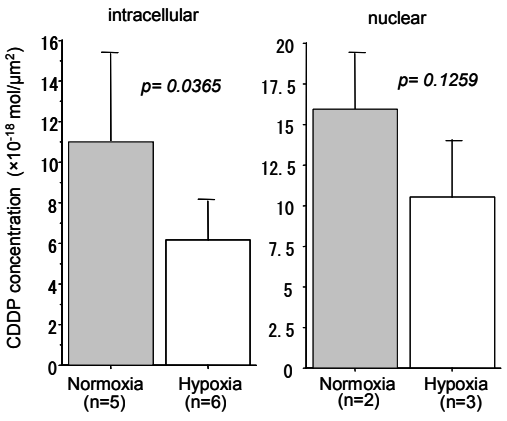

Fig. 1 Comparison of intracellular and nuclear CDDP concentration in TE-2.

3-53 The Optimum Conditions in the Analysis of Boron Micro-Distribution in Tumor Cells Using PIGE

K. Endo [a)], Y. Shibata [a)], T. Yamamoto [a)], K. Nakai [a)], A. Matsumura [a)], T. Satoh [b)], M. Oikawa [c)], K. Arakawa [b)], T. Kamiya [b)] and K. Ishii [d)]

[a)] University of Tsukuba, [b)] Department of Advanced Radiation Technology, TARRI, JAEA, [c)] National Institute of Radiological Sciences, [d)] Tohoku University

Micro particle-induced X-ray emission (micro-PIXE) was applied to determine the inter- and intracellular distribution of boron-10(^{10}B) in tumor cells. Because the energy of micro-PIXE from ^{10}B is too low, particle-induced gamma-ray emission (PIGE) was employed to detect the gamma-rays produced from the nuclear reaction of ^{10}B (p, γ) ^{7}Be.

Cultured 9L gliosarcoma cells grown on polycarbonate film were exposed to sodium borocaptate (BSH). To analyze the inter- and intra-cellular distribution of ^{10}B in 9L gliosarcoma cells, the cells were irradiated with a 1.7 MeV proton beam focused down to a 1 μm diameter and the emitted gamma-rays were detected. The inter- and intracellular distribution of ^{10}B in 9L gliosarcoma cells was directly analyzed using micro-PIGE. The results showed that the distribution of ^{10}B atoms was correctly measured. The distribution of ^{10}B should have been evenly distributed in 9L gliosarcoma cells and some ^{10}B atoms showed that distribution. However, there was a significantly high background and the detection of true ^{10}B atoms was not easy. The main purpose of this study was to determine the optimal conditions to apply this technique in an *in vitro* experiment.

Cultured 9L gliosarcoma cells were grown for 4 days on a 5 μm thick polycarbonate film. These cells were treated with 100 ppm, 250 ppm and 1000 ppm of BSH, respectively on the 3rd and 4th day. These cells were fixed on the polycarbonate film with the acute freezing on the 5th day.

The samples were analyzed to compare the distribution image of the ^{10}B atoms using the micro-PIXE analysis system with a 30 to 60 minute measuring time and a measuring range from 25×25 μm to 100×100 μm, respectively.

The peak ^{10}B atom measurement (428 keV) was small on the measurement spectrum in comparison to the circumference background. It was possible to confirm that ^{10}B atoms were measured.

And then, a mask was created from the distribution of sulphur and a suitable threshold value was determined. Thereafter, a PIGE spectrum was created which was specified by the masked portion and the whole spectrum was compared to the masked spectrum.

It was possible to confirm the presence of a correlation in the distribution of sulphur(S) (tumor cells) and the distribution of ^{10}B atoms because the peak (428 keV) of ^{10}B atoms appeared more clearly in the masked spectrum.

A more clear correlation was observed between the distribution of tumor cells and that of ^{10}B atoms distribution when the two images were combined. This demonstrated that the ^{10}B atom was accumulating around the tumor cells.

In this *in vitro* experiment, various conditions were compared to determine the optimum conditions to yield clear distribution images. The results showed that the tumor-^{10}B distribution was clearly demonstrated at a BSH concentration of 250 ppm. The best measurement ranges were from 50×50 μm to 100×100 μm and the optimal measurement time to obtain the clearest image using PIGE was from 30 to 60 minutes (Fig. 1).

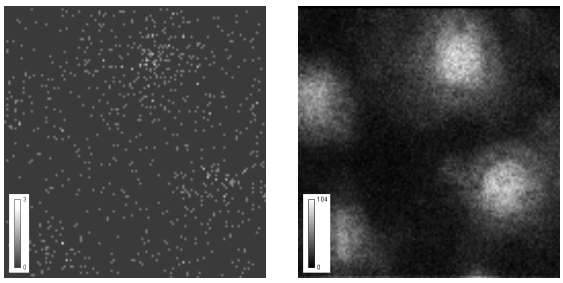

Fig. 1 Distribution of tumor cells(S) and ^{10}B(B).

However, the intracellular micro-distribution of boron could not be clearly detected in this analysis. Improvements are therefore necessary in the technical methods of cell fixation, while the micro-PIXE analyzing system also needs to be further upgraded.

References

1) J.A. Coderre et al., Radiat. Res. 149 (1998) 163-170.
2) M. Wegden et al., Nucl. Instrum. Meth. Phys. Res. B219-220 (2004) 67-71.
3) K. Endo et al., Oncol. Res. 16 (2006) 57-65.

3-54 Kinetics of Radiosensitive Microcapsules through Radiation-Induced P-selectin Guided Accumulation

S. Harada [a)], S. Ehara [a)] K. Ishii [b)], T. Satoh [c)], S. Yamazaki [b)], N. Matuyama [b)] and T. Kamiya [c)]

[a)] Iwate Medical University, [b)] Tohoku University,
[c)] Department of Advanced Radiation Technology, TARRI, JAEA

Introduction

In the first and second Takasaki Advanced Radiation Research Symposium, we reported the innovation of microcapsules for anticancer drug targeting through radiotherapy sessions[1,2]. These microcapsules should be placed in the irradiated area via iv injection. In order to accomplish this aim, we tested the radiation-induced P-selectin guided accumulation: 1) the radiation was given where the microcapsules should be placed; 2) the angigen of P-selectin was induced in the irradiated area; 3) the microcapsules that was labeled with P-selectin antibody was injected intravenously; and 4) the microcapsules was accumulated in the irradiated field through antigen-antibody reaction of P-selectin. In this study, the kinetics of intravenously injected microcapsules were studied using, micro-PIXE camera.

Methods and Materials

The Meth-A-fibrosarcoma that was inoculated in the left hind legs of BALB/c mice were irradiated by ^{60}Co γ ray at single doses of 5, or 10 Gy. The microcapsules were prepared following procedures. The mixture of 0.2% (weight/volume) and 0.1% (weight/volume) were prepared in agete pestle. To this mixture, 0.2 mmol carboplatin (a platinum (Pt)-containing anticancer drug) was added. A droplet of this mixture was sonicated using an ultrasound disintegrator and atomized to yield a solution of $CaCl_2$ that was supplemented with Fe at concentrations of 50%. The polymerization was completed within 5 min to yield microcapsules. The microcapsules thus generated were purified using a Nalgene disposable filter kit (8-0301-84 DP591) and resuspeneded in 0.1 mmol Tris hydroxymethyl aminomethane (THAM) buffer. Resulting microcapsules (1×10^{10}) were injected intravenously through tail vein of mice on 6 hours after irradiation. The accumulation of microcapsules were tested and counted in the 10 fields of 25 μm×25 μm.

Results and Discussion

There were increases of microcapsules in the irradiated tumors. The increases of microcapsules were completed until 6 hours after injection. The accumulation of microcapsules was increased dependently upon radiation doses (Fig. 1). The maximum accumulation was observed on 6 hours after the irradiation of 2.5 Gy, which was 38.1 ± 2.4%.

These accumulations were lower than we expected. In order to achieve the adequate amount of drug, more accumulation is required. The study to increase the accumulation of microcapsules into the irradiated area is underway.

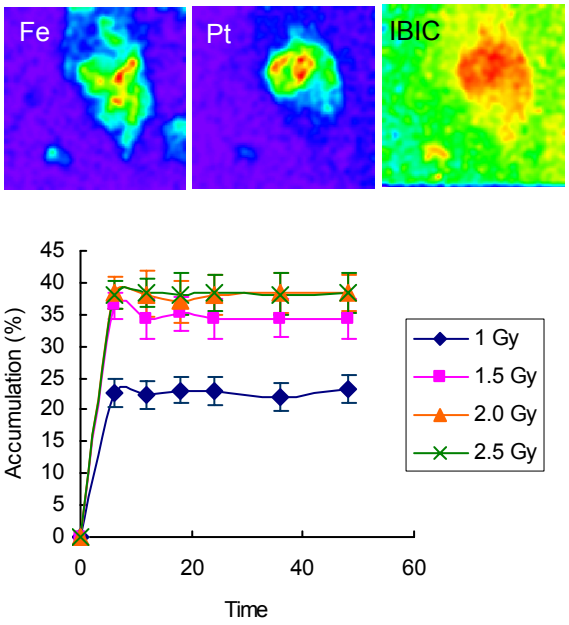

Fig. 1 The accumulation of microcapsules through radiation-induced P-selectin guided accumulation: Entrapped microcapsules that were detected by micro PIXE camera, and their percent accumulation versus time (hours) were shown.

References

1) Harada et al., TIARA Ann. Rep. 2003 (2004) 217.
2) Harada et al., Nucl. Instrum. Meth. B 260 (1) (2007) 16.

3-55 Change of Heavy Metals, Metallothionein and Heat Shock Proteins in Sertoli Cells Induced by Cadmium

Y. Tokita [a)], T. Kusakabe [a)], H. Takada [a)], K. Nakazato [a)], H. D. Moon [a)], K. Suzuki [a)], K. Nakajima [a)], T. Satoh [b)], K. Arakawa [b)] and T. Nagamine [a)]

[a)] Gunma University, [b)] Department of Advanced Radiation Technology, TARRI, JAEA

Background/Aims

Cadmium (Cd) is toxic for various tissues and cells in human, and Sertoli cell is well known to be sensitive to Cd toxicity[1)]. Heavy metals, such as Cd, iron (Fe) and zinc (Zn), are involved in testis damage caused by Cd through unknown mechanism. To identify the changes of heavy metals, we analyzed the elemental distribution in the Cd-exposed Sertoli cells by in-air micro-Particle Induced X-ray Emission (PIXE)[2-8)]. In addition, metallothionein (MT) and heat shock proteins (Hsps) levels are assayed, and apoptosis induction is evaluated.

Methods

The testis was removed from 20-24 day-old Jcl-Wister rats, and Sertoli cells were isolated using sequential enzymatic digestion[9)]. These cells were attached to myler membrane, then exposed by 10 μM of Cd for 24 h. After drying, the samples were assayed by in-air micro PIXE at TIARA. In addition, Seltori cells were sonicated and the metal contents of homogenized solution were determined by atomic absorption spectrometry (Z-6100, HITACHI). MT and Hsps expressions in Sertoli cells following various dose of Cd for 24 h were determined by immune-histochemical staining and western blotting. Apoptotic Sertoli cell death was evaluated by DNA fragmentation test.

Results

X-ray Spectra showed that the distribution of Cd and Fe were increased and Zn was decreased in Sertoli cells exposed by 10 μM of Cd, compared with control (Fig. 1). These results agree with quantitative value obtained by AAS. According to elemental maps of Sertoli cells, focal localizations of Fe were found with a spatial correlation with Cd. Apoptosis of Sertoli cells was significantly induced by more than 5 μM of Cd. MT, Hsp70 and heme oxygenase-1 (HO-1) expression were significantly increased in higher than 2.5 μM of Cd exposure.

Conclusion

Ten μM of Cd exposure induced Sertoli cells apoptosis. Such dose of Cd increased intracellular levels of Cd and Fe and decreased Zn levels in Seritori cells. Furthermore, focal localizations of Fe were found with a spatial correlation with Cd. These findings suggest the intracellular changes of theses metals may be involved in pathogenesis of Cd-induced apoptosis in Seritoli cells.

References

1) L. D. Russel et al., Am. J. Anat. 148, (1977) 313-328.
2) T. Sakai et al., Biol. Trace Elem. Res. Winter (71-72), (1999) 77-82.
3) T. Sakai et al., Nucl. Instrum. Meth. B 190 (2002) 271-275.
4) T. Nagamine et al., Cytokine 34 (2006) 312-319.
5) T. Nagamine et al., Biol Trace Elem Res 117 (2007) 115-126.
6) T. Kusakabe et al., Biometals. 21 (2008) 71-81.
7) K. Nakazato et al., Biometals 21 (2008) 83-91.
8) T. Kusakabe et al. Toxicol In Vitro. 22 (2008) 1469-75.
9) K. Gassei et al., J. Androl. 27 (2006) 611-618.

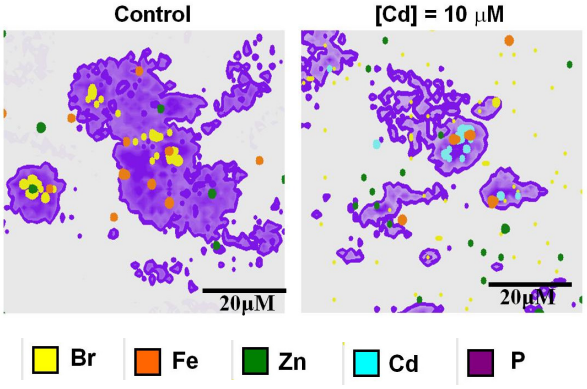

Fig. 1 Elemental map of sertoli cells exposed to Cd. Cd was increased and Br was decreased in Sertoli cells after Cd exposure. Focal localization of Cd was found with a spatial collelation with Fe.

3-50 In-Air Micro-PIXE Analysis on Contents and Distribution of Asbestos in Lung Tissue

Y. Shimizu [a)], K. Dobashi [a)], T. Kusakabe [a)], T. Nagamine [a)], S. Matsuszaki [a)], T. Ishizuka [a)], M. Oikawa [b)], T. Satoh [c)], J. Haga [c)], T. Ohkubo [c)], Y. Ishii [c)], T. Kamiya [c)], K. Arakawa [c)] and M. Mori [a)]

[a)] Gunma University, [b)] National Institute of Radiological Sciences, [c)] Department of Advanced Radiation Technology, TARRI, JAEA

Deposition of asbestos in lung is a risk factor of lung cancer or fibrosis. We demonstrated that In-air Micro Particle Induced X-ray Emission analysis (In-air Micro-PIXE) is useful for assessing the distribution and content of tissue deposited particles using asbestos bodies in raw lung tissue section. Accumulation of inflammatory cells was observed at the site of asbestos deposition. In-air Micro-PIXE system is also useful for analysis of asbestos induced immune reaction comparing its distribution.

アスベストの吸入は肺癌や肺線維症のリスクファクターである。人の肺に吸入された物質の組織内での分布や量を評価することは困難である。In-air Micro Particle Induced X-ray Emission analysis (In-air Micro-PIXE)を用いて外科的生検により得られたアスベスト肺組織、及びアスベスト肺に肺癌を合併した患者の肺癌部分に含まれるアスベストの分布と量とその成分を検討した。

コントロールとして非アスベスト吸入患者の肺組織における非腫瘍部（肺癌患者の癌以外の周辺部分）と腫瘍部を用いた。In-air Micro-PIXE解析によりアスベスト肺では、Si (珪素)、Fe (鉄)、Mg(マグネシウム)からなるアスベストボディーが同定された。アスベストボディーは長径約8 μm以下であるが、In-air Micro-PIXEによる980 μm×980 μmの比較広範囲の照射による定量では、アスベスト肺では肺組織中のバックグランドのS（硫黄）に対して、Feが優位に高かった（Fig. 1）。 50 μm × 50 μmの狭い範囲でのアスベストボディーにターゲットを絞った照射による定量では、アスベスト肺ではSiに対して、Feが優位に高かった（Fig. 2）。これらのことから解析したアスベスト肺では鉄を多く含むアスベストが沈着していることがわかった。

また、In-air Micro-PIXE解析により2次元的に得られた画像と組織のH-E染色から、アスベストボディーの存在する部位にリンパ球やマクロファージが集積していることが観察され、アスベスト沈着により肺組織に炎症を来していることが確認された。

これらのことより、In-air Micro-PIXE解析は肺組織に沈着したアスベストの分布や量及びその成分内容と併せて、沈着により疾患を引き起こしている部位の同定にも有用であることが示唆された。

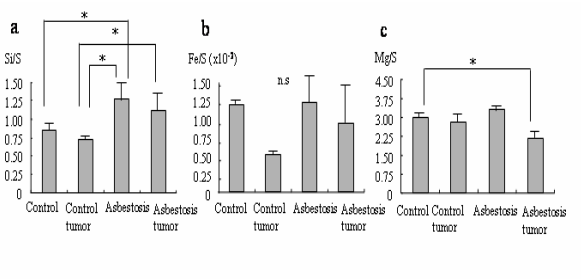

Fig. 1 Large-scale (980 μm × 980 μm) quantitative elemental analysis of lung tissue by in-air micro-PIXE. The ratio of each element relative to S (background content in lung tissue) was calculated for Si (a), Fe (b), Mg (c).

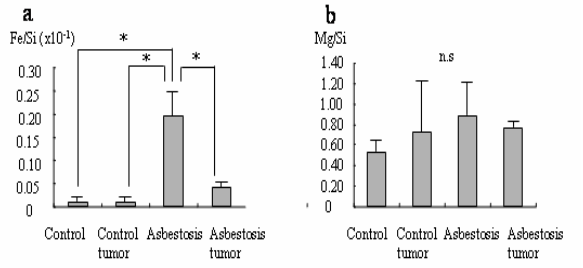

Fig. 2 Small-scale (50 μm×50 μm) quantitative elemental analysis of lung tissue by in-air micro-PIXE. The ratio relative to the Si content of lung tissue was calculated for Fe (a), Mg (b).

Reference

1) Y. Shimizu et al., Int. J. Imunopathol. Pharmacol. (2008) 567-576.

4. Advanced Materials, Analysis and Novel Technology

4-01 Effects of Ion Irradiation on Gasochromism of Polycrystalline WO_3 Films

S. Yamamoto, A. Inouye, M. Sugimoto and M. Yoshikawa

Environment and Industrial Materials Research Division, QuBS, JAEA

Gasochromic materials, coloration by gases, have considerable promise as the optical gas sensing materials. Tungsten trioxide oxide (WO_3) thin films coated with noble metal (Pd, Pt) catalysts can be used for optical hydrogen sensors with an optical fiber for the monitoring of hydrogen leakage. In this study, we investigated the effects of ion irradiation on crystalline structure and gasochromism of WO_3 films.

WO_3 films were prepared by a reactive rf magnetron sputtering from a W (purity 99.9%) target in an argon and oxygen mixture. The films with a 300 nm thickness were deposited on mirror-polished SiO_2 substrates. The substrates were maintained at 200 °C during the deposition. To fabricate stoichiometric WO_3 films, deposited films were annealed at a temperature of 400 °C in air for 2 h using an electric furnace. The crystallographic structure of WO_3 films was determined by X-ray diffraction (XRD). Ion irradiations of 350 keV helium (^{4}He) and oxygen (^{16}O) were performed in a vacuum condition (~10^{-4} Pa) using a 400-kV ion implanter at JAEA/Takasaki. The fluence of ion irradiation was up to 1×10^{17} cm^{-2}. The projected range of the 350 keV He^+ and O^+ ions in the WO_3 films are 1,080 and 455 nm estimated by SRIM2003 simulation. In this case, irradiated ions were expected to penetrate the WO_3 films. To evaluate the gasochromic coloration of WO_3 films, the films were coated with a Pd layer (15 nm) by sputtering. And then, the transmittance at a wavelength of 645 nm from a light-emitting diode (LED) was measured using a spectrometer while an argon gas including 1% hydrogen was exposed to the samples in a gas flow of 100 sccm (standard cc/min). Figure 1 shows XRD patterns of WO_3 films un-radiated and after 350 keV O^+ ion irradiated; (a) un-irradiated, (b) 1×10^{14}, (c) 3×10^{15} and (d) 1×10^{17} cm^{-2}, respectively. It can be seen that the intensity of the diffraction peaks from WO_3 film become lower, and they are broader by increasing the ion fluences, which imply that polycrystalline WO_3 films were amorphized by introducing defects with ion irradiation. The dependence of ion fluence on gasochromic coloration of the WO_3 films is summarized in Fig. 2. The ratio T/T_0 of ion irradiated films, the lower values correspond to the higher performance of gasochromic properties, was taken after an exposure of 20 minutes in 1% H_2/Ar. The ratio T/T_0 of 350 keV O^+ ion irradiated films reaches a minimum value at fluence of around 5×10^{15} cm^{-2}, then increases with increasing the ion fluence until a saturation value. On the other hand, T/T_0 of the He^+ ion irradiated films decreases at fluence of around 1×10^{17} cm^{-2}.

These results indicate that the gasochromic coloration of WO_3 film was improved by ion irradiation. In addition, the results imply an existence of critical ion fluence for the improvement of the gasochromic coloration. For 350 keV O^+ ion-irradiation, the results of XRD in Fig. 1 show the disorder of the crystalline structure in the WO_3 films increases with increasing ion fluence. It may be said that improvement of gasochromic coloration is related to the amorphization of the films with introducing defects such as oxygen vacancies.

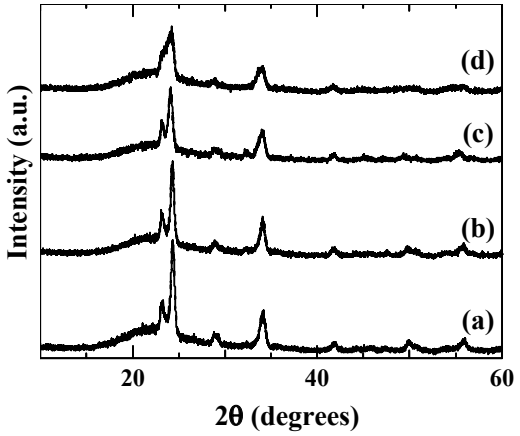

Fig. 1 XRD patterns for the WO_3 films unirradiated and after 350 keV O^+ ion irradiated; (a) un-irradiated, (b) 1×10^{14}, (c) 3×10^{15} and (d) 1×10^{17} cm^{-2}, respectively.

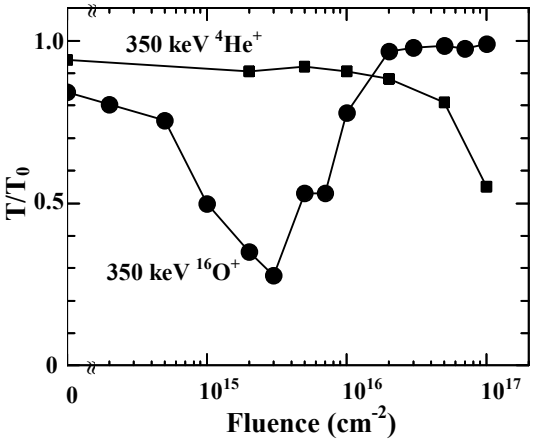

Fig. 2 The dependence of ion fluence on gasochromic coloration of the WO_3 films. The ratio T/T_0 of ion irradiated films was taken after an exposure of 20 minutes in 1% H_2/Ar.

4-02 Multi-Functional Nanowires Based on Biomacromolecules by Single Particle Nano-fabrication Technique

S. Seki [a)], S. Watanabe [a)], M. Sugimoto [b)], T. Sato [b)], M. Yoshikawa [b)] and S. Tsukuda [c)]

[a)] Division of Applied Chemistry, Graduate School of Engineering, Osaka University,
[b)] Environment and Industrial Materials Research Division, QuBS, JAEA,
[c)] Institute of Multidisciplinary Research for Advanced Materials, Tohoku University

High energy charged particles have often been characterized by their hard interaction with the organic materials, giving cylinder-like nano-space of ion tracks along the particle trajectories where reactive intermediates (ion radicals, neutral radicals, etc.) are produced non-homogeneously with extremely high density. The chemical reactions within the limited nano-space are feasible to produce one dimentional (1-D) nano-materials, and we have successfully produced 1-D nanowires based on the cross-linking reactions of the polymers. The present nano-scaled negative tone imaging technique (single particle nano-fablication technique: SPNT) is applicable to a variety of polymeric materials with equally controlled sizes (length, thickness, number density, etc.) [1-4].

Cyclodextrins (CDs) are one of cyclic oligosuccharides that several molecules of D-glucoses are combined each other by glucosidic linkage. Inside of circular configuration of CDs is a hydrophobic hole whose size is adapted for including other small molecules, so CDs indicates selective adsorbability for hydrophobic molecules fitted the hole size and applied as absorbents in the gas chromatograph, the high-performance liquid chromatograph, etc. In this paper, the nano-structures based on β-CDs and their blends with polymers were formed by SPNT. The cross-linking reactions in the ion tracks result in localized gelation, giving isolated β-CD nanowires on substrates.

The radiation sensitivity of polymers, such as G values (number of reactions per 100 eV of absorbed dose), have been studied extensively for many polymers and types of radiation. The specific properties of ion beams have been characterized by the linear energy transfer (LET), given by the energy deposition of an incident particle per unit length. In order to increase the efficiency of cross-linking reactions and the tolerance for the fragmentation, per(6-acetyl)-β-CD and poly(4-bromostyrene) (PBrS) with high cross-linking efficiency were blended and spin-coated on the Si substrate. High energy particles penetrating into thin film of the blend polymer (PBrS-β-CD) promote effectively cross-linking reaction along the trajectories. The development procedure isolated the nanowires on the substrate as shown in Fig. 1. All nanowires are no longer standing, collapsed onto on the substrate observed as the 2-D images. The size of nanowires was depended on cross-linking efficiency of sample materials with high quantitative correlation. The gelation of the polymer materials allows the derivation of energy density (ρ_{cr} eV nm^{-3}) at the boundary of an ion track as a function of cross-linking efficiency (G(x) (100 eV)$^{-1}$).

The theoretical estimate of r is given by [5,6]:

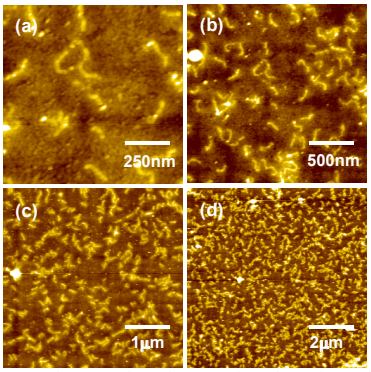

Fig. 1 AFM micrographs of nanowires based on the blended polymer of per(6-acetyl)-β-CD and PBrS produced by SPNT. Images (a) – (d) were observed in the thin films of the blended polymer at 200 nm thick after irradiation of 450 MeV Xe ion beams at the fluence of 3.0×10^9 ions cm^{-2}.

$$r^2 = \frac{LET \cdot G(x) mN}{400\pi\rho A}\left[\ln\left(\frac{e^{1/2} r_p}{r_c}\right)\right]^{-1} \qquad (1)$$

where r_c and r_p are radii of core and penumbra areas in an ion track, respectively. The radii of the PBrS-β-CD and PBrS nanowires were determined 4.4, and 5.9 nm by AFM measurement and calculation on the ellipse model, respectively [6]. The values of G(x) for PBrS-β-CD and PBrS were 0.22 and 0.39 by calculation using eq. 1, with the following empirical parameters: LET = 9300 eV nm^{-1}, ρ = 1.28 g cm^{-3}, and mN = 6.5×10^4 g mol^{-1}. The value of G(x) for PBrS were reported as 0.30 - 1.6 (100 eV)$^{-1}$, which corresponded to calculated value. The significant decrease in cross-linking efficiency between PBrS-β-CD and PBrS indicates the blended materials nanowires consisted essentially of well blended material, and the included per(6-acetyl)-β-CD inhibits cross-linking reaction, resulting in reduced G value of PBrS-β-CD. It would be possible to control the radial size of nanowires by changing the concentration of the mixtures. The lengths of nanowires on each sample also corresponds to the initial thickness of the target polymer films, thus functional addition by blended β-CD into nano-structures and the precise size controls by SPNT are effective for suger-polymer composite nano-materials.

References

1) S. Seki et al., *Phys. Rev. B,* **70** (2004) 144203.
2) S. Seki et al., *Adv. Mater.,* **13** (2001) 1663.
3) S. Tsukuda et al., *J. Phys. Chem.*, **108** (2004) 3407.
4) S. Tsukuda et al., *J. Phys. Chem. B*, **110** (2006) 19319.
5) S. Seki et al., *Macromolecules*, **39** (2006) 7446.
6) S. Tsukuda et al, *Appl. Phys. Lett.*, **87** (2005) 233119.
7) W. Burlant et al., *J. Polym. Sci*. **58** (1962) 491.

4-03 Formation of Hybrid Nano-structures by Ion Beam Irradiation to the Sol-Gel Film

S. Tsukuda [a)], S. Seki [b)], M. Sugimoto [c)], A. Idesaki [c)], S. Watanabe [b)] and S.-I. Tanaka [a)]

[a)] Institute of Multidisciplinary Research for Advanced Materials, Tohoku University,
[b)] Division of Applied Chemistry, Graduate School of Engineering, Osaka University,
[c)] Environment and Industrial Materials Research Division, QuBS, JAEA

Ion bombardment can release densely active intermediates within a cylindrical area along the passage of a single ion. The cylindrical area, which deposited high-energy form the projectile ion, is sometimes called an "ion track". The inhomogeneous energy deposition along an ion trajectory (ion track) plays a crucial role, allowing for high spatial selectivity in the distribution of radiation dose. The ionization and excitation processes that occur in ion tracks result in the generation of active intermediates at high density, leading to chemical reactions.

Our group has been examining the use of cross-linking reactions in the latent tracks for the direct formation of nanostructures [1-4]. The heavy-ion irradiation of a cross-linking polymer thin film has been shown to cause cross-linking reactions along ion tracks, yielding a nanogel with reduced solubility in organic solvents. Developing irradiated samples using an organic solvent to remove a non-cross-linked polymer affords isolated nanowires with precisely controllable size and number density [1,3]. Nanowires have been prepared in this manner from several types of polymers. In this paper, we report the direct formation of the inorganic-organic hybrid nanowires in the hybrid films using this technique (single particle nano-fabrication technique: SPNT).

The negative tone hybrid sol-gel materials were composed by typical sol-gel synthesis. Poly-(vinylpyrrolidone) (PVP) or poly(hydroxystyrene) (PHS) were dissolved in EtOH at 5 wt%, and titanium isopropoxide (TIP) or tetraethoxysilane (TEOS) were added to the solutions with 1 wt% against dissolved PVP and PHS, respectively. EtOH was used as solvent, distilled water for hydrolysis and HCl as catalysts. PVP, PHS and sol-gel materials (PVP/TEOS, PHS/TEOS, and PHS/TIP) were spin-coated on Si substrates from the respective toluene and sol-gel solutions at 5 wt%. These thin films of PVP, PHS and hybrids were subsequently placed in a vacuum chamber and exposed to 450 MeV Xe ion beams at the Takasaki Ion Accelerators for Advanced Radiation Application (TIARA) cyclotron accelerator facility of the Japan Atomic Energy Agency. After irradiation, the samples were washed using EtOH for 2 minutes. The irradiated part of the film, where a polymer gel was formed, was insoluble in EtOH. After development and drying, the direct observation of the surface of the substrates were performed using an atomic force microscope (AFM Seiko Instruments Inc.(SII) SPI-4000).

In crosslinking type polymers such as PVP and PHS, the cross-linking reactions along the ion track result in the formation of a nanowire with ~20 nm radii in thin films. The nanowires were not isolated at high fluencies (1.0×10^{12} ~ ions cm^{-2}). However, ion irradiation at low fluence (1.0×10^{9}~1.0×10^{10} ions cm^{-2}) without overlapping between ion tracks produces single ion events in target materials. Therefore, a non-cross-linked area can be removed by development with organic solvents, utilizing the change in solubility due to the gelation of the polymers. The nanowires based on PVP and PHS formed by ion bombardment can therefore be completely isolated on the substrate, as shown in Fig. 1 (a) and (b), respectively. The hybrid nanowires were also successfully formed by ion beam irradiation to the hybrid films. The nanowires based on PVP/TEOS (c), PHS and TEOS belnd polymer: PHS/TEOS (d), and PHS and TIP belnd polymer: PVP/TIP (e) can be observed on the substrate after development procedures. It is very useful for formation of the 1D hybrid nanostructures to apply the single ion events to the hybrid solgel materials.

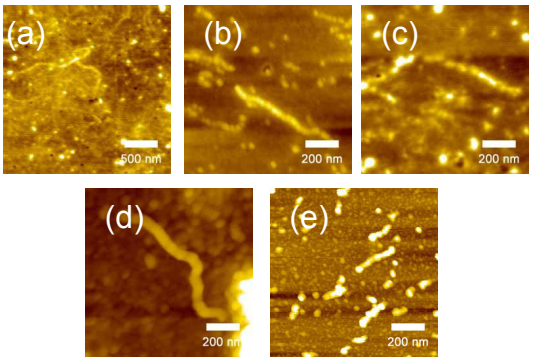

Fig. 1 AFM micrographs of nanowires formed by 450 MeV Xe ion beam irradiation to a variety of polymer thin films. (a), (b), (c), (d) and (e) are recorded in PVP, PHS, (PVP and TEOS blend polymer: PVP/TEOS), (PHS and TEOS blend polymer: PHS/TEOS), and (PHS and TIP blend polymer: PHS/TIP) with the fluence of 1.0×10^{9} ~ 1.0×10^{10} ions cm^{-2}.

References

1) S. Seki et al., Adv. Mater. 13 (2001) 1663-1665.
2) S. Tsukuda et al., J. Phys. Chem. B 108 (2004) 3407-3409.
3) S. Tsukuda et al., Appl. Phys. Lett. 87 (2005) 233119-1-3.
4) S. Tsukuda et al., Jpn. J. Appl. Phys. 44 (2005) 5839-5842.

4-04 Smart-Cut Processes for Nanopore Device Formation on SIMOX(100)

Y. Ikoma [a)], T. Motooka [a)], S. Munetoh [a)], H. Sakita [a)], Hafizal bin Yahaya [a)], H. Naramoto [b)], K. Narumi [b)], S. Sakai [b)] and Y. Maeda [b, c)]

[a)] Department of Materials Science and Engineering, Kyushu University,
[b)] Advanced Science Research Center, JAEA, [c)] Faculty of Engineering, Kyoto University

A nanometer-sized pore (nanopore) is of great interest for a possible application to molecular sensors such as DNA sequencers [1)]. Recently, we proposed a new nanopore formation which utilizes the {111} faceted pit formation during the SiC/Si(100) heteroepitaxial growth by pulse jet chemical vapor deposition (CVD) [2)]. Since our new method is suitable for mass production of nanopores on Si substrates, it is desired that these nanopores are transferred to different materials by utilizing a cut-and-paste technique. In this study, we investigated the smart cut process[3)] by hydrogen ion implantation into nanopore-formed Silicon-on-Insulator (SOI) substrates.

The nanopore samples were fabricated by pulse jet CVD system which is described elsewhere [2)]. Separation by Implanted Oxygen (SIMOX) (100) with SOI and buried oxide (BOX) layers of 180 nm and 100 nm, respectively, were cleaned by conventional RCA method [4)]. These substrates were introduced into the chamber after being dipped in aqueous 5 % buffered HF in order to remove surface oxides. Electronic grade CH_3SiH_3 was introduced into the growth chamber using a supersonic pulse valve with a nozzle diameter of 0.8 mm. The pulse width and frequency were set at 100 μs and 10 Hz, respectively. The substrate temperature was set at 850 °C. After forming the SiC heteroepitaxial layer and the {111} faceted pits on SOI layer, these samples were dipped into 5% buffered HF solution for 10 min in order to remove the BOX layer under the pits. Hydrogen ion implantation was performed at room temperature with 1.44 MeV up to the dose of 1×10^{17} /cm^2.

Figure 1 shows the scanning electron microscopy (SEM) image of nanopores on SOI substrates. Square pits oriented along <011> directions are homogeneously distributed over the surface. The size of the pit is typically 0.1~0.3 μm at the base. The density of the pit is in the order of 10^8 /cm^2. In addition to the pits, circular patterns with the diameter of ~1 μm are observed. These circular patterns are formed at large (~0.3 μm square) pits. The density of the circular pattern is ~10^6 /cm^2. The observed circular patterns are attributed to the fact that the BOX layer under the pits is removed during the buffered HF dip.

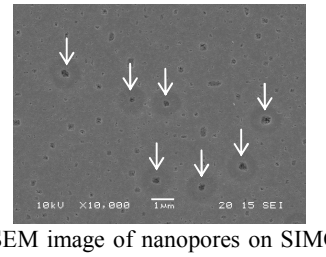

Fig. 1 SEM image of nanopores on SIMOX(100). Arrows indicate various nanopores.

In order to separate the nanopore-grown film from SIMOX substrates, we at first heated the as-implanted sample at ~500 °C in air. Figure 2 shows the SEM images of the sample after smart cut process. It is confirmed that the sample surface is successfully cut with the depth at 10 μm from the substrate surface. We carried out the pasting of the nanopore grown film on the SIMOX(100) surface. The as-implanted sample surface was contacted with a SIMOX(100) surface after hydrophilic treatment, and heated at 500 °C in N_2 ambient. Figure 3 shows the SIMOX(100) surface after smart cutting the pasted surface with nanopores. It is found that some parts of the nanopore film are pasted on the SIMOX surface. The typical size of the pasted pieces is in the order of 100 μm. These results suggest that it will be possible to fabricate the nanopore devices by utilizing and smart cut processes.

References

1) M. Rhee and M. A. Burns, Trends Biotechnol. 24 (2006) 580.
2) Y. Ikoma et al., Proc. of SPIE 6984 (2008) 69841V.
3) M. Bruel, Nucl. Instrum. Meth. B 108 (1996) 313.
4) W. Kern and D. A. Puotinen, RCA Rev. 31 (1970) 187.

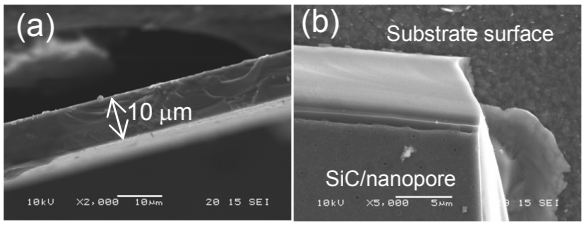

Fig. 2 SEM (a) cross-sectional image of nanopore film, (b) surface morphology of nanopore and smart cut surfaces obtained by the smart cut process.

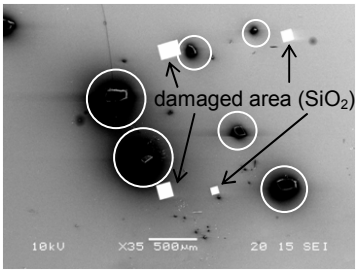

Fig. 3 SEM image of SIMOX(100) surface after smart-cutting the pasted surface with nanopores. Circles indicate the pasted samples.

4-05 Effects of Ion Irradiation on Photoluminescence of SiC Nanotubes

T. Taguchi [a)], M. Saeki [b)], K. Kodama [a)], S. Yamamoto [c)], A. Inoue [c)], H. Yamamoto [a)] and S. Shamoto [a)]

[a)] Neutron Material Research Center, QuBS, JAEA, [b)] Advanced Photon Research Center, QuBS, JAEA, [c)] Environment and Industrial Materials Research Division, QuBS, JAEA

Since the discovery of carbon nanotubes (CNTs) in 1991, significant numbers of researchers have synthesized new one-dimensional nanostructured materials such as nanotubes, nanorods and nanowhiskers for potential applications. Some of them have reported that many nanomaterials such as TiC, NbC, BN, C/C/N, SiO_2 and GaN nanostructures are fabricated from CNTs as the template. We reported that the C-SiC coaxial nanotubes, which were CNTs sheathed with SiC, were formed. Furthermore, the single-phase SiC nanotubes were successfully synthesized by heating the C-SiC coaxial nanotubes in air[1,2]. SiC is one of the most important wide-band-gap semiconducting materials and has excellent stability against irradiation. Therefore, SiC offers exciting opportunities in electronic devices and in short wavelength optical devices under irradiation environments. Applications of SiC in optical devices are limited due to its indirect band gap nature, which leads to very low light emission. It has been, however, reported that intensive light emission from nano-sized or porous indirect-band-gap semiconductors became possible. And the effect of irradiation on photoluminescence of SiC nanotubes has not been investigated. The purpose of this study is, therefore, to investigate the effect of ion irradiation on photoluminescence of SiC nanotubes.

CNTs (GSI Creos Corporation, Tokyo, Japan) was used as the template. The C-SiC coaxial nanotubes were synthesized by heating CNTs with Si powder (The Nilaco Corporation, Tokyo, Japan) at 1200 ºC for 100 h in a vacuum. Single-phase SiC nantoubes were formed by the heat treatment of C-SiC coaxial nanotubes at 600 ºC for 2 h in air. Thin films of single-phase SiC nanotubes were prepared on the alumina plates by depositing with the single-phase SiC nanotubes dispersed in ethanol. These thin films of single-phase SiC nanotubes were irradiated with 3.0 MeV Si^{2+} ions at 190 ºC to 1200 ºC. The ion fluence was 6.4×10^{20} ions/m^2. Photoluminescence of SiC nanotubes dispersed in ethanol were measured at room temperature by YAG laser with the wavelength of 266 nm.

The photoluminescence spectra of SiC nanotubes dispersed in ethanol before and after ion irradiation are shown in Fig. 1. A broad photoluminescence emission peak is observed at the center wavelength of 430 to 460 nm in the un-irradiated and irradiated SiC nanotubes.

Figure 2 shows the change of photoluminescence emission peak of SiC nanotubes by ion irradiation. This result reveals that the photoluminescence peak decreases by the ion irradiation and increases with increasing irradiation temperature. The blue emission properties of SiC nanotubes are of significant interest for their potential blue emitting device application. Moreover, these results indicate that there is the possibility of controlling the photoluminescence emission peak by ion irradiation temperature.

References

1) T. Taguchi et al., J. Am. Ceram. Soc. 88 [2] (2005) 459-461.
2) T. Taguchi et al., Physica E 28[4] (2005) 431-438.

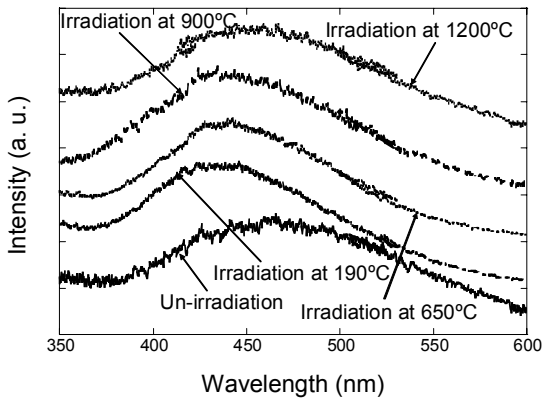

Fig. 1 Photoluminescence of SiCNTs before and after ion irradiation at several temperature.

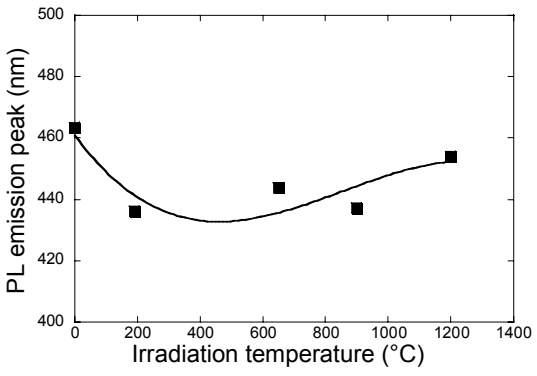

Fig. 2 Change of PL emission peak of SiCNTs by ion irradiation.

4-06 Pd-Folded Ceramic Nano Fiber Synthesis by Ion Beam Irradiation from Precursor Polymer Blend

M. Sugimoto [a)], A. Idesaki [a)], M. Yoshikawa [a)] and S. Seki [b)]

[a)] Environment and Industrial Materials Research Division, QuBS, JAEA,
[b)] Department of Applied Chemistry, Osaka University

Nano fiber with quite large surface area shows excellent characteristics of absorption and reaction activity compared with bulk materials. Recently, SiC nano fiber has been successfully obtained by ion beam irradiation that produces cross-linking within the ion track [1)]. This process suggests that a catalyst-folded ceramic nano fiber can be fabricated if a polymer blend containing catalytic metal is synthesized. In this research, we report the synthesis processes of palladium (Pd) folded ceramic nano fiber formed from the polymer blend with polycarbosilane (PCS) and Palladium(II) acetate ($Pd(OAc)_2$).

$Pd(OAc)_2$ and PCS were dissolved in tetrahydrofuran (THF) separately, then the $Pd(OAc)_2$ solution was added by dropping to the PCS solution at ambient temperature. After the mixing, the THF was evaporated, and then a polymer blend of PCS and $Pd(OAc)_2$ (PCS-$Pd(OAc)_2$) was obtained. The mass ratio of PCS / $Pd(OAc)_2$ was 15 / 1. The PCS-$Pd(OAc)_2$ solved into toluene, then the solution at 5 mass% was spin-coated on polished Si substrates to make the polymer thin films. The films were irradiated with 388 MeV $^{58}Ni^{15+}$, 450 MeV $^{129}Xe^{23+}$ and 500 MeV $^{197}Au^{31+}$ ion beams in vacuum at ambient temperature.

After irradiation, the samples were treated by toluene for 120 sec. The crosslinked part insoluble in the solvent was developed as polymer nano fibers. This was fired in argon atmosphere at 1,273 K for 1,800 sec using an electric furnace with a heating ramp rate of 250 K/h and then cooled down to room temperature, giving the final ceramic nano fibers on the substrate. Direct observation of the nano fibers was conducted using Scanning Probe Microscopy (SPM) Seiko Instruments Inc. SPA-400 using dynamic force microscope method. The size of cross-section of a nano fiber is defined as an average radius of cross-sectional measurements of a nano fiber.

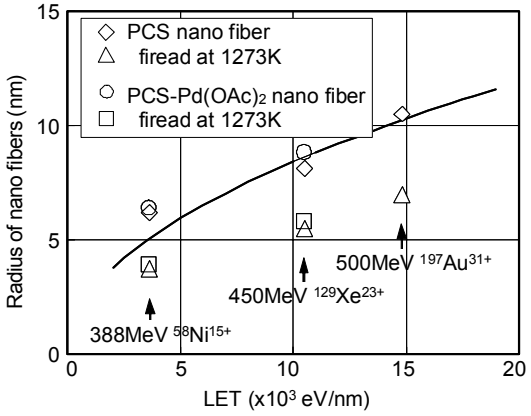

Fig. 1 Radii of nano fibers formed by various LET irradiation of PCS and PCS-Pd(OAc)2 thin films determined by the cross section profile of SPM micrograph.

The PCS-$Pd(OAc)_2$ nano fiber was observed on the surface of substrate and remained after firing. Moreover, the fiber shape did not change by heating up to 1,273 K in argon. It is considered that PCS-$Pd(OAc)_2$ changes into inorganic nano fiber via an conversion reaction similar to that of SiC fiber. Radii of polymeric and fired nano fibers formed by ion beam irradiation with various LET are presented in Fig. 1. We had reported that the radius of the nano fiber depended on the radial distribution of energy in a particle track, and the cylindrical area of energy, and Eq.(1) is corresponding to the experiment result of several kinds of polymer nano fibers well [1,2)].

$$r^2 = a \cdot LET \cdot G(x) \cdot m \cdot N \ , \qquad (1)$$

where α is proportional constant, m is the mass of the monomer unit, and N is the degree of polymerization. $G(x)$ denotes the efficiency of cross-linking reaction. Eq.(1) also gives good interpretation to the radii of the PCS-$Pd(OAc)_2$ nano fiber in Fig. 1, however, the radii are a little larger than that of the PCS nano fiber. This reason is thought to be related to the difference between G(x), because the catalytic Pd in the PCS enhances the crosslinking reaction.

By SEM observation of the fired samples, there is no Pd crystal on the substrate surface; however the Pd element was detected by EDS measurement. This indicates that PCS-$Pd(OAc)_2$ nano fiber could fired without elution and aggregation, then Pd is remain in the nano fiber after firing.

Ion beam irradiation can synthesize the catalytic elements folded nano fiber in a simple process. Further investigations are necessary to clarify the catalytic activity.

References

1) M. Sugimoto et. al., Trans. Mater. Res. Soc. Jpn., 33 (2008) 1027.
2) S. Seki et. al., Macromolecules, 38 (2005) 10164.

4-07 Synthesis of a Novel Si-based Precursor for a Catalyst-Loaded SiC Material

A. Idesaki, M. Sugimoto and M. Yoshikawa

Environment and Industrial Materials Research Division, QuBS, JAEA

Silicon carbide (SiC) ceramics which has excellent resistance for high temperature, oxidation, corrosion, and radiation, is expected as a material for use in severe conditions in the field of aerospace, fusion reactor, and so on. Polycarbosilane (PCS), which is one of the Si-based precursors, has been applied for fabrication of SiC products such as fiber, composites, micro parts, coating, and so on. High formability of PCS realizes the fabrication of SiC material with various shapes. In the fabrication process of SiC products, PCS is formed, cured, and finally pyrolyzed in an inert atmosphere. The curing process is a treatment that makes molecules in PCS crosslink in order to maintain formed shapes during subsequent pyrolysis process. A SiC fiber fabricated by using the radiation curing shows excellent thermal resistance at 2,000 K.

Recently, we have studied fabrication of SiC nano fiber utilizing high energy heavy ions, which is called as Single Particle Nanofabrication Technique (SPNT). SPNT is a unique technique in point of that the nano fiber is fabricated by the irradiation of single particle: cylindrical nano fiber is formed in the ion track based on the crosslinking of molecules in PCS. In SPNT, the diameter, length and number density of nano fibers are strictly controlled by ion species and energy, thickness of polymeric target and number of incident ions, respectively. In this process, we can expect to obtain a SiC nano fiber with catalytic performance if a precursor composed of PCS and a transition metal compound is synthesized. We chose palladium(II) acetate ($Pd(OAc)_2$) as the transition metal compound, because palladium is a well known catalyst for automotive emissions control, organic synthesis, and so on. In this work, a novel precursor composed of PCS and $Pd(OAc)_2$ was synthesized and characterized. Furthermore, the catalytic performance of Pd-loaded SiC material obtained by the pyrolysis of precursor was investigated.

PCS is a solid polymer at room temperature and has a number average molecular weight of 2,000. $Pd(OAc)_2$ is orange-brown powder with molar mass of 224.5 g/mol. Each PCS and $Pd(OAc)_2$ were dissolved in tetrahydrofuran (THF). The $Pd(OAc)_2$ solution was added by dropping to the PCS solution with stirring at ambient temperature. After the mixing, THF was evaporated. And then, a precursor composed of PCS and $Pd(OAc)_2$ (PCS-$Pd(OAc)_2$) was obtained. The ratio of PCS/ $Pd(OAc)_2$ was 1/0.8 in weight.

The obtained PCS-$Pd(OAc)_2$ was characterized by Fourier transform infrared spectroscopy (FT-IR) (Fig. 1). Comparing with the spectra of PCS and $Pd(OAc)_2$, it was found that the peak assigned to Si-H stretching (2,100 cm^{-1}) decreased and a peak assigned to C=O stretching (1,716 cm^{-1}) in carboxyl group appeared in the spectrum of PCS-$Pd(OAc)_2$. The appearance of C=O bonds indicates that PCS reacts with the carboxylate groups in $Pd(OAc)_2$. Furthermore, a peak broadening due to the formation of Si-O-Si and/or Si-O-C bonds was found at 1000-1100 cm^{-1}. According to our previous study, the decrease of Si-H bond and the appearance of Si-O-Si and/or Si-O-C bonds indicate the crosslinking of molecules in PCS, therefore, the molecules in PCS are partly crosslinked by reaction with $Pd(OAc)_2$.

The crosslinking of molecules influences on the ceramic yield. According to the result of thermogravimetric analysis (TGA) up to 1,473 K in helium gas atmosphere, the ceramic yield from PCS-$Pd(OAc)_2$ was 70%. In cases of PCS and $Pd(OAc)_2$, the ceramic yield were 56 and 42%, respectively. It was found that $Pd(OAc)_2$ acts as a crosslinking regent of PCS and enhances the ceramic yield.

Pd-loaded SiC material was obtained by the pyrolysis of PCS-$Pd(OAc)_2$ at 1,373 K in argon gas atmosphere and its catalytic performance was evaluated by evolution of CO_2 gas oxidizing CO gas. The CO_2 gas evolved with the amount of 2.4×10^{-6} mol/g from the Pd-loaded SiC material although the CO_2 gas hardly evolved from the SiC material obtained from PCS (7.1×10^{-8} mol/g). This result indicates that a SiC material with catalytic performance can be synthesized from PCS-$Pd(OAc)_2$.

As a summary, a novel precursor composed of PCS and $Pd(OAc)_2$ was synthesized and characterized for the aim of development of catalyst-loaded SiC material in this work. It was found that $Pd(OAc)_2$ acts as a crosslinking regent of PCS leading to enhancement of the ceramic yield and that Pd-loaded SiC material obtained from PCS-$Pd(OAc)_2$ shows a catalytic performance. A Pd-loaded SiC nano fiber is expected to be fabricated from the PCS-$Pd(OAc)_2$ by SPNT.

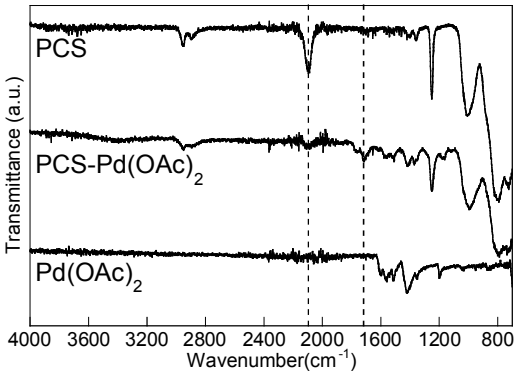

Fig. 1 FT-IR spectrum of PCS-$Pd(OAc)_2$.

4-08 Hydrogen Selectivity of Silicon Carbide Membrane with Different Number of Coatings of SiC Film

A. Takeyama, M. Sugimoto and M. Yoshikawa

Environment and Industrial Materials Research Division, QuBS, JAEA

Silicon Carbide (SiC) membrane has a potential advantage for hydrogen separation due to good heat conductivity, high temperature chemical inertness. The membrane is prepared by repeating coating SiC film in which there are many nanometer sized pores. When the diameter of pores become sufficiently small by repeating the coating, hydrogen diffuses inside pores by molecular sieving mechanism and is separated by the membrane with high selectivity. Hence, it is required to find optimum number of coatings of SiC film to obtain the membrane with high selectivity. In this report, we prepare SiC membranes with different coating number and measured hydrogen and nitrogen permeances.

Porous supports were supplied by Noritake co., limited, which were alpha–alumina tubes coated with thin gamma–alumina layer. A cycrohexan solution of polycarbosilane (PCS) of 3 mass% employed as the precursor solution, was dip-coated on the support. The support coated with the precursor film was cured and cross-linked at room temperature in helium atmosphere by an electron beam irradiation. After the irradiation, the closs-linked film was fired at 973 K for 30 minutes in argon atmosphere. Hydrogen (H_2) and nitrogen (N_2) permeances were measured at 523 K for the membrane with different coating number and the selectivity (H_2/N_2) was calculated from the ratio of H_2 to N_2 permeances.

Temperature dependence of permeances of the membrane are shown in Fig. 1. When the coating number was 1, N_2 permeance monotonically decreased. H_2 permeance was once decreased and increased by increasing the temperature. This raise of the permeance was caused by H_2 diffusion by molecular sieving mechanism. As the temperature increased, the pore diameter reduced to comparable size to mean free path of H_2 molecule by thermal expansion of SiC film. Such small pores induced H_2 diffusion by molecular sieving mechanism[1]. When the coating number was 3, H_2 permeance was monotonically increased. This means the diameter of pores was enough small to induce molecular sieving mechanism even at low temperature. In this experiment, H_2 diffused by molecular sieving mechanism over the temeperature range from 287 to 523 K when the coating number was 3.

Permeances and the selectivity at 523 K are plotted to find the optimum coating number. The decrease of permeances indicates the diameter of pores became smaller by repeating the coating. The highest selectivity was obtained when the coating number was 3. Further repeating the coating, the selectivity became low again. This means the diameter of pores became too small, not only N_2 but H_2 could not penetrate. Further investigations are necessary to clarify the mechanism behind the dependence of pearmenaces and selectivity on the coating number. In summery, we find the optimum coating number of SiC film is 3 to obtain the membrane with high selectivity using our preparation method.

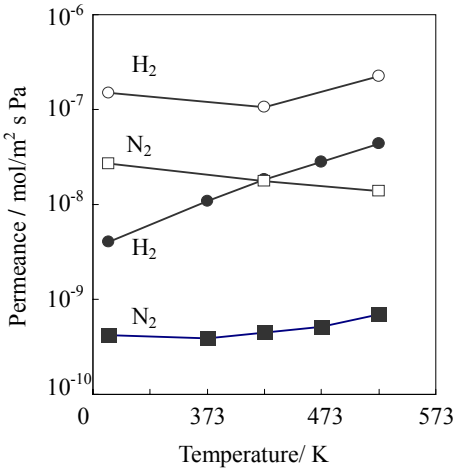

Fig. 1 Temperature dependence of permeances of the membrane. Opened and closed circles represent permeances of the membrane with coating number of 1 and 3.

References

1) J. Dong et al., J. Appl. Phys. 104 (2008) 121301-1.

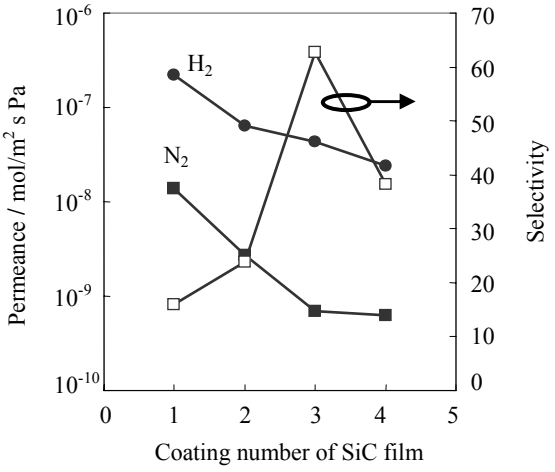

Fig. 2 Plots of H_2, N_2 permeances and selectivity of the membrane vs. coating number of SiC film.

4-09 Au and Pt Nanoclusters Formed by Sputter Deposition on Graphite with and without Ion Irradiation

K. Takahiro [a)], K. Morimoto [a)], Y. Minakuchi [a)], S. Nagata [b)], S. Yamamoto [c)], K. Narumi [d)] and H. Naramoto [d)]

[a)] Department of Chemistry and Materials Technology, Kyoto Institute of Technology, [b)] Institute for Materials Research, Tohoku University, [c)] Environment and Industrial Materials Research Division, QuBS, JAEA, [d)] Advanced Science Research Center, JAEA

Metal nanoclusters deposited on a substrate exhibit unusual physical properties, such as optical, electrical, and magnetic properties. The properties greatly depend on the size and shape of nanoclusters. It is, therefore, necessary to establish the method to control morphology of clusters. The cluster-substrate interaction is a factor to affect the morphology. Ion-irradiation damage produced on a substrate can modify the interaction between a cluster and substrate through defects, e.g., vacancies and dangling bonds. In this work, a defect density dependence of cluster size has been studied by X-ray photoelectron spectroscopy (XPS). XPS has been widely used to characterize electronic structures of metal nanoclusters on various substrates. It is known that the core level binding energy (BE) of nanoclusters shifts toward higher energy from a bulk value, depending on their size. The BE shifts for clusters arise mainly from Coulomb charging of a cluster during photoemission. The XPS BE shifts, therefore, would be sensitive to the surroundings of clusters. In addition, one can use the shape of a valence band photoemission spectrum of Au nanoclusters for cluster size estimation. The spin-orbit energy splitting in a valence band level, which is essentially insensitive to the surroundings, can be a measure of the size of nanoclusters if the charge transfer between the cluster and surroundings is negligibly small. In this case, the measurement of 5*d*-band width can be alternative. Compagnini et al. [1)] showed, in fact, that the 5*d*-band width was reduced linearly with the inverse of Au particle size.

Highly oriented pyrolytic graphite (HOPG) was used as a substrate in this experiment. In the case of ion-irradiated HOPG, it was irradiated with 1 keV-Ar ions at several irradiation times ranging from 0.1 to 2 s. The averaged ion flux was $\sim 3 \times 10^{15}$ ions/(cm^2·s) and was almost constant for the different HOPG substrates. Various defect densities are expected to be created on the HOPG by changing the irradiation time. Au or Pt clusters were deposited from respective bulk sheets by Ar-sputtering. The areal densities of Au or Pt atoms deposited on the substrate were determined by Rutherford backscattering spectrometry with 2 MeV-^{4}He ions produced from a 3MV single-ended accelerator at TIARA. XPS data acquisition was performed on a JEOL 9010 machine equipped with a sputter etching gun and non- monochromatized MgKα X-ray source ($h\nu$ = 1,253.6 eV). The base pressure in the analysis chamber was < 10^{-9} mbar. The 4*f* core level and 5*d* valence band spectra were taken with an analyzer pass energy of 10 and 20 eV, respectively. In XPS, the peak energies were calibrated by placing the C 1*s* peak.

Figure 1 shows Au and Pt $4f_{7/2}$ BE shifts from bulk values at various areal densities of deposited atoms. For deposited Au clusters at areal density of 2.5×10^{14} atoms/cm^2, for example, the BE shift is 0.52 eV for the Ar^+-irradiated HOPG, much larger than that for the pristine HOPG (0.25 eV). The results indicate that the smaller clusters form on the damaged HOPG. Throughout this study, Au or Pt clusters with smaller size tend to be created on the irradiated graphite compared with the un-irradiated one. For example, the sizes of Au nanoclusters formed on the irradiated graphite are 0.6−8.2 nm, much smaller than those on the un-irradiated one (1.6−17 nm).

By using the un-irradiated and irradiated graphite as substrates for Au nanocluster-deposition, the relationship between cluster size and 5*d*-band width in XPS was obtained for a wide range of Au cluster size. This relation can be utilized for size estimation of Au clusters embedded in non-conductive materials [2)].

References

1) G.Compagnini et al., Surf. Sci. 600 (2006) L1-L5.
2) K. Takahiro et al., to be published in Appl. Surf. Sci.

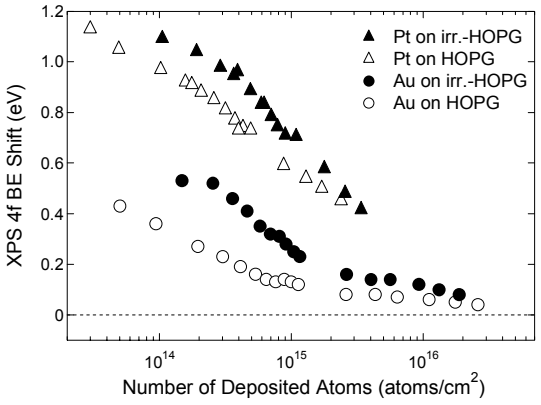

Fig. 1 XPS 4*f* core level binding energy shifts as a function of coverage (number of deposited atoms) for nanoclusters of Au/HOPG (○), Au/irradiated-HOPG (●), Pt/HOPG (△) and Pt/irradiated-HOPG (▲).

4-10 Heating and Nitriding Processes of Ti Thin Films Grown on NaCl Substrates Held at Room Temperature

Y. Kasukabe [a), b)], Y. Watanabe [b)], Y. Chen [b)], S. Yamamoto [c)] and M. Yoshikawa [c)]

[a)] Center for International Exchange, Tohoku University, [b)] Department of Metallurgy, Tohoku University, [c)] Environment and Industrial Materials Research Division, QuBS, JAEA

It has recently been reported that properties of non-stoichiometric titanium nitrides (TiN_y) such as electrical conduction, diffusion barrier, wear resistance, catalysis, etc. depend not only on chemical composition, but also on orientation relationships between TiN_y films and substrates. Therefore, much interest has been focused on studying atomistic epitaxial growth processes of TiN_y films [1)]. The purpose of the present paper is to characterize changes of the crystallographic and electronic structures of Ti thin films by heating and by nitriding during N-implantation, by using in-situ transmission electron microscope (TEM) and electron energy loss spectroscope (EELS). The characterization of the electronic structure by molecular orbital calculation and the composition analysis are also performed to clarify atomistic epitaxial growth processes of TiN_y films due to ion implantation. The ions of N_2^+ with 62 keV are implanted into deposited Ti films in the 400 kV analytic high resolution TEM combined with ion accelerators installed at JAEA-Takasaki [2)].

Both hcp-Ti and CaF_2-type TiH_x ($x \cong 1.5$) with preferred orientations have been grown in as-deposited Ti films on NaCl (001) substrates held at room temperature (RT). The as-deposited Ti films were heated up to 350 °C at a heating rate of 2 °C /min in the TEM. H atoms which constituted TiH_x were completely released from the as-deposited Ti films by heating at 350 °C, and subsequently the H-released unstable fcc-Ti sublattice was transformed into hcp-Ti. The calculated density of states (DOS) curves for the hcp-Ti and fcc-Ti cluster models are shown in Fig. 1. Each curve corresponds to superimposition of Ti 3d, Ti 4s and Ti 4p DOS for each model. The line at 0 eV represents the Fermi level, E_f. The DOS curve for the fcc-Ti exhibits a large peak indicated by the line "a" just below E_f. The corresponding peak for the hcp-Ti indicated by the line "A" is shifted to the lower energy region. The energy positions for the fcc-Ti indicated by "b", "c" and "d" are located at higher energy region than those for the hcp-Ti indicated by "B", "C" and "D", respectively. Furthermore, the averaged energies per unit electron density of states under the E_f for the hcp-Ti and fcc-Ti clusters in Fig. 1 are -2.07 eV and -1.71 eV, respectively. These mean that the electronic energy of the fcc-Ti is higher than that of the hcp-Ti. Therefore, it is considered that the H-released fcc-Ti becomes unstable and is transformed into hcp-Ti during heating of as-deposited Ti films.

The ions of N_2^+ with 62 keV were implanted into the as-deposited Ti films at room temperature and at 350 °C. It was found that the N-implantation into the as-deposited Ti films containing TiH_x crystallites at room temperature resulted in the release of H and made TiH_x crystallites unstable. Furthermore, the H-released unstable TiH_x (fcc-Ti sublattice) absorbed implanted N atoms to maintain the fcc-Ti sublattice, and the occupation of O-sites of the H-released fcc-Ti sublattice by implanted N atoms led to stabilization of the unstable fcc-Ti sublattice. These processes resulted in the formation of stable crystallites, (110)-oriented TiN_y, not of hcp-Ti. On the other hand, the (001)-oriented TiN_y is epitaxially formed by the N-implantation into the hcp-Ti films, through the transformation of the hcp-Ti to fcc-Ti sublattice, partially inheriting the atomic arrangement of the hcp-Ti and accompanying the occupation of O-sites of the fcc-Ti by N atoms. The bonding interaction of Ti sublattices with N atoms gives rise to the forming of stronger covalent bonds, and to the weakening of Ti-Ti bonds. Thus, it is considered that the shear in the <01•0> direction of hcp-Ti promoted by the forming of the strong Ti-N bonds and the weakening of the Ti-Ti bonds is the origin for the hcp-fcc transformation of Ti sublattices. Therefore, it is concluded that the shift of the atoms on the closed-packed plane induced by the change of bonding interaction of Ti sublattices with ligand H or N atoms plays an important role in the transformation between fcc-Ti sublattices and hcp-Ti sublattices due to the release of H atoms or due to the occupation by N atoms.

References

1) S. Hao, B. Delley and C. Stampfl, Phys. Rev. B **74** (2006) 035424-1.
2) H. Abe et al., JAERI-Res. 96-047 (1996) 1.

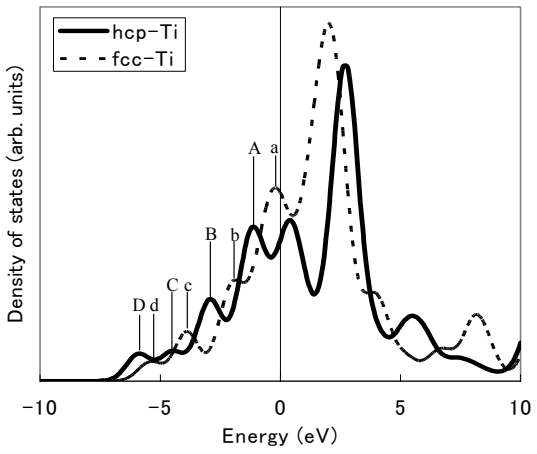

Fig. 1 DOS curves for the hcp-Ti and fcc-Ti cluster models.

4-11 Electron Irradiation Effects on Boron-Doped Superconducting Diamond Thin Films

T. Nishizaki [a] and S. Okayasu [b]

[a] IMR, Tohoku University, [b] Advanced Science Research Center, JAEA

Ekimov et al. [1] discovered superconductivity in the heavily boron-doped diamond synthesized by a high-pressure high-temperature (HPHT) method. The superconducting transition temperature T_c was 2.3~4 K for their polycrystalline bulk samples with the boron concentration $n \sim 4.9\times10^{21}$ cm^{-3} (i.e., 2.8% of the carbon atoms were substituted by boron atoms)[1]. Takano et al.[2] reported that a (111)-oriented polycrystalline boron-doped diamond film shows superconductivity at $T_c = 4.2 \sim 7.4$ K; the value is higher than that reported for the HPHT diamond [1] and for boron-doped (100)-oriented single-crystalline diamond films ($T_c < 2.1$ K)[3].

In this material, the highest T_c reached so far is 7.4 ~ 11.4 K for (111)-oriented epitaxial films with $n \sim 8.4\times10^{21}$ cm^{-3} [4]. The condition is considered to be the underdoped region according to the doping dependence [4], and the value of T_c may increase more with increasing carrier density to the optimal condition. In addition to the doping level, the value of T_c depends on the synthesized process and the orientation of the film growth [4]. It has also been suggested that the boron cluster, the boron-boron complex, and the boron-hydrogen complex reduce the value of T_c in the boron-doped diamond. These results indicate the distributions of the boron atoms and the point-like disorder in the lattice are important parameters to discuss the origin of superconductivity for the boron-doped diamond thin films.

In this study, we have studied effects of electron irradiation on the boron-doped diamond, because this method can control the distribution of the atomic arrangement and also introduce the point-like disorder in the sample. Heavily boron-doped epitaxial diamond films were grown on (111)-oriented type Ib diamond substrates by using microwave plasma-assisted chemical vapor deposition (MPCVD) method. An irradiation with 2-MeV high energy electrons was performed at room temperature using the electron accelerator of JAEA-Takasaki. The electron irradiation was repeated for the same boron-doped diamond thin film, with two kinds of irradiation doses (the first irradiation: 1×10^{17} e/cm^2, the second irradiation: 2×10^{18} e/cm^2). The defects introduced by these irradiation doses are estimated to be about 5 ppm and 100 ppm, respectively.

Figure 1 shows the temperature dependence of the magnetization $M(T)$ for a (111)-oriented boron-doped diamond film. Before the electron irradiation, the $M(T)$ data shows the superconducting transition at $T_c \sim 6.5$ K and the secondary phase is observed at low temperatures below ~2.7 K. When the irradiation dose is on the order of 1×10^{17} e/cm^2, no significant change in the $M(T)$ data is observed. After the dense irradiation with the dose of 2×10^{18} e/cm^2, however, the onset of the superconducting transition slightly decreases and the diamagnetic signal is strongly reduced. The results indicate that the volume fraction of the superconductivity is suppressed by introducing the point-like disorder in the lattice or by changing the atomic distribution. The electron irradiation effect is marked in the boron-doped diamond as compared with the high-T_c superconductor, because the volume fraction does not change by the electron irradiation with the dose of ~2×10^{18} e/cm^2 in $YBa_2Cu_3O_y$ (YBCO) single crystals [5]. Although the microscopic origin of these differences has not been clear yet, it is speculated that lattice disorder or micro-structural change due to the electron irradiation can affect the superconductivity of the boron–doped diamond more seriously than that of YBCO crystal because of a selective knock-on effect on light atoms by the electron irradiation. The boron-doped diamond is constructed with two light atoms, and the influence of the irradiation can be larger than that of YBCO. It can be the trigger of the inhomogeneity of the superconductivity in the boron-doped diamond.

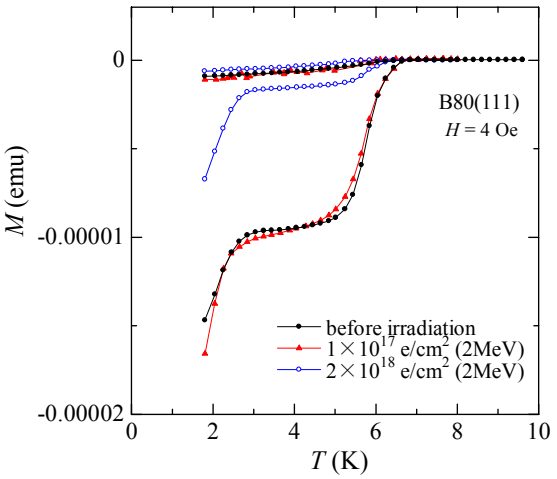

Fig. 1 Temperature dependence of the magnetization of a boron-doped diamond thin film before and after electron irradiation.

This research was performed in collaboration with Dr. Y. Takano of National Institute for Materials Science (NIMS).

References

1) E. A. Ekimov et al., Nature **428** (2004) 524.
2) Y. Takano et al., Appl. Phys. Lett. **85** (2004) 2851.
3) E. Bustarret et al., Phys. Rev. Lett. **93** (2004) 237005-1.
4) H. Umezawa et al., Cond-mat/0404286.
5) T. Nishizaki et al., Phys. Rev. B **61** (2000) 3649.

4-12 Submicron Structure Created in Oxide Ceramics Irradiated with 10-MeV Ni

N. Ishikawa

Advanced Science Research Center, JAEA

Radiation damage is one of the important causes of degradation of thermal conductivity and serious swelling in nuclear fuel ceramics. Understanding of radiation damages in nuclear fuel is important for controlling fuel properties during burn-up and for predicting fuel burn-up behavior. The objective of this study is to investigate microstructure evolution of oxide ceramic material under heavy irradiation environment. The microstructure created at the irradiated surface has been already reported for various metals or semiconductors such as carbon-based materials irradiated with energetic ions in the energy range of keV. The present study deals with the effect in the higher energy range of MeV. Oxide ceramics are chosen as target materials in order to simulate irradiation damage of ceramic nuclear fuels due to passage of energetic fission fragments. Radiation damage can be characterized in terms of various length scale, such as atomistic scale and submicron scale. One of the important radiation damages in nuclear fuel is the creation of high-burn-up structure which can be characterized by subdivision of grains and coarsening of fission product gas bubbles. Both aspects of high burn-up structure appear in the length scale of submicron. Such submicron structure can be observed by, for example, a scanning electron microscope (SEM).

Therefore, in this study, oxide materials (CeO_2 polycrystal and rutile TiO_2 single crystal) were irradiated with MeV ions (10-MeV Ni) up to relatively high fluence of 7×10^{16} ions/cm^2 in order to investigate microstructure possibly created at high fluence. It has to be noted here that CeO_2 has the same crystal structure (fluorite structure) with nuclear fuel (UO_2). In the present experiment, a CeO_2 polycrystalline sample is polished. Flat surface with no particular microstructure is confirmed by SEM before irradiation.

Figure 1 shows an SEM picture of an irradiated surface of CeO_2 polycrystalline after irradiation with 10-MeV Ni up to 7×10^{16} ions/cm^2. The figure shows that, although the surface has been originally flat, the surface evolves into a roughened surface covered with many pits with a characteristic length of around 0.2 μm. The formation of such pits is probably due to sputtering of surface atoms due to the irradiation. The sputtering itself usually takes place on an atomistic scale, but astonishingly the microstructure emerges with much larger characteristic length of submicron. As can be seen in the figure, pits are aligned along grain boundaries, indicating that pits are preferentially created at grain boundaries. Inside the grains, pits are created uniformly, and no preferential direction can be found.

Figure 2 shows microstructure created at an irradiated surface of TiO_2 single crystal irradiated with 10-MeV Ni up to relatively high fluence of 7×10^{16} ions/cm^2. The figure shows that, although the surface has been originally flat, the surface evolves into a roughened surface covered with many pits with a characteristic length of submicron order. While the pits created for CeO_2 have isotropic structure with no preferential direction except for the vicinity of grain boundaries, the pits created for single crystal TiO_2 have anisotropic structure with long axis and short axis. The anisotropy may be due to the crystallographic structure of the material. The length scale of the short axis is similar to that of microstructure created for CeO_2.

The fluence dependence is an important research objective to be investigated in order to clarify the emergence and the evolution of such microstructures.

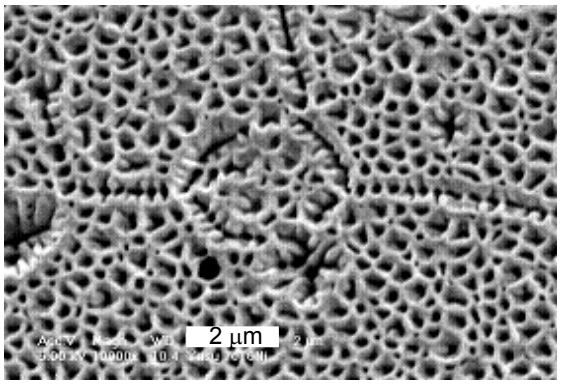

Fig. 1 Microstructure created at the surface of polished CeO_2 polycrystalline irradiated with 10-MeV Ni ions up to 7×10^{16} ions/cm^2.

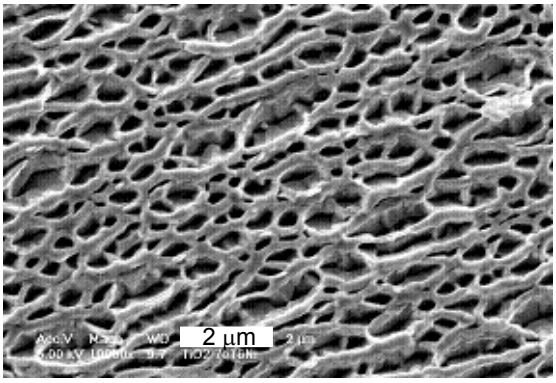

Fig. 2 Microstructure created at the surface of TiO_2 (100) single crystal irradiated with 10-MeV Ni ions up to 7×10^{16} ions/cm^2.

4-13 Non-equilibrium Surface Modification of Metallic Glass by Various Chemical Natured Ions

S. Muraishi [a)], H. Naito [a)], J. Shi [a)], Y. Nakamura [a)] and T. Aizawa [b)]

[a)] Department of Metallurgy and Ceramics Science, Tokyo Institute of Technology,
[b)] Department of Materials Science, University of Toronto

Different reactivity of ions has been implanted into metallic glass (MG) to investigate its morphology and elastic behaviors. In order to prevent crystallization of MG, non-equilibrium processing is applicable for surface modification of MG. Effectiveness of ion implantation is post-processing nature because of atom-mixing and simultaneous direct chemical reactions.

Present study focused on morphological change of MG by chemically different ions, which classified into reactive (Glass forming, nitride forming), or inert (atom-mixing).

For the above purpose, MG film of typical Zr-Cu system has been prepared by sputtering deposition with certain thickness on Si substrate. Chemical composition of as-deposited, ion-implanted film has been determined by XPS, and microstructure is mainly observed by TEM.

The mixing effect is discussed from results of inert Ar-implantation (Fig. 1). As shown in cross-section image of Ar-implanted Zr-Cu, spherical voids are induced at the mean penetration depth of amorphous matrix, where glassy phase is dominant. Comparative study by crystalline Zr_2Cu film has been revealed that similar voids formation without glass transition. Since XPS detected less than 5% of Ar inside of glassy film, Ar atoms inside of solid suddenly annihilated to gather gaseous phase as voids during implantation [2)].

On the contrary to above, chemically different 150 keV and 300 keV-Ni implantation reveals compositional dependent amorphization behavior [1)] (Fig. 2). Hence, chemical aspect of mixture enthalpy attains heating and quenching effect on amorphous mixture in proportion of implanted ions. Reactive 80 keV-N^+ induces direct formation of (Zr, Cu)N inside of MG film. As comparison with Ar^+, N concentration in MG film is consistent with total dosed amounts by XPS results.

Above results indicates implantation process would enhance local diffusivity by displacement collision and simultaneous heat production with related to energy loss of traveling ion. However, to large extent of annihilation and phase transition inevitably occurs at ambient processing temperature in accordance with phase equilibrium. These results support good post-processing nature of ion implantation and morphology of MG is controllable by different chemical nature of ions.

References

1) S. Muraishi et al., Mater. Trans. **48**(7) (2007) 1859.
2) S. Muraishi et al., Mater. Trans. **46**(12) (2005) 2751.

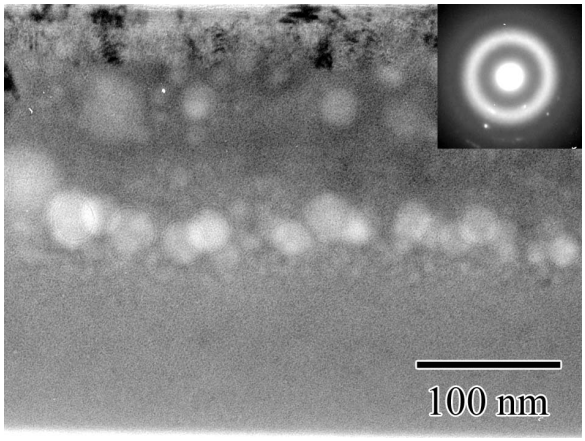

Fig. 1 Ar-implanted Zr-Cu film. Glassy phase is maintained during implantation. Spherical voids are attributed to gaseous phase of Ar.

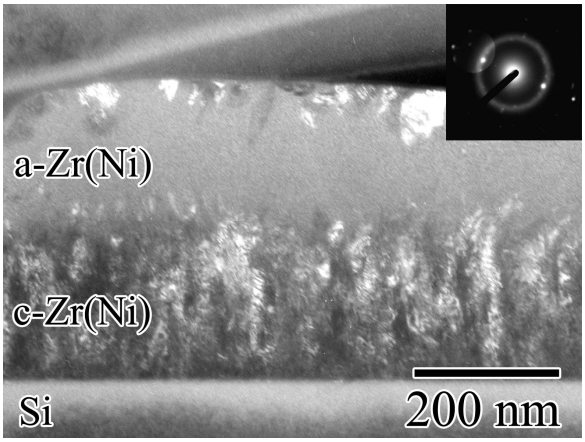

Fig. 2 Ni-implanted Zr film. Amorphization occurs proportional to Ni concentration at mean penetration depth.

4-14 Hardening of FeCu Alloys due to Electron-Irradiation Induced Cu Precipitates

S. Nakagawa [a], H. Ohno [a], F. Hori [a], N. Ishikawa [b] and A. Iwase [a]

[a] Department of Materials Science, Osaka Prefecture University,
[b] Advanced Science Research Center, JAEA

In the present experiment, we have studied the hardening of FeCu alloys under energetic electron irradiation by using Vickers hardness measurement. Specimens were prepared from three kinds of FeCu alloys with Cu concentration of 0.02, 0.6 and 1.2 wt.%. They were annealed at 850 °C, and were quenched into 0 °C water. The specimens were irradiated at 250 °C with 2 MeV electrons using a single-ended accelerator at JAEA-Takasaki. After the irradiation, the micro Vickers hardness was measured as a function of electron fluence and Cu concentration.

Figure 1 shows the dependence of change in Vickers microhardness on electron fluence for three kinds of FeCu alloys. There is little change in hardness by electron irradiation for Fe-0.02 wt.%Cu alloy. On the other hand, irradiation-induced hardness for Fe-0.6 wt.%Cu and Fe-1.2 wt.%Cu alloys increases with increasing electron fluence with a sublinear dependence on electron fluence. In Fig. 2, the hardness changes for the three specimens are plotted as a function of square root of electron fluence. The figure clearly shows that the hardness change is well proportional to the square root of the electron fluence:

$$\Delta H_v = A\sqrt{\phi}, \quad (1)$$

where ϕ is the electron fluence and A is the proportional constant which is a function of Cu concentration. Figure 3 shows that the constant, A, is proportional to Cu concentration. From the experimental result, we end up expressing the change in hardness as

$$\Delta H_v = \alpha\sqrt{(C_{Cu})^2\phi}, \quad (2)$$

where C_{Cu} is the Cu concentration and α is a constant which does not depend on C_{Cu} or ϕ.

It is well known that during irradiation at elevated temperatures, the diffusion of irradiation-produced defects enhances the diffusion of solute atoms through the interaction between defects and solute atoms. This phenomenon is called the radiation-enhanced diffusion. Cu precipitates with the diameter of a few nanometers have definitely observed in the present FeCu alloys after the electron irradiation. The dependence of the irradiation-induced hardness on Cu concentration and electron fluence, which is given by eq.(2), can be explained by considering the rate of the reaction between a defect and Cu atom, and by using the model for dispersion strengthening.

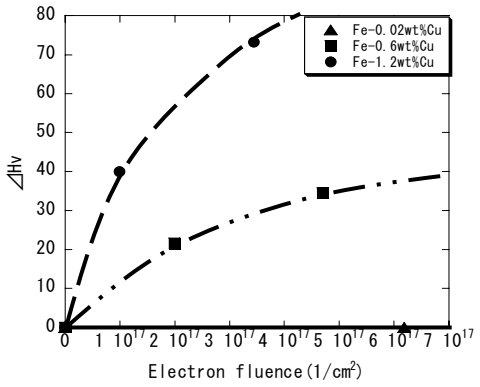

Fig. 1 Vickers hardness changes for FeCu alloys irradiated with 2 MeV electrons at 250 °C.

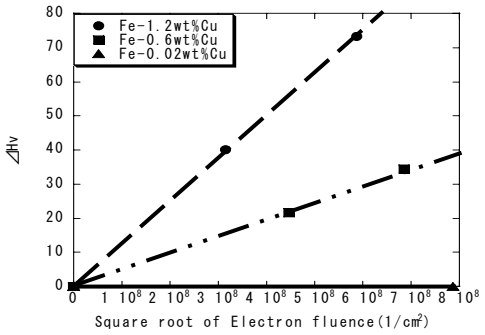

Fig. 2 Dependence of Vickers hardness change on square root of electron fluence.

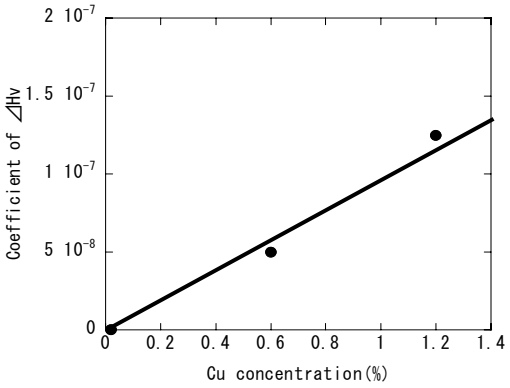

Fig. 3 Cu concentration dependence of the proportional constant, A.

4-15 Effect of 10-MeV Iodine Irradiation on Lattice Structure of FeRh Thin Films

N. Fujita [a)], S. Kosugi [a)], T. Matsui [a)], Y. Saitoh [b)] and A. Iwase [a)]

[a)] Department of Materials Science, Osaka Prefecture University,
[b)] Department of Advanced Radiation Technology, TARRI, JAEA

We have reported so far that 10-MeV Iodine ion irradiation induces the ferromagnetic state in FeRh thin film samples at low temperatures[1)]. The previous result shows that for low ion fluence (below 5×10^{12} /cm^2) the magnetization increases with increasing ion fluence, while for high ion fluence (5×10^{12} /cm^2 – 1×10^{14} /cm^2), the magnetization decreases with increasing ion fluence. In this report, we show the effect of 10-MeV Iodine ion irradiation on the lattice structure of FeRh thin films.

$Fe_{50}Rh_{50}$ thin films of about 100-nm thickness were deposited on amorphous SiO_2 substrates by using an ion beam sputtering. The samples were irradiated with 10-MeV Iodine ions to the fluence of 1×10^{12}, 2×10^{12}, 5×10^{12}, 1×10^{13}, 2×10^{13}, 5×10^{13}, and 1×10^{14}/cm^2 at room temperature using the tandem accelerator at JAEA-Takasaki. After the irradiations, the structural changes were examined by using an X-ray diffraction method (XRD). The results are shown in Fig. 1 as XRD profiles of FeRh thin films for (a) unirradiated and irradiated to the fluence of (b) 5×10^{12}, and (c) 1×10^{14}/cm^2. As can be seen in Fig. 1, compared with the unirradiated sample, we can hardly observe any change in lattice structure for the sample irradiated to the fluence of 5×10^{12} /cm^2, which exhibits the maximum magnetization. This result shows that for low ion fluence, the antiferromagnetic - B2 (CsCl type) structure is changed into ferromagnetic - B2 structure by the irradiation without any change in lattice structure. In contrast, for the high ion fluence, the magnetization of the film strongly decreases by the irradiation, and the intensity of the X-ray diffraction peaks corresponding to B2 structure also decreases. When the sample is irradiated up to the fluence of 1×10^{14}/cm^2, we can not find any diffraction peaks for the B2 structure, and a peak for A1 (fcc structure with a random distribution of iron and rhodium atoms) structure are only observed (see Fig. 1 (c)). The experimental result implies that for the high ion fluence, the ferromagnetic B2 structure is changed into nonmagnetic A1 structure, causing a strong decrease in magnetization of the samples.

In the present experiment, we observed the structural changes of FeRh thin films induced by 10-MeV Iodine ion irradiations. As the next experiment, we plan to conduct some experiments by using single crystal FeRh thin films prepared on MgO substrates to clarify the details of the ion irradiation effects on magnetic properties and lattice structure of FeRh samples.

Reference

1) N. Fujita et al., Nucl. Instrum. Meth. Phys. Res. B267 (2009) 921-924.

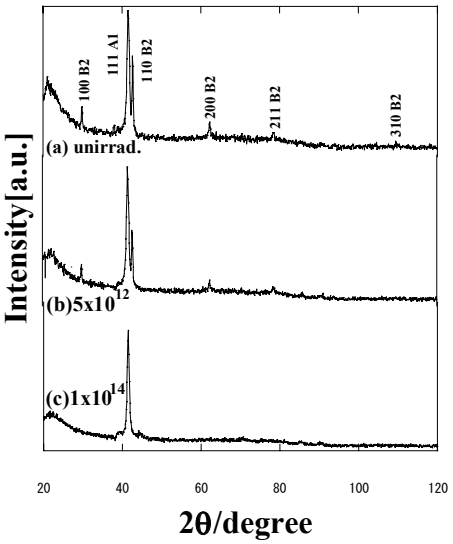

Fig. 1 Normalized XRD profiles of Fe-54at.%Rh thin films (a) uniradiated and irradiated with ion fluence of (b) 5×10^{12} ion/cm^2 and (c) 1×10^{14} ion/cm^2.

4-16 Lattice Disorder of Full Heusler Alloy Fe_2MnSi Layer Epitaxially Grown on Ge(111)

Y. Maeda [a, b], Y. Hiraiwa [a], K. Narumi [b], Y. Ando [c], T. Sadoh [c] and M. Miyao [c]

[a] Department of Energy Science and Technology, Kyoto University,
[b] Advanced Science Research Center, JAEA, [c] Department of Electronics, Kyushu University

A Heusler alloy DO_3-Fe_3Si is important as a parent material in order to synthesize some ternary Heusler alloys such as $Fe_2(TrSi)$ (Tr: Mn, V, Ti, Co) with an $L2_1$ structure. These ordered structures can be regarded as consisting of four interpenetration fcc lattices shifted along the body diagonal which originates at sites: A(0,0,0), B(1/4,1/4,1/4), C(1/2, 1/2, 1/2), and D(3/4,3/4,3/4). In the perfect DO_3-Fe_3Si, iron atoms distribute at A, B and C sites, whereas silicon atoms are located at the D site. In Fe_2MnSi, the site preference occupation of manganese at the B site was confirmed in the wide Mn/Fe ratio. These site-occupations of atoms have a great influence on magnetization and are the most important issue to control electronic structures such as spin densities of states and half-metallic properties which dominate performance of spin-injection or filtering through the interface between ferromagnetic Heusler-alloy electrodes and semiconductors. The perfect atomic rows along the <111> direction consist of periodic intervals of Fe(A), Fe(B), Fe(C), Si(D) in DO_3-Fe_3Si and Fe(A), Mn(B), Fe(C), Si(D) in the $L2_1$-Fe_2MnSi lattice.

In this study, we examined perfection of site occupation along the <111> rows of Fe atoms or Fe/Mn atoms in their Heusler alloy layers epitaxially grown on Ge(111) and discuss on origin of disorder by taking thermal vibrations predicted from the Debye model and static displacements of Fe and Mn atoms due to lattice disorders into account.

The epitaxial $Fe_{3-x}Mn_xSi$ layers with a thickness of ~50 nm were grown by low temperature- molecular beam epitaxy (MBE) on n-type Ge(111) substrates at 200 ^oC for $Fe_{3-x}Mn_xSi$, where $x = 0.36$-0.84, 9-21 at% Mn [1,2]. The three elements of Fe, Mn, and Si were co-evaporated using Knudsen cells. Axial channeling measurements and Rutherford backscattering spectroscopy (RBS) for analysis of composition of alloy layers were carried out at either SC1 or MD2 target ports in TIARA. The channeling measurement using 2.0 MeV-$^4He^+$ ions and a backscattering angle of 165 degrees was carried out at 300 K and 110 K.

Figure 1 shows the average atomic displacement u_1 as a function of the Mn content in the alloy layer. The average atomic displacement was deduced from both the minimum yield χ_{min} and the half angle $\psi_{1/2}$ measured by the axial channeling measurement and thermal vibration amplitude u_{th} calculated by the Debye model [3]. The u_1 values both for the inside of films and the interface (except for the inside of Fe_3Si) remarkably increased as the Mn content increased. The u_1 values of samples evaluated here were less than 0.011 nm at the maximum. The u_1 values for Mn-Fe and Mn-Si pairs were respectively 0.007 nm and 0.014-0.017 nm obtained from the Debye-Waller factor [4]. Therefore, it is suggested that Mn-Si pairs due to the A or C site occupation of Mn or Si atoms do not exist in our $Fe_{3-x}Mn_xSi$ layers. The u_1 value in the range of 0.006-0.011 nm is close to thermal vibration amplitudes of Fe (or Mn) atoms as shown in Fig. 1. To evaluate disorder due to the Mn content, the static displacement u_s was calculated [3]. At 300 K u_s=0.0037 nm at the interface and 0.0008 nm at the inside, at 110 K u_s=0.0048 nm at the interface and 0.0019 nm at the inside for the 21 at% Mn layer. The static disorder ratio u_s/d , (d: interatomic space) at the heteroepitaxial interface amounts 1.5% at 300 K and 2.0% at 110 K, while that at the inside of layers 0.3% at 300 K and 0.8% at 110 K. This result suggests that disordering from the interface can be fully eliminated at the inside of the layer. The Mn content causes disordering of the lattice which is originated from the increase of lattice misfit at the heteroepitaxial interface, while the inside of the layer can be relaxed fully. These results indicate that low Mn content layers with both Curie temperature above 300 K and a half metallic property [5] are promising for high quality epitaxy as well as for spin-injection electrodes in spin transistors.

References

1) Y. Maeda et al., Appl. Phys. Lett. 91 (2007) 171910.
2) K. Ueda et al., Appl. Phys. Lett. 93 (2008) 112108.
3) Y. Maeda et al., MRS Proc. 1119E (2009) 1119-L05-02.
4) J. Budnick et al., Physica B 158 (1989) 31.
5) K. Hamaya et al., Phys. Rev. Lett. 102 (2009) 137204.

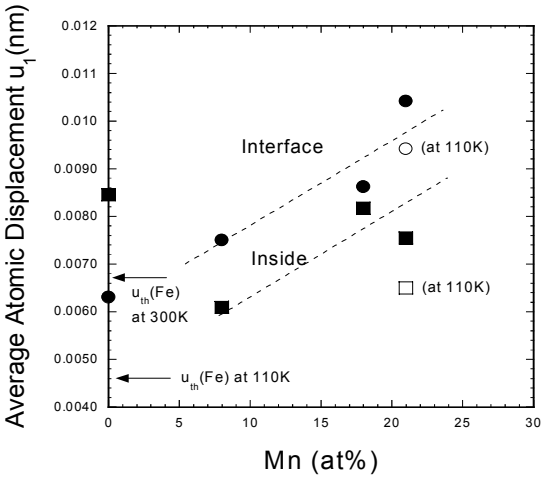

Fig. 1 The average atomic displacement u_1 as a function of the Mn content. u_{th}(Fe) is thermal vibration amplitude of Fe atoms at each temperature in the bcc lattice.

4-17 Sputtering Phenomena of Various Solid Materials Induced by Bi^+ Ion Bombardments

H. Naramoto [a)], K. Narumi [a)], Ting Hao [a)], M. Ono [a)], S. Okayasu [a)], Y. Saitoh [b)], A. Chiba [b)], K. Yamada [b)], M. Adachi [b)] and Y. Maeda [a, c)]

[a)] Advanced Science Research Center, JAEA, [b)] Department of Advanced Radiation Technology, TARRI, JAEA, [c)] Department of Energy Science and Technology, Kyoto University

Energetic ions (typically ~keV/amu) deposit their energies through the multiple collision process in the targets, resulting in the structural/compositional changes. The sputtering phenomena were studied to protect the fusion plasma from the heavy impurity contamination [1)]. Recently, the intensive studies have been made in the connection with the nano-technology [2)] and the secondary ion mass-spectrometry [3)]. The multiple collision process is reasonably assumed to induce the mass-transport in a large scale, being influenced by the existing lattice imperfections.

In the present study, we have made the effort to know the structure-sensitive nature of sputtering by analyzing the mass-spectra of sputtered species from the typical targets.

One - three hundred keV Bi^+ ions from the ion implanter in TIARA facility were bombarded under the normal incidence in the dose range of 10^{15}~10^{16} /cm^2. Annealed Sn with large grains, α-Al_2O_3(0001), ceramic Al_2O_3, annealed Al with large grains and rolled Al films were tested as typical targets. For the mass-spectrometry with the time-of-flight method, 300 keV Bi^+ ions were pulsed [4)], covering the mass-range up to 700 amu. The topographic changes on target surfaces were characterized with typical microscopic techniques: AFM and SEM.

Figure 1 shows the typical SEM micrograph from the eroded Sn surface after Bi^+ ion bombardments under the normal incidence. The ripple structure with ~100 nm width can be observed on the limited grains. This suggests the orientation-sensitive sputtering. The further systematic studies are required to elucidate the relevant mechanism.

In the Bi^+ ion incidence on Sn target, the negative target current was detected, by several times higher than the incident positive one. This can be closely related to the electronic excitation process. It is inevitable to know the charge state of sputtered species in the mass-spectrometry.

Figure 2 shows the TOF mass-spectra of ejected species with the positive (circles) and the negative (solid stars) charge when the Sn target was bombarded with 300 keV Bi^+ ions at RT. The sputtered ion yield is illustrated in the semi-logarithmic form as a function of mass-number up to 500 amu. In the low mass-region, hydrocarbon compounds with the various chemical forms are detected in the negative form. Implanted Bi, Sn and Sn_2 are detected as the positive ions, and their compounds with the low Z elements are observed as the negative ones. The comparison in the mass-spectra between high crystal-quality samples and heavily disordered samples for Al and Al_2O_3 (not shown for the simplicity) suggests that the heavily disordered samples (ceramic Al_2O_3 and rolled Al films) eject cluster type ions with the one order-higher intensity. This implies that the mass-transportation process induced by the heavy ion bombardments may release the stored strain-energies in the heavily disordered samples. The structure-sensitive nature in the sputtering should be one of the important factors especially in the secondary ion spectrometry of metallic system.

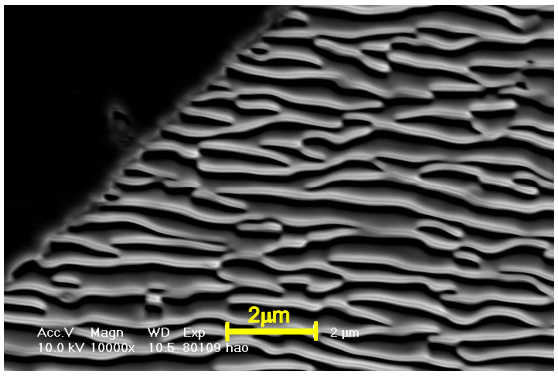

Fig. 1 SEM micrograph of annealed Sn bombarded with Bi^+ ions (150 keV, 1×10^{16} /cm^2).

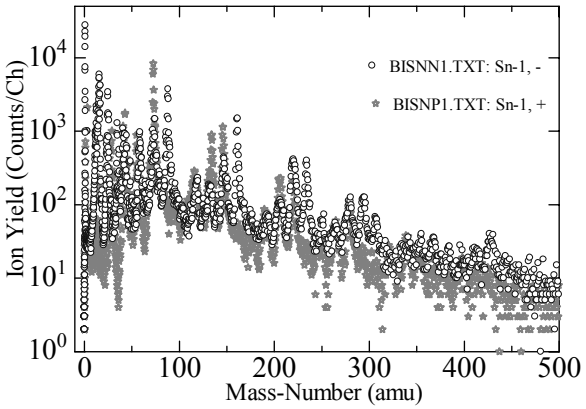

Fig. 2 TOF mass-spectra of charged species sputtered with 300 keV Bi^+ ion on polycrystalline Sn targets.

References

1) For example: J. N. Brook, Fusion Eng. Des. **60** (2002) 515-526.
2) For example: B. Ziberi, *et al.*, Phys. Rev. B **72** (2005) 235310-1~235310-7.
3) For example: K. Hirata *et al.*, Nucl. Instrum. Meth. Phys. Res. B **266** (2008) 2450-2452.
4) K. Hirata *et al.*, Appl. Phys. Lett. **65** (1994) 543.

4-18 Effects of Electron/Ion Irradiation on Hydrogen Absorption Rate of La-Ni based Alloy

H. Abe [a], S. Ohnuki [b], Y. Matsumura [c], H. Uchida [c] and T. Ohshima [a]

[a] Environment and Industrial Material Research Division, QuBS, JAEA,
[b] Course of Applied Science, Graduate School of Engineering, Tokai University,
[c] Department of Energy Science and Engineering, School of Engineering, Tokai University

Recently, Ni-MH batteries with hydrogen storage La-Ni based alloys as negative electrodes are installed many hybrid cars (HV: Hybrid Vehicle). In such metal alloys, AB_5 type metal alloys have been already used as practical materials because of their high response. We aimed to fabricate realizing alloys with a higher performance of the hydrogen absorption rate by the surface modification of the alloys using electron/ion irradiation in this report. The electron/ion beam modifications are effective methods to improve the hydrogen absorption rate in metal. The mentioned above is quite useful for the surface modification of materials, also to improve the rate of hydrogen absorption, and effectively induced defects such as vacancies, dislocations, micro-cracks or added atoms into the surface region of the metal alloy to trap hydrogen atoms[1,2]. An ion beam also caused the defects into the surface of the La-Ni based alloy[3]. In this report, the effects of hydrogen absorption characteristics La-Ni based alloy has been examined using the electron beam irradiation.

In this study, we investigate the effects of electron (e^-) and Potassium ion (K^+) irradiation on the electrochemical hydriding rate of the alkaline pretreatment La-Ni based alloys. We also analyzed the chemical compositions at the surface of the irradiated/un-irradiated La-Ni based alloys, their crystal structures, and the phases of bulk.

The samples used in this study were $LaNi_{4.6}Al_{0.4}$ alloys. These were produced like the bulk using an arc melting method. The samples were irradiated with either e^- at an acceleration energy of 2 MeV with a dose of 5×10^{16} /cm^2 using the 2 MV Cockcroft-Walton electron accelerator, or K^+ ions at an acceleration energy of 350 keV with a dose of 1×10^{16} /cm^2 using the 400 kV ion implanter, at the TIARA, JAEA. The hydrogen absorption rate measurements were also performed for the irradiated sample and un-irradiated $LaNi_{4.6}Al_{0.4}$ alloys using the electrochemical apparatus method. The hydrogen absorption rate of $LaNi_{4.6}Al_{0.4}$ alloy was measured electro-chemically in the 6M-KOH with an open cell as the current density (mA/mm^2) at a constant potential of -0.93 V and room temperature, time from 0 to 120 minutes. The chemical compositions in the surface of the irradiated $LaNi_{4.6}Al_{0.4}$ alloys were analyzed by scanning electron microscopy equipped with energy dispersive spectroscopy. The crystal structure and phase of the bulk for the irradiated $LaNi_{4.6}Al_{0.4}$ alloys were determined by X-ray diffraction (XRD).

Figures 1 and Fig. 2 show the XRD pattern of irradiated and un-irradiated $LaNi_{4.6}Al_{0.4}$ alloy samples. Some of the diffraction small peaks assigned to those of the La_2NiO_4 compound may be due to produce by plasma oxidation with irradiated e^- beam at atmospheric in air. In the case of e^- irradiation, oxide/metal interface also tend to act as dissociation of H_2O molecules into H atoms. A marked effect of surface oxidation on the hydriding kinetics of La-Ni based hydrogen absorbing alloys was reported[5].

Figure 3 shows the hydrogen absorption curves of the irradiated and un-irradiated $LaNi_{4.6}Al_{0.4}$ alloy. The current density at 120 minutes of K^+ (●: the dose of 1×10^{16} /cm^2, ▽: 1×10^{14} /cm^2), e^- (△: 5×10^{16} /cm^2) irradiated samples and un-irradiated (□) were 0.182, 0.145, 0.172 and 0.108 mA/mm^2,

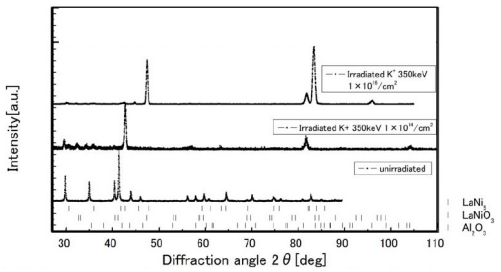

Fig. 1 XRD patterns of $LaNi_{4.6}Al_{0.4}$ alloy with K^+ irradiated/un-irradiated.

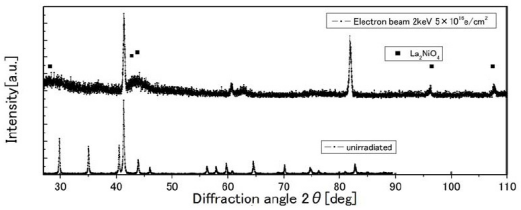

Fig. 2 XRD patterns of $LaNi_{4.6}Al_{0.4}$ alloy with e^- irradiated/un-irradiated.

respectively. The maximum value of the current density for samples of K^+ irradiation (●) and e^- irradiation (△) indicated a high value compare with another. Electron/ion irradiation onto the surface of a metal effectively induces defects, such as vacancies, dislocations, micro-cracks or impurities near the surface of a metal. As for the dissociation of the hydrogen molecule, at the surface of the samples, the nucleation site of the hydride formation might be effective for the hydrogen atom in the $LaNi_{4.6}Al_{0.4}$ surface region according to the formation vacancies with high concentration. Moreover, it was found that in the case of the K^+ irradiated sample, hydrogen absorption rate was increased with reducing of work function of surface atom related to the K atoms implanted near the surface of sample. On the other hand, this report was the first trial to the electron irradiation. As for the e^- irradiated sample, it was found that the function of the hydrogen absorption improves compared with the un-irradiated sample.

This result is considered that the effect of defects uniform in the depth direction by e^- irradiation appeared.

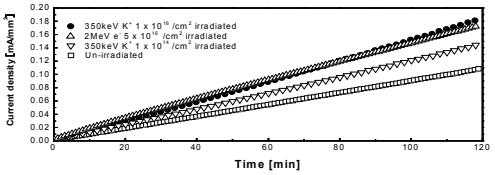

Fig. 3 Hydrogen absorption curves of the irradiated and un-irradiated $LaNi_{4.6}Al_{0.4}$ alloy.

References

1) H. Abe et al., J. Alloys and Comp. 404-406 (2005) 288.
2) H. Abe et al., J. Alloys and Comp. 408-412 (2006) 348.
3) H. Uchida et al., J. Alloys Comp. 330-332 (2002) 662.
4) H. Uchida et al., J. Alloys and Comp. 293-295 (1999) 751.
5) H. H. Uchida et al., J. Alloys Comp. 231 (1995) 679.

4-19 Effect of Ion Irradiation on the Magnetic Field Direction Dependence of Critical Current of YBCO Tapes Prepared by a PLD Method

H. Ushiki [a)], N. Chikumoto [b)], T. Machi [b)], A. Ibi [b)], S. Miyata [b)], Y. Yamada [b)], T. Kubo [a)], A. Suzuki [c)] and T. Terai [a)]

[a)] Department of Nuclear Engineering and Management, The University of Tokyo
[b)] Superconductivity Research Laboratory, ISTEC
[c)] Nuclear Professional School, The University of Tokyo

Effect of ion irradiation on the magnetic field direction dependence of critical current of YBCO superconducting tapes, which were prepared by a pulsed laser deposition (PLD) method, was studied. The samples were irradiated with 450-MeV Xe^{23+} ions perpendicular to the YBCO layer with irradiation fluences from 2.5×10^{11} to 1.0×10^{12} ions/cm^2. The linear energy transfer (LET) of Xe ion is controlled by changing the thickness of a Ag foil placed in front of the sample. After the ion irradiation, the transport critical current density (J_c) of the irradiated samples was compared to that of unirradiated samples with changing the direction and the strength of magnetic field. As a result of the ion irradiation, the enhancement of the J_c was observed when the direction of magnetic field coincided with that of ion irradiation. On the other hand, the J_c decreased for the samples irradiated at the relatively high fluence of 7.5×10^{11} ions/cm^2 when the direction of magnetic field was perpendicular to that of ion irradiation.

超伝導現象は電力や輸送、医療から情報技術などの広い範囲でその応用が期待されている。近年、酸化物高温超伝導体(HTSC)が発見され、液体窒素温度である77 Kで超伝導状態を作ることが可能になった。HTSCは第2種超伝導体に分類され、その超伝導臨界電流密度(J_c)を向上させるためには、超伝導体内に侵入した磁束を捕捉するための常伝導領域、すなわち格子欠陥などのピニングセンターを導入することが必要不可欠である。量子線照射は、製作過程によらず、照射条件を変化させることで超伝導体内のピニングセンターの形状・密度を制御できる利点がある。その中でも特に重イオン照射による円柱状欠陥は、ピニング力が強い、磁束の侵入する方向に効率的に導入できるなどの利点から特性向上に大きく寄与することが期待されている。また、現在、Pulsed laser deposition法（PLD法）で作製されたYBCO線材は、高い配向性、高いJ_c等の優れた特性を持ち、次世代の高温超伝導線材として開発がなされており、重イオン照射の効果についても報告されている[1)]。本研究では、超伝導線材が実際に使用される際には、種々の方向から磁場が印加されることを考慮し、重イオン照射がPLD法により作製されたYBCO超伝導線材におけるJ_cの磁場角度依存性に及ぼす影響を、イオンフルエンス、線エネルギー付与(Linear Energy Transfer: LET)を制御しながら輸送電流測定から調べ、より実用的なデータを取ることを目的とした。

試料は(財)国際超電導産業技術研究センター超伝導工学研究所においてPLD法により作製されたYBCO超伝導線材(YBCO層：2.25 μm)を用いた。高エネルギー重イオン照射には、日本原子力研究開発機構高崎量子応用研究所のAVFサイクロトロンを用い、超伝導層に対して垂直に照射した。照射フルエンスは2.5×10^{11}～1.0×10^{12} [ions/cm^2]の範囲で行った。照射イオン種は450 MeVのXe^{23+}を選択し、入射イオンの超伝導層でのLETは、種々の膜厚の銀箔を入射イオンと照射試料の間に挟むことで制御した。

Fig. 1に超伝導層の厚さ2.25 μmのYBCO線材におけるJ_cの磁場角度依存性を示す。○印で示した重イオン照射前の磁場角度依存性を見ると、角度90°付近(印加磁場⊥重イオン照射方向)でJ_cが急激に増加する様子が見られる。また、△で示した重イオン照射後の結果から、そのピークは重イオン照射により低下していることが分かる。角度90°付近でJ_cが急激に増加するのはYBCOの層状構造によるものであり、絶縁層に量子化磁束がトラップされることによる。また、重イオン照射によりJ_cが低下したのは、円柱状欠陥が導入されることにより、層状構造が乱され、磁束が動きやすくなったことが原因として考えられる。次に角度0°、180°においては、Ag箔2.5 μmの場合で重イオン照射の効果が大きく現れていることが分かる。この原因として、照射フルエンスの相違もあるが、個々の欠陥のピニング力の強いことが考えられる。Ag箔7.5 μmの条件では、厚さ2.25 μm のYBCO超伝導層におけるLETが小さくなり、十分な大きさの円柱状欠陥が生成されないことに対し、Ag箔2.5 μmの条件では、ピニング力の強い円柱状欠陥が導入できるためである。以上から、本研究によりXeイオン照射によるJ_c変化の磁場角度依存性についての情報を得ることができた。

Reference

1) K. Nakashima et al., Physica C, 665 (2007) 463-465.

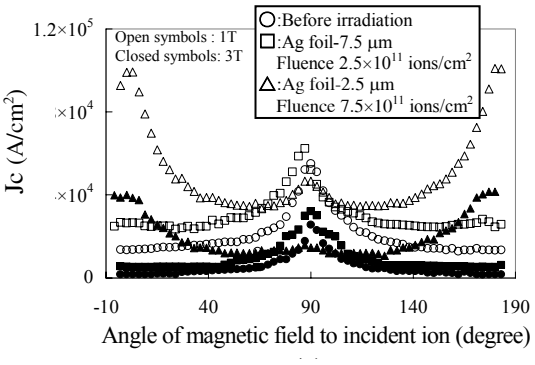

Fig. 1 Magnetic field direction dependence of J_c in YBCO (2.25 μm) at B=1.0 T or 3.0 T before and after Xe-ion irradiation.

4-20 Cathodoluminescence Characterization of Radiation-induced Halo in Feldspar (Sanidine and Albite)

H. Nishido [a)], M. Kayama [a)], S. Toyoda [b)], K. Komuro [c)] and K. Ninagawa [b)]

[a)] Research Institute of Natural Sciences, Okayama University of Science,
[b)] Department of Applied Physics, Okayama University of Science,
[c)] Earth Evolution Sciences, University of Tsukuba

Cathodoluminescence (CL) halo in quartz caused by alpha-radiation has shown the correlation between CL intensity of the halo and the dose density, suggesting its application as a geodosimeter. The halo in feldspar minerals, most common mineral in the Earth's crust, has not been studied from the point of CL characterization, although feldspar occasionally has a visible radiation damage halo surrounding radionuclide-bearing minerals within it. Until now the formation of such halo has not been investigated in detail because of the difficulty of its quantitative evaluation. In this study, CL of He^+ ion implanted feldspar minerals have been measured to characterize the halo for geodosimetry and geochronology.

Single crystals of sanidine ($Or_{82}Ab_{18}$) from Eifel, Germany and albite ($Ab_{99}Or_1$) from Galileia, Minas Gerais, Brazil were selected for CL and Raman measurements. He^+ ion implantation in the sample was performed on a 3MV-tandem ion accelerator in the facilities of TIARA (the JAEA) at 4 MeV corresponding to the energy of alpha-particles from disintegration of ^{238}U. A scanning electron microscopy-cathodoluminescence (SEM-CL), SEM (JEOL: JSM-5410) combined with a grating monochromator (OXFORD: Mono CL2), was used to measure CL spectra ranging from 300 to 800 nm at 15 kV acceleration voltage and a beam current of 1.0 nA.

CL images of sanidine and albite exhibit CL halo in the surface of He^+ ion implanted samples. Approximately 15 micro meter width of CL halo might be consistent with theoretical range of alpha-particles from disintegration of ^{238}U in these feldspar minerals. CL intensity of sanidine gradually decreases from the implantation surface to the inside up to approximately 15 micron meters, over which it jumps up to bulk emission level of non-implanted area. CL line analysis with panchromatic mode of sanidine shows that the distribution pattern of CL intensity in halo as a function of distance from the implantation surface is reciprocally related to the Bragg's curve, which indicates energy loss process of specific ionization along the track of a changed particle (Fig. 1a). CL spectrum of sanidine has two spectral peaks at 400 in blue region and 700 nm in red region (Fig. 2a). The former could be assigned to Al-O^--Al defect center and the later to Fe^{3+} impurity center. Raman spectra compose of peaks at around 480, 520, 780 and 1130 cm^{-1}, suggesting Si-O or Al-O atomic vibration. Their Raman intensities decrease from the implantation surface to the inside up to approximately 15 micron meters. These facts imply He^+ implantation appears to cause structural destruction, especially breakage of framework configuration in lattice. It might reduce emission centers such as Al-O^--Al defect center in halo. On the other hand, albite shows the increase of CL intensity exponentially from the surface to the inside, with its maximum at approximately 15 micron meters from the surface. CL line analysis in the section of halo area reveals that CL intensity increases from the implantation surface to the inside up to approximately 15 micron meters (Fig. 1b). This distribution pattern of CL intensity is reciprocally related to the Bragg's curve. CL spectrum of He^+ implanted albite shows a spectral peak at 680 nm, of which CL intensity positively correlated to dose density of He^+ ion implantation (Fig. 2b). It implies that CL emission of albite from the halo might be assigned to radiation induced luminescence centers formed by He^+ ion implantation. Furthermore, the integral intensity over the CL halo area in albite is well correlative with the irradiated dose, suggesting the use of CL halo in albite for a geodosimetry.

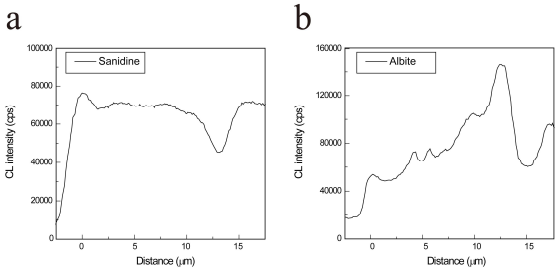

Fig. 1 CL line analyses with panchromatic mode of He^+ ion implanted (a) sanidine and (b) albite.

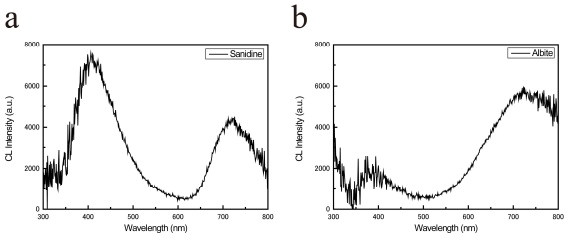

Fig. 2 CL spectra of He^+ ion implanted (a) sanidine and (b) albite.

4-21 Photoluminescence from Fused-Silica Substrates Implanted with Si Ions

K. Miura [a)], M. Honmi [a)], O. Hanaizumi [a)], S. Yamamoto [b)], A. Inouye [c)], M. Sugimoto [b)] and M. Yoshikawa [b)]

[a)] Graduate School of Engineering, Gunma University, [b)] Environment and Industrial Materials Research Division, QuBS, JAEA, [c)] Department of Advanced Radiation Technology, TARRI, JAEA

Various studies on silicon (Si)-based luminescent materials utilizing the quantum confinement effect, such as Si nanocrystals (Si-NCs), have been reported. Typical fabrication methods of Si-NCs are co-sputtering of Si and SiO_2 [1)], laser ablation [2)], and Si-ion implantation into SiO_2 plates or thermally oxidized Si wafers [3)]. We previously fabricated Si-NCs including fused-silica substrates by using the Si-ion implantation method with subsequent annealing, and observed blue [4)] and ultraviolet (UV) [5)] photo-luminescence (PL) from the substrates. The blue- and UV-light-emitting substrates were implanted with Si ions using a common energy of 80 keV but different amounts of 1×10^{17} ions/cm^2 (blue light) and 2×10^{17} ions/cm^2 (UV light). If we realize light sources by using this kind of Si-based materials, we will obtain many benefits as compared with III-V semiconductors, such as suitability for environment applications, lower cost, and matching for Si-based large-scale-integrated circuits in terms of their materials and fabrication processes.

In this study, we fabricated other Si-ion-implanted fused-silica substrates under different implanting conditions and evaluated their photoluminescence properties in order to investigate possibilities for light sources utilizing such Si-based materials.

Si ions were implanted into a fused-silica substrate (10 mm$\times$10 mm$\times$1 mm^t) at room temperature in TIARA. The implantation energy was 80 keV, and the implantation amount was 3×10^{17} ions/cm^2. The Si-ion-implanted substrate was cut into four pieces (5 mm$\times$5 mm$\times$1 mm^t) using a diamond-wire saw, and three pieces were annealed in ambient air for 25 min at 1,100, 1,150, and 1,200 ^{o}C in a siliconit furnace. PL spectra from the three samples were measured at room temperature with excitation using a He-Cd laser (λ=325 nm). A monochromator, a photo-multiplier, and a lock-in amplifier were used in our measurements. The intensities of PL spectra were calibrated by using a white-light spectrum measured with an optical spectrum analyzer at wavelengths from 350 to 1,750 nm because sensitivities of the monochromator and the photomultiplier depend on input light wavelengths.

Figure 1 presents the PL spectra of the three samples generated at room temperature. PL spectra having one or two peaks were observed from all the samples. Broad PL peaks in the UV range were observed from the samples annealed at 1,150 and 1,200 ^{o}C. Their peak wavelengths were around 390 nm (1,150 ^{o}C) and 380 nm (1,200 ^{o}C). The UV peak of the sample annealed at 1,200 ^{o}C was stronger than the one annealed at 1,150 ^{o}C. In addition to UV PL peaks, longer-wavelength peaks were observed in the red to infrared range from all three samples. Both PL peaks may originate from interface layers between Si-NCs and SiO_2 media [5,6)]. We are trying to clarify the relationship between the amounts of Si-ion implantation into fused-silica substrates and their light-emitting properties by comparing our current and previous results [4,5)].

References

1) O. Hanaizumi et al., Appl. Phys. Lett. 82 (2003) 1361-1365.
2) Y. Yamada et al., Jpn. J. Appl. Phys. 35 (1996) 1361-1365.
3) L. Pavesi et al., Nature 408 (2000) 440-444.
4) K. Miura et al., Nucl. Instrum. Meth. Phys. Res. B 263 (2007) 532-534.
5) K. Miura et al., The 2009 Annual Conference of the Illuminating Engineering Institute of Japan, to be presented, in Japanese.
6) K. Miura et al., Thin Solid Films 516 (2008) 7732-7734.

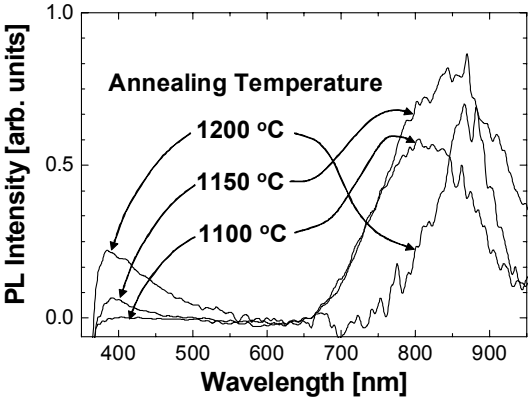

Fig. 1 PL spectra of Si-ion-implanted samples.

4-22 Characterization of the He Bubbles in Si Probed by a Positron Annihilation Spectroscopy

M. Maekawa and A. Kawasuso

Advanced Science Research Center, JAEA

It is known that helium bubbles in silicon can be formed by the high-dose He implantation. Such bubbles have been investigated as the gettering center for the impurities in silicon [1]. However, the interaction between irradiation defects and implanted He atoms, especially the role of defects for the bubble formation, are not clarified. Positron annihilation spectroscopy is suitable for the defect characterization in materials. In this study, we attempted to investigate the fundamental aspects of interaction between positrons and irradiation defects and/or the He bubbles in silicon induced by the high-dose implantation of He ions.

Samples were formed by He implantation to the *n*-type Si substrate with the energy of 50~200 keV to dose of 1×10^{17} cm^{-2}. After the implantation, the samples were annealed in argon ambient up to 900 °C. Doppler-broadening of annihilation quanta was measured and characterized by *S* and *W* parameters, which are defined as the peak and tail intensities, respectively. All the *S* and *W* parameters are normalized to the unimplanted value. When positrons annihilate at unimplanted crystal, the *S* and *W* parameters become 1.00 simultaneously. If only one kind of defect exists and positrons are trapped in it, the *S* parameter increases and the *W* parameter decreases.

Figure 1 shows the annealing behavior of *S* and *W* parameters of the ion implantation region. At 25 °C (as-implanted state), the *S* parameter became large as compared to the unimplanted state because of the implantation defects. By the thermal annealing of 200~400 °C, the *S* parameter decreased and the *W* parameter increased. This phenomenon seems to be recovery of the implantation defects. However, though the *W* parameter reached the unimplanted level, the *S* parameter did not. This means that this change was not due to the simple vacancies. In the case of the low-dose implantation, the He atoms trapped in the defects by the low-temperature thermal annealing are reported [2]. In the case of the high-dose implantation, similar vacancy clusters filled by the He atoms, i.e., He bubbles, might be formed. Figure 2 shows the result of the cross-sectional transmission electron microscope (TEM) observation. The sample was annealed at 300 °C. Many small black spots with the diameter of a few nanometers were observed. These seem to be the He bubbles.

The electron momentum distribution was measured by the detail measurement of the Doppler-broadening spectrum for the sample annealed at 300 °C. The result is shown in Fig. 3. Theoretical curves calculated by the first principal calculation for the some defective atomic models are also shown. When the V18 cluster, that is the vacancy of 18 Si atoms, was introduced, the experimental result was not reproduced at all. By introducing helium atoms into the cluster, intensity of the higher momentum region (over 5 mrad) increased. When 36 He atoms were filled to the cluster, the calculation result reproduced the experimental result. From this result, it becomes clear that positrons annihilate with the atomic structure like V18 cluster + 36 helium atoms, which is regarded as the He bubble.

In summary, the He bubbles in Si induced by the high-dose implantation were probed by the positron annihilation spectroscopy. Positrons can interact with the He bubbles.

References

1) S. E. Donnely et. al., Nucl. Instrum. Meth. 206 (2003) 422.
2) R. S. Brusa et. al., Phys. Rev. B61 (2000) 10154.

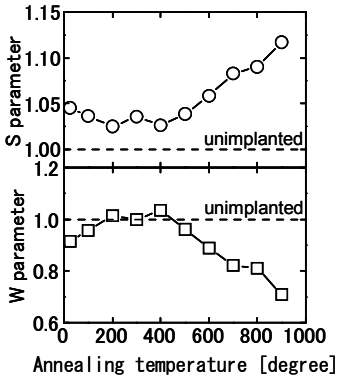

Fig. 1 Annealing behavior of *S* and *W* parameters.

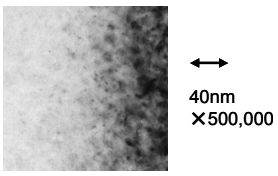

Fig. 2 The cross-sectional TEM image of ion implanted region for helium implanted Si.

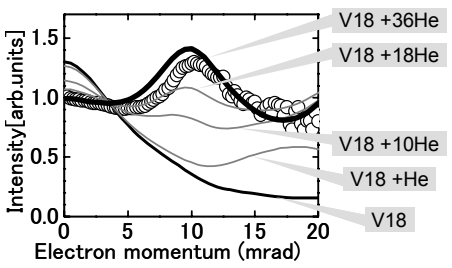

Fig. 3. Electron momentum distribution for the sample annealed at 300 °C and calculated theoretical curves.

4-23 Surface Plasmon Excitations from Al(111)-1×1 Surface studied by Reflection High-Energy Positron Diffraction

Y. Fukaya, A. Kawasuso and A. Ichimiya

Advanced Science Research Center, JAEA

Surface plasmon is one of the elementary excitations of solid surfaces. In general, the surface plasmon excitations are studied by using electron energy loss spectroscopy (EELS). Recently, using reflection high-energy electron diffraction (RHEED), the excitation process of surface plasmon by high-energy electrons has been extensively investigated [1].

The reflection high-energy positron diffraction (RHEPD) is a surface-sensitive technique owing to the total reflection [2),3)]. Due to their positive charge, positrons are totally reflected at the first surface layer when the glancing angle of incidence is small enough. In the total reflection region, the incident positron beam almost does not penetrate the surface. Therefore, under the total reflection condition, the energy loss process of positrons is considered to be different from that of electrons.

Very recently, we constructed the energy-filtered RHEPD and measured the energy loss spectrum from the Si(111)-7 × 7 surface. We found that under the total reflection condition the mean excitation number of the surface plasmon by positrons is larger than that by electrons [4]. In this study, to investigate the excitation process of the surface plasmon by positrons at metal surfaces, we measured the positron energy loss spectrum from the Al(111)-1×1 surface under the total reflection condition.

Samples ($15 \times 5 \times 0.5$ mm^3) were cut from a mirror polished *n*-type Si(111) wafer with a resistivity of 1-10 Ωcm. They were introduced into a ultra-high vacuum (UHV) chamber with a base pressure less than 6×10^{-8} Pa. They were annealed at 400 °C and flashed at 1200 °C in a few seconds several times to produce the 7×7 reconstruction. The Al atoms of 1/3 monolayer (ML) were deposited on the Si(111)-7×7 surface at 670 °C using a crucible to produce the $\sqrt{3} \times \sqrt{3}$-Al structure, where 1 ML corresponds to 7.83×10^{14} cm^{-2}. Then, the Al atoms of 3 ML were deposited on the $\sqrt{3} \times \sqrt{3}$-Al structure at 350 °C [5]. The formation of the Al(111)-1×1 surface was confirmed by RHEED.

The positron beam was generated with a ^{22}Na positron source and electrostatic lenses. The details of the apparatus were described elsewhere [6]. The retarding-field-type energy analyzer was installed into the UHV chamber to measure the energy loss spectrum of positrons. The energy resolution of the analyzer was estimated to be 4.6 eV.

Figure 1 shows the energy loss spectrum (*d*N/*d*E) of the specular spots for positrons from the Al(111)-1 × 1 surface as a function of the energy loss. The energy loss means the difference between the incident beam and retarding energy. In this energy loss region, five prominent loss peaks are observable with an interval of about 12 eV. Since the plasmon energy for the bulk Aluminum is 16 eV, the surface plasmon energy is estimated to be approximately 11.3 eV from the relation $\hbar\omega_s = \hbar\omega/\sqrt{2}$, where $\hbar\omega_s$ and $\hbar\omega$ are the surface and bulk plasmon energies, respectively. Thus, these peaks are assigned to a sequence of the surface plasmon losses. The peak intensity of the triple surface plasmon loss ($3\hbar\omega_s$) is larger than the others. Furthermore, the elastic peak (zero loss) intensity is much lower than these loss peaks. Therefore, the totally reflected positron excites multiple surface plasmons.

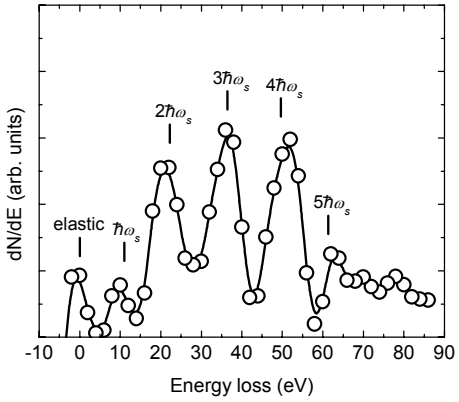

Fig. 1 Positron energy loss spectrum (*d*N/*d*E) from the Al(111)-1×1 surface as a function of the energy loss. The acceleration voltage of the incident beam was 10 kV. The glancing angle was 1.0°, which satisfies the total reflection condition. The incident azimuth corresponded to the [$11\bar{2}$] direction.

From the analysis of the loss peak intensities in Fig. 1 using Poisson distribution, we determined the mean excitation number as 2.8. This value is close to that from the Si(111)-7×7 surface [4]. Therefore, it is considered that the excitation process of the surface plasmon for positrons from the Al(111)-1×1 surface is nearly the same as the Si(111)-7 × 7 surface.

References

1) For example, Y. Horio *et al*., Jpn. J. Appl. Phys. **34** (1995) 5869.
2) A. Ichimiya, Solid State Phenom. **28&29** (1992) 143.
3) A. Kawasuso and S. Okada, Phys. Rev. Lett. **81** (1998) 2695.
4) Y. Fukaya, A. Kawasuso, and A. Ichimiya, Phys. Rev. B **79** (2009) 193310.
5) S.-T. Li *et al*., Appl. Surf. Sci. **41/42** (1989) 118.
6) A. Kawasuso *et al*., Phys. Rev. B **68** (2003) 241313.

4-24 Effect of Silica Addition on Kinetic Scheme of Radiation-induced Reduction of Dichromate Ion

Y. Kumagai, R. Nagaishi and R. Yamada

Division of Environment and Radiation Sciences, NSED, JAEA

Increase in the yields of molecular hydrogen production and reduction of metal ions has been reported in mixed systems of ceramic oxides and aqueous solutions[1-3]. It is expected that effective use of these phenomena is applicable to control of the radiation-induced reactions. Concerning the effect of ceramic oxides addition, early events, such as effect on the yields of radiolytic products of water have been studied [4,5] as well as effect on the resulting products. However little is known of the kinetic scheme bridging these two stages of different time scales. It is important for considering practical use of the addition effect of oxides. Thus we have studied the effect of silica addition on the radiation-induced reduction of dichromate ion, $Cr_2O_7^{2-}$.

The effect of the addition of silica gel (GL Science, 60-80 mesh size) was examined in the presence and the absence of 0.1 M *t*-butanol in aqueous solutions of 1 mM $K_2Cr_2O_7$ and 0.1 M $HClO_4$ deaerated by Ar. Sample of silica gel was washed with 0.1 M NaOH solution, 0.1 M $HClO_4$ solution, then rinsed with pure water and dried at 200 °C. Samples were irradiated by γ-ray from ^{60}Co, and then concentration of $Cr_2O_7^{2-}$ was measured by absorption spectroscopy. In order to distinguish addition effects relating from that not relating to radiation-induced reactions, samples added silica gel before and after irradiation were compared. Absorbed dose ranged from 1 to 7 kGy.

The reduction yield was calculated using decrease in concentration of $Cr_2O_7^{2-}$ and total absorbed energy of a sample derived from measured dose, density, and mass energy-absorption coefficient. The results are shown in Fig. 1 as a function of weight fraction of added silica gel. Since the difference between two series of samples, to which silica gel added before or after irradiation, is existence of silica gel in solutions during irradiation, addition effect on the radiation-induced reactions is indicated by the difference between the results measured in the two series.

In the absence of *t*-butanol, the addition of silica gel before irradiation increased the reduction yield compared to the addition after irradiation (SG-N-b and SG-N-a). On the contrary, in the solution containing *t*-butanol there is not a significant difference in the reduction yields between the two series (SG-B-b and SG-B-a). Additionally, when silica gel added after irradiation (SG-N-a and SG-B-a), the reduction yield was observed to be decreased. This trend is unrelated to the radiation-induced reactions and due to the adsorption of $Cr_2O_7^{2-}$ to the silica gel. This is because at lower dose, the concentration of $Cr_2O_7^{2-}$ is higher, and then the decrease in the concentration of $Cr_2O_7^{2-}$ in the solution by adsorption is relatively larger than at higher dose. Therefore decrease in the concentration of $Cr_2O_7^{2-}$ by irradiation was superficially observed to be smaller.

Difference in the reduction yields between the two series was only observed in the absence of *t*-butanol. This indicates that the addition of *t*-butanol suppresses the effect of silica gel. The main role of *t*-butanol is scavenging of $^{\bullet}OH$ and the radical of *t*-butanol, $^{\bullet}CH_2(CH_3)_2COH$, is produced, which then reduces $Cr_2O_7^{2-}$. In the absence of *t*-butanol $^{\bullet}OH$ causes the back reaction by oxidizing Cr^{3+}. Therefore it is suggested that there is an interaction between silica and $^{\bullet}OH$, and it inhibits the back reaction by $^{\bullet}OH$.

Change in the yields of products of water radiolysis is another possibility, but, if it exists, its effect is lower than the measured difference in the reduction yield because in the presence of *t*-butanol the reduction yield is almost unchanged by the addition of silica gel.

Then it is inferable that experimental results obtained in steady state radiolysis of aqueous solutions containing silica are more or less affected by this interaction with $^{\bullet}OH$. However it is still an open question whether it is redox reaction, adsorption or other modes of interaction.

References

1) R. Yamada et al., Int. J. Hydrogen Ener. 33 (2008) 929.
2) R. Nagaishi et al., Radiat. Phys. Chem. 75 (2006) 1051.
3) R. Nagaishi et al., JAEA Takasaki Ann. Rep. 2008 (2008) 160.
4) T. Schatz et al., J. Phys. Chem. B 102 (1998) 7225.
5) N. M. Dimitrijevic et al., J. Phys. Chem. B 103 (1999) 7073.

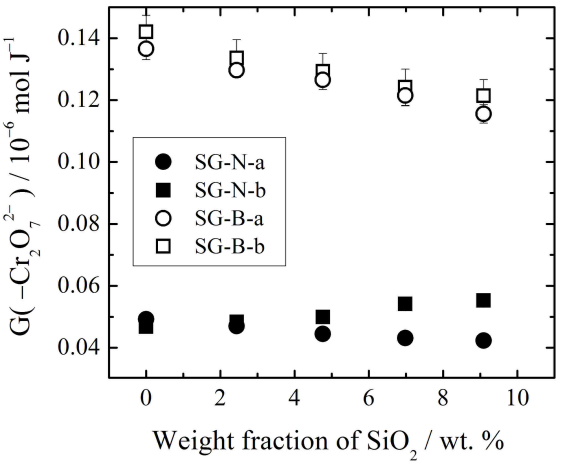

Fig. 1 The reduction yield of $Cr_2O_7^{2-}$ as a function of weight fraction of silica gel. SG-N-b (■) and SG-N-a (●): without *t*-butanol, addition of silica before and after irradiation respectively. SG-B-b (□) and SG-B-a (○): 0.1 M *t*-butanol, silica before and after respectively.

4-25 Time Resolved Absorbance Measurement System with Pulsed Heavy Ion

M. Taguchi [a)], Y. Sugo [a,b)], S. Kurashima [c)], A. Kimura [a)] and K. Hirota [a)]

[a)] Environment and Industrial Materials Research Division, QuBS, JAEA,
[b)] Division of Fuels and Material Engineering, NSED, JAEA,
[c)] Department of Advanced Radiation Technology, TARRI, JAEA

Introduction

High energy heavy ions are used as a new tool for the various basic and application studies in material and biological sciences because they induce unique irradiation effects. The irradiation effects originate in the high-density heterogeneous reaction distributions in a track of the heavy ion. Here, hydroxyl(OH) is the most important radical for reactions in aqueous samples. In a previous paper[1,2)], we estimated the formation yield of the OH radicals under the heavy ion irradiations by the product analysis methods. However, in order to understand the reactions in a track in more detail, a direct observation of radical behaviors is a good approach. The time resolved spectroscopy is a method very effective in observing directly the chemical reactions induced by the heavy ion irradiation. We constructed the highly sensitive transient absorption measurement system having a low time-jitter by synchronizing with AVF cyclotron in TIARA facility[3,4)]. The specification of the system was verified from the chemical standpoint of the spectrum changes when controlling sample conditions to the observation phenomenon.

Experimental

The time resolved absorbance measurement system consists in two parts: pulsed ion irradiation and optical measurement systems. The former made first a low energy pulsed heavy ion from a direct current generated in the ion source by the chopper, accelerated them by the cyclotron to a desired energy, and then irradiated sample solutions with them. In the latter the prove light was introduced to the sample cell at the same position of the pulsed ion, and detected by a Si photodiode. High time resolution was achieved by controlling the timing of the chopper, cyclotron and optical detector precisely. The specification of the system was evaluated by using the aqueous KSCN solution, which is a standard for the time resolved absorbance measurement using the pulsed electron.

Results and discussion

The time profile of the absorbance of the oxygen-saturated aqueous KSCN solution irradiated with 220 MeV C ions was shown in Fig. 1. It is known that the OH radical is produced by the decomposition of water molecules in the aqueous KSCN solution irradiated with the pulsed electron, and reactive species $(SCN)_2^-$, which has a large molecular extinction coefficient, is produced by the following reactions,

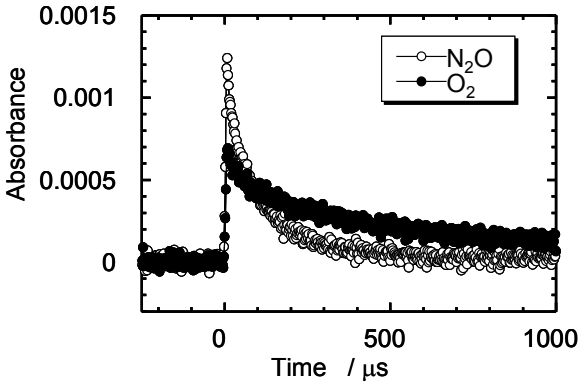

Fig. 1 Time profile of absorbance at 440 nm for aqueous KSCN solution irradiated with pulsed 220 MeV C ions. Open circle: nitrous oxide gas saturated condition, Closed circle: oxygen saturated condition.

$$H_2O \rightarrow H, OH, e^-, H_2, H_2O_2 \quad (1)$$
$$KSCN \rightarrow K^+ + SCN^- \quad (2)$$
$$SCN^- + OH \rightarrow SCN + OH^- \quad (3)$$
$$SCN + SCN^- \rightarrow (SCN)_2^- \quad (4)$$
$$(SCN)_2^- + (SCN)_2^- \rightarrow (SCN)_2 + 2SCN^- . \quad (5)$$

The optical absorption shown in Fig. 1 was identified to $(SCN)_2^-$ from the structure of the absorption spectrum measured in the range from 400 to 560 nm[3)].

In the case of nitrous oxide, N_2O, gas saturated condition, the yield of the OH radicals increases by the reaction of N_2O gas with e^- as follows;

$$e^- + N_2O + H_2O \rightarrow OH + OH^- + N_2 . \quad (6)$$

Initial absorbance under N_2O gas saturated condition is almost the double of that under oxygen saturated condition and the absorbance decayed faster as shown in Fig. 1. Increment of absorbance and faster decay are in accordance with the reaction (6) and (5), respectively.

Thus, the characteristics change of the absorbance when changing sample conditions is in good agreement with the prediction based on the chemical reaction theory, and the specifications of the time resolved absorbance measurement system were verified.

References

1) M. Taguchi et al., *Radiat. Res*., 171 (2009) 254-263.
2) G. Baldacchino et al., *Chem. Phys. Lett.*, 468 (2009) 275-279.
3) M. Taguchi et al., *Radiat. Phys. Chem*., in press.
4) Y. Sugo et al., *Radiat. Phys. Chem*., in press.

4-26 LET Effect on Degradation of Hydroxymaleimide in N_2-saturated 2-Propanol (2)

S. Nakagawa [a], M. Taguchi [b] and K. Hirota [b]

[a] Tokyo Metropolitan Industrial Technology Research Institute,
[b] Environment and Industrial Materials Research Division, QuBS, JAEA

Hydroxymaleimide was irradiated in N_2-saturated 2-propanol with 50 and 100 MeV He-ions, 350 MeV Ne-ion, and 220 MeV C-ion beams from the AVF cyclotron in the TIARA Facility. The differential *G*-values of degradation of hydroxymaleimide obtained in N_2 saturated system by heavier ion irradiation were less than those by lighter ion irradiation at the same LET value. It was opposite to the result obtained in air saturated system. The reduction of hydroxymaleimide competes with recombination of solvent radicals in N_2 saturated system. The localization of solvent radicals produced by heavier ion irradiation induces recombination of radicals effectively. Therefore, degradation efficiency of hydroxymaleimide will be decreased by heavier ion irradiation.

＜はじめに＞ マレイミド（$C_2H_2(CO)_2NH$）誘導体は、光化学重合反応の開始剤として研究が行われてきた。一方、ヒドロキシマレイミド（$C_2H_2(CO)_2NOH$）を窒素置換した2-プロパノールおよびメタノール中でγ線照射したところ、溶媒分子のラジカルが付加した化合物やダイマーが生成することがわかった。また、ヒドロキシマレイミドを含む空気飽和状態の2-プロパノール溶液をイオン照射したところ、ヒドロキシマレイミドの分解の微分G値のLET依存性の傾向は、ラジカルの生成量と同様に、Heイオン照射において重イオン照射と比較して同じLET領域で小さくなることがわかった[1)]。今回は、窒素置換した2-プロパノール溶媒中でヒドロキシマレイミドのイオン照射を行い、LET効果について空気飽和状態での照射と比較検討する。

＜実験方法＞ ヒドロキシマレイミドを2-プロパノールに溶かして（0.1モル%）窒素置換し、窒素雰囲気中で調製した試料を、原子力機構TIARA施設内AVFサイクロトンのNeイオン（350 MeV）、Cイオン（220 MeV）およびHeイオン（100 MeV, 50 MeV）を照射した。また、試料の上にアルミ箔を置き、入射イオンのエネルギーを変化させ、LET依存性を調べた。生成物およびヒドロキシマレイミドは、真空乾燥した残留物をアセトニトリルで溶解した後、液体クロマトグラフ（カラムODS、移動相アセトニトリル:水＝50：50）で分析した。

＜結果および考察＞ 吸収線量あたりのヒドロキシマレイミドの減少割合から分解効率を求めた。得られた分解効率をイオンの入射エネルギーあたりで規格化すると見かけのG値が得られる。入射イオンの初期エネルギーE_0, E_1での見かけのG値がG_0, G_1とすると微分G値dGは、

$$dG=(E_0\cdot G_0-E_1\cdot G_1)/(E_0-E_1) \qquad (1)$$

と求められる。

Fig. 1に空気飽和と比較した微分G値のLET依存性をプロットする。空気飽和の系と異なり、同じLET領域において重イオン照射ほど分解効率が減少した。

空気飽和の系では、酸化した溶媒がヒドロキシマレイミドと反応すると考えられる。一方、窒素飽和の系では、溶媒ラジカルがヒドロキシマレイミドに付加し(反応1)、付加体が生成する際に溶媒ラジカルが再生成し(反応2)、連鎖的に反応が進む。このため、ヒドロキシマレイミドの減少は、初期のラジカル生成量のイオン種による影響をほとんど受けないと考えられる。

また、ヒドロキシマレイミドの減少のメカニズムは、溶媒ラジカル同士の再結合反応(反応3)との競争であり、ラジカルの分布が重要となる。重イオン照射では生成するラジカルの分布がより局所的であるため、再結合反応が起こりやすく、ヒドロキシマレイミドの分解効率が低下するものと推測される。

$C_2H_2(CO)_2\text{-}NOH + R^{\bullet} \rightarrow {}^{\bullet}C_2H_2R(CO)_2\text{-}NOH$ (反応１)

${}^{\bullet}C_2H_2R(CO)_2\text{-}NOH + R\text{-}H \rightarrow C_2H_3R(CO)_2\text{-}NOH + R^{\bullet}$ (反応２)

$R^{\bullet} + R^{\bullet} \rightarrow R\text{-}R$ (反応３)

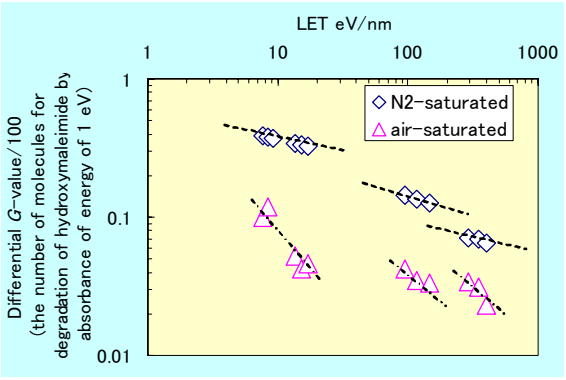

Fig. 1 The dependence of the differential *G*-values on LET value.

Reference

1) S. Nakagawa et al., *Radiat. Phys. Chem.*, 77 (2008) 1230.

4-27 Developing to the Single-Pulse Measurement of the Heavy Ion Beam Pulse Radiolysis Using Scintillator

T. Kondoh [a)], J. Yang [a)], K. Kan [a)], Y. Yoshida [a)], H. Shibata [b)], S. Kurashima [c)], M. Taguchi [d)] and K. Hirota [d)]

[a)] ISIR, Osaka University, [b)] Faculty of Engineering, Kyoto University,
[c)] Department of Advanced Radiation Technology, TARRI, JAEA,
[d)] Eenvironment and Industrial Materials Research Division, QuBS, JAEA

The characteristics of high LET radiation descends from the initial chemical reactions in the track. An ion-beam pulse radiolysis is developing to the single-pulse measurement for the initial process of ion-beam induced reactions. Our heavy ion beam pulse radiolysis system can realize high spatial resolution and high time resolution, and elucidate the characteristic of high LET effect. The refinement and the present status of our experiment system were reported here.

重イオンビームは高LET放射線で、物質に入射するとある深さで大きなエネルギーを与えて停止し、物質を局所的に高密度励起できる。近年のイオンビームを用いた物質改変、品種改良、がん治療など応用技術は、この高密度励起効果が発現したものである。これら応用技術の発展には、イオンビーム誘起反応の基礎過程を解明する必要がある。パルスラジオリシスは、物質にパルス化したビームを照射し生成した活性種を吸収分光などで直接観測する手法であり、イオンビームの場合、励起構造の特異性等から非常に困難であった。このためイオンビームが物質中で誘起する基礎過程は完全には理解されていない。一方、イオンビームの特徴である高密度励起効果は、高速に拡散して消失するため、解明するにはナノ秒の時間分解測定が必要である。我々は、イオンビームがシンチレーターを透過した時の発光を分析光として、イオンビームが試料中で停止する時の高密度励起による活性種の光吸収を測定する方法を発展してきた。この方法では、分析光源と励起場所がイオンビームの飛跡上なので、トラックの活性種濃度の直接測定と高時間分解能のイオンパルスラジオリシスを実現できる。一方、サイクロトロンからの重イオンビームを直接使用した場合、繰り返し周波数が高く、化学反応の観測が困難となる。本研究では、シンチレーターを利用した重イオンパルスラジオリシスでの、シングルパルス測定を行った。

TIARAのAVFサイクロトロンで発生した重イオンビームを、Pチョッパーを高度に制御することにより、シングルパルスで切り出した。HYポートに輸送されたビームは、サンプルセル上に設置されたシンチレーターを通過した後、試料に入射して停止する。シンチレータからの発光は全方位に放射され、このうち試料を通過した光は、光学フィルターで分光され光電子増倍管(PMT)で検出される。概要をFig. 1に示す。ビームを波形観測用のシンチレータNE-102に入射した時、主パルスの後に非常に小さな副パルスが観測されたものの、昨年度までの220 MeV Cイオンに加え、350 MeV Neイオンでもシングルパルス照射が可能となった。定常状態での強度、位置安定性が高いサイクロトロンのビームであるが、シングルパルス切り出し条件下では、長時間の照射実験中にビーム強度と位置が変動し、これが発光強度変動の原因となり正確な光吸収測定を困難にした。そこで、変動補正のために、シンチレータ上方への発光を測定しリファレンスとした。ピレン(Py)カチオンラジカルの光吸収測定に用いるCaF_2（Eu）シンチレーターを用いて測定した、ブランク試料（ジクロロメタン）、100 mM Py 溶液、さらに10 mM Py溶液の発光強度の時間変化のシグナル（それぞれ、Io、I-100 mM、I-10 mM）をFig. 2左に示した。各試料測定時のリファレンスをFig. 2右に、さらにリファレンスを用いて強度補正したシグナルをFig. 2下に示した。シグナルの生データでは、ビーム変動によりIoよりもI-100 mMが強くなり整合性に欠けるが、リファレンス測定により、このシグナル変動の大部分を補正することができた。今後この補正の精度を高めることにより、シングルパルス測定を可能にし、イオンビーム誘起初期過程を明らかにする。

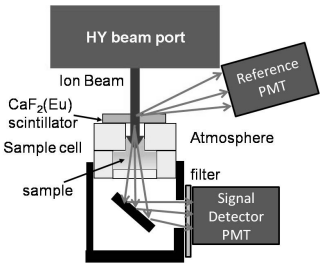

Fig. 1 Heavy ion beam pulse radiolysis system using scintillator with reference measurement.

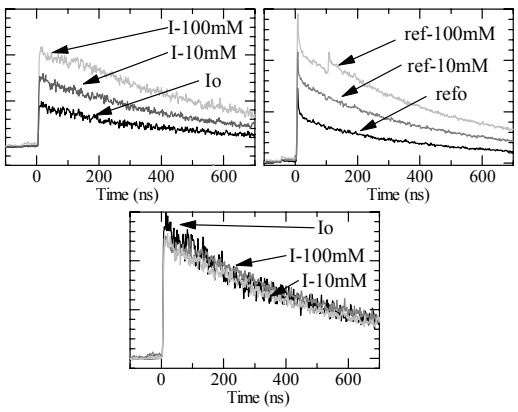

Fig. 2 Raw signal (upper left) and reference (right) and compensated signal by reference (lower).

4-28 Development of Dose Monitoring System Applicable to Various Radiations

T. Sato [a)], D. Satoh [a)], A. Endo [a)] and N. Shigyo [b)]

[a)] Division of Environment and Radiation Sciences, NSED, JAEA, [b)] Kyushu University

Introduction

For ensuring radiation safety in nuclear facilities as well as high-energy accelerator facilities, we have been developing a new device of dose monitoring system applicable to various radiations [1,2]. The system is composed of (1) a phoswitch-type scintillation detector, which consists of liquid organic scintillator coupled with ZnS(Ag) scintillator sheets doped with ^{6}Li, and (2) a data acquisition (DAQ) system for digital analysis of the waveform of the scintillation signals. The system is capable of measuring doses from neutrons, photons and muons with energy ranges from thermal energy to 1 GeV, 150 keV to 100 MeV, and 1 MeV to 100 GeV, respectively.

In the fiscal year of 2008, we examined the capability of our developing system for measuring dose rates in high-intensity radiation fields, using the quasi-monoenergetic neutron field at the LC0 beam course of the TIARA cyclotron.

Experiment

The experimental setup is depicted in Fig. 1. Quasi-monoenergetic neutrons with peak energy approximately 65 MeV were produced by bombarding protons of 68 MeV on a Li target. The phoswitch-type detector was placed behind the concrete and iron collimators at 12.9 m downstream of the target. The beam current was changed from 1 nA to 1 μA in the irradiation.

The signal from the detector was directly connected to our original DAQ system. In the system, the signal was divided into 2 branches, and their waveforms were digitized by 2 sets of ADCs at a sampling rate of 500 MHz. The 2 branches were specialized in close-up digitizing of a waveform in different voltage ranges. The digitized waveforms were immediately analyzed by FPGA. In the analysis, each event was identified as photon, neutron or muon-induced scintillation, using the pulse-shape discrimination technique. The light output of each scintillation was also determined in the FPGA analysis.

The information on the scintillation type and its light output was transferred to a tablet PC via Ethernet. In the PC, dose rates from neutron, photon and muon were calculated, using the G-function method [3], which directly relates the light output to the corresponding dose.

Results and Discussion

Figure 2 shows the time dependence of the measured neutron and photon dose rates at the LC0 beam course by changing the beam current of the TIARA cyclotron from 1 nA to 1 μA. It is evident from the figure that the measured dose rates are almost proportional to the beam current. This result indicates the accuracy of the measured dose rates even at the high-intensity radiation fields. This is owing to the high-speed waveform analysis in our developing DAQ system. For example, the count rate of the system during the irradiation at 1 μA was approximately 10^5 cps, which is much higher than the maximum count rates acceptable to conventional DAQ systems.

Conclusion

The applicability of our developing system to measuring the dose rates in high-intensity radiation fields was verified, using the LC0 beam course of the TIARA cyclotron.

Present study is the result of "Development of high-performance dose monitor applicable to various radiations" entrusted to Japan Atomic Energy Agency by the Ministry of Education, Culture, Sports, Science and Technology of Japan (MEXT).

References

1) T. Sato *et al*., J. Nucl. Sci. Technol. **42** (2005) 768.
2) T. Sato *et al*., Radiat. Prot. Dosim. **126** (2007) 501.
3) Y. Oyama *et al*., Fusion Technol. **26**, pt2, (1994) 1098.

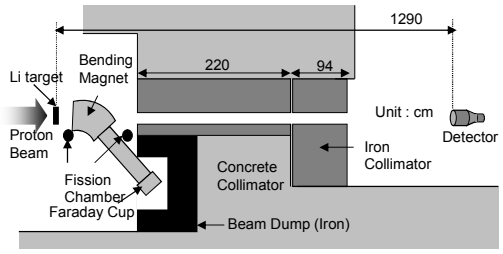

Fig. 1 Experimental setup at LC0 beam course.

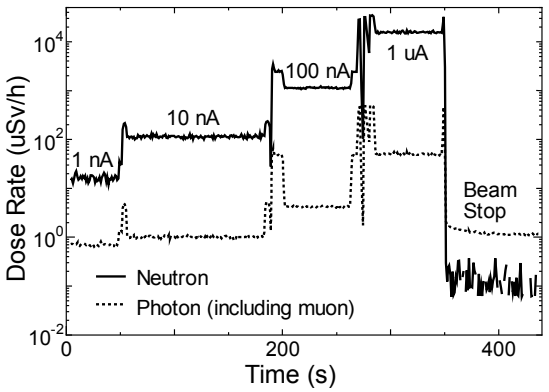

Fig. 2 Time dependence of the measured neutron and photon dose rates at the LC0 beam course by changing the beam current of the TIARA cyclotron.

4-29 Spectrum Measurement of Neutrons and Gamma-rays from Thick $H_2{}^{18}O$ Target Bombarded with 18 MeV Protons

M. Hagiwara [a)], T. Sanami [a)], Y. Iwamoto [b)], N. Matsuda [b)], Y. Sakamoto [b)], Y. Nakane [c)], H. Nakashima [c)], K. Masumoto [a)], Y. Uwamino [d)] and H. Kaneko [e)]

[a)] Radiation Science Center, KEK, [b)] Division of Environment and Radiation Sciences, NSED, JAEA, [c)] Safety Division, J-PARC, JAEA, [d)] RIKEN, [e)] TAARI, JAEA

In recent years, positron emission tomography (PET) has become a common technique of the functional imaging of a brain and organs. A number of cyclotrons are installed in medical facilities to produce radionuclides for PET. In PET, one of the most commonly used radiopharmaceuticals is fluorodeoxyglucose (FDG), which is tagged with the radioactive ^{18}F isotope. The isotope is obtained from the $^{18}O(p,n)^{18}F$ reaction when ^{18}O-enriched water ($H_2{}^{18}O$) is bombarded with a proton beam. The nuclear reaction produces neutrons and γ-rays simultaneously. The energy spectrum and angular distribution should be estimated for radiation safety and clearance of the facility.

However, the experimental data on the energy spectrum and angular distribution for neutrons and γ-rays from the $H_2{}^{18}O$ are not available especially for proton energies from 10 to 20 MeV that are used in the PET cyclotrons. Currently, shielding of the neutrons and γ-rays as well as activation of accelerator components and the room wall are calculated based on calculation codes such as PHITS[1)]. The accuracy of the codes for such a low energy region should be checked by experimental data, because most of physical models implemented in the codes were developed to describe reactions of high-energy particles. In this report, we describe the measurement of energy spectra of neutrons and γ-rays from the $H_2{}^{18}O$ induced by 18 MeV protons and comparisons between the experimental data and calculation results.

The experiments were carried out with 18 MeV proton beams delivered to the HB-1 beam line at the AVF cyclotron facility. The $H_2{}^{18}O$ target is prepared by filling a SUS container of 6 mm depth covered with a 10 μm-thick Havar foil with ^{18}O-enriched water (98 atm% enriched in ^{18}O) and installed in a vacuum chamber. The NE213 organic liquid scintillators (5.08 cm in diameter, 5.08 cm in length) were placed in directions of 15, 30, 45, 60, 75, 90, 120 and 150° with distance of 2.0 m from the target to measure the light outputs of neutrons and γ-rays and the time-of-flight (TOF). The events of neutrons and γ-rays were separated by using a pulse shape discrimination technique and analyzed by the TOF method and the unfolding method with FERDOU code[2)], respectively. Figure 1 shows the measured neutron energy spectra compared with the calculation results using PHITS and MCNPX. The calculation results generally well reproduce the measured energy spectra except for forward angle in PHITS and backward angle in MCNPX. Figure 2 shows the measured angle-integrated energy spectra of prompt γ-rays compared with the Japan Radioisotope Association (JRIA) result[3)] calculated using the MCNPX2.5 code. The JRIA result generally well reproduces the measured energy spectra except for the some peaks shown in the measured results.

In future, we will systematically measure neutron and γ-ray spectra from accelerator components induced by protons and deuterons with low energy to check the accuracy of evaluated data libraries and calculation codes.

References

1) H. Iwase et al., J. Nucl. Sci. Tech. 39 (2002) 1142.
2) K. Shin, Y. Uwamino and T. Hyodo, Nucl. Technol., 53 (1981) 78.
3) JRIA report, March 2009.

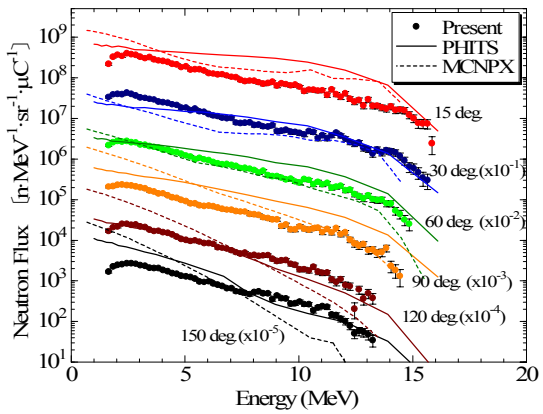

Fig. 1 Energy spectra of neutrons from the $H_2{}^{18}O$ target induced by 18 MeV protons.

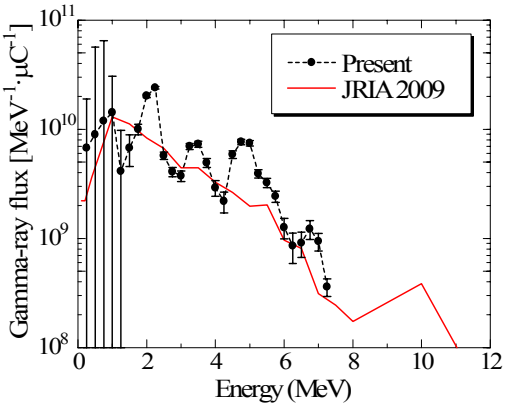

Fig. 2 Energy spectra of prompt γ-rays from the $H_2{}^{18}O$ target induced by 18 MeV protons.

4-30 Development of a Transmission Type Fluence Monitor for Quasi-monoenergetic Neutron Calibration Fields of Several Tens of MeV

Y. Shikaze [a], Y. Tanimura [a], J. Saegusa [a], M. Tsutsumi [a], Y. Uchita [a], M. Yoshizawa [a], H. Harano [b], T. Matsumoto [b] and H. Kaneko [c]

[a] Department of Radiation Protection, NSRI, JAEA, [b] National Metrology Institute of Japan, National Institute of Advanced Industrial Science and Technology, [c] Department of Advanced Radiation Technology, TARRI, JAEA

Though high energy neutron standard fields are necessary for calibrating area and individual dosimeters used in facilities of high intensity proton accelerator, the neutron standard fields above 20 MeV have not been established in Japan. Therefore, development of both the calibration fields and relevant calibration techniques has been making progress by using the quasi-monoenergetic neutron irradiation fields with 45, 60 and 75 MeV peaks at TIARA[1-2] of Takasaki Advanced Radiation Research Institute, Japan Atomic Energy Agency.

In practical calibration, neutron fluence must be monitored with enough precision. In order to achieve good correlation of count rate with neutron intensity in an irradiation room, a prototype of a transmission type neutron fluence monitor has been developed[3]. Its performance test results indicated that low collection efficiency of the scintillation light led to sensitivity lower than an existing neutron fluence monitor (a fission chamber) located at an off-line position ahead of the collimators. Therefore, in order to improve sensitivity, a transmission type neutron fluence monitor with different structure (Fig. 1) has been newly developed by changing light collection method.

The monitor has two photomultiplier tubes (PMTs) which detect the scintillation light yielded in the thin plastic scintillator ($150 \times 150 \times 0.5$ mm^3). The scintillator installed in the aluminum case is fixed on the inner surface of one of the aluminum windows (145×145 mm^2). In order to improve light collection efficiency, direct light collection method was applied by removing both acrylic light guides and reflection material coated on the scintillator surfaces.

The performance has been evaluated by using three kinds of quasi-monoenergetic neutron fields with 45, 60 and 75 MeV peaks at TIARA. In the tests, the monitor was set on the surface of the collimator exit (Fig. 1). Data on the sum of each pulse height of the two PMTs were taken. The direct light collection method raised the sensitivity of the new monitor ten times higher than that of the prototype to realize about the same sensitivity as the existing monitor (Fig. 2). As shown in Fig. 2, it was confirmed that the monitor had good linearity of count rate to beam intensity within a range of interest in ordinary use. Moreover, in order to investigate the correlation of the monitor's count rate with neutron beam intensity after passing through the collimators and the monitor, other detectors (another fission chamber and an organic liquid scintillator) in the irradiation field were used as a reference of beam intensity. The correlation of the count rate of the monitor and those of the detectors were investigated. The results indicated that the correlation of the count rate of the monitor with actual beam intensity became better than those of the existing monitors set ahead of the collimators.

In the future, remaining problems to be solved for stable use will be improved, and a user-friendly counting system that has PC based indicator and recording functions will be established for actual monitoring in calibration.

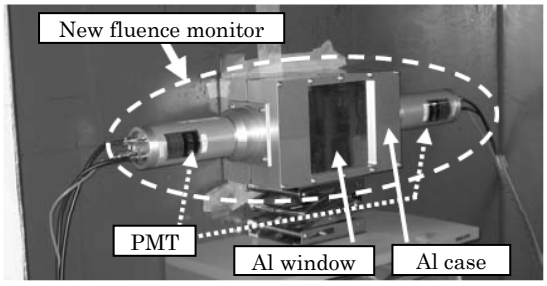

Fig. 1 New neutron fluence monitor consisting of a plastic scintillator without coating, an aluminum case with aluminum entrance windows and two PMTs.

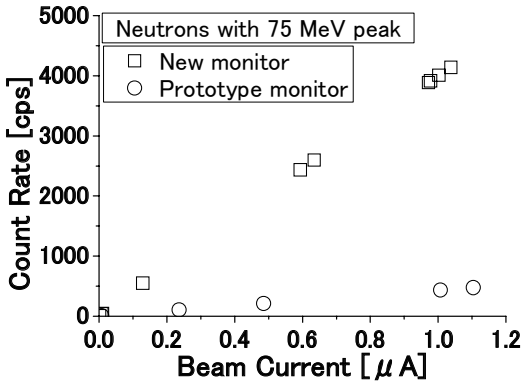

Fig. 2 Count rate v.s. beam current for neutrons with 75 MeV peak. Good linearity of the new monitor's count rate to beam current is seen.

References

1) M. Baba et al., Nucl. Instrum. Meth. A 428 (1999) 454.
2) Y. Shikaze et al., Radiat. Prot. Dosim. 126 (2007) 163.
3) Y.Shikaze et al., JAEA Takasaki Ann. Rep. 2007 (2008) 166.

4-31 Comparison of High Energy Neutron Fluence between TIARA and CYRIC

T. Matsumoto [a)], H. Harano [a)], T. Sanami [b)], M. Hagiwara [b)], Y. Unno [a)] Y. Shikaze [c)], J. Nishiyama [a)], J. Saegusa [c)], Y. Tanimura [c)], M. Tsutsumi [c)], M. Yoshizawa [c)], M. Baba [d)] and H. Kaneko [e)]

[a)] National Metrology Institute of Japan, National Institute of Industrial Science and Technology, [b)] Radiation Science Center, High Energy Accelerator Research Organization (KEK), [c)] Department of Radiation Protection, NSRI, JAEA, [d)] CYRIC, Tohoku University, [e)] Department of Advanced Radiation Technology, TARRI, JAEA

Precise measurement for high energy neutrons is important in studies on the neutron dose estimation around large accelerator facilities such as J-PARC, nuclear data, exposure in aircrafts and neutron induced soft error rate in a semiconductor devices. Therefore, measurement devices for high energy neutron above 20 MeV have been developed. Recently, the JAEA group has developed the calibration fields for quasi-monoenergetic neutrons with energies of 45, 60 and 75 MeV at TIARA. There are several similar facilities inside and outside of Japan where quasi-monoenergetic neutrons above 20 MeV can be produced. The quasi-monoenergetic neutron field at CYRIC of the Tohoku University is one of them. However, each facility has different characteristics for the neutron field and adopts different methods for high energy neutron measurements. Therefore, we have interest in comparison for the high energy neutron measurement among the neutron facilities.

In experiment for 45 MeV quasi-monoenergetic neutrons, the neutron fluence were measured with several neutron detectors, that are 5" × 5" and 2" × 2" NE213 liquid scintillators [1)], proton recoil telescope (PRT) [2)] and a spherical ^{3}He proportional counter with moderator made of polyethylene and lead[3)] as shown in Fig. 1. The results for each detector were relatively compared at first using proton beam current injected into the beam dump. The results obtained with the NE213 detectors are more than 10% larger than that of the PRT. We suspect that this discrepancy is mainly caused by the dark current through the cooling water on the beam dump, because the beam current is around 5 nA in measurements for the NE213 detectors, while it is around 1 μA in measurements for the PRT.

On the other hand, the results for the detector with the moderator were derived from the response function and neutron spectrum obtained by the TOF measurement with the NE213. Because the lower energy limit in neutron spectrum measured with the TOF method is determined by repetition rate of the proton beam from the accelerator and the flight path, the spectral component below the limit needs to be given by the extrapolation. Since the results depend on how the extrapolation is conducted, it is necessary to investigate the low energy component in the quasi monoenergetic neutron field. Therefore, we propose a novel neutron detector composed of four spherical ^{3}He proportional counters with different gas pressure and a moderator made of polyethylene and lead as shown in Fig. 2. The forward counters for the neutron beam direction have high sensitivity in the low energy region below 20 MeV, while the backward counters have high sensitivity above 20 MeV. We will try to derive the neutron fluence and to investigate the low energy component for 45, 60 or 75 MeV neutron field. Moreover, the results for the 45 MeV neutrons will be compared with those obtained at CYRIC.

References

1) M. Baba et al., Nucl. Instrum. Meth. A 428 (1999) 454.
2) Y. Shikaze et al., JAEA Takasaki Ann. Rep. 2007 (2008) 189.
3) B. Wiegel and A. V. Alevra, Nucl. Instrum. Meth. A 476 (2002) 36.

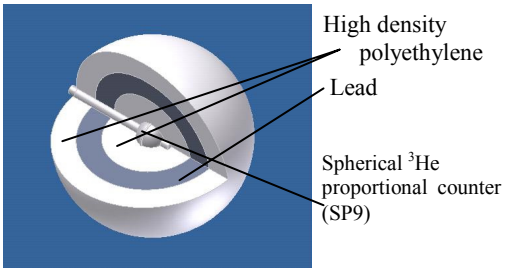

Fig. 1 The spherical ^{3}He proportional counter.

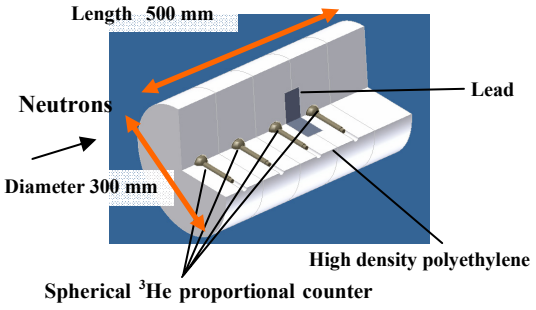

Fig. 2 Novel high energy neutron detector with cylindrical moderator made of polyethylene and lead.

Table 1 Peak neutron fluences (n/sr/μC) in the 45 MeV quasi-monoenergetic neutron field derived from the two NE213 detectors and PRT.

PRT	2"×2" NE213	5"×5" NE213
3.02E+09	3.35E+09	3.41E+09

4-32 Development of Electronic Personal Dosemeter for High-energy Neutrons

K. Oda, K. Iwano, H. Rito and T. Yamauchi

Graduate School of Maritime Sciences, Kobe University

In order to develop an active-type personal dosemeter having sufficient sensitivity to high-energy neutrons up to 100 MeV, the characteristic response of Si-semiconductor detector with a polyethylene (PE) radiator has been investigated experimentally and theoretically. Neutron irradiation experiments were carried out in a quasi-monoenergetic field of 65 MeV, where the signals caused by a recoil proton were measured as a function of the pulse height. Their distributions have been obtained for several different radiator thicknesses. On the other hand, theoretical distributions in the energy deposited in a sensitive layer of Si detector were estimated in a simplified geometry consisting of Si and PE layers, based on the angular differential cross section and the range-energy relation for protons. A good agreement in the shape and the peak height was confirmed between the theoretical and experimental results. The energy dependence of the dosemeter response could be improved by adjusting the radiator thickness.

既存の中性子用線量計は、約 20 MeV までの中性子を測定範囲としており、それ以上の高エネルギー中性子に対する線量を過小評価してしまう恐れがある。そこで、本報告では、高エネルギー中性子に対しても適切な感度を有する個人線量計の設計を目的とし、線量計レスポンスのエネルギー依存性の改善を図った。

直読式線量計用の検出素子として小型の Si 半導体検出器を選択した。また、理論計算との比較という観点から、Si 検出器とポリエチレン(PE)ラジエータから成る単純な構成が望ましいと判断した。

中性子計測実験は、検出器前部に PE ラジエータを装着した Si 検出器を用いて 65 MeV 準単色中性子場で行った。ラジエータの厚さを変化させ、得られたパルス波高分布を Fig. 1 に示す。用いた Si 検出器の空乏層は約 50 μm と薄く、ラジエータで発生する陽子の大半は貫通するため、パルス波高分布は低い領域に集中していることが分かる。また、ラジエータ厚さを厚くするにつれて、反跳陽子の検出事象が増加していることが確認できた。

一方、Si と PE のみから成る体系で、垂直入射した中性子から発生した陽子が Si の有感層に付与するエネルギーを理論的に計算した。角度微分断面積の立体角及び PE 深さに関する二重積分で表されるが、陽子の飛程－エネルギー関係から積分範囲が制限されることになる。計算した付与エネルギー分布の概形はほぼ測定したパルス波高分布と一致することが確かめられた。

次に、この計算手法を用いて、線量計の相対感度（線量当量当たりのパルス数）の中性子エネルギー依存性を異なるラジエータ厚さに対して計算した結果を Fig. 2 に示す。実際の中性子場ではγ線の影響を伴うので、γ線弁別レベルを 300 keV と仮定した。ラジエータ効果が飽和する厚さ（陽子の最大飛程）があるため、中性子エネルギーが低い場合はラジエータを変化させても感度が変わらないが、高エネルギーになるほど反跳陽子の検出事象が増加するためその効果は顕著に見られた。また、ラジエータ厚さをある程度厚くすることで高エネルギー領域の感度を上昇させることができた。

しかし、約 30 MeV 以上は PE を用いる限り、増感には限界があることもわかる。今後は、より高いエネルギー領域にも適用可能な個人線量計を開発するために、2 ウィンドー法等を適用してさらなるエネルギー依存性の改善に取り組むとともに、個人線量計として重要な角度依存性についても検討する予定である。

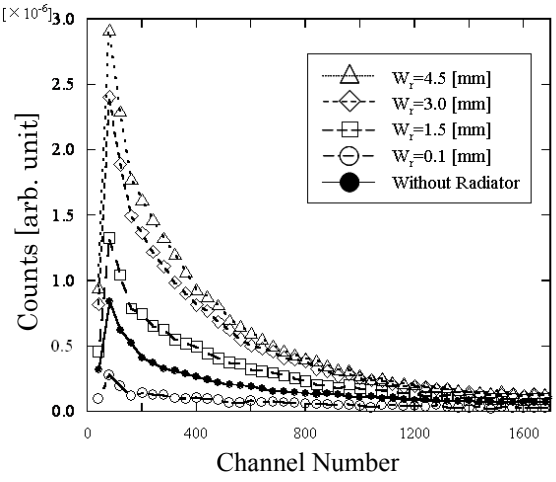

Fig. 1 Measured pulse height distribution for different radiator thicknesses.

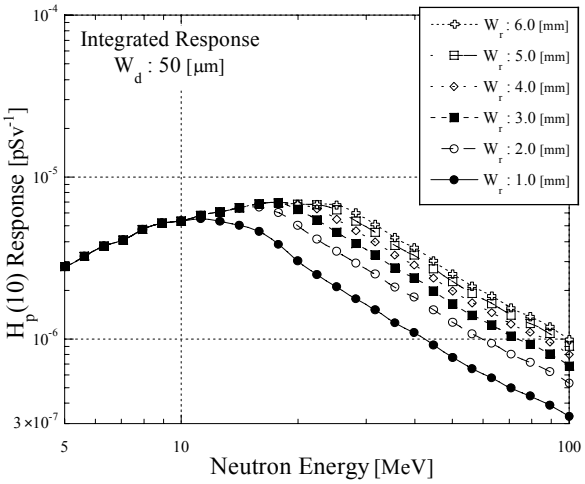

Fig. 2 $H_p(10)$ response of radiator effect as a function of neutron energy for several radiator thickness.

4-33 Properties of Blue Cellophane Film Dosimeter for ^{60}Co Gamma-rays and Electron Beams

H. Seito [a)], K. Nakai [b)], H. Kaneko [a)], Y. Haruyama [a)] and T. Kojima [a)]

[a)] Department of Advanced Radiation Technology, TARRI, JAEA, [b)] NHV Corporation

In the radiation processing of industrial materials by ^{60}Co gamma-rays and electron beams, several plastic or dyed plastic materials are commonly used as routine dosimeters for determining absorbed dose[1)]. The advantages of blue cellophane (BC) are said to be its low cost, ruggedness, ease of handling and readout, availability in large batches for routine use, and compatibility to many geometrical configurations. The thickness of BC film is thinner than that of polymethylmethacrylate (PMMA) dosimeter or cellulose triacetate (CTA) dosimeter, which can be applied to low energy electron beams. But some disadvantages like dose rate dependence and influence of humidity during irradiation were also mentioned[2)]. These dosimeters have been calibrated commonly only for ^{60}Co gamma-rays or MeV electron beams, therefore the feasibility should be studied on the calibration also for several hundred keV energy electron beams. In this fiscal year, we studied way to calibrate BC for low energy (several hundred keV) electron beams.

The BC film dosimeters with thickness of 20 μm were independently calibrated for gamma-rays and electron beams using an ionization chamber and CTA dosimeter with thickness of 125 μm, respectively. The BC film is sealed in a package in order to prevent from absorption of moisture in air. Moreover non-package type of BC film was simultaneously irradiated, in order to review moisture effect on the sensitivity. The gamma-ray irradiation was carried out using a ^{60}Co plaque source (2.6 PBq) at a dose rate of 10 kGy/h, which was measured with the ionization chamber. Irradiation of 2-MeV electron beams was carried out using an accelerator (EPS-3000) at NHV Corporation with the 180 cm wide scanning beams at absorbed dose of 10, 20, 30, 40 and 50 kGy. Irradiation of 800 keV and 300 keV electron beams was performed at the accelerator (EPS-800) at NHV Corporation. Optical absorbance change in terms of optical density change (ΔO.D) for radiation-induced coloration of dosimeters was measured for read out wavelength of 630 nm using Shimadzu spectrophotometer (model UV-1700). Thickness values were measured using a Mitutoyo micrometer (model MDC-25MJ).

Figures 1 and 2 show dose response curves of BC film dosimeters for ^{60}Co gamma-rays and electron beams, respectively. Dose response value for non-package type of film dosimeter is almost 30% smaller than film dosimeter with package. This difference is due to influence of humidity during irradiation. Humidity effects accordingly can be neglected by keeping BC film dosimeter in heat-sealed package during irradiation. In the case of electron beam irradiation, dose response is almost equal within 3% among different electron energy values. This result should enable us to achieve highly reliable dosimetry of several hundred keV energy electron beams on the basis of MeV energy electron dose reference.

References

1) H. Seito et al., Radiat. Phys. Chem. 78 (2009) 356.
2) P. Gehringer et al., Appl. Radiat. Isot. 33 (1982) 27.

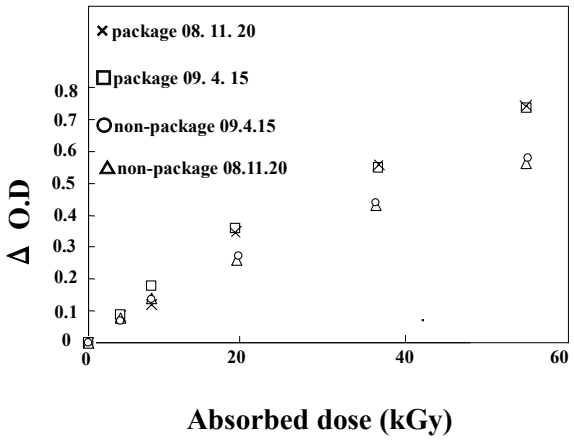

Fig. 1 Dose response curves of blue cellophane film dosimeter for ^{60}Co gamma-rays.

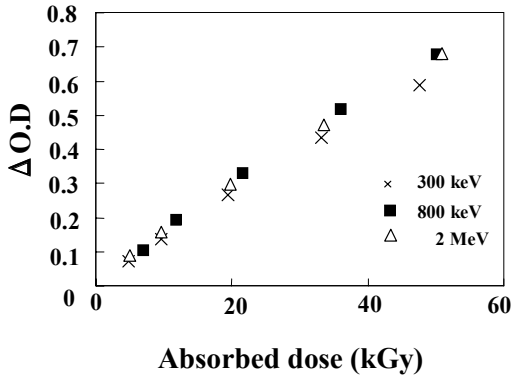

Fig. 2 Dose response curves of blue cellophane film dosimeter for electron beams.

4-34 Development of Electric Micro Filter Using Micro Structure by Proton Beam Writing

Y. Furuta [a)], H. Nishikawa [a)], Y. Shiine [a)], T. Satoh [b)], Y. Ishii [b)], T. Kamiya [b)], R. Nakao [c)] and S. Uchida [c)]

[a)] Department of Electrical Engineering, Shibaura Institute of Technology,
[b)] Department of Advanced Radiation Technology, TARRI, JAEA,
[c)] Department of Electrical and Electronic Engineering, Tokyo Metropolitan University

There has been increasing demand for a preventive approach for food safety, called HACCP (Hazard Analysis Critical Control Point), where the hazard analysis will be conducted at each critical control point in a step or procedure in a food process. To meet this demand, the dielectrophoresis has been successfully used for devices [1)] with capabilities of rapidly collecting, analyzing and even killing a food poisoning bacterium such as *O-157*, which is a bacterium *Escherichia coli (E.coli)*.

In this paper, we applied Proton Beam Writing (PBW) technique which is a promising method for micro-fabrication by a direct writing using focused beam of MeV protons[2,3)], to fabricate high-aspect-ratio pillar array using tens of micrometer thick negative resist. Utilizing the pillar array as a part of conventional electric micro filter having a capability of electrically trapping food poisoning bacteria such as *E.coli* we developed a novel electric micro filter. We also evaluate a trapping capability of bacteria for various arrangements of the pillar array by means of the PBW as a rapid prototyping tool to develop a new type of electric micro filter.

High-aspect-ratio pillar array was fabricated in area of 1.4 mm squared area by PBW on a 14-μm-thick negative-resist layer (SU-8, Kayaku-Microchem Corp.) which was spin-coated on a silica substrate [4)]. For the electric micro filter, a pair of Au surface electrodes with a gap of 200 μm was formed by vacuum evaporation on the substrate before spin-coating of the SU-8. The PBW is performed at a microbeam line of TIARA, JAEA.

Figure 1 shows a SEM image of the SU-8 pillar array on silica substrate developed after the PBW. This demonstrates the capability of the PBW to fabricate vertical pillars with an aspect ratio of 12.4 over 1.4 mm squared area.

The pillar array was introduced across the gap of the Au electrodes by PBW. The pillar array on the silica substrate was capped by a PMMA plate with PDMS sidewalls to form a few-mm width channel. Then, the electric micro filter was evaluated for trapping capability by photoluminescence (PL) measurements under AC bias with flowing suspension of *E.coli* dyed with SYTO9 (Invitrogen Corp.).

In order to demonstrate the utility of the pillar array as a part of the electric micro filter, we compare the trapping behavior of *E.coli* for filters with and without the pillar array as shown in Fig. 2. The PL intensity was measured as a function time after application of the AC bias. The amount of the dyed *E.coli* trapped at the site of the pillar array in the electric micro filter with high aspect ratio pillar array is twice as large as the one without pillars. By changing the height and spacing of the pillars by the PBW, improved performance of the new electric micro filter was confirmed.

These results indicate the utility of the high-aspect-ratio pillar array fabricated by the PBW for the development of the new type of electric micro filter.

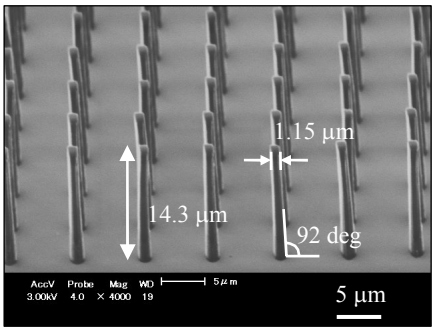

Fig. 1 A SEM image of the high-aspect ratio pillar array for electric micro filter formed by PBW using SU-8.

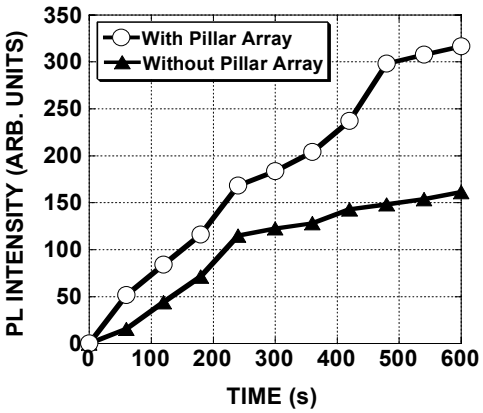

Fig. 2 Change in the PL intensity as a function time after application of the AC bias observed for electric micro filters with and without high-aspect-ratio pillar array. (Applied voltage: 71.7 V_{p-p}, Frequency: 50 kHz).

References

1) T. Enjoji et al., Journal of Institute of Electrostatics Japan, **31**, 1 (2007) 8.
2) F. Watt et al., Materials Today, **10**, 6 (2007) 20.
3) Y. Furuta et al., J. Vac. Sci. Technol. B **25**, 6 (2007) 2171.
4) N. Uchiya et al., Nucl. Instrum. Meth. B **260**, 1 (2007) 405.

4-35 Energy Dependence for 2-Dimentional Nuclear Reaction Distribution of Boron Doped in Steel

H. Shibata [a)], Y. Kohno [b)], T. Satoh [c)] and T. Ohkubo [c)]

[a)] Kyoto University, [b)] Muroran Institute of Technology,
[c)] Department of Advanced Radiation Technology, TARRI, JAEA

The microanalysis of trace amount of boron has been carried out using 3 μm proton microbeam from 3MV single ended electrostatic accelerator of TIARA facility. In 2008 steel specimens containing 100 ppm boron have been bombarded by 1.5~2.3 MeV proton beam for gamma ray detection. The 2-dimensional boron distributions dependent on proton energy have been measured by detecting 428 keV gamma ray from the ^{10}B (p, α'γ) ^{7}Be nuclear reaction. As a result of imaging, segregation of several microns sized boron precipitates has been observed, and the some correlation between energy dependent distributions could be seen.

鉄鋼材料に微量のホウ素を添加することにより強度が増大することは経験的に知られているが、鉄鋼中でのホウ素の振舞いについてはまだ十分に解明されていない。これは鉄鋼中に限らず、ホウ素の局所的かつ定量的な微量分析が難しいことによる。ホウ素の局所的な空間分布の定量分析ができるようになれば、ホウ素添加鉄鋼材料の強度特性とホウ素の分布の関係を明らかにでき、熱処理等のプロセスにおいてホウ素分布の最適化を図ることができる。これは、ホウ素の効率的な処理によって、クロム、モリブデンなどの鋼中合金元素を必要とすることなく所要強度の実現を可能にするものであり、生産コストの低減化、省資源化、そして環境に優しいリサイクルマテリアルとなる。

材料中に含まれる微量のホウ素分布を空間的、定量的に精度良く調べるために、陽子マイクロビームとホウ素との核反応を利用した分析法を採用し、新たな分析手法の確立を目指すのが本研究テーマの目的である。

2008 年度は TIARA の大気マイクロ PIXE のポートを用いて、陽子とホウ素の核反応で放出される γ 線の二次元分布の測定を行った。昨年に引き続き γ 線の二次元分布の入射陽子のエネルギー依存性の測定を行ったので報告する。

ホウ素の定量的な分布を求めるために、これまで ^{10}B (p, α'γ) ^{7}Be の核反応によって放出される 428 keV の γ 線を、HPGe 半導体検出器を用いて測定を行ってきた。分解能は 1.33 MeV において 1.7 keV である。真空チャンバー側には Si (Li)の X 線測定用の検出器が設置されており、γ 線と同時に特性X線も測定することができるようになっている。今回用いた試料は 100 ppm のホウ素を含んだ鉄の板（10×10×1 mm）で、B の他、C, Si, Mn, P, S, N, Cr, W, Co,V を含む。

Fig. 1 に核反応の全断面積を示す。この核反応では 1.5 MeV 付近に小さな共鳴があり、700 keV 位から非共鳴の断面積がなだらかに上昇する。3 MeV 位になると色々な核反応が現れてこの反応の測定が困難になるので、今回は 1.5、1.7、1.9、2.1 及び 2.3 MeV と昨年度よりもエネルギー間隔を細かくとり、ホウ素の二次元分布がどの様に変わるか、測定を行った。それぞれのイオンが核反応を起こす最大の進入深さは~8 (1.5)、~10 (1.7)、~13 (1.9)、~15 (2.1)、~19 μm (2.3 MeV) であり、2～4 μm の進入深さの差があることから、昨年度より詳細にホウ素の深さ分布の情報が得られるのではないかと考えられる。

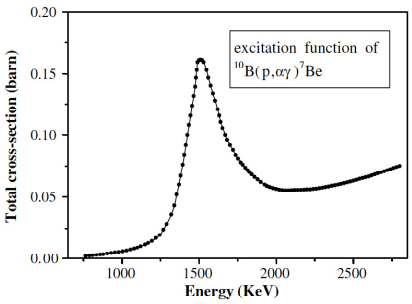

Fig. 1 Total cross-section of ^{10}B(p,α'γ)^{7}Be reaction.

Fig. 2 に 1.5、1.7、1.9、2.1 及び 2.3 MeV の入射エネルギーで得られた、ほぼ同じ領域のホウ素の二次元分布を示す。エネルギーを変えると照射野の倍率が変わることや試料セッティングの再現性の問題で全く同じ場所へ照射するのは難しく、この点は今後の課題である。図中の黒い部分がホウ素であるが、1.7 MeV から 1.9 MeV の間で若干位置がずれている。(a)から(e)で同じような場所にホウ素が存在していることが分かる。ホウ素の深さ分布を得るためには、入射エネルギー間の差分の計算法を開発する必要があり、これも今後の課題である。

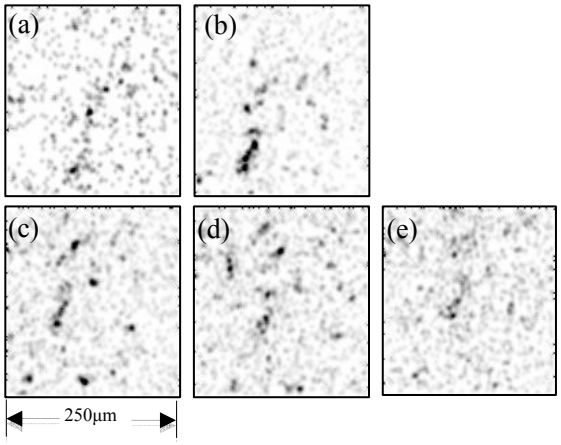

Fig. 2 A typical γ-ray images of 100 ppm boron contained steel specimen bombarded by (a) 1.5, (b) 1.7, (c) 1.9, (d) 2.1 and (e) 2.3 MeV proton microbeam.

4-36 Analysis of Emission Angle Distribution of C_2^+ Fragment Ions Exiting from Thin Carbon Foil

A. Chiba [a)], Y. Saitoh [a)], K. Narumi [b)], K. Yamada [a)], Y. Takahashi [b)] and T. Kaneko [c)]

[a)] Department of Advanced Radiation Technology, TARRI, JAEA, [b)] Advanced Science Research Center, JAEA, [c)] Department of Applied Physics, Okayama University of Science

The structure and incident angle of a cluster ion to the target are important elements to resolve a process of collisional reaction between a swift cluster ion and the solid. Dependence of the charge state distribution of fragment ions exiting the thin carbon foil on the structure of the incident cluster was recently demonstrated using 3-MeV, C^{3+} ion both experimentally and theoretically [1)]. Now, we are investigating the relationship between the charge state of the C_2^+ fragment ions dissociating in the foil and the incident angle of the cluster ion. In this report, the emission-angle distributions of the fragment ions emerging from the thin carbon foil were analyzed, using the particle trajectory simulation.

The experimental setup is shown in Fig. 1. Carbon cluster ions (C_2^+) generated by a cesium sputter ion source are accelerated to the energy of 6-MeV (3-MeV/atom) by the tandem accelerator at JAEA/Takasaki. A carbon foil of 1.0-μg/cm^2 thickness (60Å) was used as the target. To improve an S/N ratio, a shutter of a high speed CMOS camera is triggered by a detecting signal of secondary electrons from the foil. The fragment ions were deflected depending on their charge states by an electric field applied to the deflection plates placed between the foil and a MCP-2. The deflection angles depend on their charge state. The two-dimensional pattern of the deflected ions was observed as luminance points on a fluorescent screen equipped with the MCP-2. The emission-angle can be estimated from the distance between the two luminance points.

The particle trajectory simulation is treated with basically the Coulomb explosion and multiple scattering, which is evolved by the following expression:

$$V(r) = \frac{Z_1 Z_2 e^2}{r} \sum_{j=1}^{3} \alpha_j \exp\left(-\frac{\beta_j r}{\Lambda}\right)$$

Here the α_j and the β_j are the screening functional factors for Thomas-Fermi-Moliere potential, and the screening radius Λ is 0.182Å for the multiple-scattering. The screening radius on the Coulomb explosion process in the target depends on the velocity of fragment ions and the plasma frequency in the target. The charge state of fragment ions in the foil is as the average charge of the fragment ions emerging from the foil.

Figure 2 shows the experimental and calculated result of the emission-angle distribution for the C_2^+ fragment ions (pair of C^{3+}) exiting from the thin carbon foil (60Å thick). In the calculation, the total event counts are same to that of the experimental data. When the constituent atoms of the all incident C_2^+ ion at the foil surface are uniformly distributed spatially, the emission-angle distribution of the C_2^+ fragment ions that diffused by the Coulomb repulsion has an extreme peak like this calculated result in Fig. 2(a). Obviously, the both fluxes are disagreement. We speculate that the yield of smaller emission-angle is increased by the interaction of the fragments with the wake that their partners induce in the foil. However, even if the wake effect is taken account into this calculation, the spectrum will not be redistributed in this foil thickness and energy of cluster ions like the experimental value. This result implies the possibility that the spatial distribution of the constituent atoms of incident C_2^+ ions to the foil is not uniform. For example, when the rate of incident angle is a zero-mean Gaussian distribution, the calculation result agrees with the experimental value as shown in Fig. 2 (b). This consequence makes us expect that C_2^+ ions were oriented to the beam axis by the high electric field in the tandem accelerator.

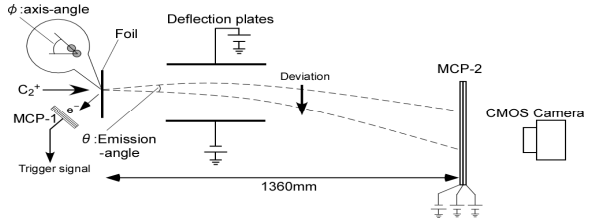

Fig. 1 Schematic diagram of the experimental setup.

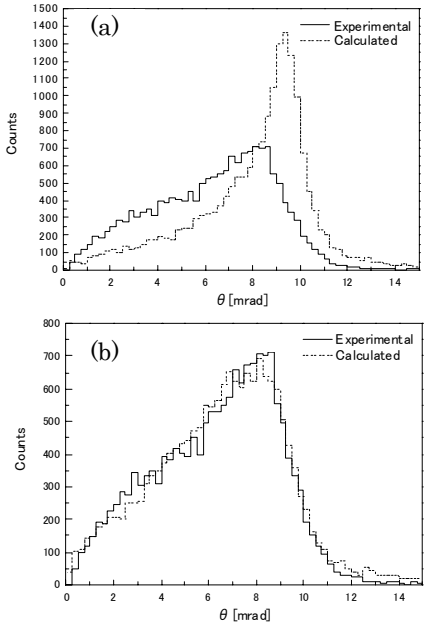

Fig. 2 Calculated and experimental emission-angle distribution of the C_2^+ fragments (pair of C^{3+}) dissociating in the 60Å thick carbon foil. The broken line is calculated result under the condition that the angular distribution of incident cluster axis is (a) uniform, (b) non-uniform.

Reference

1) A. Chiba et al., Phys. Rev. A 76 (2007) 06321.

4-37 Visualization of a Single Cluster Particle Track in Polymeric Materials

S. Seki [a)], S. Watanabe [a)], Y. Saitoh [b)], A. Chiba [b)], M. Sugimoto [b)] and K. Narumi [c)]

[a)] Division of Applied Chemistry, Graduate School of Engineering, Osaka University, [b)] Department of Advanced Radiation Technology, TARRI, JAEA, [c)] Advanced Science Research Center, JAEA

Cluster particles accelerated up to MeV-order high energy have been expected to cause unique interactions unlikely to those of *isolated* atomic particles. We have demonstrated to visualize energy releasing of a high energy particle via chemical interaction with polymeric materials along its trajectory, giving cylinder-like nano-space of particle tracks [1-5]. Theoretical formulation of the energy distribution reveals to give a good correlation with the size of the nano-space [1]. Thus we can estimate precisely the size of the 1-D nanowire, hence, the energy distribution can be "measured" with nm-resolution if we use the polymer materials of which cross-linking efficiency has been known [1,4]. In the present report, we have successfully produced the nanostructure of polymeric materials upon irradiation to the cluster particles of "light" atoms where the atomic particle has been known not to give the nanostructure because of insufficient energy releasing along the trajectories.

Commercially available high sensitive crosslinking-type polymer materials; polycarbosilane (PCS) was used as the target polymer material in the present study. The polymer was over coated onto Si substrate after an adequate surface treatment, and irradiated a series of C cluster ion beams from Tandem accelerator at Takasaki Advanced Radiation Research Institute, JAEA. The irradiated films were immersed into diethylether to isolate the nanostructures on the substrate, followed subsequently by rinsing in isopropylalcohol. The size of the nanostructures was directly measured by atomic force microscope (AFM).

Figure 1 shows the observed AFM micrographs of nanostructures formed by a variety of C cluster particles. The nanostructures represent wire-like 1-D features, and the closs-linked polymer nanowires are observed clearly upon irradiation to all the clusters except for C_2. It should be noted that atomic particles of C at the same velocity to the other cluster particles did not give any patterns of the nanostructures, suggesting the insufficient energy releasing of the single atomic or C_2 cluster particle to promote cross-linking reactions and gelation along the trajectory. Although the number density of the nanowires corresponds precisely to the number of incident "cluster" particles in the case of C_3, the number density is apparently larger than the number of the incident clusters of $C_4 - C_9$, suggesting that fragmentation of the cluster particles occurs and each fragment gives corresponding nanowire in these films. The nanowires produced by $C_4 - C_9$ (Fig. 1-c-h) show considerable non-homogeneity in the thickness of the nanowires in contrast to the uniform thickness observed in the case of C_3. The cross-linking reactions in PCS upon irradiation have been well investigated, and the G value of cross-linking ($G(x)$), therefore, has been reported as $G(x) \sim 1$ (100 eV)$^{-1}$. The theoretical formulation based on the value of $G(x)$ and LET of the cluster particles (calculated as the sum of atomic LET) gives the estimates of the cross-sectional radii of the nanostructures as 5.9 nm (C_3) ~ 10 nm (C_9). However the observed sizes of the nano- structures are 6, 7, 7, 7, 6, 9, and 8 nm, respectively for $C_3 - C_9$ cluster particles. The observed sizes show slightly lower values compared with the values predicted by our previous formulation based on the single particle (atom, ion) interaction with the polymeric materials, and small dependence on the number of atoms contributing to a cluster particles. This is also suggestive that fragmentation of the cluster particle during penetration in the polymer thin film gives a significant decrease in the radial dose distribution inside a particle tracks.

References

1) S. Seki et al., *Phys. Rev. B,* **70** (2004) 144203.
2) S. Seki et al., *Adv. Mater.,* **13** (2001) 1663.
3) S. Tsukuda et al., *J. Phys. Chem. B*, **110** (2006) 19319.
4) S. Tsukuda et al, *Appl. Phys. Lett.*, **87** (2005) 233119.
5) S. Seki et al., *Surf. Coat. Technol.*, 2007, **201**, 8486; ibid., 2007, **201**, 8526.

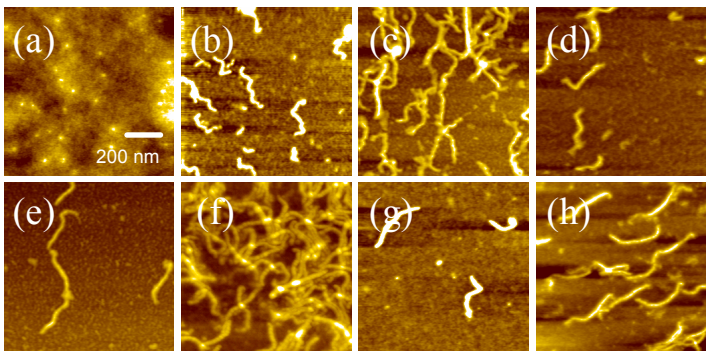

Fig. 1 AFM micrographs of polycarbosilane nanowires on Si substrate produced by $C_2 - C_{10}$ cluster ion beam at ion fluences of 3.0×10^8 - 5.0×10^9 ions cm^{-2}, followed by development in benzene. Images (a) - (h) were observed for the nanowires produced by 1.2 MeV C_2 (a), 1.8 MeV C_3 (b), 2.4 MeV C_4 (c), 3.0 MeV C_5 (d), 3.6 MeV C_6 (e), 4.2 MeV C_7 (f), 4.8 MeV C_8 (g), and 5.4 MeV C_9 (h), respectively.

4-38 Vicinage Effect on Secondary-electron Emission from Amorphous Carbon Foils Induced by Swift C_2^+ Ions

Y. Takahashi [a)], K. Narumi [a)], A. Chiba [b)], Y. Saitoh [b)], K. Yamada [b)], N. Ishikawa [a)], H. Sugai [a)] and Y. Maeda [c,a)]

[a)] Advanced Science Research Center, JAEA, [b)] Department of Advanced Radiation Technology, TARRI, JAEA, [c)] Department of Energy Science and Technology, Kyoto University

The collisions of swift (above the Bohr velocity v_0) cluster ions with a solid cause simultaneous impacts of the cluster constituents. A strong spatiotemporal correlation (~10^{-17} s and ~Å) alters the electronic-excitation process. Such process results in so called the "vicinage effect".

The vicinage effect on the electron emission form a foil in forward direction is expected to disappear at thick foil, because the cluster constituents are sufficiently far apart each other at the exit side of the foil. However, such disappearance of the vicinage effect has never been observed so far. For C_n^+ cluster ions, the foil thickness of 20.3 μg/cm^2 is not enough to observe the threshold thickness of the foil where the vicinage effect disappears [1)]. Such threshold thickness is important to estimate the threshold internuclear distance, which is also important for crude estimation of characteristic interaction length to cause the vicinage effect.

In this study, very thick carbon foils including the foil of ~7500 Å were employed to estimate the threshold thickness. We evaluated the vicinage effect on the secondary-electron yield as a function of the internuclear distance between fragment ions at the exit of the targets in forward direction.

The swift C^+ and C_2^+ ions with the energies of 62.5-250 keV/u (0.75-3.0 MeV/atom) and self-supporting amorphous carbon foils of 1.4-150 μg/cm^2 (70-7500 Å) were used. The seven target frames equipped with carbon foils were set on a movable target holder, which was tilted by 45° to the beam axis in the scattering chamber. Two microchannel-plate (MCP) detectors were placed in parallel on both sides of the target holder. The secondary electrons emitted in forward and backward directions from a carbon foil bombarded with ions were detected coincidentally by two MCPs. The pulse height was recorded with a multichannel analyzer in a list mode and distributions of the number of secondary electrons were derived by integrating them.

We derived the secondary-electron yield γ_2 in forward and backward emissions from the carbon foils bombarded with C_2^+ ions. In addition, we also measured the secondary-electron yield γ_1 using C^+ ions with the same velocity. The vicinage effect on the secondary-electron yield was derived from the ratio $R_2 = \gamma_2/2\gamma_1$. It is considered that the vicinage effect is observed when $R_2 \neq 1$.

In the backward direction, the ratio R_2 were less than unity and almost constant values as the foil thickness increases. On the other hand, the disappearance of the vicinage effect was observed in forward direction for thick foils of 61-150 μg/cm^2 for slower C_2^+ ions of 62.5 keV/u. The threshold foil thickness where the vicinage effect disappears exists between 14 and 61 μg/cm^2 in this velocity.

The vicinage effect in the forward direction was analyzed as a function of the internuclear distance between fragment ions at the exit of the targets. The forward ratio R_2 plotted as a function of the internuclear distance is shown in Fig. 1. The threshold internuclear distance where the vicinage effect disappears exists between ~6 Å and ~23 Å for the C_2^+ ion of 62.5 keV/u. Moreover, it depends on the velocity of ions and increases as the velocity of the ion increases.

The secondary-electron emission from a surface of a solid under a swift single ion impact can be explained in a three-step process: (1) *production* (excitation) of scattered electrons by the incident ion, (2) *transport* of the electrons in the solid, and (3) *transmission* of the electrons through the surface barrier.

It is expected that the vicinage effect on the electronic *energy loss* (*production* process) in this velocity region disappears at the internuclear distance of a few Å [2)]. Therefore, this result means that *transport* or *transmission* process is very important for the appearance of the vicinage effect on the secondary-electron yield. In these processes, both the internuclear distance and the charge state of the ion are important parameter to elucidate the mechanism of the vicinage effect on the secondary-electron yield.

References

1) S. Tomita et al., Phys. Rev. A 73 (2006) 060901R.
2) M.F. Steuer et al., Nucl. Instrum. Meth. 194 (1982) 277.

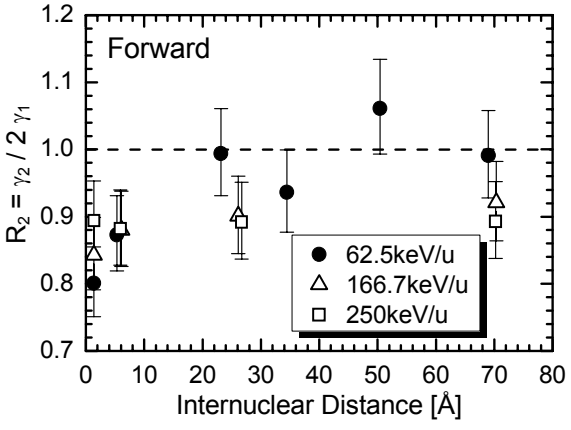

Fig. 1 Ratio $R_2 = \gamma_2/2\gamma_1$ in the forward direction as a function of the internuclear distance between fragment ions at the exit of the target.

4-39 Raman Spectroscopy Measurement of TiO_2 Irradiated with Cluster Ions

N. Ishikawa [a], A. Iwase [b], Y. Saitoh [c] and A. Chiba [c]

[a] Advanced Science Research Center, JAEA, [b] Department of Materials Science, Osaka Prefecture University, [c] Department of Advanced Radiation Technology, TARRI, JAEA

Using cluster ions as projectiles is a unique way to study the interaction between energetic projectiles and solids. When energetic cluster ions are irradiated to a solid target, atoms composing cluster ions have temporal and spatial correlation. Many studies show that, because of such correlation, damage creation due to cluster ion irradiation is not just a superposition of that due to mono-atomic ion irradiation. This effect is called nonlinear effect or collective effect.

Nonlinear effects appeared in the relatively low energy where elastic displacement takes place are investigated in the present study. In the elastic displacement regime, nonlinear damage creation is already reported for metals and semiconductors irradiated with cluster ions. However, there is no consensus on the origin of higher damage for irradiation with heavier cluster. In this paper, the damage is characterized by the change in Raman spectroscopy which reflect crystalline structure and bonding of target atoms. In the present report we report a new insight on the cluster effect observed for TiO_2 single crystal irradiated with cluster ions.

Commercial rutile TiO_2 (100) single crystals were irradiated with 1-MeV C, 2-MeV C_2 and 4-MeV C_4, all having the same velocity. These ions were irradiated at room temperature using the tandem accelerator at JAEA-Takasaki. The projected range of those ions is about 1.1 μm. However, cluster ions dissociate during the passage in the sample and they have no more spatial correlation as the clusters proceed deeper into the sample. In order to observe nonlinear effect which is expected at shallow region near irradiated surface, measurement method sensitive to sample surface should be used. In this study, Raman spectroscopy is measured to detect effects induced by cluster ion irradiation.

Figure 1 shows Raman spectra for TiO_2 single crystal before and after the irradiations. Before irradiation, peaks corresponding to A_{1g} mode, E_g mode and multi-photon process (M-P) are observed. All the spectra in the figure are normalized by the intensity of Eg peak in order to facilitate comparison of A_{1g} peak intensity relative to E_g peak intensity. The fluences are 2.6×10^{16}, 3.2×10^{16} and 1.1×10^{16} carbons/cm^2, for 1-MeV C, 2-MeV C_2 and 4-MeV C_4, respectively. From the figure, the A_{1g} peak intensity after irradiation with 1-MeV C is found to be almost the same as that before irradiation, while the A_{1g} peak intensity after irradiation with 2-MeV C_2 is relatively low compared to that before irradiation, although the fluence is almost the same for 1-MeV C and 2-MeV C_2. This demonstrates that 2-MeV C_2 ion irradiation results in heavier damage than 1-MeV C. For larger cluster like 4-MeV C_4, this tendency is more pronounced. As shown in the figure, A_{1g} peak intensity for 4-MeV C_4 is smaller than those for 1-MeV C and 2-MeV C_2, although the fluence is much less for 4-MeV C_4 (1.1×10^{16} carbons/cm^2) than for 1-MeV C (2.6×10^{16} carbons/cm^2) and for 2-MeV C_2 (3.2×10^{16} carbons/cm^2). The schematic views of A_{1g} mode and E_g mode are shown in Fig. 2.

In the framework of elastic displacements, the key parameter for the interpretation of the present result may be the energy of PKA (primay knock-on atoms). The irradiation with larger cluster is expected to cause higher PKA energy, since larger cluster has higher mass (in case of same velocity). Higher PKA energy can create larger defect agglomerates rather than simple defects. The larger decrease in A_{1g} peak for larger cluster may be related to such high PKA energy.

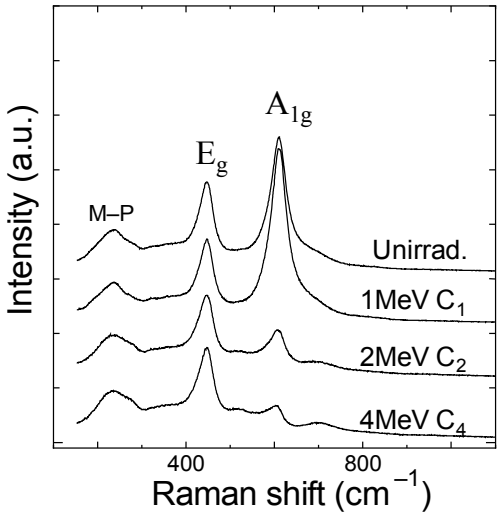

Fig. 1 Raman spectra for rutile TiO_2 before and after 1-MeV C, 2-MeV C_2 and 4-MeV C_4 ion irradiations. The fluence is indicated in the text.

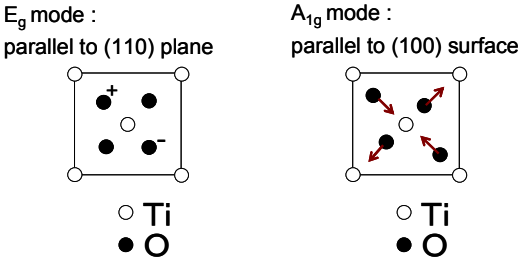

Fig. 2 Schematics of raman -active A_{1g} mode and E_g mode of rutile TiO_2.

4-40 Luminescence from Sapphire Bombarded by Swift Cluster Ion Beams

H. Shibata [a)], Y. Saitoh [b)], A. Chiba [b)], M. Adachi [b)], Y. Takahashi [c)], K. Narumi [c)], W. Yokota [b)] and T. Kojima [b)]

[a)] Graduate School of Engineering, Kyoto University, [b)] Department of Advanced Radiation Technology, TARRI, JAEA, [c)] Advanced Science Research Center, JAEA

The luminescence spectra from sapphire (α-Al_2O_3) induced by 0.5-1 MeV/atom carbon cluster ions were measured in the wave length range of 250-800 nm as a function of ion fluence at room temperature. The luminescence was observed at 326 nm (F^+ center) and 411 nm (F center) in any cluster bombardment. Result shows sub-linear feature for cluster size dependence.

高速（高エネルギー）クラスターイオンと物質との相互作用においては、単原子イオンの数の集合体として個数以上、あるいは個数以下の非線形的な効果を与えることが知られている。これまでに二次イオン粒子放出に関する高速クラスターイオン照射の特徴を調べ、主に電子励起が起きるエネルギー領域ではクラスターサイズが大きくなるとともに正負二次イオンの収量が指数的に増えることがわかったが、二次イオン収量の増加は表面付近での化学反応によるものと考えられる。このように標的表面の分子吸着の状態に強く依存する現象を避けるため、標的の照射損傷のみに依存する発光を測定し、クラスターイオンの照射効果を調べるのが本研究の目的である。今回は炭素クラスターイオンとサファイア（α-Al_2O_3）標的との衝突で放出される発光を、時間分解マルチチャンネル分光器（Hamamatsu Photonics PMA11）で測定したので報告する。

本実験に用いたクラスターイオンは TIARA 3 MV タンデム静電加速器からのエネルギー0.5 及び 1.0 MeV/atom の C_1^+～C_8^+イオンで、照射野は 3 mmϕ、ビーム電流は C_1^+で 2.5 nA、C_8^+で 40 pA 程度である。試料には発光強度が強く、発光過程が比較的良くわかっているサファイアを選んだ。Fig. 1 に 4 MeV C_8^+クラスターイオンをサファイアに照射したときの発光スペクトルを示す。測定波長範囲は 250～800 nm で、326 nm 及び 411 nm に発光が見られる。326 nm は F^+センターからの発光で、発光強度はイオンビーム照射と同時に次第に増加し、ピークに達してから少しずつ減衰する。411 nm は F センターからの発光で、これもビーム照射と同時に次第に増加し、ピークに達してから、326 nm よりも早く減衰していく。ピークに達するまでの照射量を比較すると、いずれの発光もクラスターサイズが大きくなるほど少ない照射量で最大発光量に達する。

Fig. 2 は F^+センターの発光量についてクラスターイオンサイズの依存性を調べたものである。それぞれの発光量は時間依存性があるので、本実験では発光量が最大に達する点における発光収量を比較することにした。0.5 MeV/atom C_1^+イオン照射下の F^+センターの発光収量を 1 として、0.5 および 1.0 MeV/atom クラスターイオンの発光収量に対する比を図にした。図から発光量の比はクラスターサイズに比例して増加しており、その比例係数は約 0.9 である。クラスターサイズに対応して線形的に増加した場合、比例係数は 1 なので、この場合はサブリニアな関係になる。つまり F^+センターを形成する欠陥はクラスターサイズに比例して増加するが、クラスターの個数倍よりは若干少ない量で最大値に達する。エネルギー依存性については Fig. 2 に示すように、1.0 MeV/atom の場合、0.5 MeV/atom の場合に比べ、光量は約 1.5 倍大きく、クラスターサイズに対する依存性は同じような傾向となった。

以上のように照射損傷に依存する発光（F^+センター）に関してはサブリニアな非線形性が観測された。

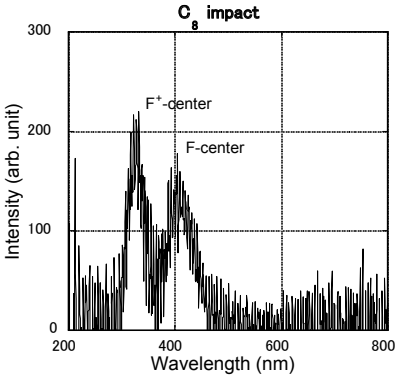

Fig. 1 Typical luminescence spectrum from sapphire target bombarded with 4 MeV C_8^+ cluster ion.

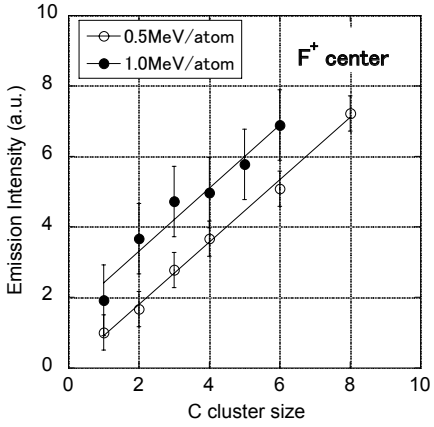

Fig. 2 The ratios of yields of luminescence from sapphire target bombarded by 0.5 and 1.0 MeV/atom C_1^+ ~ C_8^+ projectiles. The yield of luminescence from F^+ center of sapphire target bombarded by 0.5 MeV/atom C_1^+ ion is unity.

Reference

1) Y. Aoki, N. T. My, S. Yamamoto, H. Naramoto, Nucl. Instrum. Meth. Phys. Res. B 114 (1996) 276.

4-41 Energy Dependence of Sputtering Yield of Si Induced by 20-400 keV C_{60} Ions

K. Narumi [a)], H. Naramoto [a)], Y. Takahashi [a)], K. Yamada [b)], A. Chiba [b)], Y. Saitoh [b)] and Y. Maeda [a, c)]

[a)] Advanced Science Research Center, JAEA, [b)] Department of Advanced Radiation Technology, TARRI, JAEA, [c)] Department of Energy Science and Technology, Kyoto University

Recently intensive application studies using a-few-10s-keV C_{60} ions such as surface-sensitive analyses and secondary ion mass spectroscopy (SIMS) of high-polymer materials and/or biomaterials have been made based on characteristic sputtering effects [1)]. The progress of such application studies has increased an understanding of the unique sputtering phenomenon induced by C_{60}-ion bombardment. However, basic data, for example energy dependence of the sputtering yield induced by C_{60} ions, have still not been obtained enough. In this report, energy dependence of Si sputtering yield induced by C_{60} ions was measured in the energy range from 20 to 400 keV where the nuclear stopping is dominant. Obtained result was compared with the sputtering yield for a carbon single-atomic ion calculated using Sigmund's theory [2)].

Pieces of Si(100) wafer were irradiated with 200-keV Ar^+ ions by the 400-kV ion implanter of TIARA at the fluence of 5×10^{15} /cm^2 in order to make an amorphous Si layer at the surface. Then, the samples were irradiated with 20-80 keV C_{60}^+ and 200-400 keV C_{60}^{2+} ions by the ion implanter. The fluence of the C_{60} ion was 10^{14} to 10^{15} C_{60}/cm^2. After the C_{60}-ion irradiation, the change in the thickness of the amorphous layer was measured with Rutherford-backscattering spectrometry using 2-MeV He^+ ions by the 3-MV single-ended accelerator of TIARA. Sputtering yields were evaluated with the change in the thickness of the amorphous layer.

Closed and open circles in Fig. 1 show the obtained sputtering yield of Si induced by C_{60} ions as a function of the energy per atom as well as the energy of C_{60} ion. The obtained sputtering yield does not seem to depend on the charge state of the projectile C_{60} ions. The maximum sputtering yield is approximately 600 Si/C_{60} at 80 keV corresponding to approximately 10 Si/C at 1.3 keV/atom.

In order to evaluate the obtained sputtering yield, it was compared with the Si sputtering yield induced by a single-atomic carbon ion. Because there is no available corresponding experimental sputtering yield for a single-atomic carbon ion, the Si sputtering yield for a single-atomic ion was calculated based on the linear collision cascade theory by Sigmund [2)]. In the calculation, the nuclear stopping power for a carbon single-atomic ion was calculated using the SRIM2008 code [3)]. The calculated result is shown in Fig. 1 as the solid line. The maximum of the calculated sputtering yield per atom is approximately 0.9 Si/C at 4 keV/atom corresponding to approximately 50 Si/C_{60} at 240 keV. The peak position of the sputtering yield for a C_{60} ion is at lower energy per atom than that for a single-atomic carbon ion. Similar result has been observed for Au sputtering yields induced by Au clusters [4)], and it seems a general tendency for cluster-induced sputtering. The maximum of the sputtering yield per atom for a C_{60} ion is ten times larger than that for a single-atomic carbon ion, which indicates enormous nonlinear effect on the sputtering yield. What such effect is attributed to is the next issue under consideration.

References

1) For example, N. Winograd, Anal. Chem. 142A (2005).
2) P. Sigmund, Phys. Rev. 184 (1969) 383.
3) J.F. Ziegler, SRIM version 2008, <http://www.srim.org> (2008).
4) H.H. Andersen et al., Phys. Rev. Lett. 80 (1998) 5433.

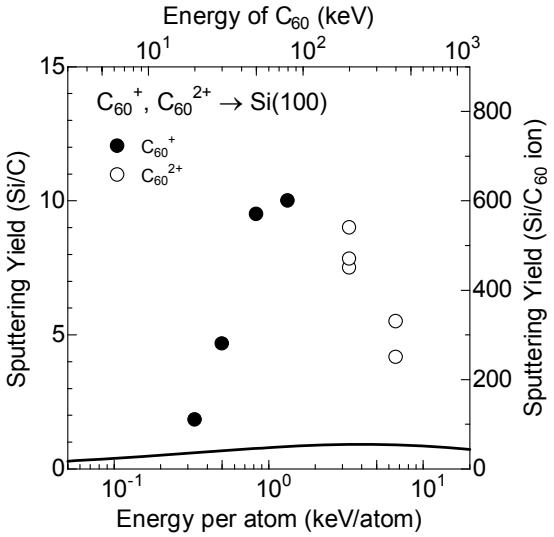

Fig. 1 Energy dependence of the sputtering yield of Si induced by C_{60} ions. The lower and upper abscissas express the energy per atom of the projectiles and the energy of C_{60} ions, respectively. The left-hand and right-hand ordinates express the sputtering yield per atom and per C_{60} ion, respectively. The solid line shows the sputtering yield induced by single-atomic ions based on the theory of Sigmund; See text.

4-42 Positive Secondary Ion Emission from PMMA upon Medium Energy C_{60} Ion Impacts

K. Hirata [a], Y. Saitoh [b], A. Chiba [b], K. Yamada [b], Y. Takahashi [b], K. Narumi [c], and T. Kojima [b]

[a] National Institute of Advanced Industrial Science and Technology (AIST), [b] Department of Advanced Radiation Technology, TARRI, JAEA, [c] Advanced Science Research Center, JAEA

Secondary ions are ejected from the surface when the primary ions bombard the target. Cluster ion impact on a target produces different secondary ion emission yields compared with those for monoatomic ions because of the unique irradiation phenomenon that the constituent atoms of an incident cluster simultaneously impact on a very small region of the target surface. Generally, the larger the primary cluster ion is, the larger the enhancement effect on secondary ion emission yields is. C_{60} is one of the most useful primary cluster ions for secondary ion mass spectroscopy due to its large cluster number and stability. We have developed time-of-flight (TOF) secondary ion mass spectroscopy using primary C_{60} ions in the medium energy range (from several tens to several hundreds of keV), where few attempts have been made to study C_{60} impacts.

The medium energy C_{60} TOF secondary ion mass spectroscopy was developed using a 400 kV ion implanter of the Japan Atomic Energy Agency (JAEA)/Takasaki [1]. Positive ions extracted from the ion source were mass-analyzed using a bending magnet in a high voltage terminal to produce C_{60} ions of a desired charge state. The direct current C_{60} ion beam was pulsed using electrostatic deflection plates triggered by a pulse generator and an aperture after acceleration at a desired energy. After collimation by a series of collimators, the pulsed C_{60} ion beam with a half-width of *ca.* 0.1μs was injected into the target. The ion beam was incident on the target at an angle of 45º to the target surface. Secondary ions produced by C_{60} impacts were accelerated between the target and a TOF drift tube before hitting a microchannel plate (MCP). The start and stop signals for TOF measurements were provided by the pulse generator used for pulsing the incident ion beam and a constant fraction discriminator (CFD) connected with the MCP output via a pre-amplifier, respectively. For quantitative comparison of secondary ion emission yields in mass spectra, incident beam current I_o and positive secondary ion current *Ip* were measured by highly sensitive electrometers, respectively, connected to a Faraday cup and a movable metal plate with a grid, as described elsewhere [2].

Figure 1 shows the positive secondary ion TOF spectra from *m*/*z* (mass to charge ratio) = 58 to 72 of a Poly(methyl methacrylate) (PMMA) target for (a) 30 keV C_{60}^+, (b) 120 keV C_{60}^+ and (c) 540 keV C_{60}^{2+}, respectively. The relative intensity on the vertical axis is proportional to the secondary ion emission yield per incident atom, as the total counts of the spectra are scaled based on *Ip*/*nIo* as described above. The major peaks observed in the figure can be attributed to $C_2H_3O_2^+$ (*m*/*z*=59) and $C_4H_5O^+$ (*m*/*z*=69), respectively. We note that the medium energy C_{60} ion (120 keV C_{60}^+ and 540 keV C_{60}^{2+}) impacts provide higher peak intensities than the lower energy C_{60} ion (30 keV C_{60}^+) impact.

Secondary ion emission yields are influenced by energy transfer processes and their deposited energy densities around the impact-points. In an incident energy range of 0.5-9 keV for C (corresponding to that of 30-540 keV for C_{60}), the energy transferred by electronic process monotonically increases with increasing the incident energy, whereas that by nuclear process shows a maximum around several keV. Considering that the relative secondary ion intensities are higher in the order of 540-keV C_{60}^{2+}, 120-keV C_{60}^+, and 30-keV C_{60}^+, the electronic process may dominantly contribute to the enhancement of the intensities of the characteristic peaks.

In conclusion, the use of medium energy C_{60} ions (120-keV C_{60}^+ and 540-keV C_{60}^{2+}) as a primary ion provided higher emission yields of the positive secondary ions of *m*/*z*=59 and 69 for PMMA than those of lower energy C_{60} ions (30-keV C_{60}^+).

References

1) K. Hirata et al., Nucl. Instrum. Meth. B **266** (2008) 2450.
2) K. Hirata et al., Appl. Phys. Lett., **86**, (2005) 044105.

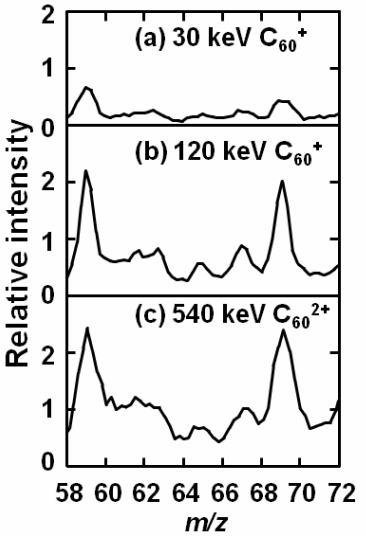

Fig. 1 Positive secondary ion TOF spectra of PMMA for (a) 30-keV C_{60}^+, (b) 120-keV C_{60}^+, and (c) 540-keV C_{60}^{2+}. Peaks at *m*/*z* = 59 and 69 are attributed to $C_2H_3O_2^+$ and $C_4H_5O^+$, respectively.

4-43 Fast Single-Ion Hit System for Heavy-Ion Microbeam at TIARA Cyclotron (II)

W. Yokota, T. Satoh, S. Okumura, S. Kurashima, N. Miyawaki, H. Kashiwagi, K. Yoshida and T. Kamiya

Department of Advanced Radiation Technology, TARRI, JAEA

The fast single-ion hit system is being developed using the focusing microbeam system at the HX beam line of the TIARA cyclotron. The highest hit rate of 25/s, 2.5 times as high as the goal value, has been obtained using a microbeam of 260 MeV-Ne last fiscal year[1]. The single-ion hit was already supplied to a number of test irradiation of biological samples and semiconductors under moderate conditions of hit rate and spatial hit accuracy.

A couple of subjects to be solved for practical single-ion irradiation were found on the way of development. One is multiple hits at the same targeted point, which appears at several percents of the total number of hit. The other subject is a miss hit around a targeted point, which appears sometimes at more than ten percents of total hit number depending on the condition of beam focusing or transport. The outline of the subjects is reported below.

The single-ion hit system includes (a) the microbeam system, (b) a scanning system, (c) an ion detection system and (d) a beam chopping system as shown in the schematic diagram in Fig. 1. The microbeam system consists of a set of a micro slit (object slit) and a divergence defining slit and of a quadruplet quadrupole lens. After a microbeam is formed, the beam intensity is reduced by some orders of magnitude shutting the beam periodically with a chopper installed in the injection line. Each ion is detected with a semiconductor or a scintillation detector mounted behind a target of CR-39 film which records actual positions of targeted points. The hit position is controlled by an electrostatic scanner placed upstream of the quadruplet quadrupole lens. Once a single ion is detected, the detection system sends a signal to the scanning system to target the next point and the high voltage of the scanner electrode is changed to a corresponding value. This is a process of delivering single-ion hit.

The multiple hits take place when more than one ion passes the scanner electrode before the scanner voltage changes. Therefore the time response of the detector system was improved, and it was verified by experiment that the multiple-hit ratio could be lowered less than one percent.

A miss hit takes place when an ion hits other than a targeted point in the following cases: 1) An ion passes the outside of the micro slit and goes through the divergence defining slit and the lens at a extremely wrong angle. 2) An ion is scattered at a small angle at some place downstream of the micro slit. The possibility of the former case was removed by experiment. While the observed fact that the miss-hit ratio strongly depends on the gap of the micro slit suggests the latter case. The micro beam system is designed on the assumption that almost all ions scattered by the micro slit deviate from the defining slit gap and do not reach the target. Moreover, every scattered ion passing through both the micro slit and the divergence defining slit is focused on the target within an area of a microbeam spot size unless its energy or charge state is changed. All the measured phenomena, however, suggest that scattering may occur at the micro slit. The elucidation of the scattering process and the solution of the miss hit are the most important subject in next fiscal year. The miss-hit ratio can be lowered with a wider micro slit gap for the present though the spatial hit accuracy worsens to some micro meters.

Reference

1) W. Yokota et al., JAEA Takasaki Ann. Rep. 2007 (2008) 180.

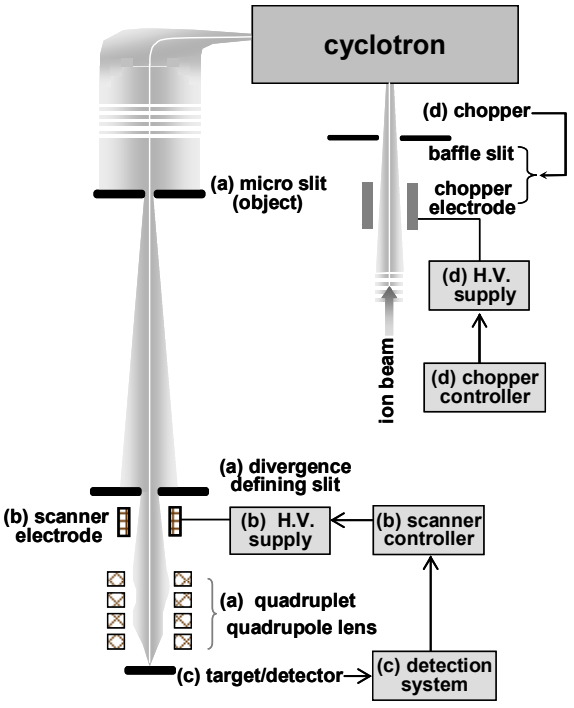

Fig. 1 Schematic diagram of the single-ion hit system. Beam generated by the ion source is transported through the injection line equipped with the beam chopper, accelerated by the cyclotron and transported to the microbeam system. See the text for the detail of the single-ion hit making process and the indices (a) to (d) for the devices.

4-44 Uniform Irradiation of Ion Beams by Means of a Nonlinear Focusing Method

Y. Yuri, T. Ishizaka, T. Yuyama, S. Okumura and I. Ishibori

Department of Advanced Radiation Technology, TARRI, JAEA

It is possible to make the beam profile uniform by applying the nonlinear focusing force of a multipole magnet to a beam. A research and development study has been carried out on a *nonlinear focusing method* for advanced uniform irradiation at the AVF cyclotron facility[1-3]. This method enables us to perform large-area irradiation both with high-uniformity and with a constant particle fluence rate at any point over the area, which compensates the shortcomings of well-known methods (beam expansion using a scattering material and beam scanning using dipole magnets)[1].

Formation of a uniform beam strongly depends on the initial beam distribution. To form a highly uniform beam, the initial distribution should be simple such as a Gaussian or parabolic distribution, while the distribution of a beam extracted from the cyclotron is usually not Gaussian. In order to obtain a sufficiently Gaussian phase-space distribution as an initial one, another thin aluminum foil (0.8 μm thick) has been installed at the waist position of the beam (TSLB1) where the horizontal and vertical phase advances are about 90*n* degrees (*n*: odd integer) from the first foil at CS0_2 to the second one.

The transverse profile on the target was tuned by monitoring beam fluorescence from a Tb-doped Gd_2O_2S screen, DRZ (Kasei Optonix Ltd.). It is suitable for real-time beam monitoring since its optical decay time is much shorter than that of an ordinary alumina screen. An example of a 2D intensity distribution of a beam focused by the octupole force is shown in Fig. 1, which was obtained using a radio-chromic film[4]. The rms uniformity of the region of about 6 cm × 6 cm was about 6%, as estimated from the optical density of the irradiated film. The central part (2 cm × 2 cm) of the uniform region has a better uniformity of 2%. A higher-intensity "wall" surrounding the uniform region is produced by over-shot tail-folding through octupole focusing, and can be removed by collimating the Gaussian tail upstream of the multipole magnet[1].

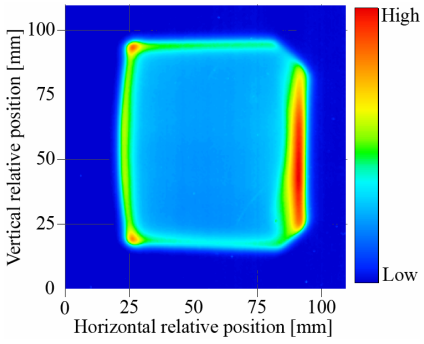

Fig. 1 2D intensity distribution of a 10 MeV proton beam on the target.

It was found that such a uniform beam exhibits unique features from the viewpoint of uniform irradiation for applications to materials science and biotechnology. In the following, we discuss the features of the nonlinear focusing method, in comparison with the raster scanning method.

In raster scanning, the uniform irradiation field is achieved by sweeping a focused (non-uniform) beam two-dimensionally at different scanning frequencies for each direction (horizontally 50 Hz, and vertically 0.25 ~ 5 Hz in the case of our cyclotron facility). Namely, the local fluence rate on the sample is not constant but periodically changes from zero to a very high value, depending on the two frequencies. This time-dependence of the fluence rate is undesirable, e.g., in the case where local target heating, induced by irradiation of a high-current beam, is intolerable.

On the other hand, in nonlinear focusing, the intensity distribution of the beam itself is uniform. The particle fluence rate is, therefore, constant at any point over the irradiation area. This feature is especially suitable to observe a transient phenomenon of the sample during irradiation.

Another merit of this method is short-time irradiation. In raster scanning, the minimum irradiation time is limited by the scanning frequency and the tolerable uniformity. If the lower frequency is, for instance, 1 Hz, the irradiation time should be longer than 100 s to tolerate a dose error of 1% caused by the difference of the number of scanning times. In order to lengthen the irradiation time, the beam current may be forced to be reduced, which sometimes makes tuning of the beam spot size difficult. On the other hand, there is, in principle, no lower limit for the irradiation time in the nonlinear focusing method. Even the irradiation time of much shorter than 1 ms is possible by chopping the beam using an electrostatic deflector. It is also possible to make the particle fluence rate very low using an attenuator mesh. The dose rate during irradiation and/or the total dose can be widely changed by combining these techniques.

In summary, we have formed a uniform beam by means of a nonlinear focusing method and demonstrated its possibilities for advanced uniform irradiation. An irradiation test of the uniform beam has been just started.

References

1) Y. Yuri et al., Phys. Rev. ST Accel. Beams **10** (2007) 104001.
2) Y. Yuri et al., Proc. European Particle Accelerator Conference, EPAC'08 (2008) 3077.
3) Y. Yuri et al., in Proceedings of the 5th Annual Meeting of Particle Accelerator Society of Japan (2008) 397.
4) T. Agematsu et al., Radioisotopes **57** (2008) 87.

4-45 Status Report on Technical Developments of the AVF Cyclotron

S. Kurashima, S. Okumura, N. Miyawaki, T. Ishizaka, T. Yuyama, Y. Yuri, H. Kashiwagi, K. Yoshida, I. Ishibori, T. Nara and W. Yokota

Department of Advanced Radiation Technology, TARRI, JAEA

Control of the beam intensity with attenuators

Attenuators composed of metal meshes with many regularly-arrayed holes are used at diagnostic stations of IS2 and IS5 in the injection line of the AVF Cyclotron for quick attenuation of the beam intensity. As a result of improvement of the attenuator, the beam distribution on the target is approximately maintained regardless of use of the attenuator [1]. However, it was found that use of the attenuator decreases the transmissivity of the beam in the cyclotron, while that in the injection line is constant. By optimizing cyclotron parameters, the transmissivity can be recovered to the original level (about 20 %) where no mesh is used.

Measurement of the cyclotron magnetic field for quick change of the beam

Reduction of the beam preparation time is required because of the shortage of the machine time, while frequent beam changing increases the ratio of the beam preparation time to the total operation time. The most time-consuming process in the beam preparation is a cycling process of the cyclotron magnetic field for ensuring the reproducibility. We plan to replace the process with a shorter one by compensating for the deviance of the magnetic field. In order to monitor the magnetic field in a wider range for compensation, an NMR probe has been installed inside the cyclotron. The installation position suitable for measurement was obtained by searching with a manipulator system. It was confirmed that the lowest magnetic field in the cyclotron, for a 10 MeV proton beam, can be measured with the probe.

Improvement of the scintillation detector for the beam phase measurement inside the cyclotron

The scintillation detector [2] inside the cyclotron has been improved for efficient measurement of the beam phase distribution. For improving the transmissivity of the induced light from the plastic scintillator to the photomultiplier, the scintillator was directly joined to the optical fiber without the light guide previously used. The transmissivity has been raised by about 1.4 times the previous case. The shape of the scintillator at the incident side was changed from a rectangular edge to a smooth one with a semi-cylinder shape to increase the collection efficiency of the scintillation light. Even the light induced at the surface of the scintillator can be transported to the optical fiber. In order to cut a signal except for the one induced by an accelerating beam, the height of the scintillator was also changed from 24 to 5 mm, which roughly equals a typical beam size. The detection efficiency of a 75 MeV $^{20}Ne^{4+}$ beam, as one of the acceleration condition of a low energy per nucleon, was increased by approximately 5 times.

Formation of a single-pulse beam by a beam chopping system under highly-stabilized magnetic field

The cyclotron has a beam chopping system [3] consisting of a pulse voltage generator (P-chopper) and a sinusoidal voltage generator (S-chopper). Simultaneous operation of these choppers can form a single-pulse beam. However, the single-pulse beam has not been utilized before installation of a magnetic field stabilization system [4] since the number of multi-turn extraction was strongly influenced by the change of the magnetic field on the order of 10^{-4}.

Formation of the single-pulse beam of a 320 MeV $^{12}C^{6+}$ was carried out under highly-stabilized magnetic field less than $\Delta B/B = 1 \times 10^{-5}$. Figure 1 shows beam pulses measured by a scintillation counter. The S-chopper reduced the beam bunches extracted every 80.3 ns to one-fifth (upper waveform). After the cyclotron had been tuned to decrease the number of multi-turn extraction less than 6, the P-chopper injected only one beam bunch. As a result, a very clear single-pulse beam was formed (lower waveform). The single-pulse beam irradiated a user's target over 3 hours without an additional tuning of the cyclotron.

References

1) T. Ishizaka et al., JAEA Takasaki Ann. Rep. 2007 (2008) 184.
2) N. Miyawaki et al., JAEA Takasaki Ann. Rep. 2007 (2008) 182.
3) W. Yokota et al., Rev. Sci. Instrum. 68 (1997) 1714.
4) S. Okumura et al., Rev. Sci. Instrum. 76 (2005) 033301.

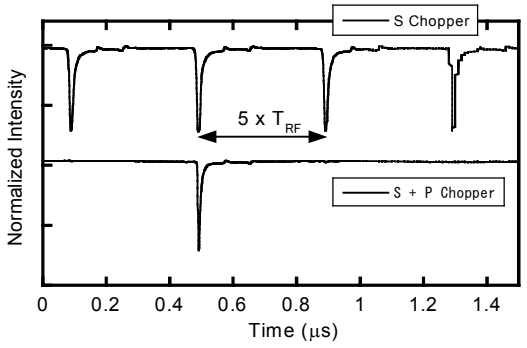

Fig. 1 Beam pulses of the 320 MeV $^{12}C^{6+}$ measured by a scintillation counter at the beam transport line.

4-46 Development of Beam Generation and Irradiation Techniques for Electrostatic Accelerators

K. Yamada, S. Uno, A. Chiba, A. Yokoyama, Y. Saitoh,
Y. Ishii, T. Satoh, T. Ohkubo and T. Agematsu

Department of Advanced Radiation Technology, TARRI, JAEA

Evaluation of stripper gas pressure in the TIARA tandem accelerator

Pressure of stripper gas in a gas cell of the tandem accelerator is an important parameter to study the mechanism of charge exchange. However, measurement of the gas pressure in the gas cell (P_{cell}) is not easy because setting of electric circuits for the measurement at high voltage terminal is difficult. The relative pressure at the gas cell can be monitored by a cold cathode gage (CCG) located just downstream of the tandem. Therefore, we studied the relationship between the pressure monitored with the CCG and that at the gas cell applying the method proposed by J. C. Acquadro et al.[1] through following experiment and calculation.

In the experiment, beam of H^- (H_{in}) was injected to the tandem and accelerated to 0.5 MeV. After traversing the gas cell at the high voltage terminal, beam current of intact H^- (H_{out}) was measured downstream of the tandem. A fraction F_H (H_{out}/H_{in}) was obtained as a function of the pressure (P_{ccg}) monitored with the CCG.

In the calculation, F_H can be expressed by the published experimental values of the charge exchanging cross-sections[2] and the rate equations for the charge state population.

$$F_H = \alpha \exp(-8.38 \times 10^2 \gamma P_{ccg}) \quad (1)$$

where α and γ are the ion optical transmission and the conversion factor to true stripper gas pressure (P_{cell}), respectively. After fitting the measured values to eq.(1) as shown in Fig. 1, the values of α and γ could be obtained. As a result, P_{cell} is written as $P_{cell} = 2.54 \times 10^4 P_{ccg}$.

Improvement of a multi Faraday cup structure

A new multi Faraday cup (MFC) to monitor ion beam profile has been improved by modifying the previous MFC structure[3] as follows: for higher resolution of beam current, the inner diameter of the Faraday cup was increased from 2 mm to 3 mm. For higher spatial resolution especially around the center of MFC, the number of FCs was increased from 21 to 33 as shown in Fig. 2. The FC consists of three parts called base, bottom and tube as shown in Fig. 3. The depth of the FC can be changed to 3, 10, and 15 mm, and two types of the FC bottom, normal and 45-degree inclined to the beam axis, are prepared to study the best aspect ratio of a FC and shape of a FC's bottom. As the result, we tried to use this new MFC for 120 keV C_{60}^+ beams, and it was found that the new MFC has good usability compared with the previous MFC, because the number of FCs increased to seven from five in axis direction and the area of a FC also increased to 7.07 mm^2 from 3.14 mm^2. The effect of the depth and the bottom shape of FC will be studied in the future.

Improvement of an emittance monitor for MeV proton beams

The improvement of the ion beam brightness and emittance of the RF ion source for the TIARA 3MV single-ended accelerator is an essential factor to form the beam spot of less than several hundred nano-meters in diameter. In this year, the emittance monitor[4] (EM) using luminescence intensity of a movable scintillator at two different positions was improved for the high angular resolution within 4×10^{-4} rad by elongating the moving distance of the scintillator. As a result of measurement, the normalized emittance and the brightness of 2 MeV proton beam were 0.8 mm•mrad(MeV)$^{1/2}$ and 0.6 $Am^{-2}sr^{-1}eV^{-1}$, respectively. Our aiming resolution of the EM was reached.

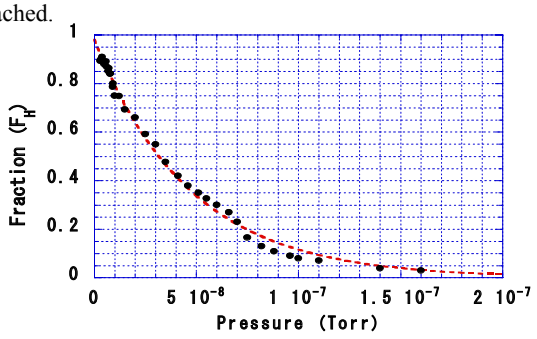

Fig. 1 Measured and calculated H^- beam fraction of 0.5 MeV H^- colliding with N_2 (dashed line).

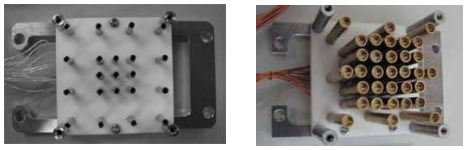

Previous MFC New MFC

Fig. 2 Photograph of the multi Faraday cup.

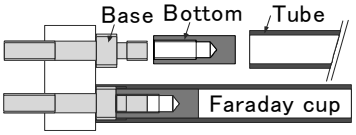

Fig. 3 Schematic drawing of each FC.

References

1) J. C. Acquadro et. al., Nucl. Instrum. Meth. B 171 (2000) 373.
2) J. Heinemeier et. al., J. Phys. B 9 (1976) 2669.
3) K. Yamada et al., JAEA Takasaki Ann. Rep. 2007 (2008) 185.
4) A. Chiba et al., TIARA Ann. Rep. 2002 (2003) 327.

4-47 Development of Irradiation Position Control Techniques for Ion Microsurgery Using an Ion Beam Induced Fluorescent Analysis

H. Shimada [a,b,e], M. Oikawa [f], T. Satoh [b], S. Okumura [b], M. Taguchi [c], T. Kamiya [a,b,d], T. Nakano [a,d,e] and K. Arakawa [a,b,d,e]

[a] 21st Century COE Program, Graduate School of Medicine, Gunma University,
[b] Department of Advanced Radiation Technology, TARRI, JAEA,
[c] Environment and Industrial Materials Research Division, QuBS, JAEA,
[d] Department of Medicine, Graduate School of Medicine, Gunma University,
[e] Gunma University Heavy Ion Medical Center, Gunma University,
[f] Fundamental Technology Center, National Institute of Radiological Sciences

The heavy particles have unique characteristics of high energy transfer localized in the vicinity of almost straightforward tracks. The heavy particles are suitable for the treatment of small tumors with the size of several millimeters or less. This research aims at developing an innovative microsurgery treatment system, using the carbon-ion pencil beam, for age-related macular degeneration (AMD).

群馬大学21世紀COEプログラム「加速器テクノロジーによる医学・生物学研究」の主要なテーマの一つとして、原子力機構・高崎研と連携して、高精度炭素イオンマイクロサージェリー技術の開発を行っている。従来のX線やγ線照射などよりも生物への照射効果の大きな重粒子線を用い、ブラッグピークを利用して狭小領域の患部に集中的にエネルギー付与し、選択的かつ集中的に治療を行うことを目指している。

本研究では、難病にも指定されている眼底疾患の一つである加齢黄斑変性症を治療想定症例として、高精度炭素イオンマイクロサージェリー技術の検討を進めている。

これまで、ビーム径0.1～5 mmφのペンシルビームを形成するための光学計算、構成機器およびその最適配置に関する検討を行ってきた。今回、照射位置決め法として、眼底蛍光造影剤を用いた重イオンビーム誘起蛍光法を考案し、重イオンビーム誘起蛍光計測システムを用いて実験を行うとともに、照射照準位置制御技術の検討を行った。

現在、眼底の狭小・微細領域にある患部を正確に3次元精密照射するために必要な照射照準制御技術の開発が最大の課題となっている。その方法として、今年度は眼底患部に注入した眼底蛍光造影剤（インドシアニングリーン；ICG）に、重粒子線を照射し、飛程をレンジシフタで微調整しながら、ICGの発光を専用特殊眼底カメラ等を用いて観測し、その発光画像を解析して照射位置の決定を行うことを検討した[1]。

眼底蛍光造影剤への照射実験は原子力機構・高崎研 TIARA 施設の AVF サイクロトロン・HA コースおよび HY コースを用いて行った。空気飽和した眼底蛍光造影剤水溶液（ICG およびフルオレセイン；Fl）に、炭素イオンビーム（$^{12}C^{5+}$-220 MeV）を照射し、眼底蛍光造影剤水溶液からの発光スペクトルおよび発光画像を撮影した。サンプルの濃度は標準的な人体に投与した際の最高血中濃度（1.0×10^{-2} mg/mL，1.3×10^{-5} M）に調整した。また、サンプル前方にフィルムミラーを設置し、ビームをフィルムミラーに透過させた後，フィルムミラーに反射した発光画像の撮影を行った。フィルムミラーには British Aerospace 社の高精度の透明ポリエステルフィルム（銀蒸着、厚み 25 μm）をアルミフレームに中空張りにしたものを使用した。

その結果、重粒子線照射による眼底蛍光造影剤からの発光画像および発光スペクトルが取得できた。光励起に比べ、発光波長はほぼ同じであるが、Flの蛍光量子収率（0.98）に対して発光強度が非常に微弱であるため、発光色素や検出系の再検討が必要であることが分かった。また、眼底蛍光撮像に向けた発光画像撮影においても、治療および位置決定用減弱ビーム強度に対して、撮像が非常に困難であった。

さらに、フィルムミラーの放射線耐性について試験を行い、治療時のビーム強度（2.0×10^9 pps）に対して、眼底蛍光造影剤及びシンチレータから発光画像及び発光強度を評価した。今回使用したフィルムミラーは比較的安価で入手可能なため、1回の治療毎に交換することを予定しており、照射ビームによるフィルムミラーへの影響はないと示唆される。

Reference

1) H. Shimada, et al., JAEA Takasaki Ann. Rep. 2007 (2008) 186.

This is a blank page.

5. Status of Irradiation Facilities 2008

This is a blank page.

5-01 Safety Measures, Utilization Status and Distribution of Research Fields at TIARA Facility

K. Mizuhashi, H. Takizawa, M. Hosono, K. Nishimura, H. Kaneko,
Y. Nakamura, S. Kaneya, S. Kanai, T. Asai, M. Yoshida, M. Kawabata and K. Daikubara

Department of Advanced Radiation Technology, TARRI, JAEA

1. Status of TIARA Facilities

Periodical inspections every month and for three months were performed and safety of the facility was also maintained certainly.

Personal access control system was renewed from 2007 to 2008. The system was installed in December, 1990 and aging deterioration went on. The renewal was divided into two periods and carried out. The personal access control system detects a person who enters the ion irradiation room and the radiation control area. In addition, it confirms the possession of the personal radiation dosimeter that is identified with the ID card. The system collects the detection signal by antenna sensor at 58 places in the TIARA radiation control area. It processes those signals and can help the safe management and monitoring of the worker in the area. At the same time, it supplies "man in the room" signal to the accelerator control system and that signal is used for the safety interlock of the accelerator and the indication of safe monitor board. In this year, we removed the ID cards, card readers and control panel whose production was stopped in the manufacturer and we renewed these to the new products. As a result of the renewal detection errors decreased and reliability was improved.

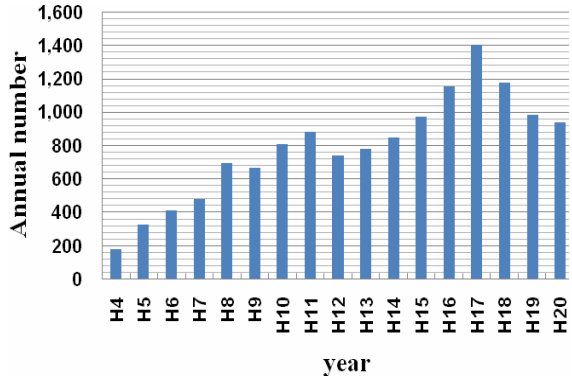

Fig. 1 Annual number of researchers who visited TIARA.

The shift of the annual number of visitor who make experiments at TIARA facility is shown in Fig. 1. The year of the biggest number of visitors was 2005, and the number was 1,404 people. The number decreased slowly from the peak year, and it was 934 people in 2008. The change of the number of visitors was related to the amount of the travel expenses budget that was provided to the experimenters. The maximum budget was 12 Myen in 2002. Afterwards, the budget was reduced year by year and no budget is offered now. However, the decrease in the number of the research subjects is not observed now.

2. Situation of TIARA Facility

From FY2008, the constitution ratio for internal, common and effective uses occupied in whole utilization frame had been designed as 75 : 17~19 : 8~6, including comprehensively 4 accelerators. The percentage for internal use increased to 75% from 70%, but it is still in a severe situation. User of the internal use can get only around 50% of the machine time that the user requires.

Four accelerators were used for various research subjects according to operation plan in FY 2008. Figure 2 shows the distribution of research fields. Annual utilization times of the AVF cyclotron and electrostatic accelerators were 2,309 hours and 475 days, respectively, which were offered to the experiments. 50% of the utilization time of the AVF cyclotron was used for the Bio technology・Medical application and the material for space. For the basic technology, 24.1% of the time was used. About the innovation, 3% (30 hours) was used.

As for electrostatic accelerators, 58% of the time was used for the basic technology and the inorganic material. The innovation use was 1.9% (9 days).

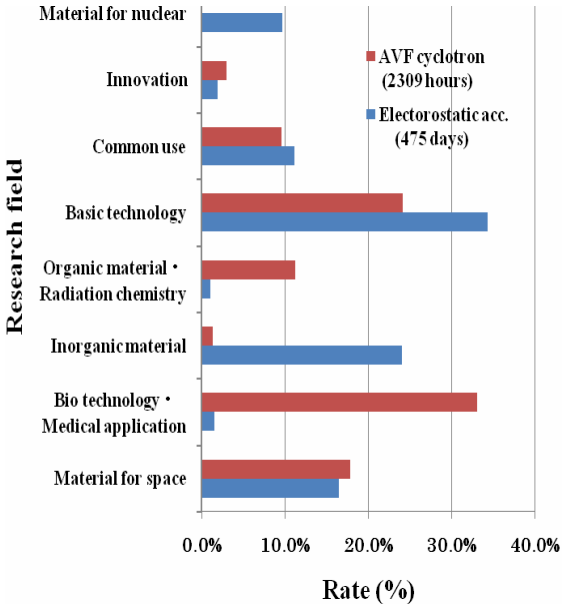

Fig. 2 Distribution of research fields for cyclotron and electrostatic accelerators.

5-02 Operation of the AVF Cyclotron

T. Nara [a)], I. Ishibori [a)], S. Kurashima [a)], K. Yoshida [a)], T. Yuyama [a)], T. Ishizaka [a)], S. Okumura [a)],N. Miyawaki [a)], H. Kashiwagi [a)], Y. Yuri [a)], W. Yokota [a)] , K. Akaiwa [b)], To. Yoshida [b)],S. Ishiro [b)], Tu. Yoshida [b)] S. Kanou [b)] A. Ihara [b)], K. Takano [b)] and S. Mochizuki [b)]

[a)] Department of Advanced Radiation Technology, TARRI, JAEA, [b)] Beam Operation Service, Co., Ltd.

Operation

The AVF cyclotron was smoothly operated in fiscal 2008 and all the planned experiments were carried out without cancellation due to troubles relating to the cyclotron. The cumulative operation time was 56,386.4 hours and the total number of experiments was 7,492 from the first beam extraction in 1991 to March 2008.

Table 1 shows the statistics of the cyclotron operation of fiscal 2008. The total operation time amounted to 3,162.1 hours, and the monthly operation times are shown in Fig. 1. The percentages of operation time of the year used for regular experiments, joint-use, the innovation program and beam tuning, and beam development are 71.6%, 6.4%, 2.1%, 19.9%, and 0%, respectively.

Table 1 Statistics for cyclotron operation in fiscal 2008.

Beam service time	2533.5 h
Machine tuning	628.6 h
Beam development	0 h
Total operation time	3162.1 h
Change of particle and/or energy	234 times
Change of beam course	308 times
Change of harmonic number	57 times
The number of experiments	642
Experiment cancelled due to machine trouble	0

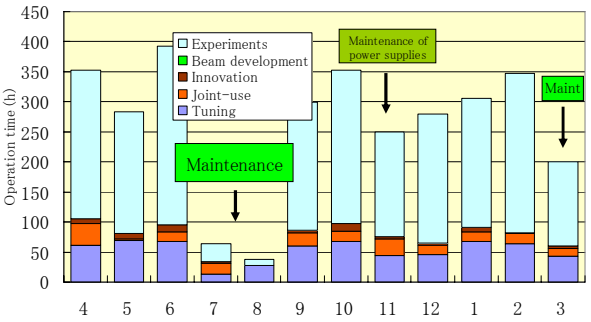

Fig. 1 Monthly operation time in fiscal 2008.

The multi-cusp ion source is used to produce H^+ ions. For production of ions heavier than Helium, two ECR ion sources are used alternatively. Table 2 shows the operation time of each ion source. Fractional distribution of major ions used for experiments is shown in Fig. 2. The tendencies of the statistics are similar to those of the past years.

Table 2 Operation times of ion sources.

Ion source	Operation time (h)	Ratio(%)
Multi-cusp	1076.1	31.0
ECR (OCTOPUS)	1036.4	29.9
ECR (HYPERNANOGAN)	1354.6	39.1

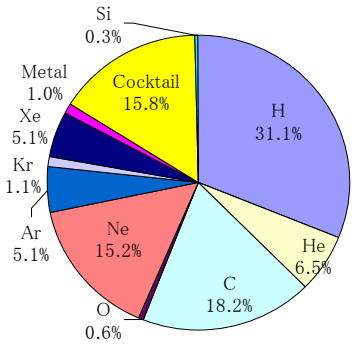

Fig. 2 Major ion species used for experiments in fiscal 2008.

Maintenance

The number of the machine troubles of the year was 251. However, they were quickly fixed and did not lead to cancellation of the experiments. The regular yearly overhaul was carried out for six weeks in July and August, and the routine maintenance of power supplies for a week in November. The principal items were as follows: 1) Change of high pressure air bellows for contact fingers of a couple of coaxial type resonator. 2) Correction of the original positions of some beam probes, the deflector, etc. 3) Cleaning of the deflector electrodes. 4) Inspection of the RF system and evaluation of its characteristics. 5) Change of lubricating oil for about 50 rotary pumps. 6) Change of amplifier for the S-chopper.

Technical Development

Four major developments are described hereafter. The beam profile change due to the attenuator in the injection line was considerably reduced by improvement of the attenuation grid pattern and location of the grids. A wide range NMR (Nuclear Magnetic Resonance) probe to measure the average magnetic field strength from 0.5 to 1.6 T has been developed and installed in the cyclotron. A uniform beam of 10-MeV H^+ was successfully formed using the nonlinear focusing system installed in the LB course last year[1)]. Its area and uniformity were 6 cm × 6 cm and 6%, respectively. The stability of single-pulse beams made by the chopping system has been extremely improved as a result of the high stabilization of the cyclotron magnetic field which was done in those several years. Single-pulse beam of 320-MeV C^{6+} was kept stable for more than 3 hours and supplied to irradiation experiments. See the reports on technical development in this annual report for the details.

Reference

1) Y. Yuri et al., Proc. Euro. Particle Accel. Conf., EPAC'08 (2008) 3077.

5-03 Operation of the Electrostatic Accelerators

T. Agematsu [a)], S. Uno [a)], A. Chiba [a)], K. Yamada [a)], A. Yokoyama [a)], Y. Saitoh [a)], Y. Ishii [a)], T. Satoh [a)], T. Ohkubo [a)], W. Yokota [a)],T. Kitano [b)], T. Takayama [b)], T. Orimo [b)], M. Kouka [b)], Y. Aoki [b)], N. Yamada [b)] and H. Saitoh [b)]

[a)] Department of Advanced Radiation Technology, TARRI, JAEA,
[b)] Beam Operation Service, Co., Ltd

1. Operation and Status

Three electrostatic accelerators were operated smoothly in FY 2008, and all the planned experiments were carried out except those canceled by users. The yearly operation time of the tandem accelerator, the single-ended accelerator and the ion implanter amounted to 2,009, 2,426 and 1,882 hours, respectively, similarly to past years. The total operation time of each accelerator since operation started is 30,322, 34,448 and 26,857 hours, respectively. The monthly operation time is shown in Fig. 1. Ion species used for experiments in FY 2008 are shown in Fig. 2.

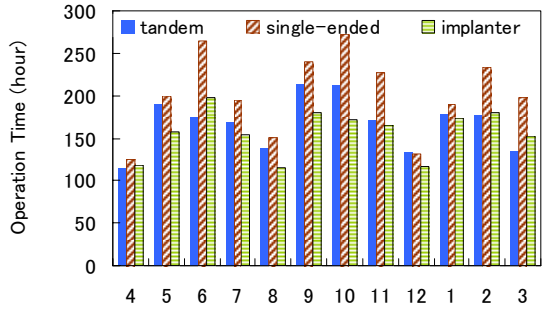

Fig. 1 Monthly operation time of each accelerator in FY 2008.

2. Maintenance

The number of troubles was smaller than that for past years. Major maintenance performed in FY 2008 is as follows;

Tandem accelerator: 1) The trouble increased at the CAMAC interface and the control computers. And it became difficult to keep spare parts of the computer. Therefore the control system was renewed in March 2009 since the last renewal in January 2001. 2) Mechanical vibration at the high-voltage terminal occurred last year and the stability of acceleration voltage was degraded. The vibration became small by changing the pellet-chain and adjusting the driving mechanism at regular maintenance, and the stability was coming back to previous level.

Single-ended accelerator: 1) The SF_6 gas was purified for the first time since gas replace in 1998. 2) The storage tank of SF_6 gas located outdoors was repainted. 3) Software limit of maximum high-voltage was set at 3.2 MV in the control system for safety operation.

Ion implanter: 1) Although the regular maintenance is performed every year by JAEA staffs, the maintenance, which was based on design knowledge, was carried out by Nissin Ion Equipment Co.,Ltd.

3. New Beam Development

As to the ion implanter, Bi_2 ion, which was required by users, was successfully generated and accelerated at intensity of 500 nA. But the inside of the ion source was seriously contaminated, and the energy was limited to 300 keV by limitation of power supplies for bending and focusing magnet. We tried to generate Nb and Pb ions for the tandem accelerator. As the generated beam intensity from the ion source was very small, the accelerated intensity was less than several nano amperes, which is insufficient for experiments.

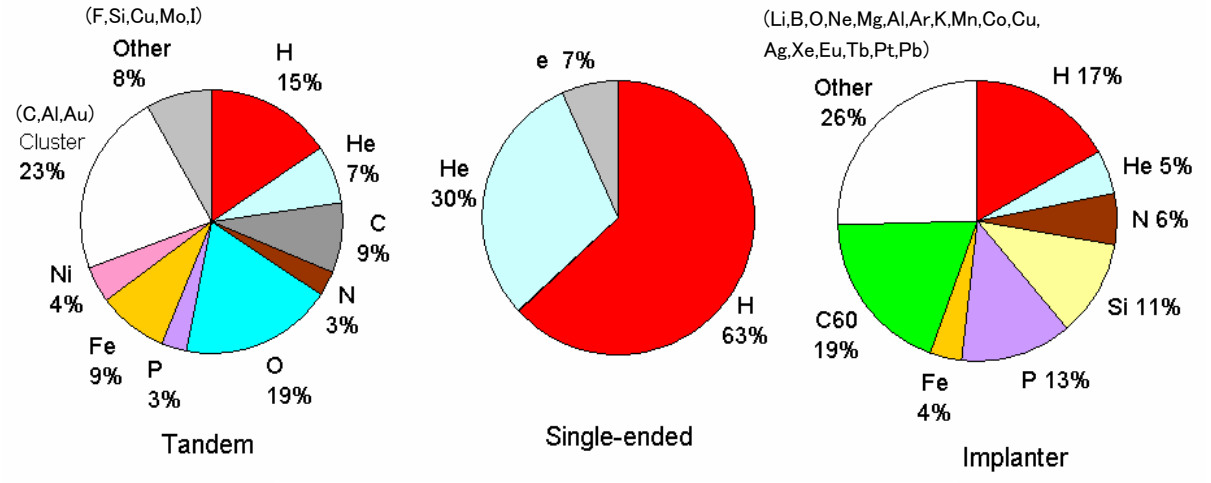

Fig. 2 Typical ion species for experiments using in FY 2008.

5-04 Operation of the Electron Accelerators and Gamma-ray Irradiation Facilities

Y. Haruyama [a)], H. Kaneko [a)], H. Hanaya [a)], R. Yamagata [a)], H. Seito [a)], T. Kanazawa [a)], T. Yamaguchi [b)], N. Yagi [b)], M. Takagi [b)], T. Hirai [b)] and S. Matsuzaki [b)]

[a)] Department of Advanced Radiation Technology, TARRI, JAEA,
[b)] Radiation Application Development Association, RADA

1. Operation

1.1 Electron accelerator

The electron accelerator No.1 was operated without any serious troubles from 9:00～17:30 on Monday and Friday, and from 8:30～23:00 on Tuesday through Thursday, to satisfy the demand of operation time for users.

Annual operation time of the electron accelerator No.1 and No.2 (operated until 2004) is shown in Fig.1 and that of No.1 in FY2008 was 860.3 h. Total operation time of the accelerator No.1 in FY2008 increased by about 23% compared with that in FY2007, and analysis of the number of research subject indicated the increase of longer-time irradiation for materials for space subject.

The accelerator served mainly for graft-polymerization for new material development, radiation effect study on semiconductors and various experiments of visiting users.

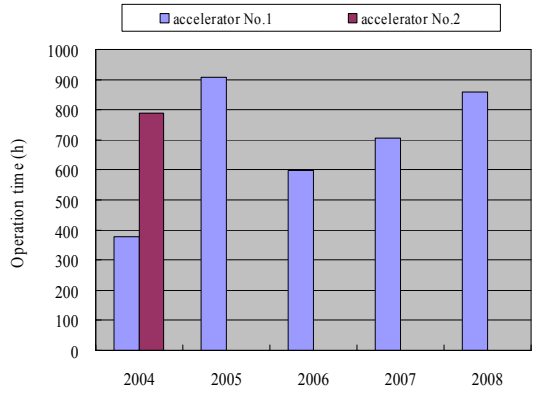

Fig. 1 Annual operation time of electron accelerators.

1.2 Gamma-ray irradiation facilities

The Co-60 gamma-ray irradiation facilities consist of three buildings and cover a wide dose-rate range from 0.04 Gy/h to 20 kGy/h with eight irradiation rooms. The annual operation time for the first, second cobalt irradiation facilities and food irradiation facility was 19,480 h, 12,503 h and 6,066 h, respectively, as shown in Fig. 2.

The first irradiation facility served mainly for radiation-resistance test of cables used in nuclear power plants and various materials used in J-PARC facility for long irradiation period. The second irradiation facility served mainly for development of new functional materials and other research subject of visiting users, involving irradiation room No.6 for hourly-scheduled operation. The food irradiation facility served mainly for development of detection method for irradiated foods and radiation resistance test at lower dose rates.

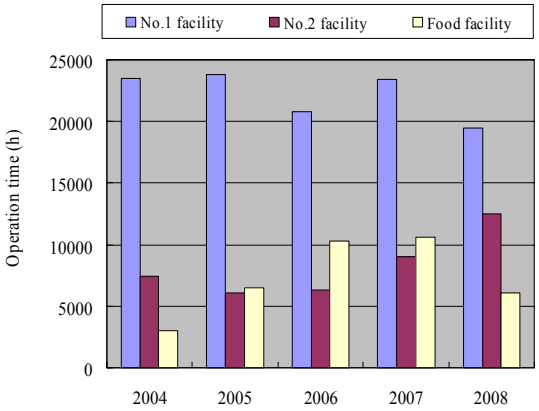

Fig. 2 Annual operation time of Co-60 gamma-ray irradiation facilities.

2. Maintenance

2.1 Electron accelerator

The operation of the accelerator was interrupted for 7 days in October, 2008 because of regular maintenance check on accelerator body, the conveyor and shielding doors of irradiation room and repair of vacuum system at the vertical beam line.

2.2 Gamma-ray irradiation facilities

The regular maintenance check mainly on mechanical system for radiation source transportation is performed every three years among three gamma-ray irradiation facilities one by one. The periodical maintenance check mainly on interlock system is performed two times a year for all the facilities.

The maintenance check and renewal of programmable logic controller of the second irradiation facility was done in June 2008, with interruption for 21 days.

The Co-60 sources were purchased and loaded to the irradiation room No.6 in the second irradiation facility to maintain total activities of the room. The old waste sources of about 20 pieces were disposed through The Japan Radioisotope Association (JRIA).

5-05 Utilization of the Electron Accelerator and Gamma-ray Irradiation Facilities

H. Kaneko [a)], Y. Haruyama [a)], H. Hanaya [a)], R. Yamagata [a)], H. Seito [a)], T. Kanazawa [a)], T. Yamaguchi [b)], N. Yagi [b)], M. Takagi [b)], T. Hirai [b)] and S. Matsuzaki [b)]

[a)] Department of Advanced Radiation Technology, TARRI, JAEA,
[b)] Radiation Application Development Association, RADA

Present status of the utilization of electron accelerator and gamma-ray irradiation facilities

An electron accelerator and three gamma-ray irradiation facilities were operated for various research subjects according to operation plan in FY 2008 without serious trouble. Distribution of research subjects and the number of experiment subjects are shown in Fig. 1 and Fig. 2, respectively. Table 1 shows irradiation time and the number of research subjects for each facility.

The number of experiment subjects at the electron accelerator increased in the research fields of material for space and material processing, and decreased in the field of basic technology and nuclear facilities. The number at gamma-ray irradiation facilities increased in the field of material processing, contrarily decreased in the field of nuclear facilities and resource & bio-technology.

Table 1 Irradiation time and the number of experiment subjects in each research field at each facility in FY2008.

Facility / Research fields	Electron Accelerator		Gamma-ray Irradiation facilities	
	Irradiation time (h)	number	Irradiation time (h)	number
Material processing	176.8	323	24475	425
Heat-resist material	96.9	31	489	6
Material for space	311.3	69	10037	51
Nuclear facilities	63.1	19	35348	71
Environment	30.0	22	472	66
Basic technology	9.6	16	1538	41
Resource & Bio-technology	0	0	310	131
Joint use	172.5	35	15947	186
Total	860.3	515	88616	977

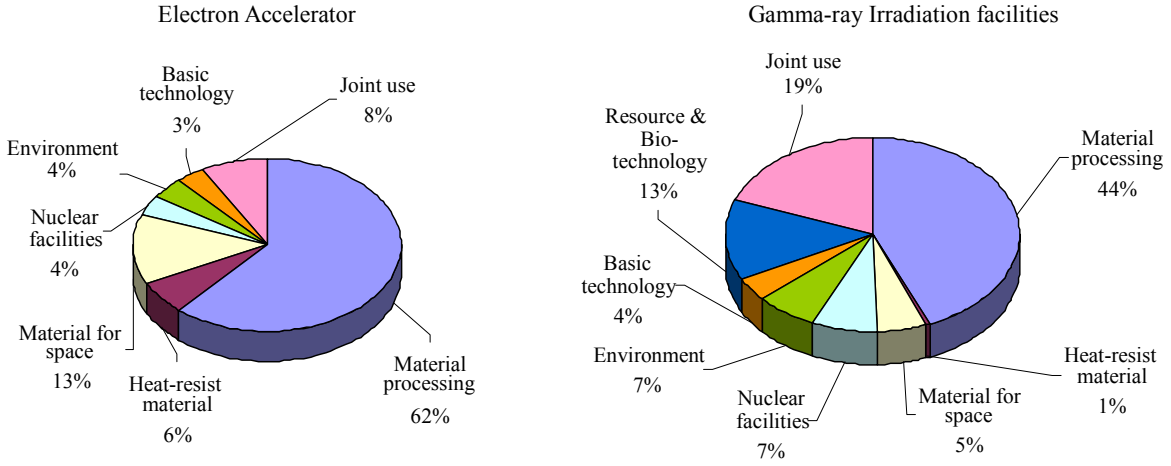

Fig. 1 Distribution of research subjects (FY 2008).

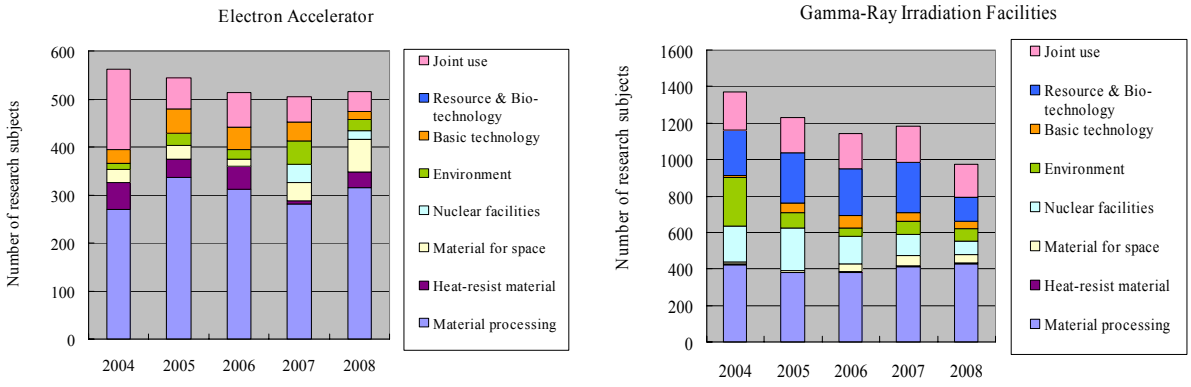

Fig. 2 The number of research subjects (FY 2004-2008).

5-06 COMMON USE PROGRAM in Takasaki Advanced Radiation Research Institute

K. Kawata, M. Hoto and H. Iijima

Department of Advanced Radiation Technology, TARRI, JAEA

1. Introduction

The facilities of JAEA are widely opened to users from universities, public institutes, and the industries, etc. COMMON USE PROGRAM, the system of facility use for the user's purpose on fee-charging basis, started in 2006 taking over the former system. There are 3 OPEN USE facilities in Takasaki; Co-60 Gamma-ray Irradiation Facilities, Electron Accelerator and TIARA. In addition to these, some of the off-line devices can be used.

We round up the Research Proposals every half year, and the execution possibility and the validity of the experimental plan are checked by the special committee. The facility usage fee is the total of the admission fee, irradiation fee and additional charge. In case of Non-proprietary research, the users must report the irradiation result to JAEA, and are exempt from irradiation fee. JAEA opens the reports to the public. It is also possible for universities to apply through the facility use program of the University of Tokyo. Those applications are accepted as priority case. Table 1 shows the outline of the program.

Table 1 Classification of COMMON USE PROGRAM.

purpose	research and development			except R&D
classify-cation	general		priority case	commercial
result	Non-proprietary	proprietary		
referee	yes	no		
charge*	A	B		C

*A= admission fee,
B= admission fee + irradiation fee,
C= admission fee + irradiation fee + depreciation.

2. Public Relations

The information like an outline of this system, guidelines for applicants, format download, etc. can be seen on JAEA website as follows:
(http://www3.tokai-sc.jaea.go.jp/sangaku/3-facility/index.html). In addition to this, we go out for publicity to search current needs of the outside of JAEA. In 2008, we participated in Seminar for advancement of RI/radiation use at Nagoya.

3. Use in FY2008

There were 21 Research Proposals in FY2008 at Takasaki institute, and 16 of them are for use with opening result. Including the users from priority case, we accepted 296 applications from 70 users and 23 users were new. We can see that the percentage of users from universities exceeds the others except Co-60 Facility from Table 2. However we expect there should be latent needs in the industries. Therefore we are trying to exhume them by the "Public relations" and improve convenience of the usage procedure by introducing new system to increase the industries user.

Figure 1 shows classification of all 296 applications. On TIARA, Non-proprietary use occupies more than 50%, while less than few percents for the other facilities.

Table 2 User's affiliation for each facility.

Facility \ User		University	Public Institute	Others	Total
TIARA	AVF Cyclotron	7	3	3	13
	3MV Tandem Accelerator	7	2	1	10
	3MV Single-ended Accelerator	2	0	0	2
	400kV Ion Implanter	3	1	1	5
Co-60 Gamma-ray Irradiation Facility		8	1	19	28
Electron Accelerator		6	2	4	12
Total		33	9	28	70

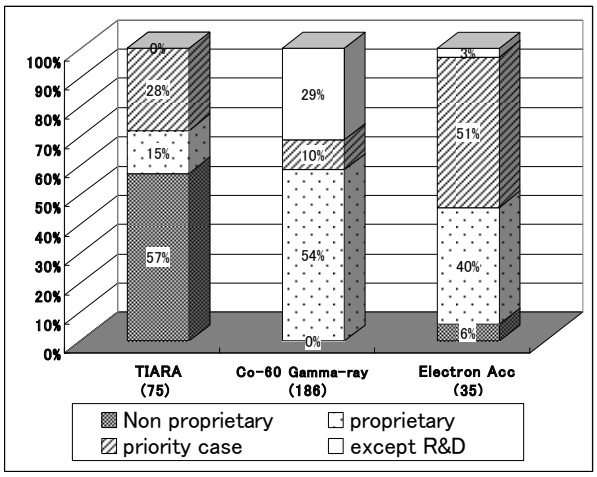

Fig. 1 Percentage of each classification. The percentage is calculated based on the number of application.

5-07 Radiation Control in TIARA

Safety Section

Department of Administrative Services, TARRI, JAEA

1 Individual monitoring

(1) Individual monitoring for the radiation workers

Table 1 shows a distribution of effective dose of the radiation workers in FY 2008. The effective dose values of almost all radiation workers were below the detection limit (0.1 mSv).

The maximum dose was 0.9 mSv/y due to the overhaul of the TIARA AVF cyclotron.

Table 1 Distributions of the effective dose of the radiation workers in FY 2008.

Items \ persons		Number of persons in each periods 1st quarter	2nd quarter	3rd quarter	4th quarter	Total
Distribution range of effective dose HE : Effective dose *1 (mSv)	HE < 0.1	547	566	572	565	669
	0.1 ≦ HE ≦ 1.0	1	6	1	2	8
	1.0 < HE ≦ 5.0	0	0	0	0	0
	5.0 < HE ≦ 15.0	0	0	0	0	0
	15.0 < HE	0	0	0	0	0
Number of persons under radiation control (A)		548	572	573	567	677
Exposure above 1mSv	Number of persons (B)	0	0	0	0	0
	(B)/(A)×100(%)	0	0	0	0	0
Mass effective dose (Person・mSv)		0.1	2.2	0.2	0.3	2.8
Mean dose (mSv)		0.00	0.01	0.00	0.00	0.00
Maximum dose (mSv)		0.1	0.8	0.2	0.2	0.8

*1 The dose induced by the internal exposure was not detected.

(2) Individual monitoring for the visitors and others

Table 2 shows the number of persons who temporally entered the radiation controlled areas. The effective dose of all persons was less than 0.1 mSv.

Table 2 The number of persons who temporary entered the radiation controlled areas in FY 2008.

Periods	1st quarter	2nd quarter	3rd quarter	4th quarter	Total
Number of persons	406	410	486	529	1831

2 Monitoring of radioactive gas and dust

Table 3 shows the maximum radioactive concentrations and total activities for radioactive gases released from the stack of TIARA, during each quarter of FY 2008.

Small amount of ^{41}Ar, ^{13}N and ^{11}C were detected for some time during operation of the cyclotron or experiment, but the pulverized substances (^{65}Zn, etc.) were not detected.

Table 3 Monitoring results of released radioactive gases and dust in FY 2008.

Nuclide \ Period / Items		1st quarter	2nd quarter	3rd quarter	4th quarter	Total
^{41}Ar	Maximum concentration	$<1.5\times10^{-4}$	$<1.5\times10^{-4}$	$<1.5\times10^{-4}$	$<1.5\times10^{-4}$	$<1.5\times10^{-4}$
	Activity	1.5×10^{7}	7.0×10^{7}	1.7×10^{8}	1.9×10^{8}	4.5×10^{8}
^{11}C	Maximum concentration	$<1.5\times10^{-4}$	-----	$<1.5\times10^{-4}$	$<1.5\times10^{-4}$	$<1.5\times10^{-4}$
	Activity	1.3×10^{8}	-----	4.1×10^{7}	4.7×10^{8}	6.4×10^{8}
^{13}N	Maximum concentration	$<1.5\times10^{-4}$	-----	$<1.5\times10^{-4}$	$<1.5\times10^{-4}$	$<1.5\times10^{-4}$
	Activity	2.4×10^{8}	-----	1.7×10^{8}	1.9×10^{8}	6.0×10^{8}
^{65}Zn	Maximum concentration	$<7.2\times10^{-10}$	$<6.0\times10^{-10}$	$<6.6\times10^{-10}$	$<6.6\times10^{-10}$	$<7.2\times10^{-10}$
	Activity	0	0	0	0	0

Unit : Bq/cm^3 for Maximum concentration, Bq for Activity.

3 Monitoring for external radiation and surface contamination

External radiation monitoring was routinely carried out in/around the radiation controlled areas and surface contamination monitoring was also carried out. Neither unusual value of dose equivalent rate nor surface contamination was detected.

Figure 1 shows a typical example of distribution of the dose equivalent rate in the radiation controlled area of the cyclotron building.

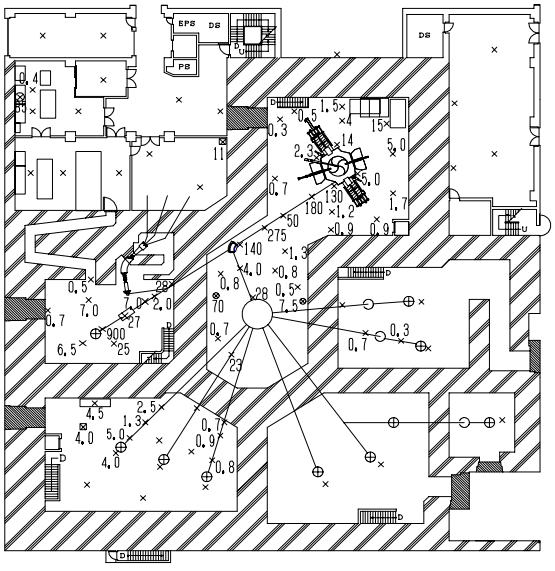

Fig. 1 Dose equivalent rate distribution in the radiation controlled area of the cyclotron building.
Measurement date : 24th March 2009,
Measuring position : Indicated with × 1 m above floor,
Unit : μSv/h. (The values are not indicated if they are less than 0.2 μSv/h.)

5-08 Radioactive Waste Management in TIARA

T. Ishibashi and N. Higuchi

Department of Administrative Services, TARRI, JAEA

1. Radioactive Wastes Management

The radioactive wastes generated in TIARA are managed by Utilities and Maintenance Section. The main radioactive wastes are the solid wastes generated from the research experiment and the maintenance of the cyclotron. Other radioactive wastes are the liquid wastes such as inorganic waste fluids generated from the research experiment and the air-conditioning machines in controlled area. These wastes are managed according to their properties.

2. Solid Radioactive Waste

Table 1 shows the amounts of solid wastes at various properties and kinds generated in each quarter of FY 2008. The main solid waste is generated from the research experiment and the maintenance of the cyclotron.

Combustible wastes are rubber gloves, paper, and clothes, etc. Incombustible wastes are metal pieces, the glasses, and contaminated parts.

3. Liquid Radioactive Waste

Table 2 shows the amounts of liquid wastes generated in each quarter of FY 2008. Most of liquid wastes was inorganic waste water generated from chemical experiments and condensed water from the operation of air conditioning units installed in each room of the first class radiation controlled area. The largest quantity of waste water in summer season (2nd quarter) is mainly due to condensed water. After treatment by evaporation, inorganic water is reused in the controlled area. Only small amounts of concentrated liquid are generated from the evaporation.

Table 1 Radioactive solid wastes generated in FY 2008.

Amounts / Items	Amounts of generation in each periods (m^3)					Number of package /drum
	1st quarter	2nd quarter	3rd quarter	4th quarter	Total	
Category A*	0.28	0.58	0.28	0.38	1.69	
1)Combustible	0.10	0.44	0.16	0.26	0.96	6**
2)Incombustible	0.18	0.14	0.08	0.33	0.73	0
Compressible	0.18	0.14	0.08	0.12	0.52	3**
Filters	0	0	0	0.21	0.21	0
Incompressible	0	0	0	0	0	0
Ion exchange resin	0	0	0	0	0	0
Category B*	0	0	0	0	0	0

* defined by dose at the outer surface of container : (A) ＜ 2 mSv/h ≦ (B).

** 200-liter drum.

Table 2 Radioactive liquid waste generated in FY 2008.

Amounts / Items	Amounts of generation in each periods (m^3)					Number of package /drum
	1st quarter	2nd quarter	3rd quarter	4th quarter	Total	
Category A*	8.91	23.10	4.97	3.44	40.42	
1)Inorganic	8.91	23.10	4.97	3.34	40.32	treatment
2)Organic	0	0	0	0	0	0
Organic	0	0	0	0	0	0
Oil	0	0	0	0	0	0
3)Sludge	0	0	0	0	0	0
4)Evaporation residue	0	0	0	0.10	0.10	1
Category B*	0	0	0	0	0	0

* defined by concentrations in Bq/cm^3 (β, γ) : (A) ＜ 3.7×10 ≦ (B) ＜ 3.7×10^4.

Appendix

This is a blank page.

Appendix 1. List of Publication

A 1.1 Publications in Journal

08J001 1-02, 1-03 C

T. Makino, D. Kobayashi, K. Hirose,
Y. Yanagawa, H. Saito, H.Ikeda, D. Takahashi,
S. Ishii, M. Kusano, S. Onoda,
T. Hirao and T. Ohshima
"LET Dependence of Single Event Transient Pulse-Widths in SOI Logic Cell"
IEEE Trans. Nucl. Sci., 56 (1) (2009) 202-207.

08J002 1-02, 1-03

牧野 高紘、柳川 善光、小林 大輔、福田 盛介、
廣瀬 和之、池田 博一、 齋藤 宏文、小野田 忍、
平尾 敏雄、大島 武、高橋 大輔、石井 茂、
草野 将樹、池淵 博、黒田 能克
"宇宙用論理 LSI で発生する放射線誘起スパイクノイズの研究"
信学技法・SANE、宇宙・航空エレクロニクス、
108 (100) 67-72.

08J003 1-05, 1-09 T, C, I

S. Onoda, T. Ohshima, T. Hirao, S. Hishiki,
N. Iwamoto, K. Kojima and K. Kawano
"Transient Response to High Energy Heavy Ions in 6H-SiC n+p Diodes"
Mater. Sci. Forum 600-603 (2009) 1039-1042.

08 J004 1-05, 1-09 T, I, E

N. Iwamoto, S. Onoda, S. Hishiki, T. Ohshima,
M. Murakami, I. Nakano and K. Kawano
"Degradation of Charge Collection Efficiency for 6H-SiC Diodes by Electron Irradiation"
Mater. Sci. Forum 600-603 (2009) 1043-1046.

08J005 1-06 E

R.D. Harris, M. Imaizumi, R.J. Walters,
J.R. Lorentzen, S.R. Messenger, J.G. Tischler,
T. Ohshima, S. Sato,
P.R. Sharps and N.S. Faatemi J. R.
"In-Situ Irradiation and Measurement of Triple Junction Solar Cells at Low Intensity, Low Temperature (LILT) Conditions"
IEEE Trans. Nucl. Sci. 55 (2008) 3502-3507.

08J006 1-06 C, T, I, E

S. Sato, M. Imaizumi and T. Ohshima
"Modeling of Degradation Behavior of InGaP/GaAs/Ge Triple-Junction Space Solar Cell Exposed to Charged Particles"
J. Appl. Phys., 105 (2009) 044504 1-6.

08J007 1-06 C, T, I, E

S. Sato, H. Miyamoto, M. Imaizumi,
K. Shimazaki, C. Morioka,
K. Kawano and T. Ohshima
"Degradation modeling of InGaP/GaAs/Ge triple-junction solar cells irradiated with various-energy protons"
Sol. Energy Mater. Sol. Cells. 93 (2009) 768-773.

08J008 1-08 I

H. Okada, K. Takemoto, F. Oikawa, Y. Furukawa,
A. Wakahara, S. Sato and T. Ohshima
"Light emitting FET based-on spatially selective doping of Eu in AlGaN/GaN HEMT"
Phys. Status Solidi C6, No. S2, (2009) S631-634.

08 J009 1-09 E

S. A. Reshanov, G. Pensl, K. Danno, T. Kimoto, S. Hishiki, T. Ohshima, Fei Yan, R. P. Devaty and W. J. Choyke
"Effect of the Shottkey Barrier Height on the Detection of Midgap Levels in 4H-SiC by Deep Level Transient Spectroscopy"
Mater. Sci. Forum 600-603 (2009) 417-420.

08 J010 1-09 I, G

S. Hishiki, S. A. Reshanov, T. Ohshima, H. Itoh and G. Pensl
"Reduction of Interface Traps and Enhancement of Channel Mobility in n-channel 6H-SiC MOSFETs by Irradiation with Gamma-Rays"
Mater. Sci. Forum 600-603 (2009) 703-706.

08 J011 1-09 I, G

S. Hishiki, N. Iwamoto, T. Ohshima, H. Itoh, K. Kojima and K. Kawano
"Effects of Fabrication Process on the Electrical Characteristics of n-channel MOSFETs Irradiated with Gamma-Rays"
Mater. Sci. Forum 600-603 (2009) 707-710.

08J012 1-10 E

H. Matsuura, K. Izawa, N. Minohara and T. Ohshima
"Mechanisms of Reduction in Hole Concentration in Al-Implanted p-Type 6H-SiC by 1 MeV Electron Irradiation"
Jpn. J. Appl. Phys., 47 (2008) 5355-5357.

08J013 1-10 E

H. Matsuura, N. Minohara and T. Ohshima
"Mechanisms of unexpected reduction in hole concentration in Al-doped 4H-SiC by 200 keV electron irradiation"
J. Appl. Phys., 104 (2008) 043702 1-6.

08 J014 1-11 E

T. Umeda, N. Morishita, T. Ohshima, H. Itoh and J. Isoya
"Photo-EPR study of vacancy-type Defects in irradiated n-type 4H-SiC"
Mater. Sci. Forum 600-603 (2009) 409-412.

08 J015 1-11 E

J. Isoya, T. Umeda, N. Mizuochi, N.T. Son, E. Janzén and T. Ohshima
"EPR identification of defects and impurities in SiC: To be decisive"
Mater. Sci. Forum 600-603 (2009) 279-284.

08 J016 1-11 E

J. Isoya, T. Umeda, N. Mizuochi and T. Ohshima,
"Pulsed EPR studies of the Tv2a center in 4H-SiC"
Mater. Sci. Forum 615-617 (2009) 353-356.

08 J017 1-11 E

A. Gali, T. Umeda, E. Janzen, N. Morishita, T. Ohshima and J. Isoya
"Identification of the di-carbon antisite defect in n-type 4H-SiC"
Mater. Sci. Forum 615-617 (2009) 361-364.

08 J018 1-11 E

P. Carlsson, N.T. Son, J. Isoya, N. Morishita, T. Ohshima, H. Itoh and E.. Janzén
"Photo-EPR studies on low-energy electron-irradiated 4H-SiC"
Mater. Sci. Forum 615-617 (2009) 401-404.

08 J019 1-11 E

N. T. Son, J. Isoya, N. Morishita, T. Ohshima,
H. Itoh, A. Gali and E.. Janzen
"Defects introduced by electron-irradiation at low temperatures in SiC"
Mater. Sci. Forum 615-617 (2009) 377-380.

08J020 1-11 E

T. Umeda, J. Isoya, N. Morishita, T. Ohshima,
E. Janzen and A. Gali
"Dicarbon antisite defects in n-type 4H-SiC"
Phys. Rev. B 79 (2009) 115211 (8 pages).

08J021 1-11 E

J. Isoya, T. Umeda, N. Mizuochi, N.T. Son,
E. Janzen and T. Ohshima
"EPR identification of intrinsic defects in SiC"
Phys. status solidi, (b) 245 (2008) 1298-1314

08J022 1-22 G, C, T

Y. Sugo, M. Taguchi, Y. Sasaki,
K. Hirota and T. Kimura
"Radiolysis Study of Actinide Complexing Agent by Irradiation with Helium Ion Beam"
Radiat. Phys. Chem., in press.

08 J023 1-29

R.L. Klueh, K. Shiba and M.A. Sokolov
"Embrittlement of irradiated F82H in the absence of irradiation hardening"
J. Nucl. Mater., 386-388 (2009) 191-194.

08J024 1-29

Johsei Nagakawa, S. Uchio, Y. Murase,
N. Yamamoto and K. Shiba
"Creep behavior of the F82H steel under irradiation with 17 MeV protons at 300 °C"
J. Nucl. Mater., 386-388 (2009) 264-267.

08J025 1-29

K. Shinozuka, M. Tamura, H. Esaka,
K. Shiba and K. Nakamura
"Creep behavior of oxide dispersion strengthened 8Cr–2WVTa and 8Cr–1W steels"
J. Nucl. Mater., 384 (2009) 1-5.

08 J026 1-29

K. Sato, K. Inoue, T. Yoshiie, Q. Xu, E. Wakai,
C. Kutsukake and K. Ochiai
"Positron annihilation lifetime measurements of vanadium alloy and F82H irradiated with fission and fusion neutrons"
J. Nucl. Mater., 386-388 (2009) 203-205.

08 J027 1-29

M. Ando, H. Tanigawa,
E. Wakai and R.E. Stoller
"Effect of two-steps heat treatments on irradiation hardening in F82H irradiated at 573 K"
J. Nucl. Mater., 386-388 (2009) 315-318.

08 J028 1-29

M. Ida, T. Chida, K. Furuya, E. Wakai,
H. Nakamura and M. Sugimoto
"Thermal-stress analysis of IFMIF target back-wall made of reduced-activation ferritic steel and austenitic stainless steel"
J. Nucl. Mater., 386-388 (2009) 987-990.

08J029 1-29

A. Hasegawa, M. Ejiri, S. Nogami, M. Ishiga,
R. Kasada, A. Kimura, K. Abe and S. Jitsukawa
"Effects of helium on ductile-brittle transition behavior of reduced-activation ferritic steels after

high-concentration helium implantation at high temperature"
J. Nucl. Mater., 386-388 (2009) 241-244.

08J030 1-29
T. Nishitani, H. Tanigawa, S. Jitsukawa, T. Nozawa, K. Hayashi, T. Yamanishi, K. Tsuchiya, A. Möslang, N. Baluc, A. Pizzuto, E.R. Hodgson, R. Laesser, M. Gasparotto, A. Kohyama, R. Kasada, T. Shikama, H. Takatsu and M. Araki
"Fusion materials development program in the broader approach activities"
J. Nucl. Mater., 386-388 (2009) 405-410.

08J031 1-29
R.J. Kurtz, A. Alamo, E. Lucon, Q. Huang, S. Jitsukawa, A. Kimura, R.L. Klueh, G.R. Odette, C. Petersen, M.A. Sokolov, P. Spätig and J.-W. Rensman
"Recent progress toward development of reduced activation ferritic/martensitic steels for fusion structural applications"
J. Nucl. Mater., 386-388 (2009) 411-417.

08J032 1-29
Y. Miwa, S. Jitsukawa and T. Tsukada
"Stress corrosion cracking susceptibility of a reduced-activation martensitic steel F82H"
J. Nucl. Mater., 386-388 (2009) 703-707.

08J033 1-29
D. Yamaki, N. Okubo, T. Nakazawa and S. Jitsukawa
"Effects of multi-ion irradiation on microstructural changes in lithium titanate"
J. Nucl. Mater., 386-388 (2009) 1065-1067.

08J034 1-29
Y. Abe and S. Jitsukawa
"Lowest energy structures of self-interstitial atom clusters in alpha-iron from a combination of Langevin molecular dynamics and the basin-hopping technique"
PHILOSOPHICAL MAGAZINE 89 (2009) 375-388.

08J035 1-34 C
R. Rohani, T. Yamaki, H. Koshikawa, S. Takahashi, S. Hasegawa, M. Asano, Y. Maekawa, K.-O. Voss, C. Trautmann and R. Neumann
"Enhancement of etch rate for preparation of nano-sized ion-track membranes of poly (vinylidene fluoride): Effect of pretreatment and high-LET beam irradiation"
Nucl. Instrum. Meth. Phys. Res. B 267 (2009) 554-557.

08J036 1-34 C
T. Yamaki, M. Asano and M. Yoshida
"Preparation of radiation-grafted ion exchange membranes for application to fuel cells: New strategies emerging with recent developments"
Current Developments of Radiation-induced Graft in Membranes (2008) 1-49.

08J037 1-34 C
T. Yamaki, H. Koshikawa, M. Asano, Y. Maekawa, K.-O. Voss and R. Neumann
"Preparation of anisotropically proton-conductive materials based on poly (vinylidene fluoride) ion track membranes"
GSI Sci. Rep. 2007 (2008) 341.

08J038 1-35 C

H. Koshikawa, Y. Maekawa and H. Usui
"Formation of composite films of ion-track membranes embedded with oblique Cu nanowires for anisotropic infrared absorption"
Radiat. Phys. Chem., 77 (2008) 453-455.

08J039 1-35 C

H. Koshikawa, H. Usui, and Y. Maekawa
"Thermally Stable and Anisotropically Conducting Membranes Consisting of Sub-micron Copper Wires in Polyimide Ion Track Membranes"
J. Membr. Sci., 327 (2009) 182–187.

08J040 1-36 E, G

Y. Maekawa, K. Yuasa, K. Enomoto,
H. Matsushita, J. Kato, S. Yamashita,
K. Ito and M. Yoshida
"Electron beam-induced color imaging of acid-chromic polymer films"
Chem. Mater., 20 (2008) 5320-5324.

08J041 1-36 E, G

S. Hasegawa, Y. Suzuki, and Y. Maekawa
"Preparation of poly (ether ether ketone)-based polymer electrolytes for fuel cell membranes using grafting technique"
Radiat. Phys. Chem., 77 (2008) 617-621.

08J042 1-36, 1-38 E, G

M. Asano, J. Chen, Y. Maekawa and M. Yoshida
"Development of fluorinated polymer electrolyte membranes using photografting-methods"
MEMBRANE, 33(2) (2008) 63-69.

08J043 1-36 E, G

Y. Maekawa, J. Kato, M. Katakai, M. Ishihara,
K. Enomoto, T. Hagiwara, T. Ishii, K. Itoh,
H. Koshikawa and M. Yoshida
"Radiation-Induced Reaction of Sulfonamide-Containing Polymers in the Film State for Color Imaging"
Macromol. Chem. Phys., 209 (2008) 625–633.

08J044 1-36 E, G

M. Zhai, J. Chen, S. Hasegawa, D. Li,
H. Oku and Y. Maekawa
"Perfluorinated polymer film with functional group prepared by radiation-induced grafting"
Eur. Polym. J., 45 (2009) 1668-1673.

08J045 1-36 E, G

M. Zhai, J. Chen, S. Hasegawa and Y. Maekawa
"Synthesis of Fluorinated Polymer Electrolyte Membranes by Radiation Grafting and Atom Transfer Radical Polymerization Techniques"
Polymer, 50 (2009) 1159–1165.

08J046 1-36 E, G

M. Zhai, S. Hasegawa, J. Chen and Y. Maekawa
"Radiation-induced grafting of perfluorinated vinyl ether into fluorinated polymer films"
J. Fluorine Chem., 129 (2008) 1146-1149.

08J047 1-36 E, G

S. Takahashi, H. Okonogi,
T. Hagiwara and Y. Maekawa
"Preparation of Polymer Electrolyte Membranes Consisting of Alkyl Sulfonic Acid for a Fuel Cell Using Radiation Grafting and Subsequent Substitution/Elimination Reactions"
J. Membr. Sci., 324 (2008) 173–180.

08J048 1-37 G

J. Chen, M. Asano, Y. Maekawa and M. Yoshida
"Fuel cell performance of polyetheretherketone-based polymer electrolyte membranes prepared by a two-step graftingmethod"
J. Membr. Sci., 319 (2008) 1-4.

08J049 1-37 G

Y. Kimura, M. Asano, J. Chen, Y. Maekawa, R. Katakai and M. Yoshida
"Influence of grafting solvents on the properties of polymer electrolyte membranes prepared by γ-ray preirradiation method"
Radiat. Phys. Chem., 77 (2008) 864-870.

08J050 1-37 G

J. Chen, M. Asano, Y. Maekawa and M. Yoshida
"Chemically stable hybrid polymer electrolyte membranes prepared by radiation grafting, sulfonation, and silane-crosslinking techniques"
J. Polym Sci. Part A: Polym. Chem., 46 (2008) 5559-5567.

08J051 1-37 G

D. Li, J. Chen, M. Zhai, M. Asano, Y. Maekawa, H. Oku and M. Yoshida
"Hydrocarbon proton-conductive membranes prepared by radiation-grafting of styrenesulfonate onto aromatic polyamide films"
Nucl. Instrum. Meth. B, 267 (2009) 103–107.

08J052 1-38 G

S. Sawada, T. Yamaki, S. Kawahito, M. Asano, A. Suzuki, T. Terai and Y. Maekawa
"Thermal stability of proton exchange fuel-cell membranes based on crosslinked-polytetrafluoroethylene for membrane-electrode assembly preparation"
Polym. Degrad. Stab. 94 (2009) 344–349.

08J053 1-38 G

S. Sawada, T. Yamaki, H. Nishimura, M. Asano, A. Suzuki, T. Terai and Y. Maekawa
"Water transport properties of crosslinked-PTFE based electrolyte membranes"
Solid State Ionics, 179 (2008) 1611-1614.

08J054 1-38 G

S. Sawada, T. Yamaki, T. Maeno, M. Asano, A. Suzuki, T. Terai and Y. Maekawa
"Solid polymer electrolyte water electrolysis systems for hydrogen production based on our newly developed membranes, Part I: Analysis of voltage-current characteristics"
Prog. Nucl. Energy, 50 (2008) 443-448.

08J055 2-10 E

T. Hakoda, K. Matsumoto, A. Mizuno, T. Narita, T. Kojima and K. Hirota
"Oxidation Process of Xylene in Air using Ag/TiO2 under Electron Beam Irradiation"
IEEE Trans. Ind. Appl., 44 (2008) 1950.

08J056 2-10 E

T. Hakoda, K. Matsumoto, A. Mizuno and K. Hirota
"Oxidation of Xylene and its Irradiation Byproducts Using an Electron Beam Irradiating a γ-Al2O3 Bed"
J. Phys. D: Appl. Phys., 41 (2008) 155202.

08J057 2-10 E

T. Hakoda, A. Shimada, K. Matsumoto and K. Hirota
"Determination of the Number of OH Radicals in

EB-irradiated Humid Gases using Oxidation of CO”
Plasma Chem. Plasma Proc., 29 (2009) 69.

08J058 2-11 G

A. Kimura, M. Taguchi, T. Kondoh, J. Yang,
Y. Yoshida and K. Hirota
“Study on the reaction of chlorophenols in room temperature ionic liquids with ionizing radiation”
Radiat. Phys. Chem., 77 (2008) 1253-1257.

08J059 3-02 C

A. Yokoya, N. Shikazono, K. Fujii, A. Urushibara,
K. Akamatsu and R.Watanabe
“DNA damage induced by the direct effect of radiation”
Radiat. Phys. Chem., 77 (2008) 1280-1285.

08J060 3-02 C

N. Shikazono, M. Noguchi, K. Fujii,
A. Urushibara and A. Yokoya
“The yield, processing, and biological consequences of clustered DNA damage induced by ionizing radiation”
J. Radiat. Res. 50 (2009) 27-36.

08J061 3-03

A. Nakasone, M. Kawai-Yamada, T. Kiyosue,
I. Narumi, H. Uchimiya and Y. Oono
“A gene encoding SMALL ACIDIC PROTEIN 2 potentially mediates the response to synthetic auxin, 2,4-dichlorophonoxyacetic acid, in Arabidopsis thaliana”
J. Plant Physiol., (2009), in print.

08J062 3-05 O

R. Yoshihara, C. Nakane, R. Sato,
A. Yasuda and K. Takimoto
“Silencing of CPD Photolyase Makes Arabidopsis Hypersensitive and Hypermutable in Response to UV-B Radiation”
Genes Environ. 30 (2008) 53-61.

08J063 3-06 C

B. Liu, A. Kanazawa, H. Matsumura,
R. Takahashi, K. Harada and J. Abe
“Genetic redundancy in soybean photoresponses associated with duplication of the phytochrome A gene”
Genetics 180 (2008) 995-1007.

08J064 3-06 C

Y. Imoto, T. Yamada,
K. Kitamura and A. Kanazawa
“Spatial and temporal control of transcription of the soybean β-conglycinin α subunit gene is conferred by its proximal promoter region and accounts for the unequal distribution of the protein during embryogenesis”
Genes Genet. Syst. 83 (2008) 469-476.

08J065 3-09 C

M. Tsuro, H. Ikedo and H.Kato
“Efficient genetic transformation in lavandin using Agrobacterium rhizogenes as vector”
J. Jpn. Soc. Hort. Sci. (2009) 236-241.

08J066 3-18 C

J. Takano and K. Namai
“Callus induction and shoot regeneration of strawberry ‘Tochiotome’”
Bull. Tochigi Agr. Exp. Stn. 63 (2008) 9-16.

08J067 3-19 G

K. Satoh, Z. Tu, H. Ohba and I. Narumi
"Development of versatile shuttle vectors for Deinococcus grandis"
Plasmid, in press.

08J068 3-23 G

M. Ukai, H. Kameya,
H. Nakamura and Y. Shimoyama
"An Electron Spin Resonance Study of Dry Vegetables before and after Irradiation"
Irradiation, Spectrochimica Acta 69(5) (2008) 1417-1422.

08J069 3-23 G

H. Nakamura, H. Kameya,
M. Ukai and Y. Shimoyama
"Synthesis and Electron Spin Resonance Spectroscopy of Biradical Molecules Containing 14N-O and 15N-O Moieties"
Spectrochimica Acta 69(5) (2008) 1367-1371.

08J070 3-23 G

小川 聡子、加恵田 庸子、亀谷 宏美、
中村 秀夫、鵜飼 光子
"標準添加法による胡椒の ESR による検知法"
食品照射、43 (2008) 9-13.

08J071 3-23 G

亀谷 宏美、川内 里紗、加恵田 傭子、小川 聡子、
中村 秀夫、鵜飼 光子、下山 雄平
"電子スピン共鳴法による照射黒コショウ中に生じた遊離基の異なる水分環境下での緩和挙動の解析"
RADIOISOTOPES 57(8) (2008) 485-490.

08J072 3-25 C

Y. Yokota, S. Wada, Y. Hase, T. Funayama,
Y. Kobayashi, I. Narumi and A. Tanaka
"Kinetic analysis of double-strand break rejoining reveals the DNA reparability of gamma-irradiated tobacco cells"
J. Radiat. Res., 50 (2009) 171-175.

08J073 3-26 G

T. Sakashita, N. Hamada, D.D. Ikeda, M. Suzuki,
S. Yanase, N. Ishii and Y. Kobayashi
"Locomotion – learning behavior relationship in Caenorhabditis elegans following gamma–ray irradiation"
J. Radiat. Res. 49 (2008) 285-291.

08J074 3-26, 3-38 G

M. Suzuki, T. Sakashita, S. Yanase, M. Kikuchi,
H. Ohba, A. Higashitani, N. Hamada,
T. Funayama, K. Fukamoto,
T. Tsuji and Y. Kobayashi
"Effects of Ionizing Radiation on Locomotory Behavior and Mechanosensation in Caenorhabditis elegans"
J. Radiat. Res. 50 (2009) 119-125.

08J075 3-27 C

T. Funayama, N. Hamada,
T. Sakashita and Y. Kobayashi
"Heavy-ion microbeams - development and applications in biological studies"
IEEE Trans. Plasma Sci. 36 (2008) 1432-1440.

08J076 3-28 C

N. Hamada
"Recent insights into the biological action of heavy-ion radiation"

J. Radiat. Res., 50 (1) (2009) 1-9.

08J077 3-28 C

N. Hamada, T. Hara, T. Funayama,
T. Sakashita and Y. Kobayashi
"Energetic heavy ions accelerate differentiation in the descendants of irradiated normal human diploid fibroblasts"
Mutat. Res., 637 (1-2) (2008) 190-196.

08J078 3-28 C

N. Hamada, M. Ni, T. Funayama,
T. Sakashita and Y. Kobayashi
"Temporally distinct response of irradiated normal human fibroblasts and their bystander cells to energetic heavy ions"
Mutat. Res., 639 (1-2) (2008) 35-44.

08J079 3-28 C

M. Iwakawa, N. Hamada, K. Imadome,
T. Funayama, T. Sakashita,
Y. Kobayashi and T. Imai
"Expression profiles are different in carbon ion-irradiated normal human fibroblasts and their bystander cells"
Mutat. Res., 642 (1-2) (2008) 57-67.

08J080 3-28 C

N. Hamada, K. Kataoka, S. Sora, T. Hara,
M. Omura-Minamisawa, T. Funayama,
T. Sakashita, T. Nakano and Y. Kobayashi
"The small-molecule Bcl-2 inhibitor HA14-1 sensitizes cervical cancer cells, but not normal fibroblasts, to heavy-ion radiation"
Radiother. Oncol., 89 (2) (2008) 227-230.

08J081 3-28 C

N. Hamada, T. Hara, M. Omura-Minamisawa,
T. Funayama, T. Sakashita, S. Sora, Y. Yokota,
T. Nakano and Y. Kobayashi
"Energetic heavy ions overcome tumor radioresistance caused by overexpression of Bcl-2"
Radiother. Oncol., 89 (2) (2008) 231-236.

08J082 3-28 C

N. Hamada, T. Hara, M. Omura-Minamisawa,
T. Funayama, T. Sakashita, S. Sora,
T. Nakano and Y. Kobayashi
"The survival of heavy ion-irradiated Bcl-2 overexpressing radioresistant tumor cells and their progeny"
Cancer Lett., 268 (1) (2008) 76-81.

08J083 3-28 C

N. Hamada, M. Ni, T. Funayama, T. Sakashita,
S. Sora, T. Nakano and Y. Kobayashi
"A LET-dependent decrease in the apoptotic response of normal human fibroblast cultures to isosurvival doses of gamma-rays and energetic heavy ions"
Biol. Sci. Space, 22 (2) (2008) 41-45.

08J084 3-28 C

N. Hamada, T. Hara, M. Omura-Minamisawa,
M. Ni, T. Funayama, T. Sakashita, S. Sora,
T. Nakano and Y. Kobayashi
"Heavy-ion microbeam irradiation induces bystander killing of human cells"
Biol. Sci. Space, 22 (2) (2008) 46-53.

08J085 3-28 C

S. Sora, N. Hamada, T. Hara, T. Funayama,

T. Sakashita, Y. Yokota,
T. Nakano and Y. Kobayashi
"Exposure of normal human fibroblasts to heavy-ion radiation promotes their morphological differentiation"
Biol. Sci. Space, 22 (2) (2008) 54-58.

08J086 3-29 C
S. Ishiuchi
"New roles of glutamate receptors in glias and gliomas"
Brain and Nerve, in press.

08J087 3-29 C
K. Shirai, Y. Suzuki, K. Oka, S. E. Noda,
H. Katoh, Y. Suzuki, J. Itoh, H. Itoh, S. Ishiuchi,
H. Sakurai, M. Hasegawa and T. Nakano
"Nuclear survivin expression predicts poorer prognosis in glioblastoma"
J. Neurooncol., 91 (2009) 353-358.

08J088 3-29 C
S. Ishiuchi and K. Tsuzuki
"GluR2 expressed by glial fibrillary acidic protein promoter decreases the number of neurons"
Front Biosci., 13 (2008) 2784-2796.

08J089 3-29 C
T. Oishi, A. Sasaki, N. Hamada, S. Ishiuchi,
T. Funayama, T. Sakashita, Y. Kobayashi,
T. Nakano and Y. Nakazato
"Proliferation and cell death of human glioblastoma cells after carbon-ion beam exposure: Morphologic and morphometric analyses"
Neuropathology, 28 (2008) 399-407.

08J090 3-29 C
E. Malchinkhuu, K. Sato, T. Maehama, C. Mogi,
H. Tomura, S. Ishiuchi, Y. Yoshimoto,
H. Kurose and F. Okajima
"S1P(2) receptors mediate inhibition of glioma cell migration through Rho signaling pathways independent of PTEN"
Biochem. Biophys. Res. Commun., 366 (2008) 963-968.

08J091 3-29 C
石内 勝吾
"ヒト神経膠芽腫細胞における重粒子線の生物学的効果"
癌の臨床、54 (2008) 115-119.

08J092 3-29 C
M. Hasegawa, I. Asakawa, T. Tamamoto,
C. Kajitani, H. Okada, E. Katayama, S. Ishiuchi,
T. Ohno, T. Nakano and T. Murakami
"Carbon Ion Beam-induced Gene Expression Profiles in Human Tumors with Different p53 Status"
Int. J. Radiat. Oncol. 72 (2008) 702-703.

08J093 3-29 C
Y. Yoshida, H. Kato, Y. Suzuki, S. Ishiuchi,
S. Kato and T. Nakano
"The Efficacy of Combining Temozolomide with Carbon Particle Therapy as a New Treatment Approach for Glioblastomas"
Int. J. Radiat. Oncol. 72 (2008) 230.

08J094 3-30 C
H. Matsumoto, M. Tomita,
K. Otsuka and M. Hatashita
"A new paradigm in radioadaptive response

developing from microbeam research"
J. Radiat. Res., 50, Suppl. (2009) A67.

08J095 3-30 C

A. Takahashi, H. Matsumoto and T. Ohnishi
"Hdm2 and nitric oxide radicals contribute to the p53-dependent radioadaptive response"
Int. J. Radiat. Oncol. Biol. Phys., 71 (2008) 550.

08J096 3-30 C

H. Matsumoto, M. Tomita,
K. Otsuka and M. Hatashita
"Revisiting sensitization mechanisms in cancer thermochemotherapy:does the production of radicals hold the key to sensitization"
Therm. Med., 24 (2008) 13.

08J097 3-32 C

M. Hino, N. Hamada, Y. Tajika, T. Funayama,
Y. Morimura, T. Sakashita, Y. Yokota,
K. Fukamoto, Y. Kobayashi and H. Yorifuji
"INSUFFICIENT MEMBRANE FUSION IN DYSFERLIN-DEFICIENT MUSCLE FIBERS AFTER HEAVY-ION IRRADIATION"
Cell Struct. Funct., 34 (1) (2009) 11-15.

08J098 3-38 O

T. Kimura, K. Takahashi, Y. Suzuki, Y. Konishi,
Y. Ota, C. Mori, T. Ikenaga, T. Takanami,
R. Saito, E. Ichiishi, S. Awaji,
K. Watanabe and A. Higashitani
"The Effect of High Strength Static Magnetic Fields and Ionizing Radiation on Gene Expression and DNA Damage in Caenorhabditis elegans"
Bioelectromagnetics 29 (2008) 605-614.

08J099 3-39

S. Takeda, H. Aono, S. Okuyama, S. Ishikawa,
H. Odaka, S. Watanabe, M. Kokubun,
T. Takahashi, K. Nakazawa,
H. Tajima and N. Kawachi
"Experimental results of the gamma-ray imaging capability with a Si/CdTe semiconductor Compton camera"
IEEE Trans. Nucl. Sci., (2009) in press.

08J100 3-39

N. Kawachi
"Development of a Prototype Compton Camera for In Vivo Imaging Using Si and CdTe Semiconductor Detectors"
Med. Imaging Technol., 27(1) (2009) 3-8.

08J101 3-39 C

K. Kikuchi, S. Ishii, S. Fujimaki, N. Suzui,
S. Matsuhashi, I. Honda,
Y. Shishido and N. Kawachi
"Real Time Analysis of Photoassimilate Translocation in Intact Eggplant Fruit using $^{11}CO_2$ and a Positron-Emitting Tracer Imaging System"
J. Jpn. Soc. Hort. Sci., 77(2) (2008) 199-205.

08J102 3-45, 3-46 C

S. Watanabe, Y. Iida, N. Suzui, T. Katabuchi,
S. Ishii, N. Kawachi, H. Hanaoka, S. Watanabe,
S. Matsuhashi, K. Endo and N. S. Ishioka
"Production of no-carrier-added 64Cu and applications to molecular imaging by PET and PETIS as a biomedical tracer"
J. Radioanal. Nucl. Chem., 280 (1) (2009) 199-205.

08J103 3-45 C

S. Watanabe, S. Watanabe, J. X. Liang,
H. Hanaoka, K. Endo and N. S. Ishioka
"Chelating ion-exchange methods for the preparation of no-carrier-added 64Cu"
Nucl. Med. Biol., (2009) in press.

08J104 3-50 S

H. Sakurai, M. Okamoto, M. Hasegawa, T.Satoh,
M. Oikawa, T. Kamiya,
K. Arakawa and T. Nakano
"Direct visualization and quantification of the anticancer agent, cis-diamminedichloro-platinum(II), in human lung cancer cells using in-air microparticle-induced X-ray emission analysis"
Cancer Sci., May, 99(5) (2008) 901-904.

08J105 3-54 S

S. Harada, S. Ehara, K. Ishii, H. Yamazaki,
S. Matsuyama, T. Kamiya, T. Sakai, T. Sato,
S. Oikawa, K. Sera and J. Ito
"Medical Application of Particle-Induced X-ray Emission"
Int. J. PIXE, 18(3&4) (2008) 101-110.

08J106 3-54 S

S. Harada, S. Ehara, K. Ishii, H. Yamazaki,
S. Matsuyama, T. Kamiya, T. Sakai, T. Sato,
S. Oikawa, K. Sera and J. Ito
"Targeted Delivery of Chemotherapeutic Agents by using Improved Radiosensitive Liquid-Core Microcapsules and Assessment of Their Antitumor Effect
Int. J. Radiato. Oncol. Biol. Phys. in press.

08J107 3-55 S

T. Kusakabe, K. Nakajima, K. Suzuki,
K. Nakazato, H. Takada, T. Satoh, M. Oikawa,
K. Kobayashi, H. Koyama,
K. Arakawa and T. Nagamine
"The changes of heavy metal and metallothionein distribution in testis induced by cadmium exposure"
Biometals 21 (2008) 71-81.

08J108 3-55 S

T. Nagamine, H. Takada, T. Kusakabe,
K. Nakazato, T. Sakai, M. Oikawa, T. Kamiya,
K. Arakawa and M. Iha
"Intracellular Changes of Metal Elements by Fucoidan Extracted from Brown Seaweed (Cladosiphon okamuranus)"
Biol. Trace Elem. Res., 124(1) (2008) 60-69.

08J109 3-55 S

T. Kusakabe, K. Nakajima, K. Nakazato,
K. Suzuki, H. Takada, T. Satoh, M. Oikawa,
K. Arakawa and T. Nagamine
"Changes of heavy metal, metallothionein and heat shock proteins in Sertoli cells induced by cadmium exposure"
Toxicol. In Vitro. 22(6) (2008) 1469-1475.

08J110 3-55 S

Y. Shimizu, K. Dobashi, T. Kusakabe,
T. Nagamine, M. Oikawa, T. Satoh, J. Haga,
Y. Ishii, T. Ohkubo, T. Kamiya, K. Arakawa,
T. Sano, S. Tanaka, K. Shimizu, S. Matsuzaki,
M. Utsugi and M. Mori
"In-air micro-particle induced X-ray emission analysis of asbestos and metals in lung tissue"
Int. J. Immunopathol. Pharmacol. 21(3) (2008)

567-576.

08J111 3-55 S

K. Nakazato, T. Nagamine, K. Suzuki,
T. Kusakabe, HD. Moon, M. Oikawa,
T. Sakai and K. Arakawa
"Subcellular changes of essential metal shown by in-air micro-PIXE in oral cadmium-exposed mice"
Biometals 21 (2008) 83-91.

08J112 3-56 S

Y. Shimizu, K. Dobashi, T. Kusakabe,
T. Nagamine, M. Oikawa, T. Satoh, J. Haga,
Y. Ishii, T. Ohkubo, T. Kamiya, K. Arakawa,
T. Sano, S. Tanaka, K. Shimizu, S. Matsuzaki,
M. Utsugi and M. Mori
"IN-AIR MICRO-PIXE ANALYSIS OF ASBESTOS AND METALS IN LUNG TISSUE"
Int. J. Immunopathol. Pharmacol., 21(3) (2008) 567-76.

08J113 4-01 S, I

A. Inouye, S. Yamamoto, S. Nagata,
M. Yoshikawa and T. Shikama
"Effects of Catalyst on Gasochromic Properties in Tungsten Oxide Films"
Trans. Mater. Res. Soc. Jpn., 33 (2008) 1127-1130.

08J114 4-03 C

S. Tsukuda, S. Seki, M. Sugimoto,
S. Tagawa, and S.-I. Tanaka
"SiC nanowires formed by high energy ion beam irradiation to polymer films and heating"
J. Ceram. Process. Res., 9 (2008) 466-469.

08J115 4-06 C

M. Sugimoto, M. Yoshikawa,
S. Tsukuda and S. Seki
"Synthesis of Ceramic Nano fiber from Precursor Polymers by Ion Beam Irradiation"
Trans. Mater. Res. Soc. Jpn., 33 (2008) 1027-103.

08J116 4-06 C

S. Seki, S. Watanabe, M. Sugimoto,
S. Tagawa and S. Tsukuda
"Multi-Functional Polymer Nanowires with Ultra-high Aspect Ratio Produced by Single Particle Nano-fabrication Technique"
J. Photopolym. Sci. Technol., 21(4) (2008) 541-543.

08J117 4-07 G

A. Idesaki, N. Koizumi, M. Sugimoto,
N. Morishita, T. Ohshima and K. Okuno
"Gas Evolution from Insulating Materials for Superconducting Coil of ITER by Gamma Ray Irradiation at Liquid Nitrogen Temperature"
Adv. Cryog. Eng., 54 (2008) 169-173.

08J118 4-09 S, I

K. Takahiro, K. Ozaki, K. Kawatsura, S. Nagata,
S. Yamamoto, K. Narumi and H. Naramoto
"Ion-induced Self-organized Ripple Patterns on Graphite and Diamond Surfaces"
to be published in Appl. Surf. Sci.

08J119 4-09 S, I

K. Takahiro, S. Oizumi, K. Morimoto,
K. Kawatsura, T. Isshiki, K. Nishio, S. Nagata,
S. Nagata, S. Yamamoto,
K. Narumi and H. Naramoto
"Application of X-ray Photoelectron Spectroscopy to Characterization of Au Nanoparticles Formed by Ion Implantation into SiO2"
to be published in Appl. Surf. Sci.

08J120 4-10 I

Y. Kasukabe, S. Nishida, S. Yamamoto,
M. Yoshikawa and Y. Fujino
"Atomistic Nitriding Processes of Titanium Thin Films due to Nitrogen-Implantation"
Appl. Surf. Sci. 254 (2008) 7942–7946.

08J121 4-13 I

S. Muraishi, H. Naito, J. Shi,
Y. Nakamura and T. Aizawa
"Microstructure and Elasticity of Glassy Surface by Ion Implantation"
Mater. Trans., 48 (7) (2007) 1859-1863.

08J122 4-15 T

N. Fujita, S. Kosugi, Y. Zushi, T. Matsui,
Y. Saito and A. Iwase
"Effect of energetic heavy ion irradiation on the structure and magnetic properties of FeRh thin films"
Nucl. Instrum. Meth. Phys. Res., B 267 (2009) 921-924.

08J123 4-16 S, I

K. Ueda, Y. Ando, T. Jonishi, K. Narumi,
Y. Maeda and M. Miyao
"Temperature dependent epitaxial growth of ferromagnetic silicide Fe3Si on Ge substrate"
Thin Solid Films 517 (2008) 422-424.

08J124 4-16 S, I

M. Miyao, K. Ueda, Y. Ando, M. Kumano,
T. Sadoh, K. Narumi and Y. Maeda
"Atomically controlled epitaxy of Fe3Si/SiGe for spintronic application"
Thin Solid Films 517 (2008) 181-183.

08J125 4-17 S, I

V. Lavrentiev, J. Vacik,
H. Naramoto and K. Narumi
"Polymerization of solid C_{60} under C_{60}^{+} cluster ion bombardment"
Appl. Phys. A 95 (2009) 867–873.

08J126 4-17 S, I

V. Lavrentiev, J. Vacik and H. Naramoto
"Structural phenomena in glassy carbon induced by cobalt ion implantation"
Appl. Phys. A 92 (2008) 673-680.

08J127 4-17 S, I

V. Lavrentiev, J. Vacik,
H. Naramoto and K. Narumi
"Fullerene nanostructure design with cluster ion impacts"
J. Alloys and Com. (2008), in press.

08J128 4-17 I

K. Hirata, Y. Saitoh, A. Chiba, M. Adachi,
K. Yamada and K. Narumi
"Development of secondary ion mass spectroscopy using medium energy C_{60} ion impact"
Nucl. Instrum. Meth. B, 266 (2008) 2450-2452.

08J129 4-18 I

H. Abe, R. Morimoto, H. Uchida and T. Ohshima
"Effects of ion beam modification on the hydrogen storage characteristics of Palladium"
App. Surf. Sci., submitted.

08J131 4-20 T

T. Okumura, H. Nishido, S. Toyoda, T. Kaneko,

S. Kosugi, Y. Sawada and K. Komuro
“Evaluation of radiation-damaged halo in quartz by cathodoluminescence as geochronological tool”
Quaternary Geochronol., 3 (2008) 342-345.

08J132 4-20
M. Kayama, H. Nishido and K. Ninagawa
“Cathodoluminescence of feldspar minerals and the assignment of luminescence centers”
Adv. ESR Appl., 25 (2009)13-18.

08J133 4-20
M. Kayama, H. Nishido and K. Ninagawa
“Cathodoluminescence characterization of tridymite and cristobalite”
American Mineralogist, 94 (2009) in print.

08J134 4-23 O
Y. Fukaya, M. Hashimoto,
A. Kawasuso and A. Ichimiya
“Surface structure and phase transition of Ge(111)-3×3-Pb studied by reflection high-energy positron diffraction”
Appl. Surf. Sci. 254 (2008) 7827-7830.

08J135 4-23 O
M. Hashimoto, Y. Fukaya,
A. Kawasuso and A. Ichimiya
“Quasi-one-dimensional In atomic chains on Si(111) at low temperature studied by reflection high-energy positron diffraction and scanning tunneling microscopy”
Appl. Surf. Sci. 254 (2008) 7733-7736.

08J136 4-25 C
M. Taguchi, A. Kimura,
R. Watanabe and K. Hirota
“Estimation of yields of hydroxyl radicals in water under various energy heavy ions”
Radiat. Res., 171 (2009) 254-263.

08J137 4-25 C
M. Taguchi, G. Baldacchino, S. Kurashima,
A. Kimura, Y. Sugo, Y. Katsumura and K. Hirota
“Transient absorption measurement system using pulsed energetic ion”
Radiat. Phys. Chem., in press.

08J138 4-25 C
G. Baldacchino, T. Maeyama , S. Yamashita,
M. Taguchi, A. Kimura,
Y. Katsumura and Murakami
“Determination of the Time-dependent OH-Yield by Using a Fluorescent Probe. Application to Heavy Ion Irradiation”
Chem. Phys. Lett., 468 (2009) 275-279.

08J139 4-26 C
S. Nakagawa, M. Taguchi, N. Ohta and K. Hirota
“Degradation of hydroxymaleimide in 2-propanol by irradiation of energetic heavy ions (I)”
Radiat. Phys. Chem., 77 (2008) 1230-1232.

08J141 4-28 C
T. Sato, D. Satoh, A. Endo, N. Shigyo, H. Yasuda,
M. Takada, K. Yajima and T. Nakamura
“The recent improvement and verification of DARWIN - Development of a new DAQ system and results of flight experiment”
Nucl. Technol., in press.

08J142 4-28 C
T. Sato, D. Satoh, A. Endo, N. Shigyo, H. Yasuda,

M. Takada, K. Yajima and T. Nakamura
"Recent Improvement of DARWIN: Dose Monitoring System Applicable to Various Radiations with Wide Energy Ranges"
Am. Nucl. Soc. Trans., 99 (2008) 589.

08J143 4-30 C

Y. Shikaze, Y. Tanimura, J. Saegusa,
M. Tsutsumi, S. Shimizu,
M. Yoshizawa and . Yamaguchi
"Development of the Neutron Calibration Fields using Accelerators at FRS and TIARA of JAEA"
J. Nucl. Sci. Technol., Suppl. 5 (2008) 209-212.

08J144 4-32 C

K. Oda, K.Iwano, T. Yamauchi, T. Nunomiya,
S. Abe and T. Nakamura
"Response of semiconductor-type electronic personal dosimeter to high energy neutron"
Radiat. Meas., 43 (2-6) (2008) 1072-1076.

08J145 4-33 G

H. Seito, T. Ichikawa, H. Kaneko, Y. Sato,
H. Watanabe and T. Kojima
"Characteristics study of clear polymethyl-methacrylate dosimeter, Radix W, in several kGy range"
Radiat. Phys. Chem., 78 (2009) 356-359.

08J147 4-34 S

N. Uchiya, Y. Furuta, H. Nishikawa, T. Watanabe,
J. Haga, T. Satoh, M. Oikawa,
Y. Ishii and Kamiya
"Ni electroplating on a resist micro-machined by proton beam writing"
Microsyst. Technol., 14(9-11) (2008) 1537-1540.

08J147 4-34 S

Y. Furuta, H. Nishikawa, T. Satoh, Y. Ishii,
T. Kamiya, R. Nakao and S. Uchida
"Applications of microstructures fabricated by proton beam writing to electric-micro filters"
Nucl. Instrum. Meth. B (2009) in press.

A 1.2 Publication in Proceedings

08C001 1-01 C

N. Ikeda, S. Kuboyama, Y. Satoh and T. Tamura
"Study of Latent Damage in Power MOSFETs Caused by Heavy Ion Irradiation"
The IEEE Nuclear and Space Radiation Effects Conference (NSREC 2008)

08C002 1-02 C

T. Makino, D. Kobayashi, K. Hirose, Y. Yanagawa, H. Saito, H. Ikeda, D. Takahashi, S. Ishii, M. Kusano, S. Onoda, T. Hirao and T. Ohshima
"Study of single event transient pulse-width in SOI logic cell"
Proc. 8th Int. Workshop on Radiation Effects on Semiconductor Devices for Space Application (RASEDA), [Tsukuba] (2008) 77–81.

08C003 1-02 C

牧野 高紘、小林 大輔、廣瀬 和之、高橋 大輔、石井 茂、草野 将樹、小野田 忍、平尾 敏雄、大島 武
"論理 LSI で発生する SET パルスによるソフトエラー断面積の推定"
2009 年春季第 56 回応用物理学会関係連合講演会、[茨城県つくば市] (2009) 30p-V-16.

08C004 1-02 C

牧野 高紘、小林 大輔、廣瀬 和之、柳川 善光、齋藤 宏文、池田 博一、高橋 大輔、石井 茂、草野 将樹、小野田 忍、平尾 敏雄、大島 武
"SOI 論理セル内で発生する SET パルス幅の LET 依存性"
2008 年秋季第 69 回応用物理学会学術講演会、[愛知県春日井市] (2008) 4a-E-4.

08C005 1-03 C

S. Abo, Y. Mokuno, A. Kinomura, S. Onoda, T. Hirao, T. Ohshima, T. Iwamatsu and M. Takai
"Irradiation Energy Dependence of Ion Probes on Soft Error Rate in SOI-SRAM"
Proc. 8th Int. Workshop on Radiation Effects on Semiconductor Devices for Space Application (RASEDA), [Tsukuba] (2008) 183–186.

08C006 1-04 C, T, I

T. Ohshima, S. Onoda, T. Hirao, Y. Takahashi, G. Vizkelethy and B. L. Doyle
"Change in Ion Beam Induced Current from Si Metal-Oxide-Semiconductor Capacitors after Gamma-Ray Irradiation"
Proc. 20th Int. Conf. on the Application of Accelerators in Research and Industry, [Fort Worth, USA] RE03-P5 (2008) 66.

08C007 1-04 C, T, I

Y. Takahashi, M. Fugane, R. Imagawa, K. Ohnishi, T. Hirao, S. Onoda and T. Ohshima
"Heavy-Ion induced Gate Current in MOSFET"
Int. Symp. on Integration of MEMS and Intelligent Electronics, [Tokyo], P-09 (2008) 65-66.

08C008 1-04 C, T, I

T. Hirao, Y. Takahashi and H. Ohyama
"Investigation of the Radiation Effects of Semiconductor using the Irradiation Facilities in Takasaki Advanced Radiation Research Institute"
Int. Symp. on Integration of MEMS and Intelligent Electronics, [Tokyo], P-10 (2008) 67-68.

08C009 1-04 C, T, I
今川 良、府 金賢、大西 一功、高橋 芳浩、平尾 敏雄、小野田 忍、大島 武
“MOS デバイスにおける重イオン照射誘起過渡電流とトータルドーズとの関係”
第 21 回タンデム加速器およびその周辺技術の研究会、3-9 (2008) 116-118.

08C010 1-04 C, T, I
平尾 敏雄、高橋 芳浩、小野田 忍、大島 武
“MOS デバイスにおける重イオン照射誘起電流”
第 21 回タンデム加速器およびその周辺技術の研究会、3-18 (2008) 150-153.

08C011 1-04 C, T, I
大脇 章弘、今川 良、竹安 秀徳、大西 一功、高橋 芳浩
“pn ダイオードにおける重イオン照射誘起電流”
日大理工学術講演会、M-19 (2008) 1292-1293.

08C012 1-04 C, T, I
今川 良、大澤 一仁、大脇 章弘、竹安 秀徳、大西 一功、高橋 芳浩
“重イオン照射による SOI-CMOS インバータ特性の過渡的変化”
日大理工学術講演会，M-20 (2008) 1294-1295.

08C013 1-04 C, T, I
高橋 芳浩
“SOI デバイスのシングルイベント効果の特徴”
第 19 回高温エレクトロニクス研究会 (2009).

08C014 1-05 T, C
S. Onoda, T. Hirao and T. Ohshima
“TRANSIENT CURRENT MAPPING USING FOCUSED HEAVY-ION MICROBEAMS WITH SEVERAL HUNDREDS OF MEV”
Proc. 27th Symp. on Materials Science and Engineering Research Center of Ion Beam Technology, [Koganei] (2008) 43-46.

08C015 1-05 C
G. Vizkelethy, S. Onoda, T. Hirao,
T. Ohshima and T. Kamiya
“Time Resolved Ion Beam Induced Current Measurements Using a Cyclotron Microbeam”
Proc. 8th Int. Workshop on Radiation Effects on Semiconductor Devices for Space Application, [Tsukuba] (2008) 187-190.

08C016 1-06 C, T, I, E
M. Imaizumi, H. Toyota, T. Shimada, H. Ogawa, M. Tajima, T. Hisamatsu, K. Nakamura, T. Takamoto, S. Sato and T. Ohshima,
“DURABILITY OF TRIPLE-JUNCTION SOLAR CELL FOR HIHT ENVIRONMENT, VENUS AND MERCURY EXPLORATION MISSIONS”
Proc. 8th European Space Power Conference, (2008), CD.

08C017 1-06 C, T, I, E
S. Sato, M. Imaizumi and T. Ohshima,
“Radiation Degradation Modeling of Triple-Junction Space Solar Cells”
Proc. 27th Symp. on Materials Science and Engineering Research Center of Ion Beam Technology (2008).37-42.

08C018 1-06 E
R.J. Walters, R.D. Harris, M. Imaizumi, J.R. Lorentzen, S.R. Messenger, J.G. Tischler, T. Ohshima, S. Sato, P.R. Sharps and N.S. Faatemi
“Irradiation and Measurement of GaAs Based Solar Cells at Low Intensity, Low Temperature (LILT)

Conditions”
Proc. 8th Int. Workshop on Radiation Effects on Semiconductor Devices for Space Applications (2008) 105-108.

08C019 1-06 T
M. Imaizumi, H. Toyota, T. Shimada, H. Ogawa, M. Tajima, T. Hisamatsu, K. Nakamura, T. Takamoto, S. Sato and T. Ohshima
“DURABILITY OF TRIPLE-JUNCTION SOLAR CELL FOR HIHT ENVIRONMENTS, VENUS AND MERCURY EXPLORATION MISSIONS”
Proc. 8th Int. Workshop on Radiation Effects on Semiconductor Devices for Space Applications (2008) 127-130.

08C020 1-06 C, T, I, E
S. Sato, M. Imaizumi and T. Ohshima
“NIEL ANALYSYS OF CARRIER REMOVAL RATE AND DAMAGE COEFFICIENT IN EACH SUB-CELL OF TRIPLE-JUNCTION SPACE SOLAR CELL”
Proc. 8th Int. Workshop on Radiation Effects on Semiconductor Devices for Space Applications (2008) 211-214.

08C021 1-06 T
C. Morioka, M. Imaizumi, S. Sato, T. Ohshima and K. Kibe
“STUDY ON OPTIMUM STRUCTURE OF AlInGaP TOP-CELLS FOR TRIPLE-JUNCTION SPACE SOLAR CELLS”
Proc. 8th Int. Workshop on Radiation Effects on Semiconductor Devices for Space Applications (2008) 215-218.

08C022 1-08 I
H. Okada, K. Takemoto, F. Oikawa, Y. Furukawa, A. Wakahara, S.-I. Sato and T. Ohshima
“New Concept Light Emitting FET Based-on Spatially Selective Doping of Eu”
Proc. Int. Workshop on Nitride semiconductors (IWN2008), [Montreux, Switzerland] (2008) Th4-E-6.

08C023 1-08 I
A. Wakahara and H. Okada
(Invited) “Development of Rare-earth Doped III-Nitride and its application for Optoelectronic”
MRS fall meeting, [Boston, USA] (2008) D2.1.

08C024 1-08 I
A. Wakahara, H. Okada and Y. Furukawa
“Nitride-based Optoelectronic Integrated Devices”
Proc. 1st Int. Symp. on Advanced Plasma and its Applications (ISPlasma2009), [Nagoya] (2009).

08C025 1-08 I
T. Hata, H. Okada, Y. Furukawa, A. Wakahara, Y. Takagi, S. Sato and T. Ohshima
“Gate controllable light emitting device based-on rare-earth ion doped AlGaN/GaN HEMT”
Proc. 1st Int. Symp. on Advanced Plasma and its Applications (ISPlasma2009), [Nagoya] (2009) Tu17.

08C026 1-09 I, G, E
T. Ohshima, S. Onoda, N. Iwamoto, K. Kojima and K. Kawano
“NIEL Analysis of Charge Collection Efficiency in Silicon Carbide Diodes Damaged by Gamma-Rays, Electrons and Protons”
Proc. 8th Int. Workshop on Radiation Effects on Semiconductor Devices for Space Application,

[Tsukuba] (2008) 175-178.

08C027 1-09 T

N. Iwamoto, S. Onoda, T. Ohshima,
K. Kojima and K. Kawano
"Charge Collection from SiC MOS Capacitors Irradiated with Oxygen Ion"
Proc. 8th Int. Workshop on Radiation Effects on Semiconductor Devices for Space Application, [Tsukuba] (2008) 191-194.

08C028 1-22 T

須郷 由美、赤松 憲、長谷 純宏、田口 光正、佐々木 祐二、広田 耕一、木村 貴海
"タンデム加速器を利用したマイナーアクチノイド分離用抽出剤へのα線照射"
第 21 回タンデム加速器及びその周辺技術の研究会報告集、JAEA-Conf 2008-012 (2008) 127-129.

08C029 1-34 C

M. Yoshida, Y. Kimura, J. Chen,
M. Asano and Y. Maekawa
"Preparation of PTFE-based fuel cell membranes by combining the latent track formation technology with graft polymerization"
Proc. 2nd Asia-Pacific Symp. on Radiation Chemistry (APSRC 2008), [Tokyo] (2008) 36.

08C030 1-35 C

H. Koshikawa, T. Yamaki, M. Asano,
M. Yoshida and Y. Maekawa
"Improvement of Chemical Stability of Grafted Electrolyte Membranes by Ion-Beam-Induced Crosslinking: Comparison with γ-ray Irradiation"
Proc. 2nd Asia-Pacific Symp. on Radiation Chemistry (APSRC 2008), [Tokyo] (2008) 145.

08C031 1-36, 1-37 E, G

J. Chen, M. Zhai, M. Asano,
Y. Maekawa and M. Yoshida
"Polyetheretherketone-based polymer electrolyte membranes for fuel cells prepared by radiation techniques"
Proc. 2nd Asia-Pacific Symp. on Radiation Chemistry (APSRC-2008), [Tokyo, Japan] (2008) 104.

08C032 1-38 G

S. Sawada, A. Kawasuso, M. Maekawa, A. Suzuki,
T. Terai and Y. Maekawa
"Positron annihilation lifetime study of graft-type fluoropolymer electrolyte membranes"
Proc. 9th Int. workshop on positron and positronium chemistry, [Wuhan, China] (2008) 62.

08C033 1-38 G

S. Sawada, Y. Yamaki, A. Suzuki,
T. Terai and Y. Maekawa
"Dissipative particle dynamics simulation of radiation-grafted fluoropolymer electrolyte membranes: Phase separation and water transport"
Proc 2nd Asia-Pacific Symp. on radiation chemistry, [Tokyo, Japan] (2008)148.

08C034 3-15 C

加納 さやか、小林 伸雄、中務 明、野澤 樹、長谷 純宏
"イオンビーム照射によって得られたアスクレピアス突然変異体の特性"
園芸学研究 7(別 2) (2008) 583.

08C035 3-18 O

J. Takano and K. Namai
"Studies on the acquisition method of Fusarium wilt resistant variants using strawberry

‘Tochiotome’ by somaclonal variation”
Hort. Res. (Japan) 7 (Suppl.2) (2008) 495.

08C036 3-23 G
小川 聡子、亀谷 宏美、大和田 滋、鵜飼 光子
“ESR スピントラップ法による食品中の抗酸化成分の定量”
酸化ストレス学会、[京都] (2008).

08C037 3-23 G
亀谷 宏美、小川 聡子、中村 秀夫、大和田 滋、鵜飼 光子
“CYPMPO を用いた各種ラジカル種の ESR スピントラップ法による評価”
酸化ストレス学会、[京都] (2008).

08C038 3-23 G
鵜飼 光子、小川 聡子
“殺菌胡椒の電子スピン共鳴法によるラジカル評価”
第 62 回日本栄養･食糧学会大会、[東京] (2008).

08C039 3-23 G
鵜飼 光子、小川 聡子
“ハスカップラジカルの ESR による研究”
日本家政学会第 60 回大会、[東京] (2008).

08C040 3-23 G
M. Ukai and Y. Shimoyama
“High-resolution Detection for OH Radical Decay by Natural Antioxidants: A Spin Trapping ESR Study”
2008 Oxygen Club California (OCC) World Congress, [Santa Barbara, California] (2008).

08C041 3-23 G
M. Ukai
“An ESR Spin Trapping Study of Antioxidant Effects on Reactive Oxygen Species Induced by UV Irradiation System”
Int. Conf. on Magnetic Resonance in Biological Systems (ICMRBS), [San Diego, California] (2008)

08C042 3-23 G
M. Ukai, S. Ogawa,
H. Nakamura and Y. Shimoyama
“CW X-band ESR studies on safety of radicals in gamma-ray irradiated pepper”
IMRP2008 (Int. Meeting on Radiation Processing), [London, UK] (2008).

08C043 3-23 G
H. Kameya, M. Ukai,
H. Nakamura and Y. Shimoyama
“Electron spin relaxation behaviors of Agaricus radicals induced by irradiation”
IMRP2008 (Int. Meeting on Radiation Processing), [London, UK] (2008).

08C044 3-23 G
小川 英之、亀谷 宏美、小川 聡子、中村 秀夫、鵜飼 光子、下山 雄平
“低線量での放射線照射処理によって誘導されるラジカルの緩和挙動に関する研究”
第 44 回日本食品照射研究協議会年次大会、[東京] (2008) 16.

08C045 3-23 G
亀谷 宏美、小川 聡子、小川 英之、中村 秀夫、等々力 節子、鵜飼 光子
“放射線照射殺菌ナツメグの電子スピン共鳴分光法による研究”
第 44 回日本食品照射研究協議会年次大会、[東京] (2008) 17.

08C046 3-24 G

菊地 正博、Mohammad Shakhawat Hussain、
森下 憲雄、鵜飼 光子、下山 雄平、小林 泰彦
“新鮮マンゴーの照射履歴判別法の開発めざして－ESR 法の適用－”
第 45 回アイソトープ・放射線研究発表会、[東京] (2008).

08C047 3-24 G

菊地 正博、小林 泰彦、森下 憲雄、
M.S. Hussain、鵜飼 光子、下山 雄平
“照射された生マンゴーにおける ESR シグナルの検出”
第 44 回日本食品照射研究協議会年次大会、[東京] (2008) 18.

08C048 3-28 C

N. Hamada, M. Iwakawa, K. Imadome,
T. Funayama, T. Sakashita, S. Sora, M. Ni,
T. Imai and Y. Kobayashi
“Distinct response of irradiated normal human fibroblasts and their bystander cells to heavy-ion radiation in confluent cultures”
Proc. 8th Int. Workshop: Microbeam Probes of Cellular Radiation Response,
J. Radiat. Res., 50: A118 (2009).

08C049 3-31 C

M. Suzuki, Y. Furusawa, C. Tsuruoka,
K. Kobayashi, N. Usami, M. Maeda, T. Funayama,
T. Sakashita, Y. Yokota, K. Fukamoto,
N. Hamada and Y. Kobayashi
“Radiation-quality-dependence in bystander cellular effects on normal human cells induced by carbon-ion and X-ray microbeams”
Proc. twenty-fourth Space Utilization Symp.,
Space Utilization Research, 24 (2008) 328-330.

08C050 3-31 C

鈴木雅雄
“放射線で誘発される生物効果のバイスタンダー効果の線質依存性”
放射線科学、51(3) (2008) 18-27.

08C051 3-32 C

M. Hino, N, Hamada, Y. Tajika, Y. Morimura,
T. Funayama, T. Sakashita, Y. Yokota,
K. Fukamoto, S. Wada, T. Kakizaki,
Y. Kobayashi and H. Yorifuji
“THE APPLICATION Of HEAVY-ION MICROBEAM TO THE ELUCIDATION OF THE MECHANISM OF PLASMA MEMBRANE REPAIR IN THE MUSCULAR DYSTROPHY”
The 21st Century COE Program, The 4th Int. Symp. on Biomed. Res. Using Accelerator Technol., [Maebashi] (2008) 31.

08C052 3-34 C

K. Akeo, N. Hamada, T. Funayama,
Y. Akeo and Y. Kobayashi
“Ion beam irradiation has different influences on glutathione peroxidase of cultured human retinal vascular endothelial cells exposed to L-dopa among ^{20}Ne, ^{12}C and ^{4}He”
The Association for Research in Vision and Ophthalmology, [Fort Lauderdale] (2008).

08C053 3-39

N. Kawachi, S. Watanabe, T. Satoh, K. Arakawa,
S. Takeda, S. Ishikawa, H. Aono, M. Yamaguchi,
T. Takahashi, H. Shimada, Y. Yoshida, Y. Suzuki,
H. Sakurai and T. Nakano
“Basic Characteristics of a Newly Developed Si/CdTe Compton Camera for Medical Imaging”
IEEE Nuclear Science Symp. and Medical Imaging

Conf. Record 2008, 3 [Deutschland] (2009) 1540-1544.

08C054 3-39

H. Aono, S. Takeda, S. Ishikawa, H. Odaka, M. Kokubun, S. Watanabe, T. Takahashi, K. Nakazawa, S. Okuyama, H. Tajima, Y. Fukazawa and N. Kawachi
"Application of double-sided silicon strip detectors to Compton cameras"
Proc. of SPIE, 7021 [USA] (2008) 70211G

08C055 3-43 C

菊地 郁、河地 有木、石井 里美、鈴井 伸郎、藤巻 秀、本多 一郎
"ポジトロンイメージング装置(PETIS)を用いた葉位によるナス果実への光合成産物移行量および移行部位の解析"
園芸学会平成 21 年度春季大会(園芸学研究）、第 8 巻(2) (2009) 104.

08C056 3-51 S

H. Komatsu
"Fluorine analysis of the tooth around fluoride-containing filling materials by the in-air micro-PIXE/PIGE system of TIARA"
The 21st Century COE Program, The Fourth Int. Symp. on Biomedical Research Using Accelerator Technology, (2008) 15.

08C057 3-53

K. Endo, Y. Shibata, T. Yamamoto, K. Nakai, A. Matsumura, T. Sato, M. Oikawa, K. Arakawa, T. Kamiya and K. Ishii
"THE CAPABILITIES AND LIMITATIONS IN THE ANALYSIS OF BORON MICRO-DISTRIBUTION IN TUMOR CELLS USING PIGE"
13th Int. Congress on Neutron Capture Therapy "A new option against cancer", [Florence, Italy] (2008) 258-260.

08C058 3-55 S

T. Nagamine, K. Dobashi, T. Kusakabe, . Shimizu, M. Oikawa and T. Sato
"Relationship between disease mechanism and elemental distribution determined by in-air microPIXE"
BioPIXE 6th Int. Symp. [Richland, USA] (2008) 26.

08C059 3-55 S

高田 久嗣、草壁 孝彦、中里 享美、及川 将一、佐藤 隆博、神谷 富裕、荒川 和夫、長嶺 竹明
"フコイダンによる細胞内微量元素の変動"
第 25 回 PIXE シンポジウム、 [前橋] (2008) 8.

08C060 3-55 S

草壁 孝彦、高田 久嗣、中嶋 克行、中里 享美、鈴木 慶二、佐藤 隆博、横田 渉、荒川 和夫 、長嶺 竹明
"肝線維化ラットを用いたフコイダンによる肝線維化の抑制"
第 19 回日本微量元素学会 [東京] (2008) 190.

08C061 4-13 C

S. Muraishi, H. Naito, J. Shi, Y. Nakamura and T. Aizawa
"Controlled Elasticity in Nano-structured Metallic Glass by Ion Implantation"
Proc. 6th Pacific Rim Int. Conf. on Advanced Materials and Processing, Materials Science Forum, 561-565 (2007) 1315-1318.

08C062 4-14

Shou Nakagawa, F. Hori, H. Ohno, N. Ishikawa, R. Oshima, M. Kitagawa and A. Iwase
"Study on copper precipitation under electron irradiation in FeCu model alloys by using Vickers hardness measurements"
Mater. Res. Soc. Symp. Proc. 1043 (2008) 1043-T09-04.

08C063 4-16 S, I

Y. Maeda, Y. Hiraiwa, K. Narumi, A. Kawasuso, Y. Terai, Y. Ando, K. Ueda, T. Sadoh, K. Hamaya and M. Miyao
"Site preference of atoms in Heusler alloys Fe3Si and Fe2MnSi grown on Ge(111) toward realization of Ge channel spin transistors"
Mater. Res. Soc. Proc., 1119E (2009) 1119-L05-02.

08C064 4-16 S, I

Y. Hiraiwa, Y. Ando, K. Narumi, K. Ueda, T. Sadoh, M. Miyao and Y. Maeda
"FERROMAGNETIC FeGe/FeSi LAYERED STRUCTURES FORMED BY INTER-DIFFUSION IN Fe3Si/Ge HYBRID STRUCTURES"
Abstract of the IUMRS Int. Conf. in Asia 2008, [Nagoya] (2008) ZO-8.

08C065 4-20 T

H. Bahadur, K. Ninagawa, H. Nishido, T. Usami, M. Kayama and S. Toyoda
"Radiation effects on Premium Q and Supreme Q cultured quartz crystals"
IEEE Proc. Frequency Control Symp. 2008, (2008) 213-218.

08C066 4-24 G

Y. Kumagai, R. Nagaishi and R. Yamada
"Reduction of Dichromate and Cerium ions in Colloidal Silica Solutions"
The 2nd Asia-Pacific Symp. of Radiation Chemistry, [Tokyo] (2008) 186.

08C067 4-24 G

Y. Kumagai, R. Nagaishi, R. Yamada, Y. Muroya and Y. Katsumura
"Effects of colloidal silica on the yields and reactions of products of water radiolysis"
The 51st Annual Meeting of Japanese Society of Radiation Chemistry, [Ibaraki] (2008) 37-38.

08C068 4-24 G

R. Yamada, Y. Kumagai and R. Nagaishi
"Hydrogen gas production in γ-radiolysis of aqueous sulfuric acid solutions containing oxide powder"
The 51st Annual Meeting of Japanese Society of Radiation Chemistry, [Ibaraki] (2008) 39-40.

08C069 4-24 G, E

永石隆二
"放射線を用いたアスベストの無害化と可溶化に関する技術開発"
テクニカルショウヨコハマ 2009（第 30 回工業技術見本市），ＪＳＴイノベーションサテライト茨城　公開ワークショップ，平成 21 年 2 月，横浜.
(社)日本機械工業連合会､かわら版､第 11 号(2009)

08C070 4-26 C

S. Nakagawa, M. Taguchi, N. Ohta and K. Hirota
"Degradation of hydroxymaleimide in N2-saturated 2-propanol by irradiation of energetic ions"
The 2nd Asia Pacific Symp. on Radiation Chemistry, [Tokyo] (2008) 108.

08C071 4-26 C

S. Nakagawa, M. Taguchi, N. Ohta and K. Hirota
"LET effect on irradiation of hydroxymaleimide in 2-propanol (3)"
Proc. 51st Annual Meeting of Japanese Society of Radiation Chemistry, [Tsukuba] (2008) 149-150.

08C072 4-27 C

T. Kondoh, J.Yang, K. Norizawa, R. Nagaishi, M. Taguchi, K. Takahashi, R. Katoh, and Y. Yoshida
"Pulse Radiolysis Study of Ion-Species Effects on the Solvated Electrons in Ammonium Ionic Liquids"
The 2nd Asia Pacific Symp. on Radiation Chemistry, [Tokyo] (2008).

08C073 4-34 S

H. Nishikawa, Y. Seki, Y. Furuta, N. Uchiya, T. Nakata, T. Watanabe, R. Nakao, S. Uchida, J. Haga, T. Satoh, T. Ohkubo, Y. Ishii and T. Kamiya
"Applications of Microstructures Fabricated by PBW to Electric-Micro Filters (Invited)"
Book of Abstracts, 11th Int. Conf. on Nuclear Microprobe Technology and Applications (ICNMTA2008), [Hungary] (2008) 61.

08C074 4-34 S

E. Yoshida, H. Nishikawa, Y. Furuta, Y. Seki and R. Tsuchiya
"Proton Beam Writer for manufacturing in Shibaura Institute of Technology"
Book of Abstracts, 11th Int. Conf. on Nuclear Microprobe Technology and Applications (ICNMTA2008), [Hungary] (2008) 118.

08C075 4-34 S

Y. Furuta, H. Nishikawa, T. Satoh, Y. Ishii, T. Kamiya, R. Nakao and S. Uchida
"Fabrication and evaluation of 3D-DEP devices utilized by proton beam writing"
Proc. 34th Int. Conf. on Micro and Nano Engineering, No. BIO4, [Athens, Greece] (2008) 05.

08C076 4-34 S

Y. Seki, Y. Furuta, H. Nishikawa, T. Watanabe, T. Nakata, T. Satoh, Y. Ishii and T. Kamaya
"Electroplating using high-aspect-ratio microstructures fabricated by proton beam writing"
Proc. 34th Int. Conf. on Micro and Nano Engineering, No. PTE, [Athens, Greece] (2008) 17.

08C077 4-34 S

古田 祐介、西川 宏之、佐藤 隆博、石井 保行、神谷 富裕、中尾 亮太、内田 諭
"集束プロトンビーム微細加工を応用した 3 次元微生物濃縮セルの作製と評価"
第 69 回応用物理学会学術講演会、講演予稿集、2a-CB-5 (2008).

08C078 4-34 S

関 佳裕、古田 祐介、西川 宏之、佐藤 隆博、石井 保行、神谷 富裕
"集束陽子線による微細構造を用いた高アスペクト比電鋳"
第 69 回応用物理学会学術講演会、講演予稿集、2a-M-8 (2008).

08C079 4-34 S

土屋 龍太郎、古田 祐介、西川 宏之、大石 知司、佐藤 隆博、石井 保行、神谷 富裕
"シロキサン系薄膜の集束イオンビーム描画によるパターニングの照射量依存性"

第 69 回応用物理学会学術講演会、講演予稿集、2a-D-5 (2008).

08C080 4-34 S

西川 宏之

“集束プロトンビーム描画による高アスペクト比微細加工技術とその応用”

第 69 回応用物理学会学術講演会、講演予稿集、2a-D-5 (2008).

08C081 4-34 S

西川 宏之、吉田 栄治、古田 祐介、土屋 龍太郎、関 佳裕、椎根 康晴

“小型プロトンビーム描画専用装置の開発と微細加工への応用 (I)”

第 56 回応用物理学関係連合講演会、1p-ZR-1 (2009) 723.

08C082 4-34 S

椎根 康晴、古田 祐介、土屋 龍太郎、関 佳裕、西川 宏之、吉田 栄治

“小型プロトンビーム描画専用装置の開発と微細加工への応用 (II)”

第 56 回応用物理学関係連合講演会、1p-ZR-2 (2009) 724.

08C083 4-34 S

関 佳裕、古田 祐介、西川 宏、渡辺 徹、佐藤 隆弘、石井 保行、神谷 富裕

“集束陽子線による微細構造を用いた電鋳のビアフィリング性”

第 56 回応用物理学関係連合講演会、講演予稿集、30p-K-7 (2009) 732.

08C084 4-36 T

斎藤 勇一、千葉 敦也、鳴海 一雅、高橋 康之

“クラスターイオン加速のための荷電変換ガスの探索”

第 21 回「タンデム加速器及びその周辺技術の研究会」報告集 JAEA-Conf 2008-012 (2008) 130-133.

08C085 4-43 C, T, S, I

W. Yokota, T. Nara, I. Ishibori, S. Kurashima, K. Yoshida, T. Yuyama, T. Ishizaka, T. Agematsu, S. Uno, A. Chiba, K. Yamada, A. Yokoyama, K. Mizuhashi, S. Okumura, N. Miyawaki, H. Kashiwagi, Y. Yuri, Y. Saitoh, Y. Ishii, T. Satoh, T. Ohkubo and T. Kamiya

“STATUS OF ACCELERATORS AND TECHNICAL DEVELOPMENT AT TIARA”

Proc. 5th Annual Meeting of Particle Accelerator Society of Japan and the 33rd Linear Accelerator Meeting in Japan, [Higashihiroshima] (2008).

08C086 4-44, 5-02 C

Y. Yuri, T. Ishizaka, T. Yuyama, S. Okumura, I. Ishibori, N. Miyawaki, S. Kurashima, K. Yoshida, H. Kashiwagi, T. Agematsu and T. Nara

“BEAM UNIFORMIZATION USING MULTIPOLE MAGNETS AT THE JAEA AVF CYCLOTRON”

Proc. European Particle Accelerator Conf., EPAC’08, [Genoa, Italy] (2008) 3077-3079.

08C087 4-44 C

Y. Yuri, T. Ishizaka, T. Yuyama, S. Okumura and I. Ishibori

“FORMATION OF A UNIFORM BEAM PROFILE USING MULTIPOLE MAGNETS”

Proc. 5th Annual Meeting of Particle Accelerator Society of Japan and the 33rd Linear Accelerator Meeting in Japan, [Higashihiroshima, Japan] (2008) 397-399.

08C088 4-46 S

横山 彰人、石井 保行、千葉 敦也、宇野 定則、
上松 敬、水橋 清、高山 輝充、江夏 昌志
“シングルエンド加速器の RF イオン源のエミッタンス測定”
第 21 回「タンデム加速器及びその周辺技術の研究会」報告集 JAEA-Conf 2008-012 (2008) 138-141.

08C089 4-46 I

山田 圭介、上松 敬、水橋 清
“TIARA イオン注入装置におけるビーム強度分布モニタの試作”
第 21 回「タンデム加速器及びその周辺技術の研究会」報告集 JAEA-Conf 2008-012 (2008) 134-137.

Appendix 2

List of Related Patents

08PAT001 1-34
八巻 徹也、浅野 雅春、吉田 勝、前川 康成（原子力機構・量子ビーム応用）他、トヨタ自動車㈱との共同出願、
「燃料電池用電解質膜及びその製造方法」
出願番号 PCT/JP2008/072396

08PAT002 2-05
廣木 章博（原子力機構・量子ビーム応用）、
吉井 文男（原子力機構・産学連携推進部）、
玉田 正男（原子力機構・量子ビーム応用）、
他、
埼玉県工業技術センターとの共同出願、
「金属材料の簡易成分分析方法」
特願 2008-173867 号

08PAT003 2-07
植木悠二、玉田正男（原子力機構・量子ビーム応用）、
「バイオディーゼル製造用触媒とその製造方法並びにバイオディーゼルの製造方法」
特願 2008-334433 号

08PAT004 3-19
鳴海一成、屠 振力、佐藤勝也（原子力機構・量子ビーム応用）、
「放射線抵抗性細菌/大腸菌シャトルベクー」
特許登録番号 特許第 3845697 号

08PAT005 3-19
I. Narumi, Z. Tu, K. Satoh (QuBS, JAEA),
「Radiation resistant bacterium/E. coli shuttle vector」
米国特許登録番号 第 6770476 号

08PAT006 3-39
山口 充孝、河地 有木、荒川 和夫、他（原子力機構・高崎量子応用研究所）、
群馬大学、宇宙航空研究開発機構、三菱重工業㈱との共同出願
「コンプトンカメラ」
特願 2008-213928 号

08PAT007 3-45
渡辺 茂樹、石岡 典子（原子力機構・量子ビーム応用）、
「キレート交換樹脂を用いた放射性銅の分離方法」
特願 2008-171032 号

08PAT008 3-46, 3-47
渡辺 智、橋本 和幸、飯田 靖彦、花岡 宏史、遠藤 啓吾（原子力機構・量子ビーム応用）との共同出願、
「抗体標識が可能な無担体 177Lu の分離精製法」
特願 2009-072558 号

08PAT009 4-06
杉本 雅樹、出崎 亮、吉川 正人（原子力機構・量子ビーム応用）他、大阪大学との共同出願、
「セラミックナノファイバー及びその製造法」
特願 2008-236572 号

08PAT010　4-07
出崎 亮、杉本 雅樹、田中 陵二、吉川 正人（原子力機構・量子ビーム応用）、
「ケイ素系ポリマーから高収率で炭化ケイ素材料を合成する方法」
特願 2009-046288 号(2009.2.27)

08PAT011　4-07
S. Ukon, H. Furukohri, K. Ishida（(株)フジクラ）、
J. Kusano（原子力機構・J-PARC センター）、
N. Morishita（原子力機構・量子ビーム応用）、
O. Takeda（原子力機構・J-PARC センター）、
A. Idesaki（原子力機構・量子ビーム応用）、
「RADIATION-RESISTANT RESIN COMPOSITION AND RADIATION-PROOF WIRE/CABLE」
European Patent Appl. No.08164201.9-2102 (2008/11/05).

08PAT012　4-07
杉本 雅樹、出崎 亮、吉川 正人（原子力機構・量子ビーム応用）、関 修平、渡辺 省伍（大阪大学）、
「ナノファイバー及びその製造方法」
特願 2008-236572 号(2008.9.16)

08PAT013　4-08
杉本 雅樹、武山 昭憲、吉川 正人（原子力機構・量子ビーム応用）、
「電離放射線無酸素架橋法によるセラミック薄膜の作製法」
特願 2009-60349 号

08PAT014　4-08
武山 昭憲、杉本 雅樹、吉川 正人（原子力機構・量子ビーム応用）、
「前駆体層の溶解による炭化珪素水素分離膜の製造方法」
特願 2009-60350 号

08PAT015　4-24
永石 隆二、青柳 登、山田 禮司（原子力機構・原子力基礎工学）、
「アスベスト処理方法及び処理装置、水素生成方法及び生成装置、重金属処理方法及び処理装置」
特願 2008-230947 号

08PAT016　4-24
永石 隆二、吉田 善行、山田 禮司、青柳 登（原子力機構・原子力基礎工学）、
「貴金属の回収方法と機能材料の製造方法、並びに機能材料を用いた強酸化性金属イオン含有水溶液の処理方法」
特願 2008-231477 号

08PAT017　4-34
西川 宏之、古田 祐介（芝浦工業大学）、
内田 諭（首都大学東京）、
神谷 富裕、石井 保行、佐藤 隆博（原子力機構・高崎量子応用研究所）による共同出願、
「三次元誘電泳動デバイス」
特願 2009-013112 号

Appendix 3

List of Related Press-Release and TV Programs

08NP001　1-31
平成 20 年 12 月 12 日、電気新聞、
日刊工業新聞、化学工業日報、鉄鋼新聞、
フジサンケイビジネスアイに掲載、
「合金製造で新技術」

08NP002　1-37
平成 20 年９月１９日、日経新聞（群馬版）、
毎日新聞（群馬版）、産経新聞（群馬版）、
上毛新聞、電気新聞、化学工業日報、
原子力産業、日刊工業新聞に掲載、
「家庭用燃料電池に最適な高耐久性電解質膜の開発に成功－“放射線グラフト重合”技術を用いて相反する電池膜特性の課題を解決－」

08NP003　3-28
平成 20 年 6 月 17 日（毎日新聞、読売新聞、
産経新聞、日本経済新聞、上毛新聞、
日刊工業新聞、フジサンケイビジネスアイ）
と平成 20 年 7 月 10 日（原子力産業新聞）、
「重粒子線は、がん遺伝子 Bcl-2 に打ち克つことを発見　—Bcl-2 高発現タイプのがんに重粒子線治療が有効—」

08NP004　3-39
平成 20 年 8 月 21 日、日刊工業新聞、
上毛新聞、化学工業日報、時事通信、
に掲載、
「群大の重粒子治療宇宙科学の技術活用－原子力、宇宙両機構と協定　精度高め患者負担軽減－」

08NP005　3-56
平成 20 年 11 月 11 日、読売新聞、上毛新聞に掲載、
「肺の中にあるアスベストの種類を細胞レベルの元素分布画像から特定-アスベスト肺の高感度診断に途-」

08NP006　4-34
平成 20 年 7 月 15 日、琉球新聞に掲載、
「水素ビームで“一筆書き”」

08NP007　4-34
平成 20 年 7 月 15 日、山陽新聞に掲載、
「電子部品を微細加工へ」

08NP008　4-34
平成 20 年 7 月 26 日、河北新報に掲載、
「微細部品に“一筆書き”」

08NP009　4-34
平成 20 年 8 月 10 日、静岡新聞に掲載、
「水素ビームで微細部品を加工」

08NP010　4-34
平成 20 年 8 月 18 日、岩手日報に掲載、
「水素ビームで微細部品を」

08TV001　3-28

平成21年7月26日23時00分ー23時30分、
NHK World TV
平成21年7月27日4時10分ー4時40分、
衛生放送第1
「What's on Japan」
「日本が世界に先駆けて取り組む重粒子線
治療」

Symbol used in the Appendix 1 to 3

An example of symbol expression is written as following.

08	J	148	4-34	S
①	②	③	④-⑤	⑥

① Number of last two orders in fiscal year

② Kind of publication

- **J** : Publication in Journal
- **C** : Publication as Proceedings
- **NP** : Press-Release (Newspaper)
- **TV** : TV Programs
- **PA** : Patent

③ Consecutive numbers for the kind of publication

④-⑤ Paper number

④ Classification number of research field

- **1** : Space, nuclear and energy engineering
- **2** : Environment conservation and resource security
- **3** : Biotechnology and medical application
- **4** : Advanced materials, analysis and novel technology

⑤ Consecutive number every research field

⑥ Accelerators or irradiation facilities utilized for the research

- **C** : AVF Cyclotron
- **T** : 3 MV Tandem Electrostatic Accelerator
- **S** : 3 MV Single-ended Electrostatic Accelerator
- **I** : 400 kV Ion Implanter
- **E** : 2 MV Electron Accelerator
- **G** : Co-60 Gamma-ray Irradiation Facilities
- **O** : Off-line (Research without the utilization of irradiation facilities)

Appendix 4 Type of Research Collaboration and Facilities Used for Research

Paper Number	Type of Research Collaboration*1					Irradiation Facilites*2						Paper Number	Type of Research Collaboration*1					Irradiation Facilites*2					
	Joint Res.	Entr. Res.	Coop. Res.	JAEA Inter.	Com. Use	C	T	S	I	E	G		Joint Res.	Entr. Res.	Coop. Res.	JAEA Inter.	Com. Use	C	T	S	I	E	G
1-01	●					◎						2-08	●									◎	◎
1-02				●		◎						2-09	●									◎	◎
1-03				●			◎					2-10				●						◎	◎
1-04	●					◎	◎					2-11				●							◎
1-05				●		◎	◎					2-12				●						◎	◎
1-06	●					◎	◎		◎														
1-07	●							◎	◎			3-01				●			◎				◎
1-08	●								◎	◎		3-02				●		◎					
1-09				●		◎				◎	◎	3-03				●OL							
1-10	●									◎	◎	3-04		●				◎					
1-11	●						◎			◎	◎	3-05				●		◎					
1-12					●		◎					3-06	●					◎					
1-13				●						◎	◎	3-07	●					◎					
1-14				●							◎	3-08				●		◎					
1-15				●							◎	3-09	●					◎					
1-16				●							◎	3-10	●					◎					
1-17				●							◎	3-11	●					◎					
1-18		●									◎	3-12	●					◎					
1-19				●							◎	3-13	●					◎					
1-20				●							◎	3-14	●					◎					
1-21		●									◎	3-15	●					◎					
1-22				●		◎	◎					3-16	●					◎					
1-23				●						◎	◎	3-17	●					◎					
1-24				●		◎						3-18	●					◎					
1-25	●										◎	3-19				●							◎
1-26	●							◎				3-20	●					◎					
1-27				●				◎				3-21	●					◎					
1-28				●		◎				◎	◎	3-22	●					◎					
1-29			●				◎					3-23	●										◎
1-30				●						◎		3-24	●										◎
1-31				●			◎					3-25				●		◎					
1-32				●			◎	◎	◎			3-26				●		◎					◎
1-33		●						◎				3-27				●		◎					
1-34				●		◎						3-28	●					◎					
1-35				●		◎					◎	3-29	●					◎					
1-36				●						◎	◎	3-30	●					◎					
1-37	●										◎	3-31	●					◎					
1-38	●									◎	◎	3-32	●					◎					
												3-33	●					◎	◎				
2-01				●						◎	◎	3-34	●					◎					
2-02	●									◎		3-35	●					◎					
2-03		●									◎	3-36	●					◎					
2-04	●									◎	◎	3-37	●					◎					
2-05	●									◎		3-38	●					◎	◎				
2-06				●						◎	◎	3-39	●					◎					
2-07				●						◎	◎	3-40	●					◎					

Paper Number	Type of Research Collaboration[*1]					Irradiation Facilites[*2]						Paper Number	Type of Research Collaboration[*1]					Irradiation Facilites[*2]					
	Joint Res.	Entr. Res.	Coop. Res.	JAEA Inter.	Com. Use	C	T	S	I	E	G		Joint Res.	Entr. Res.	Coop. Res.	JAEA Inter.	Com. Use	C	T	S	I	E	G
3-41	●					◎						4-21	●								◎		
3-42	●					◎						4-22				●					◎		
3-43	●					◎						4-23				●OL							
3-44	●					◎						4-24				●						◎	◎
3-45	●					◎						4-25				●		◎					
3-46	●					◎						4-26	●					◎					
3-47				●OL								4-27	●					◎					
3-48			●					◎				4-28		●				◎					
3-49			●					◎				4-29				●		◎					
3-50	●							◎				4-30	●					◎					
3-51			●					◎				4-31	●					◎					
3-52	●							◎				4-32					●	◎					
3-53			●					◎				4-33				●						◎	◎
3-54			●					◎				4-34	●							◎			
3-55			●					◎				4-35	●							◎			
3-56	●							◎				4-36			●				◎				
												4-37			●				◎				
4-01				●			◎	◎	◎			4-38			●				◎				
4-02					●	◎						4-39			●				◎				
4-03					●	◎						4-40			●				◎				
4-04	●							◎	◎			4-41			●					◎	◎		
4-05				●			◎		◎			4-42			●						◎		
4-06	●					◎						4-43				●		◎					
4-07				●							◎	4-44				●		◎					
4-08				●						◎	◎	4-45				●		◎					
4-09	●							◎				4-46				●			◎	◎	◎		
4-10					●			◎				4-47	●					◎	◎				
4-11				●						◎													
4-12				●			◎					5-01						◎	◎	◎	◎		
4-13					●				◎			5-02						◎					
4-14					●			◎				5-03							◎	◎	◎		
4-15					●		◎					5-04										◎	◎
4-16	●							◎	◎			5-05										◎	◎
4-17				●			◎	◎	◎	◎	◎	5-06						◎	◎	◎	◎	◎	◎
4-18	●						◎		◎			5-07						◎	◎	◎	◎		
4-19					●	◎						5-08						◎	◎	◎	◎		
4-20					●		◎																

[*1] Type of Research Collaboration

Joint Res. : Joint research with external users

Entr. Res. : Research entrusted to JAEA

Coop. Res. : Cooperative research with plural universities through The University of Tokyo

JAEA Inter. : JAEA internal use

Com. Use : Common use based on "JAEA-facility-use"

OL : Off line (research without the use of irradiation facilities)

[*2] Utilization of Irradiation Facilities

C : AVF Cyclotron System

T : 3 MV Tandem Electrostatic Accelerator

S : 3 MV Single-ended Electrostatic Accelerator

I : 400 kV Ion Implanter

E : 2 MV Electron Accelerator

G : Co-60 Gamma-ray Irradiation Facilities

Appendix 5 A Typical Example of Abbreviation Name for Organizations in Japan Atomic Energy Agency (JAEA)

◆ Directorate, Center, Department, Institute, etc.

QuBS（量子ビーム応用研究部門）: Quantum Beam Science Directorate
NSED（原子力基礎工学研究部門）: Nuclear Science and Engineering Directorate
FRDD（核融合研究開発部門）: Fusion Research and Development Directorate
GIRDD（地層処分研究開発部門）: Geological Isolation Research and Development Directorate
ANSRD（次世代原子力システム研究開発部門）: Advanced Nuclear System Research and Development Directorate
NCBD（バックエンド推進部門）：Nuclear Cycle Backend Directorate
NSRC（安全研究センター）: Nuclear Safety Research Center
NFCEL（核燃料サイクル工学研究所）: Nuclear Fuel Cycle Engineering Laboratories
NERCC（原子力エネルギー基盤連携センター）: Nuclear Engineering Research Collaboration Center
J-PARC（ J-PARC センター）: J-PARC Center
NCED（サイクル工学試験部）: Nuclear Cycle Engineering Department
TARRI（高崎量子応用研究所）: Takasaki Advanced Radiation Research Institute
NSRI（原子力科学研究所）: Nuclear Science Research Institute
KPSI（関西光科学研究所）: Kansai Photon Science Institute

◆ Division, Unit, Department, etc.

・Environment and Industrial Materials Research Division, QuBS, JAEA
（量子ビーム応用研究部門、環境・産業応用研究開発ユニット）
・Radiation-Applied Biology Division, QuBS, JAEA
（量子ビーム応用研究部門、バイオ応用技術研究ユニット）
・Neutron Material Research Center, QuBS, JAEA
（量子ビーム応用研究部門、中性子物質科学研究ユニット）
・Division of Environment and Radiation Sciences, NSED, JAEA
（原子力基礎工学研究部門、環境・放射線工学ユニット）
・Division of Fuels and Materials Engineering, NSED, JAEA
（原子力基礎工学研究部門、燃料・材料工学ユニット）
・Division of ITER Project, FRDD, JAEA
（核融合研究開発部門、ITER プロジェクトユニット）
・Division of Fusion Energy Technology, FRDD, JAEA
（核融合研究開発部門、核融合エネルギー工学研究開発ユニット）

・Advanced Science Research Center, JAEA
（先端基礎研究センター）
・Department of Advanced Radiation Technology, TARRI, JAEA
（高崎量子応用研究所、放射線高度利用施設部）
・Department of Radiation Protection, NSRI, JAEA
（原子力科学研究所、放射線管理部）
・Accelerator Division, J-PARC, JAEA
（J-PARC センター、加速器ディビジョン）
・Safety Division, J-PARC, JAEA
（J-PARC センター、安全ディビジョン）
・LWR Long-term Reliability Research Unit, NSRC, JAEA
（安全研究センター、軽水炉長期化対応研究ユニット）
・Geological Isolation Research Unit, GIRDD, JAEA
（地層処分研究開発部門、地層処分基盤研究開発ユニット）
・Nuclear Cycle Engineering Department, NFCEL, JAEA
（核燃料サイクル工学研究所、サイクル工学試験部）
・Plutonium Fuel Development Center, NFCEL, JAEA
（核燃料サイクル工学研究所、プルトニウム燃料技術開発センター）
・Advanced Reprocessing Unit, ANSRD, JAEA
（次世代原子力システム研究開発部門、次世代再処理システムユニット）
・Industrial Collaboration Promotion Department, JAEA
（産学連携推進部）
・Nuclear Cycle Backend Technology Development Unit, NCBD, JAEA
（バックエンド推進部門　バックエンド技術開発ユニット）

国際単位系（SI）

表１．SI 基本単位

基本量	SI 基本単位	
	名称	記号
長さ	メートル	m
質量	キログラム	kg
時間	秒	s
電流	アンペア	A
熱力学温度	ケルビン	K
物質量	モル	mol
光度	カンデラ	cd

表２．基本単位を用いて表されるSI組立単位の例

組立量	SI 基本単位	
	名称	記号
面積	平方メートル	m^2
体積	立法メートル	m^3
速さ，速度	メートル毎秒	m/s
加速度	メートル毎秒毎秒	m/s^2
波数	毎メートル	m^{-1}
密度，質量密度	キログラム毎立方メートル	kg/m^3
面積密度	キログラム毎平方メートル	kg/m^2
比体積	立方メートル毎キログラム	m^3/kg
電流密度	アンペア毎平方メートル	A/m^2
磁界の強さ	アンペア毎メートル	A/m
量濃度[(a)]，濃度	モル毎立方メートル	mol/m^3
質量濃度	キログラム毎立法メートル	kg/m^3
輝度	カンデラ毎平方メートル	cd/m^2
屈折率[(b)]	（数字の） 1	1
比透磁率[(b)]	（数字の） 1	1

(a) 量濃度（amount concentration）は臨床化学の分野では物質濃度（substance concentration）ともよばれる。
(b) これらは無次元量あるいは次元１をもつ量であるが、そのことを表す単位記号である数字の１は通常は表記しない。

表３．固有の名称と記号で表されるSI組立単位

組立量	SI 組立単位			
	名称	記号	他のSI単位による表し方	SI基本単位による表し方
平面角	ラジアン[(b)]	rad	1[(b)]	m/m
立体角	ステラジアン[(b)]	sr[(c)]	1[(b)]	m^2/m^2
周波数	ヘルツ[(d)]	Hz		s^{-1}
力	ニュートン	N		m kg s^{-2}
圧力，応力	パスカル	Pa	N/m^2	m^{-1} kg s^{-2}
エネルギー，仕事，熱量	ジュール	J	N m	m^2 kg s^{-2}
仕事率，工率，放射束	ワット	W	J/s	m^2 kg s^{-3}
電荷，電気量	クーロン	C		s A
電位差（電圧），起電力	ボルト	V	W/A	m^2 kg s^{-3} A^{-1}
静電容量	ファラド	F	C/V	m^{-2} kg^{-1} s^4 A^2
電気抵抗	オーム	Ω	V/A	m^2 kg s^{-3} A^{-2}
コンダクタンス	ジーメンス	S	A/V	m^{-2} kg^{-1} s^3 A^2
磁束	ウエーバ	Wb	Vs	m^2 kg s^{-2} A^{-1}
磁束密度	テスラ	T	Wb/m^2	kg s^{-2} A^{-1}
インダクタンス	ヘンリー	H	Wb/A	m^2 kg s^{-2} A^{-2}
セルシウス温度	セルシウス度[(e)]	℃		K
光束	ルーメン	lm	cd sr[(c)]	cd
照度	ルクス	lx	lm/m^2	m^{-2} cd
放射性核種の放射能[(f)]	ベクレル[(d)]	Bq		s^{-1}
吸収線量，比エネルギー分与，カーマ	グレイ	Gy	J/kg	m^2 s^{-2}
線量当量，周辺線量当量，方向性線量当量，個人線量当量	シーベルト[(g)]	Sv	J/kg	m^2 s^{-2}
酸素活性	カタール	kat		s^{-1} mol

(a)SI接頭語は固有の名称と記号を持つ組立単位と組み合わせても使用できる。しかし接頭語を付した単位はもはやコヒーレントではない。
(b)ラジアンとステラジアンは数字の１に対する単位の特別な名称で、量についての情報をつたえるために使われる。実際には、使用する時には記号rad及びsrが用いられるが、習慣として組立単位としての記号である数字の１は明示されない。
(c)測光学ではステラジアンという名称と記号srを単位の表し方の中に、そのまま維持している。
(d)ヘルツは周期現象についてのみ、ベクレルは放射性核種の統計的過程についてのみ使用される。
(e)セルシウス度はケルビンの特別な名称で、セルシウス温度を表すために使用される。セルシウス度とケルビンの単位の大きさは同一である。したがって、温度差や温度間隔を表す数値はどちらの単位で表しても同じである。
(f)放射性核種の放射能（activity referred to a radionuclide）は、しばしば誤った用語で"radioactivity"と記される。
(g)単位シーベルト（PV,2002,70,205）についてはCIPM勧告2（CI-2002）を参照。

表４．単位の中に固有の名称と記号を含むSI組立単位の例

組立量	SI 組立単位		
	名称	記号	SI 基本単位による表し方
粘度	パスカル秒	Pa s	m^{-1} kg s^{-1}
力のモーメント	ニュートンメートル	N m	m^2 kg s^{-2}
表面張力	ニュートン毎メートル	N/m	kg s^{-2}
角速度	ラジアン毎秒	rad/s	m m^{-1} s^{-1}=s^{-1}
角加速度	ラジアン毎秒毎秒	rad/s^2	m m^{-1} s^{-2}=s^{-2}
熱流密度，放射照度	ワット毎平方メートル	W/m^2	kg s^{-3}
熱容量，エントロピー	ジュール毎ケルビン	J/K	m^2 kg s^{-2} K^{-1}
比熱容量，比エントロピー	ジュール毎キログラム毎ケルビン	J/(kg K)	m^2 s^{-2} K^{-1}
比エネルギー	ジュール毎キログラム	J/kg	m^2 s^{-2}
熱伝導率	ワット毎メートル毎ケルビン	W/(m K)	m kg s^{-3} K^{-1}
体積エネルギー	ジュール毎立方メートル	J/m^3	m^{-1} kg s^{-2}
電界の強さ	ボルト毎メートル	V/m	m kg s^{-3} A^{-1}
電荷密度	クーロン毎立方メートル	C/m^3	m^{-3} sA
表面電荷	クーロン毎平方メートル	C/m^2	m^{-2} sA
電束密度，電気変位	クーロン毎平方メートル	C/m^2	m^{-2} sA
誘電率	ファラド毎メートル	F/m	m^{-3} kg^{-1} s^4 A^2
透磁率	ヘンリー毎メートル	H/m	m kg s^{-2} A^{-2}
モルエネルギー	ジュール毎モル	J/mol	m^2 kg s^{-2} mol^{-1}
モルエントロピー，モル熱容量	ジュール毎モル毎ケルビン	J/(mol K)	m^2 kg s^{-2} K^{-1} mol^{-1}
照射線量（X線及びγ線）	クーロン毎キログラム	C/kg	kg^{-1} sA
吸収線量率	グレイ毎秒	Gy/s	m^2 s^{-3}
放射強度	ワット毎ステラジアン	W/sr	m^4 m^{-2} kg s^{-3}=m^2 kg s^{-3}
放射輝度	ワット毎平方メートル毎ステラジアン	$W/(m^2 sr)$	m^2 m^{-2} kg s^{-3}=kg s^{-3}
酵素活性濃度	カタール毎立方メートル	kat/m^3	m^{-3} s^{-1} mol

表５．SI 接頭語

乗数	接頭語	記号	乗数	接頭語	記号
10^{24}	ヨタ	Y	10^{-1}	デシ	d
10^{21}	ゼタ	Z	10^{-2}	センチ	c
10^{18}	エクサ	E	10^{-3}	ミリ	m
10^{15}	ペタ	P	10^{-6}	マイクロ	μ
10^{12}	テラ	T	10^{-9}	ナノ	n
10^{9}	ギガ	G	10^{-12}	ピコ	p
10^{6}	メガ	M	10^{-15}	フェムト	f
10^{3}	キロ	k	10^{-18}	アト	a
10^{2}	ヘクト	h	10^{-21}	ゼプト	z
10^{1}	デカ	da	10^{-24}	ヨクト	y

表６．SIに属さないが、SIと併用される単位

名称	記号	SI 単位による値
分	min	1 min=60s
時	h	1h =60 min=3600 s
日	d	1 d=24 h=86 400 s
度	°	1°=(π/180) rad
分	’	1’=(1/60)°=(π/10800) rad
秒	”	1”=(1/60)’=(π/648000) rad
ヘクタール	ha	$1ha=1hm^2=10^4m^2$
リットル	L，l	$1L=11=1dm^3=10^3cm^3=10^{-3}m^3$
トン	t	$1t=10^3$ kg

表７．SIに属さないが、SIと併用される単位で、SI単位で表される数値が実験的に得られるもの

名称	記号	SI 単位で表される数値
電子ボルト	eV	$1eV=1.602\ 176\ 53(14)\times10^{-19}J$
ダルトン	Da	$1Da=1.660\ 538\ 86(28)\times10^{-27}kg$
統一原子質量単位	u	1u=1 Da
天文単位	ua	$1ua=1.495\ 978\ 706\ 91(6)\times10^{11}m$

表８．SIに属さないが、SIと併用されるその他の単位

名称	記号	SI 単位で表される数値
バール	bar	1 bar=0.1MPa=100kPa=10^5Pa
水銀柱ミリメートル	mmHg	1mmHg=133.322Pa
オングストローム	Å	1 Å=0.1nm=100pm=10^{-10}m
海里	M	1 M=1852m
バーン	b	$1\ b=100fm^2=(10^{-12}cm)2=10^{-28}m^2$
ノット	kn	1 kn=(1852/3600)m/s
ネーパ	Np	SI単位との数値的な関係は、対数量の定義に依存。
ベル	B	
デジベル	dB	

表９．固有の名称をもつCGS組立単位

名称	記号	SI 単位で表される数値
エルグ	erg	$1\ erg=10^{-7}$ J
ダイン	dyn	$1\ dyn=10^{-5}$N
ポアズ	P	$1\ P=1\ dyn\ s\ cm^{-2}=0.1Pa\ s$
ストークス	St	$1\ St=1cm^2\ s^{-1}=10^{-4}m^2\ s^{-1}$
スチルブ	sb	$1\ sb=1cd\ cm^{-2}=10^4cd\ m^{-2}$
フォト	ph	$1\ ph=1cd\ sr\ cm^{-2}\ 10^4lx$
ガル	Gal	$1\ Gal=1cm\ s^{-2}=10^{-2}ms^{-2}$
マクスウェル	Mx	$1\ Mx = 1G\ cm^2=10^{-8}Wb$
ガウス	G	$1\ G=1Mx\ cm^{-2}=10^{-4}T$
エルステッド[(c)]	Oe	1 Oe ≙ $(10^3/4\pi)A\ m^{-1}$

(c) ３元系のCGS単位系とSIでは直接比較できないため、等号「 ≙ 」は対応関係を示すものである。

表10．SIに属さないその他の単位の例

名称	記号	SI 単位で表される数値
キュリー	Ci	$1\ Ci=3.7\times10^{10}Bq$
レントゲン	R	$1\ R=2.58\times10^{-4}C/kg$
ラド	rad	$1\ rad=1cGy=10^{-2}Gy$
レム	rem	$1\ rem=1\ cSv=10^{-2}Sv$
ガンマ	γ	1γ=1 nT=10-9T
フェルミ		1フェルミ=1 fm=10-15m
メートル系カラット		1メートル系カラット = 200 mg = 2×10-4kg
トル	Torr	1 Torr = (101 325/760) Pa
標準大気圧	atm	1 atm = 101 325 Pa
カロリー	cal	1cal=4.1858J（「15℃」カロリー），4.1868J（「IT」カロリー）4.184J（「熱化学」カロリー）
ミクロン	μ	1 μ =1μm=10^{-6}m

（第8版，2006年改訂）

この印刷物は再生紙を使用しています